

Syddansk Universitet

Proceedings of the SIMS 50 Conference

Elmegaard, Brian; Veje, Christian; Nielsen, Mads Pagh; Mølbak, Tommy

Publication date: 2009

Document Version Final published version

Link to publication

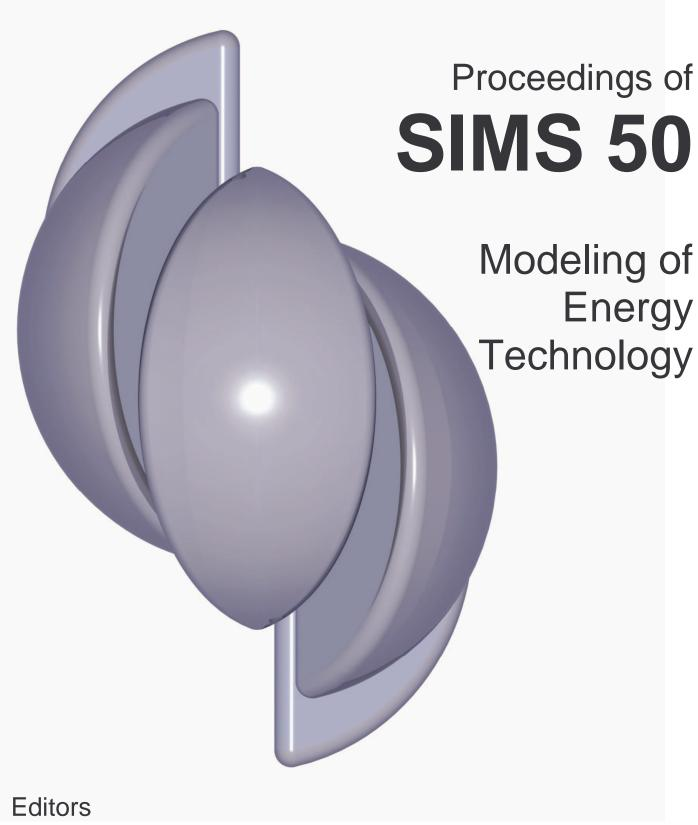
Citation for pulished version (APA): Elmegaard, B., Veje, C., Nielsen, M. P., & Mølbak, T. (Eds.) (2009). Proceedings of the SIMS 50 Conference. Lyngby: DTU.

General rightsCopyright and moral rights for the publications made accessible in the public portal are retained by the authors and/or other copyright owners and it is a condition of accessing publications that users recognise and abide by the legal requirements associated with these rights.

- Users may download and print one copy of any publication from the public portal for the purpose of private study or research.
- You may not further distribute the material or use it for any profit-making activity or commercial gain
 You may freely distribute the URL identifying the publication in the public portal?

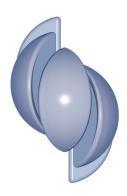
Take down policyIf you believe that this document breaches copyright please contact us providing details, and we will remove access to the work immediately and investigate your claim.

Download date: 14. jan.. 2017



Brian Elmegaard, Christian Veje, Mads Pagh Nielsen, Tommy Mølbak

Fredericia, Denmark October 7-8, 2009



Proceedings of **SIMS 50**

the

50th International Conference of Scandinavian Simulation Society

Fredericia, Denmark October 7–8, 2009

EDITORS

Brian Elmegaard, Christian Veje, Mads Pagh Nielsen, Tommy Mølbak

ORGANIZED BY

Technical University of Denmark, University of Southern Denmark, Aalborg University and DONG Energy

These Proceedings are available from: Department of Mechanical Engineering Technical University of Denmark Nils Koppels Allé Building 403 DK-2800 Kgs. Lyngby Denmark

Tel.: (+45) 45 25 19 60 Fax: (+45) 45 88 43 25

SIMS Logo Design by 3Dfacto, Denmark

ISBN 978-87-89502-88-5

Copyright © 2009

Organizing Committee

B. Elmegaard (DTU) C. Veje (SDU) M. Pagh Nielsen (AAU)

T. Mølbak (DONG Energy)

Scientific Committee

J. Ahrenfeldt DTU Risø, Denmark J. Amundsen NTNU, Norway

J. Arias KTH Royal Institute of Technology, Sweden

A. Arselis AAU Aalborg University, Denmark B. Bidoggia AAU Aalborg University, Denmark

S. Camporeale Politecnico di Bari, Italy

H. Clemmensen Pedersen
AAU Aalborg University, Denmark
T. Condra
AAU Aalborg University, Denmark
E. Dahlquist
Mälardalens Högskola, Sweden

C. Ekman Jørgensen DTU Risø, Denmark B. Elmegaard DTU, Denmark

P. Fritzson Linköping University, Sweden

F. Haglind DTU, Denmark

N. Houbak DONG Energy, Denmark

S. Juhl Andreasen AAU Aalborg University, Denmark

E. Juuso Oulu University, Finland

K. Juslin VTT, Finland

S. Knudsen Kær

B. Lie

Høgskolen i Telemark, Norway

V. Liso

AAU Aalborg University, Denmark

S. Madsen SDU University of Southern Denmark, Denmark

M. Mandø AAU Aalborg University, Denmark

T. Mølbak DONG Energy, Denmark J. Møller Munch DONG Energy, Denmark

B. Palm KTH Royal Institute of Technology, Sweden

M. Pagh Nielsen AAU Aalborg University, Denmark

M. Rokni DTU, Denmark

L. Rosendahl AAU Aalborg University, Denmark

A. Schrøder Pedersen DTU Risø, Denmark M. Skovrup IPU, Denmark

C. Veje SDU University of Southern Denmark, Denmark M. Willatzen SDU University of Southern Denmark, Denmark

Arranged by



Technical University of Denmark



University of Southern Denmark



Aalborg University



DONG Energy

Cooperating Organizations

Scandinavian Simulation Society

http://www.scansims.org/

Dansk Simuleringsforening

http://www.dksim.dk/

Preface

The members of the Organizing Committee of SIMS 50 are pleased to present the Proceedings of the conference. The SIMS 50 conference is the 50'th annual conference of the Scandinavian Simulation Society, SIMS.

The SIMS conference of 2009 is hosted in cooperation between DONG Energy and three universities, University of Southern Denmark, Aalborg University and Technical University of Denmark. The organizing committee are grateful to DONG Energy and the SIMS board who have been supporting the project of hosting a SIMS conference with focus on "Modeling of Energy Technology". We feel that this topic is very closely related to the perhaps most important issue of the modern society, solving the climate change issues.

The papers included in the proceedings show that energy technology indeed covers a very broad spectrum of technology and science. You will find papers grouped in the fields: Biomass, Fuel cells, Fuels, Industry, Power, Refrigeration, Simulation tools and methods, and Wind.

We hope you will enjoy the conference and the proceedings,

Brian Elmegaard, Christian Veje, Mads Pagh Nielsen, and Tommy Mølbak

Papers

Simulation Tools 1	1
Simulation for Decision Support in the Oil and Gas Industries	
Cameron, David;Glende, Erik;Weberg, Trond;Alne, Sveinung	. 3
Jayarathna, Sanoja A.;Lie, Bernt;Melaaen, Morten C	13
OpenModelica-Python Interoperability Applied to Monte Carlo Simulations	. 1.
Torabzadeh-Tari, Mohsen; Fritzson, Peter; Sjölund, Martin; Pop, Adrian	. 21
Fuels 1	27
Using fundamental advanced thermodynamics to understand a CO2 capture process	
Darde, Victor; Thomsen, Kaj; van Well, Willy J.M; Stenby, Erling H	. 29
Model parameters selection using sensitivity analysis on a high fidelity model of petroleum	
drilling operations.	
Lohne, Hans Petter; Nygaard, Gerhard; Time, Rune	. 37
Prediction of Condensing Flow with Relevance to Flue Gas Condenser and CO2 Captur-	
ing	
Nabati, Hamid; Mahmoudi, Jafar; Time, Rune Wiggo	. 45
Modelling of the channelling phenomenon of the pulping digester using porous media	
pourian, bijan;dahlquist, erik	. 53
Refrigeration 1	61
Implementation of the Kurganov-Tadmor High Resolution Semi-Discrete Central	
Scheme for Numerical Solution of the Evaporation Process in Dry	
Madsen, Søren; Veje, Christian T.; Willatzen, Morten	. 63
Early Measure of Synchronization Operations in Supermarket Refrigeration Systems	
Chen, Liang; Green, Torben; Izadi-Zamanabadi, Roozbeh; Larsen, Lars F. S	. 71
Comparison of two different modelling tools by static simulation of an evaporator	
Brix, Wiebke; Elmegaard, Brian	. 79
Numerical Simulation Of An Absorption Machine	
Fayad, Sahar; Younes, Rafic; Abboudi, Said	. 87
Wind	95
Integrated Desiegn of Wind Power Systems: - PowerFactory/Matlab dynamic simulation	
Hansen, Anca D.; Cutululis, Nicolaos A.; Sørensen, Poul; Barahona, Braulio	. 97
Integrated Design of Wind Power Systems: Matlab-HAWC2 interface	
Barahona, Braulio; Andersen, Peter B.; Hansen, Anca D.; Cutululis, Nicolaos A.; Sørensen, Poul .	. 107
Modelling, Operation and Control of HVDC Connected Offshore Wind Farms	
Constantin, Adrian; Agap, Adelina; Dragan, Cristina; Iov, Florin	. 115

Power	123
Model based diagnostics, maintenance on demand and decision support on Boilers	
Dahlquist, Erik; Widarsson, Björn; Avelin, Anders	125
GridLAB-D: an agent-based simulation of the SmartGrid Chassin, David;Xu, Jianhua	131
Dynamic simulation – a tool for engineering 2 800MW hard coal-fired power plants Poulsen, Kristian; Christensen, Torkild; Didriksen, Helge	143
Forecasting Renewable Energy Production and of Energy Consumption Vedel, Henrik; Pagh Nielsen, Kristian; Pedersen, Claus; Hansen Sass, Bent; Woetman Nielsen, Niels; Sattler, Kai; Feddersen, Henrik	151
Industry	155
Developing a simple Modelica library for simuluation of the Xstrata Nikkelverk Cu production plant	
Alic, Mirnes; Hauge, Tor Anders; Lie, Bernt Simulation of fouling in cross-flow heat exchanger and a fouling detection based on phys-	157
ical modeling Gudmundsson, Oddgeir;Palsson, Olafur Petur;Palsson, Halldor	165
Thermodynamic Process Simulation of the Digestion Unit in Iran Alumina Refinery Farrokh, Mohammad; Mahmoudi, Jafar	
Fuel Cells	179
Possible Future SOFC-ST Based Power Plants	1/9
Rokni, Masoud;Scappin, Fabio	181
Modelling a Combined Heat and Power Plant based on Gasification, Micro Gas Turbine and Solid Oxide Fuel Cells	
Bang-Møller, Christian; Rokni, Masoud	189
Reforming processes for micro combined heat and power system based on solid oxide fuel cell	
Liso, Vincenzo; Nielsen, Mads Pagh; Kær, Søren Knudsen	197
Biomass	209
Numerical model and infrared analysis of a hydrogen enriched gas flame Prisecaru, Tudor; Teodorescu, Mihai; Prisecaru, Malina; Petcu, Cristian; Bleaja, Gheo-	
rghe;Popa, Elena;Ciobanu, Cristina;Chiriac, Radu	211
Effects of Oxygen in Biogasification, Evaluation of ADM1-Ox model against experimental data	
Botheju, Deshai;Lie, Bernt;Bakke, Rune	221
Zero-Dimensional Model of a Dimethyl Ether (DME) Plant Based on Gasification of Torrefied Biomass	
Clausen, Lasse;Elmegaard, Brian;Houbak, Niels;Braun, Robert	229
Self-Organizing Maps for Analysis of Process Emissions in Fluidized Bed Energy Plant Liukkonen, Mika;Heikkinen, Mikko;Hälikkä, Eero;Hiltunen, Teri;Hiltunen, Yrjö	237
Power 2	245
A comparative study of computational methodology and tools of thermoelectricity	
Chen Min: Rosendahl Lassa	247

Modelling and Experimental Analysis of a Trigeneration System with a Microturbine and	
an Indirect Fired Absorption Chiller Driven by Exhaust Gases	
Moya, Marta; Marimón, Miguel Angel; Bruno, Joan Carles; Coronas, Alberto; Eguía,	
Pablo; Torres, Esther; Zamora, Inmaculada; Martínez, David	259
Design and Energy Saving Analysis of Trigeneration Configurations in Buildings	
Marimón, Miguel Angel;Ortiga, Jordi;Bruno, Joan Carles;Coronas, Alberto	267
Speeding up startup of a thermal power plant	
Didriksen, Helge; Perstrup, Claus	275
Fuels 2	283
Experimental and Computational Study of Particle Minimum Fluidization Velocity and	
Bed Expansion in a Bubbling Fluidized Bed	
Jayarathna, Chameera K.;Halvorsen, Britt M	285
Predicting optimal trim configuration of marine vessels with respect to fuel usage	
Petursson, Stefan; Sigurdsson, Sven; Runarsson, Thomas; Thorsteinsson, Jon Agust	291
Evaluating new and existing automatically controlled deep water drilling concepts using	
a high-fidelity simulation model	
Breyholtz, Øyvind;Nygaard, Gerhard	299
Refrigeration 2	313
Effect of Refrigerant Mal-Distribution in Fin-And-Tube Evaporators on System Perfor-	
mance	
Ryhl Kærn, Martin; Elmegaard, Brian; Finn Sloth Larsen, Lars	315
Numerical modeling in magnetic refrigeration	0.10
Bjørk, Rasmus; Nielsen, Kaspar; Smith, Anders; Bahl, Christian; Pryds, Nini; Hattel, Jesper	323
J. ,,,,,,,	
Simulation Tools 2	331
Solution to an Implementation Issue for a Two-Step ARX Algorithm, with Application to	
the Czochralski Crystallization Process	
Komperød, Magnus; Bones, John Atle; Lie, Bernt	333
Dynamic simulation of solar collector fields in changing operating conditions	
Juuso, Esko	341
Enhancing integrity and production of the KOC pipeline network operation through dy-	
namic simulation	
Komulainen, Tiina; Waheed, Farrukh; Davies, Ray; Alfano, Tony	349
Author Index	357

Simulation Tools 1



SIMULATION FOR DECISION SUPPORT IN THE OIL AND GAS INDUSTRIES

David Cameron¹, Erik Glende and Trond Weberg Kongsberg Oil & Gas Technologies Hamangskogen 60 1338 Sandvika Norway

> Sveinung Alne Kongsberg Defence Systems Kirkegårdsveien 45 3601 Kongsberg Norway

ABSTRACT

This paper is a review of the use of dynamic simulation as an enabling tool for integrated operations and decision support in the upstream oil and gas industry. A framework and architecture for simulator-based decision support is described. This framework is then applied to a number of case studies: (1) advanced process control, (2) multiphase flow management for sub-sea production facilities, (3) situation awareness and crisis management in environmentally and politically sensitive areas and (4) validation and maintenance of process simulators.

NOMENCLATURE

AIS: Automatic Identification System (for ships).

IO: Integrated Operations.

VTS: Vessel Traffic Services.

INTRODUCTION

Simulation is an established technology in both the oil and gas industry and the defence industries. Sophisticated dynamic models of processes and equipment are routinely used to provide users – operators, engineers, soldiers and sailors – with realistic training in the use and operation of complex, high-risk technical systems.

This paper reviews how these existing simulation technologies are being reused and developed to support *real-time*, *on-line decision making with distributed*, *collaborative teams*. The discussion focuses on upstream oil and gas production.

First, a description is given of the upstream oil and gas production domain and the challenges that can be met by using simulation. This is followed by a presentation of a framework and architecture for simulator-based decision support. This framework is then illustrated by considering four case studies: (1) using simulation to develop and speed implementation of advanced process control, (2) using dynamic simulation to manage the multiphase flow for remote sub-sea production facilities, (3) using process and defence simulators to train in situation awareness and crisis management in environmentally and politically sensitive areas and (4) using observed data to validate and maintain process simulators.

CONTEXT

Challenges in Oil and Gas Production

Modern oil and gas production involves operations in ever more remote and difficult

¹ Corresponding author: E-mail: david.cameron@kongsberg.com.

environments. For example, development in the Gulf of Mexico, Angola and Brazil is increasingly focused on wells in deep water, with depths exceeding 2000 m [3]. Other areas, such as Alaska, Newfoundland, Greenland and the Barents Sea are subject to extreme weather conditions, ice and high environmental sensitivity. Security and military interests are also tightly linked with oil and gas production. This is particularly true in the northern polar areas, in West Africa and the Gulf.

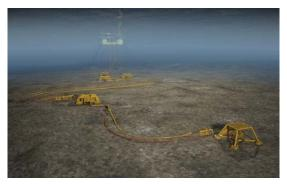


Figure 1. An artist's representation of sub-sea production facilities and connection lines to a production platform. Used by permission of StatoilHydro.

These factors all contribute to the following trends in oil and gas production:

- 1. Production wells and production facilities are placed on the sea bed.
- 2. The produced fluids (oil, gas and water) are transported to land, or to a centralised floating production unit, in a system of pipelines and manifolds. This transport system contains a three-phase mixture of gas, oil and water. The behaviour of these transport networks is dynamic, complex and difficult to manage.
- 3. Production facilities are often in isolated sites and difficult environments. Minimum levels of manning are desirable, as is remote operation and expert support from central locations.

An artist's representation of a typical production facility of this type is shown in Figure 1.

These challenges and trends are changing the way in which oil and gas production is managed. This paper calls this new way of management Integrated Operations.

Integrated Operations

In the introduction we referred to "real-time, onmaking decision with distributed. collaborative teams". This concept has been given a variety of names by different companies and interest groups. For example, the Norwegian oil and gas industry refers to Integrated Operations, the US industry to Intelligent/Digital Oil Field of the Future (DOFF) [2], BP to Field of the Future® and Shell to Smart FieldsTM. In another domain, the US military refers to Network Centric Warfare [1] and Maritime Domain Awareness and NATO refers to Network Enabled Capabilities. All these terms refer to a common set of work practices, organisational models and IT technologies that support the operation of complex systems – in this case oil production facilities.

Simulation's Role in Integrated Operations

This paper argues that, for maximum effectiveness, Integrated Operations (IO) of oil and gas facilities must take account of *all* aspects of operation of the production facility in a coherent way. This means that logistics, maritime operations, production, processing, shipping, security and emergency response need to be integrated to allow co-ordinated, interdisciplinary actions to optimize returns and minimize risk.

We believe that simulation is a key enabling technology for implementing IO: Simulation is needed to design the challenging oil and gas facilities described above. Users must be trained in the new practices, tools and organisational patterns that are needed for IO, and finally, simulation provides much of the real-time information that is needed to make the best possible real-time decisions.

The rest of this paper supports this argument by presenting a framework or architecture for using simulators of different types in IO. This description is then followed by four examples of how simulators have been used to enable better and safer operation of facilities. The examples

describe actual applications, some of which have been published in more detail previously. The purpose here is to put these applications into a common context.

Simulation is multifaceted – and a number of simulation tools and technologies need to be integrated to support IO. The simulation technologies discussed here are dynamic simulation of processing facilities and multiphase flow systems and simulation of the environment and sensor networks related to maritime situational awareness and crisis management systems.

FRAMEWORK OR ARCHITECTURE FOR SIMULATOR-BASED DECISION SUPPORT

Lifecycle Simulation: From Design to Operations

Before defining a framework for decision support we need to define the types of decisions that can be supported. We see simulators supporting decisions in both design and operation of a facility. We believe that a common architecture can be used to support both types of decisions. This is achieved by building life-cycle simulators. Thus, (a) engineering simulators are built during the design process and are used to verify design decisions and modify the design. Once the facility is being built, (b) the same simulators are used to develop operating procedures and train personnel in facility operation. Once the facility is in operations, (c) the simulators can be used with real-time data to monitor operations and provide guidance to operations personnel.

A Simulation Ecosystem

This can be done by building and maintaining an integrated *ecosystem* of simulators. These simulators are used for different purposes but share:

- A common, re-usable description of process structure and parameters.
- An iterative link to the facility's *design* basis, as stored in an engineering database.

The iterative link between the simulators and the design basis is obtained by using the design basis

to set parameters in a simulator, which is then used to evaluate *and modify* the engineering basis. The simulator is also modified to reflect the changes made. This approach needs support in organization and working practices. Simulators need to be included in the facility's change control processes, and clear responsibility for maintaining the consistency between the facility design and the simulator is needed.

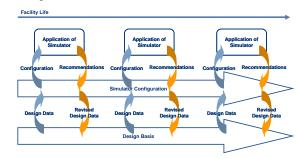


Figure 2: Iterative relationship between design basis and simulator configuration.

Note also, that a variety of simulators will co-exist in the facility, each with responsibility for a portion of the design basis. Thus, in a modern oil and gas facility, the following simulators can be found:

- Reservoir simulators, which interact with the field's geophysical, petrophysical and drilling data.
- *Production simulators*, which are steadystate models of the production system, from the wells to the production facilities. These models interact with the conceptual design and long-term operation of the wells, manifolds and transport system.
- Multiphase flow simulators, which describe the dynamic operation of the production and transport of oil, gas and water from the wells to the production facilities. These interact with the detailed physical design of the wells, manifolds and transport system.
- Dynamic process simulators, which describe the dynamic operation of the processing facilities. These interact with the detailed physical design of the

processing facilities. In addition, multiphase flow simulators are usually embedded in dynamic process simulators to provide a dynamic model of the entire oil and gas production from the wells to the outlet of the process plant.

 Operations simulators, which represent the operation of complex electronic or mechanical systems – such as maritime operations, dynamic positioning of tenders and supply boats, lifting using cranes and drilling operations. These simulators often involve some form of virtual reality.

These simulators provide information about different areas of the facility over widely differing time scales. This, somewhat subjective, view of the spread of time-scales and scope of application is shown in Figure 3.

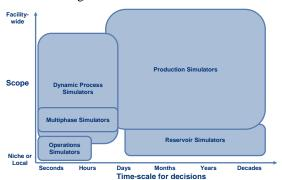


Figure 3: Scope and time-scale for the various different simulators used in the oil and gas industry.

Integrated operations need data to be available from all relevant simulators. This data must be consistent between simulators. This means that the simulators used must not contradict each other because of inconsistent input data, simplifications or assumptions.

This is often difficult to achieve in practice. Each simulator is owned and maintained by a different discipline in the oil and gas organization. In addition, there are as yet few widely accepted standards for information exchange between simulators, engineering databases and other

applications. Some moves in this direction have been organized by industry consortia such as FIATECH [7] and Energistics (through the WITSML [8] and PRODML [9] standards).

Architecture for Implementing the Simulation Ecosystem.

We have developed and implemented a software framework or architecture that allows a dynamic process simulator to be built during the design phase of a facility, installed in the facility at start-up and then used actively for operational decision support and design of modifications.

This architecture also fits well with oil companies' best practices for IT and security, in that our architecture is divided into a control layer, a process layer and an enterprise layer [11]. The architecture is shown in Figure 4.

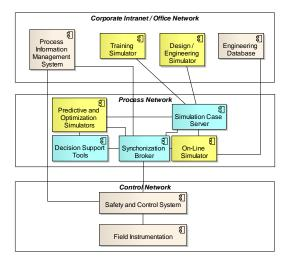


Figure 4: Architecture for Supporting and Ecosystem of Dynamic Process Simulators.

The core of our architecture is an *on-line simulator* that is located in the process layer. This simulator reads data from the control system and/or the process information management system and runs synchronized with the actual process. This simulator acts as the master copy for all other simulators used in the organization.

Because this simulator runs in real-time alongside the process, it can be used to detect faulty measurements or process failure and calculate key performance indicators, such as liquid inventory, local pressures and temperatures, energy consumption and CO₂ emissions.

Copies of this simulator, or parts thereof, can be spawned to run predictive calculations: what if studies for planned operator actions. These spawned simulations can also be used for optimization calculations. Predictive calculations can be configured to run automatically and raise alarms if undesirable events are predicted to occur.

Off-line users, such as engineers and training personnel, are located in the office network. They can obtain the latest simulator configuration – and relevant process data – by accessing a *simulation case server*. This is a web service that allows secure access to up-to-date simulator configurations. A content management database can be also installed on the office network to archive simulator configurations.

This then, is our vision of a simulation ecosystem. The rest of the paper presents some examples of how this ecosystem has evolved and the benefits that have been obtained. The examples have been published in more detail elsewhere. Our focus here is to show the benefits of re-using models and building a simulator ecosystem.

DESIGN AND IMPLEMENTATION OF ADVANCED PROCESS CONTROL

Multivariable Control

The first example has been described in more detail in reference [4]. An after-cooler on a gas compressor on an oil platform was controlled by two controllers – one on gas bypass and the other on cooling water. The existing control philosophy could not handle compressor start-up and sudden disturbances, and had resulted in several shut downs of the oil platform. An engineering design model of the process was used in a design study to evaluate different conventional approaches – using split range control – to improving the control. It was found that no conventional approach worked and that a 2 by 2 multivariable controller would give better performance. The 2 by 2 controller was designed and implemented in

the engineering simulator and was demonstrated to platform engineers. It was decided to implement the controller.

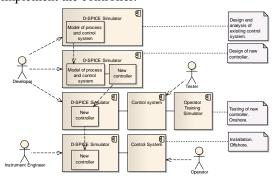


Figure 5: A simulator ecosystem: system structures and users in different phases of the development of the multi-variable controller.

The controller was implemented by using the same simulation tool (D-SPICE) as was used in the design study. This allowed the direct re-use of the controller code. This controller communicated with the platform's control system using OPC. It was essential that the controller be tested with the control system to ensure safe and proper operation before it was installed on the platform. This was done using the platform's existing operator training simulator. This simulator consisted of a dynamic model of the process (supplied by another vendor) and a copy of the actual control hardware used on the platform. The new controller was connected to the control hardware in exactly the same way as it would be when installed. Tests were made to evaluate the performance of the controller and to ensure the safe and bump-less transfer of control back to the conventional loops in the control system in the event of a communication failure. Faults in the failover logic were found and these were fixed by adding function blocks to the D-SPICE implementation of the controller. The tests showed that the system was safe and could be expected to work on the actual process.

Installation on the platform was then a straightforward and rapid procedure. Some tuning was needed; as the operator training simulator's dynamic behaviour was different from the actual

process behaviour. This sequence of simulation systems is shown in Figure 5,

The control system on the platform was replaced in 2008. The 2 by 2 controller was migrated to the new system by copying the D-SPICE software onto a new computer and connecting to the relevant points in the new control system's OPC server.

What lessons can be drawn from this? Firstly, flexible dynamic simulation tools allow effective and cost-effective transfer of ideas from design, through implementation to operation. Secondly, operator training simulators provide a valuable tool for testing and developing major and minor modifications to control systems. Risk is reduced, innovation is enhanced and implementation time is saved.

Model-predictive Control Design and Tuning

A second example involves the use of a dynamic simulator to design and test linear modelpredictive control (MPC) algorithms. A dynamic model was built of a large gas processing plant to expansion of the process interoperation of the three processing trains in the plant. This required a dynamic model of the entire process that ran faster than real time. This was achieved by splitting the process model into more than 20 sub-models, each of which can run on a separate processor. The entire process or any connected parts of the process is simulated by a master model that coordinates the flow rate and pressure of the material streams flowing between the sub-models and the control signals between sub-models. This approach is described for an LNG plant in [5].

Linear MPC is implemented on the distillation columns in the gas plant. This uses the plant operator's proprietary MPC software. The newly built dynamic simulator was applied to design the MPC algorithms using simulated step responses, and was then used to verify the expected performance of the MPC before it was implemented. The simulated step tests reduce the number and severity of step tests that need to be taken on the plant. This decreases the time required to implement and commission the MPC controllers. It also allows better and easier

maintenance of the controllers as the plant's operating point changes.

The MPC software connects to the plant's control system as an OPC client. This same approach was used to connect to the simulator. The simulator provided an OPC server that exposed the necessary simulator inputs, outputs and variables to the MPC system. This is shown in Figure 6.

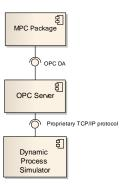


Figure 6. Structure of an MPC identification, tuning and validation system.

MULTIPHASE PRODUCTION MANAGEMENT

As noted above, the flow of oil, gas and water in a network of long pipelines from wells to production facilities is complicated and difficult to operate [10]. For this reason, a detailed dynamic design model is built during concept evaluation and process design to ensure that the fluids produced at the wells can be transported to the production facilities in a controllable way, without risk of blockage or the build-up of large accumulations – slugs – of liquid. These models are configured using specialized multiphase simulation tools.

Better design results are obtained if the multiphase simulation is embedded into a dynamic simulation of the processing facilities. In this way the tight interactions between the production facilities and the transport system can be modelled and evaluated.

Operators need information about the behaviour of fluids in the transport system. This information is only available by simulating the behaviour of the multiphase flow in real-time. This is done by connecting a lightly simplified version of the dynamic process simulator (with embedded multiphase simulator) to the plant control system. When run alongside the process, this simulator provides estimates of the pressure and fluid composition at all points in the transport network. The simulator can also be run in a predictive mode, so that operators can determine in advance the effect of actions, such as opening a well, which may otherwise cause operational problems several days later.

These production management applications are becoming widely used. They are considered to be essential technology for operating production facilities with sub-sea production in deep water. See reference [12] for more details.

Successful applications of production management systems are described in [12] and [13].

SITUATION AWARENESS AND CRISIS MANAGEMENT

If an emergency arises on an oil production facility, it is essential that all involved personnel work on the basis of the best available information and with responses conditioned by extensive, realistic training. For this reason, emergency shutdown scenarios are a routine part of the simulator-based training for process operators.

This "classic" shut-down training needs to be expanded to cover collaborative IO work practices and the challenges of operating in remote, demanding and insecure environments. Early last year, such an expanded training system was implemented for an operator in the North Sea. The system demonstrated the co-ordinated use of a simulated control and safety system and a simulated maritime surveillance system to handle two collision of ship with facility scenarios. One of the scenarios (T01) involved the slow drift of a tanker towards the platform whereas the other (T02) involved a catastrophic loss of dynamic positioning control in a tender alongside the facility. The simulated sequences of events are shown in Figure 7.

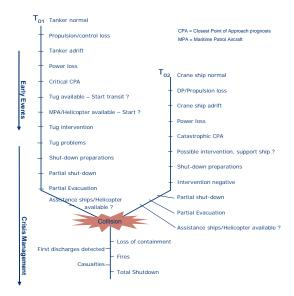


Figure 7: Sequence of events in two different ship-collision scenarios.

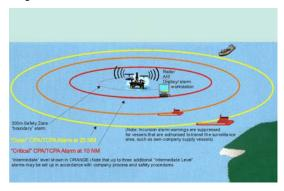


Figure 8: Alarm boundaries for a typical floating production system.

The process simulator emulated a process control system, so that operators had a realistic experience of controlling the process. The Vessel Traffic Services maritime. (VTS) simulator used real operator workstations that provided simulated information from radar, automatic identification system meteorological sensors and VHF direction finders. The VTS raised alarms when vessels passed the safety zone boundaries shown in Figure 8.

A successful exercise was held using these two systems. It was found that tying process and maritime operations together gave a more compelling experience than would have been obtained by process training or conventional emergency response training alone.

VALIDATION AND TUNING OF PROCESS MODELS

The scenarios described above pre-suppose that the simulator gives a faithful reproduction of the behaviour of the facility. Determining whether this is so – validating the model – can be difficult and laborious, although in other circumstances it is painfully clear that the model is wrong!

Engineers from the gas plant described above validated the model as it was built against actual plant data, as stored in a process historian database. The process of extracting data from the data base, entering it into the simulator and comparing results was labour-intensive and tedious. For this reason, we have collaborated with the operator of the gas plant to develop a framework for running process models using real process data and then using this data to tune the model. This system has been described in more detail in [6] and gave rise to the architecture for simulation that has been described above.

This system has been piloted with success on four facilities. The model tuning procedure has been made much more efficient, with automatic data transfer from the process historian and a tuning tool that automates the running of multiple simulator cases. A user interface also allows the simultaneous display of observed and measured data.

CONCLUSION

Figure 9 shows a typical collaboration room, such as can be supplied by Kongsberg Oil and Gas Technologies. Most oil and gas companies now have such rooms. The challenge is how to fill them with useful technology and productive work practices, so that they are not merely glorified video-conference rooms.

We believe that simulators provide the information and predictive power that is needed to make these collaboration rooms a success. This paper has presented a framework: a simulator ecosystem that supports this and provided four

examples of how this ecosystem adds value to oil and gas design and operations.

Challenges remain. Links between simulators remain ad hoc and inconsistent. For example, process simulators need to be able to access reservoir simulation results in a simple and meaningful way. As another example: consistency needs to be ensured between the thermodynamic property data used by production engineers and process engineers.



Figure 9: A typical collaboration room

Optimization capabilities need to be refined. Dynamic simulators are good at determining that something has or will go wrong. They are less capable of providing recommendations of what can be done. This gap remains to be filled.

Finally, the worker in an IO room is overwhelmed with data. This data must be filtered, analysed and visualized in novel and compelling ways.

We are working to address these challenges.

ACKNOWLEDGEMENTS

This paper builds on the efforts over more than 15 years of many colleagues in Kongsberg Oil and Gas Technologies, Kongsberg Defence Systems and their predecessor companies: Fantoft Process Technologies, Sense Intellifield, Kongsberg Maritime, Simrad Albatross and Norcontrol.

REFERENCES

[1] Alberts DS, Garstka JJ, Stein FP. Network Centric Warfare: Developing and Leveraging Information Superiority. Washington DC: CCRP, 1999.

[2] Rajan S, Krome JD. Intelligent Oil Field of the Future: Will the Future Be Too Late?, SPE Paper

- 115030, presented at SPE Annual Technical Conference, Denver, 21-24 September 2008.
- [3] Richardson GE, Nixon LD, Bohannon CM, Kazanis EG, Montgomery TM, Gravois MP. Deepwater Gulf of Mexico 2008: America's Offshore Energy Future, OCS Report MMS 2008-013, U.S. Department of the Interior, Minerals Management Service Gulf of Mexico OCS Region, New Orleans, May 2008, http://www.gomr.mms.gov/PDFs/2008/2008-013.pdf.
- [4] Cameron, DB, Bjerve Sund E, Getaz D. Simulator-Based Multivariable Control: From Troubleshooting to Implementation, 7th Asia Pacific Conf. of Chemical Engineering, Kuala Lumpur, Malaysia, August 2006.
- [5] Cameron D, With HM, Skjerven, Ø, Hyllseth M, Mannsåker, P. *Integrated Distributed Dynamic Simulation of the LNG Value Chain*. Trans. IChemE. Part A, 83(A6), 2005, pp686-691. doi:10.1205/cherd.04372.
- [6] Cameron, DB, Sperle, IL. Nordhus H, Larsson C. VALMUE: Linking process operations with training and engineering through on-line simulation and simulation data management, FOCAPO Conference, Boston, June 2008.

 [7] http://fiatech.org/
- [8] Pickering JG, Whiteley N, Roye J, Turnbull H, Cavanagh D. *A Standard Real-Time Information Architecture for Drilling and Completions*, presented at SPE Annual Technical Conference and Exhibition, 11-14 November 2007, Anaheim, California, U.S.A. SPE Paper 110388-MS. doi: 10.2118/110388-MS.
- [9] Shipley D, Weltevrede B, Doniger A, Klumpen HE, Ormerod L. *Production Data Standards: The PRODML Business Case and Evolution*, presented at Intelligent Energy Conference and Exhibition, 25-27 February 2008, Amsterdam, The Netherlands. SPE Paper 112259-MS. doi:10.2118/112259-MS.
- [10] Hagesæther L, Lunde K, Nygård F, Eidsmoen H. Flow-Assurance Modeling: Reality Check and Aspects of Transient Operations of Gas/Condensate Pipelines. SPE Projects,

- Facilities & Construction, 2(1), March 2007, pp1-17. doi:10.2118/108834-PA.
- [11] Aarset PA, Mo O. *IT Security and Architecture for Integrated Operations: Examples from Deliveries to Ormen Lange and Draugen,* presented at Intelligent Energy Conference and Exhibition, 25-27 February 2008, Amsterdam, The Netherlands. SPE Paper 112279-MS. doi:10.2118/112279-MS.
- [12] Cameron DB, Ødegaard RJ, Glende E. *Online modeling in the petroleum industry:* Successful applications and future perspectives. European Symposium on Computer-Aided Process Engineering 11, Kolding, Denmark, 27-30 May 2001, Elsevier, Amsterdam, pp111-116.
- [13] Singh A, Hannaford K. Innovative Operations Management and Flow Assurance Strategies Extend Field Life and Increase Ultimate Reserves of a Long Distance Subsea Tieback in Ultradeep Water, presented at 2007 Offshore Technology Conference, Houston, 30 April-3 May 2007. OTC Paper 18830.

Comparison of computational methods for reaction equilibrium

Sanoja A. Jayarathna¹, Bernt Lie¹, Morten C. Melaaen^{1,2} ¹Telemark University College, Norway ²Tel-Tek, Norway

Abstract

Specie concentrations for chemical equilibrium can be found in various ways such as solving a system of algebraic equations or solving a dynamic model to steady state. The algebraic equation system for reacting systems consists of multivariate polynomials with multiple solutions. Some traditional and modern methods for solving such systems are discussed together with their advantages and disadvantages.

The dynamic model results from ordinary differential equations (ODEs) based on dynamic material balances. It is shown how the ODE system contains all the information in the algebraic equation system.

Based on the comparison of methods, it is suggested that solving the dynamic model to steady state in many ways is the simplest way for computing speciation data at the equilibrium of a reacting system.

Keywords: Chemical equilibrium, computation methods, speciation diagrams.

Nomenclature

c	concentration	$[\mathrm{mol} / \mathrm{m}^3]$
MEA	Monoethanolamine	[-]
$MEAH^+$	Protonated MEA	[-]
$MEACOO^-$	Carbamate ion	[-]
r	Rate of reaction	$[\text{mol/s} \cdot \text{m}^3]$
t	Time	[s]
ν	Stoichiometric matrix	[-]

Introduction

Reactive systems are widely used in the process industry, including the CO₂ capturing field. Equilibrium concentrations of the species available in the reactive systems are considered as an important source of information regarding the reaction kinetics. Computation of the equilibrium concentrations with known equilibrium coefficients is important for checking the equilibrium with the experimental data. Equilibrium concentrations are important also for the modelling of the systems.

In chemical engineering, the values of the equilibrium concentrations are often found by solving a set of algebraic equations, [1]. The algebraic equation set consists of the relations from setting the reaction rates to zero in tandem with the atom or charge balances; the latter ensure mass conservation. Alternatively, a method like minimization of Gibbs free energy ([2], [3], [4] & [5]) can be used. Usually such methods also result a set of equations to solve for the equilibrium compositions. The set of equations to be solved is usually a set of non-linear polynomials in several variables.

A number of methods are applicable for solving such systems of non-linear polynomials with their own advantages and disadvantages. The use of some of these methods for solving for the equilibrium concentrations are discussed in this paper.

Alternatively, the dynamic mole balances (ODEs) can be solved until the steady state is reached. This gives the equilibrium concentrations.

The relationship between the algebraic equation system and the ODEs is discussed, including advantages and disadvantages of the two approaches.

The paper is organized as follows: first, the algebraic equations for chemical equilibrium are discussed, together with the possibility of multiple solutions. Methods for solving such algebraic equations are then briefly covered. Next, it is shown how dynamic models for concentrations are related to the algebraic equations, with examples. The methods are illustrated through computing a speciation curve which is relevant for post combustion CO2 capturing. Finally, some conclusions are drawn and further work is discussed.

Equilibrium Concentrations with Algebraic Equations

In chemical engineering, the equilibrium concentrations are often specified as the solution of

$$r(c) = 0 (1)$$

$$Vc = b (2)$$

$$Vc = b (2)$$

where Vc indicates a linear combination of the elements of c. Here, r(c) = 0 is a nonlinear set of equations, while the linear equations Vc = b typically are based on the idea of conservation of mass.

The use of minimization of Gibbs free energy is one of the alternative methods to find the equilibrium compositions in a reactive mixture. The numerical value of the standard

state Gibbs energy of reaction (ΔG_T^0) is used to determine the reaction coordinate (ξ) at equilibrium [3]. The Eq. 3 provides the relation between the equilibrium coefficient, the ΔG_T^0 term and the component fugacities

$$K_a = \exp\left[\frac{-\Delta G_T^0}{RT}\right] = \Pi \left[\frac{\hat{f}_i}{f_i^0}\right]^{\nu_i}.$$
 (3)

The reaction coordinates can be found by representing the component fugacities in terms of the mole fractions. With use of the known K_a 's and simplifications to the Eq. 3 a set of polynomials as presented by Eq. 4 will be resulted

$$a\,\xi^k = 0\tag{4}$$

where $a \xi^k$ is a non-linear combination of the reaction coordinates when $k \neq 1$. Ultimately, the Gibbs free energy method can also result a set of non-linear polynomials to solve for the equilibrium compositions.

In either case, numerical methods should be used if the situation is complicated for normal hand calculations. Only the $r\left(c\right)=0 \wedge Vc=b$ case will be used for the analysis in the rest of the paper while stating that the facts are common for all the similar cases.

Use of an iterative method like Newton's method is an option for solving a system of algebraic equations, [6]. A drawback of this method is that it gives only one possible solution among all possible solutions satisfying $r\left(c\right)=0 \land Vc=b$ or $a\ \xi^{k}=0$. The solution is dependant on the initial guess used to start the iterations.

Having a good guess will not always guarantee the expected results as systems of polynomials can have both stable and unstable solutions, as well as physically unrealistic solutions (negative concentrations or complex roots). Suppose the reaction is a third order polynomial in the concentration of specie *A*, leading to the ODE

$$\frac{dc_A}{dt} = -k \cdot c_A^3 + c_A. \tag{5}$$

The possible solutions are $c_{A,a}$, $c_{A,b}$ and $c_{A,c}$ for c_A , which can be depicted as in Figure 1.

Since dc_A/dt is negative between $c_{A,a}$ and $c_{A,b}$, the value of the concentration should decrease providing that any initial guesses between $c_{A,a}$ and $c_{A,b}$ will converge to $c_{A,a}$. All the initial guesses between $c_{A,b}$ and $c_{A,c}$ will settle at $c_{A,c}$ due to the positive values of dc_A/dt , leaving $c_{A,b}$ as an unstable solution. In general it is viable that the steady state solution of a dynamic model with polynomial reaction rate $r(c_A)$,

$$\frac{dc_A}{dt} = r\left(c_A\right),\,$$

is either complex (not physical), real and negative (not physically realizable), or real and positive. In the latter case, the solution may be stable or unstable. Only stable solutions are of interest.

Alternatively to Newton's method, a method such as Buchberger's algorithm for the Gröbner basis [7] can be

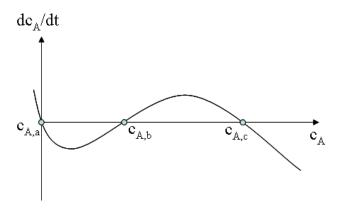


Figure 1: Possible solutions of the polynomial given by Eq. 5

used to solve the algebraic equation system. The Gröbner basis forms a "triangular" set of polynomial "bases" similar to triangular result of Gaussian elimination. As an illustrative example, consider the ammonia synthesis reaction, Eq. 6

$$\frac{1}{2}N_2 + \frac{3}{2}H_2 = NH_3. ag{6}$$

The equilibrium coefficient (K=17.653) is found in [3]. The initial N_2 and H_2 concentrations in the reactor are taken as k_1 and k_2 . The system of algebraic equations to solve for the equilibrium concentrations is given below, where Eq. 7 gives the equilibrium coefficient relating the concentrations. Nitrogen and hydrogen atom balances are given in Eqs. 8 and 9

$$K \cdot c_{N_2}^{1/2} \cdot c_{H_2}^{3/2} - c_{NH_3} \cdot c_T = 0 \tag{7}$$

$$2c_{N_2} + c_{NH_3} - 2c_{N_2, \text{in}} = 0 (8)$$

$$2c_{H_2} + 3c_{NH_3} - 2c_{H_2, \text{in}} = 0, (9)$$

where c_T is the total concentration given by Eq. 10

$$c_T = c_{N_2} + c_{H_2} + c_{NH_3}. (10)$$

The Gröbner bases can be found using Maple [8]; Figure 2 shows the steps in Maple when $c_{N_2,\rm in}$ and $c_{H_2,\rm in}$ are denoted k_1 and k_2 , respectively. In Figure 2, concentrations of N₂, H₂ and NH₃ are represented by the symbols x,y and z, respectively.

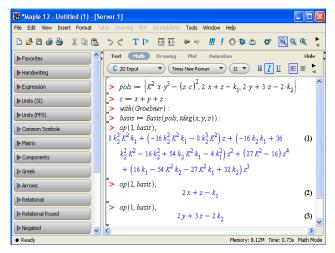


Figure 2: Calculation of Gröbner basis using Maple.

The resulting equations imply that

$$\begin{array}{lll} 0 & = & 8c_{N_2,\mathrm{in}}c_{H_2,\mathrm{in}}^3K^2 \\ & & + \left(-36c_{N_2,\mathrm{in}}c_{H_2,\mathrm{in}}^2K^2 - 8c_{H_2,\mathrm{in}}^3K^2\right)c_{NH_3} \\ & + \left(-16c_{N_2,\mathrm{in}}c_{H_2,\mathrm{in}} + 36c_{H_2,\mathrm{in}}^2K^2 - 16c_{H_2,\mathrm{in}}^2K^2 - 16c_{H_2,\mathrm{in}}^2K^2 - 4c_{N_2,\mathrm{in}}^2K^2 - 4c_{N_2,\mathrm{in}}^2K^2 \\ & + \left(16c_{N_2,\mathrm{in}} - 54c_{H_2,\mathrm{in}}K^2 - 4c_{N_2,\mathrm{in}}^2K^2 - 27c_{N_2,\mathrm{in}}K^2 + 32c_{H_2,\mathrm{in}}\right)c_{NH_3}^3 \\ & + \left(27K^2 - 16\right)c_{NH_3}^4 \\ c_{N_2} & = & \frac{1}{2}\left(c_{N_2,\mathrm{in}} - c_{NH_3}\right) \\ c_{H_2} & = & c_{H_2,\mathrm{in}} - \frac{3}{2}c_{NH_3}. \end{array}$$

From the equations above, c_{NH_3} is found by solving a fourth order polynomial in c_{NH_3} , which yields 4 solutions in the complex field; the solutions may be real positive or negative, or complex. The two subsequent equations give c_{N_2} and c_{H_2} directly from c_{NH_3} . In conclusion, there are 4 triples $(c_{N_2}, c_{H_2}, c_{NH_3})$ of solutions. In order to be a physically realistic solution, every element in a triple must be real and positive. Furthermore, it is necessary to check whether the remaining physically realistic solutions are stable or unstable. Finally, it must be determined which of the physically realistic and stable solutions belong to realistic initial concentrations c (t = 0).

The disadvantages of the Gröbner basis method are: (i) much computer memory is required, (ii) the computational time is high, (iii) the method is numerically ill-posed with current algorithms, and (iv) some post treatment is required to select the physically correct solution. The advantage is that all solutions are found, and it is not necessary to "guess" any initial value in an iteration procedure.

In [9], it is recommended to instead use ideas from continuation/homotopy to find all solutions; continuation has

better numerical properties than current implementations of the Gröbner basis method.

ODEs for Generating Equilibrium Concentrations

Solving an ODE system until steady state is reached, is an alternative to solving a set of polynomials to get the equilibrium compositions. Additional information such as forward and backward reaction rates are required, but as long as their ratio equals the equilibrium constant, the steady state equation should be correct. As long as only the steady state solution is required, exists, and is unique, and ODE solver can be looked upon as a special kind of root finder. Many other such methods exist, in addition to standard solvers such as the Newton method, see e.g. [10].

Batch reactors with perfect mixing and a constant volume have concentrations given by

$$\frac{dc}{dt} = \nu^T r \tag{11}$$

where $c \in \mathbb{R}^n$ is a vector of concentrations with elements $c_j, r(c) \in \mathbb{R}^m$ is a vector of overall reaction rates for the m reactions with elements r_i , and $\nu \in \mathbb{R}^{m \times n}$ is the stoichiometric matrix. With a given initial condition $c(t_0)$, and assuming the existence of a steady state, the steady state can be found by solving this set of ODEs until $t \to \infty$, or for a sufficiently large time. The concentrations at the steady state gives the equilibrium concentrations and is easily found with known realistic initial conditions.

It is simple to show that these ODEs contain the same information as in the system of algebraic equations being discussed earlier.

Partitioning into Reaction Invariants and Reaction Variants

The following partitioning into reaction invariants and variants is discussed in [11]. Let us introduce fictitious species with concentration s_j which are linear combinations of the real species with concentration c_j . Stacking the concentrations s_j into vector s, s can then be written as

$$s = Mc$$
.

We can then formulate the dynamic model for s as

$$\frac{ds}{dt} = M\nu^T r.$$

As long as M is invertible, this differential equation for s holds exactly the same information as the differential equation for c in the previous subsection.

Let us now choose matrix M in a particular way: let M be composed of submatrices M_N and M_C ,

$$M = \left(\begin{array}{c} M_{\mathcal{N}}^T \\ M_{\mathcal{C}}^T \end{array}\right)$$

where the columns of $M_{\mathcal{N}}$ lie in the nullspace $\mathcal{N}\left(\nu\right)$ of ν , while the columns of $M_{\mathcal{C}}$ lie in the column space $\mathcal{C}\left(\nu^{T}\right)$ of ν^{T} ; the nullspace $\mathcal{N}\left(\nu\right)$ of ν consists of all possible vectors n such that $\nu \cdot n = 0$, while the column space of ν^{T} contains all the linear combinations of the columns of ν^{T} [12].

Linear algebra tells us that it is possible to choose columns in $M_{\mathcal{N}}$ and $M_{\mathcal{C}}$ such that M is invertible [12]. With this structure of M, the differential equation for s becomes

$$\begin{array}{rcl} \frac{ds}{dt} & = & M\nu^T r = \left(\begin{array}{c} M_{\mathcal{N}}^T \\ M_{\mathcal{C}}^T \end{array} \right) \nu^T r \\ & \qquad \Downarrow \\ \frac{ds_{\mathcal{I}}}{dt} & = & M_{\mathcal{N}}^T \nu^T r \\ \frac{ds_{\mathcal{V}}}{dt} & = & M_{\mathcal{C}}^T \nu^T r. \end{array}$$

Here, $s_{\mathcal{I}}$ are the reaction invariant fictitious concentrations, while $s_{\mathcal{V}}$ are the reaction variant fictitious concentrations.

Since the columns of $M_{\mathcal{N}}, m_{\mathcal{N},i} \in \mathcal{N}(\nu) \iff \nu \cdot m_{\mathcal{N},i} = 0$, we have

$$M_{\mathcal{N}}^T \nu^T r = (\nu M_{\mathcal{N}})^T r = 0 \cdot r = 0.$$

Thus,

$$\frac{ds_I}{dt} = 0 \Longrightarrow s_{\mathcal{I}} = \text{constant}.$$

Furthermore

$$M_{\mathcal{C}}^T \nu^T = (\nu M_{\mathcal{C}})^T \in \mathbb{R}^{\rho \times \rho}$$

is square and invertible with $\rho = \operatorname{rank} \nu$ when ν is of full rank; when ν is not of full rank, superfluous reactions can be removed to ensure full rank of ν . Since $M_{\mathcal{C}}^T \nu^T$ is invertible, it follows that in steady state

$$\frac{ds_{\mathcal{V}}}{dt} = M_{\mathcal{C}}^T \nu^T r = 0 \Longrightarrow r = 0.$$

In conclusion, this shows that the steady state solution of the differential equation Eq. 11 for c is equivalent to the solution found by simultaneously setting

$$egin{array}{lll} r\left(c
ight) & = & 0 \\ s_{\mathcal{I}} & = & M_{\mathcal{N}}^T c = {
m constant.} \end{array}$$

Here, $M_{\mathcal{N}}^T$ corresponds to V in Eq. 2, while the constant corresponds to b. Using linear algebra software such as Matlab, Maple, etc., $M_{\mathcal{N}}$ can easily be computed, while the constant is given from the initial conditions $c\left(t_0\right)$. But finding the solutions of this set of equations can be difficult as already explained.

Case Study

This example will illustrate how the ODEs are related with the algebraic equations using an example found in CO_2 capturing systems [13]:

$$CO_{2} + 2H_{2}O \underset{k_{1}^{f}, k_{1}^{h}, K_{1}}{\rightleftharpoons} HCO_{3}^{-} + H_{3}^{+}O$$

$$2H_{2}O \underset{k_{2}^{f}, k_{2}^{h}, K_{2}}{\rightleftharpoons} H_{3}^{+}O + OH^{-}$$

$$MEAH^{+} + H_{2}O \underset{k_{3}^{f}, k_{3}^{h}, K_{3}}{\rightleftharpoons} MEA + H_{3}^{+}O$$

$$H_{2}O + MEACOO^{-} \underset{k_{4}^{f}, k_{4}^{h}, K_{4}}{\rightleftharpoons} MEA + HCO_{3}^{-}$$

$$HCO_{3}^{-} + H_{2}O \underset{k_{5}^{f}, k_{5}^{h}, K_{5}}{\rightleftharpoons} H_{3}^{+}O + CO_{3}^{2-},$$

where

$$K_i \triangleq \frac{k_i^{\mathrm{f}}}{k_i^{\mathrm{b}}}.$$

Here K_i , $k_i^{\rm f}$ and $k_i^{\rm b}$ are the equilibrium coefficient, forward reaction coefficient and backward reaction coefficient of reaction i, respectively. For the set of reactions considered, the stoichiometric matrix ν is

when the species are considered in the order CO_2 , MEA, MEAH⁺, MEACOO⁻, HCO $_3^-$, OH⁻, H $_3O^+$, CO_3^{2-} and H $_2O$. The overall reaction rates r_i of the system are given as

$$\begin{array}{lll} r_1 & = & k_1^{\rm f} \cdot c_{\rm CO_2} \cdot \left(c_{\rm H_2O}\right)^2 - k_1^{\rm b} \cdot c_{\rm HCO_3^-} \cdot c_{\rm H_3O^+} \\ r_2 & = & k_2^{\rm f} \cdot \left(c_{\rm H_2O}\right)^2 - k_2^{\rm b} \cdot c_{\rm OH^-} \cdot c_{\rm H_3O^+} \\ r_3 & = & k_3^{\rm f} \cdot c_{\rm MEAH^+} \cdot c_{\rm H_2O} - k_3^{\rm b} \cdot c_{\rm MEA} \cdot c_{\rm H_3O^+} \\ r_4 & = & k_4^{\rm f} \cdot c_{\rm MEACOO^-} \cdot c_{\rm H_2O} - k_4^{\rm b} \cdot c_{\rm MEA} \cdot c_{\rm HCO_3^-} \\ r_5 & = & k_5^{\rm f} \cdot c_{\rm HCO_3^-} \cdot c_{\rm H_2O} - k_5^{\rm b} \cdot c_{\rm H_3O^+} \cdot c_{\rm CO_3^2^-}. \end{array}$$

In order to solve the dynamic model based on the mole balances, the forward and backward reaction coefficients are required. The values of the forward reaction coefficients can either be found in the literature (e.g. in [14]), or fixed at some chosen value.

With given forward rates, the backward reaction coefficients are chosen in such a way that the equilibrium coefficients are correct. The mass conservation of each specie contributes with an ODE to be solved in time. Since the reactor contains nine species, the ODE system consists of nine equations which can be stacked into a vector-matrix formulation as in Eq. 11.

The nullspace $\mathcal{N}(\nu)$ of ν and the column space $\mathcal{C}(\nu^T)$ of ν^T are found using the computer algebra system Mu-PAD within the word processor Scientific Workplace, and are given by the following basis vectors $b_{\mathcal{N},i}$ and $b_{\mathcal{C},i}$ respectively:

$$\mathcal{N}(\nu) = \left\{ \begin{bmatrix} 0\\1\\1\\1\\0\\0\\0\\0\\0\\0 \end{bmatrix} \begin{bmatrix} 2\\-1\\0\\0\\1\\-1\\0\\0\\0\\0 \end{bmatrix} \begin{bmatrix} 1\\-1\\-1\\0\\1\\0\\0\\0\\1 \end{bmatrix} \begin{bmatrix} -3\\2\\1\\0\\-1\\2\\0\\0\\0\\1 \end{bmatrix} \right\}$$

and

$$\mathcal{C}\left(\nu^{T}\right) = \left\{ \begin{bmatrix} -1\\0\\0\\0\\0\\1\\0\\1\\0\\-2 \end{bmatrix} \begin{bmatrix} 0\\0\\0\\0\\1\\1\\0\\-2 \end{bmatrix} \begin{bmatrix} 0\\1\\-1\\0\\0\\1\\0\\-1 \end{bmatrix} \begin{bmatrix} 0\\1\\0\\0\\0\\-1\\1\\0\\-1 \end{bmatrix} \begin{bmatrix} 0\\0\\0\\0\\1\\1\\0\\-1 \end{bmatrix} \right.$$

Using the linear combinations of basis vectors in the nullspace $\mathcal{N}\left(\nu\right)$ of ν , the columns in $M_{\mathcal{N}}$ can be chosen. The following column vectors of $M_{\mathcal{N}}$ are used here: $m_{\mathcal{N},1}=b_{\mathcal{N},2}-2b_{\mathcal{N},3}-b_{\mathcal{N},1},\ m_{\mathcal{N},2}=b_{\mathcal{N},1}+b_{\mathcal{N},3},\ m_{\mathcal{N},3}=b_{\mathcal{N},3},$ and $m_{\mathcal{N},4}=2b_{\mathcal{N},1}+b_{\mathcal{N},2}+3b_{\mathcal{N},3}+b_{\mathcal{N},4}.$ Hence,

$$M_{\mathcal{N}} = \left[egin{array}{cccc} 0 & 1 & 0 & 2 \ 0 & 0 & 1 & 0 \ 1 & 0 & 1 & 0 \ -1 & 1 & 1 & 2 \ -1 & 1 & 0 & 3 \ -1 & 0 & 0 & 1 \ 1 & 0 & 0 & 1 \ -2 & 1 & 0 & 3 \ 0 & 0 & 0 & 1 \ \end{array}
ight].$$

The columns of $M_{\mathcal{C}}$ are chosen to be the basis vectors of $\mathcal{C}\left(\nu^{T}\right)$, i.e. $m_{\mathcal{C},i}=b_{\mathcal{C},i}$:

$$M_{\mathcal{C}} = \left[egin{array}{cccccc} -1 & 0 & 0 & 0 & 0 & 0 \ 0 & 0 & 1 & 1 & 0 & 0 \ 0 & 0 & -1 & 0 & 0 & 0 \ 1 & 0 & 0 & 1 & -1 & 0 \ 1 & 1 & 0 & 0 & 0 & 0 \ 1 & 1 & 1 & 0 & 1 & 0 \ 0 & 0 & 0 & 0 & 1 & -2 & -2 & -1 & -1 & -1 \ \end{array}
ight].$$

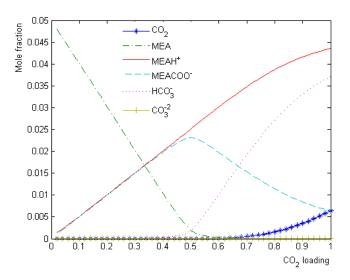


Figure 3: Speciation curves at 40 °C.

The reaction invariant set of equations is found for the fictitious species $s_{\mathcal{I}}$

$$\frac{ds_{\mathcal{I}}}{dt} = M_{\mathcal{N}}^T \nu^T r$$

$$\downarrow M_{\mathcal{N}}^T \nu^T r = 0 \in \mathbb{R}^{4 \times 5}$$

$$\frac{ds_{\mathcal{I}}}{dt} = 0$$

Since $ds_{\mathcal{I}}/dt = 0$, this shows that $s_{\mathcal{I}} = \text{constant}$, or Vc = b.

The reaction variant equation set is found for the fictitious species $s_{\mathcal{V}}$:

$$\frac{ds_{\mathcal{V}}}{dt} = M_{\mathcal{C}}^T \nu^T r$$

where matrix $M_{\mathcal{C}}^T \nu^T$ is an invertible matrix, hence in steady state the condition $r\left(c\right)=0$ is also satisfied.

This example shows that the ODEs, $\frac{dc}{dt} = \nu^T r$ contains all the information available from the system of algebraic equations, $r\left(c\right) = 0 \wedge Vc = b$.

Results of the ODEs

A dynamic model of the case study is simulated to steady state to find the equilibrium concentrations. The equilibrium coefficients for this reacting system can be found in e.g. [13], [15], and [16]. The dynamic model is simulated for a sufficiently long time and the steady state solution is taken as the equilibrium concentrations.

It can be shown that the equilibrium results depend on the initial concentrations of CO_2 and MEA, $c_{\mathrm{CO}_2,\mathrm{in}}$ and $c_{\mathrm{MEA,in}}$, respectively. It is of interest to construct a so-called speciation diagram, see Figure 3.

The speciation diagram shows the equilibrium mole fractions of the various species, as a function of the so-called ${\rm CO_2}$ loading, i.e. as a function of the fraction $c_{{\rm CO_2,in}}/c_{{\rm MEA,in}}$.

In the speciation diagram of Figure 3, a temperature of 40 °C is assumed, and the results are in good agreement with the reference work [13].

Conclusions

The equilibrium concentrations of a reactor can be found by solving a set of algebraic equations satisfying Eqs. 1 and 2. In the case of polynomial algebraic equations, the roots lie in the complex field. However, only real and positive roots are physically realistic. Furthermore, among the real and positive roots, some solutions represent unstable steady states, and the stable steady state roots are thus the only acceptable equilibrium concentrations.

A basic method for solving algebraic equations is Newton's method; this method only finds one root, and the root that is found depends on the chosen initial guess c^0 . There is no guarantee that the chosen c^0 leads to the most physically realistic solution. To study all solutions using Newton's method, it is necessary to use the method repeatedly, each time using a different value of c^0 .

When the algebraic equations are polynomials in several variables, the algebraic equations can be transformed to Gröbner bases using Buchberger's algorithm. Thereafter, all possible sets of solutions can be found using a standard solver for single variable polynomials. Finally, it is necessary to postprocess the solutions in order to find the physically acceptable equilibrium concentrations. However, Buchberger's algorithm is quite demanding when it comes to computer memory and computation time. Thus, it may be better to use continuation/homotopy methods to find all solutions.

Another alternative is to solve the dynamic model of a batch reactor to steady state. Comparing the dynamic model $\frac{dc}{dt}=\nu^T r$ with the algebraic equations, it is easily shown that the dynamic model contains all the information from the algebraic equation system $r\left(c\right)=0 \wedge Vc=b$. Additionally, dynamics of the reaction system is included in the dynamic model.

Clearly, simulating an ODE to steady state where we do not care about the transient behavior, is similar to using e.g. Newton's method; the ODE solver can be considered as just another root solver. Ensuring that steady state is reached with the ODE solver, is comparable to ensuring that the Newton solver has converged to the root. In both cases, we iterate on $\nu^T r (c^0)$ such that $\nu^T r (c^0) \to 0$.

The advantage of using a physically realistic dynamic model with an ODE solver, is that we know that the dynamic model has the equilibrium solution as the steady state solution, and that we can choose a realistic initial value for the ODEs such that the equilibrium solution is found.

Clearly, ODEs exists with complex dynamics such as limit cycle behavior where no steady state solution exist, or with bifurcations where the steady state solution is extremely sensitive to the chosen initial value or numerical inaccuracies. But these complex dynamic cases will also be difficult to solve with alternative methods.

The above factors indicate that both solving the algebraic equations using Newton's method, and solving the ODEs using an ODE solver should be equally accurate in steady state. Since it is just as simple to formulate the ODEs as formulating the algebraic equations, since it is simpler to suggest physically reasonable initial values than guessing an initial iterate for the Newton solver, and since the ODE solver automatically will lead to a stable steady state, we suggest that using an ODE solver is favorable.

Using an ODE solver to find the equilibrium concentrations has been illustrated through computing the speciation diagram relevant for post combustion CO₂ capturing using MEA.

References

- [1] Wark (Jr), K. (1995). *Advanced Thermodynamics for Engineers*. McGraw-Hill Inc, Singapore.
- [2] Thermodynamics of Chemical Equilibrium (2009). See www.chem1.com/acad/webtext/thermeg/TE5.html.
- [3] Elliot, J.R., and Lira, C.T. (1999). *Introductory Chemical Engineering Thermodynamics*. Prentice-Hall, Upper Saddle river, NJ.
- [4] Smith, M.J., Van Ness, H.C. and Abbott, M.M. (1996). *Introduction to Chemical Engineering Thermodynamics, fifth ed.* McGraw-Hill Inc, Singapore.
- [5] Skogestad, S. (2009). Chemical and Energy Process Engineering. CRC Press, Taylor and Francis group, NW, USA.
- [6] Gerald, C. F., and Wheatley P. O. (1998). Applied numerical Analysis. Addison Wesley Publishing Company, USA.
- [7] Cox, D., Little, J., and O'Shea, D. (1992). Ideals, Varieties, and Algorithms. An Introduction to Computational algebraic Geometry and Commutative Algebra. Springer, New York.
- [8] Maple (2009). See www.maplesoft.com.
- [9] Bates, D. J., Beccuti, A. G., Fotiou, I. A. and Morari, M. (2008). An Optimal Control Application in Power Electronics Using Numerical Algebraic Geometry. Proceedings of American Control Conference, Seattle, Washington, USA.

- [10] Bhaya, A., and Kaszkurewicz, E. (2006). Control Perspectives on Numerical Algorithms and Matrix Problems. SIAM, Philadelphia.
- [11] Aris, R. (1989). *Elementary Chemical Reactor Analysis*. Dover, Mineola, New York
- [12] Strang, G. (2006). *Linear Algebra and its Applications, fourth ed.* Thomson, Belmont, California.
- [13] Liu, Y., Zhang, L.,and Watanasiri, S. (1999). "Representing Vapour-Liquid Equilibrium for an Aqueous MEA-CO₂ System Using the Electrolyte Nonrandom-Two-Liquid model". *Industrial Engineering Chemical Research*, volume 38, pp 2080-2090.
- [14] Tanaka, Y. (2002). "Water Dissociation in Ion-Exchange Membrane Electro Dialysis". *Journal of Membrane Science*, volume 203, pp 227–244.
- [15] Ausgen, D. M., Rochelle, G. T., Peng, X. and Chen, C. C. (1989). "Model of Vapour-Liquid Equilibria for Aqueous Acid Gas-Alkanolamine Systems Using the Electrolyte-NRTL Equation". *Industrial Engineering Chemical Research*, volume 28, pp 1060-1073.
- [16] Kent, R. L. and Eisenberg, B. (1976). "Better Data for Amine Treating". *Hydrocarbon Processing*, pp 87-90.

OpenModelica-Python Interoperability Applied to Monte Carlo Simulation

Mohsen Torabzadeh-Tari, Peter Fritzson, Martin Sjölund, Adrian Pop PELAB – Programming Environment Lab, Dept. Computer Science Linköping University, SE-581 83 Linköping, Sweden {mohto,petfr, marsj,adrpo}@ida.liu.se

Abstract

During recent years the interest in computer aided modeling and simulation of complex multi-domain systems have increased significantly. The evolution of the declarative equation-based object-oriented (EOO) modeling language Modelica is a prime example of such a trend. The inherent acausal modeling possibilities and the hybrid modeling capabilities are two features that make Modelica superior. The Modelica community (Modelica 2009 [1], Fritzson 2004 [2]) has achieved considerable success through the development of libraries for a number of different technical domains.

OpenModelica is an open source platform for modeling and simulation of complex physical systems based on Modelica (OpenModelica 2009 [3]). It is intended for both commercial and academic use. The development is supported by the non-profit organization Open Source Modelica Consortium. The most important parts of the platform are: OpenModelica Compiler (OMC), the interactive session handler (OMShell), and DrModelica with the electronic notebook, and an Eclipse plug-in MDT for large-scale library and compiler development [4]. For interoperability with other tools and languages Modelica models can be represented in XML (The Extensible Markup Language), is in ModelicaXML (Pop 2003[5]), and a general Java-Modelica interface [7]. Furthermore, within this platform the MetaModelica extension of the Modelica language is available for modeling the meaning of languages, e.g. Modelica, and mechanisms for model transformations.

Often in a design process there is a need to make a model parameter sweep in order to find an optimal solution to a design problem, or as an improvement iteration of an existing design. For example, which design parameter values will give the minimum energy consumption in a car model. This often requires the interoperability of several tools. The aim of this paper is to illustrate the capabilities of the OpenModelica platform in this aspect. The parameter sweep is performed as a Monte Carlo simulation of a Modelica model (Källdahl 2007 [6]).

The Python language is used to set up the simulation parameters, the uncertainty distributions, as well as calling the OpenModelica compiler and simulator with the updated parameters in each step. The model variable of interest in the results can either be further analyzed in Python or exported to a Matlab file for further analyses.

Keywords: OpenModelica, Python, interoperability, Modelica.

1 The Modelica Language

In the late 90th people from both the academic community and industry joined forces to define and standardize a multi-domain modeling language, Modelica. Like other languages designed at the time the object-oriented approach for modeling the dynamic behavior of engineering systems was adopted. In December 1999, the first version of Modelica, version 1.3 was released. Since then, the Modelica design group has had many meetings, resulting new versions of the Modelica language. For example, the latest release, Modelica 3.1, introduces the decouple operator for parallel computing, among other new features (Modelica 2009 [1]).

The freely available Modelica Standard Library (MSL) contains many model components and examples from different application domains. Such components can be easily adopted by the modeler and integrated in his/her own application model. The inherent acasual capabilities built into the language lets the user express relationship between variables which gives more reusability compared to software based on assignment statements and related constructs as in conventional programming languages.

Furthermore, models in Modelica are described mathematically by Hybrid Differential, Algebraic Equations (HDAEs). The hybrid is referring to the fact that both continuous-time and discrete-time variables are handled, (Bachmann 2006 [9]).

2 OpenModelica Platform

In 2002 an initiative was taken by PELAB, [10] to develop an open source platform for the Modelica language based on more than 20 years of in-house experience of research in compiler construction. This effort was gradually expanded, and in 2007 an international consortium was formed to support the open source effort (OpenModelica 2009 [3]). Previously, the only option for the Modelica community, i.e. Modelica users, for simulating Modelica models was to use commercial tools.

The main goal for this open source platform is to create a complete environment for modeling, compiling and simulating Modelica models based on free software. Both the source code and the binaries are freely available and supported for a variety of intended uses in research, teaching as well as in industry.

The platform was originally written in a language called RML (Relational Meta Language), which is a popular formalism for compiler semantics. This formalism allows efficient compilation combined with optimized C code. This was later (2006) replaced by an extension to Modelica itself, MetaModelica, and the whole compiler was migrated to MetaModelica

The OpenModelica environment compiler translates the Modelica model into a flat Modelica code first and then into C code after a couple of more steps. Also an interactive command handler, i.e., a shell, for executing Modelica scripts and functions etc., is also provided in the environment.

3 Interoperability

Although the OpenModelica environment is a powerful tool when it comes to modeling engineering problems, there are situations when you need interoperability with other platforms. A general trend in product development is the usage of distributed resources for tackling the increasing complexity of technical systems. In the OpenPROD project, [11] the OpenModelica platform is used as the basis for integrating hardware and software models from different platforms. There are four options for interoperating with the OpenModelica platform.

The first method is via the scripting interface of the platform, The Modelica scripting language (.mos files) which is used in this paper. The OpenModelica compiler is just called with this script as an argument in each iteration.

In the second method you just need the scripting interface once for building the model. The output executable file plus the initialization file for the parameter settings is used in each iteration. The third option is to use the Corba interface for invoking the compiler and then just use the scripting interface to send commands to the compiler via this interface, [3].

The fourth variant is to use external function calls to directly communicate with the executing simulation process.

Often in a design process there are uncertainties associated with some of the design variables. One way of dealing with these uncertainties is to perform a parameter sweep, e.g. Monte Carlo simulations, in order to decide which parameter value that returns the optimal result. In this section an example of such an interoperability feature in OpenModelica is given in the form of a Monte Carlo simulation. The underlying Modelica model used in this paper for illustrating the platform's capabilities is based on ecohydrological feedbacks in arid regions, [12]. The rainfall is in this case the uncertain parameter that is swept with a uniform random density function. The result is exported to MATLAB, [13], for further analyses.

3.1 Monte Carlo Simulations

The Monte Carlo simulation is performed in such way that a random parameter is generated in a Python script and then passed to OpenModelica via the scripting interface. The Python scripts in this example for performing a parameter sweep on a Modelica model are divided in three scripts, see Appendix B, MC_RootMoisture.py, make_OMScript.py, and sim.py, see Fig. 1.

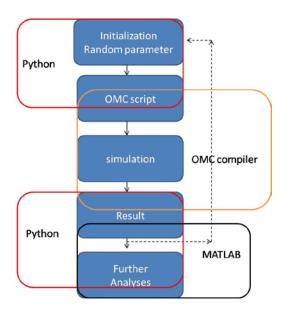


Figure 1. The execution sequence.

The first script is responsible for initiating the simulations by calling the other Python scripts and calling OpenModelica through the command interface.

In this example the result is passed to MATLAB for further calculations. The analyses performed here are the mean value and standard deviation calculations of the root biomass density against the soil moisture saturation level for each iteration.

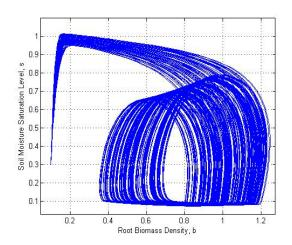


Figure 2. The biomass (x-axis) vs. the moisture saturation level (y-axis) efter each iteration

The root biomass density is plotted against the soil moisture saturation level in Fig 2.

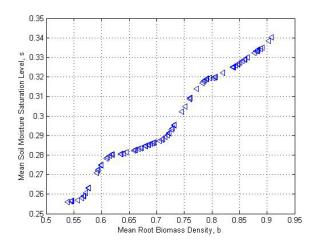


Figure 3: Mean biomass vs. moisture saturation level after each loop

In Fig 3 the mean value of biomass is plotted against the moisture saturation level after each step.

The standard deviation is illustrated in Fig 4. for the two important variables in this problem.

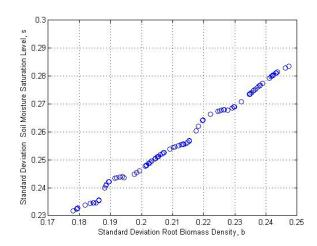


Figure 4: Standard deviation of biomass vs. moisture after each iteration

4 Conclusions

The Modelica language has proven itself when it comes to modeling complex multi-domain engineering problems such as aircraft dynamics, industry robots, etc. In addition to the usefulness of the language the free open source OpenModelica platform opens the opportunities of interoperating with other tools and platforms.

The interoperability of the platform was demonstrated in this paper where the Modelica model, described in Appendix A, was simulated from Python. In this paper the OpenModelica command interface was used to start the simulations from Python. This strategy uses the Python language for setting up the uncertain parameter and pass it to the OpenModelica and repeat this step as in Monte Carlo simulations.

In addition to the parameter sweep initiated from Python the result is passed to MATLAB for further analyses. The result is then stored in a MATLAB file as a matrix after each step with additional commands for performing on these matrixes.

A better and faster way for performing parameter sweep is to update the parameter initialization file and call the executable file in every step instead of calling the openmodelica compiler,

5 Acknowledgements

This paper was supported by the EU project Lila, (Richter 2009 [8]), by the ITEA2 OPENPROD project,[11], and by VR.

References

[1] Modelica Association (2009) "Modelica - A Unified Object-Oriented Language for Physical

- Systems Modeling Language Specification Version 3.1," May, 2009.
- [2] Fritzson Peter (2004). Principles of Object-Oriented Modeling and Simulation - with Modelica 2.1. Wiley - IEEE Press, 2004.
- [3] Open Source Modelica Consortium (2009) "OpenModelica System Documentation version 1.5 Beta", www.openmodelica.org, September 2009.
- [4] http://www.eclipse.org
- [5] Pop Adrian (2003) "ModelicaXML: A Modelica XML Representation with Applications", Modelica conference 2003, Linköping, Sweden.
- [6] Källdahl Malin (2007), Separation Analysis with OpenModelica. Linköping, Sweden, Master thesis, Dept. of Electrical Engineering, 2007.
- [7] Martin Sjölund and Peter Fritzson. An OpenModelica Java External Function Interface Supporting MetaProgramming. In Proc. of (Modelica'2009), Como, Italy, September.20-22, 2009.
- [8] Thomas Richter, David Boehringer and Sabina Jeschke. Lila: A European Project on Networked Experiments, In Proc. of International Association of Online Engineering 2009, Bridgeport, USA, 2009.
- [9] Bernhard Bachmann, Peter Aronsson, Peter Fritzson. Robust Initialization of Differential Algebraic Equations, In Proc. of (Modelica'2006), Vienna, Austria, 2006.
- [10] www.ida.liu.se/pelab
- [11] www.openprod.org
- [12] Private communications with Willis Gwenzi from University of Western Australia
- [13] <u>www.mathworks.com</u>
- [14] <u>www.python.org</u>

Appendix A The Studied Model

The used Modelica example, above, that the Monte Carlo simulations are performed on in this paper is a model for feedback interactions between root biomass and soil moisture. In this model the state variables are the root biomass density, b, and the soil moisture saturation level, s.

```
// RootMoistureModel.mo
model RootMoistureModel
Real s(start=0.3), b(start=0.1),
        T, L, Es;
parameter Real c=0.43, B=12, u=0.125,
```

```
Ke=0.01, I0=0.7, Kd=0.8,
     rainfall=0.4, Ks=0.4, Ki=0.6,
     Ku=0.3, Kc=1.0, sc=0.1, sh=0.03,
     sw=0.05, sfc=0.3, Ep=1, g=1, f=0.02,
     K3=0.1, r=0.2, Kb=1.2;
equation
     der(s)=rainfall*(b+Ki*I0)/(b+Ki)-
             T*b-L*(b+Ks*Kd)/(b+Kd)-Es*(1-
            Kb*b/(b+Ke))+r*s*b;
      //Soil water ODE //
     der(b) = c*s/(s+Kc)*T*b*(1-b)-u*(1
             -s/(s+Ku))*b7+r*s*b;
     //Root biomass balance ODE//
     Es = if s <= sh then 0
           else if (sh<s and s<=sfc) then
                   Ep*(s-sh)/(sfc-sh)
               else Ep*1;
     T = if s <= sw then 0
          else if sw<s and s<sc then
                   q*(s-sw)/(sc-sw)
               else g*1;
     L = if s<sfc then 0
          else (1/(2.718^(B*(1-sfc))-
            1))*(2.718^(B*(s-sfc))-1);
end RootMoistureModel;
```

The parameter c is the maximum water usage efficiency converting the transpiration to root biomass. The B is a drainage parameter and u the maximum intrinsic death rate depending on soil moisture. The parameters Ke and Kd are saturation levels corresponding to the dependence of the bare soil evaporation, Es, on vegetation and drainage dependence on root biomass respectively. The infiltration level in an unvegetated soil is set in K0. The parameters Ki, Ku, and Kc are saturation levels corresponding to the infiltration dependence on vegetation, intrinsic rate dependence on soil moisture, and root water usage efficiency on soil moisture. The faction of precipitation available for infiltration is set with s0 and scaled saturated hydraulic conductivity with Ks respectively. The sh and sw are responsible for the soil moisture saturation at hygroscopic point and permanent wilting point respectively. The parameter sc is the threshold of soil moisture saturation between which root mortality exceeds births. The Ep is maximum bare soil evaporation under non-limiting soil moisture and sfc the soil moisture saturation at field capacity. The q is maximum transpiration parameter under non-limiting soil moisture.

Appendix B The Python Code

The Python scripts used in this example are described below. The execution flow, also shown in Fig 1. is:

- 1. Initiating the uncertain parameter through a random generator.
- 2. Calling the make_OMScript.py for setting up the *.mos script (input argument to the Open-Modelica ompiler)

- 3. Calling the OpenModelica compiler (starting a simulation)
- 4. Retrieving the simulation result (sim.py) Iteration and passing the result to MATLAB.

The file MC_RootMoisture.py sets up the uncertain parameter, makes the mos script, calls the OpenModelica compierl with the mos script as argument and finally calling the MATLAB.

MC_RootMoisture.py

The make_make_script.py makes the OpenModelica script file, mos-file with a new value of the uncertain parameter.

The sim.py is called after each simulation for retrieving the result and pass it to MATLAB.

```
#sim.py

def zeros(n): # vector initialization
vec = [0.0]
for i in range(int(n)-1):
    vec = vec + [0.0]
return vec
```

```
res_file=open("RootMoistureModel_res.plt",
        'r',1) # Opening the result file
line= res_file.readline()
      # skip first line
size=int(res_file.readline().split('=')
        [1])
      # Read simulation interval size
time= zeros(size)
    = zeros(size)
      # Read the result to variables
while line != ['DataSet: time\n']:
  line=res_file.readline().split(',')[
for j in range(int(size)):
  time[j]=float(res_file.readline().split
         (',')[0])
while line != ['DataSet: b\n']:
  line=res_file.readline().split(',')[0:1]
for j in range(int(size)):
  b[j]=float(res_file.readline().split
            (',')[1])
res_file.close()
      # pass results to MATLAB
mat_file=open('OutputMatlab.m','a+',1)
mat_file.write("%time b" + "\n")
mat\_file.write("b = [ \n")
for i in range(int(size)) :
mat_file.write(str(time[i])+","+
str(b[i]) + "; \n")
mat_file.write("]; \n")
mat_file.write("rain = "+str(rain)+ ";
               \n")
mat\_file.write("mean\_b = mean(b(:,2)) \n")
mat\_file.write("std\_b = std(b(:,2)) \n")
mat_file.write("figure(1); \n")
mat_file.write("plot(b(:,1),b(:,2)); \n")
mat_file.write("grid; \n")
mat_file.write("hold on; \n")
mat_file.write.close()
```

It should be perhaps noted that there are other options for using the OpenModelica compiler interface. In this small example the *.mos file script was set up in every iteration. A faster way is to use the command buildModel once outside the iteration loop instead of the simulate command and set up the uncertainty parameter in the initial parameter file, RootMoistureModel_init.txt instead of using the command setComponentModifierValue. Then the file RootMoistureModel.exe is just called in each step. The reson why this method will be faster is that there is no need to restart the OMC in the iteration sequence. You only invoke one OMC. This can be improved one step further by using the Corba interface of OpenModelica, [3].

Fuels 1



Using fundamental advanced thermodynamics to understand a CO₂ capture process

Victor Darde^{1, 2}, Kaj Thomsen¹, Willy J.M. van Well² and Erling H. Stenby¹

¹Department of Chemical and Biochemical Engineering, Technical University of Denmark ²Chemical & Materials Department, DONG Energy Power, Denmark

ABSTRACT

This work deals with the study of a post combustion carbon dioxide capture process using aqueous solutions of ammonia as solvent. Amine solutions have been commonly used for the commercial production of CO_2 . The main disadvantage related to the use of amine solutions is the high energy consumption (3.5 - 4 GJ/ton CO_2) and the high degradation rate of the amines. The heat of absorption of carbon dioxide by ammonia is significantly lower than for alkanolamines. Hence, this process shows good perspectives. However, a scientific understanding of the processes is required.

In order to simulate and optimize the process, a thermodynamic model for the system is required. The properties of the NH₃-CO₂-H₂O system were previously modeled using the Extended UNIQUAC electrolyte model in the temperature range from 0 to 110°C, the pressure range from 0 to 100 bars and for a molality of ammonia up to approximately 80 [1]. In this work, the validity of this model was extended up to 150°C. Also additional data for the enthalpy of partial evaporation and speciation data were used.

The equilibrium composition and enthalpy of the different streams of the process have been studied, based on the information from the patent [2].

The results show that solid phases consisting of ammonium carbonate compounds are formed in the absorber. It also shows that the pure CO_2 stream that leaves the stripper is pressurized.

The energy requirements in the absorber and in the desorber have been studied. An energy consumption in the desorber lower than 2 GJ/ton CO_2 can be reached.

INTRODUCTION

The proportion of carbon dioxide emissions from power production is very significant in industrialized countries. In Denmark, in 2004, they represented 61% of the total CO₂ emissions [3]. Therefore, regarding the reduction objectives endorsed by many governments, efforts are being made to develop technologies allowing the decrease of the emissions from the power plants. Carbon dioxide capture implies separating the CO₂ from the flue gases from a power plant or other industry instead of releasing the CO2 in the atmosphere. Several methods can be used to capture CO₂ from coal-fired power plants. Postcombustion techniques separate the carbon dioxide from the flue gas after a traditional combustion process. The main advantage of such technique is that the combustion at the power plant is unaltered, so the process can be implemented on existing power plants. Amine solutions have been commonly used for the commercial production of CO2 and have been tested for CO₂ capture on pilot scale. However such technologies require a large amount of energy, especially in the desorption part of the process [4]. In addition, the use of amines entails some problems related to solvent degradation and corrosion [5, 6]. Therefore, new alternatives for post-combustion capture are searched for. Processes using aqueous ammonia as solvent are some of the promising alternatives. The ammonia process is found in two variants, depending on the temperature of absorption. The first variant absorbs the CO₂ at low temperature (2-10°C) and is therefore called chilled ammonia process. The low temperature process has the advantage of decreasing the ammonia slip in the absorber and decreasing the flue gas volume. This process allows precipitation of several ammonium carbonate compounds in the absorber. The second process absorbs CO_2 at ambient temperature (25-40°C) and does not allow precipitation. This study focuses on the chilled ammonia process for CO_2 capture.

DESCRIPTION OF THE PATENTED PROCESS

The use of chilled ammonia to capture carbon dioxide was patented in 2006 by Eli Gal [2]. The process described in the patent requires several steps. Figure 1 shows a schematic flow sheet of the capture process.

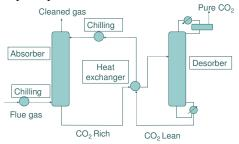


Figure 1: Flow sheet of the process

First, the purpose of the process is to absorb the carbon dioxide at a low temperature. The patent indicates a temperature range from 0 to 20°C, and preferably from 0 to 10°C. Hence, it is first necessary to cool down the flue gas that contains the CO₂. This is done by using Direct Contact Coolers at the entrance of the process. The temperature of the gas that leaves the cooling subsystem is between 0 and 10°C. This stream contains low moisture and almost no particulate matter, acidic or volatile species. Indeed, the low temperature decreases the vapor pressure of these compounds as it promotes their condensation into the water.

Then, the flue gas enters the CO_2 capture and regeneration subsystem. This subsystem consists, like the capture processes using amines, of absorption and desorption columns.

The cold flue gas enters the bottom of the absorber while the CO₂-lean stream enters the top of it. The CO₂-lean stream is mainly composed of water, ammonia and carbon dioxide. The mass fraction of ammonia in the solvent is typically to 10wt%. The pressure in the absorber should be close to atmospheric pressure, while the temperature should be in the range 0-20°C, and preferably 0-10°C. This low temperature prevents the ammonia from evaporating. According to the

patent, the CO_2 -lean stream should have a CO_2 loading (the ratio of the number of mole of carbon dioxide and ammonia in their various aqueous forms) between 0.25 and 0.67, and preferably between 0.33 and 0.67. A low CO_2 loading in the top of the absorber where the CO_2 -lean stream is fed in increases the vapor pressure of ammonia which implies its evaporation. On the other hand, a high CO_2 loading for the CO_2 -lean stream decreases the efficiency of the absorption.

Under the conditions described above and according to the patent, more than 90% of the CO_2 from the flue gas can be captured. The cleaned gas stream can leave the absorber by its top. This stream contains residual ammonia, which is washed out by using cold water and an acidic solution. The treated stream is reintroduced into the system. The cleaned gas mainly contains nitrogen, oxygen and a low concentration of carbon dioxide.

The CO_2 -rich stream leaves the bottom of the absorber. It might be composed of a solid and a liquid phase. Indeed, at this temperature and under those conditions, the solubility limits may be reached. Hence, the CO_2 -rich stream is a slurry. Its CO_2 loading is between 0.5 and 1, and preferably between 0.67 and 1. The patent mentions that a part of the CO_2 -rich stream could be recycled to the absorber in order to increase the CO_2 loading of the CO_2 -rich stream by producing more solids.

The CO₂-rich stream is pressurized and pumped to a heat exchanger where its temperature increases, and then sent to the desorber using a high pressure pump. The desorber temperature is in the range of 50-200°C, and preferably 100-150°C while the pressure is in the range of 2-136 atmospheres. Under those conditions, the vaporization of ammonia and water implied by the high temperature is reduced. The conditions cause CO₂ to evaporate from the solution. It leaves the top of the desorber as a relatively clean and high pressure stream. The water vapor and the ammonia that are contained in this stream can be recovered by cold washing, possibly using weak acid to increase the efficiency.

The desorption reaction is endothermic, but the energy that has to be supplied is much lower than for MEA or other amines according to the patent. This energy highly depends on the composition of the CO₂-rich stream that enters the desorber. In

addition, the pure CO_2 stream that is obtained with this process is already at high pressure. Hence, a part of the energy needed to compress this stream is saved. In addition, the high pressure desorption limits the vaporization of water and thereby reduces the energy consumption.

DESCRIPTION OF THE MODEL

The study of such process requires the use of a thermodynamic model that can take into account the speciation, the vapor liquid equilibrium (VLE), the solid liquid equilibrium (SLE) and the enthalpy change entailed by the mix of ammonia, carbon dioxide and water. This study uses the extended UNIQUAC model that is based on the one described by Thomsen and Rasmussen in 1999 [1]. It calculates the activity coefficient for the liquid phase using the extended UNIQUAC model, and the gas phase fugacity using the Soave-Redlich-Kwong (SRK) equation for the volatile compounds. The original version of the model has shown to be capable of describing accurately the vapor-liquid-solid equilibria and thermal properties for the CO₂-NH₃-H₂O system for a wide range of concentration (up to 80 molal NH3), for a temperature in the range of 0-110°C and for a pressure up to 100 bars [1]. In this new version of the model, additional experimental data were used in order to extend the valid temperature range up to 150°C. The following section describes this new version of the model.

Equilibrium

The analysis of the CO₂-NH₃-H₂O system implies the study of several equilibrium processes. The following reactions are considered in this new version of the model:

Speciation equilibriums

$$NH_3(aq)+H^+\longleftrightarrow NH_4^+$$
 (1)

$$CO_2(aq)+H_2O(1)\longleftrightarrow HCO_3^-+H^+$$
 (2)

$$HCO_3^- \longleftrightarrow CO_3^{2-} + H^+$$
 (3)

$$NH_3(aq)+HCO_3 \longleftrightarrow NH_2COO +H_2O(1)$$
 (4)

Vapor-liquid equilibriums

$$CO_2(g) \longleftrightarrow CO_2(aq)$$
 (5)

$$NH_3(g) \longleftrightarrow NH_3(aq)$$
 (6)

$$H_2O(g) \longleftrightarrow H_2O(l)$$
 (7)

Liquid-solid equilibriums

$$NH_4^+ + HCO_3^- \longleftrightarrow NH_4 HCO_3(s)$$
 (8)

$$NH_4^+ + NH_2COO^- \longleftrightarrow NH_2COONH_4(s)$$
 (9)

$$2NH_4^+ + CO_3^{2-} + H_2O \longleftrightarrow (NH_4)_2CO_3.H_2O(s)$$
 (10)

$$H_2O(l) \longleftrightarrow H_2O(s)$$
 (11)

$$4NH_4^++CO_3^2+2HCO_3 \longleftrightarrow (NH_4)_2CO_3.2NH_4HCO_3(s)$$
 (12)

Hence, five different solids can be formed during the process:

• Ammonium bicarbonate: NH₄HCO₃

• Ammonium carbonate: (NH₄)₂CO₃.H₂O

• Ammonium carbamate: NH₂COONH₄

• Sesqui-carbonate: (NH₄)₂CO₃·2NH₄HCO₃

• Ice: H₂O

Parameters, experimental data and upgrade of the model

The use of SRK does not imply additional parameters to be fitted as no interaction parameters are used for the gas phase.

The model requires binary interaction parameters, UNIQUAC surface area and volume parameters. In addition, the enthalpy and Gibbs energy of formation of the different solids formed were also considered as parameters to be fitted. Finally, the Gibbs energy, the enthalpy of formation and the heat capacity of the ammonium carbamate ion (NH₂COO⁻) were also fitted to experimental data. In total, 65 parameters were fitted to the experimental data compared to the previous version of the model.

In addition, changes were made from the original model. Hence, the model includes the calculation of the residual enthalpy for the gas phase. This calculation is based on the formula included in Smith JM et al. [7]

Furthermore, Henry constant correlations as a function of the temperature were included both for ammonia and carbon dioxide. The correlation used for Ammonia was proposed by Rumpf and Maurer in 1993 for a temperature range from 273.15 to 433.15K [8]. The Henry constant is expressed in $MPa \cdot kg \cdot mol^{-1}$ and the temperature in Kelvin.

$$\ln(H_{NH_3}^m) = 3.932 - \frac{1879.02}{T} - \frac{355134.1}{T^2}$$

The correlation used for carbon dioxide was proposed by Rumpf and Maurer in 1993 for a temperature range from 273.15 to 473.15K [9]. The same units are used in this expression.

 $\ln(H_{NH_3}^m) = 192.876 - \frac{9624.4}{T} + 1.441 \cdot 10^{-2} \cdot T - 28.749 \cdot \ln(T)$

The influence of pressure on the Henry's constants was estimated using the partial molar volume of carbon dioxide and ammonia in water from Brelvi and O'Connell [10].

More than 3800 experimental data from various publications were used to fit the parameters. Table 1 contains the name of the publications, the nature and number of experimental data points used to fit the parameters. VLE stands both for binary and ternary VLE data, H for enthalpy measurements and Pa Ev for the enthalpy change from partial evaporation data.

Source	Data	T, K	N
Wagman D.D, 1990	Н	298.15	9
Van Krevelen D.W, 1949	VLE	293.15-333.15	25
Pexton S, 1938	VLE	293.15-313.15	68
Geffcken G, 1904	VLE	288.15-298.15	2
Prutton CF, 1945	VLE	374.15-393.15	7
Thomsen J, 1883	Н	287.15-291.15	9
Malegaonkar M.B, 1997	VLE	274.2-278.2	9
Chernen'kaya E, 1971	Н	298.15	6
Chernen'kaya E., 1972	Н	298.15-323.15	15
Harned HS, 1943	VLE	273.15-323.15	18
Dunsmore HS, 1964	VLE	273.15-353.15	63
Markham A.E, 1941	VLE	273.15-313.15	4
Gawlick H, 1934	Н	291.15	8
Wrewsky M, 1924	Н	275.15-334.15	93
Baud E, 1909	Н	285.65	24
Barbero J.A, 1983	Н	298.15	10
Yeh SY, 1964	VLE	298.15-318.15	4
Morgan OM, 1931	VLE	273.15-298.15	67
Matous J, 1969	VLE	303.15-353.15	13
Neuhausen BS, 1921	VLE	273.15-313.15	31
Clifford IL, 1933	VLE	333.15-420.15	46
Morrison TJ, 1952	VLE	286.45-347.85	19
Abegg R, 1902	VLE	298.15	2
Kurz F, 1995	VLE	313.15-353.23	52
Göppert U, 1988	VLE	333.15-393.15	530
Mittasch A, 1926	VLE	273.45-332.85	20
Murray CN, 1971	VLE	274.19-308.15	8
Schultz JF, 1946	VLE	283.15-308.15	10
Zawisza A, 1981	VLE	323.15-473.15	33
Rizvi SSH, 1985	VLE	304.32-452.94	187
Gillespie PC, 1987	VLE	313.15-449.85	188
Nighswander JA, 1989	VLE	353.65-471.15	33
Müller G, 1988	VLE	373.15-473.15	380
Takenouchi S, 1964	VLE	383.15-473.15	3
Pawlikowski E, 1982	VLE	373.15-423.15	24
Rumpf B, 1994	VLE	323.15	7
Ellis AJ, 1963	VLE	450.15	1
Otsuka E, 1960	VLE	293.15-373.15	69
Verbrugge P, 1979	VLE	313.15-363.25	78
Dholabhai, 1993	Н	273.75-279.04	4

Rumpf B, 1997	Н	313-2.9-373.2	26
Postigo MA, 1978	VLE	288.15-328.15	5
Kiss AV, 1937	VLE	273.2-298.15	3
Wiebe R, 1939	VLE	323.15-373.15	13
Wiebe R, 1940	VLE	285.15-313.15	23
Mollier H, 1908	VLE	303.43-393.27	34
Smolen TM, 1991	VLE	293.15-413.15	188
Guillevic J-L, 1985	VLE	403.1-453.1	13
Polak J, 1975	VLE	372.2-420.1	23
	VLE	392-468	50
Sassen CL, 1990 Harms-Watzenberg F,	VLE	308.15-473.15	34
Harms-Watzenberg F, 1995	VLE	308.13-473.13	34
Ramstetter H, 1975	Н	293.15	5
Mollier H, 1909	VLE	353.32	1
Cragoe CS, 1920	VLE	273.15-343.16	15
Bartholomé E, 1956	VLE	283.15-303.15	15
Rumpf B, 1993	VLE	313.15-373.15	9
Mollier H, 1909	Н	287.15	16
Kurz F, 1994	VLE	313.15-393.15	156
Chan JP, 1964	Н	274.3-288.15	3
Iseli M, 1985	VLE	354.1-474.15	41
Staudt HJ, 1984	Н	298.15-373.15	92
Rumpf B, 1988	VLE	313.15-393.15	6
Inomata H, 1988	VLE	332.15-373.15	8
Wasmund R, 1980	VLE	273.15-333.15	130
Harvey, 1987	Н	274.3-282.9	9
Jennings BH, 1965	VLE	297-456	68
Postma S, 1920	VLE	263.15-277.51	15
Wendland M, 1999	Н	273.15-282.15	7
Graydon K, 2002	VLE	274.15-288.15	53
Yang SO, 2000	VLE	298.31	7
Novak J, 1961	VLE	284.65-313.15	23
Curry J, 1938	VLE	294	4
Van Slyke DD, 1939	VLE	295.59-298.65	6
Zelvenskii YD, 1937	VLE	273.15-285.58	95
Bamberger A, 2000	VLE	323.2-353.1	29
Kunerth W, 1922	VLE	293.15-307.15	8
Zheng DQ, 1997	VLE	278.15-338.15	10
Cramer SD, 1982	VLE	306.15-471.25	10
Ellis AJ, 1959	VLE	387.15-472.15	11
Lichtfers, 2000	SPE	333.1-393.1	83
Rumpf B, 1998	Pa Ev	313.6-393.6	89
Jänecke E, 1929	SLE	263.15-422.15	186

Table 1: Description of the data

This work uses the same solid-liquid equilibrium data published by Jänecke [11] as were used for the previous version of the model, as explained by Thomsen and Rasmussen [1]. Figure 2 shows the phase diagram for the NH₃-CO₂-H₂O system as a function of the temperature and of the CO₂ loading. Experimental data from various publications ([12, 13, 14]) have been included on the phase diagram to show the fit between the calculation from the model and the experimental data.

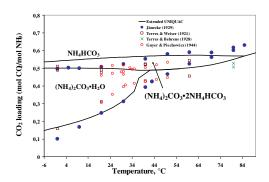


Figure 2: Phase diagram for the ammoniacarbon dioxide-water system from -6 to 90°C

To extend the valid temperature range of the model, additional data have been included for the parameter estimation. Figure 3 plots the pressure calculated with the extended UNIQUAC model for NH₃-CO₂-H₂O mixtures at 120°C and various molality of ammonia as a function of the molality of carbon dioxide. The corresponding results from two different publications have also been included [15, 16].

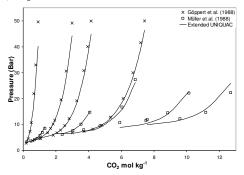


Figure 3: Total pressure in NH₃-CO₂-H₂O mixtures at 120°C

It can be observed that there is a satisfactory agreement between the results from the model and the experimental data at these conditions.

Compared to the previous version of the model, new types of experimental were used for parameter estimation.

First, data from Lichtfers et al. [17] were used. These are speciation data for the NH₃-CO₂-H₂O system that were measured at a temperature from 40 to 120°C at various concentrations of ammonia and carbon dioxide. The ratio between the amount of ammonium carbamate ion and the total amount of ammonia was used in the object function during the determination of the parameters. Figure 4 plots speciation calculation at 80°C for the NH₃-

CO₂-H₂O system for a molality of ammonia of 4.1mol/kg as a function of the molality of carbon dioxide. The experimental data from Lichtfers et al. have also been plotted.

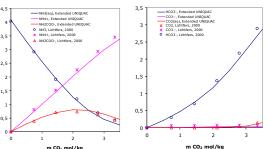


Figure 4: Speciation calculations at 80°C for a molality of ammonia of 4.1mol/kg

Enthalpy data from partial evaporation of CO₂-NH₃-H₂O mixtures published by Rumpf et al. in 1998 [18] were also used during the parameter estimation. The object function that was used consists of minimizing the difference of the calculated and the experimental enthalpy, based on a flash calculation simulating the experiment. Hence, this model is capable of describing accurately the vapor-liquid-solid equilibria and thermal properties for this system for a wide range of concentrations (up to 80 molal), for a temperature in the range of 0-150°C and for a pressure up to 100 bars.

RESULTS FROM THE MODEL

Based on the model and the information given in the patent, it is possible to calculate the composition of the different streams. The results shown here describe the compositions of the streams in the absorber and in the desorber. The initial mass fraction of ammonia that was used here is 10wt%, which corresponds to a molality of ammonia of 8.15mol kg⁻¹.

Composition of the process streams

In the absorber, the temperature should be in the range of 0-20°C, and preferably 0-10°C. The CO₂ loading of the CO₂-lean stream (lean CO₂ loading) is in the range of 0.25-0.67, and the one of the CO₂-rich stream (rich CO₂ loading) in the range of 0.5-1. Therefore it is relevant to study the influence of the CO₂ loading from 0.25 to 0.97 by maintaining the temperature at 8°C and by using an initial mass fraction of ammonia in the solvent of 10wt%.

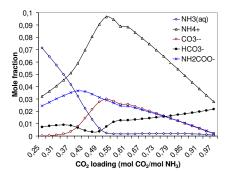


Figure 5: Composition of the liquid phase of a 10wt% ammonia solvent with a temperature of 8°C as a function of the CO₂ loading

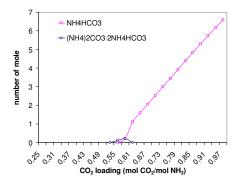


Figure 6: Nature and amount of solid phases of a 10wt% ammonia solvent with a temperature of 8°C as a function of the CO₂ loading

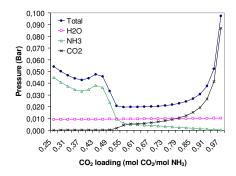


Figure 7: Bubble point pressures of a 10wt% ammonia solvent with a temperature of 8°C as a function of the CO₂ loading

Figure 6 shows that at absorber conditions, solid phases consisting of sesqui-carbonate and ammonium bicarbonate are formed. Figure 7 shows that at low CO₂ loadings (in the top of the absorber), the mole fraction of ammonia in the gas phase is very high. Therefore, it is likely that a certain amount of ammonia is swept along in the

pure gas stream that leaves the absorber. Hence, a washing section must be considered to limit the emission of ammonia.

A similar study was performed to analyze the composition of the stream in the desorber. The same initial mass fraction of ammonia was chosen (10wt%). According to the patent, the desorption preferably occurs at temperatures in the range of 100-150°C. The CO₂ loading decreases in the stripper as the carbon dioxide is desorbed there. The influence of loading on the composition of the stream in the stripper is studied in Figure 8 and Figure 9. A temperature of 110°C was chosen in the study. The CO₂ loading was varied from 0.25 to 0.77. The model is not accurate for pressures higher than 100 bars that are obtained for higher loadings.

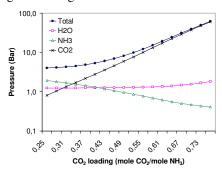


Figure 8: Bubble point pressures of a 10wt% ammonia solvent with a temperature of 110°C as a function of the CO₂ loading

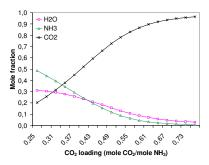


Figure 9: Composition of the bubble point gas phase of a 10wt% ammonia solvent with a temperature of $110^{\circ}C$ as a function of the CO_2 loading

It should be noticed that a logarithmic scale is used for the ordinate axis on Figure 8. Figure 9 shows that for high CO₂ loading, the mole fraction of carbon dioxide in the gas phase is very close to 1. Providing that the CO₂-rich stream that enters

the stripper has a high CO₂ loading, this figure shows that at high temperature, it is possible to get a pressurized and nearly pure CO₂ stream. Hence, some energy savings can be made during

Hence, some energy savings can be made during the compression of the CO₂ stream before it is transported and sequestrated.

Energy requirement

The energy requirement, and especially the heat required in the desorber, is a key parameter of a capture process. The use of ammonia is supposed to lower the energy requirement. The heat required in the desorber was studied. Based on the calculation of the enthalpy of each stream and using a reference configuration assuming the process conditions of each of the stream, it is possible to evaluate the energy requirement in the desorber. This study takes into account the amounts of water and ammonia that are swept along in the gas phase and eventually pumped to the desorber after the pure CO₂ stream passes through a condenser and a washing section.

NH ₃ init wt%	T CO ₂ - Lean and Pure CO ₂	T CO ₂ -Rich	Lean CO ₂ loading	Rich CO ₂ loading
10	110°C	90°C	0.33	0.67

Table 2: Desorber reference configuration

Different parameters were modified individually in order to assess their influence. Figure 10 and Figure 11 show the influence of the rich CO₂ loading and of the initial mass fraction of ammonia on the energy requirement in the desorber. Figure 10 shows that the energy requirement decreases as the rich CO₂ loading decreases. Figure 11 shows that the energy requirement decreases for an initial mass fraction of ammonia from 8 to 28wt%.

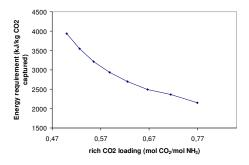


Figure 10: Energy requirement as a function of the loading of the CO₂-rich stream, at an initial mass fraction of 10% ammonia

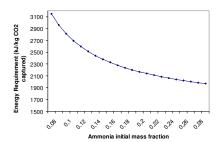


Figure 11: Energy requirement as a function of the initial mass fraction of ammonia, at a constant rich CO₂ loading of 0.67

The CASTOR project that consists of a pilot capture plant using aqueous amines showed an energy consumption in the stripper of about 3700 kJ/kg CO₂ captured for MEA, with a capture efficiency of 90% [19]. Hence, our study shows that based on the equilibrium calculations, the use of ammonia as a solvent is a way to achieve very significant decreases in the energy consumption in the desorber. In addition, the configuration studied here can be further optimized to reduce the energy requirement. Moreover, as mentioned above, the CO₂ stream that is obtained at the end of the process is pressurized when ammonia is used, which would result in additional energy savings during compression of the carbon dioxide. However, this study does not take into account the additional energy required to lower temperature of both the flue gas (including the resulting condensation of water) and the CO₂-lean stream entering the absorber. This energy requirement could be significant, and depends a lot on the location of the capture plant. Moreover, it should be realized that extensive cooling of the absorber is required for keeping a low temperature. For a similar reference configuration as shown for the desorber in Table 1, an amount of 2050 kJ/kg CO₂ produced heat was calculated for the absorber. Some energy would also be required to clean and recover the ammonia vaporized in the absorber.

Moreover, issues like the handling of the slurries and kinetics of absorption will be critical issues that have to be addressed.

CONCLUSION

The CO_2 capture using chilled ammonia process is quite recent and its study requires an advanced thermodynamic model. An upgraded version of the extended UNIQUAC model developed by

Thomsen and Rasmussen [1] used to describe the equilibrium of the CO₂-NH₃-H₂O system was presented. The data that were used for the parameter estimation come from various types of experiments. The new model parameters are valid for temperatures in the range 0-150°C and for molalities in the range 0-80mol kg⁻¹. This version of the model can accurately describe the vaporliquid-solid equilibria and thermal properties for this system. Based on indications from the patent, it was possible to describe the composition of the different streams. This study showed the presence of precipitates in the absorber, and the formation of ammonium bicarbonate from the ammonium carbonate present in the CO₂-lean stream during absorption process. The equilibrium calculation of the gas phase in the absorber shows a high mole fraction of ammonia. Hence, some cleaning subsystems at the top of the absorber should be considered in order to avoid the emission of ammonia. It was also shown that the pure CO₂ stream that leaves the desorber column is pressurized. From an energetic point of view, a reference configuration was used to assess the energy requirement both in the absorber and in the desorber. Based on equilibrium calculations, this study showed that the chilled ammonia process allows for a significant reduction of the energy consumption in the desorber compared to the energy consumption of the process using amines.

REFERENCES

- [1] K. Thomsen, P. Rasmussen, Modeling of Vaporliquid-solid equilibrium in gas-aqueous electrolyte system, Chem. Eng. Sc. 54 (1999)1787-1802
- [2] E. Gal, Ultra cleaning combustion gas including the removal of CO2, World Intellectual Property, Patent WO 2006022885 (2006)
- [3] Denmark's 4th National Communication to the United Nations Framework Convention on Climate Change and Report on Demonstrable Progress under the Kyoto Protocol (2005)
- [4] S. Freguia and GT. Rochelle, *Modeling of CO2* capture by aqueous Monoethanolamine. AIChE Journal 49 (2003) 1676-1686.
- [5] J. Reza and A. Trejo, Degradation of Aqueous Solutions of Alkanolamine Blends at High Temperature, under the Presence of CO2 and H2S. Chem. eng. Com 193 (2006) 129-138
- [6] O. Lawal, A. Bello, R. Idem, The role of methyl diethanolamine (MDEA) in preventing the oxidative degradation of CO2 loaded and concentrated aqueous monoethanolamine (MEA)-

- MDEA blends during CO2 absorption from flue gases. Ind. & Eng. chem res 44 (2005) 1874-1896
- [7] JM. Smith, HC. Van Ness, MM. Abbott, Introduction to Chemical Engineering Thermodynamics 6th edition, 2001
- [8] B. Rumpf, G. Maurer, Solubility of Ammonia Solutions of Sodium Sulfate and Ammonium Sulfate at temperatures from 333.15K to 433.15K and pressure up to 3MPa, ind. Eng. Chem. Res. 32(1993), 1780-1789
- [9] B. Rumpf, G. Maurer, An experimental and theoratical Investigation on the Solubility of Carbon Dioxide in Aqueous Solutions of Strong Electrolytes, Ber. Bunsenges. Phys. Chem. 97 (1993), 85-98
- [10] SW. Brelvi, JP. OConnell, Corresponding states correlations for liquid compressibility and partial molal volumes of gases at infinite dilution in liquids, AICHE 18 (1972) 1239
- [11] E. Jänecke, Über das System H2O, CO2 und NH3. Zeitschrift fuer Elektrochemie, 39 (1929) 332-334+716-728
- [12] E. Terres and H. Weiser, Beitrag zur Kenntnis der Ammoniak-Kohlensäureverbindungen im Gleigewicht mit ihren wässerigen Lösungen. Zeitschrift fuer Elektrochemie 27 (1921) 177-193
- [13] E. Terres and H. Behrens, Zur Kenntnis des physikalisch-chemischen Grundlagen der Harnstoffsynthese aus Ammoniak, Kohlensäure und Wasser. Zeitschrift fuer Physikalische Chemie 139 (1928) 693-716
- [14] A. Guyer and T. Piechowicz T, Lösungsgleichgewichte in wässringen Systemen. Das System CO2-NH3-H2O bei 20-50°. Helvitica Chimica Acta 27 (1944) 858-867
- [15] U. Göppert, G. Maurer, Vapor-liquid equilibria in aqueous solutions of Ammonia and Carbon Dioxide at Temperatures Between 333 and 393K, Fluid Phase Equilibria 41(1988)153-185
- [16] G. Müller, E. Bender, G. Maurer, Das Dampf-Flüssigkeitsgleichgewicht des ternären Systems NH3-CO2-H2O, Ber. Bunsenges. Phys. Chem. 92(1988)148-160
- [17] Lichtfers U, Spektroskopische Untersuchungen zur ermittlung von Speziesverteilungen im System Ammoniak-Kohlendioxid-Wasser, (2001) Aachen, Shaker Verlag
- [18] B. Rumpf, F. Weyrich, G. Maurer, Enthalpy changes upon Partial Evaporation of Aqueous Solutions containing Ammonia and Carbon Dioxide, Ind. Eng. Chem. Res 37 (1998) 2983-2995
- [19] JN. Knudsen, JN. Jensen, O. Biede, Castor SP2: Experiments on Pilot Plant, CASTOR-ENCAP-CACHET-DYNAMIS common Technical Training Workshop (2008)

MODEL PARAMETERS SELECTION USING SENSITIVITY ANALYSIS ON A HIGH FIDELITY MODEL OF PETROLEUM OPERATIONS

Hans Petter Lohne^{*} and Gerhard Nygaard International Research Institute of Stavanger 4021 Stavanger Norway

> Rune W. Time University of Stavanger Stavanger Norway

ABSTRACT

The trend towards automated drilling analysis requires high levels of reliability and accuracy of dynamic hydraulic flow models. Consequently the last decades have seen a focus on detailing the hydraulic models with respects to the dynamics in actual wells. While this work has improved understanding of hydraulic flow during drilling operations and given the possibility of predicting the future behavior of the well dynamics, very detailed and precise models are too computationally heavy to be used in real-time situations.

An alternative is to use a simpler model with sufficient performance, and then adjust poorly known or modeled parameters to make the model agree with measurements. This adjustment can be accomplished using a Kalman filter to keep the adjustments statistically sound. Before such an adjustment or calibration can be implemented, it is necessary to find the parameters which can be adjusted by reasonable amounts and still have a large enough effect on the model to compensate for the lack of accuracy.

This paper presents a set of reasonable parameters found using a sensitivity analysis. A variation range is determined for the different parameters. The method for sensitivity analysis found appropriate is a typical design of experiments using a 2^k factorial experiments method.

Keywords: Well flow model, Sensitivity analysis, Factorial experiment, Calibration.

NOMENCLATURE

C Coefficient [m⁴]

f Fanning friction factor [1]

g Acceleration due to gravity [m/s²]

N Power law index [1]

 $N_{\rm Re}$ Reynolds number [1]

p Pressure [Pa]

Q Flow rate $[m^3/s]$

t Time [s]

v Velocity [m/s]

W Mud density [kg/m³]

 α Volume fraction [1]

 ε Pipe roughness [m]

μ Viscosity [Pa s]

 ρ Density [kg/m³]

τ Shear stress [Pa]

INTRODUCTION

Models of the behavior of the flow of mud and other fluids in wells are necessary to predict potential future problems. In particular the well pressure needs to be kept between the fracturing and pore pressure, unless in underbalanced drilling (UBD – the pressure is kept below the pore pressure). If the well is drilled using MPD (Managed pressure drilling - the pressure is controlled using a valve for backpressure) the

^{*} Corresponding author: Phone: +47 51 87 50 61 Fax: +47 51 87 52 00 E-mail: hpl@iris.no

accuracy of the flow model becomes even more important. To exert control over such a complex system a flow model is needed to predict how the pressure and well environment will respond to different impulses.

Because flow models used during drilling need to be run in real-time, the most complex and numerically precise models are not viable. Simpler, faster and less precise models need to be used instead. In addition the input values for such models, such as temperature, densities etc. will always have some uncertainty associated with them. To achieve satisfactory performance from the model despite these shortcomings it is useful to calibrate the model using real-time measurements.

Previously a real-time flow model has been calibrated by multiplying the friction factor with a scaling factor [1]. Other parameters in the model closure relations have also been attempted calibrated [2], but little or no justification for the choices was made then.

The choice of parameter is significant for how a calibrated model will behave when well conditions change, such as under an increase of flow rate. See [1, 3] for the performance when calibrating a multiplicative factor to the frictional pressure loss. The lesson learned there is the importance of finding a parameter that can maintain the proper dynamic of the fluid flow, such that the calibration does not have to reset after every change in flow rate.

The calibration method is local in that the procedure takes place where measurements are available. One must therefore consider that many parameters like temperature has a gradient form along the wellbore. This is one reason a factor or addition term is tuned instead of the value itself. With wired pipe technology measurements can be gathered from the entire wellbore which will enables us to calibrate a parameter at multiple points along the wellbore. Thus how to calibrate a gradient must be considered carefully. The parameters used for calibration should in addition to the above mentioned have a physical or model significance since the tuning is to make up for poorly modeled effects or uncertainty in input. The choice of parameters tuned should be able to all represent probable discrepancy

measurements when all uncertainty in the parameters is progressed through the model.

The article is divided into 6 sections. First a theory section where basic flow equations and 2k factorial experiments will be briefly mentioned. Secondly a review of parameters considered eligible for calibration is presented and discussed. Then some data on the specific case used to perform an analysis is presented. Afterwards follows a section where the results from the sensitivity analysis are presented. Before the short summarizing conclusions of the article the last section gives the recommended choices based on the results.

THEORY

Flow model

The two phase flow model used in this work is described in [1, 4, 5, 6]. For the purpose of the simulation the well will only be filled with mud, so there is no gas phase. This section will only give a short review of the equations.

The model is based on a drift-flux formulation so two conservation of mass equations and one mixture momentum equation is used.

$$\begin{aligned}
\partial_{t}(\alpha_{g}\rho_{g}) + \partial_{x}(\alpha_{g}\rho_{g}v_{g}) &= 0 \\
\partial_{t}(\alpha_{l}\rho_{l}) + \partial_{x}(\alpha_{l}\rho_{l}v_{l}) &= 0 \\
\partial_{t}(\alpha_{g}\rho_{g}v_{g} + \alpha_{l}\rho_{l}v_{l}) + \partial_{x}(\alpha_{g}\rho_{g}v_{g}^{2} + \alpha_{l}\rho_{l}v_{l}^{2} + p) &= q
\end{aligned} \tag{1}$$

The variables α_g , α_l , v_g , v_l and p can be calculated from these equation plus a slip relation. The source terms on the right hand side as well as the densities are calculated by closure relations.

The density of the fluids, ρ_g and ρ_l , can be estimated in many different ways. A table based on laboratory data for the specific fluid can be used or base oil models such as Glasø, Standing and Sorelle.

The source term in the momentum equation is mainly gravitational forces, $F=g(\alpha_l \rho_l + \alpha_g \rho_g)\sin\theta$, and pressure loss due to wall friction and losses in bottom hole assembly (BHA) components..

The frictional pressure loss for annulus flow is based on the general equation

$$\left(\frac{\Delta P}{\Delta L}\right)_f = \frac{2f\rho v^2}{D_{hy}} R_{rot} R_{ecc}$$
 (2)

Here f is the Fanning friction factor, D_{hy} is the hydraulic diameter, and R_{rot} and R_{ecc} are correction factors that include rotation and eccentricity respectively.

The Fanning friction factor f is a factor following one equation for laminar pipe flow

$$f = \frac{16}{N_{\text{Pa}}} \tag{3}$$

where N_{Re} is the generalized Reynolds number given by

$$N_{\rm Re} = \frac{D_{\rm eff} \nu \rho}{\mu_{\rm eq}} \tag{4}$$

and a different implicit equation for turbulent flow

$$\frac{1}{\sqrt{f}} = -4\log_{10} \left[\frac{0.27\varepsilon}{D_{eff}} + 1.26^{N^{-1.2}} / \left(N_{Re} f^{1-N/2} \right)^{N^{-0.75}} \right] (5)$$

where ε is the pipe roughness, D_{eff} is the effective diameter and N is the degree of Newtonian behavior of the fluids. N is dependent on the rheological model applied to find the shear stress τ used in the calculation of the equivalent viscosity

$$\mu_{eq} = \frac{\tau_{w}}{\dot{\gamma}_{w}} \tag{4}$$

Typical rheology models are the Bingham Plastic model, the Power law model, the Robertson-Stiff model and the Herschel-Bulkley model.

It is difficult to be certain when a pipe flow is laminar and when it is turbulent, only rule of thumb criteria exist. In between these criteria a transitional friction factor can be used given by $f=C(N)N_{\rm Re}^2$ where C(N) is a transitional coefficient.

The friction factors described above are from [7]. The laminar factor is used when it is larger than the others, the transitional factor is used when it is larger than the laminar factor but smaller than the turbulent factor and the turbulent factor is used in all other cases.

Factorial experimentation

The method chosen to analyze the sensitivity of the model with respect to different parameters is 2^k factorial experiments, see [8]. This method quantifies the effect of parameters on the model based on the parameters possible low and high deviation. In addition the interaction of the parameters is quantified.

The 2^k factorial experiments are often used in the process industry to determine which factors should be the focus of further study with as few experiments as possible. Unlike for a computer model randomness in the process is usually a factor. However, it is relevant to use this method in deterministic cases as well where it is used as a screening tool to determine which parameters have large effects on the model output. In addition, as long as we assume the impact of the parameters are monotone, either non-increasing or non-decreasing, it is not necessary to fully explore between the low and high variants.

A 2^k factorial experiment uses two different values for each parameter, usually denoted "high" and "low", but does not necessarily have to be quantitative values. The full design has each level of every parameter occur with each level of every other parameter; meaning the full design requires 2^k experiments. From this the main effect of each parameter can be quantified by comparing the mean response at the "high" level of the parameter with the mean response at the "low" level.

The interaction effect between different parameters is also quantified in a similar way. Denoting + for the "high" parameter value and for the "low" parameter value the responses are added with the signs shown in Table 1 for a 2² design. There the parameters are A and B with the "a" meaning A is at "high" level while B is at "low" level and (1) meaning none are at "high" level.

Treatment	F	actorial effe	ct
combination	A	В	AB
(1)	-	-	+
a	+	-	-
b	-	+	-
ab	+	+	+

Table 1: 2^k factorial experiments.

Because we investigate a deterministic model each treatment combination does not need to be repeated. To reduce the number of experiments a fractional factorial design could be implemented, but that means throwing away higher order interaction effects as well as having to interpret aliasing. This might not be a huge problem however, as the equations tells a lot about the interactions. The reason for using a 2^k factorial design was to evaluate the effect of parameters reasonably fast and easy.

PARAMETER ALTERNATIVES

Parameters suitable for calibration should have a significant impact on the model based on its actual value in its probable value range. This section selects some of the parameters based on their importance in the equations, and determines a variation for them.

Dominant physical parameters in the flow equations are temperature, density, pressure and viscosity. In addition there are pressure losses such as pressure losses over bit, MWD, geometry and wall friction. We now consider each of them with respect to their variation, thoughts about importance and how they are defined in the globalized setting.

Temperature is a very important physical variable in that it has an impact on the physical properties of the drilling fluid, e.g. density and rheology. Further, the temperature modeling is complex in itself, particularly with rotating pipe which moves up and down. From a measurement point of view the temperature is monitored at the inlet, outlet and at some intervals down hole, but not a continuous profile as would be required for the simulator. Options are to have a multiplicative or additive factor which is constant along the wellbore, but uncertainty remains on the appropriateness of the solution.

The mud temperature depends on the heat transfer between the mud and the surrounding rock, which has an approximately known temperature called the geothermal temperature, and the heat loss when the mud is at the surface before it is pumped back into the well. To calculate the heat transfer the specific heat and thermal conductivity of the materials in the well are needed. Of these materials, the properties of the drilling fluid are usually assumed the least well known. In addition, when the mud is not circulated the temperature will slowly approach the geothermal temperature as time passes, making it difficult to estimate the temperature in the well when circulation resumes after a few hours pause in circulation.

To get an idea of the effect the temperature has on a well flow model the temperature gradient is held constant throughout the well and no dynamic temperature model is used so the temperature is constant through time as well. The temperature of the mud pumped into the well is measured to 50 degrees Celsius. For the purpose of the analysis the temperature gradient levels are set to 0.014 C/m for "low" level and 0.017 C/m for "high" level.

Pressure loss over bit, MWD etc ("singular" pressure drops) are very difficult to model; first of all because the internal flow of these devices is generally not monitored. Also their characteristics may change over time in abrasive environments drilling. Usually the manufacturing this equipment provide a number with respect to the expected pressure loss over the component. However, this value has great uncertainty and can vary a lot by flow rate; in particular outside flow rates it is intended used for. The pressure loss over the BHA can be estimated by the pressure loss equation $P = Q^2 W / C$ where Q is the flow rate, W is the mud weight and C is a coefficient given for the components in the BHA. In the analysis this coefficient uses 7.29e-7 m⁴ as "low" and 8.05e-7 m⁴ as "high", which is a 5% error to an appropriate coefficient in either direction. This error might be much larger.

Pipe roughness is a parameter in the friction factor equation for turbulent flow. The pipe roughness will increase as the pipe is used. For the analysis the pipe roughness is set to 5e-5 m which is a

value appropriate for commercial steel as "low" and 15e-5 m which is a value suitable for rusted steel as "high". The annulus is not given a different roughness due to the flow regime assumed nearly laminar there making the roughness less important.

The friction factor for turbulent flow has been approximated through experiments, and can have an error of more than 10 %. The laminar friction factor however is found analytically so there is little reason to calibrate it. Because the flow regime in the annulus is assumed approximately laminar the friction factor will only have potential for large errors in the drillstring, making it similar in effect to the roughness parameter.

Rheology models use measured shear rates and shear stresses to estimate their parameters. Rheology models can have different number of parameters that need to be estimated. Two well known models, Bingham Plastic and Power Law, use only two parameters, while others like Robertson Stiff uses three. Almost needless to say, more parameters will usually mean a more accurate model. Because the Bingham Plastic model tend to overestimate shear stress at low shear rates while the Power Law frequently underestimates shear stress at low and high shear rates these two models have been selected to be the "high" and "low" respectfully in the experiment. There is most likely some uncertainty in the measured rheology data, but in this work only the effect of the two models is measured.

Many density models for the oil based mud can be used, but here Glasø's model and Standing's model have been chosen. Both models are based on regression of measurements and will probably not give very different results, but it is useful to test the effect of density model choice. In this paper for an arbitrary reason the Glasø model will be termed "low" while Standing's model will be termed "high". To get the effect of temperature high pressure high temperature (HPHT) versions of the density models are used. Ordinarily the temperature and pressure effects are disregarded as they have opposite effects and tend to equal each other out.

Other parameters, such as the eccentricity of the drillstring in the annulus, would also be interesting to test, but due to coding issues many

parameters are not so easy to manipulate, and hence not eligible for calibration in this model.

CASE DESCRIPTION

For the purpose of the analysis of the well flow model a set of real data acquired from a North Sea well is used as background data. The well has a measured depth of 3051 meters and a true vertical depth of about 2420 meters. From the dataset covering approximately 3.5 days of drilling operations for a 8 ½ inch hole a subset with "good" data was selected. The criteria for good availability was of different types measurements such as ECD, downhole pressure and downhole temperature. In addition, to test the effects of parameters for different flow rates the dataset chosen was a stepwise increase in flow rate, see Figure 1.

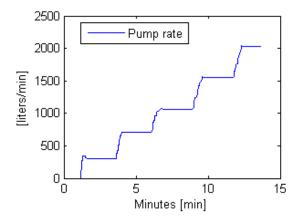


Figure 1 Flow rate

The chosen sequence starts from a short period of downtime and continues with a stepwise increase in flowrate in preparation for the continued drilling of the 8 ½ inch hole. The downtime prior to the sequence makes the temperature profile of the mud relatively unknown. The temperature of the mud pumped into the well is 50 degrees Celsius.

While doing an analysis on a single case will not provide us insight exactly valid for all cases, it is assumed that this case will be representative for similar wells.

SENSITIVITY ANALYSIS

To test how sensitive the well flow model is to each parameter previously mentioned each had defined a "high" and "low" level. The well flow model is as mentioned run for all combinations making $2^5 = 32$ simulations. Adding more parameters is easy but one more parameter will double the needed number of simulations. A fractional design could be used to reduce the number of simulations but this has its drawbacks. In this section sequences of capital letters will be used to denote "high" states with the letter being T for temperature, R for rheology model, D for density model, B for BHA coefficient and E for roughness. In this way TE will mean temperature and roughness are in their "high" states while the other parameters are in their "low" states.

The simulations had some unexpected change in behavior at the end of the sequence. Especially some of the main effects on the bottomhole pressure show a change in direction of the effect for increasing flow rates. The reason for this is the higher than expected turbulence in the annulus region for high flow rates. The spikes in the figures at around one minute are attributed to the startup of the pump.

In Figure 2 the main effects on the standpipe pressure of the parameters are displayed. It shows that the roughness has a very large effect when comparing commercial steel with rusted steel. The other parameters also have significant effects. The least effect comes from temperature and density. The density shows there is not a huge difference between Glasø's model and Standing's model.

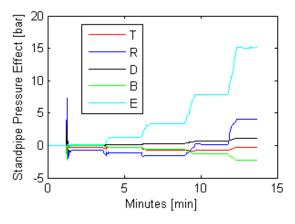


Figure 2 Main effects on standpipe pressure

In Figure 3 the main effects of the parameters on the bottomhole pressure are displayed. Not surprisingly roughness and BHA coefficient does not have much effect on the annulus pressure. Temperature gradient, rheology model and density model have significant effect on the bottomhole pressure.

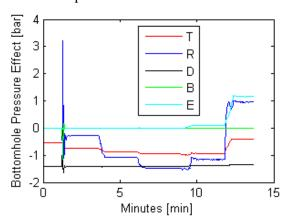


Figure 3 Main effects on bottomhole pressure

Figure 4 displays the largest interaction effects for the standpipe pressure. The temperature gradient has a small interaction effect with rheology model. The temperature-roughness interaction is negligible. By far the largest interaction effect is between the rheology model and the roughness.

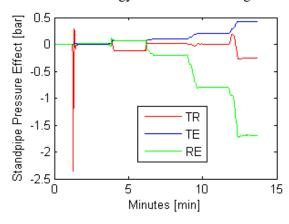


Figure 4 Interaction effects on standpipe pressure

In Figure 5 the largest interaction effects on the bottomhole pressure are displayed. There are not any large effects, but some expected interaction between temperature and density model can be seen.

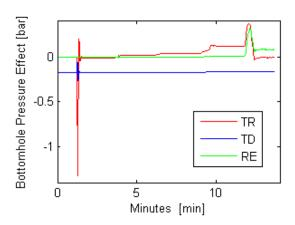


Figure 5 Interaction effects on bottomhole pressure

The figure below shows the effect on the standpipe pressure of "high" roughness and rheology model together with its reverse to get a picture of the total difference achievable.

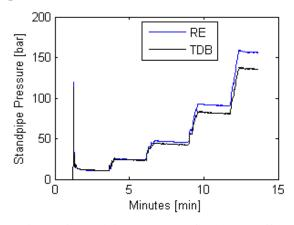


Figure 6 Standpipe pressures for largest effects

The last figure displays similarly for the bottom hole pressure "high" values for temperature, rheology and density together with the opposite.

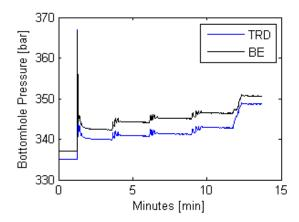


Figure 7 Bottomhole pressures for largest effects

RECOMMENDATIONS

From the figures it is apparent that the all of the parameters have some effect on the standpipe pressure, and the same for the bottomhole pressure except for the drillpipe roughness and the BHA coefficient. Thus by allowing large enough variation in these parameters they should be able to calibrate the well flow model. However, the reasonable variation in some of the parameters would not allow this.

The temperature gradient was varied between 0.014 and 0.018 degrees Celsius per meter, which corresponded to 86 C and 96 C bottomhole respectfully. These temperature values are reasonable since the known measurement for established circulation of 90 C and the geothermal temperature is estimated to 95 C there. Greater variation in temperature gradient can probably occur, but only together with a change in surface mud temperature.

The temperature gradient is interesting, however, due to the interaction effects with the rheology models and the density models. While they are quite small the rheology and density can probably vary much more than the difference between the two models. Calibrating temperature together with rheology and density is potentially interesting, but this paper does not show sufficient effect of the interactions.

The pressure loss in the BHA and the pipe roughness can have a large effect on the standpipe pressure, but not much effect on the annulus pressure. Thus it is only relevant to tune these to

make up for discrepancy in the standpipe pressure when the bottom hole pressure is fairly accurate.

SUMMARY CONCLUSIONS

A basic sensitivity analysis of the main and interaction effects of the constant temperature gradient of the drilling fluid, the rheology model used, the density model used, the coefficient for the bottomhole assembly (BHA) pressure loss and the drillpipe roughness has been performed on an advance well flow model. The method used for this was a 2^k factorial experiment. Some parameters were found to have a significant effect on the model, while others had only a small effect. The parameters which only could be shown to have a small effect will have to have a larger variation range than considered in this work in order for them to be suitable for calibration.

The analysis showed some effect from the temperature gradient, which also displayed some interaction effects, but another method than just tuning the temperature gradient would be preferred. The drillpipe roughness and bottomhole coefficient can be tuned to make the model match the measured standpipe pressure, but have no large effect on the bottomhole pressure due to the more laminar behavior in the annulus (even though there is some degree of turbulence there as well).

Both rheology and density have only a small effect, but the difference between two models is probably not sufficient to display the full possible variation in these parameters.

Further work should be conducted on more parameters and more settings to make the best founded choice of calibration parameters. In addition the effect of turbulence changing the direction of the effect of some parameters is a potential source for improving calibration.

REFERENCES

[1] Gravdal J. E., Lorentzen R.J., Fjelde K.F., Vefring, E.H. SPE 97028 Tuning of Computer Modell Parameters in Managed Pressure Drilling Applications Using an Unscented Kalman Filter

- *Technique*. In: SPE Annual technical conference and exhibition, Dallas, 2005
- [2] Lorentzen R.J., Nævdal G., Fjelde K.F. Real Time Interpretation of Measured Data during Underbalanced Drilling Operations, report 2002/192. Stavanger: RF 2002.
- [3] Lohne H.P, Gravdal J.E., Dvergsnes E.W., Nygaard G., Vefring E.H. IPTC 12707 Automatic Calibration of Real-Time Computer Models in Intelligent Drilling Control Systems Results From a North Sea Field Trial In: International petroleum technology conference, Kuala Lumpur, 2008.
- [4] Iversen F. *Pressure loss calculations in the WEMOD well flow model.* report Stavanger: RF, 2007
- [5] Frøyen J., Sævareid O., Vefring E.H. Discretization, implementation and testing of a semi-implicit method, report 2000/157. Stavanger: RF, 2000.
- [6] Frøyen J., Sævareid O. Model equations and solution techniques for multiphase flow in pipe networks, report 2000/158. Stavanger: RF 2000.
- [7] Reed, T. D., Pilehvari, A. A. SPE 25456 A New Model for Laminar, Transitional, and Turbulent Flow of Drilling Muds In: Production Operations Symposium, Oklahoma City, 1993
- [8] Walpole, R. E., Myers, R. H., Myers, S. L. Probability and Statistics for Engineers and Scientists 6th Edition, Prentice Hall 1998.

PREDICTION OF CONDENSING FLOW WITH RELEVANCE TO FLUE GAS CONDENSER AND CO2 CAPTURING

Hamid Nabati * and Jafar Mahmoudi School of Sustainable Development of Society and Technology Mälardalen University Sweden

Rune Time University of Stavanger Department of Petroleum Engineering Norway

ABSTRACT

CO2 capturing and related technologies is getting more and more important in studies, as the global temperature rising has shown its negative effects on climate change in the current decades. This paper deals with flue gas condenser for oxy-fuel process. Different available numerical model for multiphase modeling are investigated first. Then a primary design concept is proposed and water vapour condensation from a flue gas containing CO_2 and H_2O is studied upon it. The numerical model is applied to predict the flow field and heat transfer inside the condenser to investigate on condensation rate and CO_2 separation efficiency. Then based on this primary study result, some advice is made on a basic flue gas condenser design.

Keywords: CO₂ Capturing, Oxy-Fuel Power Plants, CFD, Condensation, Two Phase Flow

NOMENCLATURE

- c molar density of the mixture (mol/m3)
- cp specific heat (J/kgK)
- D diffusion coefficient of the gas mixture (m2/s)
- g acceleration of gravity (m/s^2)
- h heat transfer coefficient, enthalpy
- k thermal conductivity (W/mK)
- L surface length (m)
- m_{cd} condensation mass flux (kg/s)
- Nu Nusselt number
- p pressure (Pa)
- q heat flux (W/m2)
- R interaction force between phases
- Re Reynolds number
- S source term
- T temperature (K)
- u film velocity (m/s)
- * Corresponding author: hamid.nabati@mdh.se

- x molar fraction
- y mass fraction
- v velocity, velocity vector
- z axial coordinate (m)

Greek symbols

- α mass fraction of one phase
- λ bulk viscosity (Pa s)
- μ shear viscosity (Pa s)
- ρ density (kg/m2)

Subscripts

- i single gas species i in the mixture
- j single gas species j in the mixture
- l liquid phase
- m gas mixture
- sat saturation conditions
- bulk gas mixture

INTRODUCTION

These days it's well discussed that human activities has been caused an important increase in greenhouse gases. This increase caused the global temperature rise and eventually the rising global temperature will cause the global climate to change. Among the greenhouse gases, CO₂ is the main anthropogenic gas which comes mainly from fossil fuels used in industries like power plants. While fossil fuels account for 90 percent of global energy consumption currently and it cannot be phased out rapidly, we must rely on fossil fuels as the main energy source for the next decades [1].

Thus carbon capture and sequestration to reduce the release of CO₂ to atmosphere from stationary sources like fossil fuel fired power plants is of critical importance. One of the most recent proposed CO₂ capturing methods from flue gas is Oxyfuel process. Oxy fuel combustion systems use oxygen instead of air for combustion of the primary fuel to produce required heat for different proposes like power generation. The resulted a flue gas that is mainly water vapor and CO₂. This results in a flue gas with high CO₂ concentrations (greater than 80% by volume). The water vapor is then removed by cooling in a CO₂/H₂O condenser which is one of the key components in this system. Figure 1 shows the oxy fuel process schematically. To gain the high efficiency in H₂O removal from flue gas and preparing a pure CO₂ stream, there is a great need for precise design of the condenser. Despite of wide referring to this kind of condenser in different proposed Oxy fuel cycles, the appropriate design data are not yet available and new experimental and numerical studies are necessary to achieve the desired efficiency for CO₂ capturing and steam separation. One of the most recently research, concerning on the carbon dioxide-water mixtures, is Hailong Li thesis [2]. Operational conditions for different processes including oxyfuel process are studied and defined in the thesis. The following table shows the estimated operating pressure of the CO₂/H₂O condensation and inlet temperature of flue gas stream for a condenser used in Oxyfuel plant.

Table 1 Estimated operating pressure and inlet temperature for CO2/H2O condenser in Oxyfuel

	piani	
	Operating	Inlet
	pressure (bar)	temperature (°C)
Coal-fired	1.013	100-150
Natural gas-fired	0.9-1.013	80-150

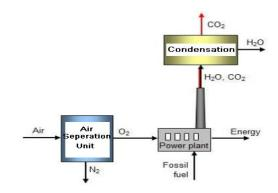


Figure 1 schematically representation of oxy-fuel process

The other important matter that should be considered for condenser study is condensation behavior of multi-component mixture. This could be rather complicated when condensing and noncondensing components forms the mixture. A.Tanrıkut and O. Yeşin have conducted an experimental study for the fundamental investigation of condensation in the presence of air as a non-condensable gas in the mixture [3]. The test section was a heat exchanger of counter-flow type, which steam/gas mixture flows downward inside the condenser tube (inner tube) and cooling water flows upward inside the outer pipe. They reported that the presence of non-condensable gases greatly degrade the performance of heat exchange when the main heat transfer mechanism is steam condensation and the system pressure has a reverse effect.

The real modeling of condenser has rarely appeared in literatures. Only few attempts have been carried out to implement CFD in study of condensing flow. Yadigaroglu[4] has also reported that computational multi-fluid dynamics is still under development and needs more research.

One of the latest works is the Charlotte Wilhelmsson paper [5]. In his study, a CFD approach is applied to model water vapour condensation and two-phase flow in a channel used in plate heat exchangers. She has developed the model based on the governing equations and solved them for the entire single and two-phase fields. In this research, the water phase change and two-phase flow are treated by employing a water liquid-phase fraction factor based on the total enthalpy in each computational cell. The density, viscosity and conductivity and other thermal-

physical properties of the two-phase region, have been calculated based on the calculated value of the liquid-phase fraction factor. She has concluded that the inlet vapour velocity has significant effects on the water phase change and two-phase flow in the channel. Another recent work that its frame is nearly similar to this paper work is Ivo Kljenak paper [6]. In this work, an experiment on containment atmosphere mixing and stratification was simulated with the Computational Fluid Dynamics code CFX4.4. The facility consists of a large cylindrical vessel in which steam, air and helium gases are injected with steam condensing on some parts of the vessel walls. During certain phases, steady states were obtained when the steam condensation rate became equal to the steam injection rate, with all boundary conditions The approach was remaining constant. modeling of flow in the domain simulation as single-phase and steam condensation on vessel walls as a sink of mass and energy. It is represented again in the work that the modeling of steam condensation are not yet commonly included in CFD codes and has to be implemented by users. The comprehensive surveying showed that the most efforts have been done to develop the mathematical modeling for multi-phase flow and no actual CFD modeling has been done for a condenser itself. This window is open for

most efforts have been done to develop the mathematical modeling for multi-phase flow and no actual CFD modeling has been done for a condenser itself. This window is open for collecting the derived models and applying them into available CFD code to obtain realistic results as guidance for better design of multiphase heat exchangers.

In the current study, a 3D condenser is analyzed numerically. The work is focused on the thermal and flow fields inside the condenser and effect of multiphase model on condensation flow. The flue gas property is considered close to what is expected from oxy-fuel power plant. The grid independency is checked severely to ensure about final results.

At the initial phase of this research, it was proposed to work on condensation in a complex direct contact and surface contact condenser. The condenser sketch is depicted in Figure 2. Then primary study showed that it is necessary to develop the condensation model based on a simple geometry and then this model could be applied to the more complex geometries. First model based on the proposed condenser design is illustrated in the Figure 3.

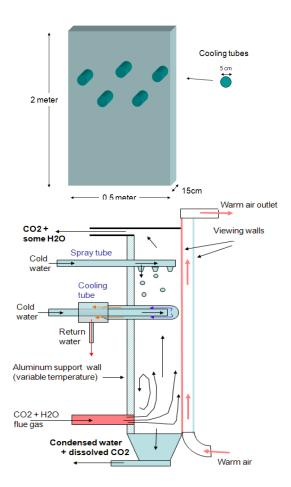


Figure 2 Proposed geometry for condensation study

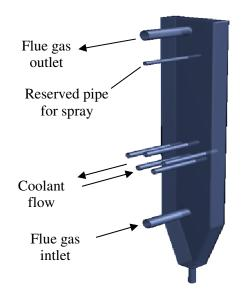


Figure 3 First implemented model for condenser

NUMERICAL APPROACHES FOR TWO PHASE FLOW MODELLING

Presently two approaches are used in numerical modeling of multiphase flows: the Euler-Lagrange approach and the Euler-Euler approach. The first step in solving the multiphase problem is to assess which of the multiphase flow regimes best represents the flow that is studied. Then the appropriate model could be selected for simulation. In the Euler-Lagrange approach, the fluid phase is represented as a continuum by solving the timeaveraged Navier-Stokes equations, while the dispersed phase is solved by tracking particles, bubbles, or droplets through the calculated flow phase can exchange The dispersed momentum, mass, and energy with the fluid phase. The essential assumption in this model is that the dispersed phase occupies a low volume fraction, even though high mass loading is acceptable. This model is appropriate for the modeling of spray dryers, coal and liquid fuel combustion, but inappropriate for the modeling of liquid-liquid mixtures, fluidized beds, or any application where the volume fraction of the second phase is not negligible.

In the second (Euler-Euler) technique, the different phases are considered as interpenetrating fluids. The volume of a phase cannot be occupied by the other phases. Conservation equations for each phase are derived to obtain a set of equations, which have similar form for all phases [8].

In the FLUENT[©], currently three different models are presented to handle the Euler-Euler approach: the volume of fluid (VOF) model, the mixture model and the Eulerian model [8]. Here a short explanation of each model is presented:

The Volume of Fluid (VOF) model is a surface tracking technique applied to a fixed Eulerian mesh. Wherever the position of the interface between the two or more immiscible fluids is of interest, this model is used. In the VOF model, a single set of momentum equations is shared by the fluids, and the volume fraction of each of the fluids in each computational cell is tracked throughout the domain. The VOF model can be applied to special flows like: the motion of large bubbles in liquid, free-surface flows, jet breakup and the steady and tracking of any liquid-gas interface.

The mixture model is a simplified model that is used to simulate multiphase flows where the phases move at different velocities. It is also possible to use this model for homogeneous

multiphase flows where all phases move at the same velocity. In practical it can be used for lots of applications including settling, cyclone separators, and bubbly flows where the gas volume fraction remains low. The limitation of this model is that only one of the phases can be defined as a compressible ideal gas and also solidification and melting cannot be modeled with the mixture model. However there is no limitation on using compressible liquids using user-defined functions. The Eulerian multiphase model is used for the modeling of multiple separate phases that could interact with each other. The phases can be liquids,

modeling of multiphase model is used for the modeling of multiple separate phases that could interact with each other. The phases can be liquids, gases, or solids in nearly any combination. However compressible flow, inviscid flow, melting and solidification are not allowed.

In CO_2 capturing technology, it is required to condense water vapour in a flue gas which contains principally CO_2 as a non-condensable gas. So in this case there is a binary gas mixture which one phase can condense (H_2O) and the other one stands as non-condensable phase. Among these models, the Eulerian multiphase model is the most suitable ones for this case modeling. So the Eulerian multiphase model has been employed in the current study to simulate the condensation.

NUMERICAL SIMULATION

The Governing equations for the problem are continuity equation, general transport equation and energy equation that are solved using Fluent software. The continuity equation for phase i in vector form is:

$$\begin{split} \frac{\partial}{\partial t}(\alpha_{i}\rho_{i}) + \nabla \cdot (\alpha_{i}\rho_{i}\overrightarrow{v}_{i}) &= \sum_{p=1}^{n} (\dot{m}_{jiq} - \\ \dot{m}_{ij}) + S_{i} \end{split} \tag{1}$$

Where \vec{v}_i is the velocity of phase i and \dot{m}_{ji} characterizes the mass transfer from the jth to ith phase, and \dot{m}_{ij} stands for the mass transfer from phase i to phase j.

The momentum balance for phase j is:

$$\begin{split} \frac{\partial}{\partial t} (\alpha_{i} \rho_{i} \vec{v}_{i}) + \nabla \cdot (\alpha_{i} \rho_{i} \vec{v}_{i} \vec{v}_{i}) &= -\alpha_{i} \nabla p + \nabla \cdot \tau_{i} + \\ \alpha_{i} \rho_{i} \vec{g} + \sum_{j=1}^{n} (\vec{R}_{ji} + \dot{m}_{ji} \vec{v}_{ji} - \dot{m}_{ij} \vec{v}_{ij}) + \\ (\vec{F}_{i} + \vec{F}_{lift,i}) \end{split} \tag{2}$$

Where τ_i is the ith phase stress-strain tensor and is expressed by following relation:

$$\tau_{i} = \alpha_{i} \mu_{i} \left(\nabla \vec{v}_{i} + \nabla \vec{v}_{i}^{T} \right) + \alpha_{i} \left(\lambda_{i} - \frac{2}{3} \mu_{i} \right) \nabla \cdot \vec{v}_{q} \bar{l}$$
(3)

 μ_i and λ_i are the shear and bulk viscosity of phase i, \vec{F}_i is an external body force, $\vec{F}_{lift,i}$ is a lift force, \vec{R}_{ji} is an interaction force between phases, and p is the pressure shared by all phases. \vec{v}_{ji} is the interphase velocity and depends on m_{ji} as follows. If $m_{ji} > 0$ that means phase j mass is being transferred to phase i then $\vec{v}_{ji} = \vec{v}_j$ and if $m_{ij} < 0$ that means phase i mass is being transferred to phase j, $\vec{v}_{ji} = \vec{v}_i$. This is similarly valid for \vec{v}_i .

The conservation of energy in multiphase applications comprises of a separate enthalpy equation for each phase:

$$\frac{\partial}{\partial t}(\alpha_{i}\rho_{i}h_{i}) + \nabla \cdot (\alpha_{i}\rho_{i}\vec{u}_{i}h_{i}) = -\alpha_{i} \cdot \frac{\partial p_{i}}{\partial t} + \tau_{i} \cdot \nabla \vec{u}_{i} - \nabla \cdot \vec{q}_{i} + S_{i} + \sum_{j=1}^{n} (\vec{Q}_{ij} + \dot{m}_{ji}h_{ji} - \dot{m}_{ij}h_{ij})$$
(4)

Where h_i is the specific enthalpy of the i^{th} phase, \vec{q}_i is the heat flux, S_i is a source term that includes sources of enthalpy. Q_{ji} is the intensity of heat exchange between the j^{th} and i^{th} phases, and h_{ij} is the interphase enthalpy. The heat exchange between phases must comply with the local balance conditions $Q_{ii} = -Q_{ij}$ and $Q_{ii} = 0$.

Built-in discretisation method included in Fluent is used to treat the above transport equations

A segregated solver is used for simulation that employs the finite volume of discretization process. The governing equations are solved sequentially. As these equations are inherently nonlinear, several iterations loop should be performed before a converged solution is obtained. Second order upwind solution is applied for momentum equation, turbulent kinetic energy, turbulent dissipation and energy equation.

Boundary conditions

In any CFD simulation, it is important to examine the mesh-independency of solution. So the mesh was checked at a certain condition by refining it and also local solution adaption features included in Fluent was used to achieve better solution. As it was mentioned earlier, the condensation rate can be calculated by two methods: 1- Mass flux in cell 2- diffusion rate law (which is known as Fick's law)

It was found that the condensation rate remains constant in the diffusions model, while it changes according to cell's dimensions change in the mass flux model. The reason is that the amount of mass flux passing through each cell depends on the cell size. It means a bigger cell size results in higher mass flux. Especially it could be a challenge in complex geometries such as what we have in a real condenser as it would be difficult to determine which mesh size is the most appropriate one.

So to prevent the errors from mesh refining, the diffusion Model was implemented for simulation of water vapour condensation from CO₂/H₂O mixture gas.

There are few inputs required in Fluent that should be set. These are including physical model definition, defining of the boundary conditions related to the condensing surface and parameters related to the UDF. All of the boundary conditions are illustrated in the Figure 4.

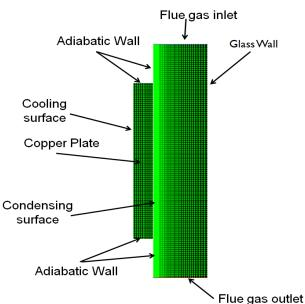


Figure 4 Illustration of solution domain and boundary condition

A fine mesh containing up to 13000 cells were created and it was refined in the vicinity of the condensing surface. This mesh refinement is adopted for the non-condensable gas accumulation in the vicinity of the wall that creates a boundary layer and water vapour should diffuse through it to condense. It was

assumed that vapor condensates only on the surface of the plate. To remove the effect of developing flow and also inverse-flow some extra adiabatic sections were added to the solution domain.

The flue gas phase is defined as fluid mixture containing water vapor and CO_2 gas. A velocity inlet considered as boundary condition at the inlet zone. Moreover, the flue gas inlet temperature and the corresponding vapor mass fractions of each component (y_{co2} and y_{h2o}) should be defined at inlet. The mixture outlet boundary condition was set to pressure outlet.

Moreover these assumptions were made prior to simulation:

- 1- In laminar condensation, the condensate film affect on the heat resistance between the gas stream and coolant surfaces is negligible and lesser than five percent.
- 2- It is assumed that the water condensation occurs only on the surface of the condensing plate. Also the volumetric condensation of water vapour itself is neglected as its amount is much fewer in comparison to surface condensation.
- 3- The gravity effect on flow field is considered.
- 4- The physical properties of the CO₂ and H₂O components in the flue gas were defined as a function of the temperature.
- 5- The physical properties of the mixture are defined depending on the mixture composition.

RESULTS AND DISCUSSION

First model was run with a binary mixture of air and water vapor. This is done first to evaluate the model and compare results with available data [9]. Heat transfer coefficient is presented in Figure 5 as a function of mass fraction of air at inlet.

It was found that there is good agreement between experimental equation and results obtained from numerical modeling in Fluent. Based on these results, the flue gas mixture then changed to CO₂/H₂O and appropriate material properties supplied to the model.

Heat transfer coefficient along the plate length is plotted in Figure 6. This graph is based on a case with high CO₂ mass fraction at inlet. It is seen that The value of heat transfer coefficient is too low and it has a sharp reduction to a certain value and remains constant after a special point of surface. The reason is that a non condensable CO₂

boundary layer has been formed and water vapour should diffuse through this layer to reach to condensing surface.

The model also showed that average heat transfer coefficient is sensitive to inlet velocity at low speeds. At higher inlet velocity (more than 1.5 m/s) the velocity effects is low. However With lower CO₂ mass fraction at inlet, this can be an affecting parameter as well.

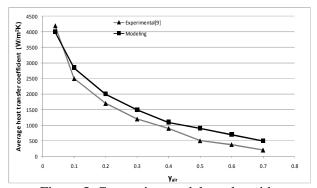


Figure 5 Comparing model results with experimental data ($\Delta T_{w-g} = 18^{\circ}C$, P = 1bar)

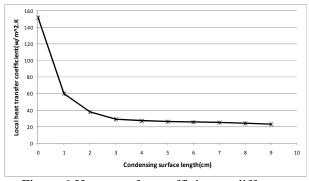


Figure 6 Heat transfer coefficient at different location along the condensing plate

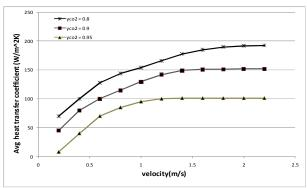


Figure 7 Average heat transfer coefficient as a function of inlet velocity and CO₂ mass fraction

Condensation rate shows more sensitivity to inlet velocity. Ideal diffusion coefficient is used for modeling. As it seen in the Figure 8 there is direct relation between inlet velocity and rate of condensation. Also lower inlet temperature causes higher condensation rate. It is natural, as water vapour reach to saturation temperature with less heat removal.

It was tried to implement the performed procedure in the proposed model for condenser. But it was found that unstructured property of mesh prevents to implement such kind of condensation in reality and it requires to make more complicated model that effort and time does not fit our research frame. However the flow filed and temperature gradients were predicted and a general mass and energy

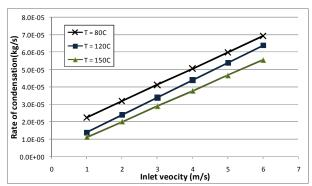


Figure 8 Condensation rate as a function of inlet velocity and inlet temperature

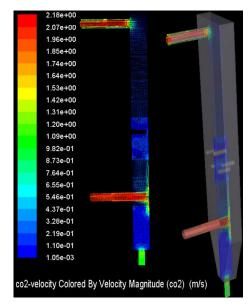


Figure 9 Velocity Profile inside the condenser model

calculation showed that results are satisfactory. Though the final tuning and results verification for a real design that would be implemented in a oxy fuel plant (or anywhere else, with similar process property) requires experimental data.

CONCLUSION

The present paper implements the numerical model for the water film condensation from a binary CO_2/H_2O mixture on a plane vertical surface considering the non-condensable gas (CO_2) effect. Results of the present model's prediction are compared with available correlation and modeling results in the literature.

- 1) Implementing the diffusion model in Fluent is capable to calculate condensation from steam and CO₂ mixture.
- 2) Surface condensation on the vertical walls can be modeled by specifying satisfactory boundary conditions.
- Condensation rate decrease along the surface as the film thickness get ticker and also the noncondensable gas layer develops simultaneously.

Theoretical and numerical study shows that in principle, it is possible to model the surface condensation using Fluent. However, this requires really good experimental data that should be inserted into the model as boundaries. Also this would require use of Eulerian model provided in the software. However it should be noted that Eulerian multiphase model is one of the most advanced models in the Fluent and requires quite a bit of experience to handle and modification of this model to suit condensation process, which itself is a very complex process, would requires a structured mesh with controlled near wall concentration of meshes. This is not an easy job when it comes to a real condenser that involves complex geometry and it most of the cases it is not possible to produce structured mesh for it.

Finally it should be noted here that the accuracy of the Fluent results depends highly on the empirical correlations specified to model the condensation process. In the industry, there is a practice to model the process with some correlations available in the open literature and then tweak various parameters to get a good agreement with the experimental results. Such a tuning is necessary most of the cases, as the general correlations may not yield accurate results for a specific set up. It

would be the same for Numerical simulation. It is required to accomplish the model with a same experimental setup in order to verify results.

It would be advisable that for applications like oxy fuel plants (as it was mentioned in introduction) choosing a condenser based on Fluent results may be a difficult task, especially if experimental data is not available. Because then it would become difficult to check the validity of the empirical correlation that is used. So this would be a high expensive method to study such kind of flow regime. However, it is possible to study the flow field and temperature profile in the real condenser. Then a simple plane condensation model like what is presented here in this study can be used for parameter study using the real data for the flue gas. These data include operation pressure, mixture gas composition, and inlet temperature and inlet mass flow rate.

ACKNOWLEDGMENTS

We would like to acknowledge the use of Fluent Inc.'S solver in the current work.

REFERENCES

- [1] Murlidhar Gupta, Irene Coyle and Kelly Thambimuthu, *Thermal CO2 Capture Technologies and Opportunities in Canada*, 1St Canadian CC&S Technology Roadmap Workshop, 18-19 September, Calgary, Alberta, Canada, 2003
- [2] Hailong Li, Jinyue Yan, Thermodynamic Properties of CO2 Mixtures and Their Applications in Advanced Power Cycles with CO2 Capture Processes, PhD thesis, ISBN 978-91-7415-091-9, KTH, Sweden, 2008
- [3] A.Tanrıkut and O. Yeşin, *In-Tube Steam Condensation in the Presence of Air*, NUREG/IA-0184, US-NRC, 2000.
- [4] G. Yadigaroglu, *CMFD* (a brand name) and other acronyms, Int. J. Multiphase Flow, 29, pp. 719–720, 2003
- [5] Charlotte Wilhelmsson, Jinliang Yuan, Bengt Sundén, Water condensation and two-phase flow modeling for a plate heat exchanger

- *channel*, ASME International Mechanical Engineering Congress and Exposition, Seattle, USA, 2007
- [6] Ivo Kljenak, Miroslav Babi'c, Borut Mavko, Ivan Bajsi', Modeling of containment atmosphere mixing and stratification experiment using a CFD approach, Nuclear Engineering and Design 236, pp 1682–1692, 2006
- [7] Krzysztof Karkoszka, Mechanistic Modeling of Water Vapour Condensation in Presence of Noncondensable Gases, Doctoral thesis, School of Engineering Sciences, Department of Physics, Div. of Nuclear Reactor Technology, KTH, Stockholm, 2007.
- [8] FLUENT 6.2, User's Guide, 2005
- [9] Dehbi AA., Golay MW, Kazimi MS, Condensation experiments in steam-air steam-air helium mixtures under turbulent natural convection. National Conference of Heat Transfer, AIChE Symp., 87(283), pp19–28, 1991.

Modelling of the channelling phenomenon of the pulping digester using porous media

Bijan Pourian, Erik Dahlquist School of Sustainable Society and Technology Development, Malardalen University (Vasteras, Sweden)

<u>Bijan.pourian@yahoo.com</u> Erik.dahlquist@mdh.se

Abstract

This paper describes the development of a dynamic model of a continuous pulping digester to characterize the channeling phenomenon. The CFD codes in FLUENT are used to compute the hydraulic behavior of the digester under both normal and various specific operating conditions. Included in this model are all the circulation flows, extractions and multiple inlets and outlets.

The digester is designed in Gambit and an axisymmetric 2d model of the digester is applied. A porous scheme is implemented in the model in order to design the fluid flow and channeling phenomenon inside the digester. A heterogeneous porous media is specified in order to take into account the compression of the pulp. The simulation can be used as a prognostic model to predict risky situations and thereby reduce economic damage. The k- ϵ turbulent model contributes to computation of the flow "regimes" or eddie formation in turbulent zones of the digester.

Key words

CFD, channeling, porous media, turbulent, axisymmetric, pulping digester

Nomenclature

C	Prescribe material
D	Prescribe material
d	Diameter
F_{X}	External body force
\overrightarrow{F}	
I	Body force (N)
G	Elasticity modulus

g	Gravitational acceleration
	(m/s^2)
G_k	Generation of turbulent
	Kinetic energy due to mean
	velocity gradient
G_b	Generation of turbulent
	kinetic energy due to
	buoyancy
k	Turbulent kinetic energy
r	Radial coordinate
S_{i}	Momentum sink
S_{m}	Mass added to continuous
	phase from dispersed phase
$X \rightarrow$	Axial coordinate
v_m	Mass-averaged velocity
V_{Z}	Swirl velocity
v	Magnitude of velocity
V_X	Axial velocity
v_r	Padial valocity
	Radial velocity
ρ	Density
	•
ρ	Density
$ ho \ arepsilon$	Density Turbulent dissipation rate

α_k Volume fraction of phase k **Introduction**

Modelling of the pulping digester has been of interest to many researchers from different areas. The digester is the major element of the pulping process. Pulp production develops in stages and different modes of cooking may occur in the digester.

The economic consequences of any disruption in the pulping process can be

1

severe. The details of the pulping process are still largely unknown and many studies have been performed to understand what really happens inside the digester.

The studies initiate from those of Vroom [1], who modelled the H-factor. The Purdue model was later established by Smith et al. [2]. This was a new approach to modelling this process and many researchers followed with improvements. The model was modified by taking different aspects of pulp processing into account and implementing them into the Purdue model. Johansson [3] implemented a temperature dependent diffusivity into the model. Hartler applied a pH dependent the Purdue diffusivity into model. Gustafson [4] improved Johansson's model by using three cooking kinetic reactions instead of a single equation.

Christinsen [5] developed kinetic models that took the wood used in the digester into account.

Harkonen [6] derived a multiphase model for use within the Purdue model.

Michelsen [7] combined the Harkonen and Christinsen models to create a more detailed model.

The study described in this paper is based on models applying commercial CFD codes within FLUENT.

The digester is a moving bed reactor where the wood chips are fed in from the top and the liquor has several inlets and outlets at the bottom, top, and around the digester. The wood chips consist of fibres, lignin and extractives. The lignin which holds the cells together reacts with the liquor chemicals and transfers to the liquid phase. The fibres within the wood chips are freed when the lignin is removed to the liquid phase. The free fibres are called pulp. In suspension solutions or granular flows, the motion of particles establishes a pressure gradient in the solution if the packing limit of the solid particles is less than the maximum allowable value of 0.63.

When the packing limit of the solid is less than the 0.63, the solid phase is compressed and a pressure gradient of the solid particles is produced independently (∇p_s). The pressure gradient is introduced by the granular momentum. The solid particles follow the Maxwell-Boltzmann distribution which is a probability distribution.

The pulping digester, shown in Figure 1, has a height of around 65 m and a diameter of 6 m at the top and of around 7 m at the bottom. The diameter increases stepwise from top to bottom.

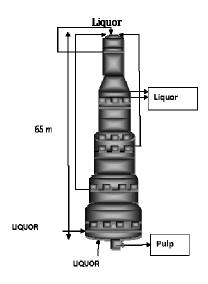


Figure 1. The pulping digester.

The compressibility of the pulp arises as a result of the transfer of the lignin to the liquid phase. The compressibility contributes a unidirectional stream of liquor in the digester. The liquor is not evenly distributed throughout the chip bed, but forms channels through it. The liquor then follows the path of least resistance. The channel formation leads to some of the wood chips not having contact with the liquor. As a consequence, dissolution of lignin declines, a non-uniform cooking develops in the digester and the channel blocks the flow of the chips and disrupts the process. A heterogeneous porous media is specified

in the digester model to represent the

compressibility of the solids. Decomposition of the wood develops when lignin is removed from the chips. The chemical dissolution process makes the chips soft and more compact. In order to model the deformation of the wood chips, the digester is divided into small sections which contribute to define different porosities in these regions. In order to investigate the behaviour of the liquor as it moves down the chip bed, the prescribed porosities are highest at the top and reduce down the digester. The void volume between the chips is called the free liquor. As the lignin dissolves, the chip bed is compressed and the free space between the chips decreases. The volume fraction of the chips in the cooking blocks increases and the volume fraction occupied by the free liquor decreases.

Governing equations

The continuity equation for 2D axisymmetric geometries (mass conservation equation)

$$\frac{\partial \rho}{\partial t} + \frac{\partial}{\partial x} (\rho v_x) + \frac{\partial}{\partial r} (\rho v_r) + \frac{\rho v_r}{r} = S_m \quad (1)$$

Axial Momentum conservation equation for 2D axisymmetric geometries

$$\begin{split} &\frac{1}{r}\frac{\partial}{\partial x}(r\rho v_{x}v_{r}) + \frac{1}{r}\frac{\partial}{\partial r}(r\rho v_{r}v_{x}) = \\ &\frac{\partial p}{\partial r} + \frac{1}{r}\frac{\partial}{\partial x}\left[r\mu\left(2\frac{\partial v_{x}}{\partial x} - \frac{2}{3}(\nabla.\vec{v})\right)\right] \\ &+ \frac{1}{r}\frac{\partial}{\partial r}\left[r\mu\left(\frac{\partial v_{x}}{\partial r} + \frac{\partial v_{r}}{\partial x}\right)\right] + F_{X} \end{split} \tag{2}$$

Radial Momentum equation

$$\frac{1}{r}\frac{\partial}{\partial x}(r\rho v_{x}v_{r}) + \frac{1}{r}\frac{\partial}{\partial r}(r\rho v_{r}v_{r}) =
\frac{\partial p}{\partial r} + \frac{1}{r}\frac{\partial}{\partial x}\left[r\mu\left(\frac{\partial v_{r}}{\partial x} + \frac{\partial v_{x}}{\partial r}\right)\right]
+ \frac{1}{r}\frac{\partial}{\partial r}\left[r\mu\left(2\frac{\partial v_{r}}{\partial r} - \frac{2}{3}(\nabla \cdot \vec{v})\right)\right] -
2\mu\frac{v_{r}}{r^{2}} + \frac{2}{3}\frac{\mu}{r}(\nabla \cdot \vec{v}) + \rho\frac{v_{z}^{2}}{r} + F_{r}$$
(3)

Porous momentum sink

Increased porosity reduces flow velocity due to generation of a pressure gradient in the cell zones. This is accounted for in the model by including an additional source term in the fluid flow equations. The source is a flow resistance and consists of two terms that are empirically determined. A viscous loss term and an inertial loss term are included in the momentum equation in the porous cell zones.

$$S_{i} = \left(\sum_{j=1}^{3} D_{ij} \mu v_{j} + \sum_{j=1}^{3} C_{ij} \frac{1}{2} \rho |v| v_{j}\right)$$
(4)

Turbulent kinetic energy

$$\frac{\partial}{\partial t}(\rho k) + \frac{\partial}{\partial x_i}(\rho k u_i) =$$

$$\frac{\partial}{\partial x_i} \left[\left(\mu + \frac{\mu_t}{\sigma_k} \right) \frac{\partial k}{\partial x_i} \right] + \tag{5}$$

$$G_k + G_b - \rho \varepsilon - Y_M + S_K$$

Turbulent dissipation rate

$$\frac{\partial}{\partial t}(\rho \varepsilon) + \frac{\partial}{\partial x_{j}}(\rho a u_{j}) = \frac{\partial}{\partial x_{i}} \left[\left(\mu + \frac{\mu_{t}}{\sigma_{o}} \right) \frac{\partial \varepsilon}{\partial x_{i}} \right] +$$

$$C_{1\varepsilon}\frac{\varepsilon}{k}(G_kC_{3\varepsilon}G_b)-C_{2\varepsilon}\rho\frac{\varepsilon^2}{k}+S_{\varepsilon}$$

Reynolds number

(6)

$$Re = \frac{\rho u d}{\mu} \tag{7}$$

Homogenous porous media

$$S_{i} = \left(\frac{\mu}{\alpha}v_{i} + C_{2}\frac{1}{2}\rho|v|v_{i}\right) \tag{8}$$

Darcy's law in porous media

$$\nabla p = -\frac{\mu}{\alpha} \vec{v} \tag{9}$$

Inertial loses in porous media

$$\nabla p = -\sum_{i=1}^{3} C_{2ij} \left(\frac{1}{2} \rho v_{j} |v| \right)$$
 (10)

Modeling set up

A turbulent model and a heterogeneous porous media are defined for the digester. In the porous media the flow velocity decreases but generation of turbulence and the dissipation rate are still modelled through the media by the default approach in FLUENT. It is not necessary to restrict the turbulence in any zone in the porous media. In order to suppress the turbulence in any zone it is sufficient to activate the "laminar zone" in the fluid panel of that zone. In this way the turbulent viscosity (μ_t) is considered zero in that section. The turbulence created in the porous media does not affect the momentum of the flow. The turbulent elements transport through the porous zones. The inertial loss term of the momentum sink is activated and specified for each porous section of the digester in both x and y directions. A porosity range is defined from 0.65 to 0.25, to account for the distribution of the fluid flow through the particles.

The effect of gravity is taken into account and a value of 9.8 m/s^2 is specified for gravitational acceleration in the positive x direction.

Results Channelling

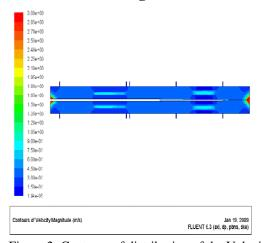


Figure 2: Contours of distribution of the Velocity inside the digester from top to bottom

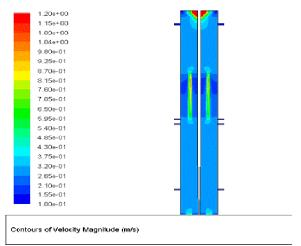


Figure 3: Contours of distribution of the Velocity at the top of the digester

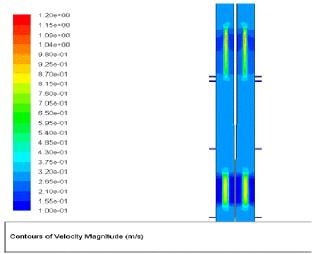


Figure 4: Contours of distribution of the Velocity in the two formed channels

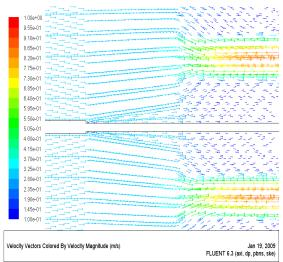


Figure 5: Contours of distribution of the Velocity vectors at the entrance of the channel

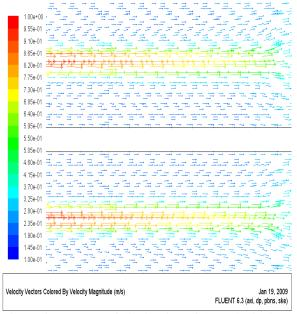


Figure 6: Contours of distribution of the Velocity in the channel

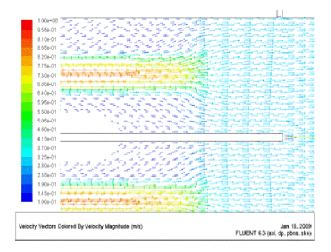


Figure 7: Contours of distribution of the Velocity vectors around the outlet of the lower channel

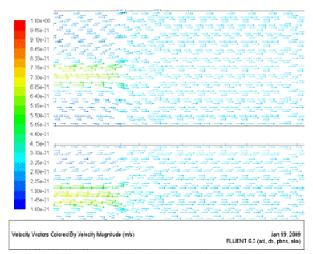


Figure 8: Contours of distribution of the Velocity vectors around the outlet of the upper channel

Discussion

Due to the unique geometric design of the reactor, the heterogeneous reaction, the hydraulic characteristics of the zones, long residence time, and the multiple inlets and outlets it is not unreasonable to assume that different flow regimes are present in different zones within the digester. In some sections the flow is unidirectional and downward and in others the flow runs against this current. These unique characteristics contribute to the formation of a double flow regime in the digester.

Therefore, assigning an exclusive flow regime to characterize the digester is an ineffective approach. Multiple Reynolds numbers may be accounted for in the multiple inlets of the digester. The free liquor flow through the chips bed follows the laminar flow regime at the top and middle of the digester. Very low velocities are observed throughout the digester despite the high velocities at the inlets. This may be due to the solid phase, which is itself mobile, and leads to a momentum exchange with the fluid flow, and also

behaves as a porous media for the liquid phase and considerably reduces its momentum. The Reynolds numbers at the inlets are defined at between 40000 and 70000. The inlet diameters are 0.35, 0.30, 0.20 and 0.16m. The viscosity is around 0.001 kg/m s

A k-ɛ turbulent model is defined due to the presence of the counter-current flow in the bottom of the digester which results in a turbulent regime. Applying a turbulent model contributes to the computation of small eddies in the lower zones of the digester.

The velocity of the liquor increases in the channels as shown by the "velocity magnitude" and "vectors of the velocity" in Figures 2 to 8.

When the liquor flow enters the channel its velocity increases due to the elimination of the momentum sink and the low amount of wood chips in the channels, as shown in Figures 2-4. When the liquor leaves the channel the velocity decreases again due to the presence of wood chips at its path, as shown in Figures 7 and 8. Inside the channel the velocity is higher at the beginning and decreases gradually as shown in Figure 6. The velocity inside the channel has a negative gradient in the vertical direction. The reaction of the lignin and liquor takes place at high temperatures of above 150 °C. One study where the temperature of the washing screen was measured showed a large variation in its temperature before and after the channeling [8].

The model of the channeling can be used to locate the channels by comparing the operating parameters before and after channeling. Channeling affects operating conditions such as the outlet flow rate, pressure and temperature.

Any deviation of these parameters from the normal operational conditions may indicate channelling. However, the magnitude of the deviation that indicates channelling must be determined because the normal operating conditions are unsteady and only deviations over a certain magnitude may indicate channelling.

Conclusion

A pulping digester has been modelled to examine the destructive phenomenon of channeling. An artificial channel modelled in the digester using a porous media model. A heterogeneous porous media is defined to represent the solid phase and its compressibility. Compared to a homogenous solid phase, using the heterogenous solid phase has the effect of increasing the volume fraction of the liquid phase in the channel while reducing the porosity outside of the channel. The channels are characterized by defining a very high porosity in the digester.

The flow behaviour is examined around and inside the channel. The results of the modelling show that the liquor velocity is higher inside the channel than outside it.

This effect can affect the circulation flow in the pipes which may be an indicator of dangerous conditions.

The liquor velocity around the channel decreases and the circulation flows which are located along the channel degenerate. However, the mass flow rate in the circulation pipes under the channel would be expected to increase under these conditions. This can lead to a pressure drop

in the pipes along the channel and an increased pressure in the pipes that are located under the channel.

These pressure changes are important parameters for the operation of the digester, and calculation of their magnitudes is an important topic for future studies.

Channel modelling improves our knowledge of the hydraulic behaviour of the pulping digester which can assist in diagnosis of dangerous operating conditions and implementation of evasive action.

References

- [1] Vroom, K, E, "The 'H' factor: A means of expressing cooking times and temperatures as a single variable," pulp and paper Mag. Can., Convention, Issue 1957
- [2] C.C. Smith, T.J. Williams, Mathematical modelling Simulation and control of the operation of kamyr continuous digester for Kraft process, Tech. Rep. 64, Purdue University, West Lafayette, USA (1974)
- [3] Johansson L, Mathematical models of the Kraft cooking process Acta Polytechnica, Scandinavia Math. Comput. Mach. Ser. No. 22, Stockholm 1971
- [4] R.R Gustafson, C.A. Slelcher, W.T. Mc Kean and B.A. Finalyson, Theoretical model of the Kraft pulping process, Ind. Eng. Chem. Process Des. Develop. 22 (1983)
- [5] Tor Christinsen, Clifford C. Smith, Lyle F. Albright, T. J. Williams, Dynamic modelling of the Kamyr digester: normal operation including hardwood-softwood

- swings, Tappi J. vol. 66, no.11, (1983), p 65-68
- [6] E.A. Harkonen, A mathematical model for two phase flow in a continuous digester, Tappi J. 70 (1987) 70(12) 122-126
- [7] F.A. Michelsen and B.A Foss, Modelling and simulation of the mass flow and reaction kinetics in a continuous Kamyr steam/liquor phase digester, Modelling identification and control,1994, vol. 15, no.1, 33-53
- [8] Toivonen, M., Optimization of the conditions in continuous cooking. Master thesis, Helsinki University of Technology, Finland, 2004. 60 p.

Refrigeration 1



IMPLEMENTATION OF THE KURGANOV-TADMOR HIGH RESOLUTION SEMI-DISCRETE CENTRAL SCHEME FOR NUMERICAL SOLUTION OF THE EVAPORATION PROCESS IN DRY EXPANSION EVAPORATORS

S. Madsen*, C.T. Veje, and M. Willatzen Mads Clausen Institute for Product Innovation University of Southern Denmark Alsion 2, DK-6400, Sønderborg, Denmark

ABSTRACT

A set of partial differential equations is derived in mass flow, enthalpy, pressure, and evaporator wall temperature based on the continuity equation, Navier-Stokes equations, and the energy equation for the refrigerant in addition to the heat exchange equation for the wall (the latter accounts for convective heat exchange with the refrigerant and the ambient). The combination of pressure and enthalpy thermodynamic variables allows for complete specification of the thermodynamic state spatially and temporally in the different zones in the evaporator. Details on the implementation of the Kurganov-Tadmor scheme for the governing equations are given and results are shown for step-responses in inlet mass-flow and outlet volume-flow.

Keywords: Evaporator modeling, Discretization scheme, Two-phase flow

INTRODUCTION

The growing concern for consumption of world energy resources and related global warming emphasizes the continuing need for increasingly higher efficiencies of energy consuming systems. Modeling and simulation of these systems is an important way of addressing this optimization problem, however, it requires a certain degree of model detail depending on the specific phenomena to be investigated. As conventional refrigeration and heat pump components approach an increasing level of maturity there is limited potential in individual component optimization as compared to a total system optimization. The benefits in carrying out such efforts are described in, e.g., Refs. [1, 2].

Two main components in the aforementioned systems are the heat exchangers which are usually subject to two-phase flow and heat transfer. Traditionally, component models for condensers and evaporators are solved using NTU- ε - methods with a fixed UA (or heat transfer coefficient) for the com-

*Corresponding author: E-mail:sma@mci.sdu.dk

ponent. The need to investigate control strategies of these systems demands realistic modeling of parameters such as superheat or subcooling hence giving rise to a widespread use of moving-boundary models [3, 4, 5]. The latter models show an advantage in demonstrating dynamical behavior of the component in relation to capacities, temperature, and pressure levels although formulated as lumped models. At the same time, the lumping also renders these models computationally fast and makes them well suited for evaluation of system control and for model predictive control. The drawback is loss of detail in the modeling and the handling of fluid-zone switching with resulting numerical obstacles.

In an effort to investigate the dynamic behavior of two-phase refrigeration-cycle systems we are seeking a mathematical formulation that provides a stable numerical solution despite a dynamically changing number of fluid zones. We further seek to capture detailed dynamics in the heat exchange between refrigerant and evaporator wall. To this end several works have been carried out on fully distributed

models solving the governing equations [6, 7, 8]. Generally, the fast dynamics of the full set of governing equations are neglected (such as pressure waves) allowing for faster computation times and numerically stable codes. Recently similar models have been used for the analysis of distribution phenomena in multi-pass evaporators [9].

In the present paper, we aim to provide a modeling framework that captures all the dynamics of the full set of governing equations and the characteristics of the components while still being numerically stable and efficient. In the first approach this includes resolving the fast dynamics of pressure propagation which may later be taken out for simplification. This is accomplished by applying the Kurganov-Tadmor (KT) scheme [10] with appropriate boundary conditions. The major strengths of the KT scheme are simplicity (e.g. non-staggered and free from Riemann solvers) and stability, the latter being a major issue with standard methods. The scheme can be formulated as a system of ODEs allowing simple integration in complete system models.

MODEL EQUATIONS

In the following, a set of partial differential equations is derived describing evaporator dynamic operation. We use the continuity equation, Navier-Stokes equations, and the energy equation [4]

$$\frac{\partial \rho}{\partial t} + \frac{\partial (\rho w_k)}{\partial x_k} = 0, \quad (1)$$

$$\frac{\partial (\rho w_i)}{\partial t} + \frac{\partial (\rho w_i w_k)}{\partial x_k} = -\delta_{ik} \frac{\partial P}{\partial x_k} + \frac{\partial \sigma'_{ik}}{\partial x_k} + \rho g_i, \quad (2)$$

$$\rho \left(\frac{\partial h}{\partial t} + w_i \frac{\partial h}{\partial x_i} \right) - \left(\frac{\partial P}{\partial t} + w_i \frac{\partial P}{\partial x_i} \right) =$$

$$\sigma'_{jk} \frac{\partial w_j}{\partial x_k} + \frac{\partial}{\partial x_j} \left(\kappa \frac{\partial T}{\partial x_j} \right), \quad (3)$$

where ρ , w_i , P, h, T, σ'_{ik} , g_i , κ , x_i , and t are the refrigerant mass density, refrigerant velocity, refrigerant pressure, refrigerant enthalpy, refrigerant temperature, the viscous tensor, the gravitation constant, the refrigerant thermal conductivity, the coordinate vector, and time, respectively. Einstein summation convention is employed in Eqs. (1)-(3).

To simplify the problem, we shall assume next that viscous heating in Eqn. (3) is neglected, that gravity effects are unimportant, and that variations in physical properties basically take place along one coor-

dinate direction (the length direction of the evaporator). Then, we have

$$\frac{\partial \rho}{\partial t} + \frac{\partial (\rho w)}{\partial z} = 0, \quad (4)$$

$$\frac{\partial (\rho w)}{\partial t} + \frac{\partial (\rho w^2)}{\partial z} = -\frac{\partial P}{\partial z} - \left(\frac{\partial P}{\partial z}\right)_{fric}, \quad (5)$$

$$\rho \left(\frac{\partial h}{\partial t} + w \frac{\partial h}{\partial z}\right) - \left(\frac{\partial P}{\partial t} + w \frac{\partial P}{\partial z}\right) = \frac{4}{D} \alpha_i (T_W - T), \quad (6)$$

where $(\partial P/\partial z)_{fric}$ is a friction factor correlation depending on local properties and conditions and w is the one-dimensional velocity along the evaporator length coordinate and the heat-transfer coefficient satisfies

$$\alpha_i \equiv \frac{D_i}{4} \frac{\partial \left(\kappa \frac{\partial T}{\partial n}\right)}{\partial n} \frac{1}{T_W - T},\tag{7}$$

with D_i , T_W , and n being the evaporator inner diameter, wall temperature, and normal direction, respectively.

We now recast the above equation set in terms of new variables (pressure, mass flow, and enthalpy) $P, \dot{m} = \rho A w$, and h

$$\frac{\partial \rho}{\partial P}|_{h}\frac{\partial P}{\partial t} + \frac{\partial \rho}{\partial h}|_{P}\frac{\partial h}{\partial t} + \frac{1}{A}\frac{\partial \dot{m}}{\partial z} = 0, \quad (8)$$

$$\frac{1}{A}\frac{\partial \dot{m}}{\partial t} + \frac{\partial \left(\frac{\dot{m}^2}{\rho A^2}\right)}{\partial z} = -\frac{\partial P}{\partial z} - \left(\frac{\partial P}{\partial z}\right)_{fric},\tag{9}$$

$$\rho \left(\frac{\partial h}{\partial t} + \frac{\dot{m}}{\rho A} \frac{\partial h}{\partial z} \right) - \left(\frac{\partial P}{\partial t} + \frac{\dot{m}}{\rho A} \frac{\partial P}{\partial z} \right) = \frac{4}{D_i} \alpha_i (T_W - T), \quad (10)$$

keeping in mind that $\rho \equiv \rho(P,h)$, $T \equiv T(P,h)$, and we have assumed that the cross-sectional area A does not depend on z. We need an additional differential equation in the wall temperature to complete the model framework. This equation is

$$(C_W \rho_W A_W) \frac{\partial T_W}{\partial t} = \alpha_i \pi D_i (T - T_W) + \alpha_o \pi D_o f_{fin} (T_A - T_W) + \lambda A_W \frac{\partial^2 T_W}{\partial z^2},$$
(11)

where C_W , ρ_W , A_W , α_o , A_o , f_{fin} , T_A , and λ are the wall heat capacity, wall mass density, wall cross-sectional area, heat-transfer coefficient between

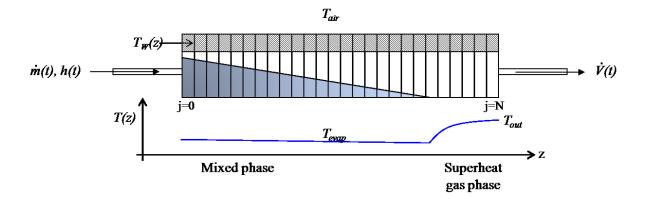


Figure 1: Schematic of evaporator model and dependent variables and parameters.

evaporator wall and ambient, outer diameter, fin factor, ambient temperature, and wall heat conductivity, respectively. The friction term is modelled as

$$\left(\frac{\partial P}{\partial z}\right)_{fric} = \frac{1}{2} f \frac{\dot{m}^2}{\rho A^2} , \qquad (12)$$

with a friction factor f corresponding to a simple model of Darcy–Weisbach friction.

The computational domain and subsequent discretization is indicated in Fig. 1. The above formulation is essentially a homogeneous flow model since we have formulated the equation set in terms of overall density and enthalpy neglecting the separation in gas and liquid phases as is more conventional in modelling two-phase flows [11]. In this first approach we assume a constant heat transfer coefficient independent of flow regime and conditions.

In principle, the only information lacking to completely specify the dependence of \dot{m} , P, h, and T_W as a function of z and t are initial conditions (all variables must be known everywhere in z at t=0) and appropriate boundary conditions at all times. For an evaporator tube of length L we have an inlet massflow at z=0 and an outlet volume flow $\dot{V}=\dot{m}/\rho$ at z=L. The pressure is then determined by the evaporator as a balance of temperatures (heat flow), mass flows and the thermodynamic relations. Pipe wall ends (z=0,L) are insulated, heat-flux conditions and refrigerant enthalpy are specified at the inlet z=0. The mathematical relations are then:

$$\dot{m}(0,t) = \dot{m}_{in} \,, \tag{13}$$

$$h(0,t) = h_{in}, (14)$$

$$\dot{m}(L,t) = \rho(L,t)\dot{V}, \qquad (15)$$

$$\left. \frac{\partial T_W}{\partial z} \right|_{z=0,L} = 0. \tag{16}$$

The above set of equations requires dynamic access to thermodynamic routines giving ρ and T as a function of the (dynamic) values of P and h. Note that P and h (in contrast to P and T) are convenient dependent variables to solve for as they specify all thermodynamic properties including the quality x (i.e., the mass percentage of vapor content in the two-phase region) unambiguously. The present model allows for determining all parameters in the evaporator spatially and dynamically.

NUMERICAL DISCRETIZATION SCHEMES

Straight-forward central finite differences applied to Eqs. (8)-(11) show spurious oscillations which quickly destroy the numerical solution. High-resolution schemes have been developed to avoid such oscillations and allow possible discontinuities in the solutions. We have implemented the KT scheme [10] in the second order semi-discrete form. The KT scheme aims to solve a set of equations:

$$\phi_t + H(\phi, \phi_z) = 0, \tag{17}$$

where ϕ is a vector of functions depending on t and z. The second-order semi-discrete KT scheme can be written as

$$\frac{d\phi_{j}}{dt} = -\frac{1}{2} \left(H(\phi_{j}, (\phi_{z}^{+})_{j}) + H(\phi_{j}, (\phi_{z}^{-})_{j}) \right)
+ \frac{a_{j}}{2} \left((\phi_{z}^{+})_{j} - (\phi_{z}^{-})_{j} \right),$$
(18)

where $z_j = j\Delta z$ with $\Delta z = L/N$ and where j = 0,...,N is the spatial discretization index

 $(\phi_j(t) \approx \phi(j\Delta z, t)), a_j$ is the maximum local speed,

$$(\phi_z^{\pm})_j = \frac{\Delta \phi_{j\pm 1/2}}{\Delta z} \mp \frac{(\Delta \phi_{j\pm 1/2})'}{2\Delta z},$$
 (19)

with

$$\Delta \phi_{i+1/2} = \phi_{i+1} - \phi_i, \tag{20}$$

and

$$(\Delta \phi_{j+1/2})' = \operatorname{minmod} \left(\Delta \phi_{j+1} - \Delta \phi_j, \frac{1}{2} \left(\Delta \phi_{j+1} - \Delta \phi_{j-1} \right), \Delta \phi_j - \Delta \phi_{j-1} \right), \tag{21}$$

where the minmod flux limiter function is defined by

$$\operatorname{minmod}(a,b,c) = \left\{ \begin{array}{ll} \min(a,b,c) & \text{if} \quad a,b,c > 0 \\ \max(a,b,c) & \text{if} \quad a,b,c < 0 \\ 0 & \text{otherwise} \end{array} \right. .$$

More details on the KT-scheme can be found in Ref. [10]. In the following, we will highlight the specific implementation details on evaporator modelling. The KT scheme is applied only to Eqs. (8)-(10). The heat equation (11) is discretized using straight-forward second order finite differences. Time-stepping is done as suggested in Ref. [10] using the modified Euler method. For the maximum local speed of propagation, a_j in Eqn. (18), we use the local speed of sound plus the local flow speed:

$$a_j = \sqrt{\frac{\partial P_j}{\partial \rho}} + \frac{|\dot{m}_j|}{\rho_j A}.$$
 (23)

The second order KT scheme has a five-point spatial stencil. At each boundary, we use two virtual points to implement physical and numerical boundary conditions. For the central second-order finite differences used for the temparature only one virtual point is needed. At the boundaries we employ:

$$\dot{m}_0 = \dot{m}_{in}, \tag{24}$$

$$\dot{m}_N = \rho_N \dot{V}, \qquad (25)$$

$$h_0 = h_{in}, (26)$$

$$T_{W_{-1}} = T_{W_{-1}}, (27)$$

$$T_{W,N+1} = T_{W,N-1},$$
 (28)

to implement the physical boundary conditions in Eqs. (13)-(16). The virtual points for the KT-scheme

numerical boundary conditions are constructed using second-order extrapolation, e.g.,

$$\dot{m}_{-1} = 3\dot{m}_0 - 3\dot{m}_1 + \dot{m}_2 , \qquad (29)$$

which assumes the functions can be approximated by a second-order Taylor series at the boundary. The thermodynamic quantities, T(h,P) and $\rho(h,P)$, are evaluated using Ref. [12]. We generate an interpolation lookup table for fast access to these relations. The working medium is R600a. The derivatives $\frac{\partial \rho}{\partial P}|_h$ and $\frac{\partial \rho}{\partial h}|_P$ are evaluated numerically from values in the lookup table.

SIMULATION RESULTS

Variable/Parameter	Value	Unit
D_i	$6 \cdot 10^{-3}$	m
D_o	$8 \cdot 10^{-3}$	m
f_{fin}	10	[-]
A	$\frac{\pi}{4}D_i^2$	m^2
C_W	385	J/K
$ ho_W$	$8.96 \cdot 10^3$	kg/m ³
A_W	$\frac{\pi}{4}(D_o^2 - D_i^2)$	m^2
λ	386	W/(mK)
$lpha_i$	1000	$W/(m^2K)$
$lpha_o$	100	$W/(m^2K)$
T_A	300	K
f	0.005	[-]
\dot{m}_{in}	$5.3 \cdot 10^{-3}$	kg/s
h_{in}	$2.5 \cdot 10^5$	J/kg
\dot{V}	$1.75 \cdot 10^{-3}$	m^3/s
P(t=0,z)	$1.091 \cdot 10^5$	Pa
T(t=0,z)	263	K
$T_W(t=0,z)$	273	K
h(t=0,z)	$200 \cdot 10^3$	J/kg
$\dot{m}(t=0,z)$	$5.31 \cdot 10^{-3}$	kg/s

Table 1: Parameters, boundary values, and initial data used in the simulations.

In the following, we use the parameters, boundary values, and initial data shown in Table 1. First, we find a steady-state by evolving the initial data in Table 1 until the temporal derivatives become zero (takes approximately 50 s). The resulting steady-state values of \dot{m} , P, h and T_W as function of position z are shown in Fig. 2. The mass-flow is constant over the tube while the pressure decreases and

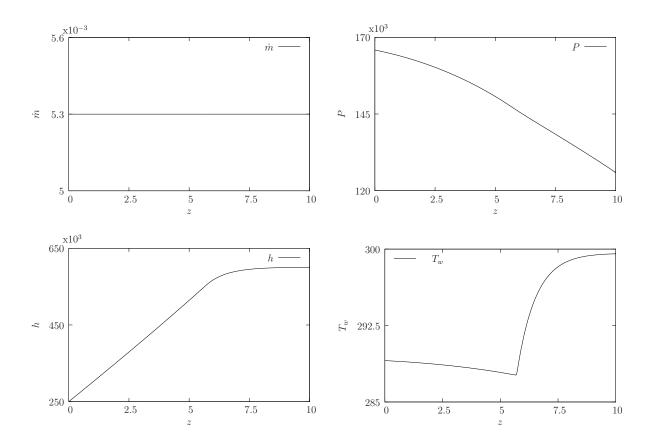


Figure 2: Steady-state solution found after letting the initial data from Table 1 evolve for 50 s. Units are according to Table 1.

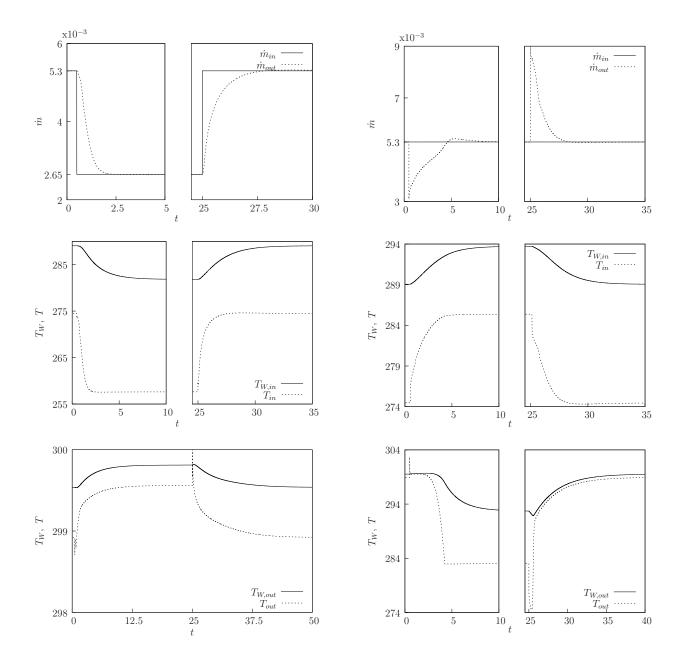


Figure 3: \dot{m} , T_W , and T at z=0 (in) and z=10 m (out) as a function of time when the inlet massflow \dot{m}_{in} is reduced by a factor of two at t=0.5 s and increased again to the initial value ($5.3 \cdot 10^{-3}$ kg/s) at t=25 s. Time axis is broken in upper and middle plot to exclude the non-varying part of the functions. Units refer to Table 1.

Figure 4: \dot{m} , T_W , and T at z=0 (in) and z=10 m (out) as a function of time when the outlet volume flow \dot{V} is reduced by a factor of two at t=0.5 s and increased again to the initial value $(1.75 \cdot 10^{-3} \text{ m}^3/\text{s})$ at t=25 s. Time axis is broken to exclude the nonvarying part of the functions. Units are according to Table 1.

the enthalpy rises. The wall temperature T_W drops slightly until dryout at $z \sim 6$ m whereafter the temperature rises quickly and becomes almost equal to the ambient temperature at z = 10 m.

To test the dynamic response and numerical stability of the model we next investigate the model response to steps in inlet massflow and outlet volume flow. In the remaining results, all simulations are started from the steady-state condition in Fig. 2.

First we reduce the inlet mass flow \dot{m}_{in} by a factor of two a t = 0.5 s and increase it again by a factor of two at t = 25 s. Figure 3 shows simulation results of \dot{m} , T, and T_W at z = 0 (in) and z = 10 m (out). The model behaves as expected and is numerically stable. The under- and over-shoot of T_{out} at t = 0.5and 25 s reflects the effects of the dynamic pressure wave propagating in the system as discussed later. In Fig. 4 we show simulation results of \dot{m} , T, and T_W at z = 0 (in) and z = 10 m (out) for the case where the outlet volume flow \dot{V} is reduced by a factor of two at t = 0.5 s and increased again to its original value at t = 25 s. The inlet massflow is kept constant and the outlet massflow returns to its original value while pressure and temperatures change so as to ensure continuity. Note that in this case the superheated zone vanishes $(T_{out} < T_{in})$ and liquid is ejected from the tube during the low volume-flow period. Again, the model behaves as expected and is numerically stable. The over- and under-shoot of T_{out} at t = 0.5 s and 25 s reflects again the instantaneous change in pressure related to the dynamic pressure wave traveling in the systems.

When the inlet or outlet flows are changed instantaneously as in Figs. 3 and 4, a pressure wave is formed shuttling back and forth a few times in the evaporator tube. Figure 5 show a detailed spatiotemporal view of \dot{m} near t=0.5 s when the outlet volume flow is reduced as in the case from Fig. 4. The wave is formed at z=10 m and moves against the flow towards the inlet. At $t\sim0.57$ s it reaches the inlet position at z=0 and reflects back into the system. The speed of the wave is not constant over the evaporator tube due to the changing speed of sound through the passage of mainly the two-phase region.

CONCLUSION

We have implemented the second order semidiscrete Kurganov-Tadmor scheme for an evaporator formulated in terms of enthalpy, pressure, mass-

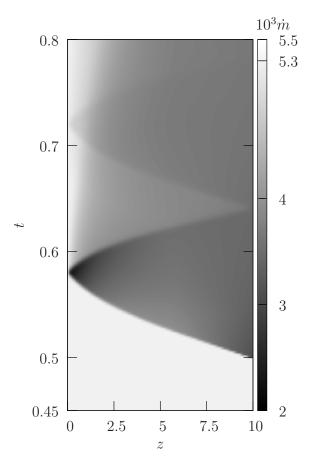


Figure 5: The space-time dependence of \dot{m} as the outlet volume flow \dot{V} is reduced by a factor of two at t = 0.5 s. A pressure wave is seen to rapidly shuttle back and forth a few times. Units refer to Table 1.

flow, and wall temperature. The scheme works well while being stable against even large steps in the inlet and outlet flows and changing number of fluid zones. Since the present model addresses the full set of partial differential equations, including the spatio-temporal details of pressure-wave effects, it is much more computational demanding than ordinary moving-boundary models or distributed models with simplified momentum equations. Thus its main purpose is to model evaporators as a benchmark for simpler and faster models ensuring similar behavior at long timescales.

REFERENCES

- [1] S. Mattsson, et. al, *Physical system modeling with modelica*, Control Eng. Practice 6 (1998) 501–510.
- [2] T. Pfafferot, G. Schmitz, Modeling and transient simulation of co2-refrigeration systems with modelica, Int. J. Refrig. 27 (2004) 42–52.
- [3] T. L. McKinley, A. G. Alleyne, An advanced nonlinear switched heat exchanger model for vapor compression cycles using the moving-boundary method, Int. J. Refrig. 31. (2008).
- [4] M. Willatzen, et. al, A general simulation model for evaporators and condensers in refrigeration. part i: Moving boundary formulation of two-phase flows with heat exchange, Int. J. Refrig. 21 (5) (1998) 398–403.
- [5] W.-J. Zhang, C.-L. Zhang, A generalized moving-boundary model for transient simulation of dry-expansion evaporators under larger disturbances, Int. J. Refrig. 29 (2006) 1119– 1127.
- [6] X. Jia, et. al, A distributed model for prediction of the transient response of an evaporator, Int. J. Refrig. 18 (5) (1995) 336–342.
- [7] X. Jia, et. al, *Distributed steady and dynamic modeling of dry-expansion evaporators*, Int. J. Refrig. 22 (1999) 126–136.
- [8] O. Garcia-Valladares, et. al, *Numerical simulation of double-pipe condensers and evaporators*, Int. J. Refrig. 27. (2004).
- [9] W. Brix, Priv. Comm., (2008).

- [10] A. Kurganov, E. Tadmor, New high-resolution semi-discrete central schemes for Hamilton-Jacobi equations, Journal of Computational Physics 160 (2000) 720–742.
- [11] G. Wallis, *One-dimensional Two-phase Flow*, McGraw-Hill, (1969).
- [12] M. Skovrup, *Thermodynamic and thermophysical properties of refrigerants*, 3.10, Departnemt of Energy Engineering, Technical University of Denmark. (2001).

EARLY MEASURE OF SYNCHRONIZATION OPERATIONS IN SUPERMARKET REFRIGERATION SYSTEMS

Liang Chen*
Donghua University
Engineering Research Center of Digitized Textile & Fashion Technology
Ministry of Education
201620 Shanghai
P. R. China

Torben Green, Roozbeh Izadi-Zamanabadi and Lars F. S. Larsen
Danfoss A/S
Refrigeration and Air conditioning
6430, Nordborg
Denmark

ABSTRACT

The objective of a supermarket refrigeration system is mainly to preserve the foodstuffs at a proper temperature. Practice shows that the temperature in one display case influences the temperature in the neighboring ones. These interactions from time to time lead to a synchronization operation in the display cases, which causes a high wear on the compressor, inferior control performance and increased energy consumption. In the paper, we analyze the synchronization dynamics using chaos theory and show that the system has the complex chaotic behavior, which is far away from the synchronization. Therefore, we propose a concept that the system may be de-synchronized by making it chaotic. The maximum Lyapunov exponent (MLE) is usually used to estimate the level of chaos. We use it as a measure of performance for the tendency of the system to synchronize. Thus, early warnings about the undesired synchronous behavior can be given to the control system for continuous optimization of the performance.

Keywords: Refrigeration, synchronization, chaos, Lyapunov exponent

INTRODUCTION

The overall task of a supermarket refrigeration system is to preserve the foodstuffs at a proper temperature without degrading in quality. The goods are usually stored in open display cases in the sales area of the supermarket. By utilizing a refrigerant in a refrigeration cycle, heat is transported from the display cases to the outdoor surroundings. Each display case is typically equipped with a hysteresis controller which adjusts the refrigerant flow such that the desired temperature is reached. Simulation and practice show that the distributed hysteresis controllers have the tendency to synchronize, meaning

*Corresponding author: E-mail:lchen.dhu@gmail.com

that the opening and closing actions of the valves coincide [1]. Consequently it causes a high wear on the compressor, inferior control performance and increased energy consumption.

The intense focus on limiting energy consumption and the global environmental awareness calls for energy efficient solutions. By monitoring the performance of the refrigeration system the "goodness" of the operation can be measured and early warnings about undesired behaviors can be given such that the control system can accommodate these and continuously optimize the system performance. In this paper, we focus on the synchronization phenomenon. Based on the simplified supermarket refrigeration model developed in [2], we analyze the system

dynamics using bifurcation and chaos theory [3, 4]. This theory is to investigate dramatic changes in the qualitative or topological structure of a system. It can be dated back to 1975 when the first mathematical definition of 'chaos' was given [5]. From the bifurcation diagram, we show that the system keeps switching between low-order and high-order limit cycles by varying the hysteresis bounds of the temperature controller. If the system converges towards a low-order limit cycle it can be seen as an indication of a risk that the system may synchronize; if the system has a high-order limit cycle, especially a chaotic behavior, it can be seen as an indication far from the synchronization. Therefore, it is a good choice to de-synchronize the system by making the system chaotic, i.e. chaotification.

Chaotification, which means creating chaos in the system when it is beneficial, has been studied for many years. It has been successfully applied in liquid mixing [6], human brain [7], resonance prevention in mechanical systems [8], and secure communications [9], etc. The maximum Lyapunov exponent is usually used to estimate the level of chaos. We use it as a measure of performance for the trend of the system synchronization. A lot of references are available on calculation of the Lyapunov exponents. Generally speaking, there are two categories: the model-based method [10, 11, 12] and the databased one [13, 14, 15, 16]. The model-based method requires explicit equations of motion, which is usually unknown in experimental settings. The databased method takes the practical view of calculating the Lyapunov exponents from experimental data and uses techniques of nonlinear time series analysis. Together with the consideration of the practical application and the future extension to the largescale supermarket refrigeration system, we adopt the data-based method. Results shows that the maximum Lyapunov exponent can give a general measure of the tendency of the system synchronization.

SYSTEM DESCRIPTION

A simple layout of the supermarket refrigeration system is shown in Fig. 1. The compressors and the display cases are connected in parallel in majority of supermarket refrigeration systems. The compressors supply the flow by compressing the low pressure refrigerant drained from the suction manifold. The refrigerant then passes through the condenser and into

the liquid manifold. Each display case has an expansion valve, through which the refrigerant flows into the evaporator of the display case. In the evaporator the refrigerant absorbs heat from the stored goods and thereby changes phase. The vaporized refrigerant flows into the suction manifold, thus closing the refrigeration cycle.

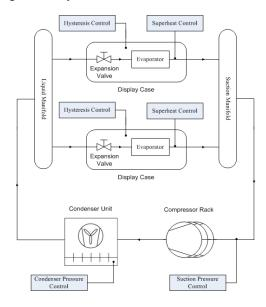


Figure 1: Layout of the supermarket refrigeration system

In a typical supermarket refrigeration system, the control structure is distributed with many local control loops. For example, the temperature in each display case is controlled by a hysteresis controller that opens and closes the expansion valve, i.e. the valve opens when the air temperature T_{air} (close to the goods) reaches a predefined upper temperature limit and stay open until T_{air} decreases to the lower temperature limit and the valve closes again; besides, the suction pressure P_{suc} is controlled by switching off and on compressors in the compressor rack. A PI controller with a dead band around the reference is normally used. If the pressure exceeds the upper bound of the dead band one or more compressors are switched on; if the pressures drops below the lower bound of the dead band a compressor is switched off. This control strategy prevents moderate changes in the suction pressure from initiating compressor switching.

Simulation and practice have found that the temperature in one display case influences the temperature in the neighboring ones. These interactions from time to time lead to a synchronization operation in

the display cases. It means that the air temperatures T_{air} in the different display cases tend to agree, which results in the coinciding opening and closing of expansion valves, thus periodic high and low amount of vaporized refrigerant flow into the suction manifold. Hence, large fluctuation in the suction pressure P_{suc} is a consequence which then induces higher switch frequencies of the compressors. This subsequently leads to excessive wear on the compressors, and thus reducing lifetime of the compressors and increasing energy consumption. The result from synchronizing display cases can be seen in Fig. 2.

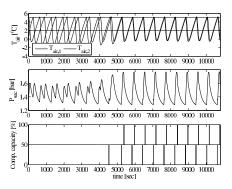


Figure 2: The effect of synchronization

In the paper, we concentrate on the synchronization phenomenon. Therefore, we only consider the dynamics relevant to the hysteresis control and the suction pressure control. The mathematical model used in the following was developed in [2].

The supermarket refrigeration system can be modeled as a piecewise-affine switched system with the general expression:

$$\frac{dx}{dt} = A_{\delta_i} x + b_{\delta_i}.$$

Here, the discrete inputs are $\delta_i \in \{0,1\}$, which is controlled by a hysteresis controller in the following way:

$$\delta_{i}(k+1) = \begin{cases} 1 & \text{if } T_{air,i} \ge \overline{T_{air,i}} \\ 0 & \text{if } T_{air,i} \le \underline{T_{air,i}} \\ \delta_{i}(k) & \text{if } \underline{T_{air,i}} < \overline{T_{air,i}} < \overline{T_{air,i}}, \end{cases}$$
(1)

where $T_{air,i}$ is the air temperature in the i th display case, k denotes the time index, $\overline{T_{air,i}}$ is the upper bound of the air temperature and $\underline{T_{air,i}}$ is the lower bound.

For a refrigeration system with two display cases and one compressor unit, the system states of the simplified model are the air temperatures $T_{air,i}(i=1,2)$ and the suction pressure P_{suc} ; the discrete inputs are $(\delta_1, \delta_2) \in \mathbf{2}^2$, where $\mathbf{2} \equiv \{0,1\}$, thus $\mathbf{2}^2 = \mathbf{2} \times \mathbf{2} = \{0,1\} \times \{0,1\}$.

SYNCHRONIZATION ANALYSIS

In the section, we use the bifurcation and chaos theory to study the synchronization dynamics. The theory is most commonly applied to investigate dramatic changes in the qualitative or topological structure of a system by varying smoothly a system parameter. We consider a refrigeration system consisting of two display cases and one compressor unit, and change smoothly the lower bound of the temperature control in one of the display cases, i.e. $T_{air,2}$. We depict the resulting behavior in the bifurcation diagram, from which we interpret the synchronization as the low-order limit cycle.

To make the situation clear, some typical limiting behaviors in the phase plots of $T_{air,1}$ and $T_{air,2}$ are shown in Fig. 3, at first. When the parameter $T_{air,2}$ = 0 (see Fig. 3a), the system switches between the two points (0,0) and (5,5) within an accepted tolerance (1e-6) in the paper). Here, we call the behavior a 2-periodic limit cycle, where the period is defined by the sum of the number of switching points on the boundary $\partial \Box = \partial([\underline{T_{air,1}}, \overline{T_{air,1}}] \times [T_{air,2}, \overline{T_{air,2}}]).$ We can see that the two system states $T_{air,1}$ and $T_{air,2}$ agree all the time corresponding to the synchronization phenomenon shown in Fig. 2. When $T_{air,2} = 0.15$, a 4-periodic limit cycle appears (see Fig. 3b) with a similar topology as Fig. 3a but a bigger difference between the two states. We call it the quasi-synchronization. As $T_{air,2}$ goes to 0.2, another topology of 4-periodic limit cycle appears (see Fig. 3c). It is totally different from the state agreement in the synchronization. If $T_{air,2}$ continues increasing to 0.3, the system tends to a high-periodic limit cycle with many switching points in the boundary of $\partial \square$. It looks like chaos, the phenomenon often happening in the nonlinear system [4]. This kind of behavior is far away from the synchronization.

To show how the system behaves with the smooth change of the parameter, a bifurcation diagram is shown in Fig. 4. It exhibits the possible long-term stable values of the system on the boundary $\partial \Box$ as a function of the parameter $T_{air,2}$. We can see that the

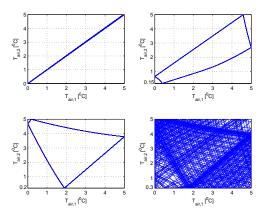


Figure 3: Typical limiting behaviors with the various values of the parameter $T_{air,2}$. (a) 2-periodic limit cycle (synchronization, $\overline{T_{air,2}} = 0$), (b) 4-periodic limit cycle ($T_{air,2} = 0.1\overline{5}$), (c) another 4-periodic limit cycle ($\overline{T_{air,2}} = 0.2$), (d) high-periodic limit cycle ($T_{air,2} = 0.3$).

system has very complicated behaviors with many bifurcations occurring when small smooth changes made to the values of $T_{air,2}$ cause sudden 'qualitative' or topological changes in the behaviors. With the varying parameter, the system behavior becomes very complex and keeps switching between order and chaos-like oscillations. If the system converges towards a low-order limit cycle we can see it as an indication of a risk that the system may synchronize; if the system has a high-order limit cycle, especially a chaotic behavior, we can see it as an indication far from the synchronization.

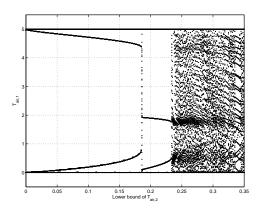


Figure 4: Bifurcation diagrams of the system state $T_{air,1}$ w.r.t the parameter $T_{air,2}$.

Next, we examine the control performance in the

synchronization and chaos situations. As stated before, synchronization of the display cases leads to large fluctuations in the suction pressure, which is unwanted. Fig. 5 shows variations of the suction pressure in the situations of synchronization and chaos-like, respectively. It can be seen that in the chaos-like situation, the fluctuation range of the suction pressure decreases from time to time, which will lead to lower switch frequency of the compressor; even for the part with the same rang as the synchronization, the pressure jumps so fast that the traditional PI controller in the compressor can fix it and it won't lead to the frequent switches of the compressors.

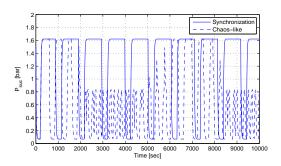


Figure 5: The suction pressure P_{suc} in the situations of (a) synchronization ($\underline{T_{air,2}} = 0$) and (b) chaos-like ($T_{air,2} = 0.3$).

The bifurcation diagram has demonstrated that a totally different topology of the behavior can be obtained in the simple refrigeration model by changing slightly the value of $\underline{T_{air}}$. Does it means that it is possible to suppress the synchronization just by adjusting a little bit value of the system parameter? It seems obvious for a small 'toy' system with only two display cases. However, for a real plant with many different display cases, selecting the appropriate parameter value becomes delicate.

Chaotification, which means creating chaos in the system when it is beneficial, has been successfully applied in many systems. In our case, it is also a good choice to make the refrigeration system chaotic once it is approaching the synchronization. Then, how to detect the synchronization early and take action to chaotify the system at proper time? The maximum Lyapunov exponent (MLE) is usually used to estimate the level of chaos. We use it as a measure of performance for the tendency of the system to synchronize, that is, the higher value of the MLE the

lower risk for synchronization.

SYNCHRONIZATION EARLY MEASURE Description of Lyapunov exponents

Lyapunov exponents are the average exponential rates of divergence or convergence of two close trajectories in phase space. Quantitatively, two trajectories $x_1(t)$ and $x_2(t)$ with initial separation $\delta x(0)$ diverge

$$|\delta x(t)| \approx e^{\lambda t} |\delta x(0)|,$$
 (2)

where $\delta x(t) = x_1(t) - x_2(t)$, λ is the Lyapunov exponent. There are n Lyapunov exponents in the spectrum of an n-dimensional dynamical system. The signs of the Lyapunov exponents provide a qualitative picture of a system's dynamics. In general, for the continuous system, we have

fixed point: $\lambda_i < 0, \ i = 1, \dots, n;$ limit cycle: $\lambda_1 = 0, \ \lambda_i < 0, \ i = 2, \dots, n;$ torus: $\lambda_1 = \lambda_2 = 0, \ \lambda_i < 0, \ i = 3, \dots, n;$ strange attractor: $\lambda_1 > 0, \ \text{at least}.$

An attractor is informally described as strange if the dynamics on it are chaotic. A positive MLE is usually taken as an indication of the existence of chaos.

General methods for calculating Lyapunov exponents

A lot of references are available on calculation of the Lyapunov exponents. Generally speaking, there are two categories: the model-based method and the data-based one.

The model-based method has been successfully applied to many "smooth" dynamical systems [10, 11]. It is based on the integration of the linearized equations for *n* linearly independent initial conditions. However, this method cannot be directly applied to non-smooth systems (with discontinuities or piecewise smoothness), like the refrigeration system in the paper, because the Jacobian matrices make no sense at non-smooth points. [12] suggested certain transitional conditions to be supplemented to the linearized equations at the instants of discontinuities. Other methods have also been proposed but only for specific non-smooth systems, e.g. [17, 18, 19].

The model-based method requires explicit equations of motion, which is usually unknown in experimental settings. Besides, to our knowledge, no literature has discussed the model-based method for nonsmooth systems consisting of more than two subsystems. It is hard to know the switching sequence of the subsystems for every independent initial condition

Another method is data-based. It uses techniques of nonlinear time series analysis and follows directly from the definition of the Lyapunov exponents. A lot of references are available on this subject, cf. [13, 14, 15, 16]. The data-based method takes the practical view of calculating the Lyapunov exponents from experimental data. Although the heuristic method hasn't been theoretically proven to be applicable to non-smooth dynamical systems and has the accuracy limit compared with the model-based method, it has been widely and successfully used in biological and economic systems where the mathematical equations are unknown, but the experimental data are easy to be obtained [20, 21, 22].

In the paper, the supermarket refrigeration system is modeled as a piecewise-smooth system with affine dynamical subsystems, where there is no obvious discontinuity in the switching. [23] has shown how the system is "glued" together to form a single dynamical system by the Poincaré map method, where the local map at the instant of discontinuity is the identity map *I*. Therefore, the system discussed in the paper has no evident non-smooth characteristics. Together with the consideration of the practical application and the future extension to the large-scale supermarket refrigeration system, the databased method is preferred to calculate the MLE as the measure of the tendency of the synchronization.

Methodology in the paper

We use the algorithm proposed by Rosenstein et al [16] to calculate the MLE. The algorithm is fast, easy to implement, and robust to changes in the size of data set, noise level, etc. Basic steps are given in the following:

1) Reconstruct the phase space:

Experimental data typically consist of discrete measurements of a single observable. The well-known technique of phase space reconstruction makes it possible to obtain the same dynamical properties in the reconstructed phase space as the original one [13]. Denote $\{x_1, x_2, ..., x_N\}$ as the N- point observable time series, the reconstructed phase space

is described as:

$$Y_i = [x_i, x_{i+\tau}, ..., x_{i+(m-1)\tau}] \in \mathbb{R}^n \ (i = 1, ..., M), \ (3)$$

where τ is the reconstruction delay, m is the embedding dimension, $M = N - (m-1)\tau$. τ and m are estimated by the C-C method [24].

2) Extract the Lyapunov points:

We employ the Tisean software package [25] implementing the formula in [16] to get the points related to the MLE.

3) Estimate the MLE:

We use the least-squares fit to the longest possible linear region of the Lyapunov points. The slope of the line is the MLE.

Results

We extract the pseudo-experimental data, a single time series of $T_{air,1}$, from the solution of the refrigeration model and treat it as an experimental observable. Fig. 6 shows the calculation result of MLE varying with the system parameter $T_{air,2}$. Generally speaking, Fig. 6 has a good correspondence to the bifurcation diagram Fig. 4, with the regions where the MLE is close to zero corresponding to the loworder limit cycle, and the regions where the MLE has a relatively larger positive value corresponding to chaotic attractors. The little delay between Fig. 6 and Fig. 4 may be caused by the inherent accuracy limit of the data-based method comparing with the model-based method. However, from Fig. 6, one can still get a general clue of the performance for the tendency of the system to synchronize, that is, the higher value of the MLE the lower risk for synchronization.

Fig. 7 shows the MLE variation after a simple bandpass filter. The slop of the fitted MLE signal Fig. 7b looks better than Fig. 6 to be as a measure of performance for the tendency of the system to synchronize.

CONCLUSION

We focus on dynamic analysis and early measure of the synchronization phenomenon frequently happening in the supermarket refrigeration system. The bifurcation diagram has exhibited that if the system converges towards a low-order limit cycle we can see it as an indication of a risk that the system may

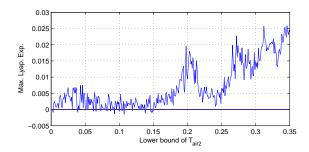


Figure 6: Variation of the max. Lyapunov exponent w.r.t the parameter $T_{air,2}$.

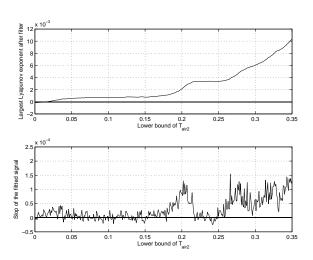


Figure 7: Variation of the max. Lyapunov exponent after filtering.

synchronize; if the system has a high-order limit cycle, especially a chaotic behavior, we can see it as an indication far from the synchronization. Simulation also has shown the significant reduction of the suction pressure variation, hence better performance when the system stays in the chaos situation than in the synchronization. Therefore, it is a good choice to de-synchronize the system by making it chaotic. Before the control system performs the continuous optimization of the performance, we must give early warnings about the undesired synchronous behavior. The MLE is usually used to estimate the level of chaos. We used it as a measure of performance for the tendency of the system to synchronize, that is, the higher value of the MLE the lower risk for synchronization.

In the paper, we considered a refrigeration system consisting of two display cases and one compressor unit. These findings for the small "toy" system may seem obvious, however they can easily be scaled to (realistic) large scale systems, where it is harder to distinguish and evaluate "good" and "bad" behavior. In the future, essential parameters to system's behaviors will be extracted and the algorithm of calculating the maximal Lyapunov exponent will be developed for commercial refrigeration systems.

REFERENCES

- [1] L. F. S. Larsen, "Model based control of refrigeration systems," Ph.D. dissertation, Department of Control Engineering Aalborg University, Aalborg, 2006.
- [2] L. Larsen, R. Izadi-Zamanabadi, R. Wisniewski, and C. Sonntag, "Supermarket refrigeration systems a benchmark for the optimal control of hybrid systems," Hycon, http://astwww.bci.unidortmund.de/hycon4b/wprelated/sr.pdf, Tech. Rep., 2007.
- [3] J. D. Crawford, "Introduction to bifurcation theory," *Reviews of Modern Physics*, pp. 991–1037, 1991.
- [4] R. L. Devaney, *An Introduction to Chaotic Dynamical Systems*. Westview Press, 2003.
- [5] T. Y. Li and J. A. Yorke, "Period three implies chaos," *Amer. Math. Monthly*, vol. 82, pp. 481–485, 1975.

- [6] J. M. Ottino, F. J. Muzzio, and M. Tjahjadi, "Chaos, symmetry, and self-similarity: Exploiting order and disorder in mixing processes," *Science*, vol. 257, pp. 754–760, 1992.
- [7] S. J. Schiff, K. Jerger, and D. H. Duong, "Controlling chaos in the brain," *Nature*, vol. 370, pp. 615–620, 1994.
- [8] I. T. Georgiou and I. B. Schwartz, "Dynamics of large scale coupled structural/ mechanical systems: A singular perturbation/proper orthogonal decomposition approach," SIAM J. Appl. Math., vol. 59, pp. 1178–1207, 1999.
- [9] M. P. Kennedy, G. Kolumban, and G. Kis, "Chaotic modulation for robust digital communications over multipath channels," *Int. J. Bifur. Chaos*, vol. 10, pp. 695–718, 2000.
- [10] G. Benettin, L. Galgani, A. Giorgilli, and J.-M. Strelcyn, "Lyapunov characteristic exponents for smooth dynamical systems and for hamiltonian systems; a method for computing all of them. part i: Theory, part ii: Numerical application," *Meccnnica*, vol. 15, pp. 9–20, 21–30, 1980.
- [11] T. S. Parker, *Practical Numerical Algorithms* for Chaotic Systems. New York: Springer, 1989.
- [12] P. C. Müller, "Calculation of lyapunov exponents for dynamic systems with discontinuities," *Chaos, Solitons and Fractals*, vol. 9, pp. 1671–1681, 1995.
- [13] A. Wolf, J. B. Swift, H. L. Swinney, and J. A. Vastano, "Determining Ivapunov exponents from a time series," *Physica D*, vol. 16, pp. 285–317, 1985.
- [14] M. S. S. Sato and Y. Sawada, "Practical methods of measuring the generalized dimension and the largest lyapunov exponent in high dimensional chaotic systems," *Prog. Theor. Phys.*, vol. 77, p. 1, 1987.
- [15] R. Gencay and W. Deckert, "An algorithm for the *n* lyapunov exponents of *n*-dimensional unknown dynamical systems," *Physica D*, vol. 59, pp. 142–157, 1992.

- [16] M. Rosenstein, J. Collins, and C. D. Luca, "A practical method for calculating largest lyapunov exponents from small data sets," *Physica D*, vol. 65, pp. 117–134, 1993.
- [17] A. Stefanski and T. Kapitaniak, "Estimation of the dominant lyapunov exponent of non-smooth systems on the basis of maps synchronization," *Chaos, Solitons and Fractals*, vol. 15, pp. 233–244, 2003.
- [18] S. de Souza and I. Caldas, "Calculation of lyapunov exponents in systems with impacts," *Chaos, Solitons and Fractals*, vol. 19, pp. 569–579, 2004.
- [19] L. Jin, Q. Lua, and E. Twizell, "A method for calculating the spectrum of lyapunov exponents by local maps in non-smooth impactvibrating systems," *Journal of Sound and Vibration*, vol. 298, p. 1019"C1033, 2006.
- [20] H. Abarbanel, *Analysis of observed chaotic data*. Springer-Verlag, 1996.
- [21] W. Dechert and R. Gencay, "Lyapunov exponents as a non-parametric diagnostic for stability analysis," *Journal of Applied Econometrics*, vol. 7, pp. S41–S60, 1992.
- [22] H. Busch, D. Camacho-Trullio, Z. Rogon, K. Breuhahn, P. Angel, R. Eils, and A. Szabowski, "Gene network dynamics controlling keratinocyte migration," *Molecular Systems Biology*, vol. 4, 2008.
- [23] R. Wisniewski and L. F. S. Larsen, "Method for analysis of synchronization applied to supermarket refrigeration system," in 17th IFAC World Congress, Seoul, Korea, 2008.
- [24] H. Kim, R. Eykholt, and J. Salas, "Nonlinear dynamics, delay times, and embedding windows," *Physica D*, pp. 48–60, 1999.
- [25] R. Hegger, H. Kantz, and T. Schreiber, Nonlinear time series analysis, TISEAN 3.0.1. http://www.mpipks-dresden.mpg.de/tisean/Tisean_3.0.1/index.html.

COMPARISON OF TWO DIFFERENT MODELLING TOOLS FOR STEADY STATE SIMULATION OF AN EVAPORATOR

Wiebke Brix *and Brian Elmegaard Technical University of Denmark Department of Mechanical Engineering 2800 Lyngby Denmark

ABSTRACT

In this paper a test case is solved using two different modelling tools, Engineering Equation Solver (EES) and WinDali, in order to compare the tools. The system of equations solved, is a static model of an evaporator used for refrigeration. The evaporator consists of two parallel channels, and it is investigated how a non-uniform airflow influences the refrigerant mass flow rate distribution and the total cooling capacity of the heat exchanger. It is shown that the cooling capacity decreases significantly with increasing maldistribution of the airflow. Comparing the two simulation tools it is found that the solutions differ only slightly depending on which software is used for solving due to differences in the thermophysical property functions. Considering the solution time, WinDali solves the equations more than 100 times faster than EES.

Keywords: Evaporator, Maldistribution, Engineering Equation Solver, WinDali

NOMENCLATURE

MIIOKL
Enthalpy [kJ/kg]
Distribution parameter [-]
Mass flow rate [kg/s]
Pressure [bar]
Heat transfer rate [W]
Relative residual
Temperature [°C]
Velocity [m/s]
Quality [-]
channel i
inlet
outlet
superheat

INTRODUCTION

Modelling and simulation of energy systems is widely used as an alternative to experimental investigations for both design and optimization of a system. The general scheme is always the same, first the rel-

*Corresponding author: Phone: +45 4525 4130 Fax: +45 4593 5215 E-mail:wb@mek.dtu.dk

evant equations describing the system in the level of details desired are found. Next, the question arises: Which tool will be suitable to help solving this set of equations? Many different modelling tools exist, which are specifically minded for solving equations describing energy systems. Each tool has its advantages, some tools are suitable for dynamic systems, while others have their strength in solving algebraic equations describing a steady state solution. It is difficult to find any guidelines in the literature of which tool to choose, mostly the choice is based on which tool is previously used, and often in-house codes are developed. In this paper a steady state model of an evaporator is developed and solved as a test case using two different modelling tools in order to compare the two tools and point out advantages and disadvantages of these two tools. The tools applied are: Engineering Equation Solver (EES) [1], and Win-Dali, [2].

The test case

Flow distribution of a fluid evaporating in parallel channels is interesting for applications of very different scales. In a steam generator of a power plant water evaporates in many parallel channels along the boiler walls. On a much smaller scale the evaporator in a refrigeration system may consist of many parallel mini- or microchannels.

Within the field of refrigeration, especially aluminum braced microchannel evaporators, with channel sizes in the 1 mm range have become very popular, since these heat exchangers both reduce the system sizes and reduce the refrigerant charge needed in order to obtain a given cooling capacity. Due to the small channel sizes a design with many parallel channels is required in order to keep the pressure drop at an acceptable level. However, parallel channels also induce the possibility of a maldistribution of the evaporating fluid. Maldistribution of the mass flow rate of refrigerant may occur due to different reasons, of which one could be an uneven heat load on the channels.

As a test case for this study, the impact of a nonuniform air velocity on the refrigerant mass flow distribution and on the cooling capacity of a microchannel evaporator is investigated. In order to keep the model relatively simple, only two, vertical microchannel tubes in parallel are considered. A microchannel tube is a flat tube with a number of small, rectangular or circular channels or ports. Two different refrigerants, R134a and CO2, are considered, while air is flowing on the secondary side of the heat exchanger. In order to enhance the air side heat transfer, the parallel tubes are connected by louvered fins. Figure 1 shows a sketch of the two channels, and table 1 summarizes the parameters, which define the geometry of the test case evaporator as well as the flow conditions.

MODELLING THE EVAPORATOR

Besides showing a sketch of the geometry, figure 1 also shows the desired model inputs and outputs. It is assumed that the thermodynamic conditions at the inlet, the total mixed outlet superheat and the airside velocity and temperature distribution are measureable and therefore used as input to the model. Output are the total mass flow rate as well as the mass flow rate distribution, the thermodynamic conditions of the refrigerant at the outlet of each channel and the cooling capacity of each tube.

In order to model the evaporator, a discretized model of a single microchannel tube is built using a fi-

Evaporator geometry	
Tube length	0.47 m
# of ports in one tube	11
Cross section of one port	$0.8 \times 1.2 \mathrm{mm}$
Flow depth	16mm
Distance between two microchannels	8 mm
Fin pitch	$727{\rm m}^{-1}$
Flow parameters	
Air temperature	35°C
Air velocity	1.6 m/s
Evaporation temperature	$7.4^{\circ}\mathrm{C}$
Quality at manifold inlet	0.3
Total superheat (R134a)	6 K
Total superheat (CO ₂)	0 K
Quality at outlet (CO ₂)	1

Table 1: Parameters defining the test case.

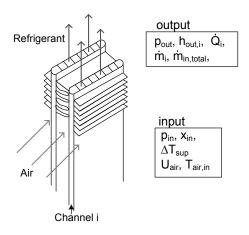


Figure 1: Sketch of two channels in parallel with input and output parameters to the model.

nite volume method. In the evaporator fins are connecting two neighboring tubes. For the single tube model half of the fin length is assumed to belong to the channel on each side. Each microchannel tube is discretized into an optional number of volumes, and each volume is treated as a small heat exchanger. For each volume the continuity equation, the momentum equation and the energy equation are solved

• The system is in steady state.

under the following assumptions:

- The refrigerant flow is one-dimensional.
- The refrigerant flow is homogeneous and vapor and liquid are in thermodynamic equilibrium.
- Axial heat conduction in the tube walls and between different tubes is negligible.

• The air is dry.

The frictional pressure drop and heat transfer coefficients are calculated using correlations from the literature, depending on the flow conditions. Table 2 summarizes the correlations that have been chosen. The different tubes are connected through, first of all, conservation of the total mass flow rate:

$$\dot{m}_{\rm in,total} = \sum_{i=1}^{N} \dot{m}_i,\tag{1}$$

where N is the total number of channels. Secondly, no pressure drop is assumed in the inlet or outlet manifolds, such that the total pressure drop over each tube has to be equal:

$$\Delta p_i = p_{\rm in} - p_{\rm out}. \tag{2}$$

Since the total superheat out of the evaporator often is used as a control parameter in refrigeration systems, this parameter is given as an input to the model instead of the mass flow rate. Both the total mass flow rate and the distribution of the mass flow rate are thus calculated from the model. The pressure drop across any tube depends on the mass flow rate, inlet quality and heat load, why almost all model equations depend on each other. This is illustrated in the model flowchart shown in figure 2. The flowchart shows the top layer of the model, while most of the calculations are performed in the box indicated as procedure HX_volume. In this procedure the pressure drop and energy balance is calculated for each volume.

MODELLING TOOLS

In order to solve the model equations, the model is implemented using two different modelling tools. Both modelling tools are implemented in equation solvers, and both tools are designed for solving models of thermodynamic processes.

Engineering Equation Solver

Engineering Equation Solver (EES) [1], is developed for numerically solving systems of algebraic equations, but it is also possible to solve differential equations. Using EES the model is written as mathematical equation in a very free form where equations are implemented in arbitrary order. The equations

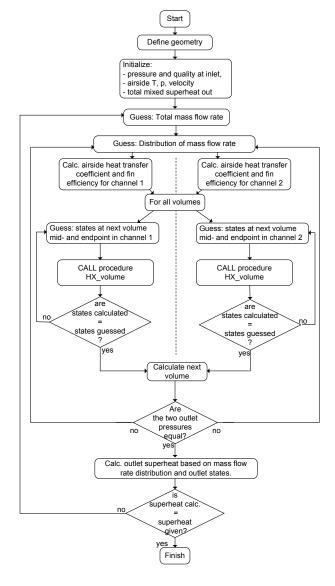


Figure 2: Flowchart of the model equations. The pressure drop and heat transfer calculations are performed inside the procedure HX_volume.

may be arranged in according to the user's preferences. Pascal-like functions and procedures may be implemented. For the numerical solution the equations are blocked, and each block is solved using a Newton-Raphson method. Convergence of the solution is reached as soon as the relative residuals are smaller than a specified value. Thermophysical properties of a large number of fluids can be found using the built in thermodynamic functions that call an equation of state in order to calculate the wanted properties.

Air side	
Heat transfer coefficient	Kim and Bullard [3]
Two-phase region	
Heat transfer coefficient (R134a)	Zhang et al. [4]
	+ smooth transition to single phase
Heat transfer coefficient (CO ₂)	Choi et al. [5]
	+ smooth transition to single phase
Frictional pressure drop	Müller-Steinhagen and Heck [6]
Single phase region	
Heat transfer coefficient	Gnielinski [7]
Frictional pressure drop	Blasius [8]

Table 2: Summary of correlations used to calculate heat transfer coefficients and pressure drop.

WinDali

WinDali [2] is a modelling and simulation software that solves systems of ordinary differential equations (ODE's) or algebraic equations (AE's). The software comprises of two parts, a model editor, which is a Free Pascal Editor, and a simulation program that reads the compiled model and solves the equations. All static equations that are part of the iterations need to be formulated as residual equations. The algebraic equations are solved using a modified Newton iteration scheme, which includes convergence and divergence control [2]. Otherwise, the software has the same main properties as EES, i.e. functions with thermodynamic properties are a builtin part, and it is possible to include procedures and functions.

Accuracy of the solution

For both modelling tools a stop criterion for the Newton-Raphson iterations needs to be given. For both EES and WinDali this criterion is given by setting the maximum allowable relative residual. The relative residual is defined as the relative difference between the solutions of two successive iteration steps:

$$R = \frac{y^k - y^{(k-1)}}{y^{(k-1)}},\tag{3}$$

where y^k is the solution found for iteration number k. The accuracy of the solution increases with decreased residuals, but so does the solution time, therefore a suitable stop criterion is found.

A relative error of the solution at a given stopping criterion is found by comparing the solutions to a more accurate solution:

Error =
$$\max\left(\left|\frac{y - y_{acc}}{y_{acc}}\right|\right)$$
, (4)

where y is a solution vector containing all static variables found by iteration, and y_{acc} is assumed to be the accurate solution. Since no analytical solution is availiable, y_{acc} is a numerical solution with a very small relative residual requirement.

In table 3 errors are summarized for the solution of the uniformly distributed case. For the Newton method quadratic convergence would be expected, such that for each iteration step, the number of correct digits is roughly doubled. This behavior is seen for the WinDali solutions. An extra iteration is performed when setting the maximum relative residual from 10^{-3} to 10^{-4} , while for the following solutions no extra iteration is needed to fulfill the residual requirement. Using EES the behavior is different, here the solution converges more slow. A stop criterion of 10^{-4} is chosen for both modelling tools.

R	10^{-3}	10^{-4}	10^{-5}	10^{-6}
Error, EES	9.1e-3	2.7e-4	6.4e-5	6.8e-6
Error, WinDali	2.1e-3	3.9e-7	3.9e-7	3.9e-7

Table 3: Error for different stop criteria.

Comparison of solutions obtained using EES and WinDali

The evaporator model is solved using both EES and WinDali. For the comparison of the solutions uniform airflow is considered, there is hence no maldistribution of the refrigerant in these cases. Two different refrigerants, R134a and CO₂, are applied using the test case parameters listed above. Figures

3 and 4 show the local heat flux and the pressure along the channel for R134a and CO_2 , respectively. It is seen, that the solutions using EES and Windali do not totally coincide for neither of the refrigerants. The largest difference in the heat flux is 309 W/m² for R134a, which corresponds to 4.6%, while for CO_2 it is 68 W/m² or a little less than 1%. The differences in the solution of the pressure are smaller, < 0.1% for R134a and < 0.01% for CO_2 . These discrepancies occur because of differencies in the thermophysical property functions. However, the solutions are considered sufficiently identical to compare the two tools.

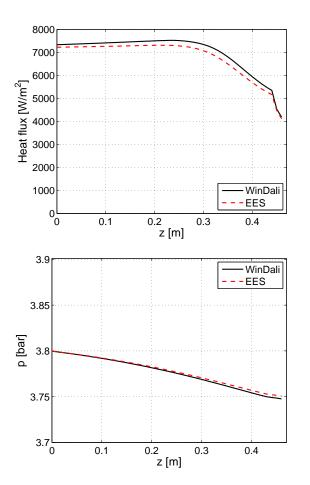


Figure 3: Comparison of the local heat flux and pressure in the channel for refrigerant R134a with uniform distribution of the airflow.

RESULTS AND DISCUSSION

The aim of modelling the parallel channel evaporator was to investigate the impact of a non-uniform

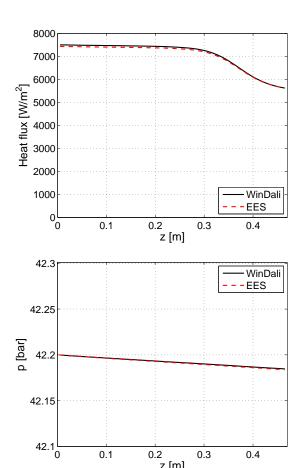


Figure 4: Comparison of the local heat flux and pressure in the channel for refrigerant CO₂ with uniform distribution of the airflow.

airflow on the cooling capacity of the heat exchanger. The airflow over the channels affects the heat load on each, which again determines how fast the refrigerant inside the channels evaporates. In order to keep the same total pressure drop over each of the channels, the mass flow rate will distribute accordingly. In order to perform the investigation, a simple airflow distribution is used, where the air velocity is increased over one channel and decreased over the other, while the mean velocity is kept constant. In order to quantify the degree of maldistribution in a simple way, a distribution parameter is defined as:

$$f_U = \frac{U_2}{U_{\text{mean}}}, \quad 0 < f_U < 1,$$
 (5)

where U_{mean} is the mean velocity and U_2 is the air velocity on channel 2, which is decreased for increased maldistribution. The parameter f_U thus takes a value

between 0 and 1, where $f_U = 1$ for a uniform air flow and $f_U = 0$, when there is no airflow on channel 2 and all air flows by channel 1.

Figure 5 shows how the mass flow rate and cooling capacity are influenced by maldistribution of the airflow for refrigerant R134a for both modelling tools. For an increasing maldistribution of the airflow. i.e. decreasing f_U , the mass flow rate decreases in both channels. In channel 1, where the air velocity is increased, the airside heat transfer coefficient will increase, which again increases the UA-value of this channel. In this channel the refrigerant therefore evaporates faster. However, since the frictional pressure gradient is higher for gas than liquid, the mass flow rate of refrigerant has to decrease in order to keep the pressure drop equal on both channels.

The lower graph in figure 5 shows how the cooling capacity is affected by maldistribution of the airflow. As it is expected, the cooling capacity decreases in the channel 2, due to the lower air velocity. Since the air side heat transfer coefficient does not change linearly, such that it increases less with higher air velocity than it decreases with lower air velocity, the UA-value of the total evaporator will decrease with increased maldistribution of the airflow. A decrease in the UA-value results in a decreased cooling capacity. Meanwhile, in order to keep the total mixed superheat out of the evaporator constant the total mass flow rate decreases, as seen in the upper graph in 5. This decrease of the mass flow rate is responsible for the decrease of the cooling capacity in channel 1, and hence for the decrease of the total cooling capacity.

The dashed lines in figure 5 show results obtained using EES, while the solid lines show WinDali results. It is seen that EES consistently predicts a slightly lower mass flow rate and heat transfer rate, but the shape of the curves are the same. For $f_U < 0.55$ EES fails to converge. WinDali does the same for $f_U < 0.525$. Since both solvers fail to converge at almost the same values, it can be assumed that this limit is given by something in the system of equations rather than the solver.

At the largest maldistribution modelled here, $f_U = 0.525$, which corresponds to a velocity of 2.36 m/s in channel 1 and 0.84 m/s in channel 2, the cooling capacity is decreased by 27%.

In figure 6 similar graphs are shown using CO₂ as refrigerant. Although the thermodynamic properties

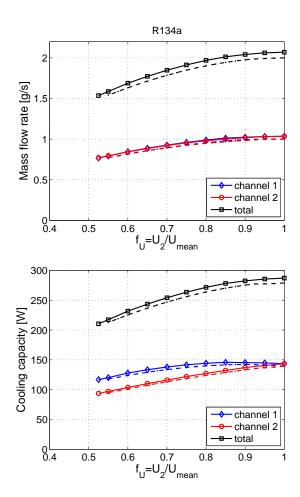


Figure 5: Influence of airflow maldistribution on the mass flow rate and cooling capacity of the two channels using R134a as refrigerant. The solid lines with markers shows the results obtained using WinDali, and the dashed lines show the results using EES.

of CO_2 are quite different from R134a, the general behavior is very similar, at least for this case. Also for CO_2 the mass flow rate decreases in both channels. The total cooling capacity stays almost constant for $0.9 < f_U < 1$, but decreases for smaller values of f_U . In channel 1, which recieves the higher air velocity, the cooling capacity increases slightly until $f_U = 0.7$. However, for smaller values of f_U the cooling capacity of this channel decreases due to the reduced mass flow rate in the channel.

Again, the solid lines show the results obtained from WinDali, while the dashed lines show the EES results. The results obtained from EES and WinDali agree very well, only for very small values of f_U small discrepancies are seen. Also for CO_2 both software fail to converge at some point. For Win-

Dali, the solver cannot converge to a solution for $f_U < 0.25$, while EES fails to converge at f_U smaller than 0.2.

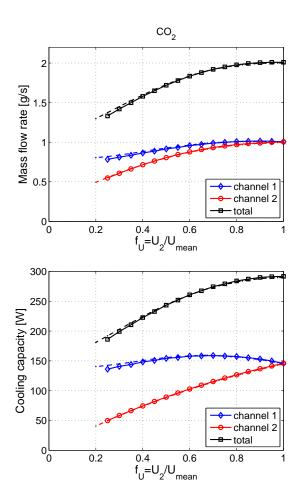


Figure 6: Influence of airflow maldistribution on the mass flow rate and cooling capacity of the two channels using CO_2 as refrigerant. The solid lines with markers shows the results obtained using WinDali, and the dashed lines show the results using EES.

Figure 7 compares the reduction of the cooling capacities due to maldistribution of the airflow. For R134a the percentwise reduction of the cooling capacity is independent of the modelling tool, despite the differences that were seen in figure 5. For the worst cases the reduction in cooling capacity for R134a is more than 20%. For CO_2 the cooling capacity is less affected by airflow maldistribution than R134a. At $f_U = 0.6$, the cooling capacity down to 80% for R134a, while it is only down to 90% for CO_2 .

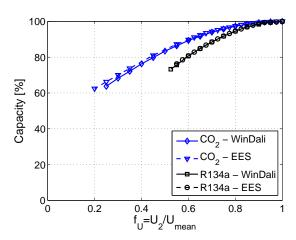


Figure 7: Comparison of the reduction of cooling capacity due to maldistribution of the airflow for R134a and CO₂ using both EES and WinDali.

General experiences with the different tools

The most significant difference between the two modelling tools when modelling the test case, is the solution time. Figure 8 shows the time used for solutions. All calculations were performed on the same personal computer, an Intel(R) Core(TM) 2 CPU, U7600@1.2 GHz and 2 GB of RAM. It was furthermore tested that the solution times were repeatable. For all points shown in the figure the same initial guesses - the solution of the uniformly distributed case - were used. This means that for the points at $f_U = 1$, the solution of the problem is used as initial guess. In this case WinDali is 25 times faster than EES for R134a and 40 times faster for CO₂. Changing the parameter f_U with increasing steps results in longer solution times. In general, if not the solution is used as initial guess, WinDali solves the equations more than 100 times faster than EES.

It is furthermore interesting to know, how dependent the solver is on accurate initial guesses when performing parameter variations. The largest parameter change (in f_U) where WinDali is still able to converge is $f_U = 0.6$ for R134a and $f_U = 0.55$ for CO₂. For EES it is also $f_U = 0.6$ when using R134a as refrigerant, while EES can go down to $f_U = 0.2$ when using CO₂. There is hence no unambiguous answer, on which tools is most stable considering parameter changes.

When running the model, WinDali thus has some considerable advantages to EES, since it is much

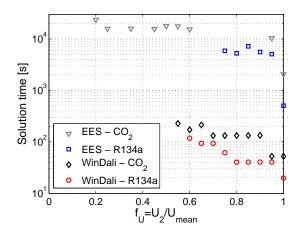


Figure 8: Time used to reach the solution when the solution of the uniform distribution case ($f_U = 1$) is used as guess values.

faster. However, on the implementation side EES has advantages. Implementation of small models in EES is extremely easy and fast and it is also straightforward to build up a larger model gradually, extending the model bit by bit. Using WinDali the model structure is more locked.

When implementing the evaporator model discussed above, EES was used for prototyping. For this purpose EES is an excellent tool. The final model was then transferred to WinDali.

CONCLUSION

In this paper a model of two parallel evaporator channels was built in order to investigate how non-uniform airflow influences on the cooling capacity of the evaporator. Furthermore the model was used as a test case in order to compare and evaluate two different modelling tools: EES [1] and WinDali [2]. Two different refrigerants, R134a and CO₂ were used in the evaporator, and it was shown, that the cooling capacity decreased considerably with increasing maldistribution of the airflow for both refrigerants. However, the cooling capacity of the evaporator using refrigerant R134a was considerably more affected by the airflow maldistribution than the evaporator using CO₂ as refrigerant.

It was furthermore found that the two modelling tools do not give identical results since the functions used for to calculate thermophysical data are not identical. Especially for CO₂ in the superheated

region significant discrepancies occur.

Comparing the two modelling tools showed that the solutions agreed very well. Only small discrepancies were found, which occured since the functions used for calculating the thermophysical data were not identical. Considering solution times WinDali was in general more than 100 times faster than EES. However, the implementation of a model in EES is much more straightforward than WinDali.

REFERENCES

- [1] EES. Engineering equation solver, 2007. Academic Professional V7.954-3D, F-Chart Software, Middleton, WI, USA.
- [2] Morten Juel Skovrup. Windali, 2008. Technical Univesity of Denmark, Department of Mechanical Engineering, http://www.et.web.mek.dtu.dk/WinDali/Index.html.
- [3] M.-H. Kim and C. W. Bullard. Air-side thermal hydraulic performance of multi-louvred fin aluminium heat exchangers. *International Journal of Refrigeration*, 25:390–400, 2002.
- [4] W. Zhang, T. Hibiki, and K. Mishima. Correlation for flow boiling heat transfer in minichannels. *International Journal of Heat and Mass Transfer*, 47:5749–5763, 2004.
- [5] J. M. Choi, W. V. Payne, and P. A. Domanski. Effects of non-uniform refrigerant and air flow distribution of finned-tube evaporator performance. *Proceedings of the International Congress of Refrigeration*, 2003. Washington D.C., USA, ICR0040.
- [6] H. Müller-Steinhagen and K. Heck. A simple friction pressure drop correlation for two-phase flow in pipes. *Chem. Eng. Process.*, 20:291– 308, 1986.
- [7] V. Gnielinski. *VDI Wärmeatlas*, chapter Ga. Springer-Verlag, 9th edition, 2002.
- [8] P. R. H. Blasius. *VDI Wärmeatlas*, chapter Lab. Springer-Verlag, 9th edition, 2002.

NUMERICAL SIMULATION OF ABSORPTION MACHINE UNDER ECHELON CONDITIONS

Sahar Fayad*, Said Abboudi*,Rafik Younes**
*Technology University of Belfort Montbeliard
90010 Belfort,Cedex French

saharfayad7@hotmail.com,said.abboudi@utbm.fr

**Lebanese University Department of Mechanical Engineering, Beirut,Lebanon ryounes@ul.edu.lb

ABSTRACT

The aim of this paper is to study a Lithium-Bromide absorption machine thoroughly. We were interested in making a numerical simulation of this system in order to find the rate of change of the temperatures in the main parts starting from the collector since the temperatures change with the variation of the heat flux density provided from the sun. We considered that the temperature changes only in the part of heat exchanger collector and the idle heat exchanger where as in all other part; we consider that the temperature does not change with time with the change of solar heat flux through the day. In other parts, we set an electric source to ensure that when the solar heat flux does not supply the required heat then the electric source will require. The proposed simulation is based on 14 heat balance partial differential equations. These equations are defined for each heat exchanger of the system (fluid 1-wall-fluid 2) and coupled between them by the inlet and the outlet boundary conditions. Keywords: Absorption machine, renewable energy, numerical simulation.

NOMENCLATURE

C: specific heat [kg/(kcal.°C)]

h: convection coefficient [W/(m 2 .°C)] L: length [m] \dot{m} : flow rate [kg/s] R: rayon [m] T: temperature [C]

 ρ : density [kg/m³]

λ: Conduction Coefficient [W/(m.°C)]

 φ : solar flux[W/m²]

INDEX:

a: absorber c: condenser e: exterior f: fluid g: glycol i: interior p: surface s: sun

v: vapor

INTRODUCTION

The absorption processes have been used to produce cooling and heating in the past few decades. Many works are available in the literature [1-4] but only a few investigations use the solar energy as a source of the absorption system [5-8]. A great part of these works is based on the study of simplified models of the various heat exchangers intervening in the absorption loop. A more complete approach of these models makes it possible to exempt the use of the empirical relations of the heat transfer coefficient between wall and fluid. For a complete study of the cycle of absorption, the use of more complete physical models for each element of exchanger

(absorber, evaporator, etc...) would require computing times much more important .A first approach consists in refining in a progressive way these models in order to better see their influences on the result of the simulation of the absorption loop.

In this study, a simultaneous numerical approach of all the heat exchangers components of the absorption system is investigated in the transient regime.

ABSORPTION CYCLE

The cycle "begins" when high-pressure liquid refrigerant from the condenser passes through a metering device (1) into the lower-pressure evaporator (2) and is collected in the evaporator sump. The heat transfer from the chilled water to the cool refrigerant causes the latter to evaporate (2), and the resulting refrigerant vapor migrates to the lower-pressure absorber (3). There, it is "soaked up" by an absorbent lithium-bromide solution. This process not only creates a low-pressure area that draws a continuous flow of refrigerant vapor from the evaporator to the absorber, but also causes the vapor to condense as it releases the heat of vaporization picked up in the evaporator. This heat—along with the heat of dilution produced as the refrigerant condensate mixes with absorbent-is transferred to the cooling water and released in the cooling tower.

- a) Solution Pump: A dilute lithium bromide solution is collected in the bottom of the absorber shell. From here, a hermetic solution pump moves the solution through a shell and tube heat exchanger for preheating.
- b) Generator: After exiting the heat exchanger, the dilute solution moves into the upper shell. The solution surrounds a bundle of tubes which carries either steam or hot water. The steam or hot water transfers heat into the pool of dilute lithium bromide solution. The solution boils, sending refrigerant vapor upward into the condenser and leaving behind concentrated lithium bromide. The concentrated lithium bromide solution moves down to the heat exchanger, where it is cooled by the weak solution being pumped up to the generator.
- c) Condenser: The refrigerant vapor migrates through mist eliminators to the condenser tube bundle. The refrigerant vapor condenses on the

tubes. The heat is removed by the cooling water which moves through the inside of the tubes. As the refrigerant condenses, it collects in a trough at the bottom of the condenser.

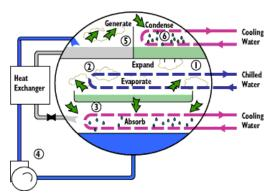


Figure 1. absorption machine

- d) Evaporator: The refrigerant liquid moves from the condenser in the upper shell down to the evaporator in the lower shell and is sprayed over the evaporator tube bundle. Due to the extreme vacuum of the lower shell [6 mm Hg (0.8 kPa) absolute pressure. the refrigerant liquid approximately 39°F (3.9°C), creating the refrigerant effect. (This vacuum is created by hygroscopic action - the strong affinity lithium bromide has for water - in the Absorber directly below.) The single effect absorption cycle uses water as the refrigerant and lithium bromide as the absorbent. It is the strong affinity that these two substances have for one another that makes the cycle work. The entire process occurs in almost a complete vacuum.
- e) Absorber: As the refrigerant vapor migrates to the absorber from the evaporator, the strong lithium bromide solution from the generator is sprayed over the top of the absorber tube bundle. The strong lithium bromide solution actually pulls the refrigerant vapor into solution, creating the extreme vacuum in the evaporator. The absorption of the refrigerant vapor into the lithium bromide solution also generates heat which is removed by the cooling water. The dilute lithium bromide solution collects in the bottom of the lower shell, where it flows down to the solution pump. The chilling cycle is now completed and the process begins once again.

HEAT BALANCE EQUATIONS:

The condenser, the evaporator and the absorber must provide regular thermal conditions of operation in order to guarantee optimum entry conditions for the remainder of the components of the system.

They will be studied only in the steady regime.

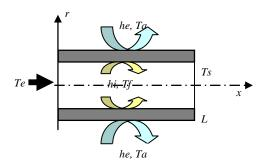


Figure 2.Physical model for the condenser, evaporator, the absorber and the collector.

Heat Balance Equations of the condenser, evaporator and the absorber:

All the above heat exchangers have a cylindrical form constituted of a thick tube and traversed by a fluid flow. The external surface of the tube is submitted to convective heat transfer with the ambient medium, figure 2

For the wall:

$$\lambda S \frac{\partial^2 T_p}{\partial x^2} = k P_e h_e (T_a - T_p) + P_i h_i (T_f - T_p)$$

$$0 < x < L$$
 (1)

k=1 for condenser and absorber, k=-1 for generator and evaporator

For the fluid (water):

$$\dot{m}_f C_f \frac{\partial T_f}{\partial x} = P_i h_i (T_p - T_f), \ 0 < x < L$$
 (2)

Boundary Conditions:

$$\lambda \frac{\partial T_p}{\partial x} = 0$$
 at $x = 0$ and $x = L$ (3)

$$T_f(0) = T_e \quad \text{at } x = 0 \tag{4}$$

Where: $P_e = 2\pi R_e$, $P_i = 2\pi R_i$, $S = \pi (R_e^2 - R_i^2)$

Transient heat balance equations of the collector:

The dynamic behaviour of the collector, the glycol and rich solution heat exchanger and the tube in tube heat exchanger are directly submitted to the solar heat flux and his variation. The study of these heat exchanger systems are realized in the unsteady regime.

For the wall:

$$(\rho CS)_{w} \frac{\partial T_{p}}{\partial t} = P_{e} \eta_{t} \varphi_{s} - P_{i} h_{i} (T_{p} - T_{g}) + \lambda S \frac{\partial^{2} T_{p}}{\partial x^{2}}$$
 (5)

For the glycol:

$$(\rho CS)_f \frac{\partial T_f}{\partial t} + (\dot{m}C)_f \frac{\partial T_f}{\partial x} = P_i h_i (T_p - T_f)$$
 (6)

Boundary Conditions:

$$\lambda \frac{\partial T_p}{\partial x} = 0 \text{ at } x = 0 \text{ and } x = L$$
 (7)

$$T_f(0,t) = T_e$$
, at $x = 0 \ t > 0$ (8)

Initial Conditions:

$$T_f(x,0) = T_{f0}, x > 0; t = 0$$
 (9)

$$T_{p}(x,0) = T_{p0}, x > 0; t = 0$$
 (10)

Transient heat balance equations of the other heat exchangers:

For the first heat exchanger, the internal fluid is the glycol and the external fluid is a rich solution while for the second heat exchanger, the internal fluid is a poor solution and the external fluid is a rich solution.

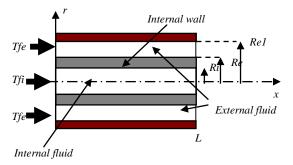


Figure 3. Physical model of the other components of the system.

For the internal fluid:

$$(\rho CS)_{fi} \frac{\partial T_{fi}}{\partial t} + (\dot{m}C)_{fi} \frac{\partial T_{fi}}{\partial x} = P_i h_i (T_p - T_{fi}) \quad (11)$$

For the internal wall:

$$(\rho CS)_{w} \frac{\partial T_{p}}{\partial t} = P_{i}h_{i}(T_{fi} - T_{p}) - P_{e}h_{e}(T_{p} - T_{fe}) + \lambda S_{i} \frac{\partial^{2}T_{p}}{\partial x^{2}}$$
(12)

For the external fluid:

$$(\rho CS)_{fe} \frac{\partial T_{fe}}{\partial t} + (\dot{m}C)_{fe} \frac{\partial T_{fe}}{\partial x} = P_e h_e (T_p - T_{fe}) (13)$$

Boundary Conditions:

$$\lambda \frac{\partial T_p}{\partial x} = 0$$
 at $x = 0$ and $x = L$ (14)

$$T_{fi}(0,t) = T_{ei}, x = 0, t > 0$$

$$T_{f2}(0,t) = T_{e2}, x = 0, t > 0$$

Initial Conditions:

$$T_{fi}(x,0) = T_{fe}(x,0) = T_0, x > 0; t = 0$$
 (15)
 $T_n(x,0) = T_{n0} \quad x > 0; t = 0$

NUMERICAL RESULTS

The system of the coupled heat balance equations (1) and (2) are solved numerically by finite difference method. The numerical results, for the distributions of the temperatures of the wall and the fluid, are presented in the following figures.

a) For the Condenser

The input data are presented in table 1.

Data for Condenser Simulation					
L	R_e	R_i	h_i	h_e	λ
1.6	0.0254	0.00635	6428	11966	395

Table 1.

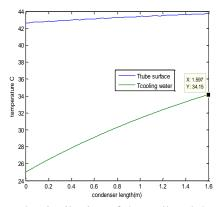


Figure 4. Distribution of the wall and the fluid temperatures for the condenser.

Parameters variation

The material used for condenser tube is the copper. The metal that has higher conductivity is brass, but this one doesn't give big differences in results and is more expensive. Variation in fins thickness (1.8 mm to 2 mm) gives shorter condenser (1.5 m instead of 1.6 m), Figure 5. We obtain $T_g(L)=33.73^{\circ}C$ so no important variation in heat required.

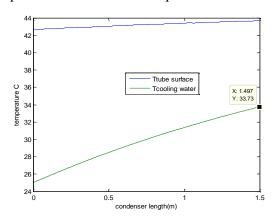


Figure 5. Distribution of the wall and the fluid temperatures for the condenser

If we decrease fins length from 19 mm to 12.7 mm and we decrease also fins thickness we can obtain condenser length 1122 mm (Figure 6)

The difference in cooling water temperature at x=L becomes = 34.15-31.98=2.17°C so we get small optimization.

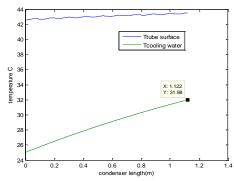


Figure 6. Distribution of the wall and the fluid temperatures for the condenser

b).For the Evaporator

The input data are presented in table 2.

Data for Evaporator Simulation						
L	R_e	R_i	h_i	h_e	λ	
8	0.0156	0.0039	18056	1300	395	

Table 2.

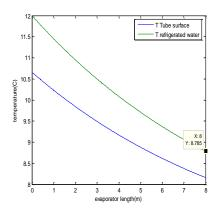


Figure 7. Distribution of the wall and the fluid temperatures for the evaporator

The influence of the external heat transfer coefficient, not presented here, shows that the value $h_e=15019~W/(m^2.{}^{\circ}C)$ gives better results. Then evaporator length becomes 5~m and the quantity of heat gained is bigger, Figure 8.

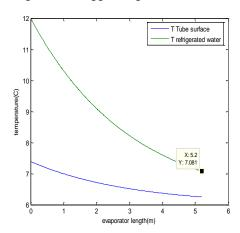


Figure 8. Distribution of the wall and the fluid temperatures for the evaporator.

c. For the Absorber

The input data simulation is presented in table 3.

Data for Absorber Simulation					
L	R_e	R_i	h_i	h_e	λ
1.668	0.0254	0.00635	7649	11966	395

Table 3.

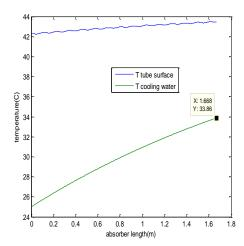


Figure 9. Distribution of the wall and the fluid temperatures for the absorber.

TRANSIENT SIMULATION

For the unsteady systems, the finite difference method is used for the solution; a central form is used for the spatial direction and an explicit form for time

One iteration of the numerical algorithm has the following form of calculation:

$$T^{n+1} = A. T^n + B$$

Where:

 T^n is the vector of the temperatures at time t_n involving the internal fluid, the wall and the external temperatures at different positions, for each heat exchanger.

A is a matrix which depends on the parameters of the system

B is a vector, which depends on the boundary conditions.

The evolutions of the distributions of the temperature of the collector and the first (or intermediate) heat exchanger are presented in figures 10a-f, for the following conditions:

Length of collector = 300 m;

L1 = 10 m;

Solar sensor efficiency = 0.8;

Copper Conductivity = $395 W/m^{\circ}K$;

 $\dot{m}_g = 0.05 \text{ kg/s};$

Glycol density = 1110 kg/m^3 ;

Copper density = 8940 kg/m^3 ; $\dot{m}_{sr} = 0.05 \text{ kg/s}$;

In these figures, the variations of the temperatures of the wall and the glycol inside the collector are presented respectively.

We note that glycol temperature increases continuously with time if we have constant solar flux 500w/m^2

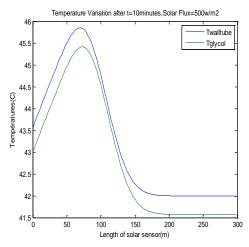


Figure 10a

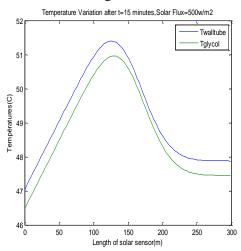


Figure 10b

Figure 10c

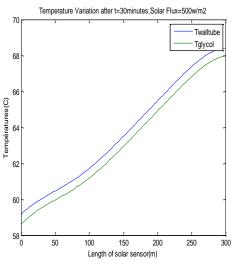


Figure 10d

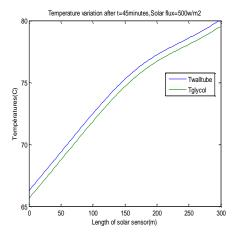
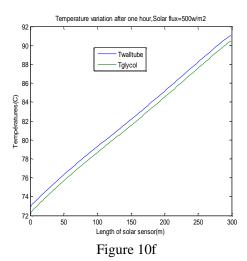


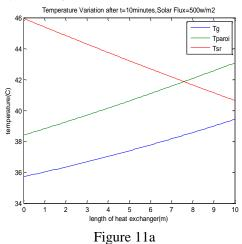
Figure 10e



Distribution of the temperature of the first heat exchanger glycol-rich solution:

The temperature evolutions are presented in figures 11a-e, for different times. We note that after 15 minutes heat transfer begins, rich solution temperature increases and glycol temperature decreases. Glycol heat losses are gained with rich solution. Thermal equilibrium is established after 20 minutes, and the difference between temperature losses and saved are very near.

We note also that long solar exposition increase heat quantity exchanged.



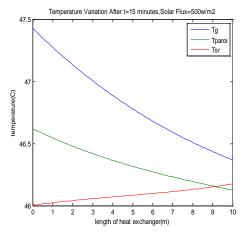


Figure 11b

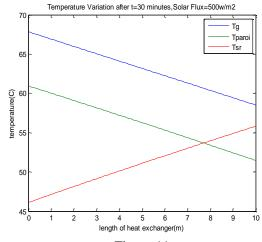


Figure 11c

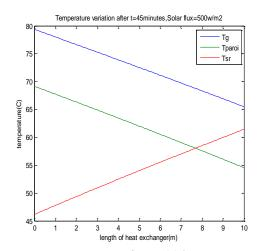
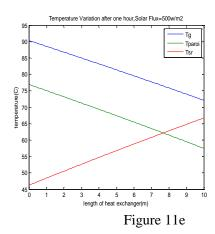


Figure 11d



Second heat exchanger: poor solution-rich solution:

Fluids circulating in this heat exchanger are not affected with solar flux variation. Its role is to heat rich solution circulating outside and cool interior poor solution, Figure 12.

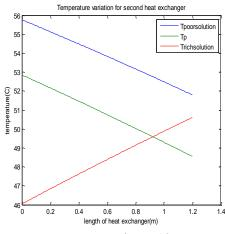


Figure 12

CONCLUSION

In this work, a numerical simulation of an absorption machine under variable solar heat flux, is presented. The condenser, the evaporator and the absorber are studied in steady state and the collector and the glycol and rich solution heat exchanger are studied in the unsteady state. Moreover, we showed the method of resolution taking the tube in tube heat exchanger as an example. The simulation of the absorption machine helps us in showing the variation of temperature through all parts of the machine.

The variation would be the first step to optimization, since to get the absorption machine to respond quickly we must optimize all its parts mainly the heat exchangers. In the heat exchanger, we can optimize their diameter, their thickness and their material, where as for those with fins we optimize their thickness and the distance that separates them. Since, we had already formulated the software that shows us the variation of the temperature throughout the machine, then we put the optimized data and observe how does the temperature change still we reach the most optimized parameters.

REFERENCES

- [1] F. Meunier, Solid sorption heat powered cycles for cooling and heat pumping applications, Applied Thermal Engineering 18 (1998) 715–729.
- [2] G. Cacciola, G. Restuccia, Progress on absorption heat pumps, Heat Recovery Systems & CHP 14 (4) (1994) 409–420.
- [3] N.C. Srivastava, I.W. Eames, A review of developments in solid–vapour adsorption refrigeration and heat pump systems, Journal of the Institute of Energy 70 (1997) 116–127.
- [4] L.M. Sun, N.Y. Feng, M. Pons, Numerical investigation of adsorptive heat pump systems with thermal wave heat regeneration under uniform-pressure conditions, International Journal of Heat and Mass Transfer 40 (2) (1997) 281–293.
- [5] Z.Tamainot-Telto, R.E. Critoph, Adsorption refrigerant using monolithic carbon–ammonia pair, International Journal of Refrigeration 20 (2) (1997) 146–155.
- [6] M. Pons, D. Laurent, F. Meunier, Experimental temperature fronts for adsorptive heat pump applications, Applied Thermal Engineering 16 (5) (1996) 395–404.
- [7]N. C. Srivastava And I. W. Eames. (1997), "A review of developments in solid-vapour absorption refrigeration ans heat pump systems". Journal of the Institute of Energy, 70, pp 116-127.
- [8] T. F. Lin, J.C. Kuo, Transient conjugated heat transfer in fully developed laminar pipe flow, *Int. J. Heat Mass Transfer* 31, 5, 1093-1102, (1988).

Wind



INTEGRATED DESIGN OF WIND POWER SYSTEMS: -DIGSILENT/MATLAB DYNAMIC SIMULATION-

Anca D. Hansen*, Nicolaos A. Cutululis, Poul Sørensen and Braulio Barahona Risø-DTU, Wind Energy Department P.O. Box 49, DK-4000 Roskilde, Denmark

ABSTRACT

The paper presents a modeling and simulation approach for dynamic integrated design studies for wind power systems. Two complimentary simulation tools, such as the detailed power system simulation tool PowerFactory from DIgSILENT and the powerful control system design software MATLAB/SIMULINK, are coupled dynamically online. This modelling approach combines jointly the strengths and abilities of complimentary simulation tools and it is therefore useful to asses a thorough insight into an integrated design of a wind turbine. The idea is that instead of writing and running a whole wind turbine model in only one simulation tool, the simulation is splitted into two parts, one performed in DIgSILENT and the other in MATLAB. These two parts are linked to each other continuously through a communication interface, which is designed in such a way that it is possible to exchange information online between the simulation tools. A model for an active stall wind turbine equipped with a fault ride-through controller is used as an exemplification to emphasize the simulation approach.

Keywords: integrated design, active stall wind turbine, grid fault, DIgSILENT, MATLAB/SIMULINK

INTRODUCTION

At the moment, there is no any complex simulation platform able to investigate simultaneously an integrated wind turbine design.

The need for integrated design of wind turbines is therefore the main justification of a research project carried out at Risø-DTU*. The first stage of this research work is presented in this paper, where the attention is on how to establish and evaluate an online dynamic coupling approach between two different simulation tools, i.e. DIgSILENT and MATLAB/SIMULINK. The paper is thus presenting an approach on how these two tools are coupled dynamically online in a continuous, simultaneous and adjoin simulation.

The communication interface, presented in this paper, is designed in such a way that DIgSILENT and MATLAB/SIMULINK are able to exchange

properly information online during simulations. Besides the communication interface, some wind turbine modeling and control issues are also presented. The aerodynamic part, the mechanical part and the control system of the turbine that regulates wind turbines power both during normal and fault operation conditions, are modeled and simulated in MATLAB/SIMULINK, while the electrical components of the wind turbine and the network are modeled inside DIgSILENT.

The dynamic performance of the presented adjoin simulation approach between DIgSILENT and MATLAB/SIMULINK is assessed and emphasized by means of a set of simulations for an active stall wind turbine, equipped with a fault ride-through controller. The proposed adjoin simulation approach is assessed by a quantitative comparison of the results with a DIgSILENT benchmark model for an active stall wind turbine, developed and validated by Risø-DTU [1]. The idea of this comparison, in the first step, is to assure that, the dynamic properties of an active

^{*}Corresponding author: Phone: +45 4677 5073 Fax: +45 4677 5080 E-mail: anca@risoe.dtu.dk

stall wind turbine are simulated correctly with the new proposed approach. The benchmark model presented in [1] is, in this work, further developed with a fault-ride through controller, developed based on [2].

NEED FOR INTEGRATED DESIGN

Nowadays, the design of wind turbines take typically place in specific dedicated simulation tools, which are specialised either in the mechanical, electrical or control design area. These tools are typically not coupled online in simultaneous and adjoin simulations, but only sequentially in offline approaches, as described for example in [3].

The expertise in these wind turbine design areas is thus built-up independently, with very specific focus and without any influence from one design area to another. Network faults are, for example, typically simulated in dedicated power system simulation tools, based on very detailed models for the electrical components of the wind turbine and for the network, while structural loads of wind turbines are typically assessed in advanced aeroelastic computer codes, which take the flexibility of the tower, blades and other components of the wind turbines into account.

In spite of this fact, practical experience shows that there is a considerable interplay between the mentioned design areas and therefore it is a real need for integrated design investigations for wind turbines. This interplay became even stronger in the last years, due to the continuously increasing size of wind turbines. An example for such interference, especially related to large wind turbines, is the risk for a coupling between the generator electrical eigenfrequency and the tower structural frequency, aspect described in details in [4]. It is known that, the low natural frequency of the generators, determined by the generator inertia, decreases with the generator size and it can therefore get closer to the structural frequencies of the wind turbine.

A better understanding of the interference between different design areas of wind turbines is strongly conditioned by being able to perform integrated design of wind turbines and thus to combine and draw on the abilities and expertise of complimentary simulation tools.

This is the background of two on-going research projects carried out at Risø-DTU, whose overall objective is to develop an integrated simulation environment that combines dedicated tools for control, mechanical, electrical and power system, respectively [5], [6].

As sketched in Figure 1, an integrated design of wind turbines is possible, if the strengths and the knowledge regarding different specialized design research areas (i.e. mechanical, electrical and control design) can be jointly used.

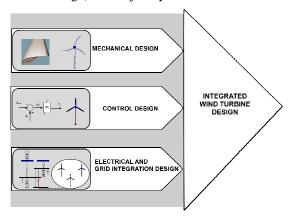


Figure 1: Integrated wind turbine design.

The long term objective of the integrated design research is to combine continuously and, if possible, simultaneously the complimentary abilities of three different simulation tools, i.e. the power system simulation detailed DIgSILENT, the advanced aeroelastic computer code HAWC2 and the popular control system design software MATLAB. These and other similar simulation tools are used intensively by the wind energy industry at the moment. By using these tools in the attempt to connect them continuously and simultaneously, to the extent that is possible, it can be thus achieved a detailed insight into the structural as well as the electrical design and control.

The attention in this paper is directed toward to establish and evaluate an online (simultaneous) simulation approach betweentwo different

simulations tools, as a first step: DIgSILENT and MATLAB/SIMULINK. The wind turbine model is thus splitted into two parts, which are linked to each other continuously through a communication interface, i.e. the electrical components of the wind turbine and the network are modeled inside DIgSILENT, while a simplified aerodynamical and mechanical model are implemented in MATLAB SIMULINK. A detailed aerodynamic modeling of the wind turbine, as it is provided by the third simulation tool, i.e. HAWC2, will be taken into account in a near future work, as it is a natural step of the research.

DIgSILENT and MATLAB description

DIgSILENT is a dedicated electrical power system simulation tool [7]. It covers a full range of applications like: load flow calculations, RMS simulations for dynamic stability, power quality assessment and analysis of wind turbines grid integration and **EMT** simulations investigations into electromagnetic transients. DIgSILENT provides a comprehensive library of component built-in models (i.e. generators, motors, controllers, power plants, loads). The program also provides a DSL (Dynamic Simulation Language), which makes it possible for the users to create its own models library.

MATLAB/SIMULINK is a popular mathematics and control systems design software package, very suitable for modeling complex control systems [8-9]. It is an open interpreted language, which offers a large library of mathematical and control functions. These are invoked using statements entered either directly onto the MATLAB command line or directly called through a m- MATLAB file, or graphically inside a mdl- SIMULINK file.

One practical feature of MATLAB is that it can be started from a user written C program. This feature makes possible to connect MATLAB to communicate with other tools like i.e. DIgSILENT.

DigSILENT's solver is Newton-Raphson. MATLAB may use different types of solvers (i.e. Newton-Raphson, Runge-Kutta, etc) depending on the application. MATLAB solver can be set

directly inside the interface file or in the properties of the mdl- SIMULINK model file.

DIGSILENT TO MATLAB INTERFACE

The simultaneous synergy of a dedicated electrical power system simulation tool, as DIgSILENT, with MATLAB can have several advantages.

For example, the powerful control system modeling capabilities of MATLAB/SIMULINK can be accessed through the fast and powerful dedicated electrical-network modeling simulation tool DIgSILENT. Another aspect is the fact that, although the power system network equations can be programmed into MATLAB, there is at the moment no yet a comprehensive MATLAB toolbox. which is suffice for industrial applications. Moreover, in case of specialized power network simulation studies, it is more practical and faster to run a software like DIgSILENT, specifically developed for this purpose, instead of running MATLAB/SIMULINK code.

Structure of the communication interface

A communication interface is established and designed in order to make it possible for the two software packages to run simultaneously and to exchange data to each other during the online simulations.

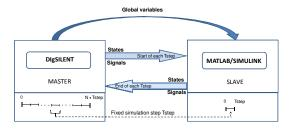


Figure 2: Communication interface DIgSILENT – MATLAB/SIMULINK

DigSILENT can be connected to MATLAB/SIMULINK using an interface function, which is given via DSL. As illustrated in Figure 2, such connection of DIgSILENT with MATLAB is only possible using DIgSILENT as

MASTER and MATALB/SIMULINK as *SLAVE* in the time-domain simulation.

As illustrated in Figure 2, DIgSILENT inserts into MATLAB workspace a set of global variables, which are necessary to successfully run the SIMULINK model. Besides global variables, DIgSILENT transfers a set of signals and states to MATLAB at each simulation step.

It should be noted that DIgSILENT triggers MATLAB at each DIgSILENT time step. In each step of DIgSILENT simulation, the SIMULINK model is completely evaluated. MATLAB runs thus the SIMULINK model one time step and then at the end of each time step gives the values of signals and of states back to DIgSILENT.

DIgSILENT needs the state variables at the end of each integration period. After each time step DIgSILENT recalculates thus the states using linear interpolation, based on the state variable vector returned by MATLAB. The calculation is done using the first two points from the state variable vector and the time vector. If the same fixed time step is used in both simulation tools, then the values of the states are simply equal to the second row in the state vector. The new values for the states are then used for the next simulation in MATLAB. DIgSILENT sends thus them back to MATLAB, which initializes the model, performs the integration and returns the new state and outputs values. After each time step, it is possible to view the values of the state-, outputs and time vector in MATLAB console window. This command window is automatically started when running the simulation.

In general, it is advisable to use the same fixed step size in both DIgSILENT and MATLAB, and due to this, the simulation speed may be slower for the online DIgSILENT – MATLAB/SIMULINK simulation than for the pure DIgSILENT simulation run.

SIMULATION EXAMPLE

In order to show how a MATLAB/SIMULINK model can be interfaced to DIgSILENT and to demonstrate the adjoin simulation between them, an example of an active stall wind turbine

(ASWT) model, splitted-up between these two softwares, is presented along with simulation results.

Simulation setup

In this respect, a simplified simulation scenario of a short circuit in a reduced wind power installation is performed, as sketched in Figure 3. A 2MW active stall wind turbine, equipped with a squirrel-cage induction generator (SCIG) is connected to a typical-medium voltage (MV) distribution network through a step-up transformer.

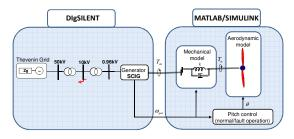


Figure 3: Splitting the task of simulation between DIgSILENT and MATLAB/SIMULINK.

The grid model is represented by a Thevenin equivalent, consisting of a constant magnitude/frequency voltage source and a serial impedance. Such representation is typically used when no specific grid is in focus and generalised conclusions are sought. In this case study, it is assumed that, the wind turbine protections are not taken into account, but they can of course be conveniently modelled inside DIgSILENT, if it is required.

As shown in Figure 3, a 3 phase short circuit closest to the wind turbine, i.e. on 10kV busbar, with duration 100ms, is simulated in DIgSILENT by using the RMS (electromechanical transient models) simulation feature for longer-term dynamics.

Two set of simulations are compared in order to evaluate the performance of the proposed modeling approach: one simulation where the whole wind turbine model and its control are implemented and run inside DIgSILENT, and another one where the wind turbine model (excepting electrical components: generator and

power electronics) and its whole control system are implemented in MATLAB/SIMULINK, while the electrical components and the grid are modeled inside DIGSILENT. This quantitative comparison, as a first step in the integrated design research process, is done in order to ensure that, the proposed modeling approach simulates correctly the dynamic behavior of an active stall wind turbine.

It is assumed that the wind turbine operates at 12 m/s, corresponding to a rated power operation. The parameters of the wind turbine model and pitch controller are of course the same in both simulations. The SIMULINK solver parameters are set to integrate over one small time step, e.g. start time = 0s, end time = 0.01s, and step size = 0.01s

Wind turbine configuration

The model of ASWT has been presented in a variety of publications [10-11] and it is therefore only summarized in the following.

The ASWT model consists of an aerodynamic model of the wind turbine rotor, a mechanical model of the shaft system, a generator model and a generic pitch control model.

The pitch controller, used in this work and illustrated in Figure 4, is designed in such a way that enables a fast control of the wind turbine power P^{meas} to its reference power P^{ref} , through the pitch angle θ [2],[12]. In case of normal operation conditions, depending on wind speed conditions, the wind turbine has either to produce maximum power (e.g. in power optimisation mode) or to limit its production to its rated power e.g. (power limitation operation mode). In the optimization mode, when the power from the wind is less than the nominal power, the error through the controller is a positive value. This is integrated up until the pitch reference θ_{ref} reaches the upper limit of the controller, which is chosen to be the optimal pitch.

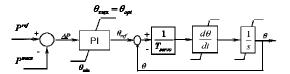


Figure 4: Normal operation pitch control.

In the power limitation mode, the power error of the controller becomes negative and therefore the pitch angle is moving out the upper limitation and starts actively to control the power.

In case of fault operation condition, the fault ridethrough capability of an ASWT, can be achieved by reducing the wind turbine power production for a duration of few seconds from the moment of fault occurrence. This is done in order to prevent wind turbine from going overspeed.

During grid faults, the normal operation condition controller is thus switched off and replaced by an open loop fault operation controller, which reduces directly the mechanical power of the rotor to a predefined level. When the grid fault is cleared, the wind turbine continues running at the reduced power for still few seconds, after which it starts to ramp up the mechanical power of the rotor and to re-establish the normal operation conditions control of the wind turbine.

Development and operation of the model

As illustrated in Figure3, in this simulation example, the electrical parts of the turbine, i.e. generator, transformer and network as well as network faults and system disturbances are modeled in DIgSILENT, while the aerodynamic part, the mechanical part and the control system of the turbine are modeled and simulated in MATLAB/SIMULINK. Measurements of power and voltage are also modeled in DIgSILENT.

The chain of the joint simulation starts from the power system due to the network fault simulated in DIgSILENT. This affects firstly the generator, whose electrical torque drops to zero. Due to the imbalance between the electrical torque and the mechanical torque, the generator speed increases. The mechanical side of the turbine and its control are then affected through generator speed and shaft torque.

Figures 5, 6 and 7 show how the wind turbine part modeled inside MATLAB/SIMULINK (including mechanical, aerodynamical and control components) is interfaced to the electrical parts of the turbine, modeled in DIgSILENT.

Figure 5 illustrates the DIgSILENT file, where one of the slots contains the MATLAB interface.

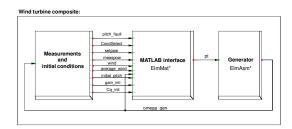


Figure 5: DIgSILENT configuration with MATLAB interface.

Notice that DIgSILENT inserts into the MATLAB interface a set of signals (fault operation pitch setpoint, setpoint power, measured power, wind speed, average wind speed), and initial conditions (pitch angle, gain of the controller, aerolastisc efficiency C_q). The signals, which connect MATLAB interface with the generator in DIgSILENT, are the mechanical power signal pt from the transmission system and the generator speed signal $omega_gen$.



Figure 6: Access of the MATLAB interface file inside DIgSILENT window.

As sketched in Figure 6, the MATLAB interface file is accessed inside DIgSILENT, by indicating the MATLAB path to the MATLAB interface file.

Notice that the state variables ('InitialState') inside MATLAB interface, as seen in Figure 6, are assigned to SIMULINK model in each step of the simulation. To avoid limitation of SIMULINK model, which allows only one instance of the model running at the same time, DIGSILENT must send all parameters in the each step of simulation.

Figure 7 shows the MATLAB/SIMULINK model and control part of the wind turbine, called inside MATLAB interface model. As already mentioned, the models consists of an aerodynamic block, mechanical block and a pitch controller block, which also includes a gain scheduling block for the compensation of the aerodynamic nonlinearities. model is The of independently written and stored in a mdl-file in the same directory as the MATLAB interface file.

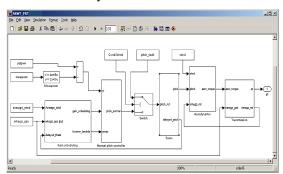


Figure 7: MATLAB/SIMULINK mdl-file, called by MATLAB interface model in Figure 6.

It should be noted that the order of the state variables and thus their initialization settled in DIgSILENT is crucial for a successful online running between DIgSILENT and MATLAB/SIMULINK. The order of the elements in the state vector inside DIgSILENT must be the same as in the state variable vector constructed internally by MATLAB.

To determine the order of the MATLAB state variable vector, the command "[sizes,x0,xstring]= *ModelName*" can be used in the MATLAB console, which is started automatically when the online simulation is started. The *ModelName* is

the name of the SIMULINK model (without the .mdl extension). The output of the string variable xstring contains the names of the dynamic blocks in the SIMULINK model in the desired order.

Simulation results

Figure 8 shows the results of both simulation sets, i.e. the generator stator voltage, generator speed, pitch angle and the mechanical power of the wind turbine. The dotted-line in Figure 8 indicates the results from the simulation set, where DIgSILENT and MATLAB/SIMULINK are coupled dynamically online. Notice that, the results from the two considered simulation sets are on top of each other.

As expected, the generator voltage drops right after the grid fault and recovers to its initial value when the fault is cleared after 100ms. During grid fault, the turbine accelerates as the aerodynamic torque is no longer balanced by the electromagnetic torque of the generator. Notice that, as soon as the fault is detected, the normal operation control strategy is switched off and replaced by the open loop fault operation controller, which has to reduce the power

production to a predefined level. As illustrated in Figure 8, the pitch angle ramps down to a fault operation pitch setpoint. The change in the pitch angle is limited by the pitch rate limiter existing in the servo mechanism. As soon as the fault is cleared and the voltage is recovered to the required range, the wind turbine continues still running at reduced power for still few seconds, before it ramps up the mechanical power of the rotor. The pitch system ramps then up the pitch angle to its normal operation conditions value.

As the results from the two considered simulation sets are on top of each other, the proposed modeling approach assesses the dynamic properties of an active stall wind power system in a similar manner as the benchmark model for an active stall wind turbine developed and run in DIgSILENT does. This means that by using the proposed modeling approach, where DIgSILENT and MATLAB/SIMULINK are coupled dynamically online, one can combine the strengths of both simulation tools in the purpose to achieve an integrated design of a wind turbine.

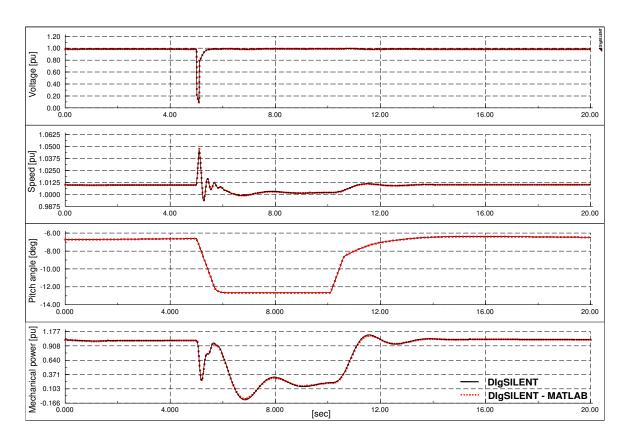


Figure 8: Simulation comparison between the benchmark model inside DIgSILENT and the proposed online simulation approach between MATLAB and DIgSILENT.

CONCLUSIONS

This paper presents an approach for dynamic integrated simulation studies for wind power systems, where two different simulation tools, ie. DIgSILENT and MATLAB/SIMULINK, are coupled dynamically online.

The performance of the proposed modeling approach is assed and illustrated through two sets of simulations, which are carried out and compared, i.e. one where the whole wind turbine model and its control is implemented inside DIgSILENT (benchmark model), and another one where a simplified aerodynamic wind turbine model (excepting electrical components: generator and power electronics) and its whole control system are implemented MATLAB/SIMULINK, while the electrical

components and the grid are modeled inside DIGSILENT.

The online coupling approach between the two simulation tools, i.e. DIgSILENT and MATLAB/SIMULINK, proposed in this paper, is the result of the first investigations regarding integrated design research carried out at Risø-DTU. The long term idea of this research is to be able at the end to combine and to develop a continuous online communication between three simulation tools with complimentary abilities.

The presented approach simulates the dynamic properties of an active stall wind turbine in a similar quantitative way the benchmark model implemented in DIgSILENT does. This means that the presented modeling and simulation approach between DIgSILENT and MATLAB/SIMULINK, can be used to further

develop the complex simulation platform necessary in the investigations of an integrated wind turbine design. This is the goal of our future work, where the now presented simulation approach between two simulation tools, is to be extended in order to be able to simulate at the same time with three different softwares, i.e. MATLAB/SIMULINK, DIgSILENT and HAWC2, the last one having strong skills in the aerolastic modeling part of wind turbines.

ACKNOWLEDGEMENT

This paper describes the ongoing results of a EFP project titled "Integrated design of wind power systems". The Danish Energy Agency is acknowledged for funding this work in contract number EFP07-II. The work is carried out by the Wind Energy Department at Risø-DTU National Laboratory in cooperation with Aalborg University.

REFERENCES

- [1] Sørensen P., Hansen A.D., Christensen P., Meritz M., Bech J., Bak.Jensen B., Nielsen H., Simulation and verification of transient events in large wind power installations, Risø-R-1331(EN), 2003.
- [2] Akhmatov V., Knudsen H., Nielsen A.H., Pedersen J.K., Poulsen N.K., *Modelling and transient stability of large wind farms*, Electrical Power and Energy Systems 25 (2003), 123-144.
- [3] Hansen A.D., Cutululis N., Sørensen P., Florin Iov, Torben J. Larsen, *Grid faults' impact on wind turbine structural loads*, NWPC 2007, Denmark, 6p.
- [4] Larsen T.J., Hansen M.H., Iov F. Generator dynamics in aeroelastic analysis and simulations, Risø-R-1395(EN), 2003
- [5] EFP07-II, *Integrated Design of Wind Power Systems*, Risø-DTU National Laboratory project, http://www.risoe.dtu.dk/Research/sustainable-energy/wind-energy.aspx.
- [6] PSO-F&U 2006-1-6319. Grid fault and design-basis for wind turbines, Risø-DTU

- National Laboratory project, http://www.risoe.dtu.dk/Research/sustainable energy/wind energy.aspx.
- [7] DIgSILENT GmbH, DIgSILENT Technical

 Documentation PowerFactory DSL Models,

 August 2008. www.digsilent.de
- [8] MATLAB, http://www.mathworks.com/
- [9] MATLAB/SIMULINK, http://www.mathworks.com/products/simulink/
- [10] C. Jauch, A. D. Hansen, P. Sørensen and F. Blaabjerg, Simulation Model of an Active-stall Fixed-speed Wind Turbine Controller, Wind Engineering, Vol. 28, no.2, pp. 177-195, 2004
- [11] A. D. Hansen, C. Jauch, P. Sørensen, F. Iov, F. Blaabjerg, *Dynamic wind turbine models in power system simulation tool DIgSILENT*, report Risø-R-1400(EN), 2003
- [12] Hansen, A.D.; Sørensen, P.; Iov,F.; Blaabjerg, F., *Grid support of a wind farm with active stall wind turbines and AC grid connection*, Wind Energy 2006, vol. 6, pp 341-359.

INTEGRATED DESIGN OF WIND POWER SYSTEMS: MATLAB - HAWC2 INTERFACE

Braulio Barahona, Peter B. Andersen, Anca D. Hansen,
Nicolaos A. Cutululis and Poul Sørensen
Risø-DTU National Laboratory
Wind Energy Department
P.O. Box 49, DK-4000 Roskilde, Denmark

ABSTRACT

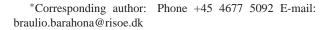
This paper explores basic concepts for coupling two dedicated software packages in order to simulate the dynamics of wind power systems. The objective is to develop an integrated simulation environment that combines dedicated tools for mechanical and electrical analysis, control and power system integration. This work presents the interfacing of Matlab/Simulink and HAWC2. The latter is an aeroelastic simulation tool, developed at Risø DTU. The technical possibilities of interfacing with Matlab and Simulink are described and discussed. An integrated model of a fixed-speed wind power system is presented. It includes structural, aeroelastic, mechanical and electrical systems of the wind turbine. The electrical components are modeled in Matlab/Simulink; while the structural, aeroelastic and mechanical components are modeled in HAWC2. The dynamic interfacing between Matlab/Simulink and HAWC2 is done using dynamic libraries and TCP/IP. A fixed-speed wind turbine under normal operation is simulated to test the interface.

Keywords: wind power, dynamic simulations, Matlab application programing interfaces, HAWC2, shared libraries, TCP/IP, fixed-speed wind turbine

INTRODUCTION

In the context of higher penetration of wind energy in the power system [1], the wind power plant's ability to provide services such as fault-ride-through and frequency control is becoming increasingly more important. Such operating conditions impose loads on wind turbine mechanical and structural components that may be significant. Furthermore, other services that may be required in the short term, such as storm control will also have an impact on the loads of wind turbines.

Therefore, it is considered relevant to study the dynamical interactions of wind turbines with the grid from an integrated perspective and with the goal of better integration of wind power into the grid. Thus the motivation to couple dedicated tools for aeroelastic design with dedicated tools for control and power system analysis. The first step towards an integrated design simulation platform, is the actual



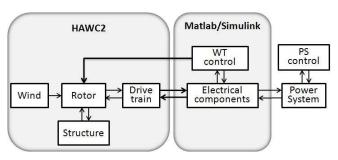


Figure 1: Wind power integrated design platform: HAWC2 - Matlab

coupling of HAWC2 (Horizontal Axis Wind Turbine Code) with Matlab/Simulink. Figure 1 shows the concept of an integrated design platform, where aeroelastic, structural and mechanical components are simulated in HAWC2 while the electrical components are wind turbine controls are simulated in Matlab/Simulink.

HAWC2 is an aeroelastic simulation software, based

on blade element momentum theory and multi-body dynamics, developed at Risø DTU. It is aimed at simulating wind turbine loads under dynamic loading conditions and control. It is mainly coded in Fortran and licensed as a Windows OS executable. Matlab/Simulink is a well know scientific computing high level language with a graphical environment particularly suited for design and simulation of dynamic system and controls.

In the following Section the available options for interfacing Matlab with other applications and the method implemented to interface it with HAWC2 are described. The section The Dynamic System Under Study describes in a general manner the wind turbine system under study and its dynamics. Following, the results of simulating a fixed-speed wind turbine under normal conditions of turbulent wind are presented. Finally, conclusions regarding the perspective of this interface towards an integrated design platform are presented.

INTERFACING APPLICATIONS

There are several possibilities to interface a given application with Matlab and Simulink. This section explores some of the concepts and methods commonly used to interface with Matlab/Simulink. Fundamentally, making available for Matlab a program or function written in a different language is done with the objective of taking advantage of the given application for use in Matlab programs. In some cases, saving computation time can be the driver for accessing shared libraries. Also the matrix manipulation, visualization and control tools in Matlab are attractive to other applications.

For example, the interfacing of GAMS (optimization software) and Matlab as described in [2], is done in order to combine the GAMS ability for large nonlinear optimization with the Matlab visualization tools. This is achieved by having a *gams mex interface*, which basically comes down to a shared library compiled as Matlab executable (MEX-file) that is available from the Matlab command line as any other built-in function.

Another example is how PSCAD/EMT (electromagnetic transients simulation program) and Matlab are coupled[3]. This interface takes advantage of interprocess communication capabilities in both software using a Fortran subroutine (for PSCAD/EMT) and the "Matlab engine" for Matlab. The Fortran sub-

routine starts a Matlab engine and initiates the communication process, making in this way the relevant Matlab mathematical functions and control system blocks (written in a Matlab m-file) available to PSCAD. This interface also allows the Matlab engine to run on a different computer on the same network, thereby allowing *parallelism* of the computation time.

Another way of interfacing with Matlab is the socalled *parallelization* of Matlab. In the sense that some of the tools used in order to run various Matlab engines (slaves) in a cluster called by another Matlab engine (master), can be attractive to interface Matlab with other applications. There has been more than a few initiatives to develop a parallel Matlab [4]. Nowadays, Matlab provides a Distributed Computing Server interface that supports a variety of platforms and operating systems. Also other platforms can be integrated using other generic application programing interfaces (APIs) [5].

The power system simulation tool PowerFactory, also provides possibilities of interfacing with Matlab/Simulink. Mainly, with the objective of taking advantage of the control design capabilities in Simulink [6].

Options for interfacing with Matlab/Simulink

Shared libraries

The concept of *shared libraries* can be ambiguous to some extent. In this document a shared library is considered a collection of functions that can be dynamically loaded by Matlab at run time [7]. The objective of shared libraries is that various programs can access a given set (i.e. library) of functions, subroutines, classes, etc., coded in another language (C, C++, Fortran, Delphi). It can be said that a shared library consists of a header file and the library itself (a * .dll file in Windows OS). The header file provides the *signatures* (or *prototypes*) of the functions, in other words the declaration of the function's name, type and number of arguments. Where as the library file provides the actual definitions of the functions.

In order to give Matlab access to an external function in a shared library the user needs to:

• load the shared library, and

• call the desired function.

This simple process involves knowing the full path of the library and the header file. It is then necessary to know the signature of the shared library functions (SL functions) and the type of arguments to be passed to it. Some argument types in Matlab are, in practical terms, the same as the corresponding type in the language the library is programmed. However, if the types are different they can be automatically or manually converted using Matlab functions as described in [7].

MEX-files

Similarly, MEX-files are functions originally written in another programming language (i.e. source MEX-files in C or Fortran) and compiled to be *Matlab executable files* (namely, *.mexw32 files in Windows OS). Once these binary files are loaded, they work like Matlab built-in functions. These definitions are further explained in [7]. The structure of a source MEX-file is basically:

- comments,
- headers,
- computational routine and
- gateway routine.

standard gateway routine, named mexFunction, is available. This is the actual interface to Matlab. Within mexFunction there is a section of declaration of variables, then the inputs and outputs are assigned to the corresponding Finally the computational routine is called, again with arguments corresponding to the input and output variables requested from Matlab. A MEX-file can actually contain a set of functions, therefore it is similar to a shared library, with the difference that the MEX-file functions can be called like native Matlab functions.

S-functions

A system-function (S-function) is a Simulink block written in computer language (i.e. Matlab, C, C++, Fortran) [8]. Basically, it can be implemented as:

• a Level-1 or Level-2 M-file S-function (written in Matlab) or

 as a C MEX S-function (hand written in practically any modern language, via the S-Function Builder or via the Legacy Tool Code).

TCP/IP communication

The Transmission Control Protocol/Internet Protocol is a mechanism for transferring data between applications over multiple networks [9]. The origins of this protocol lie in the predecessor of the Internet and it is the under laying working architecture of the Internet as it is known today. Some of the features of TCP/IP are:

- quick and simple to configure,
- one end is the client and the other server, but once the link has been establish both can send and receive data,
- non-transactional, not persistent (i.e. it uses memory buffer),
- no built in security, and
- no standard way of signaling end and start of message.

It is possible to make applications talk to Matlab using TCP/IP. Such feature is included in the Instrument Control Toolbox and it is oriented to communicating with instruments that support this protocol [10]. It has been used to communicate with remote applications as described in [11].

Matlab engine

This feature allows external applications to call Matlab software and running it in the background as a separate process. In Windows OS it uses a Component Object Model (COM) interface [7], which enables interprocess communication between applications. The engine library has routines available that allow the external application to control Matlab computation engine. These functions basically come down to start up/shut down and send/receive data.

Matlab - HAWC2 coupling

The task of dynamically interfacing Matlab and HAWC2 for solving complex dynamic systems,

such as a wind turbine, can be approached in various ways. If the objective is to be able to access HAWC2 libraries directly from Matlab or to create shared libraries for HAWC2 directly with Matlab, then some of the options described in the previous Section are applicable. However, the overall objective of this work is to create an interface that allows HAWC2 and Matlab to interact dynamically in order to simulate complex wind power systems, while bearing the possibility of connecting a third application (e.g. DIgSILENT) with Matlab and HAWC2. The solution developed is based on keeping HAWC2 as a stand-alone application while letting Matlab manage some HAWC2 processes and have dynamic access to data and input variables every time step. Thereby, an interface as described by figure 2 using dynamic libraries and TCP/IP sockets was implemented and tested. With this interface HAWC2 and Matlab run as separate processes on the same computer, Matlab acts as a client and HAWC2 as a server using local TCP/IP sockets (i.e. local IP addresses and port numbers). Once the connection is established both ends can send and receive data. HAWC2 is set to remaining listening for the client to send inputs and requests.

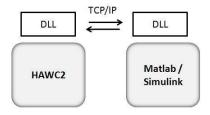


Figure 2: HAWC2 - Matlab interfacing using shared libraries and TCP/IP sockets

THE DYNAMIC SYSTEM UNDER STUDY

A wind turbine is a complex dynamic system subject to stochastic loads driven mainly by the wind. From a general functional perspective, it can be considered to be composed of structure, rotor, drive train, electrical components and control components (figure 1). These systems interact dynamically with each other and with the power system.

For this work an active stall fixed-speed wind turbine was implement. This wind turbine concept is often described in the literature, the main components are: rotor, drive train, generator and pitch control. Typically, the generator is a squirrel cage induction generator (SCIG) directly connected to the grid. Therefore, the speed of the wind turbine rotor is practically fixed to the electrical frequency of the grid [12]. The power is regulated by varying the angle of the blades with the pitch control, for wind speeds below rated this is done to maximize the efficiency. Above rated wind speed the blades are pitched to a stall position (i.e. active stall) to limit the power of the rotor.

In this study the wind turbine is considered to operate under normal conditions and the grid is considered infinitely stiff, thus the dynamics considered in this work are:

- Turbulent wind (based on the Mann model, compliant with IEC61400-1 ed. 3 [13])
- Aerodynamics (state-of-the-art aerodynamics considering dynamic inflow, dynamic stall, skew inflow, wind shear and large deflections [13])
- Mechanical components (rotor and drive train)
- Structural components (tower)
- Electrical generator (reduced order model of SCIG based on [14] and [15])
- Control (a pitch servo modeled as a first order filter)

Turbulent wind, aerodynamics, structural and mechanical components are simulated in HAWC2. The generator model and the control are implemented in Matlab. The generator model is a reduced order model formulated in state-space and solved with standard differential equation solvers available in Matlab. The state-space equations are referred to the dq0 frame, in order to avoid time-varying inductances [16]. The flux linkages of the stator and rotor are selected as state variables, however, the transient of stator fluxes are neglected as described in [14]. The pitch control implemented is described in figure 3, it consists of a moving average of the wind speed with a 60 seconds window, a sample hold of the moving average every 10 seconds, a look up table for the optimal pitch as a function of the wind speed and a pitch servo that is modeled as a first order filter. This simple control strategy works for this case study where the mean wind speed is kept constant at the nominal value of the machine (12 m/s) and standard operating conditions are assumed. The objective is to test the qualitative performance of the HAWC2 - Matlab interface.

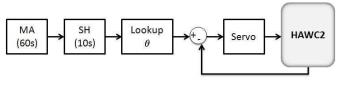


Figure 3: Pitch control for active stall under nominal operating conditions

Integrated simulation

An active stall, fixed-speed, 2 MW wind turbine is simulated with the dynamics described to test the performance of the interface. The simplified flow diagram in figure 4 describes the integrated simulation computational flow.

Previous to the flow depicted in figure 4, time-data management variables and generator model are initialized in Matlab. Then the shared library developed to interface with HAWC2 is loaded and functions of this library are used to startup HAWC2. At startup, HAWC2 uses specified input files and sets a local TCP/IP socket listening to Matlab. Matlab then asks HAWC2 to step to a given *initialization* time and wait.

Once the systems in both applications are initialized, the simulation continues with Matlab reading information of the relevant states (shaft speed ω) and variables (wind speed ν , blade angle θ) from HAWC2, then solving the generator model and estimating a control input. The output of the generator model (torque T) and the control input (blade angle θ) are sent back to HAWC2 along with the indication of iterating to find the solution of the next time step. HAWC2 solves its system, sends states and variables back and waits again for Matlab. The process is then repeated, keeping the same time step size in both simulation tools, until the end of the simulation.

SIMULATION RESULTS

This section presents a simulation of the active stall fixed-speed wind turbine, previously described, un-

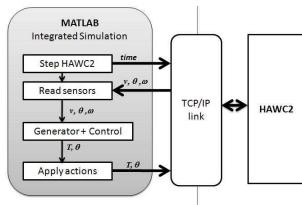


Figure 4: Integrated simulation simplified flow diagram

der normal operating conditions. Figure 5 shows the wind speed perpendicular to the rotor at hub height (80 meters), the pitch angle of the blades and the power produced by the wind turbine. Figures 6 show the tower top and bottom bending moments and figure 7 the flapwise (M_x) and edgewise (M_y) blade root moments.

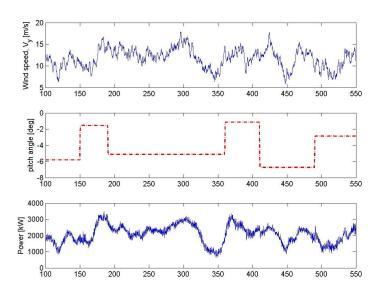
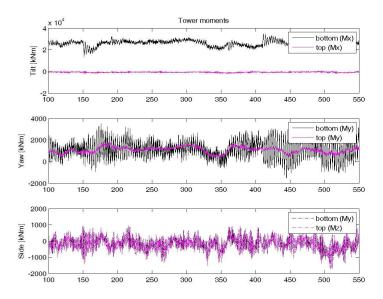


Figure 5: Wind speed, pitch angle and power

CONCLUSION

An interface for Matlab/Simulink and HAWC2 based on shared libraries and TCP/IP sockets has



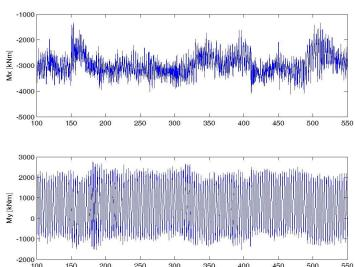


Figure 6: Tower bending moments

been introduced. This interface lets Matlab interact with HAWC2, making possible to perform dynamic simulations with models written in Matlab/Simulink. The interface was tested qualitatively with a fixed-speed active stall wind turbine under normal operation conditions. Generator and pitch control were developed in Matlab while turbulent wind, aerodynamics, structural and mechanical components were implemented in HAWC2.

The interface developed takes advantages of the capabilities and tools built-in in Matlab for interfacing with external applications. It combines such tools in a particular manner specific to this problem. The next step is to increase the complexity of the system and the control to simulate wind power systems under conditions that are relevant for grid integration issues. In this stage, it is considered possible to extend the interface described here to include a power system simulation tool. However, it will very much depend on the built-in interfacing capabilities of the software, particularly when it comes to commercial software.

ACKNOWLEDGMENT

This paper describes the ongoing results of a EFP project titled "Integrated Design of Wind Power Systems". The Danish Energy Agency is acknowledge for funding this work in contract number EFP07-II.

Figure 7: Blade root moments

The work is carried out by the Wind Energy Department at Risø-DTU National Laboratory in cooperation with Aalborg University.

REFERENCES

- [1] "IEA WIND ENERGY Annual Report 2007," tech. rep., International Energy Agency, July 2008.
- [2] M. C. Ferris, "Matlab and GAMS: Interfacing Optimization and Visualization Software," *University of Wisconsin, Computer Science Department.*
- [3] A. Gole and A. Daneshpooy, "Towards Open: Systems A PSCAD/EMTDC to MATLAB Interface," in *ISPT '97*, June 1997.
- [4] R. Choy and A. Edelman, "Parallel MATLAB: Doing it Right," *Proceedings of the IEEE*, vol. 93, pp. 331–341, February 2005.
- [5] The MathWorks Inc., MATLAB Distributed Computing Server 4.0.
- [6] DIgSILENT GmbH, DIgSILENT Technical Documentation PowerFactory DSL Models, August 2008.

- [7] The MathWorks, Inc., *MATLAB External Interfaces*, online edition ed., October 2008.
- [8] The MathWorks Inc., Writing S-functions, on line ed., October 2008.
- [9] A. S. Tanenbaum, *Computer Networks*. Pearson Education International, 4 ed., 2003.
- [10] The MathWorks, Inc., *Instrument Control Toolbox*, July 2005.
- [11] E. J. Mayhew, "Building a Distributed Aircraft Tracking Simulation Using TCP/IP," *MATLAB Digest*, July 2005.
- [12] I. Munteanu, A. I. Bratcu, N. A. Cutululis, and E. Ceangă, *Optimal Control of Wind Energy Systems*. Springer, 2008.
- [13] T. J. Larsen, "How 2 HAWC2, the user's manual," tech. rep., Risø DTU, January 2009.
- [14] F. Iov, A. D. Hansen, P. Sørensen, and F. Blaabjerg, "Wind Turbine Blockset in Matlab/Simulink. General Overview and Description of the Model," tech. rep., Aalborg University, 2004.
- [15] N. A. Cutululis, T. J. Larsen, P. Sørensen, F. Iov, and A. D. Hansen, "Electrical Components Library for HAWC2," tech. rep., Risø DTU, 2007.
- [16] P. C. Krause, O. Wasynczuk, and S. D. Sudhoff, Analysis of Electric Machinery and Drive Systems. IEEE Press Series on Power Engineering, WileyBlackwell, 2002.

MODELLING AND CONTROL OF WIND POWER SYSTEMS FOR STABILITY STUDIES

Adrian Constantin, Adelina Agap, Madalina Cristina Dragan, Florin Iov Aalborg University – Department of Energy Technology 9220 Aalborg Øst – Pontoppidanstræde 101 Denmark

ABSTRACT

Nowadays, the Transmission System Operators are dealing with an increasing share of wind power, thus issuing new grid code requirements in order to maintain power system stability. The Wind Farms must provide grid support capabilities similar with conventional power plants. The purpose of this project is the implementation of a wind power control system in accordance with the grid regulations in Denmark. Modelling of the wind power system, grid connection techniques and the Wind Farm control architecture have been performed and analyzed on generic study cases. The active and reactive power control functions implemented in the model verify the powerful grid support that a Wind Farm can provide to the stability of the power system. A simulation platform for stability studies including a reduced model of a Wind Farm, a VSC-HVDC transmission system and a Wind Farm controller, has been implemented in a power system simulation tool and is available for future studies.

Keywords: Wind Farm Modelling, Stability Studies, Grid Support Functions

INTRODUCTION

The Danish Transmission System Operator (TSO), Energinet, provides grid code requirements defined specifically for Wind Turbines (WTs) and Wind Farms (WFs) connected at voltage levels below and above 100 kV [1] and [2]. More interest is being given to the development of large scale wind power plants with power ratings of hundreds of MW. Such WFs are usually connected to the high and extra high voltage levels of the transmission grid. Also, in countries where there are fewer available onshore sites for developing wind power projects, the development goes offshore. In this situation the Voltage Source Converter (VSC) - High Voltage Direct Current (HVDC) transmission system can be taken into consideration due to its lower power losses than its AC counterpart.

The reliable operation of the WF is verified by developing a simulation model of the entire system in a dedicated power system simulation tool and afterwards analyzing the performance of the system for specific cases.

The grid code details requirements on the active (P) and reactive (Q) power output/demand, power quality issues and Low Voltage Ride Through (LVRT). With respect to the active power requirements of WFs connected to voltage levels above 100 kV, a number of control techniques are

defined in [2] with the following priority (from high to low): system protection, frequency control, stop regulation, balance regulation, power gradient constraint, absolute production constraint and delta production constraint.

Also, the WF must be equipped with reactive power compensation devices in such a manner that Q of the WF in the Point of Common Coupling (PCC) will result in operating points always located in the control band interval in Figure 1. If the WF system can control reactive power outside these limits, special agreements can be settled. All the previously mentioned requirements are difficult to comply without the use of frequency converters installed on each WT in the WF or on a group of WTs (VSC-HVDC case).

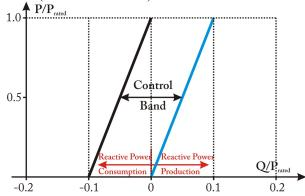


Figure 1: Reactive power control requirements

Several other important grid support functions are mentioned in the grid code such as: low voltage ride through capability and voltage quality aspects. Further verifications of the WF's compliance with the grid code for these latter requirements can expand the functionality of the model. Assessment of the P and Q control capability of the WF has been performed by developing an RMS simulation model of the WF system.

SYSTEM DESCRIPTION

The developed WF model comprises a relatively large WF connected through an VSC-HVDC transmission system to the PCC as it is presented in Figure 2. The simulation platform is intended to be applied successfully to other similar configurations as well (number of WT, voltage and power ratings). It contains 30 WTs, each rated at 2.3 MW, therefore, with a WF rated active power of 69 MW. The WTs are pitch-controlled, fixed-speed equipped with induction generators. A power transformer is connected at the terminals of each WT and raises the voltage to medium voltage distribution levels. A collecting grid with a defined length connects to another power transformer and afterwards to the WF side converter of the HVDC system. The "sending end" station transmits power to the "receiving end" station which will finally inject the energy in the PCC of the main power grid. Consider also that the PCC is a HV or extra HV transmission node of the power system. The voltage ratings have been chosen so as to fulfill the DC voltage requirements of the power converter modules, as stated in [3] and specific modulation index values as in [5].

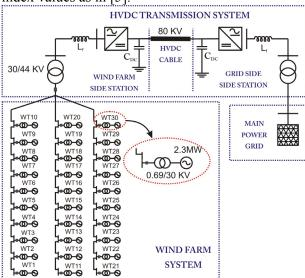


Figure 2: Considered Wind Power System Layout

Large WFs may contain tens or hundreds of WTs, each of them being made of many more individual elements that require modelling efforts in order to be able to analyze the entire system. It is therefore practically impossible to simulate in a reasonable time frame the whole system without having to perform simplification steps. Two main options are available [6]:

- The concept of WF system aggregation represents one solution to the analysis of large wind power systems. Using this method implies the implementation of (1) the corresponding electrical components of each WT e.g. AC generator, transformer, no-load capacitor, power converter and (2) aggregated models for the wind, aerodynamic and mechanical components of the WT;
- The solution in which the WF is represented using reduced models: similar components of the WTs are aggregated into one cumulative model e.g. wind, aerodynamic, mechanical and electrical models. In this case, certain assumptions must be taken in order to obtain accurate results.

As argumented in [6], for power system stability studies where the overall response of the WF is of interest, the latter solution is reasonable, thus obtaining valid results. Consequently, a reduced model is implemented in the simulation model of the WF.

The structure of the WF system implemented in the power system simulation tool Power Factory DIgSILENT is presented in Figure 3, where one WT group is representing 10 WTs.

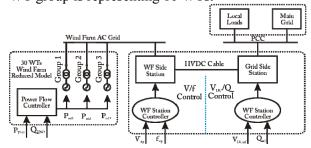


Figure 3: Control structure of the Wind Power System

The HVDC system is coordinated by the overall WF controller. Design of the WF and HVDC control system has been taken into consideration.

The WF controller contains power (active and reactive) regulation functions which send reference setpoints to the corresponding controllers in the system e.g. pitch controllers, PWM converter control. The HVDC control system is split into the "receiving" and "sending" end station controllers acting on their associated converters.

A two level control system is implemented in this paper as described in Figure 4. The WF controller is at the user control level, thus all external or manually set references in the power plant are integrated in this block. The lower level controllers, called the equipment controllers are mainly consisting of the pitch angle controller corresponding to each reduced model of WTs, the WF and Grid side converters controllers.

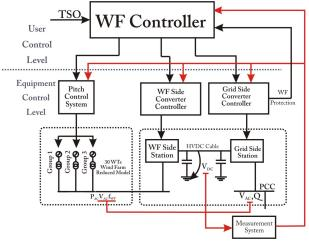


Figure 4: Control architecture of the WF and transmission system

WIND TURBINE MODEL

The block diagram and the signal transfer between each component of one WT is sketched in Figure 5. The wind turbine model is based on [7] and [8] and previously implemented in [9]. It is intended to model a fixed speed variable pitch WT.

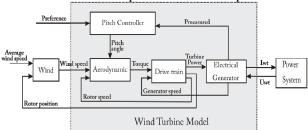


Figure 5: Block diagram of Wind Turbine system

Several additional modifications are made to the system with the purpose of adapting the one turbine model to a higher number of WTs. The WT system

has been chosen to represent a commonly found, modern, 2.3 MW WT with the parameters as in [9].

The wind model is based on [7]. Using measurement data from specific site in Denmark as the average wind speed, the model generates time series wind speed values depending on wind turbine's characteristics e.g. blade radius, rotor position and on environment characteristics e.g. turbulence intensity, terrain's scale etc. This block is essential for simulating realistic power fluctuations occurring in WTs due to variations in the wind speed at WT's hub. The WF smoothing effect that characterizes the power output is also analyzed and additional modifications to the wind model are performed.

The aerodynamic model converts the wind energy into mechanical rotor low speed torque fed to the drive train. It is built around the power coefficient dependence on tip speed ratio and pitch angle, $C_p(\lambda,\theta)$, which is characteristic for the studied type of wind turbine.

The pitch control system of the WT basically is one PI controller that receives the error signal based on the difference between the power reference received from the WF controller and the WT power. The electrical active power, is controlled by setting the pitch angle reference to the aerodynamic model.

The mechanical model of the WT represents the drive train as a two mass model, adequate for power system stability and transients studies [5]. It is based on the model implemented in [9], designed specifically for the simulation software used, namely Power Factory DIgSILENT.

The electrical model comprises a squirrel cage induction generator, typically found in WT installations. A build-in model of the asynchronous machine, available in DIgSILENT has been used with the parameters as in [9].

WIND FARM MODELLING

In this paper, the multi-machine equivalent has been adopted for the WTs placed on each column as in Figure 6. For the 30 WTs WF it results, therefore, three reduced models of 10 WTs each. Characteristic for this simplification are the fast simulation time while still keeping a good accuracy of the results.

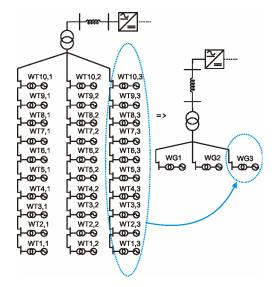


Figure 6: Multi-machine equivalent

Realistic representation of the collective power output of one group of 10 WTs should also include the power smoothing effect. Figure 7 shows the power output of each WT in one group (with green) and their collective response (with red). It is obvious that the power output of the WF has a smoother characteristic than the one of a single WT system.

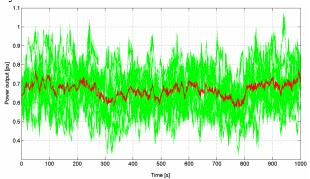


Figure 7: Power output of each WT (green) and their cumulated response (red)

Tuning of the turbulence intensity parameters for the wind model implemented in the reduced WF model has been performed so that the power spectra density of the reduced WF model (one equivalent machine) and the detailed WF model with 10 WTs are overlapping each other as in Figure 8. Although for higher frequencies than the one corresponding with the 3p effect there are small differences, the power contents is insignificant for this region.

The WF controller has the block diagram as in Figure 9 and has been implemented in Power Factory DIgSILENT using DIgSILENT Simulation

Language (DSL). The WF Controller implements a number of functions that coordinate and protect the reliable operation of the WF. For active power control, all the constraints schemes have been implemented. Also, the TSO must be allowed to set references of the reactive power balance in the PCC. Protection measures of the WF are included in this control block.

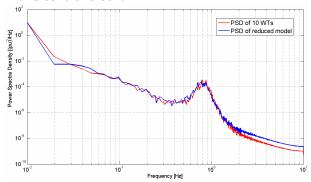


Figure 8: Power spectra density for reduced WF and WF with 10 WTs

The WF controller's inputs are measurement parameters (wind speeds, AC grid frequency etc) and references provided by the TSO (delta, absolute, stop, balance regulation constraints, reactive power setpoints in the PCC). For power system protection reasons, error signals are received from the grid side converter control block. The output signals are the active power reference to the pitch controllers of the WT systems and the reactive power reference to the grid side converter.

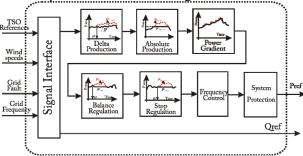


Figure 9: WF Controller block diagram

VSC-HVDC TRANSMISSION SYSTEM

The WF side converter is responsible for controlling the voltage and frequency in the internal WF grid. The control structure adopted for the WF controller is based on [4] and [5], and presented in Figure 10. The internal grid can be viewed as a microgrid and therefore voltage and frequency stability can be achieved using voltage and frequency droop control [11]. Using the voltage

reference two Proportional-Integral (PI) controllers are employed for voltage and current regulation respectively. The PWM modulation index |M0| and the frequency setpoint f0 are the parameters fed to the WF converter. |M0| and |f0| can be adjusted independently by the control algorithm to give any combination of voltage magnitude and phase as desired to maintain the grid balance.

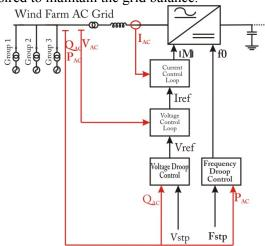


Figure 10: Block diagram of the WF Side Converter Controller

Voltage stability in the internal AC grid is dependent on the demand of Q required by the asynchronous generators [11]. The voltage reference V_{ref} applied to the outer voltage loop is defined by the variation of the AC voltage with the measured Q given by w:

$$V_{ref} = V_{stp} + k_{v} \cdot Q_{meas} \tag{1}$$

where $k_{\rm v}$ is the voltage droop coefficient and $V_{\rm stp}$ represents the voltage set-point fed by the V/f control system.

The frequency active power droop control developed in [4] and [5] is ensuring stable active power operation within the internal WF grid setting the frequency reference f_{ref} for the PWM converter as in (2), where K_f is the droop coefficient for frequency.

$$f_{ref} = 1 - K_f (1 - P_{meas})$$
 (2)

The grid side converter controller is designed for mid and long term power system stability studies. The control variables in this structure are the DC voltage Vdc and Q in the PCC as it can be observed in Figure 11. The following assumptions have been

taken in the control model: (1) only positive sequence components are considered, therefore the system is assumed to be operating in balanced and symmetrical conditions; (2) the voltage phase angle in the PCC is zero (where the reference machine the main grid - is connected).

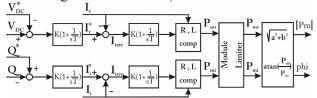


Figure 11: Control structure of the Grid Side Converter

Since I_r and I_i are the effective values of the sinusoidally alternating currents i_r and i_i , the control can contain PI controllers with no steady state error. The advantage of using this converter control structure is the elimination of the phase locked loop (PLL) block which is known not to perform well in the case of severe voltage unbalances and without being required to implement advanced PLL structures [13]. In the control block the outputs of the controller are $|P_m|$ and phi which represent the magnitude and angle of the PWM generated voltage with reference to the grid voltage.

SIMULATION RESULTS

Study cases on all the active and reactive power support functions have been performed, in this paper only the most relevant have been further on presented.

A simulation study is set up in order to verify the performance of the delta production control algorithm. As it is known, the TSO may require active power reserves to be assured by the WF as in Figure

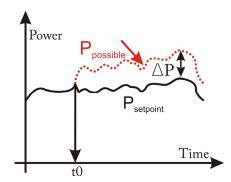


Figure 12: Delta production constraint

The following simulation conditions are adopted: (1) a reserve margin reference with the characteristic (blue color) in Figure 13 is provided externally by the TSO, (2) wind speeds vary in the optimization range, thus not allowing the required reserve margin to be maintained all the time; (3) simulation time frame of 200 seconds.

Figure 13 presents the overall WF reserve power margin (red), while in Figure 14 the electrical power output of the WF in the remote site is viewed. The power margin is well maintained in the case of values greater than 0.1. Larger errors appear when the reserve margin is 0.05, therefore, differences in the setpoint and the reference power are present. Relatively good results are obtained, though in a realistic scenario the change in reserve margin demand will not happen so often, therefore smaller errors will be obtained.

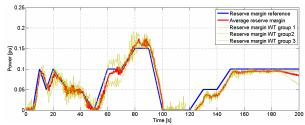


Figure 13: Reserve power margin compliance of the WF

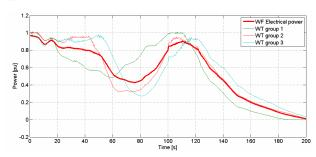


Figure 14: WF electrical power output

The reactive power control algorithm designed to comply with the requirement in Figure 1 has been verified by adjusting Q accordingly with a reference provided by the TSO as in Figure 15 (blue). The actual reactive power output (green) is following steadily the reactive power reference from the TSO while the power output of the WT is unaffected by the reactive power demand. A different situation appears when the reactive power demand increases above the possible total instantaneous power output of the PWM converter. Priority in this case has the active power output over the reactive power demand in order to

maintain the DC link voltage stable and thus WF system stability.

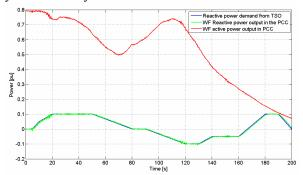


Figure 15: P and Q generated in the PCC by the WF

Power unbalance is directly related to frequency fluctuations; therefore, keeping the frequency in a desired margin ensures power system stability for active power. Usually the frequency stability is mainly the responsibility of the large power stations. For this purpose the grid model in DIgSILENT has been used in parallel with a synchronous machine. Its purpose is strictly related to the increase or decrease of power injection in the main grid, which will have the inherent result of increasing or decreasing the electrical frequency. Practically, this synchronous generator corresponds to a small CHP plant that has no control of P or Q.

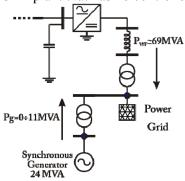


Figure 16: Study case for assessing the frequency control function

This addition at the initial system configuration has been done due to the fact that frequency increase cannot take place in the simulation without the increase of generated power in the PCC above the value of the initial steady state conditions from which the simulation starts. For testing the frequency control of the WF the study case in Figure 16 has been simulated.

A study case has been performed in which the performance of the frequency control algorithm is assessed. The following simulation conditions are assumed: standard frequency control setpoints as in [2]; long start up at 0.5 pu and relatively fast shutdown of the synchronous generator as in Figure 17; the average wind speed is at rated value; the electrical grid has an acceleration time constant $T_a = 100s$ and a short circuit power $S_{sc} = 1200MVA$; no frequency control action is taken from the grid; simulation time - 150 seconds. Figure 17 shows the power output from the WF and the synchronous generator.

In case there is no frequency control action from the WF nor the power grid, the maximum frequency reached is 52.75 Hz, therefore above the maximum accepted range. It is evident that the system loses its frequency stability and the circuit breakers will inherently trip in a real case situation. The results for the Frequency control algorithm are displayed in Figure 18 and Figure 19. In Figure 18, the maximum frequency deviation that resulted in this simulation test was of 0.8 %, respectively 0.4 Hz deviation from the nominal 50 Hz, which is as expected in the control band. Also, it is important to observe that the power grid will remain in an accelerated state even though the synchronous generator is stopped, namely at the limit of normal operation, with an operating frequency of 50.15 Hz (1.003 pu). Further control action from the WF is not required by the grid code. In Figure 19, the power output of the WF (red) is being reduced, thus keeping the grid frequency in the control band.

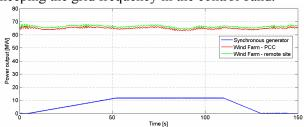


Figure 17: P for the WF and synchronous generator

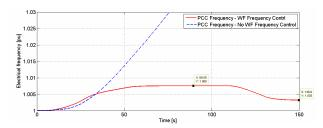


Figure 18: Frequency stability in the PCC

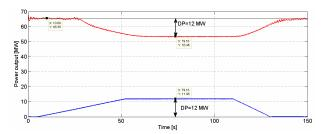


Figure 19: P of the WF (red) and synchronous generator (blue)

CONCLUSIONS

This paper deals with simulation techniques of Wind Power Systems for grid integration studies. A wind model describing the smoothing effect of WF on power production has been implemented in this paper. Smaller power variations (caused by wind turbulence) are "seen" at the WF output as the number of WTs increase. A reduced model of a WF that is valid for grid integration analyses of WFs (for cumulative response of the WF in the power grid) is also presented. Active power regulation functions implemented in the WF controller model prove stable operation of the WF even if in the PCC there is a main power grid with small or no frequency control capability. Furthermore, delta production control characteristic accounts for the reserve power of large power plants, thus creating an energy buffer in the system. Reactive power regulation helps maintaining the PCC voltage level in the designed control interval. An simulation platform of an WF for power system stability studies implemented in Power Factory DIgSILENT is available for future studies.

This model's functionality can be further expanded by implementing other grid support functions. Among them, low voltage ride through is one of the main requirements a WF must comply with in most of the grid codes. Island operation of the WF in case of loss of the main power grid can also be studied using the simulation model of the WF.

References

- [1] Elkraft System & Eltra. English version of Technical Regulations TF 3.2.6 Wind Turbines Connected to Grids with Voltages below 100 kV Technical regulations for the properties and the control of wind turbines. May 19, 2004;
- [2] Elkraft System & Eltra. Regulation TF 3.2.5 Wind Turbines Connected to Grids with Voltages above 100 kV Technical regulation

- for the properties and the regulation of wind turbines. Dec. 3, 2004;
- [3] ABB AB, Grid Systems HVDC. It's time to connect Technical description of HVDC Light® technology. Available from www.abb.com/hvdc;
- [4] F. Iov, P. Sørensen, A. Hansen, F. Blaabjerg. Modelling, Analysis and Control of DCconnected Wind Farms to Grid. International Review of Electrical Engineering. Praise Worthy Prize, February 2006, pp.10, ISSN 1827-6600;
- [5] F. Iov, P. Sørensen, A. Hansen, F. Blaabjerg. *Modelling and Control of VSC based DC Connection for Active Stall Wind Farms to Grid.* in IEE Japan Trans. On Industry Applications, Vol. 126-D, No. 5, April 2006,
- [6] V. Akhmatov. Analysis of dynamic behaviour of Electric Power Systems with Large Amount of Wind Power Phd Thesis. Electrical Power Engineering, Ørsted-DTU, April 2003. ISBN 87-91184-18-5/3;
- [7] F. Iov, Anca D. Hansen, Poul Sørensen, Frede Blaabjerg. Wind Turbine Blockset in Matlab/Simulink General Overview and Description of the Models. Aalborg University, March 2004. ISBN 87-89179-46-3;

- [8] Poul Sørensen, Anca Hansen, Lorand Janosi, John Bech and Birgitte Bak-Jensen. Simulation of Interaction between Wind Farm and Power System. Risø National Laboratory, Roskilde, December 2001. Risø-R-1281(EN);
- [9] Adrian Constantin. Advanced Modelling and Control of Wind Power Systems Master Thesis. Aalborg University, June 2009.
- [10] Anca D. Hansen, Poul Sørensen, Frede Blaabjerg and John Becho. *Dynamic modelling of wind farm grid interaction*. Wind Engineering Volume 26, NO. 4, 2002. PP 191–208;
- [11] Robert H. Lasseter. Microgrids and Distributed Generation. Journal of Energy Engineering, American Society of Civil Engineers, Sept. 200
- [12] DIgSILENT Gmbh. Power Factory User Manual v. 14. PF Manual 14v0E
- [13] M. Ciobotaru, F. Iov, P. Zanchetta, S. Biffaretti. UNIFLEX-PM. Advanced power converters for universal and flexible power management in future electricity network Report on Control Strategies. Deliverable D5.1, EC Contract no. 019794(SES6), June 2008, p. 162, (available on-line at www.eee.nott.ac.uk/uniflex/Deliverables.htm)

Power



MODELBASED DIAGNOSTICS, MAINTENANCE ON DEMAND AND DECISION SUPPORT ON BOILERS

Erik Dahlquist 1), Björn Widarsson 1) 2) and Anders Avelin 1)

1) Mälardalen University, Västerås, Sweden 2) Fjärrvärmebyrån AB

erik.dahlquist@mdh.se, +46-21-151768

ABSTRACT

At a CFB boiler a system has been tested based on a Modelica model together with a decision support system. The model is a physical model including energy and material balances, chemical reactions like combustion and gasification reactions. For the combustion system we primarily consider equilibrium conditions while for gasification the kinetics is important and thus PLS-models built on experimental data in a pilot plant are combined with literature data and a physical model. The simulation model is first developed in Modelica, but then placed as an object in Simulink/Matlab, from which data is communicated to and from the data base through OPC-server. Measured data are collected from the process data base and inserted as initial data into the simulation model, including the boiler, separator, heat exchangers and steam system. A simulation during 300 seconds is performed and the data after this is compared to the initial data. If we have steady state conditions, the values after the simulation will be the same as the initial data, while if the data are not balanced, the difference will correspond to a balanced state between all measured data and the physical correlations in the boiler. This procedure is repeated on a regular basis and the trend of the difference between the measured and the balanced data is plotted and analyzed with respect to slope respectively variance. These data are combined with other type of information like standard deviation of sensors, which corresponds to noise; is the data value changing at all? Input of manual information like lab-data, unexpected events like noise; maintenance actions; activities like how many times a valve has been opening and closing; combination of data like Energy and Mass balances combined with conductivity in blow down from steam drum to detect possible leakages in piping or boiler systems;

All this information is introduced into a BN, Bayesian Net, which has been built from known relations, but where the quantitative data is built from experience and statistics. In this way we can then detect possible faults or probable faults coming up. This information is used by both the operators and maintenance staff. The mathematical simulation model over the CFB boiler and results from the utilization is presented in this paper.

Key words: CFB boiler, mathematical model, simulation, diagnostics, decision support

INTRODUCTION

In most process industries and power plants we always are operating under variable conditions. Steady state operations is always strived for, but seldom reached due to variations in the feed stock, fouling of heat exchanger surfaces, deterioration in sensors etc. To make it possible to both understand the process dynamics better and to make it possible to control the process in an optimal way we propose a method where a simulation model is

built over the process, and this model then is used to compare the real operations with the "optimal operations". By doing this we can both get a tool to diagnose the process performance as well as the sensor status.

The models normally used for data reconciliation normally include only steady state mass balances, and not energy balances like in Sanchez et al [1] and Crow et al [2], Leibman et al[3] Romagnoli et al[4]. These applications all have been primarily focusing

on chemical industry applications. For CHP plants papers have been presented by e.g. Avelin [5], Karlsson et al [6,7,8]. Concerning decision support there are many publications, but here a few are mentioned related to the methodology we are using. Genrup [9] and Bebe [10] have studied degradation in gas- and steam turbines, and the output can determine when it is time to do service. Hess [11] used physical models for the production planning and optimization of a reactor. The output from the algorithm was implemented by the operators, and as such worked as a decision support. Decision support can be structured by using e.g. Bayesian networks. These are giving relations between different input variables and different faults, including statistical probability for the different faults to be present. Jensen [12] has presented the methodology in his "Bayesian Networks and Decision book Graphs". Applications for different industry usage has been presented in e.g. Weidl's thesis [13] "Root Cause Analysis and Decision support on Process Operation" as well as by Widarsson et al [14] specifically for a boiler application and by Bell [15] in operations decision support based on dynamic simulation and optimization in pulp and paper. A more general evaluation of the use of Bayesian networks for diagnostics has also been presented by Przytula et al [16]. Procedure for sensor diagnostics using Dynamic Characteristic Curve Estimation was presented by Latva-Käyrä et al [17].

SYSTEM DESCRIPTION

At a CFB boiler at Malarenergy, Vasteras, a system has been tested based on a Modelica model together with a decision support system. The model is a physical model including energy and material balances, chemical reactions like combustion and gasification reactions. For the combustion system we primarily consider equilibrium conditions while for gasification the kinetics is important and thus included, built on experimental data in pilot plants combined with literature data.

The simulation model is first developed in Modellica, but then placed as an object in Simulink/Matlab, from which data is communicated to and from the data base through OPC-server. See figure 1. Measured data are collected from the process

data base and inserted as initial data into the simulation model, including the boiler, separator, heat exchangers and steam system. A simulation during 300 seconds is performed and the data after this is compared to the initial data. If we have steady state conditions, the values after the simulation will be the same as the initial data, while if the data are not balanced, the difference will correspond to a balanced state between all measured data and the physical correlations in the boiler. This procedure is repeated on a regular basis and the trend of the difference between the measured and the balanced data is plotted and analyzed with respect to slope respectively variance. In figure 2 we have a simple example with a tank, a pump and two valves. The sum of the flows do not match, but by including also information on level in the vessel, valve positions and pump motor power as well a balance can be calculated by a physical model. In figure 3 we see the measured, the calculated and the difference for the three positions for three time steps with 15 minutes in-between. Here we can see that for position 1 the difference is the same for all three time steps. while for position 3 it is increasing, indicating drift in a sensor or clogging of a valve.

These data from the model calculations are combined with other type of information like standard deviation which of sensors. corresponds to noise. Different types of deviations are considered. First of all - is the data value changing at all? If so, is there a significant trend in the deviation in one direction, or is it fluctuating but at a principally constant level? Is the fluctuation random or more like a sinus curve, indicating oscillations?

Aside of on-line data also input of manual information like lab-data are used. Unexpected events are noticed, both manually as input from operators, as well as input from maintenance staff. Maintenance actions are registered and statistics about different type of actions stored and used as input to the decision support system.

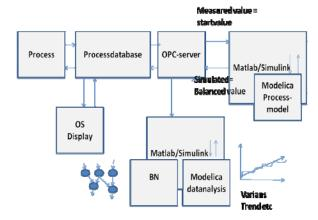
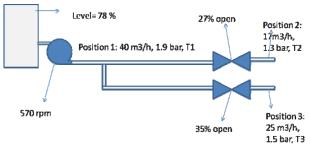


Figure 1. System layout for on-line application of the decision support system for maintenance on demand and process performance diagnostics

Activities like how many times a valve has been opening and closing can give an indication on both how well the control of the valve is tuned but also indicate the need for service.



From data-base: 40 m3/h - 17 + 25 m3/h - no balanceBalance calculation with model gives: 39 m3/h = 17.5 + 21.5 m3/h,

Figure 2 A simple example of a system to illustrate the procedure

Sometimes different type of information can be combined to give indications on most probable cause of a problem as well as an isolation of where a problem has occurred. Combination of data like Energy and Mass balances together with conductivity in blow down from a steam drum can give information not only about a possible leak in the boiler tubes but also where the leakage can be. If the conductivity is constant it indicates a leakage in the Economizers, while if the conductivity drops, it indicates a leakage in the actual boiler room, as the concentration of salts in the water going back to the steam drum is reduced as less water goes back.

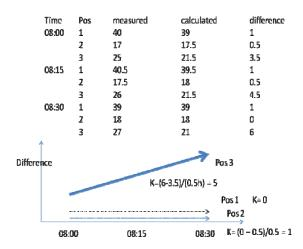


Figure 3. Measured data for each position respectively calculated data for the same positions using the simulation model, for three times

Other type of information can be information about local diagnosis, like noise in sensors due to poor electrical contact or similar.

All this information is introduced into a belief tree, e.g. a BN, Bayesian Net, which has been built from known relations between cause and effects principally. The quantitative data is gathered from specific experience from operators and maintenance staff as well as from statistics on different measurements etc described earlier. In this way we can detect probable faults coming up. An example of this using the previous example is shown in figure 4.

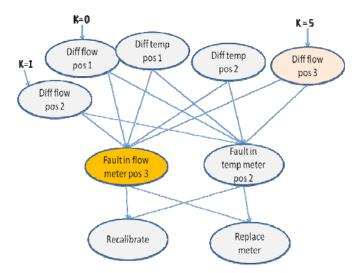


Figure 4. Decision support on possible faults from the previous example

This information can be used by both the operators and maintenance staff. What information that should be used by different categories will have to be defined, but principally immediate actions should be taken by the operators, while more planned service should be performed by the maintenance staff.

The procedure can be summarized as a set of calculations using the physical model combined with data from the process data base.

- 1. The data base is filtered with different filters as a "moving window": filtered value of variable x1 (t+1) = v* old value variable x1 (t) + (1-v)*new value variable x1 (t+1) where 0 < v < 1.0. For a high damping v is close to 1.0. Different values of v are used in parallel during the development phase, but later the value is fixed for a specific variable.
- 2. The filtered data are sent to the simulation model as "initial values". The simulator runs for a specific predefined time period. 300 seconds gave a stable situation.
- 3. The final data from the simulation were sent back to the database and stored
- 4. The data set for each variable with both simulation and measured data were sent to the calculation of the deviation trends as well as a variance analysis of the time series for different time horizons
- 5. The data then are sent to the BN tree as input data.On a frequent basis the weighting factors in the BN tree are calculated

EXAMPLE FOR A CFB BOILER

The method has been tested of line at Malarenergy but will be implemented on-line later this year. The simulation model contains the following elements [18]:

The mass in the bed inventory by time is given from:

$$\partial m_{inventory}/\partial t = \sum m_{i,in}$$
 - $\sum m_{i,out}$

where m $_{i,in}$ is the mass in-flow of each single component i (C,H,O,N,CO₂,H₂O,NO₂,ash) and m $_{i,out}$ is the corresponding out-flow. The change in concentration of each component i is given by c_i in the bed inventory:

$$\partial c_{i}/\partial t = \left(\sum c_{i} * m_{j,in} - \sum c_{i} * m_{k, \text{ out}}\right)/m_{\text{ inventory}}$$
(2)

where j are all incoming flows and k all flows out of the inventories. Except the bed inventory we also have one inventory for the Intrex and one for the steam system. The steam system has only water and steam components, while the Intrex has the same components as the bed. The temperature $T_{inventory}$ in the inventory is calculated from the energy balance:

$$\partial T_{inventory} / \partial t = \sum_{k} T_{j} * C_{p_{i}} * c_{i} * m_{j,in} - \sum_{k} T_{k} * C_{p_{i}} * c_{i} * m_{k, out}) + \Delta H - U * A * (T_{inventory} - T_{outside}) / (m_{inventory} * (\sum_{k} c_{i} * C_{p_{i}}))$$
(3)

Here ΔH is the energy released during combustion and U is the heat transfer number, A the area of the heat exchanger area and T outside the temperature at the other side of the heat exchanger surface – steam temperature vs exhaust gas temperature. Cp_i is the heat capacity for component *i*. These equations are the most important. Aside of them we also need correlations describing the change in each single component. Carbon, C, in the biomass is combusted to CO₂, and the hydrogen is forming H₂O. Oxygen in the fuel is used for the combustion aside of the oxygen in the air.

The boiler is seen in figure 5. It is a 170 MW CFB boiler operating on biomass. As seen in the figure the steam system is quite complex where two steam lines are in parallel but not symmetric. In the model we have run a simplified configuration with the Modelica model while a complete model was used using APROS, to see the impact of detailed modeling for the diagnostic purpose, where the exhaust gas train heat exchangers were not in focus, but the bed and the Intrex. The model was used together with input data from the database.

(1)

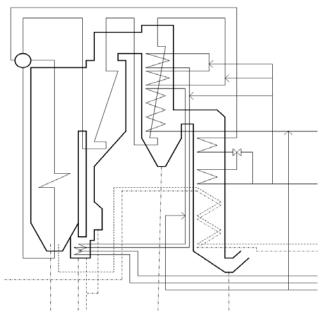


Figure 5. The boiler 5 at Malarenergy

In figure 6 we see the development of the deviation between the simulation calculation and the measured values for the temperature in the separator ("cyclone") over a 14 day period to the left and the steam temperature in the Intrex super heater to the right.

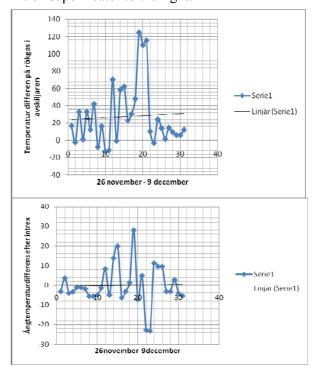


Figure 6. The deviation between calculated and measured temperature in the separator ("cyclone") to the left and in the Intrex Super Heater steam temperature during a two week period to the right.

What we can see is that first the deviation is oscillating around an average for five days, but then it moves away almost 100 oC for several days, until it goes back again at the end of the period. This indicates that we had combustion high up in the separator instead of in the bed. at least to some extent, during several days. For the steam temperature in the super heater we can see that deviation first is very small, but then starts to oscillate. When the temperature is high in the separator, it goes down in the Intrex steam compared to what it should have been from a balance point of view. indicating that the solids going down to the Intrex is affecting also the Intrex performance. In figure 7 we have made a cause tree for the Intrex steam temperature, showing possible relations. This tree can then be used to identify possible problems and the probable cause of these. By tuning the tree formulated as a BN we can also determine the probability for different causes in relation to each other. We have not had time to do that tuning yet, but it will be implemented later this year.

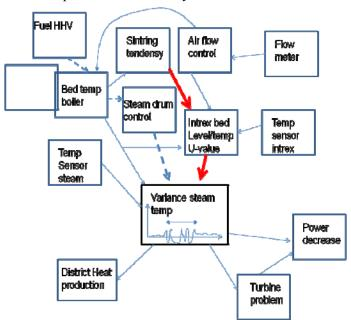


Figure 7. A tree structure showing the possible root causes of the increased variation in the steam temperature in the super heater inside the Intrex

DISCUSSION AND CONCLUSIONS

From the example we can see that it may be interesting to use simulation models to correlate different variable to each other through physical relations. By calculating the probable balance as a function of time

development of different type of faults can be detected at an early stage. This includes both process problems and sensor problems. By structuring the information we can achieve a decision support system that can be used both for the daily operations as well as for maintenance on demand. By feeding back information on true causes of different problems we can tune e.g. a BN to get the quantitative information about the relative probability of different possible faults in relation to each other. By then checking more in detail the status of each possible problem, the operators and maintenance people can identify the true fault and the model can be upgraded on a continuous basis.

By doing this more advanced control will make sense, to optimize the performance of the process, in this case the power boiler.

ACKNOWLEDGMENT

We want to thank Varmeforsk, KKS (Swedish Competence Foundation) and Swedish Energy Agency as well as Malarenergy for the support of the project.

REFERENCES

- [18] Avelin A., Widarsson B., Dahlquist E. and Lilja R.: Time based data reconciliation and decision support for a CFB boiler. IFAC Power Plant Control conference in Tampere July 5-8, 2009.
- [6] Avelin A., Widarsson B. and Wester L. (2006), "Moisture content determination of biomass fuel supported by Bayesian Networks", Proceedings ASCC-2006, Jul 18-21, Bali, Indonesia
- [10] Beebe R., "Condition monitoring of steam turbine by performance analysis", Journal of Quality in Maintenance Engineering, vol 9, no 2, pp 102 112, 2003.
- [15] Bell J., Dahlquist E.,Holmstrom K.,Ihalainen H.,Ritala R.,Ruis J.,Sujärvi M.,Tienari M: Operations decision support based on dynamic simulation and optimization. PulPaper2004 conference in Helsinki, 1-3 June 2004.Proceedings
- [2] Crowe C.M., Campos Y.A.G., Hrymak A., "Reconciliation of process flow rates by matrix projection. Part I: Linear case", *American Institute of Chemical Engineers Journal*, vol. 29. pp 881-883, 1983.
- [9] Genrup M., "On Degradation and Monitoring Tools for Gas and Steam

- Turbines", PhD thesis, Lund University, 2005, ISBN: 91-628-6470-X
- [11] Hess T. (2000): Process optimization with dynamic modeling offers big benefits, I&CS, August, p 43-48.
- [12] Jensen, F.V., "Bayesian Networks and Decision Graphs", Springer Verlag, 2001, New York, ISBN 0-387-95259-4
- [6] Karlsson C., Dahlquist E., "Process and sensor diagnostics Data reconciliation for a flue gas channel", Värmeforsk Service AB, 2003, (in Swedish).
- [7] Karlsson C., Dahlquist E., Dotzauer E.: Data Reconciliation and Gross Error Detection for Sensors in the Flue Gas Channel in a Heat and Power Plant, Proceedings PMAPS, Iowa, USA, 2004
- [8] Karlsson C., Arriagada J., Genrup M., "Detection and interactive isolation of faults in steam turbines for maintenance decision support", accepted for Journal of Modelling and Simulation, Practice and Theory in 2008
- [17] Latva-Käyrä K. and Ritala R. Sensor Diagnostics based on Dynamic Characteristic Curve Estimation", 10th International Conference on Technical Diagnostics, Budapest, Hungary, June 9-10th, 2005.
- [3] Leibman M. J., Edgar T. F. and Lasdon L. S.: Efficient data reconciliation and estimation for dynamic processes using nonlinear programming techniques. Comput. Chem. Engng, 1992, 16(10/11), 963-86.
- [16] Przytula K.W., Dash D., Thompson D., "Evaluation of Bayesian Networks Used for Diagnostics", Aerospace Conference, 2003, IEEE Proceedings, vol 7, pp 3177-3187, 2003
- [4] Romagnoli JA, Sánchez MC; "Data Processing and Reconciliation", Academic Press, San Diego July 1998.
- [1] Sanchez M. A., Bandoni A., Romagnoli J., "PLADAT A package for Process Variable Classification and Plant Data Reconciliation." *Journal of Computers and Chemical Engineering* (suppl. 1992), pages 499-506.
- [13] Weidl G., "Root Cause Analysis and Decision support on Process Operation", PhD Thesis, paper I, page 18, Mälardalen University Press 2002, ISBN 91-88834-36-0.
- [14] Widarsson B., Karlsson C., Dahlquist E., "Bayesian Network for Decision Support on Soot Blowing Superheaters in a Biomass Fuelled Boiler", Conference on Probabilistic Methods Applied Power Systems, Iowa, Ames, USA, 2004

An agent-based simulation of SmartGrid

Jianhua Xu and David P. Chassin, Pacific Northwest National Laboratory, USA

Abstract

Demand response and dynamic pricing programs are emerging in greater numbers as policy makers look for new mechanisms to integrate distributed resources into system operations. The behavior of demand resources, their interaction with the power system, and their operating characteristics under different electric market scenarios raise many questions for system operators, market operators, and regulators. This paper discusses the use of GridLab-D as simulation environment to understand the behavior of distributed resources in new market environments.

Introduction

The most important characteristic of a "smart grid" is its ability to flexibly incorporate distributed energy resources (DER) from the generation, storage, and demand sides into system operations. The integration of large number of resources presents serious technical challenges, which lead many to ask whether and how they can be effectively and reliably coordinated while preserving the integrity and resilience of the overall system. A simulation system, GridLAB-D, and an experiment on the Olympic Peninsula of Washington State were created and conducted to help answer these questions [1] [2].

GridLab-D is an agent-based system simulation tool that models end-use loads coupled with power distribution models [3]-[10]. As a SourceForge-hosted product, this tool is under continuous development, but many of the most important capabilities have already been implemented and demonstrated, such as extended quasi-steady state time-series solutions, end-use models of homes and appliances, appliance-based load shedding technologies, and distribution-level market systems.

The experimental demonstration was conducted on the Olympic Peninsula to examine how information-based technologies can affect user behavior. Specifically, the project tested what benefit distributed generation and demand response resources offered to relieve transmission and distribution congestion, how heterogeneous distribution-level resources could be integrated, and whether real-time communication of incentives elicited prolonged voluntary demand reduction.

The conduct of such large-scale experimental demonstrations is time-consuming and very costly. A priori simulation is an important part for ensuring the success of such projects. Part of our research therefore is focused on validating against the data obtained to determine whether the tool will be effective for other such projects that are in the planning stages today. The research is on-going and in this paper, we only present the comparison of simulated residential energy consumption and the measured residential energy consumption.

The GridLAB-D System

As an agent-based simulation tool, GridLAB-D implements an advanced algorithm that determines the simultaneous state of millions of independent objects, using the process illustrated in Figure 1. Each object is solved independently for both its state as a function of time and time as a function of state. This algorithm has important advantages over traditional finite difference-based simulators: it is an implicitly parallel process; it can handle widely disparate time scales, ranging from sub-second to many years; and it is very easy to integrate new models. The advantage over traditional differential-based solvers is that it is not necessary to integrate every device's behavior into a single set of equations that must be solved simultaneously.

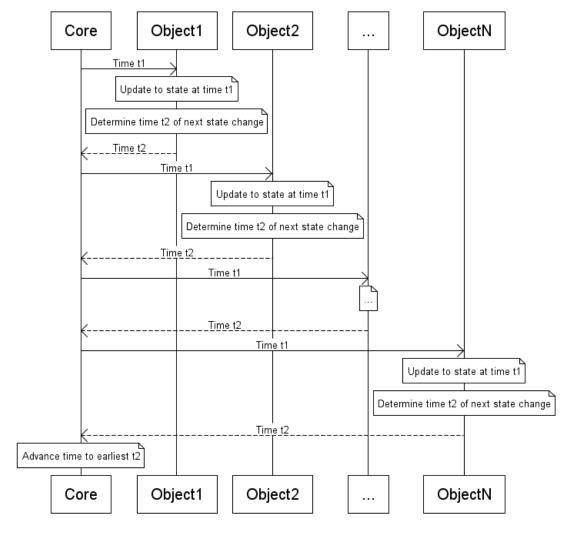


Figure 1 : UML sequence diagram for a single GridLAB-D agent synchronization event that advances the simulation time from t_1 to t_2 .

GridLAB-D can examine in detail the interplay of every part of a distribution system with every other. GridLAB-D does not require the use of reduced-order models, so the danger of oversimplifying assumptions can be mitigated to the extent that the modeler desires. An extensive suite of tools are available to build, run and analyze studies. For instance, users can create detailed studies of how new end-use technologies, distributed energy resources, distribution automation, and retail markets interact and evolve over time, to create and validate rate structures, examine consumer reaction, and verify the interaction and dependence of programs with other technologies and wholesale markets. The focus of this paper is on using GridLAB-D to simulate smart residential energy technology, hence we introduce the two major parts of the system that are involved which are end-use load modeling, and market systems.

End-Use Load Modeling

Commercial and residential end-uses are implemented using the Equivalent Thermal Parameters (ETP) model [11]. These are differential models solved for both time as a function of state and state as a function of time. Currently residential end-uses such as heat-pumps, residential heating, electric hot water heaters, washer and dryers, cooking (range and microwave), electronic plugs and lights are supported. Commercial loads are simulated using an aggregate multizone ETP model that will be enhanced with more detailed end-use behaviors.

Market Systems

GridLAB-D implements a simple double auction for all market clearing processes. Devices submit price/quantity bids to buy or sell energy on the distribution system. Loads bid to purchase energy over the coming five-minute interval at a particular price. The bulk supply is obtained at the wholesale price for the available capacity on the feeder under the present conditions. Distributed generators use a cost function to adjust their bid prices for the generator's available capacity. The complete supply and demand curves are assembled at five-minute intervals and the market is cleared, with the clearing price being published. The clearing quantity establishes the expected feeder load and any distributed generation dispatch request.

Model Validation

GridLAB-D has been validated with both existing end-use simulations and standard power flow analysis tools. Testing on the power system components of GridLAB-D is done in two steps which are unit tests and integrated tests. The unit tests are designed to ensure that the objects that represent individual components, such as a line section, are properly implementing their functions. This is especially important since the distribution system is modeled in accordance with Kersting's method [12] which gives a complete representation of the system. The integrated tests use the 4-node, 13-node, and 37-node IEEE Distribution Test Feeders [13].

Integrated validation is much more challenging to perform. For one thing, there are no other equivalent simulation environments that can be used to compare coupled end-use and power flow calculations. In addition, the complexity of the models and the huge volume of output make direct comparison of results very difficult and possibly inconclusive. This requires that higher level comparisons be employed, such as statistical techniques and comparisons of integrated results, such as energy use, load shape statistics, price and load duration curves, etc. These challenges have not been fully overcome to date, and we foresee a need for significant work to identify more formal approaches to validating simulation systems of the complexity of GridLAB-D. Nonetheless, the results from the simulation of the Olympic Peninsula demonstration are a good start.

The Olympic Peninsula Demonstration

The Olympic Peninsula project was conducted from April 2006 to April 2007 to demonstrate smart grid technologies [14] by the US Department of Energy, Bonneville Power Administration, and a number of industry and academic collaborators. Specifically, the project "tested weather automated two-way communication between the gird and distributed resources will enable resources to be dispatched based on the energy demand and price signals that they receive"[2]. This project included a number of municipal, commercial and residential customers whose equipments responded to energy price signals. These equipments include five water pumps, two asynchronous diesel generators, a synchronous micro-turbine, and roughly 100 residential electric water heaters, electric dryers, and electric space heating and cooling systems. Two additional virtual generators were simulated in order to assure that sufficient supply was provided for a balance market.

Each water pump submitted a bid every five minutes based on the measured height of the reservoir at the pumping station. The pump bid high when its reservoir level became low, and bid low when its reservoirs level became high. The start and stop of the pumps were determined by the market clearing results in relation to the bids. Detailed control and communications for the pumps were modeled as described in the project report [2]. The two diesel generators are connected to commercial buildings (an office/laboratory building and a research annex in Sequim, Washington). When running, the generators are isolated from the grid using automatic transfer switches. The bids are submitted as a demand bid (buy) using the start-up price for operating the generator and the current load of the building [2].

For residential customers, their thermostat, water heaters and dryers were programmed to respond to the price signals, but only the thermostats could submit demand bids, with the remainder of the household load bidding as unresponsive load. A total of 111 residential participants were recruited and provided a compensation for their involvement in the project. To study the response of participants and their equipments to various pricing schemes, the participants were divided into four groups with each being billed with a different pricing scheme. These four groups [15] were (1) the control group, who were

given the equipments but no incentive for demand response, (2) the fixed price group, who are billed using the traditional fixed price model, (3) the time-of-use group, who were billed based on the time of day when the electricity was used, and (4) the real-time-price group who were billed based on the 5-minute distribution market price. The electricity pricing scheme lies at the heart of the hypotheses tested, electricity price structure for the four groups is shown Table 1.

Table 1 - Residential electricity price contract assignment				
Fixed	29	8.1 ¢/kWh		
Time-of-use	27	Seasonal: peak ~ 3 × offpeak		
Real-time	30	5 minute distribution capacity market		
Control	25	No price signal/equipement only		

Distribution capacity market

The bids from both demand resources and supply resources were gathered and the distribution market was cleared every five minutes, as shown in Figure 2. When the feeder was running below capacity, the distribution market would clear at the wholesale price, obtained daily from the Dow Jones index for day-ahead Mid-Columbia hourly energy.

Figure 2 illustrates a typical on-peak condition in the distribution market. The feeder capacity (a) and distributed generators (b) compose the supply curve. The non-bidding loads (c), commercial non-parallel distributed generators (d) and residential loads (e) compose the demand curve. The clearing price P and quantity Q are found at the intersection of the supply and demand curves.

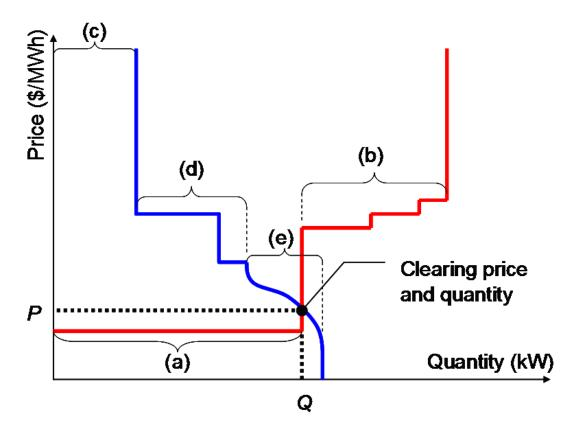


Figure 2 - Double auction for distribution feeder capacity

The clearing price was posted to all resources, including those that could not or did not bid. Each resource was then free to decide what action should be taken in response to the new price: (a) turn off, (b) continue as before, or (c) turn on. In the event the resource consumed electricity, the resource was charged according to the group that it is affiliated to. There was no penalty to failing to operate as bid. Because water heaters could not bid, they were only price-responsive. Their loads were included in the market in the non-responsive bid group, even though some actually could respond. This may have distorted the market somewhat, resulting in slightly higher prices than if they had bid. But loads have no motive to not bid, so the defect was not expected to detract significantly from the results obtained.

The commercial and residential customers who used RTP required a bidding strategy that would allow them to choose the desired objective (economy versus comfort) and the setpoints for the different times of day, and days of week. This control strategy was implemented with the controller code and the simulation model includes the same control code: controllers observe the present conditions every five minutes and compute a bid price and quantity for the next five minutes. The utility's distribution market is then cleared at the end of each five-minute interval and the clearing price is posted to all customers. Each device that cleared the market is allowed to run, and all the devices that do not clear are not allowed to run. The price response for air-conditioners was

implemented by adjusting the setpoint temperature and the water heaters simply increase the probability of curtailment as the price went up.

A similar approach was used for both commercial building HVAC systems as well as the municipal water pumping loads. The details of these implementations are provided in the previously cited report [2].

Simulation Results

In this paper, we focus on the simulation of residential end-uses. Using GridLAB-D, we estimated the energy consumption in the four residential groups by utilizing the clearing market price information in the demonstration as if the auction has been settled with GridLAB-D. Unfortunately, many end-uses that are found in the homes could not be accurately simulated by GridLAB-D at the current time. In our simulation, only the energy consumption for space heating and space cooling is modeled and the energy consumption from other household appliances (e.g., water heater, dryer etc.) is given by the measured load.

The comparison of the measured energy consumption and the simulated energy consumption for the studied four groups is shown from Figure 3 to Figure 6. From the figures, it can be seen that although the energy consumption pattern in a year obtained with simulation was similar to that of the measured results, the simulated results were lower than the measured results in general. The difference in the annual energy consumption obtained with the two methods (simulation and experimental measurement) is shown in Table 2.

Table 2 - Comparison of simulated and measured annual energy consumption							
Group Cont		Fixed price	Time of use	Real time price			
Simulation error	-12.6%	-14.1%	-16.9%	-24.8%			

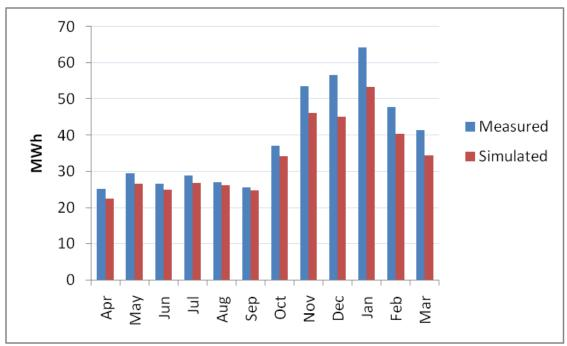


Figure 3 - Energy consumption of the control group

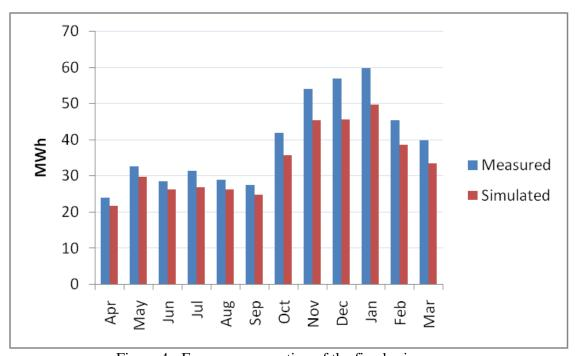


Figure 4 - Energy consumption of the fixed price group

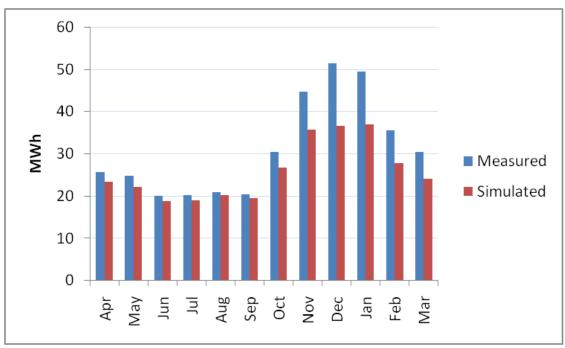


Figure 5 - Energy consumption of the time-of-use price group

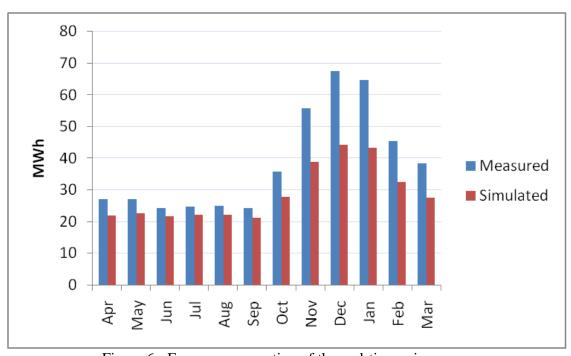


Figure 6 - Energy consumption of the real-time price group

Discussion

The house model used in this simulation is based on the ASHRAE Cooling Load Temperature Difference (CLTD) method. This method is known to not model thermal

mass as accurately as other methods, such as the Equivalent Thermal Parameters (ETP) method. This can be expected to introduce an error, particularly when pre-heating and pre-cooling strategies are being employed.

But the observed error is significantly different across the various contract types. This suggests that the different control strategy employed by the RTP and TOU in the field demonstration may be partly responsible for the discrepancy. Indeed, the demonstration used what is possibly a flawed price-response strategy for low price periods while heating that was too aggressive and would often engage auxiliary or supplemental heating coils instead of simply running the heat-pump for longer time intervals. The GridLAB-D simulation does not model this flaw and consequently we should expect that in winter months the observed heating energy would be somewhat higher than simulated, especially when significant price-induced load shifting is occurring. Based on the errors observed, as much as 50% of the heating energy error may come from this flawed price-response control system.

The GridLAB-D model is therefore probably a more accurate representation of what would have been observed on the Olympic Peninsula demonstration if the thermostat setpoint control had been done correctly.

Conclusions

This paper introduces an agent-based system simulation tools that can be used to model power distribution systems, end-use loads, and distribution-level capacity markets. The study focused mainly on the simulated residential energy consumption for a set of households for which the experimental energy consumption were known as one of the early steps for validating the simulation model.

By comparing the magnitude of the simulated annual energy consumption and the experimental results, we have established that the simulation tools can be used to estimate the energy consumption of a large number of households under a variety of pricing regimes and maintain reasonable accuracy.

Although the energy consumption pattern across a year obtained with the simulation tool is consistent with the experimental energy consumption pattern, the simulation underestimates the energy consumption. The ASHRAE CLTD method used is expected to introduce some errors, but the residual error for the winter heating conditions most likely corresponds to a known problem with the TOU and RTP heating control strategies used in the demonstration project.

Significant additional validation work on the end-use models within household remains to be completed, as well as validation of the commercial building models and municipal water pumping systems.

References

- [1] D. P. Chassin, K. Schneider, and C. Gerkensmeyer, 2008. "GridLAB-D: An Open-Source Power Systems Modeling and Simulation environment", IEEE Power Engineering Society, 2008 Transmission and Distribution Conference & Exposition, 21-24
- [2] D. J. Hammerstrom, R. Ambrosio, J. Brous, T. A. Carlon, D. P. Chassin, J. G. DeSteese, R. T. Guttromson, G. R. Horst, O. M. Jarvegren, R. Kajfasz, S. Katipamula, L. Kiesling, N. T. Le, P. Michie, T. V. Oliver, R. G. Pratt, S. Thompson, and M. Yao, 2007. "Pacific Northwest GridWiseTM Testbed Demonstration Projects: Part I. Olympic Peninsula Project", Pacific Northwest National Laboratory, PNNL-17167
- [3] N. Lu, Z.T. Taylor, D.P. Chassin, R. Guttromson, and S. Studham, 2005. "Parallel computing environments and methods for power distribution system simulation", IEEE 2005 Power Engineering Society General Meeting, vol. 1, 12-16 June 2005, 215 220
- [4] J. M. Roop, E.M. Fathelrahman, S.E. Widergren, 2005. "Price response can make the grid robust: an agent-based discussion", IEEE 2005 Power Engineering Society General Meeting; vol. 3, 12-16 June 2005, 2813 2817
- [5] R. T. Guttromson, 2003. "Modeling distributed energy resource dynamics on the transmission system", IEEE 2003 Power Engineering Society General Meeting, vol. 4, 13-17 July 2003.
- [6] S. E. Widergren, J. M. Roop, R. T. Guttromson, Z. Huang, 2004. "Simulating the dynamic coupling of market and physical system operations", IEEE 2004 Power Engineering Society General Meeting, vol. 1, 6-10 June 2004, 748 753.
- [7] J. Nieplocha, A. Marquez, V. Tipparaju, D. Chavarria-Miranda, R. Guttromson, Z. Huang, 2006. "Towards efficient power system state estimators on shared memory computers", IEEE 2006 Power Engineering Society General Meeting, 18-22 June 2006.
- [8] R. T. Guttromson, D.P. Chassin, S.E. Widergren, 2003. "Residential energy resource models for distribution feeder simulation", IEEE 2003 Power Engineering Society General Meeting, vol. 1, 13-17
- [9] N. Lu, D. P. Chassin, 2004 "A state-queueing model of thermostatically controlled appliances", IEEE Transactions on Power Systems, vol. 19, no. 3, August 2004, 1666—1673
- [10] N. Lu, D. P. Chassin, S.E. Widergren, 2004. "Simulating price responsive distributed resources", IEEE 2004 PES Power Systems Conference and Exposition, vol.3, 10-13 Oct. 2004, 1538 – 1543
- [11] R. G. Pratt and Z. T. Taylor, "Development and Testing of an Equivalent Thermal Parameter Model of Commercial Buildings From Time-Series End-Use Data", Richland, WA: Pacific Northwest Laboratory, Apr. 1994.
- [12] W. H. Kersting, 2007. Distribution System Modeling and Analysis. Boca Raton: CRC Press, 2007
- [13] IEEE Radial Test Feeders- Available through the IEEE Distribution System Analysis Subcommittee: http://ewh.ieee.org/soc/pes/dsacom/testfeeders.html
- [14] D. P. Chassin, D. J. Hammerstrom, and J. G. DeSteese, 2008. "The Pacific Northwest Demand Response Market Demonstration", 2008 IEEE Power & Energy Society General Meeting, p 6,
- [15] L. Kiesling and D. P. Chassin, "Beneficial Complexity: A field Experiment in Technology, Institutions, and Institutional Change in the Electric Power Industry", working paper, www.hks.harvard.edu/hepg/Papers/2009/Kiesling%20Chassin%20OlyPen%20complexity.pdf (Accessed on April 28, 2009)

DYNAMIC SIMULATION – A TOOL FOR ENGINEERING 2 × 800MW HARD COAL FIRED POWER PLANTS

Kristian Bøcher Poulsen*, Torkild Christensen, Helge Didriksen, Robert Hvelplund
DONG Energy
Engineering and Technology
7000 Fredericia
Denmarks

ABSTRACT

This paper describes the method and experiences for introducing dynamic simulation as a tool for engineering two 800MW hard coal-fired power plants in Greifswald (GFW) Germany. Dynamic simulation is used throughout the project period covering the early project start where the process design is matured, to development of the control, sequences, interlocks to the testing of the actual DCS (decentralized control system) control code and HMI (human machine interface), to the commissioning and finally to potentially training of the operating personnel. During the project, dynamic simulations will mainly be used to support process engineers (mechanical), C&I engineers (control and instruments) and in particular DCS engineers. The model will to a wide extent be prepared for training of the plant operating staff, eg for investigating new operating procedures. Both process and C&I plant supporting engineers can use it as a tool to test "what if" cases for further development on the dynamics of the process design and controls. The paper deals with the experiences of defining a strategy for the development of a dynamic simulation tool that ensures a model structure which is module based, will have increasing fidelity and scope as the project develops, should be quick to debug and investigate, and which will have a high level of autogenerated simple models based on database parameters. Furthermore, the paper deals with documentation of the model and simulations through partly auto generated reports.

Keywords: Modelling tools, simulation tools and technology, simulation in control of energy systems, training simulators and real-time simulation, visualization of modelling and simulation results, process plant simulation, MMS/ACSL from nHance technologies

INTRODUCTION

DONG Energy intends to build two seawater-cooled 800MW hard coal fired power plants in Greifswald Germany. In order to ensure a fast commissioning of the DCS, high availability of the plant and high performance of the plants dynamics DONG Energy uses dynamic simulation as a tool during the engineering phase.

At the point of time where the article is released the DCS system has not yet been chosen and the model building and simulation is not completed.

MOTIVATION FOR A DYNAMIC SIMULATION TOOL

DONG Energy is for the GFW project using a multi vendor strategy which requires a lot of involvement from the owner and which is opposite to the turn-key contract strategy. The multi vendor strategy choice is based on a high level of know-how from the owner during long time experience as the process here is split up into sub processes which are overall designed individually by the owner. Technical demands for eg materials, functionality, backup, safety and documentation is setup by DONG Energy according to its standards. The specific design is made together with the contractor of the specific sub-process which means that DONG Energy's engineers are involved from design, tendering, engineering to commissioning and optimising.

^{*} Phone: +45 9955 4191, Email: krbop@dongenergy.com

One advantage of the multi-contract is here that the complete process design is not directly fixed to a specific contractor's standard. This gives some degrees of freedom as more contractors can be invited to tender for each sub-system and the overall topology of the process is kept flexible. The flexible overall design is important to ensure that state of the art in materials, equipment and methods go into the design. All the experiences (C&I and electrical side, process and mechanical side (pumps, valves, tubes, vessels), chemical side (choice of material, water/steam chemistry, slag, ashes, fluegas cleaning, potential CCS (carbon capture storage), water treatment), civil and structural side (foundation, building)) from constructing, installing and operating power plants over the years can be fed back to the engineering phase of each sub-system which in the end ensures a robust and high performance power plant.

Also regarding the functionality of the power plant, the flexibleness is important as a modern power plant in DONG Energy rather functions as an energy refinery with multi-fuel inputs such as coal, oil, gas, industrial waste and biomass and outputs such as electrical power, district heat, process steam, ethanol, minerals from flue gas cleaning and potential extraction of CO2 for eg storage. Both inputs and outputs have time, quality and economical constraints which are constantly changing according to regulations and market. The production schedule for the energy refinery hour by hour is therefore getting increasingly more complex and as a consequence the production can be carried out in many different ways or operating points. In order for the energy refinery to be able to change load and composition of inputs and outputs at an acceptable rate the automatic control and an intelligent process design is a necessity. [1], [2].

It is central to the load dispatcher that the automatic controls can be depended upon to carry out the load schedule for particularly the main output electrical power (secondary control) and react to demands for net balance support (primary control) without manual interventions from the operating staff at the plant. The need for a high level of automatic control has increased over the years because of the market mechanisms and the increasing number of wind turbines in the net [3],

[1]. As the market demonstrates strong daily variations in electricity prices – prices are relatively high in the daytime and low in the night time – the overall design targets are high efficiency combined with excellent load-following capabilities. In periods, daily shifts between full load and technical minimum load is expected.

To match this flexible engineering strategy of the multi vendor, the complexness of the automatic control and the process design task, dynamic simulation during designing, prototyping and testing has been chosen as a new tool to help the engineers fulfil the expectations. [4], [5], [2].

CHOSING THE PLATFORM FOR THE DYNAMIC SIMULATION TOOL

DONG Energy has a long history of using dynamic simulation to support process optimisations and control designs at different levels of fidelity and scope.

The following tools have been used:

- Matlab with more toolboxes including Simulink
- Vissim
- Dymola
- MMS(modular modelling system)/ACSL(advanced continuous simulation language)

In order to keep evolving the modelling and simulation capabilities in house and having the model to full disposal for future support and new jobs it was chosen to do the model building inhouse.

The ambition is, through high fidelity and high scope simulation:

- to design/mature, test and roughly tune control loops and sequences together with the C&I engineers.
- to support the process engineers design including valves, pumps, and vessels
- to have the option that the model could be used for training of the future operating staff.

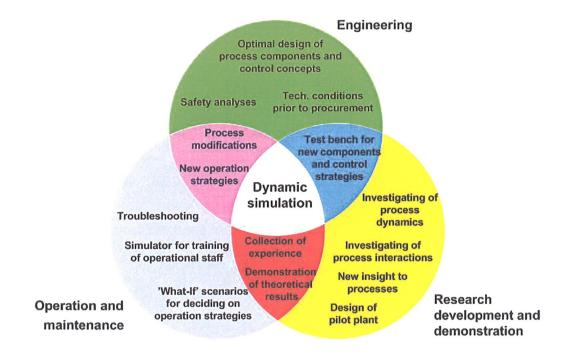
As the GFW project is a relative large-scaled project the strategy of a high fidelity and high

scope model had the necessary cost benefit relation.

From the listed simulation tools the MMS/ASCL programme was chosen because:

- It has proven to be stabile for large models on former jobs
- Has a build-in model library
- High-quality support (the supplier has a long experience with large models of complete power plants – 25 years)
- Prepared for instructor station operation (supplier has solid experience with different types of setup. See eg [6])

- the project requires <u>a lot of rebuilding</u> as the process design evolves over time.
- 2) Dynamic simulation of different plant trips together with extreme secondary and primary load changes are important to the general design of the plant. Therefore they are required to be carried out at the early project stage. Dynamics for these types of simulation involve boiler, turbine, and condensate system which results in a high-scoped model though relatively low fidelity exists at this stage in the project.
- 3) Today, several DCS suppliers are capable of not only supplying an application test platform for the simple DCS control code testing (very low



STRATEGY FOR THE MODEL CONSTRUCTION

A strategy for the construction of the process model faced different challenges:

1) As the idea was mainly to support engineers throughout the design phase with dynamic simulation, the model building potentially had to start at a very <u>early stage</u> together with process engineers when they started to work on the balance of plant. But choosing high fidelity process modelling and starting at an early stage in

Figure 1 : The different use for a dynamic simulation tool

fidelity model, and limited scope of simultaneous running code), but also of supplying an emulator with DCS and HMI system. The emulator fully simulates the complete DCS software and hardware 1:1, but the owner has to supply his own process model and instructor station. The emulator will together with the process model and instructor station define a training platform

for operating staff and would be a high-quality test platform for the engineers. When using the emulator the process model has to reflect all the I/O's from the DCS, which means that the process model has to be greatly expanded in order to be able to generate sensible feedbacks to all the DCS/emulator commands.

To deal with these three challenges, a strategy for the construction of the model had to be made.

The answer to the first and second challenge was to divide the process model into many subsystems which then together constituted the total process model. Each sub-system had to be updated when new information was available. In this way, the total model consisted of many different sub-systems with increasing fidelity as the project evolved.

It was recognized that the model would have to go through three phases of development and use.

The scope of the process model was high from the beginning, which meant that boiler, turbine and condensate system was included at an early stage. In order to do a realistic simulation at an early stage with little manual interaction, the controls for the boiler, turbine, and condensate system had to be included in the model also with a low to medium fidelity at this point. This was the first work phase - named phase one.

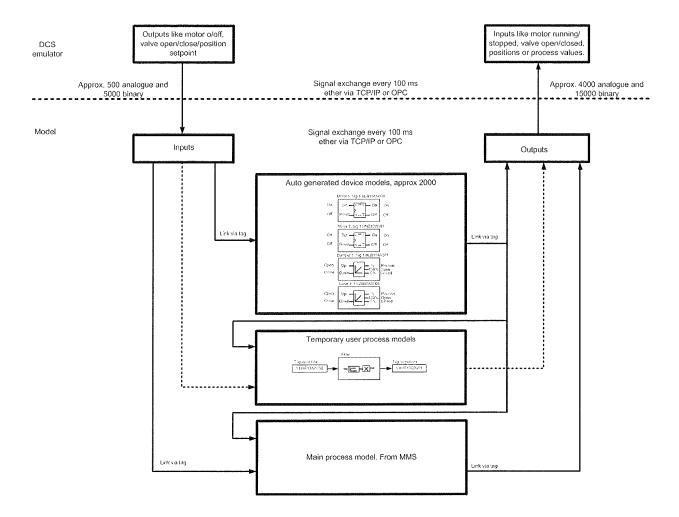
The controls are part of the total model in MMS (different sub-models) at this early stage and the DCS system contractor is not chosen at this point. The controls are matured (together with boiler, turbine supplier) through simulations and updated in fidelity subsystem by subsystem along with the process model during the project. When a DCS contractor is chosen and DCS software at some point (parallel to the work of updating the MMS control and process fidelity) has evolved to a minimum for starting using the emulator together with the MMS model, a given simulation will be based on control code distributed between the MMS model and the emulator. In the end, the DCS code will include control for most process systems and only a small part of the controls will stay in the MMS model.

The phase of work where the control code is distributed is named phase two.

Answer to the third challenge is autogenerated models. The emulator will have approximately analogue and 5000 binary outputs (commands) and approximately 4000 analogue and 15000 binary inputs (feedbacks). Many of these I/O's are not related directly to the main process dynamics, but are used for interlocking and monitoring the state eg valves and motors. However if the extra I/O's are not addressed by the process model the emulator will generate alarms and simulation will be impossible. Therefore approximately 2000 autogenerated device models (number will increase from 0-2000 as the DCS code evolves during the project) has to be created from database information about type and signal numbers and included in the total model. These types of models will be very simple eg flip-flops, integrators or first order responses which makes it relatively simple to autogenerate using typicals. Macros in Excel is used to autogenerate these models by merging DCS information with MMS model typicals. The autogenerated models is linked and compiled together with the other process and control submodels to form the total MMS model.

Even with the resulting level of fidelity the process model do not include all interacting dynamics of the plant. Not all of the autogenerated models will be connected to the main process model and as such unable to influence main model dynamics. For instance sootblowers are not modelled in the main process but an autogenerated drive model for the sootblowers valves and motor will be. In order to have the possibility to make a soodblower influence eg a slag coefficient in the main process, the engineer can define links between command and feedback in a small sub-model. It therefore possible to make software connections from the output of the DCS emulator to input of the DCS emulator via analogue and binary model modules, enabling also the construction of a simple process model. For instance connecting the open command for a burner oil valve to the flame detecting feedback signal by means of a time on delay module, which then automatically generates the flame signal when the oil valve is opened.

In phase three of the model construction, the control code is still distributed between MMS-



model and emulator but now it has been setup as a training station. The resemblance in topology of the hardware and software (DCS and models) that goes into simulating during phase two and the phase three is high.

To sum up, the model construction was divided into three phases:

Phase one:

- DCS contractor is not known. Controls are modelled in MMS in sub-models. HMI is through MMS.
- Dynamic simulation is used for maturing control concepts and process design against best practice.
- Process model and controls start off with high scope and low fidelity, but fidelity evolves over time through model updating.

Phase two:

• DCS contractor is known. Controls are distributed between MMS and emulator

Figure 2: A schematic illustration of the emulator and simulator (MMS model) topology

from contractor. HMI is 1 to approx. 0.95 compared to real plant.

- Dynamic simulation is used for first maturing interlocks and sequences and finally testing complete analogue and binary controls including alarms.
- Process model is high scope and fidelity and analogue controls starts off at high fidelity in the MMS model and are reprogrammed in the DCS and will end up at max fidelity (1:1).

Phase three:

• DCS contractor is known. Controls are distributed between MMS and emulator. The controls are mainly executed by the emulator. HMI is 1:1 compared to real plant.

- Dynamic simulations are used for training of operating staff, maturing operating procedures and testing special control scenarios and process optimisation.
- Process model with very high scope and very high fidelity and controls are 1:1 compared to real plant.

EXPERIENCES WITH THE MODEL CONSTRUCTION STATEGY UNTIL NOW

The work of erecting the model is currently in phase one so the experiences are related to this period:

To reduce the time for the recurring updating of subsystems, the model builder has to be very structured in his work. But even then, updating a high fidelity model of this scale is still time consuming. Still the investment for maturing of the control concepts and process design is very valuable when process and production schedule becomes more and more complex.

The structural dividing of the model into sub models is crucial for efficiently updating the system fidelity, isolating subsystem models during debugging, restructuring between new/old sub model versions, performing special simulations, and testing/verifying the steady state and dynamics of each subsystem.

The process structure has from experience a surplus of valves in the process sub-models and switches (plus rate limiting modules) in the control sub-models. These are used instead of boundaries so the isolating and activating/deactivating of the sub-systems can be achieved semiautomatic through scripts.

From experience special attention has been taken to initial conditions for all modules in the total model during model building even through most are feedback controlled. This to ensure that the solver would not have any problems as the total model evolved in number of differential equations over time.

Supporting process engineers with simulation during the construction of the model can create a bottleneck problem when the modelling team is small. The advantage of the structured model cannot always make up for the time that goes into a simulation especially one that includes complete plant dynamics. The optimum is here to have a small resetting time for the model boundaries and scripting files so the simulation results are generated relatively fast. As the fidelity of the process model increases the reaction time for the model engineer to respond to a process engineer's request will on the one hand be reduced as the number of boundaries and scripting files are reduced on the other hand special request that requires adjustment to model will take more time.

In order to keep the response time acceptable low from process engineer's request to responding simulation results, increasing the process model fidelity in the project was prioritised as follows over time (V=version – eg. V1 equals version 1.0):

- 1) Turbine model(V1) with boundaries is modelled.
- 2) Turbine model(V1) with full feed water preheater(V1) and condensate preheater train (V1). Boundaries for boiler.
- Boiler fidelity increased to simple boiler(V1), same turbine(V1), feed water(V1) and condensate preheater train(V1) model.
- 4) Boiler fidelity increased(V2), same turbine(V1), feedwater (V1) and condensate(V1) model.
- 5) Turbine(V2), feedwater(V2) and condensate(V2) system fidelity increased. Same boiler (V2)
- 6) Boiler air/gas system (V3) fidelity increased. Same turbine(V2), feedwater(V2) and condensate(V2) model

Development on the fidelity of the model should ideally be scheduled to the point in time where a request for particular simulation is expected to occur.

INTERFACE BETWEEN THE DCS EMULATOR AND PROCESS MODEL

The emulator and the total model will together normally simulate real time but asynchronously. In order to achieve repeatability for the simulation, tight synchronization between total model and emulator is necessary. A simulation

master (part of MMS programme) insures that the total model and the emulator are kept in sync so neither is working on old data at any point.

The closed-loop (MMS and emulator in the loop) simulation will be able to handle control of all main systems around boiler, turbine and condensate without introducing unrealistic data latency in an event rich simulation (load change, primary and secondary control scenarios, sudden disturbances eg malfunctions, load limiting). The fastest control loop in the DCS will be 100ms.

The interface between the emulator master and total model simulation master will be master/slave and will be able to accommodate the following simulator modes of operation:

- Freeze/run (stop/start simulation of DCS emulator and process model)
- Slow time (the simulation runs slower than real time)
- Backtrack/replay (continuously record initialisation data for later recovery – and replay those data)
- Snapshots (initial conditions save/load in order to store and replay from a particular condition)
- Simulated equipment malfunctions (hardware faults in the DCS)

Potentially the instructor station setup will conform to ANSI/ISA-77.20-1993, se [7]. Also the recommendations from VGB PowerTech [4] are weighted strongly.

FIDELITY AND SCOPE OF THE MODEL

Fidelity levels are relative for models and finding the right level for a particular job have to be based on experience. In [8] some different fidelity levels are compared to its utilization. In our case the model would have different use over time starting from early overall simulations on the turbine alone to detailed analyses of subsystems dynamics. To ensure that a simulation requests could be answered in a wide sense a relative high fidelity model strategy was chosen from the beginning. In this way the number of "rule of thumb"-factors, and adjusting of boundaries is kept to a minimum.

The high fidelity process model simulates the dynamics of the main systems:

- Feedwater system (tank, pumps, valves, feedwater preheaters)
- Furnace including storage vessel system.
- HT system incl. attemperation
- Reheat system incl. attemperation
- Coal mills (primary air system, sealing air system, dynamic classifier, feeder)
- Fuel oil system (pumps, valves)
- Air/gas system (secondary air system, over fire air system, steam air preheater, flue gas air preheater, ID fan system)
- Condensate system (preheaters, pumps, valves)
- Steam turbine including seal steam system to some extent.

Scope for process model was limited to main systems that are dynamically important for the operation and load changing capabilities of the plant. Auxiliary and support systems like for instance hydraulic oil coolers, soot blowers and condensate polishing plant were not included.

Modelling and simulation work are scheduled to 4.3 man years which in itself is a significant investment. Given the wide use of model throughout the project period and the potential option for operator training and support to future plant engineers, after the project, the investment is relative low. Other dynamic simulation vendors can for the same amount typically deliver a dynamic model for operator training after the plant have been in operation for a period.

VERIFICATION OF MODEL DYNAMICS WITHOUT A RUNNING PLANT

The many sub-models and the total model dynamics cannot be truly evaluated before the plant has been built and put into operation. However DONG energy has a large database with logged operation data from several plants over the years, which are used to justify time constants and gains throughout the dynamic model.

DOCUMENTING DYNAMIC SIMULATIONS

Steady state simulations results can easily be documented in a table, but dynamic simulations typically require a plot with a time scale in order to preserve the historic information and the initial

conditions. Matlab scripts and Excel macros are used to create the most popular collection of plots that are used at every simulation. Two schematic figures for the boiler and the turbine including feed water preheater and condensate preheaters are used to display the most addressed states prior to a simulation – initial steady state condition. The same schematics a be used to display same states after x seconds/minutes, but an autogenerated report with groups of plots is normally preferred.

For steady state modelling stroke time and time constants for valves, motors and measurements are not an issue but for dynamic simulation this part can be crucial to document. A parameter list for all drives, motors and measurements is therefore suggested to be collected in an Excel sheet for documentation of given total model. Many of these parameters will be delivered from sub-system vendors and will be used for the DCS programming and as such updated as the project evolves. Therefore the parameter list is also suggested to be input to the autogeneration of the input-/out-layer to ease the recurring updating of the model.

CONCLUSIONS

In this article a strategy for using dynamic simulation as tool throughout the project phase of designing and commissioning a hard coal fired power plant has been presented.

The strategy requires experience in power plant modelling in order to insure adequate scope and fidelity of model as the project evolves to ensure expected precision in the dynamic simulations. A key factor here is model structure and a high level of autogenerated models to minimize human error, updating time and at same time maximizing the quality of the documentation.

The need for dynamic simulation as a help to process and control engineers is expected to increase in the future as more wind power is introduced to the power grid and the input and output side of the power plant are becoming more complex.

As a consequence of the complexness not two plants will be the same; therefore there is still need for maturing the design with regards to different types of fuel, boiler designs, condensate systems design, feed water preheating, turbine for steam extractions for district heat, process steam eg. ethanol.

Retrofit is part of a plants lifecycle, at least in Denmark. Also here an updated dynamic model would also be very valuable for the engineers as well as for the operating staff.

Dynamic simulations is therefore a valuable tool for the design phase, engineering phase, commissioning phase as well as for the future support of the plant.

REFERENCES

- [1] M. Kurth, F. Greiner. Herausforderungen an die Kraftwerksleittechnik durch steigende dynamiche Anforderungen an die Verfahrenstechnik. In: VGB PowerTech 8/2008
- [2] W. Zethner, H.Spliethoff, W. Woyke. Betriebsanalyse und –optimierung moderner Steinkohlekraftwerke durch Simulation. In: VGB PowerTech 11/2008
- [3] H. Weber, T. Haase, F. Gottelt, J. Nocke, E Hassel. Universitet Rostock: *Kraftwerksbetrieb bei Einspeisung von Windpark*.In: VGB KELI 2008
- [4] VGB PowerTech. Einsats von Simulator training unter den aktuellen bedingungen von Anlagentechnik, Anlagengrösse und Energimarkt. First draft issue 2008.
- [5] M. Kröck, K.Fehse, H. Nacke. Neue Schulungssimulatoren moderner Kohlekraftwerke bei der KRAFTWERKSSCHULE E.V.In:VGB PowerTech 9/2008.
- [6] W. Todd Sneed: TVA Brown Ferry Simulator EHC System Upgrade Using Woodwards's NetSim Simulation Package
- [7] American National Standard for: Fossil Fuel Power Plant Simulators –Functional Requirements. ANSI/ISA–77.20–1993.
- [8] Karsten-Ulrich Klatt. *Trainingssimulation Erfahrungen und Perspektiven aus Sicht der chemisch-pharmazeutischen Industrie*. In: ATP 1-2/2009, P66-71

FORECASTING RENEWABLE ENERGY PRODUCTION AND ENERGY CONSUMPTION

Henrik Vedel, Kristian P. Nielsen,* Claus Petersen,
Bent Hansen Sass, Niels Woetmann Nielsen,
Kai Sattler and Henrik Feddersen.
The Danish Meteorological Institute
Department of Research
2100 Copenhagen Ø
Denmark

ABSTRACT

The Danish Meteorological Institute (DMI) is the leading provider of weather forecasts for the Danish territory. Currently DMI's suite of numerical weather prediction models is being revised, with the special purpose of improving the forecasting of energy production from renewable sources. This includes in-model integration of cumulative wind power production, and the use of new, high resolution ensemble forecasting systems to quantify the uncertainty of wind power production estimates. It also includes better handling of radiation transport and cloud formation, leading to improved estimates of solar heating, potential of solar electricity production, and need for electrical light. Further DMI model output can be used to forecast the need of energy for heating and light, as well as the potential energy production from wave energy plants.

Keywords: Wind forecasting, solar irradiance forecasting.

AIM

The aim of the project is to develop at DMI refined meteorological forecasting methods, enabling reliable assessment of the weather related uncertainty of forecasts of energy production from renewable energy sources (such as wind power and solar energy) and of energy consumption (heating and light). A second goal is to optimise, in collaboration with other institutions (*e.g.* the Department of Informatics and Mathematical modelling (IMM) at the Technical University of Denmark (DTU) regarding statistical treatment) and the main companies on the energy market, the use of such information in decisions when planning energy production and trading. However, lack of funding means the second part is currently inactive.

Wind forecast errors are currently the cause of energy system imbalances. To the operators better forecasting tools will mean better knowledge when

trading, more effective production, and cost reductions. This should result in lower power prices for consumers. In Denmark, forecasting solar energy, is expected to be of particular importance for local energy consumers with solar thermal energy units.

High quality forecasts of wind production will allow the traders of wind energy to offer the right amounts of electricity into the day ahead spot market, thus allowing the spot market to send the right price signals to the rest of the producers, in turn enabling those to move production away from timeslots with a high forecast degree of wind energy coverage relative to demand, or to move consumptions from e.g. heat pumps into such periods. Accurate predictions of heat requirement to combined heat and power (CHP) plants, together with big thermal stores, allow CHPplants to plan better production and consumption of electricity, and allow the plants to participate in the spot market and the regulating power market in a more efficient way. In addition to this, we will soon in Denmark be in a situation, where the necessary electrical reserves will be determined by the unpre-

^{*}Corresponding author: Phone: +45 39157 403 Fax: +45 39157 400 E-mail:kpn@dmi.dk

dictability of the wind production instead of being determined by the shortfall of the biggest component in the electricity grid. In this situation good forecasts of wind power are expected to reduce the necessary electrical reserves.

Improved energy forecasts are expected to be of direct benefit to companies in Denmark producing and selling energy, reducing the 'overhead' in Danish energy production. A successful project will help Denmark maintain its edge regarding renewable energy systems. Inclusion of significant amounts of renewable energy in an existing production and distribution network is a complicated task - to Danish exporters it will be of high value to demonstrate that in Denmark intelligent solutions exist and to export the product. With a better forecasting tool higher amounts of renewable energy can be included in the energy production system, without having to finance extra backup systems. This can help reduce CO₂ emissions. Increasing the use of renewable energy and reducing CO₂ emissions is a political goal.

INTRODUCTION

NWP (Numerical Weather Predictions) ensemble models have existed for more than a decade (Houtekamer and Derome, 1994; Molteni et al., 1996; Toth and Kalnay, 1993).

But these systems were designed for the medium forecasting range, beyond day two. It has been demonstrated that downscaling of global ensembles is not adequate (Feddersen and Sattler, 2005 and Marsigli et al., 2005). Development of ensemble systems for short-range and high resolution predictions has been initiated (e.g., Molteni et al., 2001, Frogner and Iversen, 2002), and is a process requiring years of work. Examples of current projects are GLAMEPS (Grand Limited Area Models Ensemble Prediction Systems), SRNWP-PEPS (Short Range Numerical Weather Prediction - Poor Man's Ensemble Prediction System), MOGREPS (UK Met Office global and regional ensemble prediction system). GLAMEPS is a project of the HIRLAM-ALADIN groups. The goal is that each partner contribute a short-range ensemble to a combined grand ensemble system. DMI is a partner in the HIRLAM (HIgh Resolution Limited Area Models) consortium, and establishment of a short-range DMI-ensemble to contribute to the GLAMEPS system will enhance the ensemble forecasting quality and magnify the benefit for DMI as well as for GLAMEPS.

In the present project DMI focuses on the improvement of the NWP forecast and ensemble aspects.

Today rather advanced methods for predicting the expected wind power, electricity and heat consumption exist (Giebel et al., 2005, Nielsen and Madsen, 2001, Landberg et al., 2003, Madsen et al., 2005, Nielsen et al., 2006). Most of the methods are, however, either purely statistical or purely physical based (lacking feedback from the measured data). Most methods provide a point forecast only and an estimation of the uncertainty of the forecast is typically not available. This lack of information about the uncertainty leads to a rather poor possibility for optimal use of the energy sources.

The ultimate approach to energy forecasting calls for an integrated method for simultaneous and consistent forecasting of all the terms entering the energy balance. However, today the methods or tools for energy forecasting are not well integrated; very often it is rather difficult to use the forecasts consistently in the same software of optimal scheduling. A need for such methods becomes more evident as the amount of weather related energy sources (e.g. wind and solar energy) become more prevalent. Altogether we observe a need for consistent forecasting of energy sources and consumption, which also provides reliable estimates of the uncertainty. Furthermore a better integration between the NWP forecasts and the energy forecasts is needed.

Collaboration

DMI is a member of several international meteorological communities such as WMO, ECMWF and HIRLAM. As the Danish member of WMO (the World Meteorological Organization), DMI has access to the international meteorological data from weather stations, ships, buoys, radio sondes, satellites, an so forth, which are essential for initial data analysis for the meteorological forecasts. ECMWF (the European Centre for Medium-Range Weather Forecasts) makes global weather forecasts, into which HIRLAM is nested.

Weather forecasting is only one of the elements needed for energy forecasting. Therefore, DMI collaborates with the main experts in Denmark on other fields: Statistical treatment, decision models, solar energy, and energy production and trade on the Danish market. Consideration of end user preferences will have a high priority and also other end users are involved. New collaborations are always welcome.

PRELIMINARY RESULTS

In Fig. 1 an example of windproduction forecasts at Karup in Denmark is shown. It is an epsogram with several members of an ensemble forecast plotted. One of the many parameters that can be varied between different ensemble members is the cloud formation schemes. The colors of the curves each represent cloud schemes that can be used in the DMI-HIRLAM model including the Rasch-Kristjansson Kain-Fritsch (RKKF) scheme (Rasch & Kristjansson, 1998; Kain & Fritsch, 1998) and two versions of the STRACO scheme (Sass, 2002). The three subplots show the windproduction in percentage of maximum as a function of forecast time for 50, 100 and 150 meters height above ground, respectively. In Fig. 1 a power curve for a standard wind turbine has been used for calculating the wind energy production. In an operational setup, it is necessary to know the the power curve of each given wind turbine.

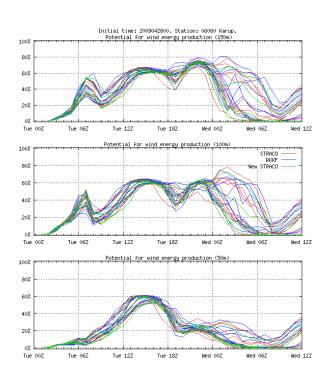


Figure 1: An epsogram of windproduction forecasts at Karup 2009-04-28 0h UTC.

In this case a considerable spread at forecast times of 24 to 36 hours can be seen between ensemble members. At 100 meters above ground, this ranges from 0% to 80%. This is a "cherry picked" example. In most cases the spread is not so large. Nevertheless, it demonstrates the potential of high resolution ensemble forecasting.

Another feature worth noticing in Fig. 1 is how there on the first afternoon (12h-18h) is approximately the same wind energy production at all three height levels, whereas there in the evening (18h-0h) is more than a factor of three in difference between the wind energy production at 50 and 150 meters height. This is not unexpected, but quantifying such differences for long periods of time might be worthwhile, when considering wind turbine construction and placement.

In Fig. 2 a forecast of the cloud drop effective radius for one of the DMI-HIRLAM areas is shown. The white areas in the plot are either outside the area of the model of areas without cloud drops.

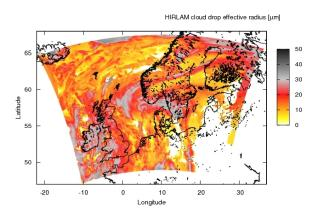


Figure 2: A 36 hour forecast of cloud drop effective radius run at 2009-04-26 0h UTC.

In order to forecast global radiation on cloudy days, it is essential to forecast the cloud drop effective radius r_e [m], since the (scattering) cloud optical thickness of visible light τ_{VIS} , from Mie-Debye scattering theory can be derived to depend inversely on this

$$\tau_{VIS} = \frac{3CLWP}{2r_e \rho_{H_2O}}. (1)$$

Here *CLWP* is the cloud liquid water path [kg m⁻²] and ρ_{H_2O} is the density of water [kg m⁻³].

DISCUSSION

The main scientific idea in the project is to overcome the lack of resolution (in space and time) of current NWP ensemble forecasting systems, to simultaneously improve the aspects of NWP models themselves of particular importance to energy forecasting, both with regards the physics of the models, and with regards to the properties derived from the models. The introduction of the 'wind energy production' measure, which is integrated at each timestep in the model, is an example of the latter.

A limiting factor thus far has been the access to ensemble NWP forecasts focusing on the relevant scales. Computer resources and understanding on a level facilitating this have only recently become available.

Another important aspect is to overcome the problem that ensembles, contrary to how they are interpreted by many people, do not provide quantitative uncertainties or probabilities. With access to the latter a powerful set of mathematical and statistical tools can be applied to aid in planning and decision making. We expect this to be done in collaboration with IMM/DTU, when funding become available.

REFERENCES

- [1] Feddersen H, Sattler K. Verification of wind forecasts for a set of experimental DMI-HIRLAM ensemble experiments. HIRLAM Newsletter 2005; 47.
- [2] Frogner I-L, Iversen T. High-resolution limited-area ensemble predictions based on low resolution targeted singular vectors. Quart. J. Roy. Soc. 2002; 128: 1321-1341.
- [3] Giebel G, et al. Wind Power Prediction using Ensembles. Risø-R-1527(EN), 2005.
- [4] Houtekamer PL, Derom J. *Prediction Experiments with Two-member Ensembles*. Mon. Wea. Rev. 1994; 122: 2179-2191.
- [5] Landberg L, Giebel G., Nielsen HAa, Nielsen TS, Madsen H. *Standardizing the perfomance evaluation of short-term wind prediction models*. Wind Engineering 2005; 29(6): 475-489.
- [6] Kain JS, Fritsch MJ. Multiscale convective overturning in mesoscale convective systems:

- Reconciling observations, simulations and theory. Monthly Weather Review 1998; 126: 2254-2273.
- [7] Marsigli C, Boccanera F, Montani A, Paccagnella T. The COSMO-LEPS mesoscale ensemble system: validation of the methodology and verification. Nonlin. Processes Geophys. 2005; 12: 527-536.
- [8] Molteni F, Buizza R, Marsigli C, Montani A, Nerozzi F, Paccagnella T. A strategy for highresolution ensemble prediction. I: Definition of representative members and global-model experiments. Quart. J. Roy. Soc. 2001; 127: 2069-2094.
- [9] Molteni F, Buizza R, Palmer TN, Petroliagis T. The ECMWF ensemble prediction system: methodology and validation. Quart. J. Roy. Soc. 1996; 122: 73-119.
- [10] Nielsen HAa, Nielsen TS, Madsen H. *Using* quantile regression to extend an existing wind forecasting system with probabilistic forecasts. Wind Energy 2006; 9: 95-108.
- [11] Nielsen HAa, Madsen H. A generalization of some classical time series tools. Computational Statistics and Data Analysis 2001; 37: 13-31.
- [12] Rasch PJ, Kristjansson JE. A comparison of the CCM3 Model climate using diagnosed and predicted condensate parameterizations. Journal of Climate 1998; 11: 1587-1614.
- [13] Sass BH. A research version of the STRACO cloud scheme. DMI Technical report 1998; 02-10.
- [14] Toth Z, Kalnay E. Ensemble Forecasting at NMC: The Generation of Pertubations. Bull. Am. Meteor. Soc. 1993; 74: 2317-2330.

Industry



DEVELOPING A SIMPLE MODELICA LIBRARY FOR SIMULUATION OF THE XSTRATA NIKKELVERK COPPER PRODUCTION PLANT

Mirnes Alic and Bernt Lie Telemark University College Department of Electrical Engineering, IT and Cybernetics 3913 Porsgrunn Norway

> Tor Anders Hauge Xstrata Nikkelverk and University of Agder Kristiansand Norway

ABSTRACT

Xstrata Nikkelverk (Norway) refines copper by leaching and electrowinning. Matlab implementation of the model of copper refinement has already been published in previous work. The process contains seven stages with a chemical reaction, a number of buffer stages, and one stage where electrolysis takes place. Recirculation of liquid plays an important role in the refinement operation. This process is a prime example where developing a library units in Modelica greatly simplifies the model development. In this paper, the development of a simple process unit in Modelica is illustrated. The flow sheet of the process is developed from the Modelica library. Finally, a comparison of the newly developed Modelica model and the Matlab model is carried out. It is also indicated how the developed model can be used for estimation and control.

Keywords: Modelica, library, modeling, simulation, copper leaching.

NOMENCLATURE

- a Number of molecules [-]
- A Specie
- b Number of molecules [-]
- B Specie
- c Concentration [g/l]
- C Faraday's constant
- i Inlet [-]
- Ī Overall electrical current [A]
- j Species index [-]
- k Reaction coefficient [1/h]
- m Mass flow [g/h]
- M Molecular weight [g/mol]
- n Amount of substance [mol]
- N Stoichiometric matrix [-]
- o Outlet [-]
- r Reaction rate [g/(hl)]
- u Input signal [-]

- $\dot{V}_{i,o}$ Volumetric flow [l/h]
- V Volume [1]
- x Number of molecules [-]
- X Specie
- y₁ Measurement [-]
- y Number of moles [-]
- Y Specie
- z_{Cu} Element valence (Cu) [-]
- $\bar{\eta}$ Overall currency efficiency [-]

INTRODUCTION

Process background

Apart from the main product of Xstrata Nikkelverk, nickel (Ni), a substantial amount of other metals is produced. Among them most important are cobalt (Co) and copper (Cu), and traces of some precious metals. This work

focuses on modeling of the copper production line. The process of copper production is extracted from a fairly complex plant and treated separately. On the one hand, the copper production line is relatively simple regarding the variety of different units present in the plant, and on the other hand, it is characterized by a time delay, a non-linear behavior and being a multivariable system.

Previous work and current goal

A detailed model development and simulation of the Cu production line has been previously addressed in the paper by Lie and Hauge [1] in which Matlab was used as the main instrument of modeling and simulation analysis. Such an implementation in Equation-based Object Oriented environment (EOO) (Modelica/Dymola) has not been done yet, as to the best knowledge of the author. The main current applications of Modelica and its numerous tools are in the area of electrical, mechanical, thermal and aerospace engineering for which extensive libraries have been developed [9]. The work in similar area of simulating batch plants has been done by Poschlad et al. [3]. A comparison of equationbased and procedural modeling language in the area of building energy simulation is presented in the paper by Wetter and Haugstetter [4]. Useful guidelines discussing modeling and development in Modelica can be library extracted from dissertations by Tummescheit [5] and Eborn [6]. For a general reference on EOO in Modelica see Fritzson [7] and Tiller [8].

The aim of this paper is to explore and gain some knowledge about the possible (benefits of) application of EOO tools, in particular Modelica/Dymola in the modeling of chemical processes.

Process description

The Cu production line consists of four sections where each section, as a main element, contains a number of tanks. The four sections are: slurrification, leaching, purification and electrowinning.

The slurrification section, shown by Figure 1, is represented by the two tanks in which a screw

conveyor supplies matte, a raw material containing copper oxide (CuO), and mix it with the recycled stream of anolyte (a liquid stream out of the electrolysis section assumed to be composed of sulfuric acid (H₂SO₄) and copper sulfate (CuSO₄)). The mass flow rate of the raw material at the entrance of the slurrification section is defined by the conveyor velocity and the weight measurements.

The leaching section, shown in Figure 2, is represented by five sequential tanks, where added sulphuric acid reacts with the metal oxide (MeO(s)) forming a metal sulfate (MeSO4).

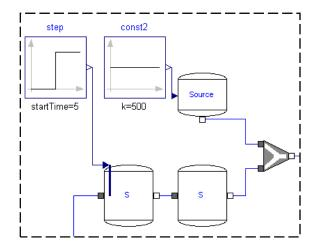


Figure 1: Slurrification section (tank S)

The reaction with the copper is given by (1):

$$CuO + H_2SO_4 \rightarrow CuSO_4 + H_2O$$
 (1)

There are three external inflows in this section: sulfuric acid inflow, water make-up and hydrogen chloride inflow. This will be explained in more detail in the following sections. The leaching section and the slurrification section are sections with the chemical reaction (1).

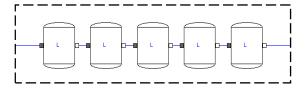


Figure 2: Leaching section (tank L)

The purification section, shown by Figure 3, is represented by a series of filter presses, scrap columns and buffer tanks.

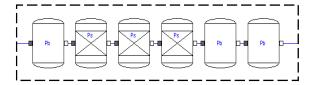


Figure 3: Purification section: Scrap column (Ps) and Buffer tank (Pb)

The modeled elements are the three scrap columns and the three buffer tanks. The parallel filter presses remove remaining non-dissolved metal oxides (MeO(s)) of nickel, cobalt, copper and precious metals. After the filter presses, which are not shown in the figure, the feed is further treated through the scrap columns. Before and after the scrap columns there are buffer tanks used for smoothing out the concentrations in the process stream.

The electrowinning section is represented by three interconnected tanks: a dilution tank, a mixing tank, and a cluster of small parallel electrolysis tanks which can be modeled as one tank of equivalent volume, given in Figure 4. A high concentration of copper sulfate at the exit from the purification section is not suitable for direct use in electrolysis, thus dilution is required. Dilution process is achieved in the dilution tank, with the recycled stream of anolyte from the mixing tank that follows after the electrowinning tank itself. The diluted feed is distributed into a large number of small tanks in which the electrolysis process is carried out in parallel.

Tanks are characterized by the common following assumptions: perfect mixing, constant liquid volume and constant liquid density. In addition, some tanks will have a reaction and some not. The chemical reaction is present only in the slurrification and the leaching section. An important issue is the volume flow between the tanks which is, in this model of the plant, calculated from the mass balance. The least squares method constrained by a steady state model is used to find initial states, the reaction

rate coefficient, and the overall currency efficiency.

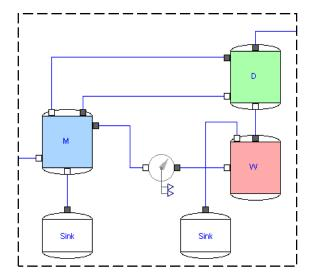


Figure 4: Dilution tank (D), Mixing tank (M) and Electrowinning tank (W)

OPERATIONAL INPUTS AND MEASUREMENTS

There are three inputs used to control the process: u_1 which is the mass flow of the raw material containing CuO, u_2 which is the volume flow of the recycled analyte from the electrowinning section to the slurrification section, and u_3 which is the volume flow of H_2SO_4 into the leaching section.

There are three measurements in the process used for assessing the quality of the process: y_1 which is the mass concentration of H_2SO_4 entering the electrolysis volumes, y_2 which is the mass concentration of the Cu in the form of $CuSO_4$ at the outlet of the electrolysis section, and y_3 which is the mass concentration of sulfates (H_2SO_4 and $CuSO_4$).

CAUSAL AND ACAUSAL MODELLING

Explicit statements (assignments) are the basic constructing element of the Matlab syntax and, as such, prevent a natural way of looking at the mathematical equality (=). The unknowns have to be explicitly expressed on the left side of the equation. Causal modeling is a consequence of such an approach. As model is becoming more

complex, the implementation becomes more difficult and challenging since components have limited reusability.

An implicit construct (similar to implicit equation) is providing a natural mathematical way of understanding the equality sign, i.e. it does not matter at which side of the equality sign the unknown is as long as the overall system remains consistent (number of equations equals number of unknowns). This has resulted in a component based modeling. The components are designed irrespective of their inputs and outputs, and are able to resemble real systems more truly. Such a modeling implementation is supported for e.g. by Modelica (1996) [7] and [8].

BUILDING THE LIBRARY

The main structural elements in the CuPlant library are the control volumes satisfying the conservation of mass and the constant liquid level. The attention is focused on representing the process flow sheet of tanks the way it appears in the real plant (except for the elements that were not presently taken into consideration such as filter presses, pumps, and heat exchangers).

A screenshot of the first and second hierarchical level of the library's main components is given in Figure 5.

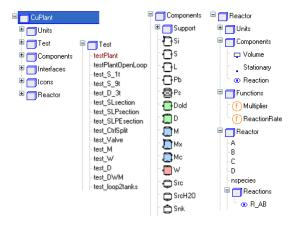


Figure 5: Hierarchical representation of the CuPlant library

Simple reacting/non-reacting tank model

The main characteristic of modeling in Modelica is the idea of independent components (or independent cluster of components) being connected to describe a physical system. A mathematical description of the physical phenomena in the tanks is derived from the fundamental principle of mass conservation, equation (2) of each specie j expressed by concentration c_j,

$$\frac{dc_j}{dt} = \frac{1}{V} \left(c_{j,i} \dot{V} - c_{j,o} \dot{V} + r_j V \right) \tag{2}$$

The basic tank unit in this library is formed by joining the conservation laws and tank general properties (for example volume), defined in the partial model of the control volume, with the tank specific characteristics (for example electrolysis phenomena described by equation (3)), as shown in Figure 6

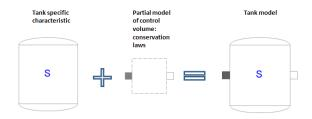


Figure 6: Forming a tank

$$\dot{m}_{Cu,o} = \frac{M_{Cu}}{z_{Cu}C} \overline{\eta} \overline{I}. \tag{3}$$

Depending on the tank specification, the reaction term can be switched on or off. Each tank in the plant is modeled in such a way. There are two ways of defining the chemically reactive volume of species in equation (2). The first way, is to define the reaction rate of each species individually, as it is done in this library (which will be changed in the future). Such a way gives a solution to only one chemical system, in this case the Cu-production plant. The other way, not fully implemented in this library yet, is to use certain assumptions and make a model of a chemical reaction in a general matrix form. The general reaction, with the reaction coefficient k, can be written as (4):

$$xX + yY \xrightarrow{k} aA + bB$$
 (4)

The reaction rate r, can be computed under the assumption of elementary reaction, as in equation (5):

$$r = -k \left[X \right]^x \left[Y \right]^y \tag{5}$$

The vector of mass/mole change of species inside the volume is given by equation (6):

$$\frac{d}{dt} \begin{pmatrix} n_X \\ n_Y \\ n_A \\ n_D \end{pmatrix} = NrV \tag{6}$$

where N is the stoichiometric matrix. The reaction volume defined in such a way is able to represent a large number of chemical systems when each species is explicitly defined.

Aggregating the model

When faced with complex models, visual representation plays a significant role in understanding the structure of the model. An important tool in achieving readability of the model is aggregation.

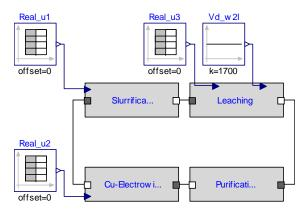


Figure 7: Plant aggregation

Here, each of the four sections is represented by its own block, and important inputs/outputs of the system are being extracted in a fairly simple way as shown in the Figure 7.

MODEL SIMULATION AND VALIDATION

The model components were developed in Modelica/Dymola, and the plant simulation results are compared to the results from the Matlab simulation.

The model is validated using: the varying input of the raw material, mass flow u_1 , into the slurrification section, the varying input of the of the recycled analyte, volume flow u_2 , into the slurrification section, and the varying input of the sulphuric acid, concentration u_3 , into the leaching section, shown in the Figure 8.

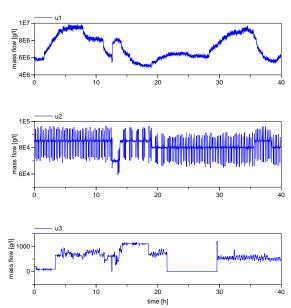


Figure 8: Input data for the model simulation

Using inputs from data collected over a period of 41 hour, simulation in Dymola gave results as shown in Figure 9. The profiles of the system responses from the simulation and from the measurements are in relatively good correspondence. The diagram showing the concentration of available H2SO4eq in Figure 9, expresses the difficulty of truly representing the model dynamics due to non-linear behavior, time delay, and unmodeled dynamics (additional utilities in the real process, such as filter presses, heat exchangers, etc.).

Validation of the model was not of primary concern for this paper, but it can be concluded from the Figure 9 that the model needs further improvements via for e.g. parameter estimation.

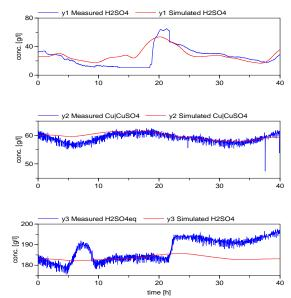


Figure 9: Simulated system response (Dymola) and measured system response

Simulations were also performed in Matlab. The results are given in the Figure 10. The Matlab simulation gave identical results as the Dymola simulation which is to be expected since we have used the same model for both implementations.

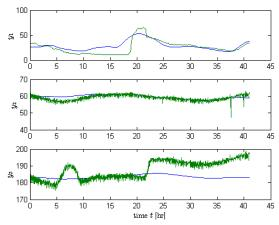


Figure 10: Simulated system response (Matlab) and measured system response

DISCUSSION, CONCLUSIONS AND FUTURE WORK

From a personal experience, time spent on implementing the process of Cu production plant with low complexity in the procedural modeling language, is comparable to the time used for modeling in EOO.

The advantage of being able to represent the model in Modelica, using the object-oriented approach, is actually found in the further work with the model. Once the model component (unit) is confirmed to work properly, it is relatively easy to continue building more complex units, and add complementary units.

The true difference in the implementation time and achievable complexity comes when the system grows larger (reflected through additional physical phenomena and additional equipment). The EOO approach takes the advantage of inherent, reusable and hierarchical model structures supported by handy drag-and-drop facilities, to provide tractable, fast and systematic way of implementing additional complexity.

Modelica's approach to modeling can be effectively applied to chemical processes. The model can be exported into Matlab/Simulink and analyzed from the control point of view. Matlab/Simulink still offers powerful support for control engineering, and it is this symbiotic relationship between Modelica and Simulink that presently ensures the best results.

The aim of our future efforts is to improve the model by parameter estimation methods and extend the library to provide the tools by which it will be possible to model the whole plant (encompassing nickel, cobalt, and sulphuric acid production).

Acknowledgments: gratitude belongs to Juan Videla for useful suggestions on Modelica, and master student Hu Ying for providing the preprocessed input data for the simulations.

REFERENCES

- [1] Lie B, Hauge TA, Modeling of an industrial copper leaching and electrowinning process with validation against experimental data. In: Modelling and Simulation, Proceedings of 49th Modeling and Simulation Conference, Oslo, 2008.
- [2] Hauge TA, *Cu process introduction*. Internal report, Xtrata Nikkelverk, Kristiansand, 2007.

- [3] Poschlad K, et al., *Modeling of an Experimental Batch Plant with Modelica*. Proceedings Modelica Conference, 2006.
- [4] Wetter M, Haugstetter C, Modelica versus Trnsys A comaprison between an Equation-based and Procedural modeling language for building energy simulation. Proceedings of the 2nd SimBuild Conference, 2006.
- [5] Tummescheit H, Design and Implementation of Object-Oriented Model Libraries Using Modelica. PhD thesis. Lund Institute of Technology, 2002.
- [6] Eborn J, *On Model Libraries for Thermo-hydraulic Applications*. PhD thesis. Lund Institute of Technology, 2001.
- [7] Fritzson P, Principles of object-oriented modeling and simulation with Modelica 2.1. United States of America, John Wiley and Sons Inc., 2004.
- [8] Tiller M, *Introduction to Physical Modeling with Modelica*. Springer, 2001.
- [9] Modelica Association, *Modelica Standard Library 3.0.1*,2009
- [10] Dymola, *Dymola User Manual*, *Version* 6.1. Dynasim AB, 2006.

SIMULATION OF FOULING IN CROSS-FLOW HEAT EXCHANGER AND A FOULING DETECTION BASED ON PHYSICAL MODELING

Oddgeir Gudmundsson; Halldor Palsson and Olafur Petur Palsson University of Iceland

Faculty of Industrial Engineering, Mechanical Engineering and Computer Science Hjardarhagi 2-6, IS-107 Reykjavik, Iceland

Abstract

Heat exchangers are frequently used in number of industrial fields and it is important to prevent unnecessary energy loss due to fouling in heat exchangers. Finding data that can be used for fouling analysis can be hard to come by, it is therefore good to be able to simulate fouling to test methods for detecting the fouling. The aim of this paper is to introduce a method to simulate cross-flow heat exchanger data that are usually gathered in normal operation of heat exchangers and introduce a method that can be used to detect the fouling online. The detection method uses the simulated inlet and outlet temperatures and the mass flow of the hot and cold fluid. In both the simulation and the detection method, the heat exchanger is divided into sections on each side (hot and cold side). In the simulation the energy balance is described by two coupled partial differential equations where the field variables are the hot and cold temperatures. In the detection method energy balance equations are set up for each section and the total model is written in a state space form and the model parameters are formatted as states in the model. The Extended Kalman filter (EKF) is used to follow the changes in the model parameters as the process evolves. Fouling detection is done by monitoring the model parameters that are a priori known to depend on the heat transfer and hence the fouling. The conclusion of this study shows that the derived detection method can detect fouling in the data from a simulated cross-flow heat exchanger, with a reasonable accuracy and consistency. Further analysis on real data is scheduled.

Keywords: Fouling, Cross-flow heat exchanger, Kalman filter, State space methods, On-line monitoring

NON	MEN	CI	ATI	IRE
	רועווע	IV.I.	/A I I	

- A System matrix
- A Surface area when used with subscript [m²]
- **B** Input matrix
- C Measurement matrix
- c Specific heat $[kJ/kg^{\circ}C]$
- Co Courant number
- Cus Cumulative sum
- d/dt Derivative with respect to time
- d Depth [m]
- F Correction factor
- H CuSum chart parameter
- *h* Height [m]
- K CuSum chart parameter

- M Mass [kg]
- \dot{m} Mass flow rate [kg/s]
- q Heat transfer rate [kW]
- **Q** Covariance matrix
- R Measurement noise covariance
- R_f Fouling factor [m²°C/W]
- T Temperature [$^{\circ}$ C]
- t Time [s]
- U Overall heat transfer coefficient [kW/m 2 °C]
- v White Gaussian noise
- W Width [m]
- w White Gaussian noise
- α Model parameter
- β Model parameter
- Δ Difference
- δ Partial derivative
- ε Effectiveness

^{*}Corresponding author: Phone: +354 691 0481 Fax: +354 525 4632 E-mail: oddgeir@hi.is

 θ Parameter vector

u Mean value

 ρ Density [kg/m³]

 τ Model parameter [1/s]

Subscripts

c Cold side h Hot side

i Section indicator or index number

in Inlet

j Section indicator or current time step

LMTD Log mean temperature difference

s Separating wall

out Outlet

T Relative to temperatures θ Relative to parameters

INTRODUCTION

Heat exchangers are widely used in domestic and industrial applications involving transfer of energy from one fluid to another. Many types exist of various complexity, but a rudimentary classification results in parallel flow, counterflow and cross flow heat exchangers. Heat exchanger operation can furthermore be divided into two classes, steady operation where mass flow and temperatures are constant, and dynamic operation where big variations can occur during operation.

Models of heat exchangers are commonly used for design purposes and to understand their behavior in operation. For steady state conditions this has proven to be relatively simple, since analytical and empirical relations can be derived for different heat exchanger types and used for all necessary calculation regarding time invariant conditions, see e.g. [1]. However, if flow and temperature of the fluids change, things become more involved and more complex mathematical models are required, see e.g. [2] and [3].

In this study, a model has been developed to simulate accurately the temperature and flow transients in a cross flow heat exchanger. The model is based on the finite volume method (FVM) where a mathematical representation of a general cross flow heat exchanger is solved numerically. One possible application of such a model is to generate data that can be used to compare and tune more simple dynamic models based on either black box methods or state space modeling. An important application in this context involves methods to detect fouling in heat

exchangers under dynamic operation.

Fouling in a heat exchanger is described as a process where the metal inside the heat exchanger accumulates deposits from the fluids. This is very common and poses problems and results in reduced efficiency of the heat exchangers. Usually, fouling starts when the metal that is placed between the fluids accumulates deposits from the fluids, builds up biofilm or starts to corrode. Nevertheless numerous methods are available to address the effect of fouling, see [4], [5], [6] and [7].

There are number of ways to detect fouling but according to [8], classical methods involve a) examination of the heat transfer coefficient, b) simultaneous observations of pressure drops and mass flow rates, c) temperature measurements, d) ultrasonic or electrical measurements and e) weighing of the heat exchanger plates. Methods a-c) require the heat exchanger to be operating in steady state condition, d) can only monitor local fouling and e) requires the process to be stopped. These restrictions can be too strict or costly. Another approach is to model the heat exchanger and look for discrepancy between model predictions and what is actually measured. In this study a effect of fouling in a cross flow heat exchanger is simulated with the FVM and a state space model is used to detect the fouling. The detection model is based on the mass flow rates and the inlet/outlet temperatures and the extended Kalman filter (EKF) is used to estimate the states inside the heat exchanger as well as the model parameters.

SIMULATION MODEL

This section describes the simulation model, which has the primary purpose of calculating outflow conditions of the two fluids, based on mass flow and inflow temperature history. This simulator should represent the physics of the problem in an accurate way and if this is fulfilled, it can be argued that the validity of the identification methods can be proven with simulated data representing the real world. One concern though are measurement errors, which are not present in an accurate simulator, and should therefore be added if appropriate.

Mathematical formulation

The model is based on a mathematical representation of two fluids flowing perpendicular to each

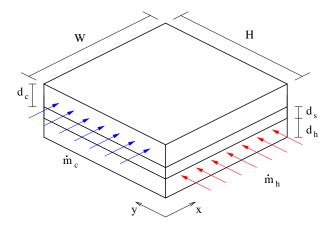


Figure 1: A simple illustration of a cross flow heat exchanger

other, separated with a fixed wall. Various parameters can be adjusted in order to represent different sizes of cross flow heat exchangers, as seen in Figure 1.

The state of the heat exchanger at a given point in time is represented by three field variables $T_c(x,y)$, $T_h(x,y)$ and $T_s(x,y)$, representing temperatures of cold fluid, hot fluid and the wall (the subscript s could denote steel). Three coupled partial differential equations describe the temperature fields and how they are related to changes in time, namely

$$\rho_c c_c d_c \frac{\partial T_c}{\partial t} + \frac{\dot{m}_c c_c}{h} \frac{\partial T_c}{\partial x} = U_c (T_s - T_c)$$
 (1)

$$\rho_h c_h d_h \frac{\partial T_h}{\partial t} + \frac{\dot{m}_h c_h}{W} \frac{\partial T_h}{\partial y} = U_h (T_s - T_h) \qquad (2)$$

$$\rho_s c_s d_s \frac{\partial T_s}{\partial t} = U_c (T_c - T_s) + U_h (T_h - T_s)$$
 (3)

The equations above describe advection (convection) without diffusion, but with source terms on the right hand side that represent heat flow from the hot fluid to the wall and from the wall to the cold fluid. It is furthermore assumed that the inflow is uniform for both fluids and that complete mixing takes place just before the fluids exit each passage. Note that the heat capacity of the wall ($\rho_s c_s$) will delay the heat transfer between fluids in dynamic situation, which is the main reason for including the wall.

To summarize, the inflow temperature, mass flow and heat transfer coefficient U are generally assumed to be time dependent in the model while other parameters are constant. Thus, Eq. (1-3) represent a real heat exchanger if they are solved in a consistent and accurate manner. The following section

describes a numerical method suitable for this.

Numerical scheme

Various numerical methods are available for dealing with advective-diffusive problems, both finite element methods as in [9] and also finite difference methods, see [10]. Comparison between available methods, see [11], indicate that the method presented in [10] as well as an improved version in [12] can be considered state of the art for such problems and therefore the QUICKEST numerical scheme is applied for the advective part of the problem. The only boundary conditions in this case are the inflow temperatures, which require alternative treatment for finite difference points close to the inlets, as discussed in [13].

The source terms on the right hand sides of Eq. (1-3) are approximated by a central difference method in time, while the advection terms are explicit according to the QUICKEST scheme. Therefore the time stepping method here can be regarded as a semi-implicit method. The Courant number characterizes advection and is defined as

$$\operatorname{Co}_{c} = \frac{\dot{m}_{c}}{\rho_{c} d_{c} h} \frac{\Delta t}{\Delta x}$$
$$\operatorname{Co}_{h} = \frac{\dot{m}_{h}}{\rho_{h} d_{h} W} \frac{\Delta t}{\Delta y}$$

for the cold and hot side of the heat exchanger. Now let the superscript j denote the current time-step and j+1 a new one. Also, let \hat{T}_c^j and \hat{T}_h^j denote temperatures calculated with the QUICKEST scheme, which would result in a pure advective temperature at time-step j+1. Then the coupled system becomes

$$\left[C + \frac{\Delta t}{2}A\right] \begin{bmatrix} T_c^{j+1} \\ T_s^{j+1} \\ T_h^{j+1} \end{bmatrix} = \left[C - \frac{\Delta t}{2}A\right] \begin{bmatrix} T_c^j \\ T_s^j \\ T_h^j \end{bmatrix} - C \begin{bmatrix} \hat{T}_c^j \\ 0 \\ \hat{T}_h^j \end{bmatrix}$$

where C and A are matrices defined as

$$C = \begin{bmatrix} \rho_c c_c d_c & 0 & 0 \\ 0 & \rho_s c_s d_s & 0 \\ 0 & 0 & \rho_h c_h d_h \end{bmatrix}$$

and

$$A = \begin{bmatrix} U_c & -U_c & 0 \\ -U_c & U_c + U_h & -U_h \\ 0 & -U_h & U_h \end{bmatrix}$$

The result is a numerical scheme for updating the three fields in time, with an accurate high order advection part and a source part based on central differences in time. There is one stability requirement that must be fulfilled, which is that both Co_c and Co_h must be smaller than one.

Here, a numerical model has been derived that represents the physical behaviour of cross flow heat exchangers. In the following sections, the model is applied to the problem of fouling detection, where a new approach is investigated to deal with consistent fouling detection of a cross flow heat exchanger.

FOULING

The simulator was used to simulate and generate data from a heat exchanger, with and without fouling. The fouling factor was allowed to progress to a maximum of $R_f = 0.0004$, which corresponds to 25% decrease in the overall heat transfer coefficient. During design the heat exchanger is commonly designed to operate under mild fouling by assuming a fouling factor in the interval 0.0001 to 0.0007. According to [14] and [15] there is usually an induction time before a noticeable amount of fouling has accumulated. In [16] it is shown that the fouling will grow with increased rate during the fouling period. Figure 2 shows the evolution of the fouling factor from the time the heat exchanger starts to accumulate fouling until the simulation is stopped.

In the following section a description of the detection model is given and then results from the following aspects of the method a) step size for the parameter changes, b) sensitivity for initial values, c)

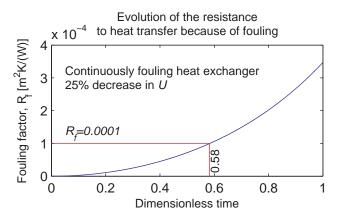


Figure 2: Evolution of the fouling factor from the time the heat exchanger starts to accumulate fouling

sensitivity for the sampling time and d) sensitivity of fouling detection.

The detection model

The model is based on dividing the heat exchanger into *ns* sections on each side. Using the assumptions that a) the heat exchanger is perfectly insulated, b) there is no heat conduction in the direction of the flow in the medium between the fluids nor the fluids themselves, c) there is uniform temperature in each section of the heat exchanger and d) the specific heat capacities are constant through the heat exchanger, it is possible to derive a differential energy balance equation for each section of the heat exchanger. Note that these assumptions are the same as in the simulator.

For the hot section this results in

$$M_{h}c_{h}\frac{dT_{h,ij}(t)}{dt} = \dot{m}_{h}(t)c_{h}[T_{h,ij-1}(t) - T_{h,ij}(t)] -A_{h}U_{ij}(t)F\Delta T_{ij}(t)$$
(4)

and for the cold section the corresponding heat balance is

$$M_{c}c_{c}\frac{dT_{c,ij}(t)}{dt} = \dot{m}_{c}(t)c_{c}[T_{c,i-1j}(t) - T_{c,ij}(t)] + A_{c}U_{ij}(t)F\Delta T_{ij}(t)$$
(5)

In [17] it is recommended to use the representation of $\Delta T_{ij}(t)$ of a counter flow heat exchanger with a correction factor F, and in [18] it is recommended to use the arithmetic mean temperature in cells instead of log mean temperature difference to avoid extra nonlinearities in the model. The correction factor depends on the inlet and outlet temperatures of the hot and cold fluid streams. For the case of cross flow heat exchanger with both fluids unmixed it is not possible to derive explicit formula for the correction factor. The calculations for the correction factor are presented in [19].

Parametrization

Several parameters are part of the detection model and they must be determined in a way that allows the model to represent the actual behaviour of the heat exchanger. The following model parameters are introduced

$$\alpha(t) = \frac{FA_h U_{ij}(t)}{\dot{m}_h(t)c_h} \tag{6}$$

$$\beta(t) = \frac{FA_c U_{ij}(t)}{\dot{m}_c(t)c_c} \tag{7}$$

$$\tau_h(t) = \frac{M_h}{\dot{m}_h(t)} \tag{8}$$

$$\tau_c(t) = \frac{M_c}{\dot{m}_c(t)} \tag{9}$$

and by inserting the model parameters into the model it can be written in a state space form as

$$\frac{d}{dt}\underline{T} = \mathbf{A}(\underline{\dot{m}}, \underline{\theta})\underline{T} + \mathbf{B}(\underline{\dot{m}}, \underline{\theta})\underline{T}_{\text{in}}$$
 (10)

The **A** and **B** matrices will be ns by ns and ns by 4 sized respectively, where ns indicates the total number of section in the model. A model that represents the connection between outlet temperatures and states must also be presented. This measurement model is described by

$$\underline{T}_{\text{out}}(t) = \mathbf{C}\underline{T}(t) \tag{11}$$

In [20] it is shown that by using empirical relations for the heat transfer coefficient it is possible to use very low model order, and that procedure is followed in this study.

Parameter estimation

The heat exchanger model presented in Eq. (10) is deterministic by definition. To compensate for deviations in correct temperatures and measurement, a noise term should be added models. The resulting model is

$$\frac{d}{dt}\underline{T} = \mathbf{A}(\underline{\dot{m}}, \underline{\theta})\underline{T} + \mathbf{B}(\underline{\dot{m}}, \underline{\theta})\underline{T_{in}} + \underline{w}_T$$
 (12)

and the measurement model similarly becomes

$$\underline{T}_{out} = \mathbf{C}\underline{T} + \underline{v}_T \tag{13}$$

where $w_T(t) \in N(1, \mathbf{Q}_T)$ and $v_T(t) \in N(1, \mathbf{R}_T)$, i.e. independent normal distributed white noise with zero mean

By viewing the parameters in Eqs. (6) and (7) it can be seen that the overall heat transfer coefficient is part of the parameters and it is therefore enough to estimate the α and β parameters. The τ_h and τ_c are easily computed since they represent the median residence time of the fluids in each section. For simplicity it is assumed the effect of fouling is negligible for those parameters. By letting α and β be model

states it is possible to observe the changes in \boldsymbol{U} indirectly. Thus two differential equations are added to the model

$$\frac{d}{dt} \begin{bmatrix} \alpha(t) \\ \beta(t) \end{bmatrix} = \frac{d}{dt} [\underline{\theta}] = \underline{w}_{\theta}(t)$$
 (14)

where α and β are described as purely random processes and $\underline{w}_{\theta}(t) \in N(0, \mathbf{Q}_{\theta})$, i.e. independent normal distributed white noise process with zero mean. After expanding the model in Eq. (10) with Eq. (14) it becomes

$$\frac{d}{dt} \left[\begin{array}{c} \underline{\theta} \\ \underline{T} \end{array} \right] = \left[\begin{array}{c} \underline{0} \\ f(\underline{\dot{m}}, \underline{T}, \underline{\theta}, T_{in}) \end{array} \right] + \left[\begin{array}{c} \underline{w}_{\theta} \\ \underline{w}_{T} \end{array} \right] \quad (15)$$

The EKF is used to estimate the states of the model. A good introduction to the EKF can be found in [21] and [22] where the EKF is used to estimate the parameters in counterflow and parallel flow heat exchanger. The parameters of the model are found by minimizing the squared difference between the actual measurements and the estimated output temperatures that are found by Eq. (11).

Fouling detection

When fouling accumulates in a heat exchanger the resistance to heat transfer increases. The increased resistance will decrease the overall heat transfer coefficient, U. If there are frequent mass flow changes it can be hard to detect changes in U since U is correlated with the mass flow through the Reynolds number, see [17].

It is not possible to observe the changes in U directly, so the model parameters α and β are used to indirectly observe changes in U. If U decreases so will the model parameters as can be seen in Eqs. (6) and (7), and by using this relation of the parameters to U it is possible to detect fouling through a shift in the parameters. To detect the shift in the parameters the Cumulative sum control chart (CuSum) is used, see [23].

The test is defined as follows:

a) Compute the cumulative sum:

$$Cus(i) = \max[0, \mu_0 - \overline{x}_i - K + Cus(i-1)]$$

b) If Cus(i) > H then a drift is detected.

The moving average value of the parameter under investigation, \bar{x} , is calculated over a window of a specific length. The parameters K and H are used to assess if the process is going out of control.

RESULTS

This section summarizes the main results from using the FVM simulation model to simulate fouling in the data and use the proposed method to detect fouling in a cross flow heat exchanger. The results are based 100 slow and fast fouling simulations and 100 simulations equally long without fouling.

Step size

When estimating the parameters of the model with the EKF the parameter values are allowed to move with certain maximum step size each time, the step size is controlled through the process noise defined in the covariance matrix \mathbf{Q}_{θ} . If the step size is to small the method will be too slow to follow the changes in the parameters but on the other hand if the step size is to big the method might exaggerate changes in the parameters. In Figure 3 effects of different values of the covariance matrix \mathbf{Q}_{θ} are shown for the slow fouling data series. By choosing to have $\mathbf{Q}_{\theta}(1,1) = \mathbf{Q}_{\theta}(2,2) = 10^{-7}$ the parameters are allowed to change 2-3% in few steps, which allows the parameters to follow the changes in the parameters fairly well.

Sensitivity for initial values and sampling time

To be sure that the effect of initial values does not play significant role in the parameter estimation, 200 random initial values on the interval 0 to 2 were tried out for both the α and β parameters. Additional effect of sampling time were furthermore investigated. In the left of Figure 4 it can be seen that the method converges relatively quickly even though high sampling step is used. From the right of Figure 4 it can be seen that the standard deviation between different estimation runs is less than 1% of the parameter values after less than 100 samples. During fouling detection the first 100 values are removed before detection method is applied.

Sensitivity of fouling detection

As stated above fouling detection is done by monitoring for changes in the α and β parameters. To evaluate detection sensitivity first 100 different data series were simulated without fouling and the fouling detection performed on each of the data series.

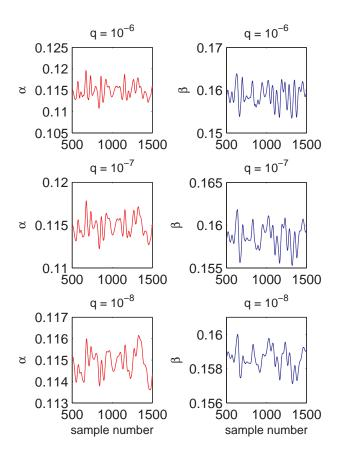


Figure 3: The effect of different scale of the covariance matrix \mathbf{Q}_{θ} in the slow fouling data series

The CuSum parameters were chose from the clean data sets such that it minimizes the likelihood on false detection. Fouling detection on the fouled data series were quite similar for both the slow and fast fouling which indicates that the method is not dependant on the fouling rate. For the fast fouling the median dimensionless detection time was made at 0.83 and 2.5% and 97.5% percentiles were 0.59 and 0.98 respectively. As for the slow fouling the median dimensionless detection time was made at 0.81 and 2.5% and 97.5% percentiles were 0.63 and 0.93 respectively. In few cases the CuSum chart detected an early shift in the parameters but the process got back to a normal state shortly after, a correct detection was seen later in the data sets. Those results can be compared to the fouling factor in Figure 2.

The fouling detection interval correspond to a fouling factors on the interval [0.0001, 0.00033]. Typical fouling factors are, as stated above, on the interval [0.0001, 0.0007]. The results therefore indicate that the method can be used to detect fouling with

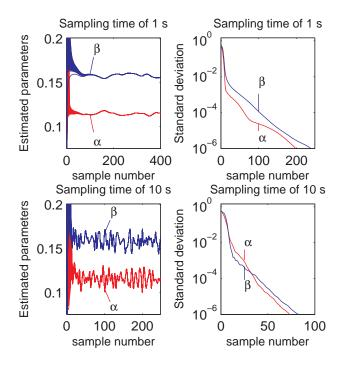


Figure 4: Effects of different sampling times on the slow fouling data series. Right: Estimated values of α and β . Left: Evolution of the standard deviation.

reasonable accuracy in heat exchanger that are operating in non-steady state condition.

DISCUSSION AND CONCLUSION

The results of application show that it is possible to use a simulation model for a cross flow heat exchanger to simulate data with and without fouling and detect the fouling in the data with the described detection method. The detection method is physically based and some of its parameters contain the overall heat transfer coefficient. By monitoring those parameters it is possible to detect changes in the overall heat transfer coefficient that are due to fouling. Unlike conventional methods this method can detect fouling in heat exchangers that are not operated in steady state conditions. It has been shown that the method is invariant for initial values and sampling steps. The fouling detection is made within the designed fouling factor interval. The results are in agreement with the results of studies made in [8] and [24] that used similar methods on counter flow heat exchangers and [19] that studied cross flow heat exchanger.

The main conclusion can be summarized to the fol-

lowing

- 1. The results show that the method can be used to detect fouling in a cross flow heat exchangers.
- 2. The method uses measurements that can be obtained under normal operation.
- 3. The method is invariant to initial values and can cope with large sampling steps.

Further work will include application of the method on a data from a real heat exchanger as well as increasing the number of sections in the detection model.

ACKNOWLEDGEMENT

This work has been supported by the Icelandic energy company Orkuveita Reykjavíkur.

REFERENCES

- [1] Holman JP. *Heat Transfer*. Ninth edition, McGraw Hill, 2002.
- [2] Mishra M, Das PK, Sarangi S. Effect of temperature and flow non-uniformity on transient behaviour of crossflow heat exchanger. International Journal of Heat and Mass Transfer, 2008, p. 2583-2592.
- [3] Kou H, Yuan P. Thermal performance of crossflow heat exchanger with nonuniform inlet temperatures. International Communications in Heat and Mass Transfer, 1997; 51(9-10):357-370.
- [4] Pope WL, Pines HS, Fulton RL, Doyle PA. Heat exchanger design "why guess a fouling factor when it can be optimized?. Enery Technology Conference and Exhibition. Huston, Texas, 1978.
- [5] Nejim A, Jeynes C, Zhao Q, Müller-Steinhagen H. Ion implantation of stainless steel heater alloys for anti-fouling applications. In: Proceedings of the International Conference on Ion Implantation Technology, 1999;2:869-872.
- [6] Nema PK, Datta AK. A computer based solution to check the drop in milk outlet temperature due to fouling in a tubular heat exchanger.

- Journal of Food Engineering. 2005;71:133-142.
- [7] Sanaye S, Niroomand B. Simulation of heat exchanger network (HEN) and planning the optimum cleaning schedule. Energy Conversion and Management. 2007; 48:1450-1461.
- [8] Jonsson GR, Lalot S, Palsson OP, Desmet B. *Use of extended Kalman filtering in detecting fouling in heat exchangers*. International Journal of Heat and Mass Transfer, July, 2007;50(13-14):2643-2655.
- [9] Westerink JJ, Shea D. Consistent higher degree petrov-galerkin methods for the solution of the transient convection-diffusion equation. International Journal for Numerical Methods in Engineering, 1989, p. 1077-1101.
- [10] Leonard BP. A stable and accurate convective modelling procedure based on quadratic upstream interpolation. Computer methods in Applied Mechanics and Engineering, 1979, p. 59-98.
- [11] Choi SK, Nam HY, Cho M. *A comparison of higher-order bounded convection schemes*. Computer methods in Applied Mechanics and Engineering, 1995, p. 281-301.
- [12] Leonard BP. The ultimate conservative difference scheme applied to unsteady onedimensional advection. Computer methods in Applied Mechanics and Engineering, 1991, p. 17-74.
- [13] Sousa E. *High-order methods and numerical boundary conditions*. Computer methods in Applied Mechanics and Engineering, 2007, p. 4444-4457.
- [14] Bansal B, Chen XD. Fouling of heat exchangers by dairy fluids a review. In: Proceeding of Heat Exchanger Fouling and Cleaning Challenges and Opportunities, Kloster Irsee, Germany, June 5-10, 2005.
- [15] Fahiminia F, Watkinson AP, Epstein N. Calcium sulfate scaling delay times under sensible heating conditions. In: Proceeding of Heat Exchanger Fouling and Cleaning Challenges and Opportunities, Kloster Irsee, Germany, June 5-10, 2005.

- [16] Bohnet MW. Crystallization fouling on heat transfer surfaces 25 Years research in Braunschweig. In: Proceeding of Heat Exchanger Fouling and Cleaning Challenges and Opportunities, Kloster Irsee, Germany, 5-10th of June, 2005.
- [17] Cengel YA, Turner RH. Fundamentals of Thermal-Fluid Sciences. Washington: McGraw Hill, ed 2, 2005.
- [18] Jonsson G, Palsson OP, Sejling K. *Modeling* and parameter estimation of heat exchangers a statistical approach. Journal of Dynamic Systems, Measurement and Control, Transactions of the ASME, Dec, 1992;114(4):673-679.
- [19] Gudmundsson O, Palsson OP, Palsson H, Lalot S. Fouling detection in a cross flow heat exchanger based on physical modeling. In: Proceeding of Heat Exchanger Fouling and Cleaning, Schladming, Austria, 14-19th of June, 2009. (To be published)
- [20] Jonsson G, Palsson OP. *Use of empirical relations in the parameters of heat-exchanger models*. Industrial and Engineering Chemistry Research, June, 1991;30(6):1193-1199.
- [21] Welch G, Bishop G. An introduction to the Kalman filter. http://www.cs.unc.edu/~welch/media/pdf/kalman_intro.pdf, updated July 24, 2006.
- [22] Jonsson G, Palsson OP. Application of extended Kalman filtering to heat exchanger models. Journal of Dynamic Systems, Measurement and Control, Transactions of the ASME, June, 1994;116(2):257-264.
- [23] NIST/SEMATECH e-Handbook of Statistical Methods, April 30, 2009, http://www.itl.nist.gov/div898/handbook/.
- [24] Lalot S, Palsson OP, Jonsson GR, Desmet B. Comparison of neural networks and Kalman filters performances for fouling detection in a heat exchanger. International Journal of Heat Exchangers, June, 2007;8(1):151-168.

THERMODYNAMIC PROCESS SIMULATION OF THE DIGESTION UNIT IN IRAN ALUMINA REFINERY

Mohammad Farrokh*
ACECR, TDI and Sharif branch
Box: 13445-686 Tehran
Iran
and Mälardalens University
Akademin för hållbar samhälls- och teknikutveckling
721 23 Västerås
Sweden

Jafar Mahmoudi Mälardalens University Akademin för hållbar samhälls- och teknikutveckling 721 23 Västerås Sweden

ABSTRACT

Jajarm bauxite is of the chamosite-diasporic type, one of the hardest types of bauxite for alumina production. The Iran Alumina Refinery uses Jajarm deposits and currently operates at 65-70% of its nameplate capacity. Digestion is one of the most important processes in the refinery and has become the main bottleneck in the production. In this paper we study the effect of selected parameters on the behavior of this important section of the refinery using thermodynamic simulation of the digestion unit. The ASTM tables property method was used for vapor streams and the Elec-NRTL property model was used for the global digestion process. The digestion process was simulated with Aspen plus software. The results show good agreement with experimental data. The relationship between the incoming slurry temperature in the first flash tank and the preheater cold stream (slurry into the furnace) temperature and energy consumption is discussed.

Key words: Bauxite, Diaspore, Bayer process, Slurry, Alumina digestion, Simulation, Electrolyte NRTL property model

E-mail: mohammad.farrokh@mdh.se

^{*} Corresponding author: Phone: +46 76 5824058 and +98 912 3022771 Fax: +46 21 101370 and +98 21 66012497

INTRODUCTION

Jajarm bauxite has a fine grain structure, generally smaller than 10 microns, and is of the chamosite-diasporic type which is one of the hardest types of bauxite for alumina production. The main aluminous Jajarm mineral is diaspore, which contains 39% of the Al₂O₃ content of the bauxite. The highly stable lattice of diaspore results in poor digestibility and a low Al₂O₃ equilibrium solubility during the Bayer process. The hardness of diaspore also causes abrasion problems during the Bayer process. Alumina extraction must therefore be carried out under conditions suitable for processing diaspore, which include high temperature and pressure, and specific caustic concentrations during the digestion stage[1, 2].

Although technology and empirical data of tube digestion are available for gibbsitic and boehmitic bauxite, only a few sporadic studies have been performed on tube digestion of diaspore bauxite. Despite these limitations, considerable amounts of diaspore bauxite are processed in various production plants around the world [3, 4, 5]. As a result of the discovery of the bauxite deposits at Jajarm, the Jajarm alumina plant was funded to refine alumina from locally mined bauxite. The average chemical composition of Jajarm diaspore is shown in Table 1.

Component	Percentage
Al_2O_3	47.4
SiO ₂	10
Fe_2O_3	22.4
TiO_2	5.6
L.O.I	11.3
Others	Rem

Table 1: Average chemical composition of Jajarm diaspore

Jajarm alumina plant

The Jajarm Alumina Plant was designed and built by Technoexport (TEX) from the Czech Republic between 1990 and 1999 and has an annual capacity of 280,000 tons. The plant uses the tubular digestion process. The function of the refinery is to separate the alumina from other minerals and refine it to a purity of 98% Al₂O₃ in the form of sandy alumina. Table 2 shows the main parameters of the process. The refinery plant is currently limited to operating at

65-70% of its nameplate capacity. This is a result of several problems that have emerged during alumina production in the refinery. Several modifications were therefore made on the production line and in particular the digestion stage. As described above, and because of the complexity of the process, it is very important to determine the effect of changing parameters on the behavior of the process.

The present study was performed on a macro simulation of the Jajarm digestion unit using a thermodynamic model to determine the influence of parameters such as pressure, temperature and flow rate on the slurry behavior and on other sections of the digestion unit, in particular the flash tanks and preheaters, with the aim of optimizing the energy consumption of the digestion unit.



Figure 1: Part of the Jajarm digestion line

THEORETICAL STUDY

The main function of the digestion unit is to dissolve the alumina which exit in the bauxite using caustic liquor and to precipitate out undesirable components such as silicates. This is done at high temperature and pressure. Diasporic alumina dissolves in the caustic solution during the Bayer process according to the simplified equation shown below [6,7].

AIOOH _{diaspore} + OH $^{-}$ + H₂O \Rightarrow Al(OH)₄ $^{-}$; OR DIASPORE + 2NAOH \Rightarrow 2NaAlO₂ + 2H₂O

In order to recover the thermal energy following digestion, the slurry is passed through a series of flash tanks where the excess energy in the superheated liquid is flashed off as steam. There are

frequent disturbances and a large number of interacting processes in the overall digestion process which contribute to there being considerable dead time. The challenge to any alumina refinery is to maximize the production rate (plant flow and yield) and minimize the energy costs per ton of produced alumina. Successful chemical process development and operation requires the ability to accurately predict process conditions. Changes in material and energy consumption can be determined through heat and mass balance calculations. Process simulation is an important tool for evaluating and improving performance in the plant [8].

As the success of process simulation is highly dependent on the modeling method used to model the process, particular attention should be paid to model selection. The most important point when modeling the Bayer process is the strong non-ideality of phase equilibria due to solids and electrolytes. The effect of dissolved ions in the digestion liquor in raising the boiling point of water has a large influence on the process and has to be modeled accurately [9,10,11]. A thermodynamic model that is capable of reliable simulation of the Bayer type solution over a wide range of temperatures, pressures and compositions is therefore of great interest. The Electrolyte NRTL model was originally proposed by Chen et al., for aqueous electrolyte systems and is the most versatile electrolyte property method. It can handle very low and very high concentrations of electrolytes [11, 12, 13].

ASPEN represents the latest generation of production scale chemical process simulation programs. It considers solid components and allows users to write specific unit operation and physical property models. It also contains many useful property models for electrolyte systems and ASTM steam table correlations. The software allows users to mathematically model or simulate a process to predict what happens when different variables (such as heat, pressure, or raw material composition) are changed, thereby making possible increased efficiency and lower costs [10,12,13,14].

A number of studies have been published about the digestion process and its reactions and the effects of additives. However, there are few reports on the energy consumption and optimization of the process. This study considers thermodynamic simulation of the Jajarm digestion unit.

EXPERIMENTAL DATA

After grinding and pre-desilication, bauxite slurry enters the digestion line at around 100 bars and about 100°C and passes through high pressure tube preheaters consisting of nine sections where the slurry is heated by exit vapor from the flash tanks. The slurry is further heated in the digestion furnace to 275°C from where it flows through the tube reactor and digestion tanks to achieve sufficient retention time at the required temperature. After digestion, about 73 percent by mass of the Al₂O₃ in the bauxite is converted to a soluble form of sodium aluminate, meaning the amount of Al₂O₃ in the liquor increases from 87 g/l to 244 g/l.

Parameter	Amount
Al ₂ O ₃ content in bauxite	48.8%
Silica ratio of bauxite	4.61
Caustic concentration Na ₂ Ok	190 g/l
αk of digested liquor	1.42
Digestion temperature	275°C
Addition of Lime	12%
Caustic ratio of pregnant liquor	1.49

Table 2: Main parameters of the process

The other solid constituents remain insoluble. About 30% of the bauxite therefore remains in suspension as a thin red mud slurry of silicates and oxides of iron and titanium. The average chemical composition of the red mud slurry is shown in Table 4.

Component	mass%
Al_2O_3	49.1
SiO ₂	10.7
Fe ₂ O ₃	20.6
TiO ₂	5.8

Table 3: Average chemical composition of the bauxite slurry at entry

The mud-laden liquor leaving the digestion vessels is flash-cooled by directing the aluminate slurry through a series of flash vessels. The purpose of the flash line is to gradually reduce the pressure and temperature of the aluminate slurry. Pressure is reduced by using orifices of different diameters at

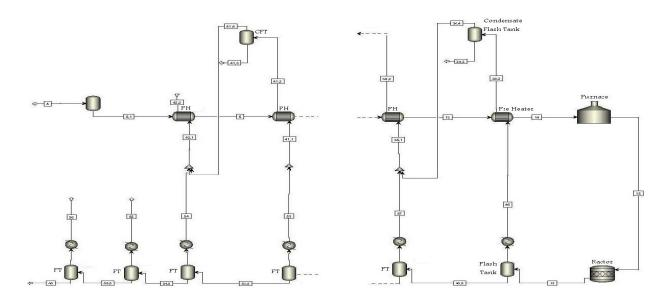


Figure 2: Flow diagram of the Jajarm Refinery digestion process

the inlet of each flash tank. Exhaust vapor from the first nine flash tanks is used to heat the bauxite slurry in preheaters before it enters the reactor. The exhaust vapor then enters condensate flash tanks. Aluminate slurry leaves the last flash tank at a temperature between 125 and 130°C and a pressure of around 0.16 MPa and precipitates as alumina hydrate in subsequent units.

Component	mass%
Al_2O_3	17.9
SiO_2	14.8
Fe_2O_3	27
${ m TiO_2}$	7.8
CaO	15.2

Table 4: Average chemical composition of the red mud slurry

SIMULATION PROCEDURE AND RESULTS

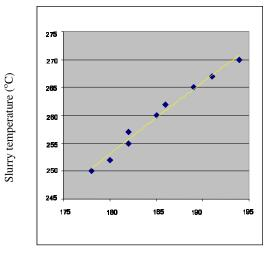
The Electrolyte NRTL property model was used for the entire digestion line and ASTM steam tables were used for the vapor phase. The rise in the boiling point of the liquor was also considered. The simulation was run in the Aspen plus software. The composition of the incoming and outgoing slurry and other parameters of the digestion are shown in Tables 2, 3 and 4. The digestion unit was simulated based on data from the Jajarm Refinery. Simulations were first carried out on individual blocks, followed

by sections containing groups of blocks (such as flash tanks), and finally on the entire line. The flow diagram of the simulated digestion process is shown in Figure 2.

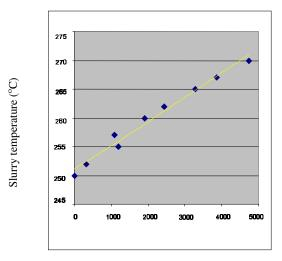
Using the simulation program, the amount of vapor created in each flash tank (which is used as a hot stream to each preheater) and the preheaters outlet cold stream (bauxite slurry) temperature were calculated and are shown in Table 5.

Flash tank No.	Vapor created (kg/hr)	Preheater No.	Cold stream temperature (°C)
V06	1899	(9)	174
V07	2146	(8)	166
V08	1567	(7)	160
V09	2681	(6)	151
V10	2352	(5)	144
V11	1992	(4)	137
V12	2713	(3)	120
V13	2427	(2)	115
V14	1595	(1)	101
V15	2170	-	-
V16	3195	-	-

Table 5: Preheaters hot stream mass (vapor exiting flash tanks) and cold stream (bauxite slurry) temperature



Outgoing preheater cold stream temperature (°C)



V06 flash tank vapor created (kg/hr)

Figure 3: The effect of increasing slurry temperature on the generation of vapor by V06 and the preheater cold stream temperature

The effect of incoming slurry temperature on the generation of vapor by V06 flash tank and also on the last preheater cold stream (slurry to furnace) temperature was calculated by the simulation and is shown in Table 6 and Figure 3.

DISCUSSION AND CONCLUSIONS

The data shown in Table 5 was computed by the simulation program for the 130 kg/m³ volume flow rate condition. The data agrees well with the current digestion line conditions and has been accepted by the refinery. Figure 3 shows that the temperature of the incoming slurry into the first flash tank (V06) has a large effect on the efficiency of the preheaters. Decreasing slurry temperature below a specific limit should eliminate flashing and vapor creation. This agrees well with the refinery conditions. Increasing incoming slurry temperature in 2 to 3°C steps showed that vapor was created by flashing slurry inside the flash tank and this increased according to Figure 3 (right). The last preheater cold stream (outgoing bauxite slurry) temperature is therefore increased by the vapor as shown in Figure 3 (left). There is an upper limit for incoming slurry temperature into the flash tank due to heat loss in the digestion line. 260°C is therefore an acceptable

the temperature and is close to the operating condition of refinery.

The Jajarm Alumina Refinery digestion line was simulated using the Elec-NRTL property model and Aspen simulating tool. The simulation showed good agreement with the real conditions and experimental data. This simulation program can be used to optimize energy consumption and operation of the digestion line.

slurry temperature(°C)	Vapor created(kg/hr)	Cold stream (Preheater)(°C)
250	0	178
252	306	180
255	1178	182
257	1094	182
260	1900	185
262	2446	186
265	3283	189
267	3853	191
270	4731	194

Table 6: The effect of slurry temperature on vapor generated in V06 flash tank and the last preheater cold stream temperature

ACKNOWLEDGMENTS

The authors would like to acknowledge the Iran Alumina Company and their managers and engineers for their kind help in providing essential data for this research. We would also like to thank Miss Zeinab Farrokh for her assistance in preparing this paper.

REFERENCES

- [1] Shadloo M.T, Ramezani M. *Elburz bauxite* mining treatment in a high temperature tube digestion plant. Travaux 2000;31(27):47-62.
- [2] Technical Description of Heaters11-H-1ABCD. TR:226 Rev.1 Techno Export Erection Documentation
- [3] Taxiarchou M., Paspaliaris J, Papanastassiou D. *Possibilities for improved digestion of diasporic bauxites for alumina production.* TRAVAUX de ICSOBA 1997;28(26):235-245.
- [4] Papanastassiou D.J. Research directions for improved digestion of Greek diasporic bauxites. TRAVAUX de ICSOBA 1999;30(26):137-145.
- [5] Wargalla G., Brandt W. *Processing of diasporic bauxites*. Light Metals 1981:83-100.
- [6] Panias D., Asimidis P, Paspaliaris I. Solubility of boehmite in concentrated sodium hydroxide

- solutions: model development and assessment. Hydrometallurgy 2001;59:15-29.
- [7] Mock B., Evans L. B. and Chen C.C, Thermodynamic representation of phase equilibria of mixed-solvent electrolyte systems, AICHE J. 1986;32(10):1655-1664.
- [8] Handbook of Chemistry and Physics, 56th Edition, CRC Press, 1975, p. E-1
- [9] Dewey John L. *Boiling point rise of Bayer plant liquors*. Light Metals 1981:185-197.
- [10] Zigao L., Shu Lu, Experimental data on the Bayer digest process for Pingguo bauxite. Light Metals 1993:21-25.
- [11] Konigsberger E., Eriksson G., May P. M., Hefter G. *Comprehensive model of synthetic Bayer liquors, Part 1, Overview.* Ind. Eng. Chem. Res. 2005;44:5805-5814.
- [12] Kumagoe Y., Simulation of the Bayer digestion process with solids and electrolytes. Light Metals 1990:69-72.
- [13] Chen C.C, Evans L.B, A local compositions model for the excess Gibbs energy of aqueous electrolyte system AICHE. 1986;32(3):444.
- [14] Langa J.M, Russell T.G, O'Neill G.A, Gacka P. Aspen modeling of the Bayer process, Process Control and Computer Technology 1991:169-178

Fuel Cells



POSSIBLE FUTURE SOFC – ST BASED POWER PLANTS

Masoud Rokni ¹ and Fabio Scappin Technical University of Denmark, Dept. Mechanical Engineering, Thermal Energy Systems, 2800 Lyngby, Denmark

ABSTRACT

Hybrid systems consisting of Solid Oxide Fuel Cell (SOFC) on the top of a Steam Turbine (ST) are investigated. The plants are fired by natural gas. A desulfurization reactor removes the sulfur content in the NG while a pre-reformer breaks down the heavier hydrocarbons. The pre-treated fuel enters then into the anode side of the SOFC. The gases from the SOFC stacks enter into a burner to burn the rest of the fuel. The off-gases now enter into a heat recovery steam generator to produce steam for a Rankine cycle. Different system setups are considered. Cyclic efficiencies up to 67% are achieved which is considerably more than the conventional combined cycles (CC). Both ASR (Adiabatic Steam Reformer) and CPO (Catalytic Partial Oxidation) fuel reformer reactors are considered in this study.

Keywords: SOFC, Rankine cycle, steam plant, steam cycle, hybrid system

INTRODUCTION

The Solid Oxide Fuel Cell (SOFC) is an electrochemical reactor currently under development by several companies for power-heat generation application. Depending on the type of the electrolyte they are operating at temperature levels of more than about 750°C up to 1000°C. The lower temperature alternative is now being developed for market entry during the next decade. Due to material complication on the BoP (Balance of Plant) components some companies are trying to find new materials for the SOFC cells to decrease the operating temperature of the SOFC stacks. Temperatures of about 650°C are also mentioned.

The biggest advantage of the SOFC in comparison with other types of fuel cells may be in its flexibility in using different types of fuels. However, in planar SOFCs one needs to preprocess most kind of fuels in order to break down the heavier hydro-carbons which may otherwise poison the solid oxide fuel cells. The sulphur content in the fuels must firstly be removed and then pre-reformed before entering the anode side of the SOFC. Such pre-processing can be done in two different catalytic reactors operating at

different temperature levels indicated by reactor manufacturers.

SOFC – based power plants have been studied for a while and some companies, such as Wärtsilä, are trying to realize such a system for CHP (Combined Heat and Power) applications; see e.g. [1]. The SOFC is also combined with CC (Combined Cycles) in the literature to achieve ultra high electrical efficiencies, see e.g. [2-3]. Due to the current operating temperature of the SOFC stacks (more than about 750°C), hybrid SOFC and GT (Gas Turbine) systems have also been studied extensively in the literature, e.g. in [4] for CHP (Combined Heat and Power). Characterization, quantification and optimization of hybrid SOFC-GT systems have been studied by e.g. [5]. In [6] modeling results are compared with measured data for a 220 kW hybrid planar SOFC-GT power plant. Details on design, dynamics, control and startup of such hybrid power plants are studied in [7]. While hybrid SOFC-GT plants have been extensively studied by many researchers, the investigations on combined SOFC and ST (Steam Turbine) are very limited see [8].

By decreasing the operating temperature of the SOFC stacks, then the combination of SOFC-ST

hybrid system would be more attractive than the SOFC- GT systems.

Fuel pre-reforming can be done in different reactors such as ASR (Adiabatic Steam Reformer) and CPO (Catalytic Partial Oxidation). The disadvantages of an ASR reactor is that it needs superheated steam during start-up (depending on the operating temperature of the reactor, i.e. 400°C) which is an extremely power consuming process. During normal operation steam is available after the anode side of the SOFC stacks, which can be recycled into the system. In a CPO reactor additional air is needed for the fuel prereforming process, which in turn increases the plant power consumption (compressor power) and thereby the plant efficiency will be decreased. In this study, ASR reforming process versus CPO reforming process is studied in terms of plant design, plant efficiency and plant output power.

A single pressure level for the Rankine cycle is investigated in this study. Plants characteristics of such system configurations are also studied. In addition, the off–gases from the Heat Recovery Steam Generator (HRSG) are used to preheat the incoming air into the SOFC stacks. The effect of such suggested air preheating on plant efficiency and output power is thus studied. All the configurations studied here are novel in terms of designing new plants with very high efficiencies.

METHODOLOGY

The results of this paper are obtained using the simulation tool DNA (Dynamic Network Analysis), see [9–10], which is a simulation tool for energy system analysis.

Some of the important features are:

- Simulation of both steady state (algebraic equations) and dynamic models (differential equations)
- Handling of discontinuities in dynamic equations
- Use of a sparse-matrix-based simultaneous solver for algebraic equations
- No causality implied on the model input, i.e. no restriction of the choice of inputs and outputs
- Medium compositions can be variables
- Models of thermodynamic states, transport

variables and radiative properties for relevant fluids, e.g. steam, ideal gases and refrigerants. The component library includes models of various components such as; heat exchangers, burners, gasifiers, turbo machinery, dryers and decanters, energy storages Engines, valves, controllers, as well as more specialized components and utility components. The user may also implement additional components.

In DNA the mathematical equations include mass and energy conservation for all components, as well as relations for thermodynamic properties of the fluids involved. In addition, the components include a number of constitutive equations representing their physical properties, e.g. heat transfer coefficients for heat exchangers and isentropic efficiencies for compressors and turbines. During the development of DNA the four key terms, portability, robustness, efficiency, and flexibility have been kept in mind for making a generally applicable tool for energy system studies. The program is written in FORTRAN.

Modeling of SOFC

The SOFC model used in this investigation is based on the planar type developed by DTU-Risø and TOPSØE Fuel Cell. The model is calibrated against experimental data in the range of 650°C to 800°C (operational temperature) as described in [11]. The operational voltage (E_{FC}) is found to be

$$E_{FC} = E_{Nernst} - \Delta E_{act} - \Delta E_{ohm} - \Delta E_{conc} - \Delta E_{offset}$$
(1)

where E_{Nermst} , ΔE_{act} , ΔE_{ohm} , ΔE_{conc} , ΔE_{offset} are the Nernst ideal reversible voltage, activation polarization, ohmic polarization, concentration polarization and the offset polarization respectively. The activation polarization can be evaluated from Butler–Volmer equation (see [12]). The activation polarization is isolated from other polarization to determine the charge transfer coefficients as well as exchange current density from the experiment by curve fitting technique. It follows,

$$\Delta E_{act} = \frac{RT}{(0.001698T - 1.254)F} x$$

$$\sinh^{-1} \left[\frac{i_d}{2(13.087T - 1.096 \times 10^4)} \right]$$
(2)

where R, T, F and i_d are the universal gas constant, operating temperature, Faradays constant and current density respectively. Ohmic polarization depends on the electrical conductivity of the electrodes as well as the ionic conductivity of the electrolyte and can be described as

$$\Delta E_{ohm} = \left(\frac{t_{an}}{\sigma_{an}} + \frac{t_{el}}{\sigma_{el}} + \frac{t_{ca}}{\sigma_{ca}}\right) i_d \tag{3}$$

where $t_{an} = 600 \, \mu \text{m}$, $t_{el} = 50 \, \mu \text{m}$ and $t_{ca} = 10 \, \mu \text{m}$ are the anode thickness, electrolyte thickness and cathode thickness respectively. σ_{an} , σ_{el} and σ_{ca} are the conductivity of anode, electrolyte and cathode respectively.

$$\sigma_{an} = 10^5 \tag{4}$$

$$\sigma_{ca} = \frac{5.760 \times 10^7}{T} \exp\left(-\frac{0.117}{8.617 \times 10^{-5} T}\right) (5)$$

$$\sigma_{el} = 8.588 \times 10^{-8} T^3 - 1.101 \times 10^{-4} T^2 + 0.04679T - 6.54$$
(6)

Concentration polarization is dominant at high current densities for anode – supported SOFC, wherein insufficient amounts of reactants will be transported to the electrodes and the voltage will then reduce significantly. Neglecting the cathode contribution (see e.g. [13]), it can be modeled as

$$\Delta E_{conc} = B \left(ln \left(1 + \frac{p_{H2} i_d}{p_{H2O} i_{as}} \right) - \frac{1}{n} \left(1 - \frac{i_d}{i_{as}} \right) \right)$$

$$(7)$$

where B is the diffusion coefficient and is calibrated against experimental data which found to be,

$$B = (0.008039X_{H2}^{-1} - 0.007272)\frac{T}{T_{ref}}$$
 (8)

In the above equations p_{H2} and p_{H2O} are the partial pressures for the H₂ and H₂O respectively, while T_{ref} is the reference temperature (1023 K). The anode limiting current is defined as

$$i_{as} = \frac{2F \ p_{H2} D_{bin} V_{an}}{R T \ t_{an} \tau_{an}} \tag{9}$$

where V_{an} and τ_{an} are the porosity and tortuosity of the anode and are the physical characteristics as

30% and 2.5 μm in the experimental setup. The binary diffusion coefficient is given by

$$D_{bin} = \left(-4.107 \times 10^{-5} X_{H2} + 8.704 \times 10^{-5}\right) \left(\frac{T}{T_{ref}}\right)^{1.75} \frac{P_{ref}}{P}$$
(10)

which is also calibrated against the experimental data. P_{ref} is the reference pressure as 1.013 bar and X_{H2} is the mass reaction rate of H_2 . Finally the current density i_d is directly proportional to the amount of reacting hydrogen according to the Faraday's law;

$$i_d = \frac{n_{H2} \, 2F}{A} \tag{11}$$

where n_{H2} is molar reaction rate of H₂. The area A is the physical property of the cell and is 144 cm².

Modeling of Fuel Pre-Reforming

The reforming process is assumed to be equilibrium by minimizing the Gibbs free energy as described in [13]. The Gibbs free energy of a gas (assumed to be a mixture of k perfect gases) is given by

$$\overset{\bullet}{G} = \sum_{i=1}^{k} \overset{\bullet}{n_i} \left[g_i^0 + RT \ln(n_i p) \right]$$
 (12)

where g^0 , R an T are the specific Gibbs free energy, universal gas constant and gas temperature respectively. Each atomic element in the inlet gas is in balance with the outlet gas composition, which yields the flow of each atom has to be conserved. For N elements this is expressed as

$$\sum_{i=1}^{k} \overset{\bullet}{n}_{i,in} \mathbf{A}_{ij} = \sum_{i=1}^{k} \overset{\bullet}{n}_{i,out} \mathbf{A}_{ij} \quad \text{for } j = 1, N \text{ (13)}$$

The *N* elements corresponds to H_2 , CO_2 , H_2O and CH_4 in such pre–reforming process. $\mathbf{A}_{i,j}$ is a matrix with information of the mole j in each mole of i (H_2 , CO_2 , H_2O and CH_4). The minimization of Gibbs free energy can be formulated by introducing a Lagrange multiplier, μ , for each of the N constraints obtained in Eq. (13). After adding the constraints, the expression to be minimized is then

$$\phi = \overset{\bullet}{G}_{out} + \sum_{j=1}^{N} \mu_{j} x$$

$$\left[\left(\sum_{i=1}^{k} \overset{\bullet}{n_{i,out}} - \overset{\bullet}{n_{i,out}} \right) A_{ij} \right) \right]$$
(14)

The partial derivation of this equation with respect to $n_{i,out}$ can be writes as

$$\frac{\partial \phi}{\partial n_{i,out}} = \frac{g_{i,out}^{0}}{RT} + \ln(n_{i,out} p_{out}) + \sum_{i=1}^{k} \mu_{j} \mathbf{A}_{ij} \quad \text{for } i = 1, k$$
(15)

At the minimum each of these is then zero. The additional equation to make the system consistent is the summation of molar fractions of the outlet gas to be unity.

RESULTS

The first configuration studied is shown in Fig. 1a. The fuel (NG) is preheated in a heat exchanger before it is sent to a desulphurization unit to remove the sulphur content in the NG. This unit is assumed to be using a catalyst, operating at temperature of 200°C. Thereafter the heavier carbon contents in the NG are cracked down in a CPO type pre-reformer catalyst. Before that the fuel must be preheated again to reach to the operational temperature of the CPO catalyst. The CPO catalyst needs additional air which is supplied by a small pump as shown in the figure. It is assumed that the supplied NG is pressurized and therefore no pump is needed for the fuel. The pre-reformed fuel is now sent to the anode side of the SOFC stacks. Due to the exothermal nature of the CPO catalyst, no preheating of the fuel is required. The fuel has a temperature of about 650°C before entering the stacks. The operating temperature of the SOFC stacks as well as outlet temperatures is assumed to be 780°C. The burned fuel after the stacks is used to preheat the fuel using a heat exchanger. On the other side, air is compressed in a compressor and then preheated in a recuperator to about 600°C before entering the cathode side of the SOFC stacks. Lower entering temperature may shut down the

automatically. Since the fuel in the SOFC stacks will not burn completely the rest of the fuel together with the air coming out of the cathode side of the stacks are sent to a burner (catalytic burner) for further burning. The off-gases from the burner have a high heat quality which can be used to generate steam in a Heat Recovery Steam Generator (HRSG).

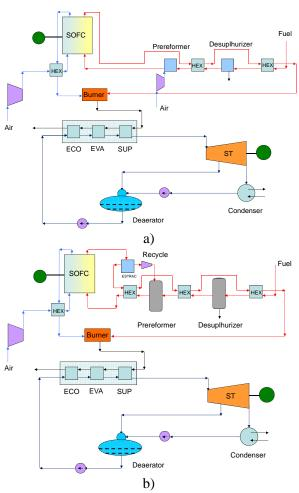


Figure 1. Combined SOFC – ST cycle plants, a) with CPO reformer, and b) with ASR reformer. Rankine cycle with a single pressure level.

In the Rankine cycle, the pressurized water after the feed pump is heated up to steam in the economizer (ECO), evaporator (EVA) and superheater (SUP). The generated steam is then expanded in a steam turbine to generate electricity. Part of the expanded steam is then is extracted for the deaerator. The expanded steam is then cooled down in a condenser (including a sub

-cooler part) before pumping to the deaerator. The water is preheated before in the deaerator being recycled. As mentioned earlier the ASR reformer needs super heated steam for operation. Such steam must be supplied to the reformer externally during start-up. However, during normal operation steam is available after SOFC stacks due to reactions of hydrogen and oxygen. Therefore, the stream after the anode side of SOFC is recycled as shown in Fig. 1b. There are three alternatives for such a recirculation unit, a pump, a turbocharger and an ejector. In a real plant, due to high temperature of this stream (more than 700°C) the cost of a pump working will be rather expensive. This is also true for a turbocharger which is working at such mass flows and pressures. Moreover, using an ejector brings up problems associated with the size and dimensioning of the ejector (due to combination of pressure drop and mass flows). Based on these facts and for the sake of simplicity a pump is used in this investigation. Besides the recycle part, the plant configuration is the same as in the CPO reformer case, see Fig. 1b.

The main parameters for the plant are set in table 1. Number of SOFC stacks is assumed to be 10000 and number of cells per stacks is assumed to be 74. The pressure drops in the cathode and anode sides of the fuel cell are assumed to be 0.05 respective 0.01 bars. These values are the setting values for the program, however, pressure drops are a function of channel sizes and mass flows and the channel geometry is not kwon. Therefore, these values are calculated based on the available data for each channel mass flow and dimensions. In addition, the calculations show that the final values in terms of plant power and efficacy do not change significantly if these values are changed slightly. The SOFC plant provides direct current and must be converted to AC through a converter. Further, the efficiency of the DC/AC converter is assumed to be 100%, due to lack of such component in the DNA program. In reality there would be some losses trough the converter and efficiencies of 97% could be assumed for plants of such sizes studied in this investigation. The output power would therefore be somewhat lower while the plant efficiency would not change significantly. Several calculations have been

carried out to find the optimal extraction pressure as well as the optimum live steam pressure which are not included in this study. The main calculated parameters are provided in Table 2.

Parameter	CPO	ASR
Compressor intake T	25°C	25°C
Compressor η _{isentropic}	0.85	0.85
Compressor n _{mechanical}	0.95	0.95
SOFC cathode inlet T	600°C	600°C
SOFC cathode outlet T	780°C	780°C
SOFC utilization factor	0.80	0.80
SOFC number of cells	74	74
SOFC number of stacks	10000	10000
SOFC cathode side Δp	0.05 bar	0.05 bar
SOFC anode side Δp	0.01 bar	0.01 bar
HEXes pressure drops	0.01 bar	0.01 bar
Fuel inlet temperature	25°C	25°C
Desulphurizer operation T	200°C	200°C
SOFC anode inlet T	650°C	650°C
SOFC anode outlet T	780°C	780°C
Burner efficiency	0.97	0.97
ST isentropic efficiency	0.9	0.9
Feed water pump pressure	70 bar	60 bar
Extraction pressure	2 bar	2 bar
Extraction steam T	120.2°C	120.2°C
Generators efficiency	0.97	0.97
Tr-1.1. 1 Main management	. C 1	

Table 1. Main parameters for design point calculations of Fig. 1.

The main difference in the Rankine cycle from CPO and ASR are the off-gases temperatures entering the HRSG. The CPO pre-reforming plant provides much higher temperature for the off-gases, which is due to the fact that the air mass flow to its burner is lower than the corresponding one for the ASR pre-reforming plant. Consequently, the feeding temperature for the Rankine cycle will be higher in the CPO type, which will results in higher net power from the its steam cycle, see Table 3.

The plants net powers and thermal efficiencies (based on LHV, Lower Heating Value) are shown in Table 3. The net power output of the hybrid plant with CPO pre-reforming is calculated to be about 1 MW higher than the corresponding plant with the ARS pre-reforming. The main reason is that the steam cycle in the CPO type plant

produces somewhat higher power than the corresponding ASR type plant (higher off – gases temperature for the CPO pre-reforming). As a result the thermal efficiency of the plant with CPO pre-reforming will be higher than the corresponding plant with ASR pre-reforming.

Parameter	CPO	ASR
Compressor massflow	51.4 kg/s	59.0 kg/s
Fuel massflow	1.32 kg/s	1.30 kg/s
SOFC fuel massflow	1.45 kg/s	1.72 kg/s
Burner fuel massflow	5.17 kg/s	5.13 kg/s
Burner inlet air mass	47.7 kg/s	55.1 kg/s
flow		
HRSG inlet gas T	526.3°C	455.6°C
HRSG outlet gas T	218.2°C	232.0°C
HRSG inlet water T	121.1°C	121.0°C
ST inlet steam T	496.3°C	425.6°C
ST pressure	69.97 bar	59.97 bar
ST inlet mass flow	6.33 kg/s	5.47 kg/s
Extraction mass flow	5.40 kg/s	4.64 kg/s

Table 2. Main calculated parameters for design point calculations of Fig. 1.

Parameter	CPO	ASR
Net power output	38.03 MW	36.72 MW
SOFC cycle power	31.04 MW	31.23 MW
ST cycle power	6.99 MW	5.49 MW
Steam cycle η _{thermal}	0.382	0.368
SOFC cycle η _{thermal}	0.514	0.524
Plant η _{thermal}	0.630	0.617

Table 3. Net powers and efficiencies of the plants for Fig. 1.

However, the thermal efficiency of the SOFC plant (not the hybrid one) with ASR prereforming is calculated to be about 1% higher than the SOFC plant with CPO pre-reforming. This is due to the fact that CPO pre-reforming needs additional air mass flow which must be provided by additional compressor flow (or additional compressor) which in turn needs additional electrical power. In order to optimize the systems presented above, the plants efficiencies versus live steam pressures and moisture contents are presented in Fig. 2.

The results indicate that for the CPO case the maximum efficiency appears to be at about 45 bar

while for the ASR case this maxima is around 22 bar.

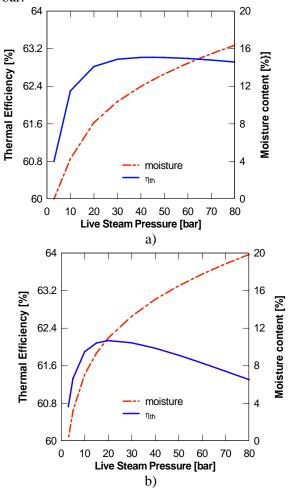


Figure 2. Thermal efficiency and moisture content of the combined SOFC – ST plants as function of live steam pressure, a) with CPO reformer, and b) with ASR reformer.

At optimal live steam pressure the efficiency of the CPO pre-reformer case is higher than the corresponding optimal live steam pressure for the ASR pre-reformer case. The moisture content after the steam turbine is an important issue to be considered. Too high level of moisture (more than about 16%) may cause blades corrosion located at the last stage, see e.g. [15]. Further, the results indicate that for the CPO pre-reforming plant the moisture content more than 16% may occur for pressures above 75 bar, while for the ASR pre-reforming plant this true for pressures above 48bar. Although, both are much higher than the optimized pressures mentioned above.

Effect of Cathode Preheating

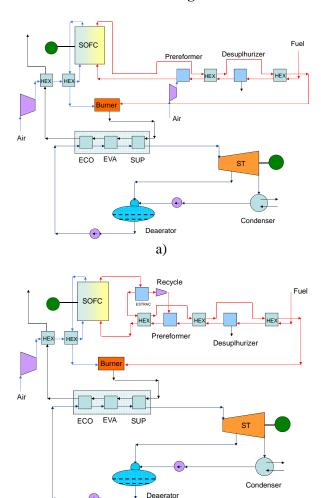


Figure 3. Combined SOFC – ST cycle plants with cathode preheating in the SOFC cycle, a) with CPO reformer, and b) with ASR reformer.

b)

The energy left after the HRSG in the previous designs are rather high; see the outlet temperatures of HRSG in both cases. This energy can be used to preheat the cathode air flow and thereby decrease the energy from the SOFC cycle which is used for preheating. Figure 3 shows the suggested plants. The SOFC cycle efficiency will not decrease significantly by such preheating. Such a preheating cannot be done in a combined cycle (gas turbine on the top of a steam turbine) since the temperature after the compressor is too high because of compressor pressure ratio. Several calculations are carried out to find the

optimal thermal efficiency for each pre-reformer case. Main important calculated results are shown in Table 4. In Table 4, the results are presented for the HRSG outlet gas—side temperature of 90°C. However, the thermal efficiencies of the proposed systems decreases if the HRSG outlet gas temperatures are increased see Fig. 4.

Parameter	CPO	ASR
Net power output	41.06 MW	40.34 MW
SOFC cycle power	30.92 MW	31.13 MW
ST cycle power	10.14 MW	9.21 MW
Dissipated gas T	90°C	90°C
Steam Pressure /	70 bar /	60 bar /
Temperature	569.9°C	532.2°C
Steam cycle η _{thermal}	0.395	0.381
Moisture after ST	11.5%	12.9%
SOFC cycle η _{thermal}	0.512	0.523
Plant η _{thermal} (LHV)	0.680	0.677

Table 4. Net powers and efficiencies of the plants for Fig. 3.

At 120°C the thermal efficiency of the CPO case drops to 0.668, while for the ARS it is decreased to 0.664. However, these efficiencies are still much higher compared to the traditional plants for such sizes. Further, the drop in efficiency for the ASR pre-reforming case is more sensible than the CPO case, the lines are getting wider.

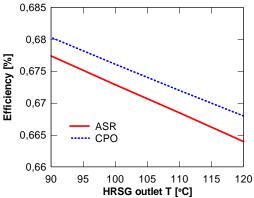


Figure 4. Thermal efficiencies as function of HRSG outlet gas temperature.

CONCLUSIONS

Hybrid combined SOFC – ST plants are presented and analyzed. The plants are fired by natural gas

and therefore the fuel is desuphurized and then pre-reformed before sending to the anode side of the SOFC. Both CPO and ARS pre-reforming processed are used.

The results indicate that for simple combinations the thermal efficiencies of the system can reach to about 62% –63 % depending on the pre-reforming process. The SOFC cycle efficiency in the ASR performing type is higher than the corresponding SOFC cycle with CPO pre-reforming. However, the efficiency of the hybrid plants with CPO case is larger than the corresponding hybrid plant with ARS case. This is due to the fact that in the CPO case the temperature of the off-gases entering the HRSG is larger than the corresponding temperature in the ARS case. This results in higher efficiency in the bottoming cycle (steam cycle) and thereby better efficiency for the hybrid plant. Using cathode preheating the efficiency will be increased to about 67% - 68%.

REFERENCES

- [1] Fontell, E., Kivisaari, T., Christiansen, N., Hansen, J.-B. and Pålsson, J. 2004, "Conceptional study of a 250 kW planar SOFC System for CHP Application", *J. Power Sources*, Vol. 131, pp. 49 56.
- [2] Rokni, M., 2003, "Introduction of a Fuel Cell into Combined Cycle: A Competitive Choice for Future Cogeneration", *ASME Cogen Turbo*, IGTI vol. 8, pp. 255 261.
- [3] Riensche, E., Achenbach, E., Froning, D., Haines, M. R., Heidug, W. K., Lokurlu, A., and von Andrian, S., 2000, "Clean Combined-cycle SOFC Power Plan Cell Modeling and Process Analysis", *J. Power Sources*, Vol. 86, pp. 404 410.
- [4] Pålsson, J., Selimovic, A. and Sjunnesson, L., 2000 "Combined Solid Oxide Fuel Cell and Gas Turbine System for Efficient Power and Heat Generation", *J. Power Sources*, Vol. 86, pp. 442 448.
- [5] Subramanyan, K. and Diwekar, U. M., 2005 "Characterization and Quantification of Uncertainty in Solid Oxide Fuel Cell Hybrid Power Plants", *J. Power Sources*, Vol. 142, pp. 103 116.

- [6] Roberts. R. A. and Brouwer, J. 2006, "Dynamic Simulation of a Pressurized 220 kW Solid Oxide Fuel-Cell – Gas-Turbine Hybrid System: Modeled Performance Compared to measured Results", J. Fuel Cell Science and Technology, Vol. 3, No. 1, pp. 18 – 25.
- [7] Rokni, M., Fontell, E., Ylijoki, Y., Tiihonen, O., Hänninen, M., 2005, "Dynamic Modeling of Wärtsilä 5kW SOFC System", Ninth International Symposium on Solid Oxide Fuel cell (SOFC IX), Quebec, Eds. S.C. Singhal and J. Mizusaki, pp. 865 875.
- [8] Dunbar, W.R., Lior, N., Gaggioli, R.A., 1991, "Combining Fuel Cells with Fuel Fired Power Plants for Improved Exergy Efficiency". *J. of Energy*, Vol. 16, No. 10, pp. 1259 1274.
- [9] Elmegaard, B, Houbak, N, 2005, "DNA A General Energy System Simulation Tool," Proceeding of SIMS 2005, Trondheim, Norway.
- [10] Petersen, T.F., Houbak, N. and Elmegaard, B., 2006, "A Zero-Dimensional Model of a 2ND Generation Planar SOFC With Calibrated Parameters", *Int. J. Thermodynamics*, Volume 9, issue 4, pp. 161 168.
- [11] Keegan, K. M., Khaleel M., Chick L. A., Recknagle K., Simner S.P. and Diebler J., 2002, "Analysis of a Planar Solid Oxide Fuel Cell Based Automotive Auxiliary Power Unit", SAE Technical Paper Series No. 2002-01-0413.
- [12] Kim, J.W. and Virkar, A.V., 1999, "The Effect of Anode Thickness on the Performance of Anode Supported Solid Oxide Fuel Cell", *Proc. of the Sixth Int. Symp. On SOFCs*, (SOFC VI), PV99 19, The Electrochemical Society, pp. 830 839.
- [13] Elmegaard, B, Houbak, N, 1999, "On the Implementation of Energy Simulators with Emphasis on Chemical Equilibrium Gasifier Models", Proceedings of ECOS'99 (ISBN: 4-9980762-0-5), pp. 258-263, Tokyo.
- [14] Kehlhofer, R.H., Warner, J., Nielsen, H. and Bachmann, R., 1999, "Combined – Cycle Gas Steam Turbine Power Plants", PennWell, ISBN: 0-87814-736-5.

MODELLING A COMBINED HEAT AND POWER PLANT BASED ON GASIFICATION, MICRO GAS TURBINE AND SOLID OXIDE FUEL CELLS

Christian Bang-Møller* and Masoud Rokni **Technical University of Denmark Department of Mechanical Engineering** 2800 Kgs. Lyngby Denmark

ABSTRACT

A system level modelling study on two combined heat and power (CHP) systems both based on biomass gasification. One system converts the product gas in a micro gas turbine (MGT) and the other in a combined solid oxide fuel cell (SOFC) and MGT arrangement. An electrochemical model of the SOFC has been developed and calibrated against published data from Topsoe Fuel Cells A/S (TOFC) and Risø National Laboratory, and the modelled gasifier is based on an up scaled version of the demonstrated low tar gasifier, Viking, situated at the Technical University of Denmark. The SOFC converts the syngas more efficient than the MGT reflected in the electrical efficiency of the gasifier and MGT system in opposition to the gasifier and SOFC-MGT configuration - η_{el} =28.1% versus η_{el} =50.3%.

Keywords: System modelling, biomass gasification, micro gas turbine, SOFC

NOMENCLATURE

TIOTIE	EITTERE
$a_{\rm ohm},b_{\rm ohm}$	coefficients for Eq. (24)
ASR	area specific resistance
E	reversible open circuit voltage
F	Faradays constant
$oldsymbol{g}_{\mathrm{f}}$	Gibbs free energy of formation
$g_{ m f}$ i	current density
LHV	lower heating value
'n	molar flow
$n_{\rm e}$	transferred electrons per molecule of fuel
p	pressure/partial pressure
\overline{P}	power production
R	universal gas constant
T	temperature
UF	fuel utilization factor for SOFC
V	potential/overpotential
y	molar fraction
δ	SOFC layer thickness
η	efficiency
•	•

Subscripts:

anode c cathode con consumption electrolyte e interconnect

INTRODUCTION

Development of sustainable and efficient production plants of combined heat and power (CHP) tends to gain more attention as climate changes, security of supply and depletion of fossil fuels have become well known issues. The share of biomass in CHP production are expected to increase in the future and decentralized CHP plants are also of interest to avoid costs of biomass transportation. Efficient power producing technologies for small scale productions are typically gas engines, micro gas turbines (MGT) and fuel cells – all requiring gaseous fuel. Gasification can deliver biomass based gaseous fuel so the combination of biomass gasification and efficient syngas conversion are potentially a sustainable and efficient CHP plant.

Solid oxide fuel cells (SOFCs) can electrochemically convert H2 and CO as well as internally reform CH₄ into more H₂ and CO due to their high operating temperature. This makes SOFCs very fuel flexible and ideal for converting syngas compared to other fuel cell types.

The performance and system design of integrated biomass gasifier and SOFC systems in the 100-

Corresponding author: Email: chrbm@win.dtu.dk Phone: +45 45254123

1000kW_e class have been investigated by several. An innovative design including heat pipes between a SOFC stack and an allothermal gasifier is described in [1]. Fryda et al. [2] studies the performance of a CHP system of less than 1MW_e and consisting of an autothermal gasifier combined with a MGT and/or SOFC.

This study focus on the performance of a system combining an up scaled version (\sim 500kW_{th}) of the two-stage gasifier named Viking and a MGT or a SOFC-MGT system. Viking is a 75kW_{th} autothermal (air blown) fixed bed biomass gasifier demonstrated at the Technical University of Denmark and it is described in detail in [3]. The Viking gasifier produces almost no tars, which is favourable for downstream SOFC operation. Hofmann et al. [4] has operated a SOFC on cleaned syngas from the Viking gasifier for 150 hours without degradation.

The present study is based on zero dimensional and steady-state modelling in the simulation tool DNA [5]. DNA has incorporated thermodynamic property data, is component based and is developed at The Technical University of Denmark.

SYSTEM DESCRIPTION

Two different combined heat and power systems are investigated in this study, both based on syngas production from an up scaled Viking gasifier. A flow sheet of the two systems is depicted in Figure 1. The modelled gasifier system is slightly simplified, but aims at the same resulting gas composition and cold gas efficiency as for the Viking gasifier. In the gasifier model the dryer is heated by hot syngas. The steam production from the dryer is added to the preheated air and dry wood and mixed air and steam are fed to the gasifier. The raw product gas are cooled to 90°C in three steps; air preheating, wood drying and syngas cooling producing hot water for district heating. The cooled syngas are then cleaned from impurities as particles and sulphur compounds before some of the water in the gas are condensed through cooling to 50°C. The cleaned and partly dried syngas are then converted into electricity and heat in a bottoming cycle consisting of a MGT or both a SOFC and a MGT. These two system configurations will from now on be referred as the Gasifier-MGT and the GasifierSOFC-MGT configuration, respectively. In the Gasifier-SOFC-MGT configuration all the components in the flow sheet are in use. With respect to Figure 1 the SOFC and preheaters are bypassed in the Gasifier-MGT arrangement. In addition the syngas compressor works as a roots blower for the gasifier system and not illustrated is a generator.

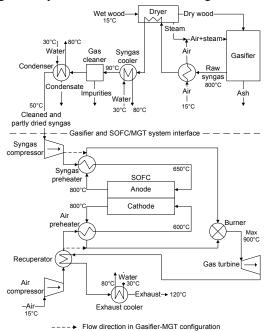


Figure 1: Flow sheet of the hybrid systems

Operating pressure	$p_{ m gasifier}$	0.998 bar
Operating temperature	$T_{\rm gasifier}$	800°C
Pressure loss	$\Delta p_{\rm gasifier}$	5 mbar
Non-equilibrium methane	METH	0.01

Table 1: Inputs to the gasifier submodel

GASIFIER MODEL

The gasifier component calculates the produced syngas composition as well as the produced ashes based on the inlet media composition and the operating conditions. The input parameters defining the operating conditions for the gasifier submodel are given in Table 1. The gasifier pressure loss is defined as the difference between the inlet air and steam mixture and the outlet syngas.

In the gasifier the incoming flows are converted into a syngas and ashes. The ashes come from a defined content in the biomass. The syngas can consist of the following species: H₂, O₂, N₂, CO,

NO, CO₂, H₂O, NH₃, H₂S, SO₂, CH₄, NO₂, HCN, COS and Ar. It is assumed that equilibrium is reached at the operating temperature and pressure, where the total Gibbs energy has its minimum value. With this assumption the syngas outlet composition can be found by the Gibbs minimization method [6]. A possibility for bypassing an amount of methane from the equilibrium calculations is added in order to reach syngas compositions, which contain more methane than the corresponding one at equilibrium. Thus the syngas composition can be adjusted to match real syngas compositions, e.g. from the Viking gasifier. The input parameter METH is used for this bypassing and is defined as the fraction of the methane that is not included in the equilibrium calculations and instead flows through the gasifier and appears in the outlet syngas.

Gasifier model validation

The model validation for the gasifier is done for all of the gasification plant from the biomass input to the cleaned and dried syngas. Thus the data from the Viking gasifier plant can be used for validation.

Wood chips from beech with small amounts of oak are used in the modelling as for the Viking gasifier reported in Ahrenfeldt et al. [3].

As seen in Table 2 the produced syngas composition and the lower heating value (LHV) from the gasifier model is close to the Viking data. The overall performance of the modelled gasifier is also similar to the Viking gasifier expressed in the cold gas efficiencies.

SOLID OXIDE FUEL CELL MODEL

The SOFC stack component calculates the air and fuel outlet compositions as well as the power production. The calculations are based on the inlet air and fuel compositions and flow rates as well as the other operating conditions of the SOFC. The SOFC submodel includes an electrochemical model for predicting the performance of the SOFC. The operating conditions are partly described by input parameters given to the SOFC submodel and these are presented in Table 3.

In the submodel only H₂ is electrochemically converted in the SOFC anode, but the model takes into account that CO produces an extra H₂ through

	Viking [3]	Gasifier model
H ₂ (vol-%)	30.5	29.9
CO (vol-%)	19.6	20.8
CO ₂ (vol-%)	15.4	13.5
CH ₄ (vol-%)	1.16	1.19
N ₂ (vol-%)	33.3	34.2
LHV (MJ/kg)	6.2	6.3
Cold gas eff.	93%	94%

Table 2: Dry syngas composition, lower heating value as well as cold gas efficiency for the Viking gasifier and the modelled gasifier, respectively

Fuel utilization factor	UF	0.85
Operating temperature	$T_{ m SOFC}$	800°C
Anode pressure loss	Δp_{a}	5 mbar
Cathode pressure loss	$\Delta p_{ m c}$	10 mbar
Current density	i	300 mA cm ⁻²

Table 3: Inputs to the SOFC submodel

the water-gas-shift (WGS) reaction, while four additional H₂ molecules are produced from CH₄ through internal steam reforming and WGS of produced CO (full conversion is assumed). The total mole flow of H₂ on the anode after internal steam reforming and WGS is expressed in Eq. (1).

$$\dot{n}_{\rm H_2,tot} = \dot{n}_{\rm H_2,in} + \dot{n}_{\rm CO,in} + 4\dot{n}_{\rm CH_4,in}$$
 (1)

$$H_2 + O^{2-} \rightarrow H_2O + 2e^-$$
 (2)

$$\frac{1}{2}O_2 + 2e^- \to O^{2-} \tag{3}$$

$$H_2 + \frac{1}{2}O_2 \rightarrow H_2O \tag{4}$$

The amount of hydrogen that is converted depends on the fuel utilization factor (*UF*) and this amount is electrochemically converted in the anode. The electrode reactions and the overall fuel cell reaction are as shown in Eq. (2) to (4).

From the overall fuel cell reaction it is seen that the amount of consumed oxygen is half the amount of consumed hydrogen. The cathode outlet composition can then be found by the following equations if the only species taking into account are O₂, N₂, CO₂, H₂O and Ar.

$$\dot{n}_{\rm O_2,con} = \frac{UF\dot{n}_{\rm H_2,in}}{2} \tag{5}$$

$$\dot{n}_{\text{c,out}} = \dot{n}_{\text{c,in}} - \dot{n}_{\text{O}_2,\text{con}} \tag{6}$$

$$y_{O_2,\text{out}} = \frac{\dot{n}_{c,\text{in}} y_{O_2,\text{in}} - \dot{n}_{O_2,\text{con}}}{\dot{n}_{c,\text{out}}}$$
 (7)

$$y_{j,\text{out}} = \frac{\dot{n}_{\text{c,in}} y_{j,\text{in}}}{\dot{n}_{\text{c,out}}}, \ j = \{N_2, CO_2, H_2O\}$$
 (8)

$$y_{\text{Ar,out}} = 1 - y_{\text{O}_2,\text{out}} - y_{\text{N}_2,\text{out}} - y_{\text{CO}_2,\text{out}} - y_{\text{H}_2\text{O,out}}$$
(9)

The fuel composition leaving the anode is calculated by the Gibbs minimization method [6] as described for the gasifier submodel. Equilibrium at the anode outlet temperature and pressure is assumed for the following species: H₂, CO, CO₂, H₂O, CH₄ and N₂. The equilibrium assumption is fair since the methane content in this study is low enough for such kind of assumption to be made. The heat consumed by the endothermic internal reforming reactions is taken into account by the Gibbs minimization method. More internal reforming means more cooling of the SOFC.

The power production from the SOFC depends on the amount of chemical energy fed to the anode, the reversible efficiency (η_{rev}), the voltage efficiency (η_v) and the fuel utilization factor (*UF*). It is defined in mathematical form in Eq. (10).

$$P_{\text{SOFC}} = \begin{bmatrix} LHV_{\text{H}_{2}} \dot{n}_{\text{H}_{2},\text{in}} \\ + LHV_{\text{CO}} \dot{n}_{\text{CO,in}} \\ + LHV_{\text{CH}_{4}} \dot{n}_{\text{CH}_{4},\text{in}} \end{bmatrix} \eta_{\text{rev}} \eta_{\text{v}} UF$$
 (10)

The reversible efficiency is the maximum possible efficiency defined as the relationship between the maximum electrical energy available (change in Gibbs free energy) and the fuels LHV. This is shown in Eq. (11) and the definition of the change in Gibbs free energy is shown in Eq. (12). The voltage efficiency express the electrochemical performance of the SOFC and the calculation of the voltage efficiency is described in the following subsection.

$$\begin{split} &\eta_{\text{rev}} = \frac{\left(\Delta \overline{g}_{\text{f}}\right)_{\text{fuel}}}{LHV_{\text{fuel}}} \\ &\left(\Delta \overline{g}_{\text{f}}\right)_{\text{fuel}} = \left[\left(\overline{g}_{\text{f}}\right)_{\text{H}_{2}\text{O}} - \left(\overline{g}_{\text{f}}\right)_{\text{H}_{2}} - \frac{1}{2}\left(\overline{g}_{\text{f}}\right)_{\text{O}_{2}}\right] y_{\text{H}_{2},\text{in}} (12) \\ &+ \left[\left(\overline{g}_{\text{f}}\right)_{\text{CO}_{2}} - \left(\overline{g}_{\text{f}}\right)_{\text{CO}} - \frac{1}{2}\left(\overline{g}_{\text{f}}\right)_{\text{O}_{2}}\right] y_{\text{CO,in}} \\ &+ \left[\left(\overline{g}_{\text{f}}\right)_{\text{CO}_{2}} + 2\left(\overline{g}_{\text{f}}\right)_{\text{H}_{2}\text{O}} - \left(\overline{g}_{\text{f}}\right)_{\text{CH}_{4},\text{in}} \right] \end{aligned}$$

Electrochemical model

The electrochemical model is used to calculate the cell potential and the voltage efficiency of the SOFC. Both depend on the operating conditions such as temperature, pressure, gas compositions, fuel utilization and load (current density). The cell potential and voltage efficiency is defined in Eq. (13) and (14), respectively.

$$V_{\text{cell}} = E - V_{\text{act}} - V_{\text{ohm}} \tag{13}$$

$$\eta_{\rm v} = \frac{V_{\rm cell}}{E} \tag{14}$$

In the following the reversible open circuit voltage (E), the activation overpotential $(V_{\rm act})$ and the ohmic overpotential $(V_{\rm ohm})$ are calculated. Traditionally a concentration overpotential term is included in Eq. (13). The concentration overpotential is a result of the limitations of transporting the reactants to the active cell area. In Larminie et. al. [7] it is described as a voltage drop caused by the pressure change associated with the consumption of reactants. As a result of the current being drawn from the cell the average partial pressure of reactants is lower than at the inlet. Thus, in this study the concentration overvoltage is taken into account by using average partial pressures when calculating E and $V_{\rm act}$.

E can be calculated from the Nernst equation:

$$E = \frac{-\Delta \overline{g}_{f}^{0}}{n_{e}F} + \frac{RT}{n_{e}F} \ln \left(\frac{\overline{p}_{H_{2}, \text{tot}} \sqrt{\overline{p}_{O_{2}}}}{\overline{p}_{H_{2}O}} \right)$$
(15)

Since it is assumed that all CO and CH₄ are converted to H₂ before the electrochemical reactions takes place, the change in standard Gibbs free energy ($\Delta \overline{g}_{\rm f}^{\ 0}$) and the number of electrons transferred for each molecule of fuel ($n_{\rm e}$) is determined for the reaction of H₂ only. Thus, $n_{\rm e}=2$ and $\Delta \overline{g}_{\rm f}^{\ 0} = (\overline{g}_{\rm f}^{\ 0})_{\rm H_2O} - (\overline{g}_{\rm f}^{\ 0})_{\rm H_2} - \frac{1}{2}(\overline{g}_{\rm f}^{\ 0})_{\rm O_2}$. The partial pressure of species j is an average across the respective electrode and is here defined as an arithmetic mean between inlet and outlet as shown in Eq. (16) and (17). The average partial pressure of available hydrogen after internal steam reforming and WGS of CH₄ and CO can be determined from

the overall steam reforming and WGS reaction including all species. It is defined in Eq. (18):

$$\overline{p}_{j} = \left(\frac{y_{j,\text{out}} - y_{j,\text{in}}}{2}\right) p_{a}, \tag{16}$$

$$j = \left\{H_{2}, \text{CO}, \text{CH}_{4}, \text{CO}_{2}, \text{H}_{2}\text{O}, \text{N}_{2}\right\}$$

$$\overline{p}_{\text{O}_{2}} = \left(\frac{y_{\text{O}_{2},\text{out}} - y_{\text{O}_{2},\text{in}}}{2}\right) p_{c} \tag{17}$$

$$\overline{p}_{\text{H}_{2},\text{tot}} = \left(\frac{\overline{p}_{\text{H}_{2}} + \overline{p}_{\text{CO}} + 4\overline{p}_{\text{CH}_{4}}}{\overline{p}_{\text{H}_{2}} + \overline{p}_{\text{CO}} + 3\overline{p}_{\text{CH}_{4}} + \overline{p}_{\text{CO}_{2}} + \overline{p}_{\text{H}_{2}\text{O}} + \overline{p}_{\text{N}_{2}}}\right) p_{a}$$
(18)

The activation overpotential is due to an energy barrier (activation energy) that the reactants must overcome in order to drive the electrochemical reactions. The activation overpotential is non-linear and is dominant at low current density (i). The activation overpotential is defined as (cf. [8]):

$$V_{\text{act}} = V_{\text{act,a}} + V_{\text{act,c}}$$

$$= \frac{2RT}{n_{\text{e}}F} \left[\sinh^{-1} \left(\frac{i + i_{\text{n}}}{2i_{0,\text{a}}} \right) + \sinh^{-1} \left(\frac{i + i_{\text{n}}}{2i_{0,\text{c}}} \right) \right] (19)$$

The internal current density (i_n) is added to the actual fuel cell current density in order to account for the mixed potential caused by fuel crossover. The importance of the internal current density in the case of SOFCs is much less than for low temperature fuel cells and the value of i_n is usually very small [7]. The exchange current density (i_0) is a measure of the level of activity on the electrode at i=0 mA cm⁻² and is defined as (cf. [9]):

$$i_{0,a} = 2.13 \times 10^{7} \left(\frac{\overline{p}_{H_{2}, \text{tot}} \overline{p}_{H_{2}O}}{p_{a}^{2}} \right) \exp \left(\frac{-110000}{RT} \right) (20)$$

$$i_{0,c} = 1.49 \times 10^{7} \left(\frac{\overline{p}_{O_{2}}}{p_{c}} \right)^{0.25} \exp \left(\frac{-110000}{RT} \right)$$
 (21)

The ohmic overpotential is caused by the electrical resistance for the ions passing through the electrolyte as well as for the electrons passing through the electrodes and interconnects. The

R	8.314 J K ⁻¹ mol ⁻¹	
F	96485 C mol ⁻¹	
$n_{\rm e}$	2	
$i_{\rm n}$	2 mA cm ⁻²	[9]
$\delta_{\!\scriptscriptstyle a}$	750×10 ⁻⁴ cm	[10]
$\delta_{ m a} \ \delta_{ m c}$	50×10 ⁻⁴ cm	[10]
$\delta_{ m e} = \delta_{ m i}$	40×10 ⁻⁴ cm	[10]
$\delta_{\rm i}$	100×10 ⁻⁴ cm	[11]
$a_{ m ohm,a}$	$0.00298 \times 10^{-3} \mathrm{k}\Omega\mathrm{cm}$	[12]
$b_{ m ohm,a}$	-1392 K	[12]
$a_{\rm ohm,c}$	$0.00811 \times 10^{-3} \mathrm{k}\Omega\mathrm{cm}$	[12]
$b_{ m ohm,c}$	600 K	[12]
$a_{\rm ohm,e}$	$0.00294 \times 10^{-3} \text{ k}\Omega\text{cm}$	[12]
$b_{ m ohm,e}$	10350 K	[12]
$a_{\rm ohm,i}$	$0.1256 \times 10^{-3} \text{ k}\Omega\text{cm}$	[12]
$b_{ m ohm,i}$	4690 K	[12]

Table 4: Inputs for the electrochemical model

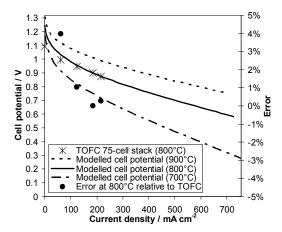


Figure 2: Single cell polarization curves based on a 75-cell stack and the SOFC model, respectively.

ohmic overpotential is defined below (cf. [9] and [12]).

$$V_{\rm ohm} = i \, ASR \tag{22}$$

$$ASR = ASR_a + ASR_c + ASR_c + ASR_i$$
 (23)

$$ASR_j = \delta_j a_{\text{ohm},j} \exp\left(\frac{b_{\text{ohm},j}}{T}\right), \ j = \{a, c, e, i\}$$
 (24)

The thicknesses of the different layers (δ) and the constants a_{ohm} and b_{ohm} used are listed in Table 4.

SOFC model calibration

The described electrochemical model has been calibrated against experimental data. Since the model aims at the performance of 2^{nd} generation SOFCs from Topsoe Fuel Cell A/S (TOFC) and Risø National Laboratory, published data from this SOFC type has been used. The ASR has been calibrated against a value of $0.15~\Omega$ cm² at 850° C as published by [13] and the resulting cell potential has been calibrated against a polarization curve (800° C and fuelled with H_2 and N_2) published by [14]. An active cell area of $81~\text{cm}^2$ has been assumed. Both modelled and experimental data as well as the error relative to the experimental data are presented in Figure 2.

The model shows excellent agreement with the experimental data above a current density of 100 mA cm⁻². The current density of 300 mA cm⁻² is chosen to represent the SOFC load in the following results.

PERIPHERAL EQUIPMENT

Modelling of peripheral components like compressors, turbines and heat exchangers are standard and therefore not described in detail.

The throughput of wet biomass is 154.8 kg h^{-1} (corresponds to 499.2 kW_{th} (LHV)). Thus it is assumed that the Viking gasifier can be scaled up from a nominal ~75 kW_{th} [3]. The biomass dryer reduces the water content in the biomass from 32.2 wt-% to 5 wt-% by heating it to $150 ^{\circ}\text{C}$ and the air for the gasifier is preheated to $780 ^{\circ}\text{C}$ by the hot product gas.

The inlet temperature to the SOFC anode and cathode are maintained at 150°C and 200°C below the outlet temperature, respectively.

The pressure loss in every component in the SOFC air supply stream and burner exhaust stream is assumed to be 10 mbar, while the pressure loss in each of the rest of the components is assumed to be 5 mbar, except the burner that has a pressure loss of 0.6‰ (equals 1.5 mbar when 2.5 bar at inlet)

The gas cleaner is a baghouse filter removing particulates and it is assumed that the cleaned syngas can be used directly in a SOFC. The condenser removes some of the water content in the syngas resulting in a content of water in the cleaned and dried syngas of 12.7 vol-%. The re-

sulting steam to carbon ratio (S/C) is 0.41, which is somewhat low, but is justified by the very low tar content in the Viking syngas.

The isentropic and mechanical efficiency of the compressors are 75% and 98%, respectively, and the isentropic efficiency of the MGT expander is 84%. The turbine inlet temperature (TIT) is limited to 900°C in the Gasifier-MGT case, while varied in the Gasifier-SOFC-MGT arrangement. The performance of the compressors and the MGT expander are taken from Fryda et al. [2] and corresponds to common performance data for a MGT of this scale. The recuperator effectiveness is assumed to be 85% and the generator efficiency is assumed to be 99%. In the Gasifier-MGT configuration the burner operating pressure is 3.75 bar and in the Gasifier-SOFC-MGT case the SOFC operating pressure is 2.5 bar (these pressures are varied in the results section).

No heat losses are taken into account. Introducing heat losses from the gas cleaner will only affect the heat production from the condenser since the temperature after the condenser is fixed to 50°C.

The outlet pressure from the MGT depends on the total pressure loss downstream the MGT, since it is the exhaust pressure which is fixed to 1.013 bar. Because of the recuperator and exhaust cooler the outlet pressure from the MGT is 1.033 bar. The district heating (DH) water is assumed to be 30°C at inlet and 80°C at outlet.

RESULTS AND DISCUSSION

In the following results the inputs presented in the previous sections are used unless something else is stated. The system configurations are previously described in detail.

The performance of the different system configurations vary greatly with the operating conditions and namely the pressure ratio of the MGT (in the Gasifier-MGT case) and the operating pressure of the SOFC (in the Gasifier-SOFC-MGT case) are of great importance to the resulting system performance. The two system configurations have different optimum with regard to their operating pressure and these can be seen in Figure 3. When operating at a constant TIT of 900°C the Gasifier-MGT configuration shows an optimum at 3.75 bar performing an electric efficiency of 28.1%. It is the recuperator that ensures an optimum at a rela-

tively low operating pressure. By combining the SOFC and MGT in the Gasifier-SOFC-MGT configuration the electrical efficiency reaches 50.3% at an optimum operating pressure of 2.5 bar. This is a substantial increase in efficiency caused by the efficient SOFC. With a fuel utilization of 85% a part of the fuel passes through the anode, but this amount is used in the MGT. In this case the TIT is varying with the SOFC operating pressure and has a value of 697°C at 2.5 bar.

The Gasifier-MGT system performance also depend on the allowed TIT as depicted in Figure 4. Decreasing the TIT by 100°C to 800°C lowers the electrical efficiency to 25.4% - a drop of 2.7 percentage points. In the Gasifier-SOFC-MGT configuration a drop in SOFC operating temperature by 100°C to 700°C decreases the electrical efficiency to 44.4% - a drop of 5.9 percentage points. This indicates that the SOFC operating temperature has more influence on the SOFC performance than the TIT has on the MGT performance. The research and development working on lowering the SOFC operating temperature in order to use cheaper materials will influence the system performance presented here and potentially other bottoming cycles could be beneficial, e.g. a Rankine cycle.

The sensitivity of the model results to the chosen SOFC current density is shown in Figure 5. At the reference current density value of 300 mA cm⁻² the SOFC voltage efficiency (defined in Eq. (14)) is 40.8%. Raising the SOFC load to 500 mA cm⁻² lowers the voltage efficiency to 35.7% meaning a reduction in the total electrical efficiency to 46.7% - a drop of 3.6 percentage points. This is a relative change in electrical efficiency of 7% for a 66.7% increase in current density.

Key data for the two system configurations studied are presented in Table 5 and the respective optimal operating pressure is used in each configuration as well as the reference input values presented in the previous sections. The Gasifier-SOFC-MGT configuration clearly has the best electrical efficiency, while the CHP efficiencies do not differ significantly. In the Gasifier-SOFC-MGT case, the power production is mainly from the SOFC producing 76.4% of the power. The exact values of the efficiencies will be slightly lower when incorporating heat losses, a more

accurate efficiency of the gasifier system and possible more extensive gas cleaning, but the comparison of the systems performance is still valid.

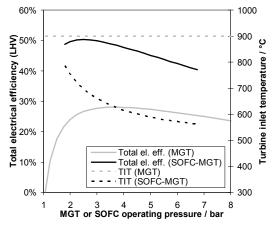


Figure 3: Electric efficiency and TIT at different MGT or SOFC operating pressures

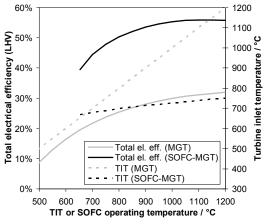


Figure 4: Electric efficiency and TIT at different TIT or SOFC operating temperatures

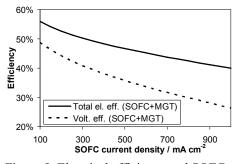


Figure 5: Electrical efficiency and SOFC voltage efficiency as a function of SOFC current density

		Gasifier	Gasifier
		-MGT	-SOFC-MGT
Biomass	/ kg h ⁻¹	154.8	154.8
input	/ kW _{th,LHV}	499.2	499.2
$p_{\rm MGT}$ or $p_{\rm SO}$	_{orc} / bar	3.75	2.5
P _{MGT,net} / kW _{el}		140.1	59.2
$P_{\rm SOFC, net}$ / k		-	191.8
P _{total,net} / kW _{el}		140.1	251.0
DH production / kJ s ⁻¹		239.7	146.7
$\eta_{\rm el}$ / % (LHV)		28.1	50.3
η_{CHP} / % (LHV)		76.1	79.7

Table 5: Key data for the studied systems

CONCLUSION

A study on the system performance of an up scaled Viking gasifier (~500 kW_{th}) with either a downstream MGT or SOFC-MGT has been conducted by zero dimensional process modelling. A SOFC submodel has been developed including an electrochemical model predicting the SOFC performance at different operating conditions. This submodel has been calibrated against published TOFC stack performance data. The reference conditions for the SOFC has been an operating temperature of 800°C, a fuel utilization of 85% and a current density of 300 mA cm⁻². The optimal operating MGT and SOFC-MGT pressure has been found for the two system configurations to 3.75 and 2.5 bar, respectively. The SOFC converted the syngas more efficient than the MGT reflected in the efficiency of the gasifier and MGT system configuration in opposition to the gasifier and SOFC-MGT configuration - η_{el} =28.1% versus $\eta_{\rm el}$ =50.3%. These efficiencies were very sensitive to the SOFC operating temperature (or TIT in the Gasifier-MGT arrangement), while only a moderate sensitivity to the SOFC current density was observed.

REFERENCES

- [1] Karellas S, Karl J, Kakaras E. An innovative biomass gasification process and its coupling with microturbine and fuel cell systems. Energy 2008;33:284–291.
- [2] Fryda L, Panopoulos KD, Kakaras E. *Integrated CHP with autothermal biomass gasification and SOFC–MGT*. Energy Conversion and Management 2008;49:281–290.

- [3] Ahrenfeldt J, Henriksen U, Jensen TK, Gøbel B, Wiese L, Kather L, Egsgaard H. Validation of a Continuous Combined Heat and Power (CHP) Operation of a Two-Stage Biomass Gasifier. Energy & Fuels 2006;20:2672-2680.
- [4] Hofmann Ph, Schweiger A, Fryda L, Panopoulos KD, Hohenwarter U, Bentzen JD, Ouweltjes JP, Ahrenfeldt J, Henriksen U, Kakaras E. High temperature electrolyte supported Ni-GDC/YSZ/LSM SOFC operation on two-stage Viking gasifier product gas. J. Power Sources 2007;173:357–366.
- [5] Elmegaard B, Houbak N. *DNA A General Energy System Simulation Tool*, In: Proceedings of the 46th Conf. on Simulation and Modeling, Trondheim, 2005. (cf. http://www.scansims.org/sims2005)
- [6] Smith JM, Van Ness HC, Abbott MM. Introduction to Chemical Engineering Thermodynamics. 7th ed. Boston: McGraw-Hill, 2005.
- [7] Larminie J, Dicks A. Fuel Cell Systems Explained. 2nd ed. West Sussex: John Wiley & Sons Ltd., 2003.
- [8] Aloui T, Halouani K. Analytical modeling of polarizations in a solid oxide fuel cell using biomass syngas product as fuel. Appl. Therm. Eng. 2007;27:731-737.
- [9] Calise F, Dentice d'Accadia M, Palombo A, Vanoli L. Simulation and exergy analysis of a hybrid Solid Oxide Fuel Cell (SOFC)—Gas Turbine System. Energy 2006;31:3278-3299.
- [10] Chan SH, Khor KA, Xia ZT. A complete polarization model of a solid oxide fuel cell and its sensitivity to the change of cell component thickness. J. Power Sources 2001;93:130-140.
- [11] Chan SH, Low CF, Ding OL. Energy and exergy analysis of simple solid-oxide fuelcell power systems. J. Power Sources 2002;103:188-200.
- [12] Bessette NF II, Wepfer WJ, Winnick J. A Mathematical Model of a Solid Oxide Fuel Cell. J. Electrochem. Soc. 1995;142:3792-3800.
- [13] Christiansen N, Hansen JB, Holm-Larsen H, Linderoth S, Larsen PH, Hendriksen PV, Mogensen M. Solid oxide fuel cell development at Topsoe Fuel Cell and Risø. Fuel Cells Bulletin 2006;2006(8):12-15.
- [14] Linderoth S, Larsen PH, Mogensen M, Hendriksen PV, Christiansen N, Holm-Larsen H. Solid Oxide Fuel Cell (SOFC)

 Development in Denmark. Materials Science Forum 2007;539-543:1309-1314.

REFORMING PROCESSES FOR MICRO COMBINED HEAT AND POWER SYSTEM BASED ON SOLID OXIDE FUEL CELL

Vincenzo Liso¹, Mads Pagh Nielsen, Søren Knudsen Kær Department of Energy Technology IET Aalborg University Denmark

ABSTRACT

Solid oxide fuel cell (SOFC) is a promising technology for decentralized power generation and cogeneration. This technology has several advantages: the high electric efficiency, which can be theoretically improved through integration in power cycles; the low emissions; and the possibility of using a large variety of gaseous fuels.

The high operating temperature (700-1000°C) of SOFCs has a number of consequences, the most important of which are the possibility to partially reform the raw fuel in the fuel cell anode compartment and the possibility to use high quality heat for cogeneration.

In this work, different configurations of SOFC systems for decentralized electricity production are considered and studied.

The balance of plant (BoP) components will be identified including fuel and air supply, fuel management, start-up steam, anode re-circulation, exhaust gas heat management, power conditioning and control system.

Using mass and energy balance, different types of fuel reforming including steam reforming, autothermal reforming and partial oxidation will be investigated for each configuration.

Also effective system concepts and key performance parameters will be identified.

Keywords: Solid Oxide Fuel Cell, Micro CHP System

INTRODUCTION

State of the art SOFC micro CHP

Fuel cell systems are being developed for supplying primary power (heat and electricity) for residential applications of the near future. Residential power generation systems can be operated to provide primary or backup power for the home. They can run independently or in parallel to an existing power grid.

Residential application of fuel cell technologies will require selection of appropriate operating conditions. By varying operating conditions, a wide range of power and efficiency may be

Corresponding author: Phone: +45 9940 9259 Fax: +45 9815 1411 E-mail:vli@iet.aau.dk

derived from a SOFC system.

Fuel reforming systems can extract hydrogen from a variety of conventional fuel sources for the residential micro cogeneration application with fuel cell. Existing infrastructures such as natural gas pipelines and propane distribution systems can be used for these systems. Hydrogen rich gases can be produced via various fuel processing technologies. Steam reforming, partial oxidation and autothermal reforming are the three major fuel-processing technologies.

The SOFC based micro-CHP unit will replace the gas heating boiler and will provide heat and hot water as usual and additionally will provides the majority of the home's electricity needs. In figure 1 the integration of the unit in a household is depicted.

The basic idea of this SOFC based CHP unit is represented as a block diagram in figure 2.

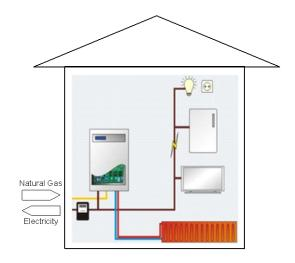


Figure 1 Household micro CHP system based on SOFC

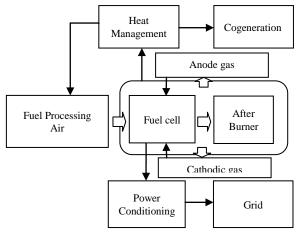


Figure 2 Micro CHP system configuration

The analyzed system is a SOFC-based heat and power generator operates on natural gas. The flow of natural gas is preheated in the system to reach the required temperature (200–300 C) for the desulphurization stage in which H₂S content is reduced by the action of an activated carbon bed. Prior to enter the SOFC stack, the fuel is pre-reformed (methane is partially converted into hydrogen and carbon monoxide) via a reforming process. In this paper differ types of fuel reforming have been analyzed namely steam reforming, autothermal reforming and partial oxidation.

Air is supplied by a blower and preheated prior to enter the SOFC stack. Non-recycled gases are sent to the catalytic after-burner where the remaining fuel is burnt with part of the excess air. Internal demand of electricity and heat is self supported by the system. The operating parameters may be selected based on requirements for power, efficiency, or a function of both variables such as cost of electricity.

Reforming of natural gas for solid oxide fuel cells is achieved either internally as described above or externally by a pre-reformer reactor [1] [2]. Further processing of the fuel is not required, because of the unlimited tolerance of the fuel cell to carbon monoxide. The re-circulation of anode off-gas to the pre-reformer [3] is an interesting option for solid oxide fuel cells. Through these means, addition of water can omitted, which clearly decreases the complexity of the system and reduces cold start problems. Besides an enhancement of system efficiency occurs.

Since the average annual consumption in a single-family detached dwelling is around 5000 kWh, a 1 kW electric power output should be a good trade off for an electricity generation systems for residential applications working for long periods under steady state operation [4]. In fact due to continuous fluctuations in the electricity demand, it would not be possible to follow the demand using a solid oxide fuel cell system.

In theory, SOFC can also operate with a full internal reforming, i.e.: without any prereforming process. However, this circumstance should always be avoided.

The use of a pre-reformer is required to crack the higher hydrocarbons included in the fuel; in addition the pre-reforming promotes the internal reforming process and the electrochemical reaction. In fact, a cell not equipped with a pre-reformer would not produce any current at its bottom, since the corresponding active area would be used for the reforming process and not for the electrochemical reaction [5]. It is also well-known that the reforming process occurring in the fuel cell is strongly endothermic, resulting in a dramatic decrease of the fuel temperature. In fact the reforming process results to be much faster than the heat exchange between the reacting stream and the hot gases [6].

Complete reforming in the solid oxide fuel cell incentives carbon deposition. This phenomenon should be prevented because it results in the growth of carbon filaments that are attached to anode crystallites, which generate massive forces within the electrode structure and, thereby, result in its rapid breakdown. Temperature, steam to carbon ratio, and electrode material are influential on carbon deposition [7].

It is also well-known that high temperature gradients in the SOFC must be avoided. Thus, it is not possible to feed the stack with low temperature air and fuel. The air inlet temperature can be increased by means of an external preheater, supplied by the SOFC outlet stream. On the other hand, the fuel can be preheated by increasing the length of the pre-reformer, since this component also acts as a tube-in-tube counter-flow heat exchanger. However, the larger the length of the pre-reformer, the higher is the de-methanization rate achieved in the same component. Therefore, an increase in the prereformer length would result in a better heat exchange but also in a complete reforming process within such component. circumstance must be avoided, since the internal reforming is crucial to provide additional cooling to the stack, avoiding unacceptable values of the stack temperature

FUEL PROCESSES

The analyzed micro CHP system operates on natural gas, therefore a pre reformer process is required.

The reforming process can be considered a general oxidative conversion of hydrocarbons to hydrogen. The generic chemical equation for this process is:

$$C_nH_m+O_x\rightarrow xCO+yCO_2+xH_2$$
 (1)

where C_nH_m is a hydrocarbon ($n \ge 1$, $m \ge n$) and O_x is an oxidant such as O_2 , H_2O , and CO_2 . The chemical reaction occurs at high temperatures, typically, above 700°C, in the presence of oxidants.

Depending on the nature of the oxidant O_x the oxidative process could be exothermic (e.g., when $O_x = O_2$), endothermic (when $[O_x] = H_2O$, CO_2 , or H_2O-CO_2 mixture), or near thermoneutral (when $[O_x] = O_2-H_2O$ or O_2-CO_2 , or O_2-CO_2), or O_2-CO_2 0.

 H_2O – CO_2 mixture with the suitable molar ratio of the reagents) [8].

The overall fuel process is endothermic therefore a certain amount of energy is required during the fuel process. High operational temperatures of the oxidative conversion processes are due to the relative "inertness" of methane and other saturated hydrocarbons (or alkanes) that make up most of the hydrocarbon feedstock for hydrogen production.

Water and CO₂ are also very inert compounds requiring high temperatures (in excess of 1000°C), for their activation and interaction with other chemical compounds. Therefore any fuel process will require a certain amount of energy changing the internal demand of the mCHP system.

Catalysts are widely used to accomplish these processes at the practical range of temperatures (750–950°C) and a combination of different gases is used as oxygen (air), steam and CO₂. The main drawback of the catalyst is the use of the poisoning effect of sulphur compound that should be properly filtered in the desuphurazer.

In general, the processes for oxidative conversion of hydrocarbons to hydrogen are well-established technologies, and most of the industrial hydrogen production processes. Steam methane reforming [SMR], partial oxidation [POx], autothermal reforming [ATR] belong in this category. Even though many companies produce large scale reforming system, small scale reformers for micro-CHP system are still under development. In fact, scalability issue rises from big to little size apparatus.

The extent of the pre-reforming reaction is one of the parameters to be optimized in the system because of its strong influence in heat balance and global efficiency. A compromise between the avoidance of carbon deposition in the inlet manifold of the fuel cell stack (external reforming reaction consumes steam reducing S/C ratio in the inlet flow) and the minimization of oxidant flow to cool down the stack must be reached to set an optimal degree of pre-reforming [9].

In the next sections the reforming processes mentioned above (SMR, POx, ATR) will be briefly described.

Steam Reforming Process

The steam reforming process is typically used to reform heavy hydrocarbon and oil fuels in industrial processes where the required heats of reaction are provided in-situ by oxidizing a fraction of the feedstock. One of the main drawbacks of this technology is a long time of reaction during the start up phase.

The steam reforming reaction is endothermic and takes place in a high-alloy tube reformer loaded with a nickel-based catalyst, which is placed inside a furnace equipped with burners in the side or at the top of the furnace. The use of combustion provides for a direct heat exchange where no heat transfer surface area is required. The major reactions can be represented as follows.

$$\begin{array}{ll} CH_{4} + H_{2}O \rightarrow CO + 3H_{2} & \Delta H_{298} = 206 \frac{kJ}{mol} \ \, (2) \\ CO + H_{2}O \rightarrow C_{2}O + H_{2} & \Delta H_{298} = -41 \frac{kJ}{mol} \ \, (3) \\ C_{n}H_{m} + nH_{2}O \rightarrow nCO + \left(n + \frac{m}{2}\right)H_{2} & (4) \end{array}$$

The process is typically operated with excess steam-to-carbon ratios at temperatures at about 750 to 900°C, depending on the use of the gas.

Because the number of moles changes for reaction (2), the process should be carried out at the lowest possible pressure to maximize the methane conversion rate (principle of Le Chatelier).

The exit raw synthesis gas composition is a mixture of H₂, CO, CO₂, and unreacted methane, which is near the equilibrium of the steam reforming reaction and water–gas shift (WGS) reaction. The complete reforming process is represented in figure 3.

conversion, therefore, it is necessary to operate at high temperature, low pressure and relatively high steam to carbon ratios [10].

According to the literature, SMR can be modeled by considering only chemical equilibrium. Hence, it is possible to predict the outlet composition by only knowing the H/C, O/C, pressure and temperature. This claim is based on measurement validation.

Table 1 Typical Reformer Outlet Gas Composition [2]

Furnace outlet temperature, °C	890.0
Furnace outlet pressure, bar	3
S/C ratio	24.0
Component, vol%	
Hydrogen	51.0
Carbon monoxide	10.4
Carbon dioxide	5.0
Methane	2.0
Water vapor	31.6

Partial Oxidation Process

The second important reaction for generating hydrogen suitable for mCHP application is partial oxidation (POx). This technology is already been applied in other SOFC mCHP system prototypes [3].

It can be seen as oxidation with less than the stoichiometric amount of oxygen for full oxidation to the stable end products, carbon dioxide and water. Oxygen can be supplied by through air.

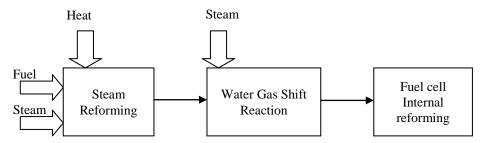


Figure 3 Fuel reforming process

A typical outlet gas from the steam reforming phase is shown in the table 1.

Steam reforming of methane is a reversible reaction. In order to ensure a high methane

Below the main reaction for methane are shown:

$$CH_4 + \frac{1}{2}O_2 \rightarrow CO + 2H_2$$
 $\Delta H_{298} = -36 \frac{kJ}{mol}$ (5)

$$CH_4+O_2 \rightarrow CO_2+2H_2$$
 $\Delta H_{298}=-319 \frac{kJ}{mol}$ (6)

The oxygen is usually supplied by air which will result in a dilution of the hydrogen product by nitrogen. Dilution of hydrogen means a lower fuel cell voltage and hence reduced efficiency. Reactions (5) and (6) may take place as low as 850°C for methane POx over Ni/Al₂O₃ heterogeneous selective catalysts. Without the benefit of catalysts, the operating temperature of the reforming process must be increased (1100-1500°C). Because this process yields a lower amount of hydrogen per mole of hydrocarbon input than SMR processes, as well as consuming a portion of its heating value to supply the heat for the endothermic reforming reaction, it results in lower system efficiencies (~1-5% below systems using SMR).

Despite this inefficiency, POx reformers are likely to see use in SOFCs for remote power applications where such inefficiencies are acceptable in light of other advantages, such as cost and weight [5].

POx reforming makes possible designs that are compact and lightweight, and respond rapidly to fluctuating power demands after a rapid start from cold conditions [4]. POx may produce harmful soot nano particles in their normal operating range therefore a soot trap is required. A representation of the POx process is depicted in Figure 4.

$$H_2+CO \rightarrow H_2O+C$$
 (7)

$$2CO \rightarrow CO_2 + C \tag{8}$$

$$CH_4 \rightarrow 2H_2 + C \tag{9}$$

Coke formation can be avoided lowering O/C ratio.

The main drawbacks are the comparatively low hydrogen yield and the tendency to produce soot at sub-stoichiometric air/fuel.

Autothermal reforming

Many developers of fuel cells and reformers have turned to autothermal reforming as a more effective alternative to the inefficient POx process and to SMR process characterized by a long start up phase.

Autothermal reforming is a process where both steam and oxidant are reacted with a fuel in a catalytic reactor to produce a hydrogen rich gas. As such, autothermal reforming can be regarded as a combination between pure steam reforming and pure partial oxidation. The idea of autothermal reforming is such that endothermic steam reaction and the exothermic oxidation are balanced and no heat is to be supplied or removed. This greatly simplifies the reactor design. Autothermal reforming can have the same dynamic response as partial oxidation, if only air is supplied to the reactor at start-up.

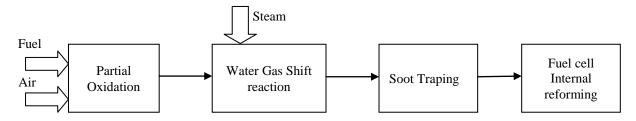


Figure 4 Partial oxidation fuel reforming process

It has been shown that under extremely short residence times, in the order of milliseconds, methane may be partially oxidized forming H_2 and CO as the main product. Thus, it is possible to avoid the slower steam, reforming reactions interfering to any significant extent.

One of the main advantages of this reforming process is that steam is not required. On the other hand high amount of coke formation is one of the drawbacks of the reactions. The reactions can be described in the following:

$$C_{x}H_{y}+zH_{2}O_{(1)}+\left(x-\frac{1}{2}z\right)O_{2} \leftrightarrow xCO_{2}+\left(z+\frac{1}{2}y\right)H_{2}$$

$$\Rightarrow CO, CO_{2}, H_{2}, H_{2}O \qquad (10)$$

The value for the steam to carbon ratio, here shown as z/x, should be chosen such that the

reaction is energy neutral, neither exothermic nor endothermic [15].

In figure 5, it is shown the combination of reactions that occur in autothermal reforming process, also water shift gas reaction is considered.

The maximum hydrogen production efficiency (η_{H_2}) occurs under pure steam reforming and decreases as the operation moves towards pure oxidation. The carbon monoxide production efficiency (η_{CO}) increases when moving from pure steam reforming towards pure oxidation and reaches a maximum under partial oxidation operation.

In figure 6 is represented the continuum of operating conditions for producing hydrogen rich fuel cell feeds form partial oxidation and steam reforming processes.

Comparison among external reforming processes

In table 2, a comparison among the reforming processes previously analyzed is shown. Of course, every process has pros and cons and none of them can be considered in absolute terms the best reforming process.

In fact, the best choice depends by different parameters; among this we can mention fuel cell type and CHP system size.

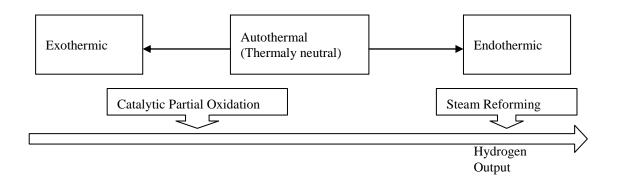


Figure 5 Hydrogen output as function of operating conditions

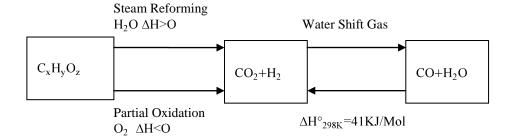


Figure 6 Flow diagram of different combination of reforming reactions

	Steam Reforming	Partial Oxidati on	Authotherm al Reforming
Type of	Endothermi	Exother	Neutral
process	c	mic	
System	Complex	Very	Simple
Complexity		simple	
System	Slow	Fast	Fast
Start Up			
and			
dynamic			
response			
Outlet	70-80%	35-45%	40-50%
Hydrogen			
Content			
(Dry Basis)			
Carbon	9% CO	19% CO	3% CO 15%
yield	15% CO ₂	1% CO ₂	CO_2
Pollutant	low	Soot,	low
emission		HCs	
Durability	High	Low	High
and			
reliability			
System	Careful	Low	Careful
control	thermal		control to
	managemen		balance
	t to provide		endothermic
	heat for		and
	reaction for		exothermic
	start-up and		processes
	dynamic		during the
	response	~	load change
System	Complex	Simple	Complex
configurati	pre-		pre-
on	reforming		reforming
	system due		system due
	to		to additional
	additional		heat
	heat		exchangers
	exchangers		

Table 2 Comparison among different external fuel reforming

Fuel Processing in SOFC

Solid oxide fuel cells contain solid electrolytes, which are frequently based on zirconia stabilised by yttria. On the cathode side strontium or calcium doped lanthanum manganese oxide (LaMnO₃) is most commonly used, while the anode side comprises of yttria stabilized zirconia frequently doped with nickel to achieve electrical

conductivity. To achieve sufficient mobility of the oxygen anions, high operating temperatures of between 800 and 1000°C are usually required [16]. However, the nickel catalyst is subject to coke formation when carbon monoxide is present in the reformate. Addition of steam is one possible way to reduce coke formation. Through the addition of steam, internal reforming of light hydrocarbons, such as methane, becomes feasible within the solid oxide fuel cell.

Internal reforming may either be performed at the catalyst positioned adjacent to the anode or at the anode itself. However, the efficiency of the fuel cell is reduced due to the dilution of anode feed by the steam. On the other hand, steam reforming consumes energy, which helps to cool the fuel cell. Various alternative anode materials are under investigation. Copper is relatively inert towards the carbon-formation reactions that occur on nickel, and stable operation has been observed with even large hydrocarbons over copper-based anodes [17].

The working fluid in an SOFC is usually a reacting mixture of gases composed of H_2 , H_2O , CO, CO_2 , and possible higher hydrocarbons in the anode stream, O_2 , N_2 , in the cathode stream. Chemical reactions take place in the gas channels (typically the anode) in the triple-phaseboundary (TPB), i.e. a reaction zone very close to the electrode-electrolyte interface [18].

If the cell operates on a hydrocarbon, rather than on hydrogen, the reforming reaction takes place in the anode gas channel:

$$C_n H_m O_p + (n-p) H_2 O = nCO + (n-p + \frac{m}{2}) H_2$$
 (11)

Furthermore, carbon monoxide reacts with water generate additional hydrogen and carbon dioxide through the exotermic shift reaction:

$$CO+H_2O \rightarrow CO_2+H_2$$
 $\Delta H_{298}=-41 \frac{kJ}{mol} (12)$

Both reactions can be assumed to reach equilibrium quickly because of the high operating temperature and the high water vapor content. In addition, nickel is present in the anode which acts as a catalyst for both reactions [19]

SYSTEMS INTEGRATION

As discussed earlier, fuel process occurs over different stages, each taking place in a separate reactor. In addition, some of them require air supply, some require steam supply, and all require some kind of temperature control.

The equipment for air supply, steam supply, and temperature control must be incorporated in the fuel processor subsystem. There are numerous ways the components and the flows between them can be arranged. The goal is to have a system with highest possible efficiency.

When carbon is present in the fuel, the Steam To Carbon Ratio (STCR) must be above 2 at 400°C for methane to avoid carbon deposition which may destroy the anode[21].

Reforming reactions is the most economical route to produce hydrogen for hydrogen production, mainly because they extract the hydrogen of both the hydrocarbon and the water. For methane:

$$\begin{array}{ccc} CH_{4} + H_{2}O \rightarrow CO + 3H_{2} & \Delta H_{298} = 206 \frac{kJ}{mol} \ (13) \\ Energy \ Cost = 68.7 kJ/mole \ H_{2} \\ CH_{4} + 2H_{2}O \rightarrow CO_{2} + 4H_{2} & \Delta H_{298} = 165 \frac{kJ}{mol} \ (14) \\ Energy \ Cost = 41.25 \ kJ/mole \ H_{2} \end{array}$$

Reaction (13) uses around 67% more energy per mole H2 produced than reaction (14). The second reaction is the most efficient for hydrogen production (4 moles H_2 per mole CH_4) and energy efficiency. STCR is used to incentive reaction (14) instead of (13).

For the highly endothermic steam reforming reactions, the process can be autothermic if there are other exothermic reactions balancing it. A good configuration of the reformer apparatus is also a way to achieve a good balance between endothermic and exothermic reaction.

Under a thermodynamic point of view, there are different techniques to achieve a balance between endothermic and exothermic reactions. A simple approach is a material/energy balances to find out their basic characteristics with special emphasis on Hydrogen production. This criterion can be applied both in fuel processing and fuel cell modeling.

Combining Oxidative reforming to Steam reforming we have the following reactions.

$$CH_4 + \frac{1}{2}O_2 \rightarrow CO + 2H_2$$
 $\Delta H^{\circ}_{298} = -36 \frac{kJ}{mol}$ (15)
 $CO + H_2O \rightarrow CO_2 + H_2$ $\Delta H^{\circ}_{298} = -41 \frac{kJ}{mol}$ (17)

The two reactions produce 3 moles of hydrogen per mole of CH4, and produce 77kJ/mole of reacted CH4.

The most efficient steam reforming reaction is:

$$CH_4+2H_2O \rightarrow CO_2+3H_2 \qquad \Delta H^{\circ}_{298}=165 \frac{kJ}{mol}$$
 (18)

For autothermal operation in a reforming process, through mole and energy balances, the maximum H_2 yield to be equal to ~3.15 mol H_2 /mol CH_4 (78.8% of the theoretical yield of 4 moles H_2 per mole CH_4).

Autothermic operation can be also operated coupling the complete oxidation or methane combustion with steam reforming. This process results more efficient than the oxidative reforming/steam reforming coupling (even the efficient one with shift conversion). Full methane oxidation reaction is:

$$CH_4+2O_2 \rightarrow CO_2+2H_2O$$
 $H^{\circ}_{298}=-802 \frac{kJ}{mol}$ (19)

This reaction is strongly endothermic and by coupling it with Steam Reforming reaction for autothermal operation, maximum H₂ yield is around 3.317 mol H₂/mol CH₄.

Internal Reforming

In design of fuel cell systems, the fuel cell electrical efficiency is the key parameter. In solid oxide fuel cell fuels may be converted directly on the anode resulting in improved overall efficiency.

The fuel cell thermodynamic efficiency is given by the ratio of the Gibbs function change to the Enthalpy change in the overall cell reaction. The Gibbs function change measures the electrical work and the enthalpy change is a measure of the heating value of the fuel. Assuming that all reactants and products are in their standard state follows that

$$\eta_{\text{ideal}} = \frac{\Delta G}{\Delta H} \tag{20}$$

The ideal voltage in the cell is calculated from Gibbs free energy, but this reversible voltage is reduced due to the actual activities of the reactants and products in the cell as expressed by the Nernst equation, and by the polarization on

the cathode and anode and the internal resistance of the electrolyte when current is drawn from the cell.

This case is especially attractive, since the heat produced by the electrochemical reactions in the stack can be absorbed by the steam reforming reaction.

The modeling of internally reforming natural gas fuelled SOFC systems requires an in-depth knowledge of the rate of methane steam reforming on nickel-zirconia anodes. A number of kinetic studies of the steam reforming of methane on nickel, nickel catalysts, and SOFC anodes are found in the literature and have been reviewed. Unfortunately there is little agreement between the rate equations reported by different workers. [17].

At this level only the main reactions occurring in the fuel cell will be considered. For these so called direct reforming fuel cells with internal steam reforming, the coupling of the catalytic steam reforming and the electrochemical reactions of hydrogen and oxygen at the electrodes takes place as follows:

$$CH_4+2HO_2=CO_2+4H_2 -Q_{SMR} \Delta H_{1023}=191\frac{kJ}{mol}$$
 (21)

$$4H_2 + 2O_2 = 4H_2O$$
 $+Q_{OX} + E \Delta H_{1023} = -991 \frac{kJ}{mol}$ (22)

Appling the Hess's law we obtain:

$$CH_4+2O_2=2H_2O+CO_2+Q_{OX}+E$$
 $\Delta H_{1023 \text{ tot}}=-800 \frac{kJ}{mol}$

(23)

where the heat of reaction for the steam reforming and the electrochemical reaction of hydrogen and oxygen, ΔH, are shown for 750°C and E is the electric energy.

For full conversion of the steam reforming reaction ΔH equals Q_{SMR} , and ΔH equals $Q_{OX}+E$ in the hydrogen oxidation reaction. Since usually the electrochemical reaction is not completed, a fuel utilization constant, $U_f,$ corresponding to extent of reaction shall be introduces. We should keep in mind that these values should be adjusted considering also the influence of the rate of reaction.

In order to maintain the temperature of the cell, the heat required for the reforming reaction must not exceed the electrochemically produced heat.

$$Q_{SMR} < Q_{OX}$$
 (24)

It is essential that the reforming reaction is coupled to the electrochemical reactions on the anode. If the reforming reaction took place outside the SOFC anode chamber, complete conversion of methane would not be possible. Therefore either an external reformer with high exit temperature or a recycle of non-converted methane is required.

$$E < \Delta H_{SMR} + U_f * \Delta H_{OX}$$
 (25)

$$\eta_{\text{max}} = \frac{\Delta E}{\Delta H} = \frac{\Delta H_{\text{SMR}} + U_{\text{f}} * \Delta H_{\text{OX}}}{\Delta H_{\text{tot}}}$$
(26)

Because higher fuel utilizations generate lower cell voltages, but they also reduce the system fuel and air flow requirements, and because the cell voltage cannot be higher than the lowest local potential in the cell, fuel utilization limits the efficiency, see [20]. Besides, if the degree of pre-reforming is enhanced, the power production increases, because of the higher H₂ content in the inlet anodic gas.

CONCLUSION

The reforming process both in the fuel processes stage and in the fuel cell was analyzed. In particular steam reforming, partial oxidation and autothermal reforming were identified as most suitable to mCHP application. Internal reforming is also a viable alternative since hydrocarbon can be used as a fuel in solid oxide fuel cell.

It is essential to note that if the reforming reaction took place outside the SOFC anode chamber, complete conversion of methane would not be possible. Therefore either an external reformer with high exit temperature or a recycle of non-converted methane is required.

Due to the high efficiency of the fuel processing system and the high H_2 output, steam reforming is the most suitable reforming process for mCHP operation at base load. Increasing the degree of pre reforming, the steam outlet flow from the reforming process will decrease whereas H_2 concentration will increase.

Partial oxidation is also suitable for SOFC mCHP application for its high controllability and fast activating reaction. However, the actual level of development of solid oxide fuel cell does not allow a high variability in the operation

conditions. In this perspective steam reforming is recommended.

Autothermal reforming conserves the benefits of controllability of POx and makes the process more efficient. However, since the SOFC systems are still steady state operation it would not be possible to fully take advantages of the autothermal reforming benefits.

It has also been shown that fuel utilization, U_f , is one of the most important operation parameter for fuel cell handling hydrocarbons as a fuel. In particular it affects electrical efficiency and thermal efficiency through a higher fuel concentration in the afterburner. Therefore, in mCHP systems electrical and thermal efficiency follows different trends. In particular an increase in electrical efficiency determines a reduction of heat for cogeneration. The electrical efficiency increases also with anodic recirculation, however due to the high temperatures involved in the process, anodic recirculation system is still under development.

Carbon formation may seriously damage the anode when carbon is present in the fuel. Increasing the steam to carbon ratio can facilitate the water gas shift reaction thereby increasing the consumption of carbon monoxide. A steam to carbon ratio higher than two should be used in order to avoid carbon deposition at the anode.

Steam reforming is an endothermic reaction. Thus, a strong internal reforming should be avoided since it leads to a reduction in temperature and consequently to thermal stresses in the stack.

On the other hand, by reducing of stack temperature, the internal reforming decreases the need of cooling air. These two effects should be kept in consideration when operating the mCHP system. The heat exchangers dimensions will decrease and consequently the cost of the system. Finally, due to a narrow range of operations in the fuel cell, the global efficiency follows the trend of thermal efficiency, as it is much more sensitive to variations of operation parameters.

REFERENCES

[1] Chan, S.H. and Wang, H.M. Effect of natural gas composition on autothermal fuel reforming products. 2000, Fuel Process. Technol., pp. 64, 221–239.

- [2] Costamagna, P., Cerutti, F., Di Felice, R., Agnew, G., Bozzolo, M., Collins, R., Cunnigham, R. and Tarnowski, O. Production and utilization of H2 in a reforming reactor coupled to an integrated planar solid oxide fuel cell (IP-SOFC): Simulation analysis. 2004, Chem. Eng. Trans., pp. 4,81-86.
- [3] Borup, R.L., Inbody, M.A., Tafoya, J.I., Guidry, D.R. and Jerry, W. New Orleans: s.n. *SOFC anode recycle effect on diesel reforming.*, 2004. in Proceedings of the AIChE Spring Meeting.
- [4] Wit, Jan de. Amsterdam: s.n.Implementation of micro chp in single-family houses., 2006. 23rd World Gas Conference.
- [5] R.J. Braun, S.A. Klein, D.T. Reindl. Varna, Bulgaria: s.n. Evaluation of system configurations for solid oxide fuel cell-based micro-combined heat and power generators in residential applications., 2006. 6th International Conference on Lead-Acid Batteries. pp. 1290-1305.
- [6] Francesco Calise, Massimo Dentice d'Accadia and Adolfo Palombo *A Detailed One Dimensional Finite-Volume Simulation Model of a Tubular SOFC and a Pre-Reformer.* 2007, Int. J. of Thermodynamics, pp. Vol. 10 (No. 3), pp. 87-96.
- [7] Clarke SH, Dicks AL, Pointon K, Smith TA, Swann A Catalytic aspects of the steam reforming of hydrocarbons in internal reforming fuel cells.. 1997, Catalysis Today, pp. 38:411–423.
- [8] Muradov, Mazim Z. Production of Hydrogen from Hydrocarbons. [book auth.] Ram B. Gupta. Hydrogen Fuel: Production, Trasport, and Storage. s.l.: Taylor Francis Group, 2009, pp. 33-101.
- [9] Pilar Lisbona, Alessandro Corradetti, Roberto Bove and Piero Lunghi. Analysis of a solid oxide fuel cell system for combined heat and power applications under nonnominal conditions. 2007, Electrochimica Acta, pp. 1920-1930.
- [10] Joensen, Finn and Rostrup-Nielsen, Jens R. Coversion of Hydrocarbons and alcohols for fuel cells. 2002, Journal of Power Sources, pp. 195-201.

- [11] Dicks., Andrew L. *Hydrogen generation* from natural gas for the fuel cell systems of tomorrow. 1996, Journal of Power Sources, pp. 61(1-2):113 124.
- [12] Song, X. and Guo, Z. 2006, Energy Conv. Manag., p. 47: 560.
- [13] A. Raimondi, D. Fino, N. Russo, G. Tortone, E. Morella, S. Specchia. Emission and trapping of particulates from TPOX and CPOX reformers. 30th Meeting on Combustion - Italian Section of the Combustion Institute.
- [14] M. Krumpelt, S. Ahmed, and R. Kumar. Nagoya, Japan: s.n. *Partial oxidation fuel reforming for automotive power system.*, 1999. 3rd International Fuel Cell Conference.
- [15] Ryan O'Hayre, Suk-Won Cha, Whitney Colella, Fritz B. Prinz. *Fuel Cell Fundamentals*. New York: John Wiley & Sons, Inc., 2006.
- [16] Park, S., Gorte, R.J. and Vohs, J.M. *Application of heterogeneous catalysis in the direct oxidation of hydrocarbons in a solid-oxide fuel cell.* 2000, Appl. Catal., pp. 200, 55–61.
- [17] Park, S. D., Vohs, J. M. & Gorte, R. J. *Direct oxidation of hydrocarbons in a solid-oxide fuel cell.* 2000, Nature, pp. 404, 265–267.
- [18] Ubertini, R. Bove S. *Modeling Solid Oxide Fuel Cells*. s.l.: Springer, 2008.
- [19] Larminie, J. and Dicks, A. Fuel Cell System Explained. Chichester: John Wiley & Sons Inc., 2004.
- [20] EG&G Technical Services, Inc. Fuel cell handbook 7th edition. Morgantown, West Virginia: U.S. Department of Energy Office of Fossil Energy, National Energy Technology Laboratory, 2004.
- [21] Gunther Kolb, Fuel Processing for fuel cell, Wiley VCH

Biomass



NUMERICAL MODEL AND INFRARED ANALYSIS OF A HYDROGEN ENRICHED GAS FLAME

Tudor Prisecaru*!, Mihai Teodorescu *, Malina Prisecaru*, Cristian Petcu**, George Bleaja**, Elena Popa *, Cristina Ciobanu*, Radu Chiriac*, Petre Dumitru*, Lucian Mihaescu*

* Politehnica University of Bucharest, Romania

ABSTRACT:

Industrial applications of the flames produced by hydrogen enriched gas (HRG) are spreading more and more, raising a new series of technical problems at the same time. This paper presents an interesting behavior of a HRG flame, used for metal cutting and brazing. HRG is an industrial gas with a cvasistoichiometric composition, obtained from an electrolytic patented installation. The industrial patent belongs to some of the authors of this paper. Industrial processes involve premixed flames which are usually very short, but here a very long and luminous flame with a low temperature has been produced; it has been visualized by a Cedip Silver infrared camera. A numerical model prepared by Fluent CFD simulation code and based on Warnatz kinetic reactions mechanism has been prepared to analyze and to explain this unexpected behavior of the HRG flame. Due to this CFD model two different flames have been identified: the first one with premixed characteristics and the secondary flame with a diffusive aspect. This conclusion has been then validated by infrared analysis when different regions of flame have been focused with care. This paper presents the two flame structures also.

Key words: hydrogen, HRG, thermal cutting

1. INTRODUCTION

A new type of electrolyzer [1] has been developed by Hydrogen Technology Applications, Inc., from Clearwater, Florida to produce hydrogen from water. According to the physical patented process, hydrogen is generated together with oxygen in a stoichiometric proportion called "HRG gas". An important particularity of this process consists of the sliding characteristics of the whole installation. The main features of this new system are the following: gas flow rate - 1500 Nm³/h; gas pressure - 0.2÷0.6 MPa; gas temperature - 20÷45°C.

One important field of using this gas phases mixture (HRG) can be found in cutting/brazing the metallic products and other hard materials, such as sintered products. This paper presents some theoretical and practical analysis developed in order to explore the gas properties and the applying

conditions for the HRG gas. Also, the work! describes the adequate procedures adopted by the authors and the main results obtained on each applied process, concerning the ecological performances mainly.

2. HRG GAS BEHAVIOR UNDER PRESSURE

The oxygen/hydrogen combination can create in extreme case malfunctions or explosions in the apparatuses or the gas cylinders. The explosion limits for hydrogen/oxygen or hydrogen/air mixtures have been already investigated and consistent literature data have been presented in [2, 3].

Although the HRG gas obtained with the new patented generator seems to be a stoichiometric

^{**} Rokura Industrial Applications, Bucharest, Romania

¹ Corresponding author: Phone: +40752064123, Fax: +403181019, e-mail: tudor prisecaru@hotmail.com

hydrogen/oxygen mixture, the possible presence in this gas of impurities, like special species of hydrogen/oxygen combination in quantities up to 5÷7%, has been theoretically demonstrated [4]. Under these conditions, some experiments seems to be necessary to evaluate the behavior of the HRG gas, at least at pressures up to 0.6 MPa and

temperatures until 50°C which can be developed in the present cutting and brazing investigations. Static compressing tests at ambient temperature have been executed up to 5.4 MPa (fig.1) without HRG gas tendency to condensate or to wet the metallic walls of the chamber.

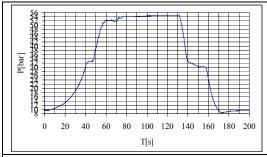


Fig.1. HRG gas slow compression cycle between 1.0 MPa and 5.4 MPa

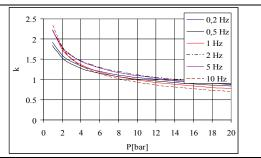


Fig.2. Polytropic factor at dynamic HRG gas compression cycles with frequencies between 0.2 Hz and 10 Hz

Similar stability of the HRG gas has been observed also during dynamic compression/decompression tests at frequencies between 0.2÷10 Hz and maximal pressure until 1.8 MPa [5].

A certain influence of the cycle frequency appears in the pressure/volume variation. Those anomalies were characterized by polytropic factors with values between 0.8÷1.5 (fig.2).

3. AUTO-IGNITION LIMITS AND BURNING VELOCITY OF THE HRG GAS

Auto-ignition tests have been executed by continuous heating a closed vessel containing HRG gas at different initial pressures between 0.2÷0.5 MPa [6]. Some gas instability processes, expressed by minor anomalies in gas pressure variation, were observed at temperatures higher than 350°C (fig.3). The auto-ignition moment appears at temperatures between 440°C and 470°C and is well defined by explosive pressure rise up to 18 MPa (fig.4).

HRG gas burning process has been studied by means a closed combustion camera provided with electrical discharge high voltage system, pressure sensors and optical access for flame propagation analysis by Schlieren technique [7]. A typical pressure-time history it is to be observed in fig.5. The necessary time for formation and development

of the flame kernel was 0.115 ms and laminar burning velocity was estimated at 10.46 m/s.

4. OPEN FLAME CHARACTERISTICS FOR THE HRG GAS MIXTURE

The flame of HRG gas generated by a cutting torch has been studied by a high speed infrared camera. One typical temperature profile it is to be observed in (fig.6).

A short and condensed flame at very high temperature has been expected, but surprising a low temperature values have been registered. Due to this fact, the physical - kinetic mechanism involved in this process has been evaluated by means of a numerical combustion model developed in Fluent code [8, 9]. For the numerical simulation a cylindrical domain of 800 mm height and a radius of 20 mm (greater than ten times the nozzle diameter) have been adopted. The Fluent model used an unstructured quad-tetrahedral mesh containing a number of 234348 cells. The nozzle has been considered as a pressure inlet surface characterized by 6 Pa gauge pressure. The Magnusen [8,9] procedure (based upon the Warnatz kinetic mechanism) has been adopted to simulate the chemical process instead of the chemical equilibrium analysis of the combustion.

The last method usually gives a higher level of temperatures and when using it, Fluent code is not capable to complete further the NOx formation by its own module. The results of this analysis showed very clear that at atmospheric pressure the flame of HRG gas has a special behavior due to a

huge oxidation rate of hydrogen being in stoichiometric ratio, and more, already premixed with oxygen. Post-processed flame aspect and the calculated temperature distribution (in Kelvin scale) are presented in fig.7.

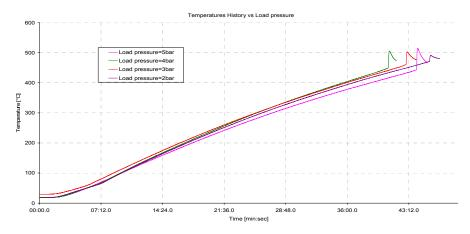


Fig. 3. Pressure-temperature history at HRG gas heated in a bomb with initial 0.5 MPa pressure

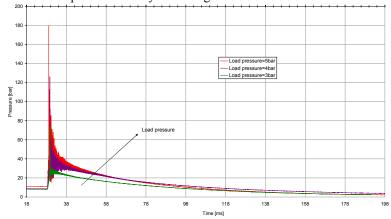


Fig.4. Auto-ignition moment of the HRG gas combustion heated in a bomb

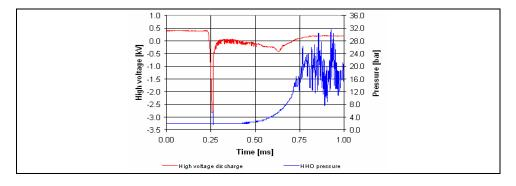


Fig. 5. Electrical discharge high voltage and pressure-time history at HRG gas burning

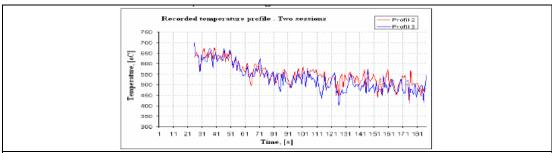


Fig.6. Recorded temperature values in two successive experiments in order to reveal the repeatability of the test. (decreasing values due to the HRG outlet decreasing pressure)

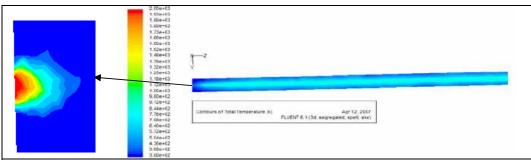


Fig.7. Global contour of the HRG flame post-processed of a Fluent numerical simulation. The domain has been cropped and sloped upwards. Detailed temperature at the nozzle is presented into the detail.

Details of the incipient flame showed that in the initial zone, the temperature values are about 3036°C, but this zone is a very small one, comparable with the nozzle torch diameter. Focusing the nozzle's outlet with a double wave infrared thermometer OS3753, temperature values in the range of 2860 – 2950 °C have been obtained. To do this measurement an InGaAs detecting element has been used working with 0.9/1.55 µm wavelength and an emissivity compensation of 0.065. Next to the primary zone, the process continues in a special space for water vapors dissociation, having 10÷15 times more the torch nozzle diameter. It follows a secondary combustion zone, with bigger length, were temperature values are about 645°C. This zone can be described by Warnatz mechanism [10] (Table1) and practically constitutes the visible part of flame; the temperature of this zone has been explained by its volume and the influence of oxygen that diffuses from environmental air with low caloric supply.

To develop this numerical model, some important assumptions have been adopted:

- The HRG gas has been perfectly mixed (hydrogen and oxygen) at the cutter tool outlet, due to the relative long path (l/d) from the gas generator to the cutter, lap over the multitude of bents, even within the cutter;
- The HRG composition has been a stoichiometric one, based upon the electrolyzing process;
- Kinetic mechanism of the HRG burning process has been adopted after Table 1 [10].

Within the Fluent case a standard k- ε model of turbulence has been adopted [11], considering the turbulence kinetic energy, k, and its rate of

dissipation, ε , from the following transport equations:

$$\frac{\partial}{\partial t}(\rho k) + \frac{\partial}{\partial x_{i}}(\rho k u_{i}) = \frac{\partial}{\partial x_{j}} \left[\left(\mu + \frac{\mu_{t}}{\sigma_{k}} \right) \frac{\partial k}{\partial x_{j}} \right] + G_{k} + G_{b} - \rho \varepsilon - Y_{M} + S_{k}$$
and
$$\frac{\partial}{\partial t}(\rho \varepsilon) + \frac{\partial}{\partial x_{i}}(\rho \varepsilon u_{i}) = \frac{\partial}{\partial x_{i}} \left[\left(\mu + \frac{\mu_{t}}{\sigma_{\varepsilon}} \right) \frac{\partial \varepsilon}{\partial x_{i}} \right] + C_{1\varepsilon} \frac{\varepsilon}{k} (G_{k} + C_{3\varepsilon}G_{b}) - C_{2\varepsilon} \rho \frac{\varepsilon^{2}}{k} + S_{\varepsilon}$$

In these equations, G_k represents the generation of turbulence kinetic energy due to the mean velocity gradients, G_b is the generation of turbulence kinetic energy due to buoyancy, Y_M represents the contribution of the fluctuating dilatation in compressible turbulence to the overall dissipation rate and $C_{1\epsilon}$, $C_{2\epsilon}$, and $C_{3\epsilon}$ are constants; σ_k and σ_ϵ are the turbulent Prandtl numbers for k and ε , respectively. S_k and S_ϵ are user-defined

source terms. The turbulent (or eddy) viscosity, μ_t , is computed by combining k and ε as follows:

$$\mu_t = \rho C_\mu \frac{k^2}{\varepsilon}$$
, where C_μ is a constant.

The model constants $C_{1\varepsilon}$: $C_{2\varepsilon}$: $C\mu$; σ_k ; and σ_{ε} have the following default values [11]:

$$C_{1\varepsilon} = 1.44$$
, $C_{2\varepsilon} = 1.92$ $C_{\mu} = 0.09$
 $\sigma_k = 1.0$ $\sigma_{\varepsilon} = 1.3$

Table 1. Presentation of the Warnatz model, for hydrogen oxidation

Nr.	R1	R2	ITC1	P1	P2	ITC2	A	ь	E
							cm, mol, s		kJ/mol
React	tions H2	-O ₂							
1	02	+H		=OH	+0	- 3	2.000E+14	0.00	70.3
2	H ₂	+0		=OH	+H		5.060E+04	2.67	26.3
3	H ₂	+ОН		=H ₂ O	+H		1.000E+08	1.60	13.8
4	ОН	+ОН		=H ₂ O	+0		1.500E+09	1.14	0.42
Reco	mbining F	Reactions			161			8 1	ž.
5	H	+H	+M*	$=H_2$	135	+M*	1.800E+18	-1.00	0.00
6	0	+0	+M*	$=O_2$		+M*	2.900E+17	-1.00	0.00
7	H	+OH	+M*	$=H_2O$		+M*	2.200E+20	2.00	0.00
Reac	tions H(\dot{D}_2			100				ž.
8	H	+02	+M*	$=HO_2$	100	+M*	2.300E+18	-0.80	0.0
9	HO_2	+H		=OH	+OH		1.500E+11	0.00	4.2
10	HO_2	+H		$=H_2$	+02		2.500E+13	0.00	2.9
11	HO_2	+H		=H ₂ O	+0		3.000E+13	0.00	7.2
12	HO_2	+0		=OH	+02		1.800E+13	0.00	-1.7
13	HO ₂	+ОН		=H ₂ O	+02	8	6.000E+13	0.00	0.0
Reac	tions H2	O2			(6)		2	30	20
14	HO ₂	+HO ₂		=H ₂ O ₂	+02		2.500E+11	0.00	-5.2
15	ОН	+ОН	+M*	=H ₂ O ₂	23	+M*	3.250E+22	2.00	0.0
16	H ₂ O ₂	+H		=H ₂	+HO ₂		1.700E+12	0.00	15.7
17	H ₂ O ₂	+H		=H ₂ O	+OH		1.000E+13	0.00	15.0
18	H ₂ O ₂	+0		=OH	+HO ₂	-	2.803E+13	0.00	26.8
19	H ₂ O ₂	+ОН		=H ₂ O	+HO ₂	-	5.400E+12	0.00	4.2

5. CUTTING TESTS WITH HRG GAS FLAME

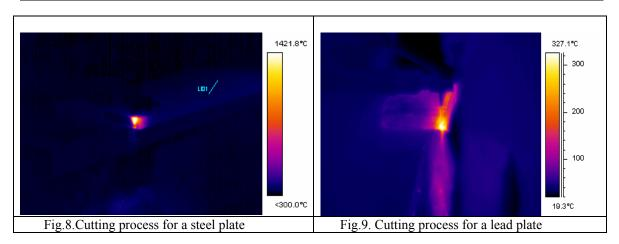
The presented research helped us to develop some incision or adhesion advanced technologies based on HRG ignition and combustion phenomenology. The first has been upgraded the experimental system from gas generator and under pressure vessel till cutting/brazing torch, in view to assure good health and safety testing conditions. After this, somewhat in opposite with theoretical estimations, we observed that HRG flame had the power to melt the steel and other metals until to realize a melt pool in products with considerable

thickness. This is very important for the steel products at witch, in conditions of oxygen blazing it is possible to assure consistent exothermic reactions needed in real economic and ecological cutting processes [12].

Cutting tests were executed on steel and lead heavy plates. For steel plate cutting a RHONA RK 20 torch has been utilized, with a LS-1B nozzle with a central bore for oxygen and multiple peripheral slots for HRG gas. In case of lead plates, the tests were executed with a VIKTOR torch having a nozzle with a unique central bore. Experienced cutting tests executed in a semiautomatic regime for torch moving are presented in Table 2 [13].

Table 2. Semiautomatic	thermally	cutting	process	paramet	ters

Material	Nozzle	HRC	i gas	Oxygen	Cutting pa	rameters
Thickness	diameter	Pressure	Flow rate	Pressure	Nozzle/materia	Cutting speed
	mm	MPa	1/min	MPa	l distance, mm	mm/min
S335J2 EN10025	1×0,9	0.6	40	0.5	8.5	330
20 mm	10×0,5					
13 CrMo 4.5	1×0,9	0.6	40	0.5	8.5	330
EN10028	10×0.5					
18 mm						
Pb 99.97	1×0,9	0.5	22	_	9.0	220
45 mm						



The temperature distributions observed in cutting process showed a consistent energy density in the process core (fig. 8, 9).

The macroscopic aspect of the cut surfaces obtained with HRG/oxygen flame, respectively, with HRG flame is presented in fig.10 and 11.

The quality of the thermally cut surfaces analyzed according to EN ISO 9013 are presented in Table 3.

The integrity of the thermally cut surfaces has been performed by penetrating liquid method according to EN 571-1/EN 1289. Results of the control

proved that the surfaces are free from flaws, cracks or other local imperfections.

6. BRAZING TESTS WITH HRG GAS FLAME

The moderate temperature of the HRG gas flame offers excellent conditions to execute brazed joints. The possibility to assure a controlled local heating in similar and dissimilar material joints has been tested [10].

The most important condition to reach the uniform joint heating was the correct adaptation of the flame shape and the gas burning intensity on joint type and dimensions. To obtain a large and soft HRG gas flame, the RHONA RK 20 torch has been selected, with multiple peripheral gas slots. Also, the HRG gas pressure has been reduced comparatively to values considered in cutting process. A large material qualities and joint types have been tested [11]. In Table 4 some examples are presented.

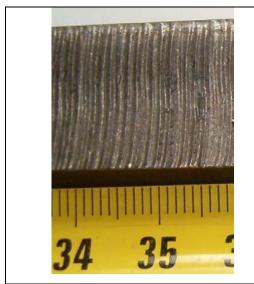


Fig.10. Cut surface of the S 335 J2 steel plate with 20 mm thickness



Fig.11. Cut surface of the lead plate with 45 mm thickness

Some interesting aspects can be mentioned here concerning the fig. 10 and 11: stability of the cutting process due to the flame uniformity and the almost non-chamfered edge the cut surface which was much closed to the first stage of the HRG flame in the spite of the magnitude of the plate thickness. In the fig.10 it is about high yield

point steel for construction where the pure HRG flame has not been sufficient and a supplementary oxygen jet has been added. The differences in the general aspect of the surface are obvious in comparison with the fig.11 where only HRG has been used.

Table 3. The quality of the thermally cut surfaces obtained with HRG gas flame

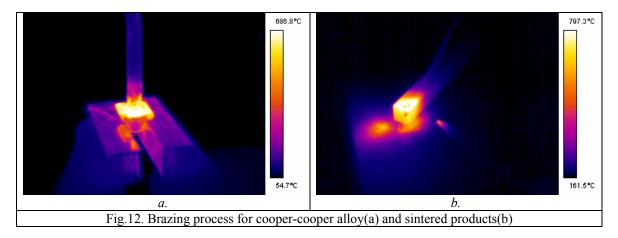
<u>Material</u>	Cutting				Quality	
Thickness	flame	u^{l} , mm	$R_{y5}^{2)}$, µm	n^{3} , mm	$r^{4)}$, mm	class
<u>S335J2</u> 20 mm	Oxygen/ HRG gas	0,4÷0,7	37÷49	0,8÷0,9	< 1,0	II

13 CrMo 4.5 18 mm	Oxygen/ HRG gas	0,4÷0,6	85÷112	0,6÷0,9	< 1,0	II
Pb 99.97 45 mm	HRG gas	0,8÷1,1	5,3÷5,6	6,6÷7,2	< 1,0	II

Obs.: 1) perpendicularity deviation; 2) surface roughness; 3) cut delay; 4) edge radius

Table 4. Examples of brazed joints with HRG gas flame

Table 4. Examples of brazed joints with TIKO gas frame							
Brazed	Base m	aterials	Joint	Filler	Fluxes	Brazing	
product	1	2	type	metal		temp, ⁰ C	
Pipe to flange	Cu-OF	CZn40Sn	Lap	AG 104	FH 10	680	
joint	EN 13347	EN 13347	joint	EN 1044	EN 1045		
Pipe to flange	Cu-OF	CuSn6	Lap	AG 104	FH 10	680	
joint	EN 13347	EN 13347	joint	EN 1044	EN 1045		
Pipe to	EN AW-Al99	EN AW-Al99	Lap	AL 104	AL1	585	
Pipe joint	EN573/EN754	EN573/EN75	joint	EN 1044	DIN		
		4			8511		
Strip to	EN AW-Al99	EN AW-Al99	Lap	AL 104	AL1	585	
Strip joint	EN573/EN755	EN573/EN75	joint	EN 1044	DIN		
		5			8511		
Carbide tip	A12/K10	C45 W	Lap	AgCu400	FH 10	779	
turning tool	ISO 513	EN 10083-1	joint	STAS8903	EN 1045		



The temperature profiles in joining moment are illustrated in fig.12. It is to observe that basic metals are not exposed on overheating and heat affected zones are minimal in dimensions. Here (in the fig.12) the temperature values indicated in the Table 4 cannot be surpassed due to the ablation phenomenon during the brazing process even it is about cooper or sintered metallic carburized plates. Due to the small emissivity of the primary HRG flame the heating process is much focused on the brazing area. Nondestructive macroscopic and microscopic tests acc. to EN 12797 and penetrating

liquid tests acc. to EN 571-1/EN 1289 has been successfully executed on all types of joints.

7. ECOLOGICAL EVALUATION OF THE CUTTING AND BRAZING PROCESSES EXECUTED WITH HRG GAS FLAME

Health and safety are important factors in selecting a technological solution in cutting or brazing processes. HRG gas with hydrogen as combustible gas, mixed with oxygen in stoichiometric proportions, offers the best conditions for a controlled flame heating process with ecological attributes.

Gases (NO_x) and airborne particles measurements executed in the operator's breathing zone during the cutting process with HRG flame in steel and lead products showed low emissions values, situated in the limits of the EN recommendations. Practical, no CO_x and SO_x emissions were observed.

8. CONCLUSIONS

- ➤ The flame of HRG gas mixture at atmospheric pressure has a special behavior due to a huge oxidation rate of hydrogen being in stoichiometric ratio and more, already premixed with oxygen. Due to this fact the numerical model of combustion pointed out temperature values around 3036°C within the primary zone of the flame. Validation measurements gave a range temperature values between the ranges of 2860 2950 °C.
- ➤ Next to the primary zone, comparable as length with injection nozzle diameter, the process continues in a special space for water vapors dissociation having 10 15 times nozzle diameter. It follows a secondary combustion zone, with bigger length, were temperature values are about 645 °C. In this zone, which practical constitutes the visible part of flame, the temperature is explained by its volume and the influence of oxygen that diffuses from environmental air with low caloric supply.
- ➤ The research presented will help to develop more ecological brazing and cutting technologies based on HRG mixture ignition and combustion phenomenology.

REFERENCES

- [1] Klein, D., *Patent No. US 6689259 B1*, Feb. 10, 2004, United States Patent Office.
- [2] Schroder, V., Emonis, B., Janssen, H., Scultze, H., Explosion Limits of Hydrogen/Oxigen

- Mixtures at Initial Pressures up to 200 bar, in Chem. Eng. Technology, 2004, 27, No.8, pag.847-851
- [3] Safety Standard for Hydrogen and Hydrogen Systems, NASA NSS 1740.16, 2005, Washington, SUA.
- [4] Santilli, R.M. *A new Gaseous and Combustible form of Water*, in Int. Journal of Hydrogen Energy, Elsevier, 2006, No.31, pag.1113-1128,.
- [5] Vasiliu, N., Calinoiu, C., Teodorescu, M., Dica, C., *Comportarea la compresiune a amestecului gazos HHO*, in Buletinul Universității Politehnica București, Seria Mecanică, 2008, Vol.IV.
- [6] Dica,C., Petcu,C., Bleaja,G., Chiriac,R., Vasiliu,N., *Hydrogen rich gas a possible challange for the fuels future*, in H-2_FUEL_CELLS_MILLENNIUM_CONVERGE NCE, 2007, pag. 39-48, Bucharest, Romania.
- [7] Chiriac,R., Apostolescu, N., Dica,C. Effects of Mixing Diesel Fuel HHO Gas on Performance and Emissions of a Diesel Engine, in Acta Technica Napocensis, 2007, No.50, vol.IV, pag. 1-10.
- [8] Prisecaru, T., Dica, C., Teodorescu, M., Prisecaru, M., Mihaescu, L., Berbece, V., Experimental Validation of an HHO Gas Cutting Flame CFD Model, in EHTP Proceedings, Cracovia, 2008.
- [9] Evaluarea comportarii la taiere a gazului ecologic Klein in cazul unor aplicatii din oteluri nealiate cu grosime intre 3,5 si 14 mm, Raport ISIM nr. 149, 2004.
- [10] J. Warnatz, Survey of the C/H/O reactions, Combustion Chemistry II, Springer Verlag, New York, 1991.
- [11] B. E. Launder and D. B. Spalding. *Lectures in Mathematical Models of Turbulence*. Academic Press, London, England, 1972.
- [12] Elaborare tehnologie ecologica de lipire componente metalice si nemetalice cu materiale de adios performante, ISIM Report nr. 164, 2004.
- [13] Tăierea termică ecologică a metalelor grele și a oțelurilor de înaltă rezistență, CEEX "X2C38" Project Report, 2008.

EFFECTS OF OXYGEN IN BIOGASIFICATION; EVALUATION OF ADM1-Ox MODEL AGAINST EXPERIMENTAL DATA

Deshai Botheju*, Bernt Lie and Rune Bakke Telemark University College Faculty of Technology Porsgrunn, Norway

ABSTRACT

The previously presented free oxygen included anaerobic digestion model, ADM 1-Ox, is evaluated against experimental data obtained using a laboratory batch test array comprising miniature anaerobic bio-reactors of 100 ml total volume each, operated under different initial air headspaces giving rise to the different oxygen loading conditions. The reactors were initially fed with a glucose solution and incubated at 35 °C for 563 hours duration. Under the oxygen load conditions of 22, 44 and 88 mg/L, the ADM1-Ox model simulations predicted the experimental methane potentials quite adequately. Both the experimental data and the simulations suggest a linear reduction of methane potential with respect to the increase in oxygen load within this range.

Keywords: ADM1, oxygen, modeling, simulation

NOMENCLATURE

Often used symbols

C – oxygen concentration (mg/L)

 C^* - saturation concentration (mg/L)

 $k_L a$ – oxygen transfer coefficient (d⁻¹)

M – oxygen mass (mg)

T – absolute temperature (K)

t – time (days)

V – reactor liquid volume (L)

INTRODUCTION

The previously presented ADM1-Ox model [1] which is based on the standard Anaerobic Digestion Model no. 1 [2] developed by the International Water Association (IWA) attempted to describe the impacts of oxygenation in anaerobic biogasification. This paper aims to compare the simulation predictions from the ADM1-Ox model against experimental data obtained in a laboratory batch test array where the variation of methane potential due to different air headspaces is observed.

*Corresponding Author: Tel. +47 45075165; Fax: +47

35575001; Email: Deshai.Botheju@hit.no

METHODS

Experimental Methodology

An experimental test array was established to test the methane potential under different initial oxygen loading conditions. BD Plastipak 100 ml polypropylene syringes (supplied by VWR International), transformed into miniature biowere used to carry experimentation for 563 hours time duration (23.5 days) incubated at 35 °C. After filling the syringes with the inoculum together with the substrate up to the 50 ml volume mark, hypodermic needles were attached. The needle was then inserted into a rubber stopper to close and isolate the system. As gas is produced the piston is displaced outwards and the produced biogas volume is read on the After 563 hours, the observed gas generation had stopped. The reactors were initially provided with different air head space displacements of 0, 4, 8, 16 and 32 ml to introduce different oxygen loading conditions. Triplicates of reactors were used for each test condition and the measurement and analysis results were averaged for final evaluation. The test reactors were fed with 1 ml of 0.5 M glucose solution at the start up of the experiment (equivalent to an initial substrate concentration of 1.92 kg COD/m³). Control reactors without feeding were also included in order to quantify the gas generation potential of the inoculum alone.

The inoculum was taken from an active municipal wastewater anaerobic digester (Knarrdalstrand municipal wastewater treatment facility, Porsgrunn, Norway). This digester is operated at 35 °C and fed with chemically precipitated primary sludge from municipal wastewater. Also the digester is preceded by a micro-aerobic contactor with a short hydraulic retention time. Before used in the experiment, inoculum was kept stored at room temperature condition for 30 days in order to deplete the remaining degradable substrate from the wastewater. This ensures minimum gas generation due to remaining substrate in the inoculum (Fig. 1(a)), making it easier to distinguish the most relevant experimental results and also simulate the process. Prior to being used in the batch test array, the inoculum was filtered through a 0.5 mm sieve to remove the larger particulate material. While filling the miniature reactors, the inoculum vessel was constantly mixed and de-aerated by nitrogen purging. The dissolved oxygen reading was kept below 0.35 mg/L.

Analytical methods

Measurements and analyses were conducted to determine gas generation, gas composition, soluble and total COD (chemical oxygen demand), pH, VFA (volatile fatty acids), NH₄⁺, TSS/VSS (total/volatile suspended solids) and TS/VS (total/volatile solids). The total gas generation is measured daily (or twice a day at the beginning) by taking readings volumetrically labeled piston displacement. Gas composition analysis is carried out at three different occasions (140.4 hrs, 299.5 hrs. and 563.2 hrs. – at the end of the exp.) during the course of the experiment using a Gas Chromatograph (Hewlett-Packard -P series, micro GC) with helium as the carrier gas. Compositions of methane, carbon dioxide, nitrogen and oxygen were determined accordingly. Then the amount of methane gas generated was calculated based on the total gas volume. Liquid phase analyses were carried out according to the established standard test methods [3].

Oxygen loads

Table 1 summarizes the different oxygen loading conditions tested for this study. Supplied oxygen mass in moles indicated in column 3 is obtained using the ideal gas law relation (n = pv/RT) at 298 K temperature (filling temperature of the head spaces) and 1 atm pressure. The rightmost column indicates the corresponding oxygen load provided in the 50 ml reactor mixed liquor. These oxygen load values (mg O_2 / L reactor content) are consistently used here for indicating the reactor oxygen loading conditions while elaborating the experimental and simulation results.

Table 1: Oxygen loading conditions tested in experiments and in simulations

Initial air	Initial	Initial	Initial	Equivalent
headspace	O_2	O_2	O_2	O_2 load
vol. (mL)	vol.	mass	mass	(mg/L)
	(mL)	(mol)	(mg)	
		$\times 10^5$		
0	0	0	0	0
4	0.8	3.4	1.10	22
8	1.7	6.9	2.2	44
16	3.4	13.7	4.4	88
32	6.7	27.5	8.8	176

Oxygen transfer coefficients (k_La)

The following analysis is carried out to estimate the equivalent oxygen transfer coefficients ($k_L a$) corresponding to the oxygen loads indicated in Table 1.

The rate of aeration can be expressed as,

$$\frac{dC}{dt} = k_L a (C^* - C) \tag{1}$$

Here, C is the oxygen concentration and C^* represents the saturation oxygen concentration in the system. Assuming that the free oxygen concentration in the liquid phase is near zero due to rapid oxygen consumption by facultative biomass [1], then equation 1 can be re-arranged to give the oxygen mass transfer rate into the reactor,

$$\frac{dM}{dt} = V k_{L} a C^{*}$$
 (2)

Here *V* is the liquid volume of the reactor and *M* is the oxygen mass. It follows that,

$$\Rightarrow \int dM = V k_{L} a C^{*} \int dt + k_{o}$$
 (3)

$$\Rightarrow M = V k_{L} a C^{*} t + k_{o}$$
 (4)

Neglecting the initial oxygen content in the liquid phase, k_0 =0, hence,

$$k_L a = \frac{M}{VC^* t} \tag{5}$$

The M values are given in the 4th column of Table 1, and V = 0.05 L (reactor liquid volume). For the approximation of "uniform aeration" of reactor liquor due to initial headspace, t may be taken as 23.5 days (experiment duration). It can be reasonably assumed that all the oxygen supplied through the headspaces is depleted during this time period.

Saturation oxygen concentration C^* is calculated according to the empirical formula by Weiss [4]. For zero salinity solutions,

$$\ln(C^*) = A_1 + A_2(100/T) + A_3 \ln(T/100) + A_4(T/100)$$
(6)

Here, T is the absolute temperature and the C* is given in mL/L. The empirical constants have the values, A_1 =-173.4292; A_2 =249.6339; A_3 =143.3483; A_4 =-21.8492.

From equation 6, $C^* = 6.95$ mg/L at 308 K (operating temperature).

The equivalent $k_L a$ values (d⁻¹) corresponding to the different air head spaces are calculated according to equation 5 and are given in Table 2. These $k_L a$ values were used in the ADM1-Ox model simulations to represent the different oxygen loading conditions tested in the experiment.

 Table 2: Estimated k_La values

 Equivalent O_2 Equivalent k_La

 load
 (d^1)

 (mg/L) 0

 22
 0.14

 44
 0.27

 88
 0.54

 176
 1.08

ADM1-Ox simulations

Development of the oxygen included anaerobic digestion model ADM1-Ox is described elsewhere [1]. The ADM1-Ox is a modified version of the standard anaerobic digestion model, ADM 1. The key features of ADM 1-Ox includes; three new aerobic oxidation processes, oxygen inhibition of obligatory anaerobic organisms, and modified first order hydrolysis kinetics to include acidogenic biomass concentration. The amended model has 25 components and 22 biochemical processes.

The computer aided simulation tool AQUASIM 2.1 [5] is used to simulate the developed ADM1-Ox model under the operating conditions of the experimental trials described above. According to the preliminary simulations carried out before [1], it is observed that the low oxygen loading conditions such as oxygenated influent streams cannot cause significant detrimental effects in anaerobic digesters, primarily due to the rapid ability oxygen consuming of facultative acidogenic biomass. In order to include the prolonged aeration effect due to the headspaces provided in the experimental trials analyzed here, a continuous aeration process is introduced in the model as an additional dynamic process. The aeration rate is described according to equation 1. Each experimental oxygen loading condition is then simulated using corresponding k_La value (Table 2). The applied glucose feed concentration (1.92 kg COD/m³) is specified as the initial condition of the monosaccharide concentration in the simulation program. Initial conditions for the other degradable substrates were given diminutive

values (putting them as zeros hinder the initialization of the simulator).

In order to simulate the cumulative gas generation in the Aquasim built ADM1-Ox model, the reactor headspace is defined as a variable volume complete mixed reactor. The model was calibrated by multiplying the initial biomass concentrations used in the original ADM1 simulation program [6] by 0.1 fold. This calibration approximately predicted the experimental methane generation at zero oxygen loading condition. No attempt is made to optimize the simulated initial biomass concentrations. Also, no kinetic parameter was modified or optimized from their values given in the original ADM1 [2; 6].

RESULTS AND DISCUSSION

Total cumulative gas generation

Total cumulative biogas generation measured and simulated under the operating conditions investigated, are shown in Fig. 1(a) and Fig. 1(b), respectively. The experimental curves exhibit three distinguishable phases having markedly different gas generation rates (Fig. 1 (a)): an initial high generation of short duration, an extended period of an approximately constant production rate, and eventually a final period of very low gas production. Simulation curves display a similar behavior (Fig. 1 (b)) with the general order and the magnitudes of gas generation. Simulations, though somewhat overpredicts the total gas generation, still substantiate the experimentally shown exhaustion of gas generation within 20 days. The final total biogas production is on average approximately the same with and without oxygen loads. This can be expected, as the possible reduction in methane yield due to oxygen is compensated by increased CO₂ production. The experimental curves are not as congregated as the simulated ones.

The oxygen appears to speed up the initial biogas production rate, observed both in the experiments and in the simulations (Figure 2). It is further observed that the simulated initial production rates are much larger than the measured (Figure 2). This difference between simulations and measurements in initial production can be due to

the less than ideal mixing condition in the experimental reactors, while the simulations assume ideal mixing conditions. Besides that, the early dynamic behavior of the model simulated curves, in general, are highly sensitive to the initial conditions used. Apart from the monosaccharide concentration, the initial values of the most of the other state variables are somewhat subjectively chosen, though founded on the values given in original ADM1 simulator.

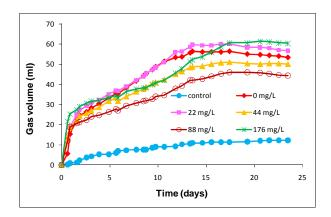


Fig. 1 (a): Experimental

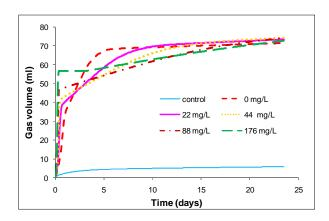


Fig. 1(b): Simulated

Figure 1: Experimental (a) and simulated (b) total cumulative gas generation for the control and for different oxygen loading conditions

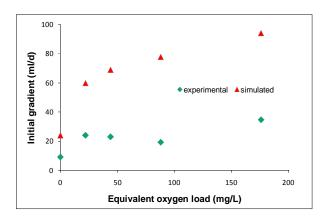


Figure 2: Initial gas generation rates under different oxygen loading conditions

Methane generation potential

The methane fractions of the produced biogas under different oxygen loading conditions, simulated and measured, are presented in Figure 3. The measured methane generations for different oxygen loading conditions are quite closely predicted by the model simulations except for the case of 176 mg/L oxygen load (Fig. 3(a) – 3(f)). For the oxygen loads of 22, 44 and 88 mg/L, the simulated data are, most of the time, within the error margins of the experimental data (Fig. 3(c)-3(e)). The large differences observed for the oxygen load of 176 mg/L case are not fully understood. The experimental data in this case shows a significantly higher methane generation compared to the simulation predictions (Fig. 3(f)).

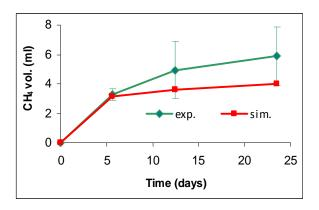


Fig. 3(a): Unfed control

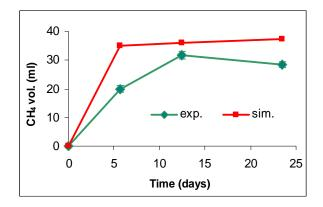


Fig. 3(b): 0 mg/L

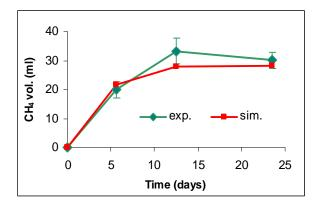


Fig. 3(c): 22 mg/L

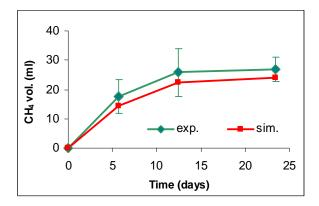


Fig. 3(d): 44 mg/L

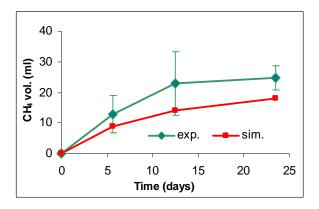


Fig. 3(e): 88 mg/L

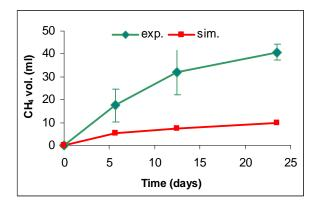


Fig. 3(f): 176 mg/L

Figure 3(a-f): Cumulative methane generation measured in the control and in different air headspace experiments (average±SD) compared against simulation predictions

According to the experimental data (Fig. 4(a)), 22 mg/L oxygen load only induce a minor (not statistically significant) impact on the methane generation potential, while 44 and 88 mg/L loads induced increasingly negative impacts on the methane potential. 176 mg/L load had no significant impact initially but eventually ended up being the case with highest ultimate methane generation. Simulations predict distinguishable and increasingly negative impacts on the methane generation potential at increasing oxygen loads (Fig. 4(b)). This suggests that some yet un-known effects of oxygen on methane generation may need to be included in the model to better simulate these cases.

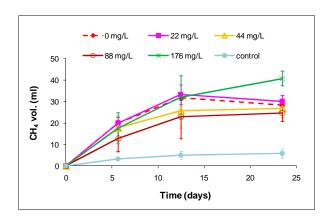


Fig. 4(a): Experimental

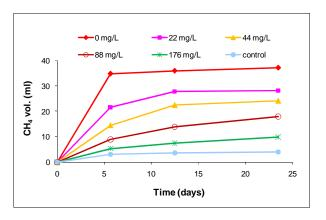


Fig. 4(b): Simulated

Figure 4(a-b): Relative placement of methane generation curves under different oxygen loading conditions according to the experimental data (average±SD) and the simulation predictions

Figure 5 displays experimental and model predicted ultimate methane generation against different oxygen loads. Though the model somewhat over-predicted the methane potential at zero oxygen load, it quite closely predicted the methane potential under the oxygen loads of 22, 44 and 88 mg/L cases. As observed earlier, the observed methane production for the 176 mg/L oxygen load is significantly higher than the simulation value.

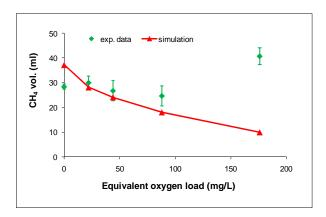


Figure 5: Experimentally determined (average±SD) and simulation predicted ultimate methane generation vs. oxygen load

Linear reduction of methane potential

experimental and simulated methane generation data at 22, 44 and 88 mg/L oxygen loads demonstrate a linear decrease of methane potential with increasing oxygen load (Figure 6). The coefficients of determination (R²) values for the experimental data (0.908) and simulated data (0.995) indicate above 90% confidence in linearity. The case of 176 mg/L oxygen load is removed from this analysis due to the significant deviations pointed out earlier. Also, the data for zero oxygen condition do not fall within this linear region. Apparently, there is a certain nonlinear behavior when the condition changes from fully anaerobic to oxygen affected methane generation. Both the experimental and simulated data suggest the existence of such a non-linearity at this transition region. If not for this initial nonthen interestingly enough, linearity, experimental and simulation lines have a similar intercept on the y- axis suggesting the exact same value of methane potential at zero oxygen load (31.1 mL). This value is 16.4 % below the simulation prediction for the zero oxygen condition and 9.5 % above the experimentally determined value for zero oxygen load. The higher slope of the simulation line (0.15)compared to the experimental line (0.076) causes the simulation data to increasingly over predict the negative impacts of increasing oxygen loads.

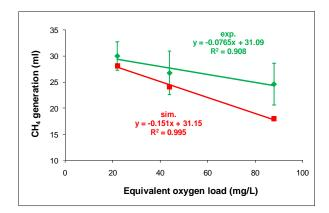


Figure 6: Analysis of linearity for experimental (average \pm SD) and simulated data in the 22 – 88 mg/L oxygen load range

Rationale

The reduction of methane potential observed in experiments and in simulations can be attributed to the substrate oxidation by facultative acidogenic organisms and the partial inhibition of the activity of strictly anaerobic biomass. Since a soluble substrate is used (glucose), an increase in hydrolysis due to aerobic activity of facultative organisms cannot be expected. Previous studies indicated that even with the increased hydrolysis (~50 % increase) due to micro-aeration, the ultimate methane yield has been reduced (by ~50 %) [7].

The experimental data point obtained for 176 mg/L oxygen load, suggesting an increased methane yield, is yet to be explained. Some other physical or biochemical phenomenon that has not been captured in the model might have taken place in the experiment. This may warrant further studies on extended range of oxygen loads and alternative loading scenarios.

The use of simulation and experimental data discussed here are restricted to the specific operating conditions and oxygen load levels tested. However the general ability of the ADM1-Ox model to predict oxygen impacts in anaerobic digestion is demonstrated based on this experimental study.

CONCLUSIONS

The anaerobic digestion model where effects of free oxygen are included is evaluated based on laboratory batch test data. Under the experimental conditions tested (batch condition of 23.5 days, COD/m³ 1.92 initial glucose concentration, 35 °C operating temperature, 22 – 88 mg/L equivalent oxygen loading range), the previously developed ADM 1-Ox model can be used to predict the oxygen impact on anaerobic digestion with satisfactory results. Experimental and simulation data suggest a linear decrease of methane potential at increasing oxygen loads under these operating conditions. The simulation, however, increasingly over-predicts this negative impact on methane potential at increasing oxygen loads.

ACKNOWLEDGEMENTS

This study is funded by the grants from the Research Council of Norway. Authors acknowledge the valuable support extended by Damien Batstone and Jorge Rodríguez by providing original ADM1 simulators. A special thank goes to Laboratory Engineer at Telemark University College, Ms. Hildegunn H. Haugen for her technical support and encouragement.

REFERENCES

- [1] Botheju D, Lie B, Bakke R. *Modeling free oxygen effects in anaerobic digestion*. Proceedings of the MATHMOD 2009 6th Vienna International Conference on Mathematical Modeling, Vienna, 2009.
- [2] Batstone DJ, Keller J, Angelidaki I, Kalyuzhnyi S, Pavlostathis SG, Rozzi A, Sanders W, Siegrist H, Vavilin V. *Anaerobic digestion Model No.1*. London: IWA publishing, 2002.
- [3] APHA, AWWA and WEF. Standard methods for the examination of water and wastewater. 19th edition, Washington DC, USA, 1995.

- [4] Weiss RF. The solubility of nitrogen, oxygen and argon in water and seawater. Deep-Sea Research 1970; 17: 721-735.
- [5] Reichert P. AQUASIM 2.0-User manual; Computer program for the identification and simulation of Aquatic Systems. Swiss Federal Institute for Environmental Science and Technology (EAWAG), 1998.
- [6] Batstone DJ. Anaerobic Digestion Model no.1; AQUASIM 2.1 simulator program. Personal communication. March, 2009.
- [7] Johansen JE, Bakke R. *Enhancing hydrolysis with micro-aeration*. Water science and Technology 2006;53(8): 43-50.

ZERO-DIMENSIONAL MODEL OF A DIMETHYL ETHER (DME) PLANT BASED ON GASIFICATION OF TORREFIED BIOMASS

Lasse Røngaard Clausen* and Brian Elmegaard
Technical University of Denmark, Department of Mechanical Engineering
2800 Lyngby, Denmark

Niels Houbak DONG Energy 2450 Copenhagen, Denmark

Robert J. Braun Colorado School of Mines, Engineering Division Golden, Colorado USA 80401

ABSTRACT

A model of a DME fuel production plant was designed and analyzed in Aspen Plus. The plant produces DME by catalytic conversion of a syngas generated by gasification of torrefied woody biomass. Torrefication is a mild pyrolysis process that takes place at 200-300°C. Torrefied biomass has properties similar to coal, which enables the use of commercially available coal gasification processing equipment. The DME plant model is integrated with a steam cycle that utilizes waste heat from the plant and covers the on-site electricity consumption. The plant model predicts a fuel production efficiency of 67 % (LHV) from torrefied biomass to DME and 70 % (LHV) if the exported electricity is included. When accounting for raw, untreated biomass, the efficiency for DME production is reduced to about 60 %.

Keywords: biorefinery, biofuel, dimethyl ether, DME, torrefication, gasification, syngas, CO₂ capture.

INTRODUCTION

One of the ways of reducing the CO₂ emissions from the transportation sector is by increasing the use of biofuels in vehicular applications. Dimethyl ether (DME) is a diesel-like fuel that can be produced from biomass in processes very similar to methanol production processes. Combustion of DME produces lower emissions of NO_x than combustion of diesel, with no particulate matter or SO_x in the exhaust [1], however it also requires storage pressures in excess of 5 bars to maintain a liquid state. The DME production plant investigated in this paper is of large-scale (> 2,000 tPD) because of the better economics compared to small-scale production of DME [2] [3]. Larger-scale plants, however, have higher feedstock transportation costs which increase the attractiveness of torrefied wood pellets as a feedstock instead of conventional wood pellets. Torrefication of biomass also makes it possible to use commercially available coal gasification processing equipment¹. This paper documents the design of a DME plant using Aspen Plus modeling tools with a focus on process integration and waste heat recovery. Thermodynamic performance of the resulting plant configuration is presented and discussed.

Torrefication of biomass

Torrefaction of biomass is a mild pyrolysis process where biomass is heated to 200-300°C.

^{*}Corresponding author. Phone: +45 45 25 41 65, email: lacl@mek.dtu.dk

¹ See the Gasification World Database [4] for a list of commercial plants.

The process alters the properties of biomass in a number of ways, including increased energy grindability/pulverization, density, improved better pelletization behavior, and resistance to biodegradation and spontaneous heating. This conversion process enables torrefied biomass to achieve properties very similar to coal, and therefore allows the altered biomass feedstock to be handled and processed using conventional coal preparation methods. Additionally, torrefied biomass can be stored in environments and outdoor the electricity consumption for milling and pelletization is significantly lower than that of wood [5] [6].

DESIGN OF THE DME PLANT

A process flow sheet of the DME plant design is shown in Figure 1. Plant design aspects related to feedstock preparation, gasification, syngas cleanup, and DME synthesis and distillation are described next and are followed by a brief discussion of electricity co-production and Aspen Plus modeling techniques.

Feedstock

The feedstock employed in this design analysis is torrefied wood pellets. The composition is (Weight-%): 50.0 % C, 40.8 % O, 5.7 % H, 1.5 % H₂O, 0.29 % N, 0.01 % S, 1.7 % Ash [7].

Pretreatment & feeding

The pretreatment and feeding of torrefied biomass is assumed to be accomplished with existing coal-based commercial technology [5] [6]. The torrefied biomass is milled to powder with an electricity consumption similar to milling of bituminous coal [5]; a power input equivalent to $0.29~\%^2$ of the thermal energy input (LHV) of torrefied biomass [8] is utilized. The resulting biomass powder is pressurized with lock hoppers using CO_2 from the carbon capture process downstream. It is envisioned that pneumatic feeders - also driven by captured CO_2 gases - are used for feeding the torrefied biomass to the gasifier.

_

Gasification

A commercial, dry-fed, slagging entrained flow coal gasifier is used for gasifying the torrefied wood powder. The gasifier is oxygen blown, pressurized to 40 bar and steam moderated [7]. The oxygen supply is provided by a cryogenic air separation plant which delivers oxygen with a purity of 99.6 % while consuming electricity at a rate of 1.0 MWe/(kg O₂/s) [9]⁴. A gas quench using 200°C recycled product gas downstream of the cyclone lowers the temperature of the syngas from 1300°C to 900°C⁵. The composition of the syngas is calculated by assuming chemical equilibrium at 1300°C. The steam used for gasification is generated by waste heat boilers in the plant.

Gas cooling and water gas shift

The syngas is further cooled to approximately 200°C by generating superheated steam for primarily the integrated steam cycle. A sulfur tolerant⁶ water gas shift (WGS) reactor adjusts the H₂/CO-ratio to 1 in order to optimize DME synthesis⁷ [11]. The gas is then cooled to 25°C prior to acid-gas cleaning step.

Gas cleaning incl. CCS

Gas cleaning of biomass syngas for DME synthesis includes an acid-gas cleaning step, a filter and/or cyclone for particle removal and guard beds⁸ placed just before the synthesis reactor [12] [8]. The acid-gas cleaning step is done with Selexol⁹ and removes sulfur

² In [5] the power consumption is reported to be around 1 % of the thermal input of torrefied biomass (LHV). It is assumed that the size of the mill used in the experiments is the reason for the higher value (heavy-duty cutting mill, 1.5 kWe).

³ Chosen instead of 95 % purity in order to minimize inert buildup in the synthesis recycle loop. 95 % purity would only give a 1.6 % reduction in electricity consumption and a 4 % reduction in capital cost [9].

 $^{^{4}}$ 0.36 kWe / (m_{n}^{3} O₂/h) used in reference.

⁵ The electricity consumption for recycling gas is not accounted for since pressure drops through components are not included.

⁶ E.g. Haldor Topsoe produces such catalysts [10]

⁷ Given by the chemical reaction equation: $3H_2+3CO \leftrightarrow CH_3OCH_3+CO_2$

⁸ ZnO and active carbon filters

⁹ Another physical solvent such as Rectisol could also be used. Rectisol can clean the gas to lower sulfur concentrations (0.1 ppm [13] compared to 1 ppm for Selexol [14]) which is preferred because of the very low sulfur tolerance of the synthesis catalysts [12]. Cleaning with Rectisol is more expensive than Selexol. This increased expense might however be offset by the less frequent need to regenerate the guard beds [12].

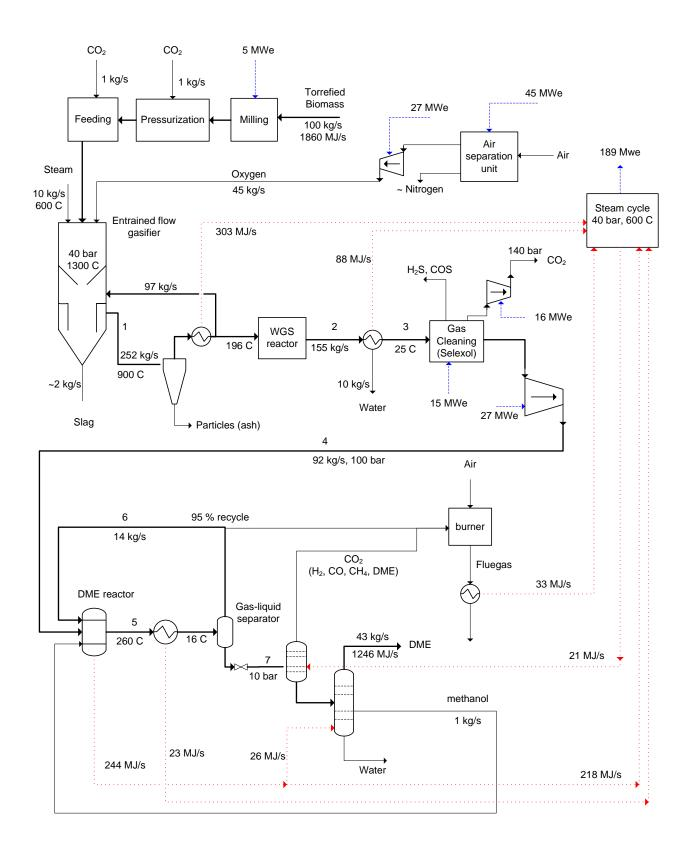


Figure 1. Flow sheet of the modeled DME plant. Some important parameter values are shown.

components (H_2S and COS) and CO_2 in either two separate streams or one combined stream. The latter is an option because the sulfur content in biomass syngas is very low. If CO-removal is not used, the sulfur components are oxidized and vented [8]. The captured CO_2 is compressed to 140 bar for underground storage. The CO_2 content in the syngas after the wash is 2 % and the H_2S + COS content is about 1 ppm [14].

The only energy input for the Selexol process is electricity to run a pump that pressurizes the physical solvent.

Synthesis of DME

The syngas is compressed to 100 bar before entering the synthesis reactor. The reactor is modeled as a liquid-phase reactor operating at 260°C ¹⁰ where the product stream is assumed to be in chemical equilibrium [15]. The reactor operating temperature is maintained at 260°C by a water-jacketed cooler that generates saturated steam at 40 bar. The product gas is then cooled to about 16°C and a gas-liquid separator separates the liquid DME from the unconverted syngas. 95 % ¹¹ of the unconverted syngas is recycled to the synthesis reactor ⁵ and the remaining 5 % is sent to an off-gas burner that augments the steam generation for electricity co-production in the Rankine power cycle.

Distillation

The liquid stream from the gas-liquid separator is distilled by fractional distillation in two columns. The first column is a 10-stage topping column operating at 10 bar. The purge gas from the topping column is mixed with the separator offgas and sent to the same burner previously mentioned. The second column separates the water and methanol from the DME. The methanol is recycled to the synthesis reactor and the water is either sent to waste water treatment or injected into the gasifier as steam. The column

A low temperature moves the chemical equilibrium towards DME but slows down the chemical reactions. A too high temperature can cause catalyst deactivation. "In practice, a reactor operating temperature of 250-280°C balances kinetic, equilibrium, and catalyst activity

considerations" [16].

is modeled with 15 stages at 10 bar. In this configuration, the DME liquid product achieves a purity of 99.99 mol %.

Power production

A simple steam cycle power plant is thermally integrated into the biorefinery configuration. It produces enough electric power from waste heat recovery to meet both the on-site electricity demand as well as excess for export to the utility grid. Approximately 58% of the heat addition to the steam power cycle comes from cooling of the syngas after gasification, 36% from the synthesis reactor and about 6% from on-site gas burner/boiler. The temperature of the steam entering the steam turbines is 600°C at 40 bar.

Modeling tool

The modeling was done with Aspen Plus, which is a component-based commercial modeling tool with integrated thermodynamic, chemical and physical properties for a large number of gases and liquids. Aspen Plus excels at modeling of chemical process plants, but its library of unit operations also enables detailed modeling and simulation of power plants. The handling of solids is however not optimal¹². The ability to estimate physical properties of gas-liquid mixtures was particularly helpful in the plant design and simulation effort, especially in unit operations containing distillation columns and liquid fuel reactor product streams that need to account for the solubility of CO₂.

Aspen Plus has two built-in solvers – a sequential solver and a simultaneous solver (EO). The sequential solver was used primarily for generating start guesses for the simultaneous solver. The simultaneous EO solver was employed due to improved convergence and robustness of the process flowsheet, especially where recycle streams play a prominent role in the plant configuration.

RESULTS

The results from the simulation of the DME plant are presented in the following. In the flow sheet in figure 1 some of the important thermodynamic

¹¹ The recycle percentage is maximized in order to increase DME production while not generating a too high recycle mass flow. For comparison the Haldor Topsoe fixed-bed system design uses a recycle percentage of 93-98 % [17].

¹² E.g. solids are not supported when using the simultaneous solver (EO)

parameters are shown. In Table 1 the gas / liquid composition at specific nodes in the flow sheet is shown.

Node no.	1*	2*	3*	4*	5*	6*	7 ¤
H2	29	38	41	49	8	30	2
CO	46	38	41	49	9	28	4
CO_2	9	17	18	2	45	32	48
H ₂ O	16	8	0	0	1	0	1
N_2	0	0	0	0	1	4	0
Ar	0	0	0	0	0	1	0
Methanol	-	-	-	-	1	0	2
DME	-	-	-	-	35	6	43

Table 1: Gas / liquid composition in mol % at specific nodes in figure 1. *Gas *Liquid

Table 2 shows important energy efficiencies for the DME plant. It can be seen that 67 % of the input chemical energy in the torrefied wood is converted to chemical energy stored in the output DME. If the torrefication process – that occurs outside the plant – is accounted for, the efficiency drop by 7 %-points.

Input	Torrefied	Untreated
	biomass	Biomass*
Output		
DME	67 %	60 %
DME + electricity	70 %	63 %

Table 2: Energy conversion efficiencies for the DME plant (LHV basis). *Assuming an energy efficiency of torrefication of 90 %.

The electricity produced in the plant by the integrated steam cycle is primarily used on site, but 54 MW is exported to the grid (Table 3).

	Power consumption
Compressors	54 MW
ASU	45 MW
Compression of CO ₂	16 MW
Gas cleaning*	15 MW
Milling of biomass	5 MW
Steam cycle	-189 MW
Net power	-54 MW

Table 3: Power consumption/production in the DME plant. *Incl. CO₂ capture.

The 30 % of the chemical energy in the torrefied biomass input that is not converted to DME or

electricity is lost in the form of waste heat in the condenser of the integrated steam plant. In order to improve the total energy efficiency of the plant, the steam plant could produce district heating instead. This would however result in a small reduction in power production.

It is mainly in the gasifier and the DME reactor that chemical energy is converted to thermal energy (Table 4). There is some potential for improvement in the gasification efficiency, e.g. by lowering the output temperature of the gasifier¹³. The DME reactor efficiency is however difficult to improve since the chemical reaction that produces DME generates heat.

	Chemical	Efficiency ⁿ
	energy loss*	
Gasifier	312 MW	83 %
WGS reactor	26 MW	98 %
DME reactor	231 MW	86 %
Purge gas	6 MW	-
Topping gas	30 MW	-

Table 4: Chemical energy conversion in selected components together with 2 waste streams containing chemical energy (LHV based).

*Chemical energy converted to thermal energy "Chemical energy output divided by chemical energy input

The steam cycle converts 665 MW of waste heat to 189 MW of electricity - corresponding to an electrical efficiency of 28.4 %. The low efficiency performance is largely due to the low steam pressure generated – limited by the DME reactor operating temperature (boiling point of the water). When comparing the efficiency of the steam cycle configured within the biorefinery with the efficiency of a more conventional steam power plant, it should be noted that the heat used in this plant is (on average) of lower quality than the heat used in a conventional steam plant 14.

There are more constraints in this plant than in a steam power plant – in this plant the heat is available in certain temperature intervals. E.g. heat from cooling of syngas from gasification: 900-200°C, heat from reactor cooling: 260°C.

¹³ Could be by doing a chemical quench instead of a gas quench or changing from entrained flow gasification to fluid bed gasification.

Carbon analysis

Since the feedstock for DME production is biomass, it is not considered a problem - with regards to the greenhouse effect - to vent CO_2 from the plant. But since CO_2 is captured in order to condition the syngas, the pure CO_2 stream might as well be stored, as vented. This gives a positive greenhouse effect and might be economic in the future, if CO_2 capture from the atmosphere is rewarded in the same way as emission of CO_2 is taxed. If not, some of the biomass could be substituted by coal – matching the amount of CO_2 captured.

In the designed plant the feedstock contains 50 kg/s of carbon and the DME product (43 kg/s) contains 22 kg/s of carbon. This means that 45 % of the input carbon is stored in the product DME, this will eventually be combusted and the CO_2 will most likely be vented to the atmosphere.

The rest of the carbon (28 kg/s) is either captured in the syngas conditioning (14 kg/s) or vented as flue gas from the burner (14 kg/s). The vented CO_2 from the burner could be captured as well – the most economical way probably being oxyfuel capture since most of the fuel is CO_2 and an air separation unit is already available on-site.

CONCLUSION

A zero-dimensional model of a DME plant was designed and analyzed using Aspen Plus. A simple steam cycle was integrated with the DME plant in order to use the waste heat from the plant to co-produce electricity. The produced electricity meets the on-site electricity consumption (135 MW) with a surplus (54 MW) being exported to the grid.

The DME plant model simulation resulted in an energy efficiency of 67 % from torrefied biomass to DME (LHV) and 70 % if the exported electricity is included. However if the torrefaction process is included the energy efficiencies drops to 60 % and 63% respectively.

REFERENCES

[1] International DME association (IDA). *DME*- Clean Fuel for Transportation.
http://www.aboutdme.org/index.asp?bid=2
19

- [2] Boerrigter H. *Economy of Biomass-to-Liquids (BTL) plants*, report: ECN-C--06-019. Petten, The Netherlands: ECN, 2006. http://www.ecn.nl/publications/
- [3] Larson ED, Williams RH, Jin H. Fuels and electricity from biomass with CO2 capture and storage. In: proceedings of the 8th International Conference on Greenhouse Gas Control Technologies, Trondheim, Norway, June 2006.
- [4] The National Energy Technology Laboratory (NETL) (a part of the U.S. Department of Energy), Gasification World Database 2007, http://www.netl.doe.gov/technologies/coalpower/gasification/database/database.html
- [5] Kiel JHA, Verhoeff F, Gerhauser H, Meuleman B. BO2-technology for biomass upgrading into solid fuel pilot -scale testing and market implementation. In: Proceedings for the 16th European Biomass Conference & Exhibition, Valencia, Spain, 2008, p. 48-53. http://www.ecn.nl/publications/
- [6] Bergman PCA, Boersma AR, Kiel JHA, Prins MJ, Ptasinski KJ, Janssen FJJG. Torrefaction for entrained-flow gasification of biomass, report: ECN-C--05-067. Petten, The Netherlands: ECN, 2005. http://www.ecn.nl/publications/
- [7] van der Drift A, Boerrigter H, Coda B, Cieplik MK, Hemmes K. Entrained flow gasification of biomass; Ash behaviour, feeding issues, system analyses, report: ECN-C--04-039. Petten, The Netherlands: ECN, 2004. http://www.ecn.nl/publications/
- [8] Kreutz TG, Larson ED, Liu G, Williams RH. Fischer-Tropsch Fuels from Coal and Biomass, report. Princeton, New Jersey: Princeton Environmental Institute, Princeton University, 2008.

 http://www.princeton.edu/pei/energy/public ations

- [9] Andersson K, Maksinen P. *Process* evaluation of CO2 free combustion in an O2/CO2 power plant, report no. T2002-258. Göteborg, Sweden: Chalmers University of Technology, 2002.
- [10] Haldor topsoe. Sulphur tolerant shift conversion.

 http://www.topsoe.com/Business_areas/Gas
 ification-based/Processes/Sour_shift.aspx
- [11] Larson ED, Jin H, Celik FE. Large-scale gasification-based coproduction of fuels and electricity from switchgrass. Biofuels, Biorprod. Bioref. 2009;3:174–194.
- [12] van der Drift A, Boerrigter H. *Synthesis gas* from biomass, report: ECN-C--06-001. Petten, The Netherlands: ECN, 2006. http://www.ecn.nl/publications/
- [13] Linde Engineering. Rectisol wash.

 Homepage accessed January 28 2009.

 http://www.linde-engineering.com/process-plants/hydrogen-syngas-plants/gas-processing/rectisol-was-h.php
- [14] Sharp CR, Kubek DJ, Kuper DE, Clark ME, DiDio M. Recent Selexol operating experience with gasification, including CO2 capture. In: Proceedings for the 5th European Gasification Conference, Noordwijk, the Netherlands, 2002.
- [15] Gogate MR, Vijayaraghavan P. A single-stage, liquid-phase dimethyl ether synthesis process from syngas: thermodynamic analysis of the LPDME process system. Fuel Science and Technology International 1992;10(3):281-311.
- [16] Larson ED, Tingjin R. Synthetic fuel production by indirect coal liquefaction. Energy for Sustainable Development 2003;7(4):79-102.
- [17] Voss B, Joensen F, Hansen JB. *Preparation* of fuel grade dimethyl ether, US Pat. 5908963. June 1, 1999.

SELF-ORGANIZING MAPS FOR ANALYSIS OF PROCESS EMISSIONS IN FLUIDIZED BED ENERGY PLANT

Mika Liukkonen*, Mikko Heikkinen and Yrjö Hiltunen University of Kuopio Department of Environmental Science 70211 Kuopio Finland

> Eero Hälikkä and Teri Hiltunen Foster Wheeler Power Group 78201 Varkaus Finland

ABSTRACT

In this study, a self-organizing map (SOM) -based analysis methodology was used to the emission analysis of a circulating fluidized bed process. The aims were to find dependencies between process variables and the concentrations of gaseous emission components, and to model their formation in the process. Data processing included two stages. First, the process was modeled by using a self-organizing map to create the general process model, and the model was clustered to create subsets representing the different states of the process. These process states may include for example start-ups, shutdowns, and idle times in addition to the normal process flow. Second, emission models were formed on the basis of both the general process model and the high boiler load area of the process. This methodology revealed dependencies that could otherwise be difficult to observe. In conclusion, the methodology used showed potential in the emission analysis of fluidized beds.

Keywords: Self-organizing map, Fluidized bed, Emission modeling, Neural networks

INTRODUCTION

The world-wide efforts to reduce harmful process emissions, such as nitrogen oxides (NO_x) , sulfur dioxide (SO_2) and carbon monoxide (CO), are affecting increasingly the production of energy. In the meantime the requirements for the efficiency of combustion processes are increasing. However, efficient combustion of fuels with lower emissions is increasingly difficult in power plants. The pressure to lift the price of electricity is causing an additional challenge because the producers are forced to search for cheaper fuels of lower quality, such as waste, recycled fuels or poor-quality coal.

Fortunately, the data gathered from the process may involve essential information on the

performance of the process and on different phenomena influencing the formation of emissions and the energy efficiency of combustion. This information can be extracted by using suitable data mining methods. If used and interpreted in an appropriate way this information can be valuable in the analysis and optimization of the process. Therefore it is reasonable to develop such data analysis methods that can respond to the new challenges in the production of energy.

The self-organizing map (SOM) [1] was originally developed by Kohonen in the early 1980s. Thereafter the use of the self-organizing map algorithm for different purposes has produced a diversified range of applications. The SOM has

*Corresponding author: Phone: +358 40 351 0644 Fax: +358 17 163 191 E-mail: mika.liukkonen@uku.fi been used in many different practical applications, including exploratory data analysis, pattern recognition, speech analysis, industrial and medical diagnostics, robotics and instrumentation, and even control [1]. In addition, Kasslin *et al* [2] and Alhoniemi *et al* [3] have introduced SOM-based applications to process monitoring and modeling in many industrial cases.

Furthermore, several of our recent studies [4–7] have shown the power of SOM in the modeling of the fluidized bed combustion. These contributions present a relatively large variety of applications related to process modeling, involving for instance modeling and identification of process states, emission modeling, variable selection and even optimization. In this paper we expand the methodology presented in [7] for the analysis of NO_x to the modeling of other gaseous emissions in a CFB power plant.

PROCESS AND DATA

Fluidized bed combustion is a widely used technology for producing energy. The process is designed principally for the combustion of solid fuels such as coal. A conventional circulating fluidized bed boiler, or a *CFB*, comprises a combustion chamber, a separator and a return leg to circulate the bed particles. The bed material is composed of sand, fuel ash and some sulfur capturing material, for example limestone. The mixture of bed material is fluidized by the primary combustion air brought in from the bottom of the chamber.

In CFBs the bed particles are in consistent movement with the flue gases because of high fluidizing velocities. The particles advance through the combustion chamber into a separator, where the larger particles are extracted and diverted back to the chamber. In the meantime the finer particles are separated from the cycle. Characteristic combustion temperatures in CFB boilers are between 850 and 900 °C. The advantages of CFBs include multi-fuel combustion, low NO_x emissions relatively low temperatures, desulfurization during combustion, which means that no additional cleaning systems are needed for sulfur emissions.

The original process data were averaged to the resolution of five minutes. After averaging, the

data matrix used in the modeling included 10 000 rows with 38 variables in columns.

METHODOLOGY

Self-organizing maps were used in the analysis of the process emissions. The data processing stages and their outcome are presented in Figure 1. The area of high boiler load was selected to the analysis because it best presents the typical situation in the combustion process.

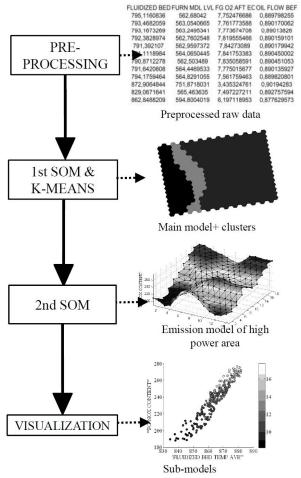


Figure 1: Schematic presentation of the methodology used in the analysis.

Self-organizing maps (SOM)

The common use of SOM is based on mapping *n*-dimensional input vectors to nodes, or *neurons*, for example in a two-dimensional lattice, or *map*. The map of neurons describes variations in the statistics of the input data, and the topological organization of the original data is maintained on the SOM by connecting the input vectors sharing common

features to the same or neighboring neurons. The size of the map can be varied according to the application; the bigger the map, the more details appear. In contrast, a smaller map can be chosen to ensure an adequate generalization capability.

The learning of SOM involves an unsupervised process. First, the reference vectors are initialized randomly by using an even distribution whose limits are determined by the input data. During learning the input vectors are categorized successively into best matching units, *BMU*s, on the map. The BMU is the neuron whose reference vector has the smallest *n*-dimensional Euclidean distance to the input vector. At the same time, the nearest neighbors of the BMU are activated as well, according to a neighborhood function (e.g. Gaussian distribution). Ultimately the reference vectors of all activated neurons are updated.

The parameters of the SOM and the size of the map were determined by experimental testing. Linear initialization, batch training algorithm, and a Gaussian neighborhood function were used in the training. The map was taught with 10 epochs, and the initial neighborhood had the value of 6. The SOM Toolbox (http://www.cis.hut.fi/projects/somtoolbox) was used in the analysis under a Matlab (version 7.6) software (Mathworks Inc., Natick, MA, USA, 2008) platform.

K-means clustering

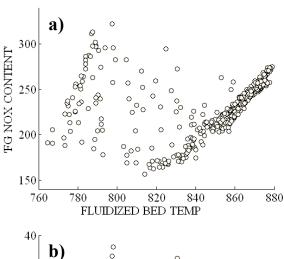
The k-means [8] is a widely used non-hierarchical method for data clustering. The basic approach is to first create k cluster centers at random, and then classify each sample to the cluster whose mean value is the most similar on the basis of Euclidean distances. In the meantime the cluster centers are updated iteratively by calculating the average of the data rows assimilated in each cluster. The optimal cluster structure can be determined by using the Davies-Bouldin -index [9]. This way clusters beforehand knowing the becomes unnecessary.

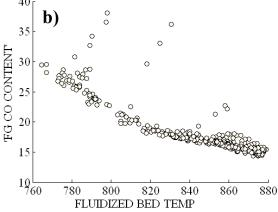
RESULTS

Generic model and its process states

A self-organizing map having 24*16 neurons was created to obtain the overall process model. The emission models in Figure 2 involve the use of the

whole data set before the identification of process states. The markers in these figures represent the neurons of the SOM, which are plotted in a 2-dimensional space in respect to their variable components shown in the axes.





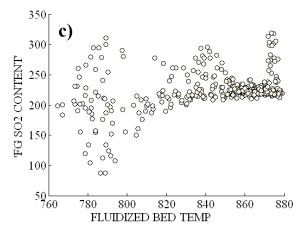
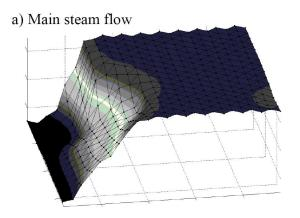


Figure 2: Emission models after creating a 24*16 SOM. a) NO_x, b) CO and c) SO₂ content [mg/Nm³] of flue gas (FG) as a function of the bed temperature [°C] by using the reference vectors of SOM neurons.

After modeling, the process states of high, medium and low boiler load were identified. This was done by clustering the reference vectors of the 24*16 SOM with the k-means algorithm, as presented in Figure 3. As can be seen, in this case the borders achieved by clustering seem to follow the degree of steam flow, i.e. the boiler load.



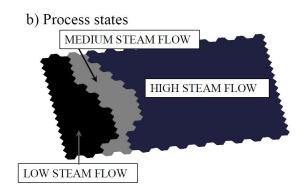
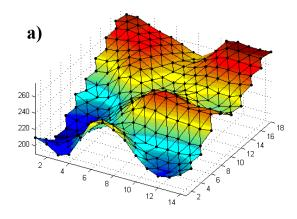


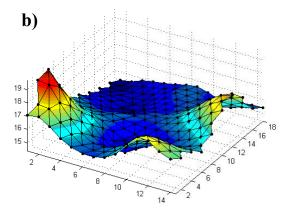
Figure 3: a) The behavior of the main steam flow on a 24*16 SOM, and b) Clustered SOM (k = 3), which shows the separation of process states into three categories.

Process state of high power

For emission models, a SOM having 18*14 neurons was created within the process state of high steam flow. The emission models for NO_x, CO and SO₂ are presented in the Figure 4a, b and c, respectively. In Figures 5a, b and c, each emission component is presented as a function of the bed temperature, the color scale indicating the deviation of the bed temperature. The markers in these figures represent the neurons of the SOM, which are plotted in a 2-dimensional space in respect to their variable components shown in the axes. Figures 6 and 7 illustrate the SO₂ content of

flue gas as a function of the fluidized bed temperature and the total limestone flow, respectively. The color scale indicates the deviation of the middle level temperature in the furnace.





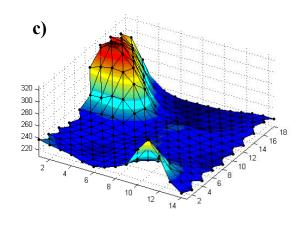


Figure 4: The component planes of different emission components $[mg/Nm^3]$, a) NO_x , b) CO and c) SO_2 , on 18*14 SOM grids after modeling the process state of **high steam flow**.

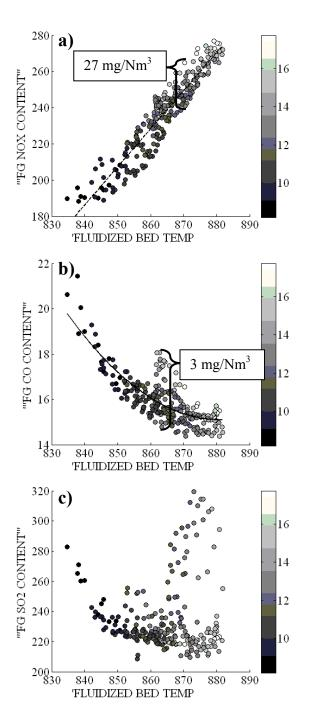


Figure 5: Emission models of the process state of **high steam flow**. a) NO_x, b) CO and c) SO₂ content [mg/Nm³] of flue gas (FG) as a function of the bed temperature [°C] by using the reference vectors of SOM neurons. Color scale indicates the deviation of the bed temperature [°C].

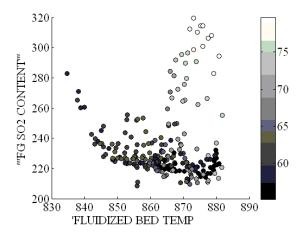


Figure 6: Flue gas (FG) SO₂ content [mg/Nm³] as a function of the bed temperature [°C] by using the reference vectors of SOM neurons in the process state of high steam flow. Color scale indicates the deviation of the furnace middle level temperature [°C].

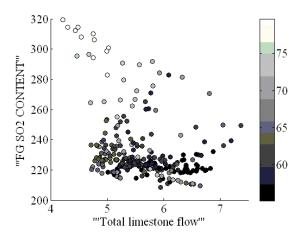


Figure 7: Flue gas (FG) SO₂ content [mg/Nm³] as a function of the limestone flow [kg/s] by using the reference vectors of SOM neurons in the process state of high steam flow. Color scale indicates the deviation of the furnace middle level temperature [°C].

DISCUSSION

The results of the study reflect the complexity of the problem. Figure 2 indicates the difficulty of modeling the emissions. Carbon monoxide is the only emission component that could be modeled well without the information on the different process states. Perhaps the foremost conclusion can be drawn from Figure 4: the areas of minimum emission rates are at variance with each other in the process state of high power. Situations with relatively low NO_x and SO₂ emissions can be found on the map, but those areas are also characterized by a relatively high concentration of CO. This leads to compromises in the minimization of emissions.

In respect to nitric oxides (see Figure 5a), the most distinct factor involved with their formation in the state of high power is the bed temperature; however the relationship is not clear in respect to the overall process model (see Figure 2a). It seems nonetheless that the NO_x concentration increases when there is instability in the bed temperatures (see Figure 5a). In addition, an important observation is that the NO_x content of flue gas could be reduced by as much as 10 % (27 mg/Nm³) by optimizing the process.

Higher bed temperatures seem to favor the reduction of CO in the flue gas (see Figures 2b and 5b). In this respect the CO emissions behave conversely to the NO_x emissions. Nevertheless, the effect of the deviation of the bed temperature is similar on both the CO and NO_x concentrations: a stable bed temperature generally favors the reduction of these emissions. Even as high as 18 % (3 mg/Nm³) reduction of CO can be achieved by optimizing the process.

Figure 5c indicates that the formation of SO_2 can be reduced in the process state of high power with a higher bed temperature; however, it seems that there are cases where the SO_2 concentration becomes suddenly high in the higher temperatures. Generally speaking it seems that the formation of SO_2 is a more complex issue than the other emission components that were studied.

Figure 6 suggests that a high deviation of the middle level temperature in the furnace explains the high concentrations of SO₂ in the higher bed temperatures. However, Figure 7 suggests that a certain level of limestone flow should be maintained to keep the SO₂ concentration below 300 mg/Nm³. It is presumable that the changes in the sulfur content of fuel can affect greatly the formation of sulfur dioxide in the process, which can explain the high deviation in the SO₂ concentration with higher bed temperatures.

CONCLUSION

The world is struggling for cleaner environment and searching for solutions to different environmental problems. It is evident that in the future the energy plants have to be able to produce their energy with a lesser amount of harmful, gaseous emissions. The method presented provides a fruitful way to diagnose processes, and offers new possibilities for the analysis of process emissions in the near future.

For instance, presently only a few gaseous emission components are included to the international emission trading. Nonetheless, the emission regulations are becoming tighter worldwide due to the growing interests in different environmental issues. As new emission types will be added to the trading of emissions in the future, the method can be used for emission cost modeling after the definition of an appropriate cost function. Alternatively, the methodology can be used to more generic process optimization, for example to optimize the total profit of producing steam in fluidized bed boilers.

REFERENCES

- [1] Kohonen T. Self-Organizing Maps. Springer-Verlag, Berlin Heidelberg New York, 2001.
- [2] Kasslin M, Kangas J, Simula O. Process State Monitoring Using Self-Organizing Maps. In: Aleksander I, Taylor J, editors. Artificial Neural Networks 2, Vol. I. North-Holland, Amsterdam, 1992. p. 1532-1534.
- [3] Alhoniemi E, Hollmén J, Simula O, Vesanto J. *Process Monitoring and Modeling Using the Self-Organizing Map.* Integrated Computer Aided Engineering 1999; 6(1): 3-14.
- [4] Heikkinen M, Kettunen A, Niemitalo E, Kuivalainen R, Hiltunen Y. SOM-based method for process state monitoring and optimization in fluidized bed energy plant. In: Duch W, Kacprzyk J, Oja E, Zadrożny S, editors. Lecture Notes in Computer Science 3696. Springer-Verlag Berlin Heidelberg, 2005. p. 409-414.

- [5] Liukkonen M, Hälikkä E, Kuivalainen R, Hiltunen Y. *Process State Identification and Modeling in a Fluidized Bed Energy Plant by Using Artificial Neural Networks*. In: Proceedings of Finnish-Swedish Flame Days. The Finnish and Swedish National Committees of the International Flame Research Foundation (IFRF), 2009.
- [6] Liukkonen M, Heikkinen M, Hiltunen T, Hälikkä E, Kuivalainen R, Hiltunen Y. Modeling of Process States by Using Artificial Neural Networks in a Fluidized Bed Energy Plant. In: Troch I, Breitenecker F, editors. Proceedings of MATHMOD 09 VIENNA [CD-ROM]. Vienna University of Technology, 2009.
- [7] Liukkonen M, Heikkinen M, Hälikkä E, Kuivalainen R, Hiltunen Y. *Emission Analysis of a Fluidized Bed Boiler by Using Self-Organizing Maps*. In: Kolehmainen M. et al., editors. Lecture Notes in Computer Science 5495: Proceedings of ICANNGA' 09 International Conference on Adaptive and Natural Computing Algorithms. Springer-Verlag Berlin Heidelberg, 2009 (in press).
- [8] MacQueen J. Some methods for classification and analysis of multivariate observations. In: Proc. Fifth Berkeley Symposium on Mathematical Statistics and Probability, Vol. I: Statistics. Berkeley and Los Angeles: University of California Press, 1967. p. 281-297.
- [9] Davies DL, Bouldin DW. *A cluster separation measure*. IEEE Trans. Pattern Recognition and Machine Intelligence 1979; 1(2): 224-227.

Power 2



A COMPARATIVE STUDY OF COMPUTATIONAL METHODOLOGY AND TOOLS OF THERMOELECTRICITY

Min Chen*and Lasse A. Rosendahl†
Alborg University
Institute of Energy Technology
9220 Pontoppidanstraede 101
Denmark

ABSTRACT

The governing equations used in the thermoelectric device modelling can be based upon irreversible thermodynamics and energy conservation, respectively. This paper presents a comparative study of the two different computational methodologies for thermoelectric numerical modelling. Firstly, boundary conditions for the simplified but classical and well known one-dimensional analytical model are formulated for a thermoelectric generator example. The analytical derivation from irreversible thermodynamics is compared with that based on energy conservation, and a unified result for the analytical model under the both theoretical frameworks is arrived at. Secondly, numerical results of the commercial code ANSYS, which is from irreversible thermodynamics and Onsager flux, are evaluated by a comparison to those of the numerical formulation from energy conservation for a three-dimensional generator case, where the nonlinear differential equation system with temperature dependent material properties must be solved. Although numerical results of electric parameters as well as the temperature profile from the both computational tools match almost exactly, several additional effects on the simulation regarding connection between the temperature field and the thermal flux, flexibility of incorporating additional heat transfer terms, and quantification of the Thomson heat, are brought by the energy conservation based numerical tool to support its numerical applications with practical notes.

Keywords: Thermoelectric; Heat transfer; Irreversible thermodynamics; Numerical simulation; Boundary conditions;

INTRODUCTION

Thermoelectric generators (TEG) and coolers have been of great interest to energy applications in recent years as highly reliable, environmentally friendly, and easy-to-use energy devices. The optimization of such devices requests for the precise simulation of thermoelectric effects. The solution of the entire thermoelectric multi-physics process, however, relies on numerical approximation methods of a nonlinear differential equation system, where energy production by the irreversible Joule effect, the reversible Peltier and Thomson heat, and temperature dependent material properties are included. There have been two approaches to writing the comprehen-

*Phone: +45 9940 9284 E-mail:mch@iet.aau.dk

†Phone: +45 9940 9263 E-mail:lar@iet.aau.dk

sive governing equation system for the thermoelectric numerical approximation. Inspired by Onsager's heat flux formulation [1], the first governing equation system [2] has roots in irreversible thermodynamics with the famous assumption of local equilibrium, necessarily postulating a discontinuous system consisting of a finite number of regions, on which the constitutive relation is achieved. Each region is with uniform values for the state variables, hence different regions have different variable values. On the other hand, the second approach to express governing equations uses a more conventional energy conservation theory, simply applying heat balance on the control volume of thermoelements [3].

In the field of thermoelectric numerical approximation, it is most often that one accounts nonlinear features by the first approach that some state intensive variables are analytically presumed discontinuous, and there have been a number of works on numerical modelling of thermoelectric devices by such methodology as well as the development of general computational tools, regardless whichever the concrete numerical solution algorithm, finite element method (FEM) [4, 5, 6, 7], finite volume method (FVM) [8, 9], or others regarded as one form of the Galerkin method, is actually used. But so far little attention is paid on the advantages and disadvantages of the first approach in practical simulation when compared with the second. One opinion on the first technique is that "it is theoretically superior because of its ability to treat the problem without separating the energy fluxes into conducted heat, electrical heat dissipation, and etc" [10]. However, since the local heat flow is regarded as one form of the Onsager flux in the approximation, this particular formulation of thermal flux certainly does not have a direct connection with the temperature gradient field, amongst other usual heat characteristics.

The full understanding of the computational methodology and the simulation results even requires more careful examinations, especially on discontinuous conditions across boundaries. Such analyses can be carried out more easily with the analytical treatment of governing equations. In fact, if the one-dimensional (1D) device model neglects temperature dependent material properties, the differential equations given in both [2] and [3] have been analytically solved. For the classical formulation of the simplified 1D model from irreversible thermodynamics [11], the boundary condition issue has been noticed recently by Gurevich and Logvinov [12], whose comment bears repeating:

"However, the absence of precisely formulated boundary conditions does not allow for the presentation of a clear picture of the Peltier effect in this case."[12]

This paper compares the two numerical approximation methods of thermoelectricity, i.e., the one based upon the irreversible thermodynamics, and the other, being more intuitive and closer to the physical insight, based upon the energy conservation formulation. The main intention is to analytically clarify the unified result of irreversible thermodynamics and energy conservation for thermoelectric device modelling, whether the both are equivalent or not, and

to numerically study the effects of different computational methods and tools on the simulation results. First we examine the two analytic derivations of solving the 1D governing differential equations in order to deal with the boundary condition issue considered in [12]. Afterwards a comparative study is done between the two different computational strategies. ANSYS coupled-field analysis capability is evaluated by a comparison to the numerical formulation from conventional energy conservation realized by FLUENT, where three-dimensional (3D) differential equations are solved using a FVM scheme and User Defined Functions and Scalars. Some conclusions are summarized in the last section.

ANALYTICAL COMPARISON Energy Conservation

In order to address the contention in [12] against the formulation based on irreversible thermodynamics for the boundary condition, we firstly consider a rather idealized single-couple TEG, used in [11] and shown here in Figure 1. The TEG is composed of an n-type semiconductor leg and a p-type semiconductor leg that are in parallel thermally and connected electrically in series by metal strips. The legs are sandwiched between two thermally conducting but electrically insulating substrates mounted above and below, as expressed by K_1 and K_2 , respectively; the hot side is an idealized heat source with a constant temperature T_w while the cold side is an idealized cold source with a constant temperature T_a ; Q_h is the rate of heat transfer from the heat source to the hot junction at temperature T_h , and Q_c the rate of heat transfer from the cold junction at temperature T_c to the heat sink; Q_p is the rate of heat transfer in the p-type leg, and Q_n the rate of heat transfer in the n-type leg; Q is the sum of Q_p and Q_n ; I is the electrical current generated under the load resistance R_l .

Following the same assumptions of [11], the TEG is adiabatic from the surroundings except the heat flows at the cold and hot side. The electrical resistivities ρ_p and ρ_n , the thermal conductivities k_p and k_n , and the Seebeck coefficients α_p and α_n of the p- and n-type semiconductor material are assumed independent of temperature. Hence the Thomson effect is negligible. S_p and S_n are uniform cross-sectional areas of p- and n-type legs, respectively.

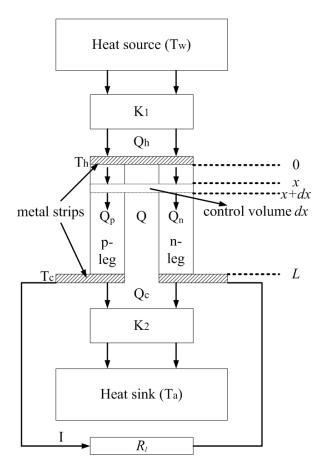


Figure 1: Schematic representation and thermal model of a single-couple TEG.

The manufacturing requirements usually dictate the lengths of the two legs are identical, and represented here by L.

In terms of conventional energy conservation [3], the 1D differential equation governing heat transfer of the infinitesimal element with a length of dx in the p-type leg under steady state can be written as,

$$dQ_p = Q_p(x+dx) - Q_p(x) = I^2 \frac{\rho_p}{S_p} dx,$$
 (1)

and according to Fourier's heat conduction law, the relationship between heat flow and temperature gradient is:

$$Q_p(x) = -k_p S_p \frac{dT_p(x)}{dx},\tag{2}$$

where $T_p(x)$ is the temperature profile of the p-type leg and a function of position x. With the tempera-

ture boundary condition at the hot and cold side,

$$T_p(0) = T_h, (3a)$$

$$T_p(L) = T_c, (3b)$$

(1) and (2) can be solved to yield

$$Q_p(0) = K_p(T_h - T_c) - \frac{I^2 R_p}{2},$$
 (4a)

$$Q_p(L) = K_p(T_h - T_c) + \frac{I^2 R_p}{2},$$
 (4b)

where

$$K_p = \frac{k_p S_p}{L} \tag{5}$$

is the thermal conductance of the p-type leg, and

$$R_p = \frac{\rho_p L}{S_p} \tag{6}$$

is the internal electrical resistance of the p-type leg. Using the same method and the same temperature boundary conditions, the heat flow Q_n can be expressed in exactly the same form by treating the 1D heat transfer differential equation of the infinitesimal element dx in the n-type leg, with the value of ρ_n , k_n , and S_n . Since the thermal energy flow Q transferred in a TEG such as shown in Fig.1 is defined as the sum of Q_p and Q_n , more general equations for the whole device can be obtained as:

$$Q(0) = Q_p(0) + Q_n(0) = K(T_h - T_c) - \frac{I^2R}{2},$$
 (7a)

$$Q(L) = Q_p(L) + Q_n(L) = K(T_h - T_c) + \frac{I^2R}{2},$$
 (7b)

where

$$K = \frac{k_p S_p}{L} + \frac{k_n S_n}{L} \tag{8}$$

and

$$R = \frac{\rho_p L}{S_p} + \frac{\rho_n L}{S_n} \tag{9}$$

are the total thermal conductance and internal electrical resistance of the single-couple TEG, respectively. When the energy removal αIT_h from Q_h and energy supply αIT_c to Q_c by the Peltier effect, occurred at each junction, are considered respectively, the heat flow boundary conditions at both sides are given as

$$Q(0) = Q_h - \alpha I T_h, \tag{10a}$$

$$Q(L) = Q_c - \alpha I T_c, \tag{10b}$$

where $\alpha = \alpha_p - \alpha_n$ is defined as the Seebeck coefficient of the thermocouple. Eqs. (7) can now be changed to

$$Q_h = \alpha I T_h + K(T_h - T_c) - \frac{I^2 R}{2},$$
 (11a)

$$Q_c = \alpha I T_c + K(T_h - T_c) + \frac{I^2 R}{2}.$$
 (11b)

Equations (11a) and (11b) are the heat flow balance equations of the hot and cold junctions, upon which most previous analytical works are based.

Irreversible Thermodynamics

In his work [11], Goldsmid arrived at the same heat flow equations as Eqs. (11) by a somewhat different method where thermodynamic heat flow is adopted rather than conduction flow. Still taking the p-type leg as the paradigm, the heat flow is redefined as

$$Q_p(x) = \alpha_p IT_p(x) - k_p S_p \frac{dT_p(x)}{dx}.$$
 (12)

Whilst it is easy to recognize that the second term is simply the heat conduction, it should be noted that the first term is the reversible (Peltier) heat flow, one special form of Onsager's flow, to reflect the reversible thermoelectric heat brought by current. However, Goldsmid treated only the heat conduction term in a way akin to the treatment described above for governing equations of conventional energy conservation method. With the same temperature boundary condition, $-k_pS_p\frac{dT_p(0)}{dx}=K_p(T_h-T_c)-\frac{l^2R_p}{2}$ and $-k_pS_p\frac{dT_p(L)}{dx}=K_p(T_h-T_c)+\frac{l^2R_p}{2}$ can be derived thus

$$Q_p(0) = \alpha_p I T_h - k_p S_p \frac{dT_p(0)}{dx} = \alpha_p I T_h + K_p \Delta T - \frac{I^2 R_p}{2}, \text{ duction term } -k_p S_p \frac{dT_p(0)}{dx} \text{ (=0 due to the isothermal-ity); } \alpha_p I T_h + K_p (T_h - T_c) - \frac{I^2 R_p}{2} \text{ should only be ap-$$

$$Q_p(L) = \alpha_p I T_c - k_p S_p \frac{dT_p(L)}{dx} = \alpha_p I T_c + K_p \Delta T + \frac{I^2 R_p}{2}.$$
(13b)

When the same results for the n-type leg are included, Eqs. (11) can be obtained.

Gurevich and Logvinov's contention about [11] is on the boundary, i.e., whether Goldsmid's derivation of Eqs. (13) where the junctions are assumed to have a finite temperature gradient requires new insightful explanations for Peltier effect as described in their work [12]. For the sake of clearness, we

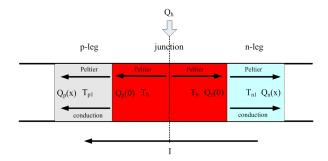


Figure 2: An assumed isothermal hot junction of the single-couple TEG.

magnify the hot junction part by Figure 2, where the metal strip is removed without loss of generality. According to irreversible thermodynamics, the micro regions in Figure 2 are all assumed in local equilibrium, each with uniform temperature values $(T_h, T_{p1}, T_{n1}, ...)$. Different regions have different temperature value, hence the temperature is discontinuous across boundaries.

As is pointed out by Gurevich and Logvinov, in the application of Onsager's reciprocal relation to Peltier effect it is usual to assume the isothermality of the junction of dissimilar materials [13, 14]. So if the assumption is a condition for Peltier effect, the heat conduction should vanish in the junction region in this case, and the only thermal term is the Peltier heat flow, shown in Figure 2 (the red elements). Here Gurevich and Logvinov's contention in effect implies the following: Provided that the Peltier heat is assumed as an isothermal effect, the right side of (13a), $\alpha_p IT_h + K_p (T_h - T_c) - \frac{l^2 R_p}{2}$, should not be equal to $Q_p(0)$ because $Q_p(0)$ does not have the conity); $\alpha_p IT_h + K_p (T_h - T_c) - \frac{I^2 R_p}{2}$ should only be approximated by the heat flow in the neighboring region next to the junction, i.e., T_{p1} (same result for T_{n1}), where a finite temperature gradient exists. This result obviously disagrees with what has been got from the conventional energy conservation method. One important point missed herein, however, is that the intention of the assumption of isothermality is just to make the mathematic treatment, particularly the relation between the Seebeck factor and the Peltier heat, easier, and to allow a clearer physical picture. It is a misunderstanding that the assumption of isothermality [13, 14] is a condition for the Peltier effect in terms of irreversible thermodynamics. To eliminate such confusions and to show why a simple renouncement of using the isothermal assumption is not questionable, below from a new pedagogical viewpoint the application of Onsager's reciprocal relations to thermoelectric phenomenon is re-formulated in a strictly sequential order.

In terms of the phenomenological law of irreversible thermodynamics, if an 1D conductor with both heat and electric currents flowing (like the thermoelements in Fig.1) can be assumed local equilibrium, we have the electromotive force and temperature gradient force, written as

$$X_1 = \frac{1}{T} \nabla \mu, \tag{14a}$$

$$X_2 = \nabla \frac{1}{T},\tag{14b}$$

to drive the electric current and thermodynamic flow of heat (same significance as Eq.(12)), i.e.,

$$J_1 = L_{11}X_1 + L_{12}X_2, (15a)$$

$$J_2 = L_{21}X_1 + L_{22}X_2, (15b)$$

respectively, where μ is the electromotive and L_{ij} the phenomenological coefficients between flows and forces.

To treat Eq.(15), the next step is to calculate L_{ij} according to the physical definitions of the electrical resistivity ρ , the thermal conductivity k, the Seebeck coefficient α , and the Peltier coefficient Π (henceforth α , ρ , and k refer to properties of the conductor material). Now let us discuss the first phenomena: if no electric current passing through the aforementioned conductor, i.e., $J_1 = 0$, from Eq.(15a) we have

$$\nabla \mu = \frac{L_{12} \nabla T}{L_{11} T}.\tag{16}$$

Eq.(16) clearly shows that the electric potential in the conductor is not zero if there is an accompanied temperature gradient, even if there is no electric current passing. According to the definition of Seebeck effect, this potential is the Seebeck electromotive potential, where

$$\alpha = -\frac{\nabla \mu}{\nabla T} = -\frac{L_{12}}{L_{11}T},\tag{17}$$

and L_{12} can be obtained as $-\alpha L_{11}T$. From Eq.(15b) we also have

$$\frac{J_2}{\nabla T} = \frac{L_{21}\nabla\mu}{T\nabla T} - \frac{L_{22}}{T^2}.$$
 (18)

According to the definition of heat conduction (Fourier's law), and using the result of Seebeck electromotive potential obtained above for the same zero current configuration,

$$-k = -\alpha \frac{L_{21}}{T} - \frac{L_{22}}{T^2},\tag{19}$$

and L_{22} can be obtained as $-\alpha T L_{21} + kT^2$.

Let us now discuss the second phenomena: if no temperature gradient existing in the aforementioned conductor, i.e., $X_2 = 0$, from Eq.(15b) we have

$$J_2 = \frac{L_{21}\nabla\mu}{T} = J_1 \frac{L_{21}}{L_{11}}. (20)$$

Eq.(20) clearly shows that the heat flow in the conductor is not zero if there is an accompanied nonzero electric current, even if there is no temperature gradient existing¹. According to the definition of Peltier effect, this non-conduction heat flow J_2 , brought by the electric current J_1 from one end to the other end, is the reversible Peltier heat absorbed at one isothermal junction and evolved at the other, where

$$\Pi = \Pi - 0 = -\frac{J_2}{J_1} = -\frac{L_{21}}{L_{11}},\tag{21}$$

and L_{21} can be obtained as $-\Pi L_{11}$. From Eq.(15a) we also have

$$\frac{J_1}{\nabla \mu} = \frac{L_{11}}{T}.\tag{22}$$

According to the definition of electrical conduction, the left side of Eq.(22) is $1/\rho$, and L_{11} can be obtained as T/ρ .

Substituting L_{11} into L_{21} and L_{12} , and then substituting L_{21} into L_{22} , all phenomenological coefficients are expressed by material properties,

$$L_{11} = \frac{T}{\rho},\tag{23a}$$

$$L_{12} = -\frac{\alpha T^2}{\rho},\tag{23b}$$

$$L_{21} = -\frac{\Pi T}{\rho},\tag{23c}$$

$$L_{22} = kT^2 + \frac{\alpha\Pi}{\rho}T^2$$
. (23d)

¹External heat reserviors around the 1D conductor are certainly necessary to remove the temperature gradient, i.e., supply Peltier heat and/or eliminate Joule heat transfer, etc. Another necessary condition for this configuration is that the two ends of the conductor must be in electric contact with two inhomogeneous lead wires by which the current is applied to the conductor, i.e., the two ends of the conductor are two isothermal junctions. Without loss of generality, the Peltier coefficients of the both two lead wires are however assumed zero.

Substituting Eqs.(23) and Eqs.(14) into Eqs.(15) yields the complete flow-force equation system for the case of thermoelectricity:

$$J_{1} = \frac{\nabla \mu}{\rho} + \frac{\alpha}{\rho} \nabla T,$$

$$J_{2} = -\frac{\Pi}{\rho} \nabla \mu - (k + \frac{\alpha \Pi}{\rho}) \nabla T = -\Pi J_{1} - k \nabla T.$$
(24a)
(24b)

Eqs.(24) had been extensively discussed in 19th century, firstly by Thomson (Lord kelvin) in a somewhat different form [15], where he made his famous conjecture of $\Pi = \alpha T$, an equivalent to $L_{12} = L_{21}$ in flow-force equations. Thomson's conjecture of thermoelectric relations is not a complete proof because he did not bring the necessarily accompanied irreversible processes into his derivation. Many researchers attempted to solve this problem such as [16] based on the flow-force equation form, but the enigma why $L_{12} = L_{21}$ is thermodynamically legal was not clarified until 1931 when Onsager developed the reciprocal relations expressing the equality of certain relations between flows and forces in thermodynamic systems out of but close to equilibrium [1]. Elegantly formulated by the principle of microscopic reversibility, Onsager's reciprocal relations have been well confirmed by a number of experiments and generalized as the footstone of irreversible thermodynamics. For those frequently cited references discussing thermoelectric effects where zero current and the isothermal junction of dissimilar materials are used, such as [13, 14], it should be remarked that they are just explanatory works of Onsager's reciprocal relations.

It is clear that neither is the assumption of $J_1=0$ nor $X_2=0$ relevant to Onsager's theory. It is also clear that, from the above formulations, the intention of the both assumptions is nothing but to simplify the calculation of phenomenological coefficients. By assuming a zero electric current, Seebeck effect and heat conduction are left alone and L_{12} and L_{22} can be easily expressed by α and k; By assuming a zero temperature gradient, Peltier effect and electrical conduction are left alone and L_{21} and L_{11} can be easily expressed by Π and ρ . However, when these physical effects are interfered by each other, the correctness of the above treatment for them is not affected because the phenomenological law itself is left unchanged. In other words, removing

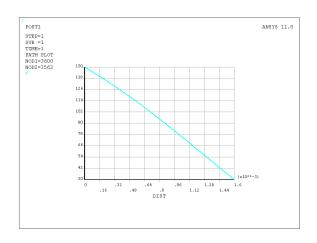
the both assumptions does not have any influence on the phenomenological coefficients already obtained with such assumptions. Of course, one cannot say that if there is an electric current in the conductor, then Seebeck effect would not follow the same rule as without current. Completely similarly the assumption of isothermality is not a condition for the manner how Peltier effect occurs either.

Therefore, once the phenomenological coefficients have been obtained, Eqs.(24) is arrived as a general theorem, and the assumption of isothermality does not have to always exist any more for the application of the equations. Nothing is required to be additionally done to renounce the isothermal junction. In fact, maintaining the isothermal state necessarily requires external reservoirs to remove any Joule heat produced in the junction out of it immediately. Otherwise there must be accompanied temperature gradients. In the case of the thermoelectric generator hot junction in Fig.2, the only reservoir attached to the junction is of a higher temperature T_w , hence the assumption of isothermality is not possible. Another much more straightforward approach to show that the Peltier effect cannot be isothermal in this 1D thermoelectric generator is: if both the hot and the cold junctions are isothermal, then referring to Fig.2 the input and output heat of the generator can only be αIT_h and αIT_c , respectively; the generator would be a carnot engine! Obviously both the Peltier heat flow and the heat conduction must appear simultaneously in the junction. Thus the renouncement of using the isothermal assumption in [11] is not only appropriate but also necessary for this 1D generator, and the derivation of Eqs. (11) is free of unclear boundary condition.

Moreover, a note should be addressed to the concept of the so called induced thermal diffusion flux by Gurevich and Logvinov [12]. Its effect to give rise to a temperature heterogeneity in the junction region is the same as that of the heat entering the hot junction in Fig.1 from the external heat reservoir T_w , a part of which becomes the conduction flow to produce the temperature heterogeneity, in parallel the other part absorbed as Peltier heat flow [17], because the induced thermal diffusion also follows Fourier's law, and must be from some heat sources outside. In fact, the temperature heterogeneity can be caused by either configuration. Far from being able to suggest a new physical interpretation of the Peltier effect,

Gurevich and Logvinov's 'cooling junction' model seems to us by no means different from the disturbed temperature distribution described by Bridgman [18, 19], as well as the analyse afterwards with more details for the Peltier effect in segmented thermoelements [20].

NUMERICAL COMPARISON



(a)

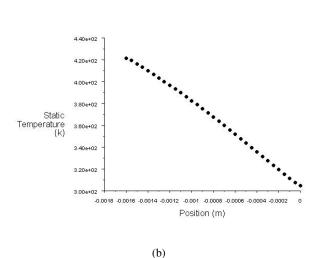


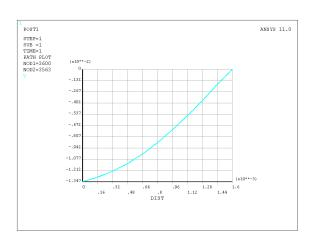
Figure 3: Predicted Temperature distribution in an x-y plane corner line along z direction. (a) ANSYS. (b) FLUENT.

The commercially available software ANSYS is the most representative thermoelectric analysis tool that based on irreversible thermodynamics's constitutive equations. Applying the Galerkin FEM procedure to the equations, it can approximate the tempera-

ture and electric scalar potential over the full 3D thermoelectric field [7]. On the other hand, in order to ease the co-design and co-optimization of the fluid or combustion system and the TEG, a 3D TEG model has been proposed and implemented in a computational fluid dynamics (CFD) simulation environment (FLUENT) based on energy conservation [21]. Temperature dependent properties can also be described in terms of a polynomial as a function of temperature of various orders in the both models.

The simulation example is the performance of the TEG described in the previous study [22], the thermoelectric module TEC1-12706 made by Tianjin Institute of Power Sources, China. Initially the constant temperature boundary condition is set on the top and bottom surfaces for 1D simulation, where no heat loss from the other four sides of the legs is assumed. The 1D temperature and electric potential distributions in a left leg axis line of a single-couple TEG are depicted in Fig. 3 and Fig. 4, where the both models show very similar characteristics. It is of our main interest herein to observe the thermal flux from the simulation results, whence the element solution by ANSYS is shown in Fig. 5. It is very interesting to find out that the thermal flux monotonically decreases from the hot junction to the cold junction. This observation applies to the thermal flux in both n-type and p-type legs, an equivalence to Q_p and Q_n , as is shown in the 3D Fig. 6. This means that the computational results express irreversible thermodynamics flow rather than the usual conduction heat flow, as is decided by the governing equations.

In the analysis of relevant thermal simulation results by ANSYS, therefore, one should not expect a direct connection between the temperature field and the thermal flux. Fig. 7 shows the 1D temperature gradients by both ANSYS and FLUENT. When the same conditions are used, it is not surprising that the ANSYS temperature gradient (heat flow) monotonically increases from the hot junction to the cold junction. The explanation is that all Joule heat generated in the legs flows towards the cold side through heat conduction. For the FLUENT temperature gradient, its main part (middle) shows very similar characteristics to that of ANSYS, but at the hot and cold junctions it is largely augmented dut to the conduction heat change brought by the Peltier effect. This becomes clearer with the 1D heat flow distribution



(a)

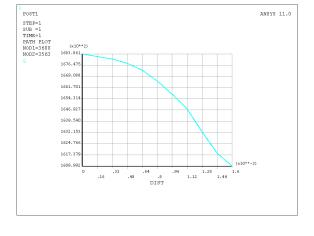


Figure 5: ANSYS 1D thermal flux in an x-y plane corner line along z direction.

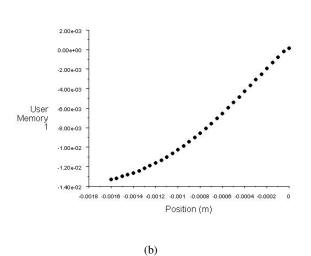


Figure 4: Predicted Voltage distribution in an x-y plane corner line along z direction. (a) ANSYS. (b) FLUENT.

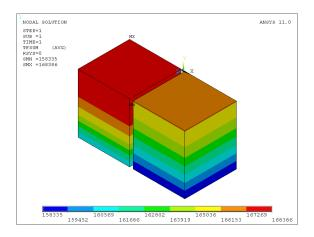
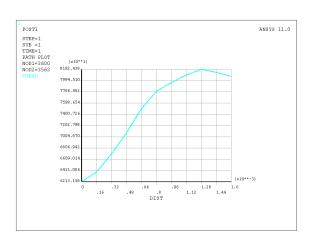


Figure 6: ANSYS 3D thermal flux.



(a)

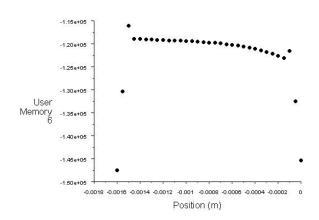


Figure 8: FLUENT 1D heat flow distribution in an x-y plane corner line along z direction.

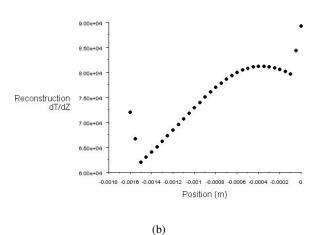


Figure 7: Temperature gradient distribution in an x-y plane corner line along z direction. (a) ANSYS. (b) FLUENT.

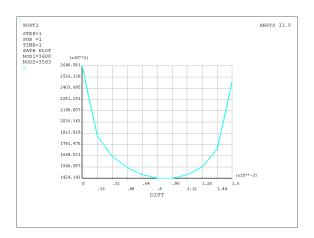


Figure 9: ANSYS 1D thermal flux in an x-y plane corner line along z direction with convection.

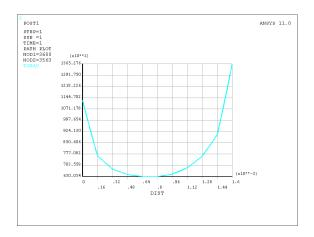


Figure 10: ANSYS 1D temperature gradient in an x-y plane corner line along z direction with convection.

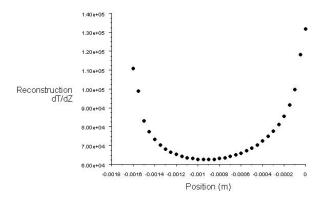


Figure 11: FLUENT 1D temperature gradient in an x-y plane corner line along z direction with convection.

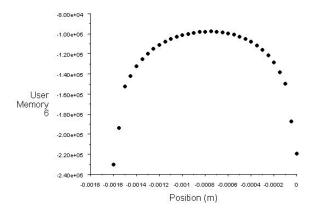


Figure 12: FLUENT 1D heat flow in an x-y plane corner line along z direction with convection.

of FLUENT simulation, shown in Fig. 8, where the heat difference between the two ends reflects the power produced, like the disclosure by the analytical heat flow diagram [17].

In order to illustrate how the surface heat loss can produce multidimensional effects, the 1D thermal flux and temperature gradient distributions in the thermocouple by the ANSYS model are depicted in Fig. 9-10, where all leg surfaces except the top and bottom junctions are assumed exposed to a heat transfer rate specified as 500 W/m^2K . The bulk mean temperature in the module cavity is set to be the arithmetic average of T_h and T_c . i.e., 363K. It can be seen that the thermal flux and temperature gradient distributions become similar when the convection dominates the heat transfer. With the same parameters, the FLUENT temperature gradient distribution shows similar characteristics in Fig. 11, whilst the FLUENT heat flow distribution is still able to indicate the energy balance around the TEG (Fig. 12). Evidently, the results thus obtained is closer to physical reality, and in this method the governing equations can be more easily revised by simply incorporating additional heat transfer terms.

CONCLUSIONS

We have tackled and reformulated the boundary condition issue considered for irreversible thermodynamics [12]. It is rigorously proven that the renouncement of using the isothermal approach to the Peltier effect in thermoelectric device analysis is appropriate. So the the numerical approximation methods based on irreversible thermodynamics do not suffer more essentially theoretical drawbacks than the energy conservation methods. A preliminary comparison of two different computational tools shows that they both have the ability of convenient interaction between thermal and electrical circuits, calculating temperature dependency of materials properties, and others. However, since the energy conservation based numerical formulation has more customized governing equations and is more flexible, its results might be easier to analyze and to truly understand from a viewpoint of energy balance.

REFERENCES

[1] L. Onsager, Reciprocal Relations in Irreversible Processes. I., Phys. Rev. 37 (1931)

- 405–426, Reciprocal Relations in Irreversible Processes. II., Phys. Rev. 38 (1931) 2265–2279.
- [2] C.A. Domenicali, Stationary Temperature Distribution in an Electrically Heated Conductor, J. App. Phys. 25 (1954) 1310–1311.
- [3] A.E. Burshstein, An investigation of steady state flow through a current-carrying conductor, Sov. Phys. Tech. Phys. 2 (1957) 1397–1406.
- [4] L. Helmers, W.E. Müller, J. Schilz, W.A. Kaysser, Graded and stacked thermoelectric generators-numerical description and maximisation of output power, Mat. Sci. Eng. B. 56 (1998) 60–68.
- [5] H. Saber, M. El-Genk, A three-dimensional, performance model of segmented thermoelectric converters, AIP Conference Proceedings, 608, 2002 pp. 998-1006.
- [6] E. Müller, S. Walczak, W. Seifert, C. Stiewe, G. Karpinski, Numerical performance estimation of segmented thermoelectric elements, Proceedings of 24th International Conference on Thermoelectrics, Clemson, USA, 2005, pp. 349–354.
- [7] E. Elena, D.C. Looman, Finite Elements for Thermoelectric Device Analysis in ANSYS, Proceedings of 24th International Conference on Thermoelectrics, Clemson, USA, 2005, pp. 200–203.
- [8] T. Hogan, T. Shih, Modeling and Characterization of Power Generation Modules Based on Bulk Materials, in: D. M. Rowe (Eds.), Thermoelectrics Handbook: Macro to Nano, Taylor & Francis, London, 2006, 12.1-12.23.
- [9] R. Harris, T. Hogan, H.J. Schock, T. Shih, Heat transfer and Electric Current Flow in a Thermoelectric couple, Proceedings of AIAA 44th meeting and exhibit, Reno, Nevada, 2006, 0575.
- [10] J.A. Brandt, Solutions to the differential equations describing the temperature distribution, thermal efficiency, and power output of a thermoelectric element with variable properties

- and cross sectional area, Adv. Energ. Convers. 2 (1962) 219-230.
- [11] H. Goldsmid, Conversion efficiency and figure-of-merit, in: D. M. Rowe (Eds.), Handbook of Thermoelectrics, CRC Press, London, 1995, pp. 9-25.
- [12] Y. Gurevich, G. Logvinov, Physics of thermoelectric cooling, Semicond. Sci. Technol. **20** (2005) 57-64.
- [13] H. Callen, The Application of Onsager's Reciprocal Relations to Thermoelectric, Thermomagnetic, and Galvanomagnetic Effects, Phys. Rev. 73 (1948) 1349–1358.
- [14] S.R. DeGroot, P. Mazur, in: Nonequilibrium Thermodynamics, Interscience, New York, 1962.
- [15] W. Thomson, Proc. Roy. Soc. Edin. Collected Papers I, 21 (1854) 237, Proc. Roy. Soc. Edin. 21 (1854) 123.
- [16] L. Boltzmann, Ber. Wien. Akad. 96 (1888) 1258–1297.
- [17] M. Chen, L. Rosendahl, I. Bach, T. Condra, and J. Pedersen, Irreversible transfer processes of thermoelectric generators, Am. J. Phys. 75 (2007) 815–820.
- [18] P.W. Bridgman, On the application of thermodynamics to thermo-electric circuit, Proc. Nat. Acad. Sci. 15 (1929) 765–768.
- [19] P.W. Bridgman, in: The Thermodynamics of Electrical Phenomena in Metals, Macmillan, London, 1934.
- [20] R.W. Ure, R.R. Heikes, in: Thermoelectricity, Interscience, New York, 1961.
- [21] M. Chen, L. Rosendahl, and T. Condra, A three dimensional numerical model of thermoelectric generators in fluid power system,
- [22] M. Chen, L.A. Rosendahl, T.J. Condra, J.K. Pedersen, Numerical Modeling of Thermoelectric Generators with Varying Material Properties in a Circuit Simulator, IEEE. Trans. Energ. Convers. 24 (2009) 112–124.

MODELLING AND EXPERIMENTAL ANALYSIS OF A TRIGENERATION SYSTEM WITH A MICROTURBINE AND AN INDIRECT FIRED ABSORPTION CHILLER DRIVEN BY EXHAUST GASES

M. Moya, D. Martínez, M.A. Marimon, J.C. Bruno*, A. Coronas Universitat Rovira i Virgili, CREVER-Research Group on Applied Thermal Engineering, Dept. of Mechanical Engineering, Av. Paisos Catalans, 26, 43007 Tarragona (Spain)

P. Eguia, E. Torres, I. Zamora University of the Basque Country - Department of Electrical Engineering -Alda. Urquijo s/n, 48013 Bilbao (Spain)

ABSTRACT

This study describes the modelling and experimental investigation of the performance of a trigeneration system with a microgasturbine and an indirect fired absorption chiller. The microturbine has a net power output of 28 kW and a thermal output power of 60 kW. The absorption chiller is an ammonia/water air-cooled chiller with a rated cooling capacity of 17 kW. The unit was extensively modified to be driven by thermal oil at high temperature instead of a conventional burner. The trigeneration system was tested at different operating conditions by varying the output power of the microgasturbine, the external temperature of the absorption unit, the cooling water outlet temperature and the thermal oil inlet temperature. The modelling of the absorption air-cooled chiller driven by thermal oil is presented and the simulation results are compared with the testing results.

Keywords: Microgasturbine, absorption chiller, trigeneration, heat exchanger

INTRODUCTION

The integration of trigeneration technologies in buildings is an alternative to the current situation in which electricity is purchased wholly from the grid and heating is generated locally. A building demands different energy services: electricity, hot water for heating and DHW, steam (in such specific cases as hospitals) and cooling for air conditioning. These needs can be covered by buying electricity from the grid and producing heat locally with boilers and cooling with conventional air-conditioned units or with a trigeneration system that can produce all the

energy required with a single source of primary energy.

Trigeneration is the simultaneous production of mechanical power (usually converted into electricity), heat (at low and high temperature) and cooling (with heat recovered at high temperature) using only one source of primary energy as fuel or solar energy. The thermal energy recovered is used to generate heat and cooling, thus making the system more efficient than the more conventional separate production of electricity and heating and/or cooling.

559 691 E-mail: juancarlos.bruno@urv.cat

^{*} Corresponding autor: Phone: +34 977 257 891 Fax +34 977

Several distributed generation technologies can produce electricity using different types of fuels. Some are mature technologies, such as gasturbines and I.C. engines, while others are still in the development process, such as fuel cells (solid oxide phosphoric acid, residential PEM), Stirling engines, etc.

All the above mentioned technologies produce thermal waste heat at different temperature levels. Depending on the quality of the recoverable thermal energy of the cogeneration technology selected it will be possible to use different thermally-activated cooling technologies. Gasturbine and solid oxide fuel cells generate recoverable heat at very high temperatures suitable for efficient double effect chillers. Microturbines and small I.C. engines, on the other hand, are suitable for driving single-effect absorption chillers desiccant or cooling technologies. PEM fuel cells produce waste heat at low temperature range so they can be integrated with adsorption chillers.

New technologies and products are being developed to respond to the increasing demand for small scale systems for trigeneration in buildings.

The current market includes power generation technologies with a capacity lower than 200 kW: new reciprocating engines, Stirling engines, ORC (organic Rankine cycles), MGT and fuel cells. And the options for thermal small-scale cooling production are mainly water/LiBr chillers activated with low-temperature heat, ammonia/water chillers, adsorption chillers and thermochemical heat pumps. These units have a cooling capacity that ranges from 5 to 100 kW.

Trigeneration technology is in many cases a good energy saving solution for supplying energy to the building sector (commercial, residential, offices, hotels, etc.).

In industrial applications, the energy demand is very regular throughout the year, but in buildings it varies considerably due to the external ambient conditions, occupancy, different building uses, etc. The flexibility of trigeneration equipment can adapt to the customer's service requirements, despite the high variability in energy demands so characteristic of building applications.

The main objective of this paper is to describe the modelling, design and preliminary test results of a small trigeneration system that consists of the integration of an MGT and an absorption chiller activated indirectly by the exhaust gas of the MGT. The exhaust gas of the microturbine, is used to produce heat and cold. The trigeneration system analysed in this paper is based on a Capstone C30 Microgasturbine and an air-cooled absorption chiller driven by thermal oil to produce 17 kW of cooling (see figure 144).

This project has been financed by the European Project HEGEL (High Efficiency polyGEneration applications) and the Spanish national project TRIGENED which are developing co- and trigeneration technologies to be integrated in various buildings.

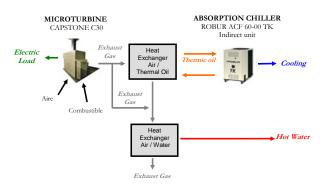


Figure 1: Trigeneration configuration

DESCRIPTION OF THE TRIGENERATION SYSTEM

Microturbines are excellent power generators for combined heat and power systems. They produce waste heat at very high temperatures. This provides greater overall efficiency rather than greater electrical efficiency with the simultaneous production of cold (with an absorption chiller) and heat.

The Capstone C30LPNG system is a compact, ultra-low-emission generator providing up to 28 kW of power and 60 kW of heat for combined heat and power applications. It uses high-pressure natural gas [14].

All the above features mean that microturbines have some advantages over other competing technologies such as natural gas reciprocating engines. These advantages are:

- They are lightweight and very compact systems.
- Their noise levels are low and they are vibration free.
- Their exhaust gas emissions are lower than those of competing technologies, with the one exception of fuel cells.
- Like other gas turbines, the heat recovery system is less complex than that of engines.
- They require less maintenance, particularly the oil-free MGT.
- Fuel flexibility. MGTs are available for operation with various gaseous fuels, including natural gas, propane, diesel, sewage and landfill bio-gas [2].

Integrating the MGT with an absorption chiller requires the best integrated configuration to make the global energy efficiency of the trigeneration system better than the efficiency of a conventional system.

The vast majority of absorption chillers for small scale applications are water/LiBr systems driven by hot water, so the energy efficiency is quite limited (COP about 0.7). A cooling tower is required for waste heat dissipation from the chiller and the chilled water temperature is also limited to 7°C [3]. The present project overcomes some of these problems by using an air-cooled ammonia/water chiller driven by thermal oil.

Most small-scale ammonia/water chillers are activated with natural gas or propane [3], because driving temperatures need to be high, but new versions of these chillers, which use thermal oil or pressurized hot water, are now being developed.

The absorption chiller analysed in this paper is the Hot Oil Driven ROBUR ACF 60-00 TK, modified so that it can be fed by thermal oil instead of a gaseous fuel (natural gas or LPG) to produce water chilled to 3°C. The fluid used as thermal source is Repsol Multigrado thermal oil. The ACF 60-00 TK chiller does not need a cooling tower, because it is air cooled.

The original burner was replaced by a patented heat exchanger.

Two flanged fittings on the lateral panel of the unit enable the hot fluid feed piping to be connected.

The ACF 60-00 Robur consists of a high efficiency water chiller with an air-cooled condenser, for outdoor installation, to produce water chilled to 3°C. It uses a refrigerant absorption cycle with a water-ammonia mixture in which the ammonia is the refrigerant and the water is the absorbent These products are innocuous to the environment. Ammonia diluted in the water is absolutely safe and has the following advantages over other refrigerants [4]:

- It is not subject to any international limitation on the protection of the ozone layer.
- It does not contribute to the green-house effect.
- It is used in thousands of refrigeration appliances.
- In comparison with other natural and synthetic fluids, its thermodynamic performances are among the best.

To integrate the MGT and the chiller a configuration had to be designed to recover the exhaust gas heat of the MGT so that the thermal oil could be heated to the required temperature to drive by the Absorption chiller using a cross flow gas/thermal oil heat exchanger. An additional heat exchanger is also used to recover the remaining exhaust gas heat after the thermal oil heat exchanger to produce hot water (see figure 2).

In summary, the main components of the trigeneration system are:

- Microturbine C30 LPNG of 28 kW
- Thermal oil driven absorption chiller, ACF 60-00 TK condensed by air
- Exhaust gas thermal oil, heat exchanger
- Exhaust gas hot water, heat exchanger.

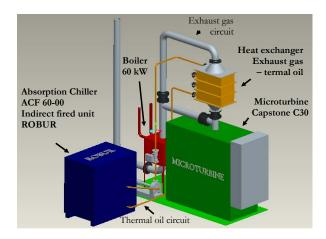


Figure 2: Main components of the trigeneration system

The measuring instruments of the system were selected to control the overall trigeneration system and to analyse the performance of each component. They were the following:

- Four flowmeters: an Annubar flowmeter with integrated pressure and temperature compensation located in the exhaust gas pipeline; a variable area flowmeter (Krohne) for the thermal oil flow rate and two magnetic flowmeters for the hot water and the chiller water circuit flow rate, all controlled by a PLC.
- PT100 temperature sensors (inlet and outlet in all the circuits)
- A thermostat to prevent overtemperature in the thermal oil circuit
- A pressure switch for thermal oil and exhaust gas

A SCADA (Supervisory Control and Data Acquisition system) was selected to control the trigeneration system.

EXPERIMENTAL ANALYSIS OF THE TRIGENERATION SYSTEM

The trigeneration system was installed in CREVER's new test bench at the Rovira i Virgili University in Tarragona (Spain).

In this project the absorption was tested inside an environmental chamber so that its performance could be evaluated in a controlled environment at steady state.

The other components were installed outside the chamber (see figure 3).

A comprehensive database of system conditions was obtained from the test program so that the system performance could be analysed.

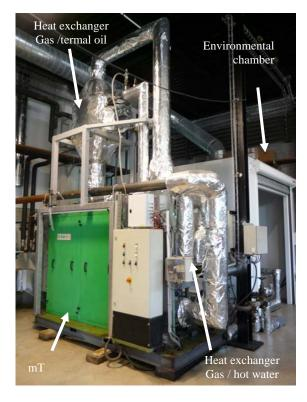


Figure 3: Trigeneration system in the CREVER-URV test bench

Figures 4 and 5 show that as the environmental test chamber temperature increases from 25°C to 35°C, the COP and the cooling capacity of the absorption chiller remain fairly constant and is about 35°C when it begins to decrease rapidly.

The heat input and cooling capacity of the absorption chiller were also evaluated as a function of the MGT output power (see figure 6).

The effect of the thermal oil on the chiller cooling capacity was analysed and showed that as this temperature increases, the cooling capacity also increases (see Figure 7) for a thermal oil temperature range of 145°C to 205°C.

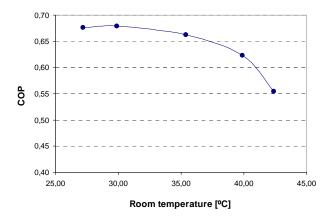


Figure 4: COP of the absorption chiller as a function of ambient temperature for an electrical output power of 20 kW, a chiller temperature of 8° C and a thermal oil flow rate of $2400 \, l/h$

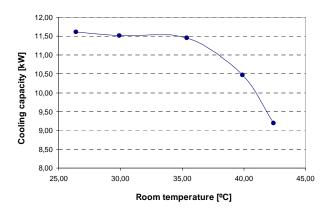


Figure 5: Cooling capacity of the absorption chiller as a function of ambient temperature for an electrical output power of 20 kW, a chiller temperature of 8°C and a thermal oil flow rate of 2400 l/h

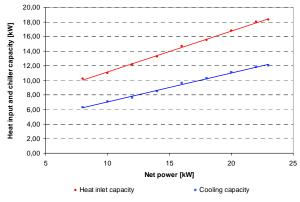


Figure 6: Heat input and capacity of the absorption chiller versus MGT electrical power output for an environmental chamber temperature between 25 and 35°C and a chilled water temperature of 8°C

Experimental results show a marked influence of the output power of the MGT and the driving thermal oil temperature on the cooling capacity of the absorption chiller. The effect of the ambient temperatures between 25°C and 35°C on the cooling capacity of the absorption unit is quite small. However, there is a considerable decrease in the cooling capacity for ambient temperatures higher than 35°C.

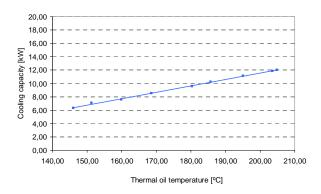


Figure 7: Cooling capacity of the absorption chiller versus thermal oil temperature for an ambient temperature of 35°C and a chilled water temperature of 8°C

MODELLING OF THE AIR-COOLED AMMONIA / WATER ABSORPTION CHILLER

The absorption chiller was modelled using the flowsheet process simulator Aspen Plus (Aspen Plus, 2006) [5]. This program is useful for a variety of steady state modelling applications. It works as a modelling system based on 'blocks'. These blocks are unitary operations which can simulate numerous industrial processes. The various blocks are connected through mass and energy streams in such a way that the complete flowsheet of the process is constructed. Aspen Plus also includes an extensive database that contains the thermo-physical properties of a wide range of chemical compounds, and numerous thermodynamic models to simulate any chemical system.

Darwish et al. (2008) [6] propose a model made with Aspen that simulates a water/ammonia absorption chiller. They compare their results with the experimental data obtained by Lazzarin et al.

(1996) [7] and Hourz & Callander (2004) [8] when testing a direct fired commercial unit. According to Darwish, their Aspen Plus model is in good agreement with the experimental and manufactured data found in the open literature. The model is also useful for studying how modifications in the cycle can improve the COP.

In the present study the model constructed is based on the model developed by Darwish. The specifications of some blocks and operating conditions of the original model have been modified to adjust it to the unit tested, which is driven by thermal oil and not a direct flame using natural gas. The following blocks make up the absorption chiller system model (figure 8):

- The generator. It is modelled through a multistage distillation column, with a partial condenser, a reboiler, a reflux of 0.2 and 6 separation stages. The thermal energy input is the heat transferred by the thermal oil.
- The refrigerant condenser. It is modelled as a total condenser. A stream of air at ambient pressure and temperature given by the climatic chamber is used to produce the condensation effect.
- The subcooler. This block is a heat exchanger in which 20 °C of superheating for the cold stream is specified.
- The evaporator. This is the unit that produces the cooling effect. It is modelled using a heat exchanger in which saturated vapour conditions at the outlet of the equipment are specified.
- The solution cooled absorber. This is the unit where the poor solution (low ammonia concentration) absorbs the refrigerant vapour. It is modelled as a heat exchanger in which the minimum temperature between the hot and cold streams at the outlet is specified at 1 K.
- The air-cooled absorber. After the primary absorber there is still a vapor fraction, so a second absorption stage with heat dissipation by air is required to ensure the total absorption

of the ammonia in the water. This block is modeled through a heat exchanger which uses an external stream of air (at ambient pressure and environmental chamber temperature) to remove the absorption heat. A vapor fraction of zero for the solution is specified at the exit from the block.

The rectifier is the component that minimizes the quantity of water vapour at the generator outlet. Two units are used to model this equipment: the rectifier and a component separator. The rectifier is simulated with a heater in which the energy input is the condensing heat from the generator, and the component separator is the unit that separates the traces of water at the exit from the generator in the model.

It is assumed that there are no pressure drops in any unit, except in the valves.

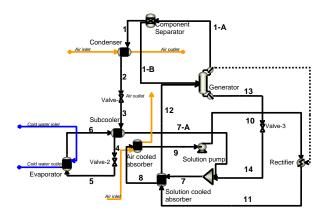


Figure 8: Flowsheet of the absorption chiller model in Aspen Plus

SIMULATION OF THE AMMONIA/WATER CHILLER

The experimental data of the thermal energy transferred by the thermal oil to the generator, and the cooling capacity (therefore the COP) are the principal outputs used to compare the model with the real performance of the chiller, working under the same operating parameters. The principal adjustable model parameters are the operation pressures and the chiller internal flow rates,

because they cannot be directly measured. As an example, table 144 presents the results of one of the simulations for a microturbine power capacity of 18 kW and an ambient temperature of 37°C.

Figures 9 and 10 compare the values of the cooling capacity and the COP obtained experimentally with the same parameters obtained by simulation using data from some of the trigeneration system tests. The agreement between the simulation and experiment results is satisfactory, the highest difference being approximately 4% in cooling capacity and COP.

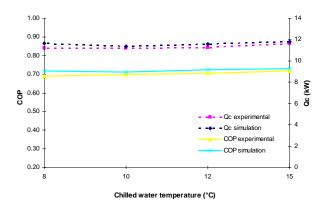


Figure 9: COP and cooling capacity (Qc) with an MGT output of 18 kW and an ambient temperature of 27 °C inside the environmental chamber.

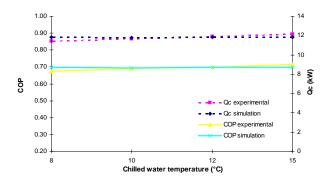


Figure 10: COP and cooling capacity (Qc) with MGT output of 20 kW and air temperature at 28 °C inside the environmental chamber.

Table 1 shows the results of the simulation for all the streams in figure 10 when the microturbine produces 18 kW of electricity and the environmental chamber temperature is 37 °C for a chilled water outlet temperature of 8 °C. Table 2 shows the heat duties of the main components of the cycle for the same conditions as in table 3. For these conditions the simulation returns a solution pump work input of 0.09 kW and a cycle COP of 0.65. This is an interesting scenario because of the high environmental chamber temperature, which implies that the air that is used as a heat sink is still able to dissipate the condensation and absorption heat of the cycle, thus allowing the chiller to produce 10 kW of cooling capacity with a COP of 0.65.

CONCLUSIONS

From the analysis of the experimental tests results for different operating conditions it can be concluded that:

- For an environmental test chamber temperature between 25°C and 35°C, the COP and the cooling capacity remain fairly constant.
- When the environmental test chamber temperature is higher than about 35°C the COP and the cooling capacity decrease rapidly.
- The higher the output power of the MGT and thermal oil driving temperature, the higher the cooling capacity produced.
- The simulation of the ammonia/water absorption air cooled chiller can predict the cooling capacity and COP of the chiller with a deviation below 4%.

ACKNOWLEDGMENTS

The authors would like to acknowledge the funding for this work provided by the Ministry of Industry, Commerce and Tourism of Spain, Plan Nacional de I+D+I, TRIGENED Project, ENE2006-15700-C02-01/CON, and the European Project HEGEL (Contract n° 20153), the Catalan Energy Institute (ICAEN) and IDAE.

Table 1. Simulation results for all the streams of the absorption cycle for the microturbine producing 18 kW of electricity,
an environmental chamber temperature of 37 °C and a chilled water outlet temperature of 8 °C

Stream	Temperature (°C)	Pressure (kPa)	Vapor fraction	Mass flow (kg/h)	NH ₃ concentration (mass %)
1	41.7	1575	1	31.344	99.99
1-A	41.7	1575	1	31.342	100
1-B	41.7	1575	0	0.002	0
2	40.7	1575	0	31.342	100
3	31.2	1200	0.042	31.342	100
4	31.2	1200	0.005	31.342	100
5	6.8	545	0.099	31.342	100
6	6.8	545	1	31.342	100
7-A	26.8	545	1	31.342	100
7	106.6	545	0.510	67.997	48.47
8	93.0	545	0.412	67.997	48.47
9	40.5	545	0	67.997	48.47
10	41.3	1575	0	67.997	48.47
11	71.1	1575	0	67.997	48.47
12	92.0	1575	0.113	67.997	48.47
13	189.2	1575	0	36.655	4.46
14	148.0	545	0.100	36.655	4.46

Table 2 – Heat duties of the main components of the absorption cycle for the microturbine producing 18 kW of electricity, an environmental chamber temperature of $37 \,^{\circ}\text{C}$ and a chilled water outlet temperature of $8 \,^{\circ}\text{C}$

Component	Heat duty (kW)
Evaporator	9.99
Generator	15.47
Condenser	9.96
Solution-cooled absorber	4.49
Air-cooled absorber	15.59
Rectifier	2.68

REFERENCES

- [1] Capstone C30 natural gas or gaseous propane, Product Datasheet, 2003
- [2] Bruno J.C., Massagués Ll., Coronas A., Standalone and grid-connected performance analysis of a regenerative micro gas turbine cogeneration plant. Proc. Instn Mech. Engrs Vol.218 Part A: J. Power and Energy, 2004
- [3] Bruno, J.C., Ortiga, J., Vives, G., Domínguez, F., Cejudo, J.M., Coronas, A., Techno-economic viability of a microtrigeneration system integrated in a low energy demand public building. Int. Conf. on Improving Energy Efficiency in Commercial Buildings, Frankfurt, 2006.
- [4] Catalogue: Hydronic heating and cooling with absorption heat pumps, chillers and chiller-heaters, http://www.robur.com, 2008.

- [5] Aspen Plus, 2006. Aspen Technology, Inc., Ten CanalPark, Cambridge, MA, USA. See also: http://www.aspentech.com.
- [6] Darwish N.A., Al-Hashimi S.H., Al-Mansoori A.S. Performance analysis and evaluation of a commercial absorption-refrigeration water-ammonia (ARWA) system., International Journal of Refrigeration 31, 1214-1223, 2008
- [7] Horuz, I.; Callander, T.M.S., Experimental investigation of a vapor absorption refrigeration system, Int. Journal of Refrigeration 1, 10-16, 2004.
- [8] Lazzarin, R.M.; Gasparella, A.; Longo, G.A., Ammonia-water absorption machines for refrigeration: Theroretical and real performances, International Journal of Refrigeration 19, 239-246, 1996

DESIGN AND ENERGY SAVING ANALYSIS OF TRIGENERATION CONFIGURATIONS IN BUILDINGS

M. A. Marimón, J. Ortiga, J.C. Bruno*, A. Coronas Universitat Rovira i Virgili, CREVER-Research Group on Applied Thermal Engineering, Dept. of Mechanical Engineering, Av. Paisos Catalans, 26, 43007 Tarragona (Spain)

ABSTRACT

The electricity demand for air-conditioning applications in buildings has increased considerably in Europe in recent years, expanding the market potential of small scale trigeneration systems. Trigeneration technology supply all the energy services required in a building with a single integrated unit that produces electricity and recovers waste heat to provide heating, domestic hot water and cooling with different thermally-activated HVAC technologies. The objective of this paper is to analyse and evaluate different trigeneration configurations for buildings. The configurations are designed with three cogeneration technologies and different thermally activated technologies for cooling production. By using the fundamental thermodynamic principle, steady-state thermodynamic modeling and simulation have been done using the Engineerig Equation Solver (EES) software to predict the performance of absorption chillers integrated with CHP units. The technical performance, of each configuration like thermal power, refrigeration and waste heat recovered are presented. For each trigeneration configuration, the calculated parameters are mainly the primary energy saving, CO₂ emissions savings and global performance. The results will be the initial point for selecting the appropiate technology in building applications. This work is carried out in the framework of the TRIGENED project, which aims to provide a technical solution that covers all electrical, environmental and regulatory aspects of trigeneration in buildings.

Keywords: Absorption chiller, trigeneration, energy saving

NOMENCLATURE

Cw: Cooling water Chw: Chilled water

DE: Double effect absorption Chiller

 h_i : Enthalpy of the stream j

HVAC: Heating ventilation and air conditioning

 m_{in} , m_{out} : Input – output mass flow rate

 Q_g : Heating capacity in the high pressure generator

 Q_{gb} : Heating capacity in the low pressure generator

SE: Single effect absorption Chiller x_{in} , x_{out} : Input – output composition

* Corresponding autor: Phone: + 34 977 55 78 91 Fax +34 977 559 691 E-mail: juancarlos.bruno@urv.cat

INTRODUCTION

In the tertiary and residential sector energy demand has experienced a great increase for air conditioning applications in Spain. One of the consequences of this is a high peak load during the summer season and also power supply security problems.

Furthermore the current increasing energy prices and the limitated primary energy resources promotes the use of more efficiency and reliable systems. Trigeneration technologies are able to supply all the energy services required in a building. Several trigeneration configurations with different overall performances could be used to satisfy the energy demand of a building, reducing

their environmental load and energy costs. The performance or viability of the traditional trigeneration systems using single effect absorption chillers, is in many cases low compared with the current state of the art of conventional systems such as high efficiency compression chillers or heat pumps, using electriciy from highly efficient combined cycle power stations. The purpose of this paper is to propose and analyse advanced trigeneration configurations for building applications more efficient and competitive than the traditional trigeneration systems. In this paper the basic and advanced configurations are presented and the results of their simulations are discussed in terms of energy saving and reduction of CO₂ emissions. This work is carried out in the framework of the TRIGENED project, founded by the Spanish Science and Education Ministry. In the next phases of the project the analysed configurations will be tested by the partners of the project.

COGENERATION TECHNOLOGIES AND THERMALLY DRIVEN ABSORPTION CHILLERS

The cogeneration and thermally driven technologies that are considered in this paper are briefly introduced in this section.

Micro gas turbine (MGT)

MGTs can be defined as small, compact highspeed turbo-generators with nominal capacities ranging from 28 to 200 kWe. The exhaust gas heat can be used to drive a thermal cooling technology, delivering simultaneously electrical, thermal and cooling energy. Basically, MGTs are based on a Brayton cycle and usually consist of a centrifugal compressor, a radial turbine, a regenerator and a permanent magnet alternator rotor. In a typical MGT regenerative system, the inlet atmospheric air is filtered and used as a cooling medium for the alternator and electronic devices. The air leaving the alternator is later compressed and passed through the regenerator, where it is preheated with the hot gases leaving the turbine before the combustion chamber. This reduces the amount of fuel used to reach the operating temperature. In the combustion chamber, compressed fuel is burned with excess compressed air to produce hot gas at high temperature and pressure, that is expanded through the turbine. The turbine drive the compressor and the alternator. The turbine exhaust gas goes through the regenerator and can later be fed to a boiler [1], a direct driven absorption chiller [2], or used in any other process.

Internal Combustion Engine (ICE)

The ICE is a proven technology with a wide range of nominal capacities. In addition to fast start-up capability and good operating reliability, these engines has a high effiency at partial load operation obtaining a flexible power source, suitable for a range of different energy applications. Reciprocating engines are by far the most commonly used power generation equipment and recently its application for buildings is growing. CHP systems based on natural gas internal combustion engines are increasingly used as small scale distributed cogenerators taking a very important role in the cogeneration market [3]. The type of cogeneration engine considered in this paper is based on a automotive derived internal combustion engine of 120 kW electrical and 195 kW thermal capacity [3,4]. This engine has a high part load electrical efficiency due to a variable speed operation strategy and uses an advanced exhaust gas after-treatment to meet the most stringent pollutant emission regulations.

Fuel Cell (FC)

A fuel cell is an electrochemical energy device that converts hydrogen (fuel) and oxygen (air) into electricity and heat. The hydrogen can be obtained from a variety of sources but the most common is the reforming of natural gas or other gaseous or liquid fuels. A lot of cases of application and simulation of fuel cells can be found in the literature for example, are presented in Bizarri et al [5] or Erlich and Morini [6]. The fuel cell used in this paper is based on a PEMFC Teledyne Perry 72-cell, supplied by Teledyne Energy Systems and able to operate with pure hydrogen or reformate gas.

Thermally driven absorption chiller

A refrigeration system uses an energy input to produce a cooling effect. In vapor compression system, the energy input is mechanical work, usually an electric motor. In absorption system, the energy input is heat. The water/LiBr absorption chiller can be categorised by the number of effects:

- Single effect (SE), COP ≈ 0.75
- Double effect (DE), $COP \approx 1.2$
- Single/Double effect (SE/DE), COP ≈ 0.9

MODELING OF THE ABSORPTION COOLING SYSTEM

The equations for each component includes mass, energy balance, heat transfer equations. The properties, such as enthalpy and equilibrium functions, are related to the pressure, temperature, composition, and vapor quality of water/steam and sorbent solutions by the empiric correlations in the EES software [7]. EES solves the equations simultaneously by adjusting the estimates to reach a solution.

The model the SE, DE, and SE/DE absorption chillers in steady-state conditions each point of the cycle is characterised by its temperature, pressure, enthalpy, flow rate and composition. The assumptions for each model are shown below.

Model basic assumptions

The following assumptions are used to properly represent the absorption cycle:

- The system operates at steady-state conditions.
- The dilute solution leaving the absorber is in phase equilibrium at the same pressure as the refrigerant from the evaporator.
- Flow restrictors, are isoenthalpic.
- Pump work is isentropic.
- The solution pump is adiabatic.

The stream nomenclature and thermodynamic state points in the SE, DE and SE/DE absorption chillers are shown in Figures 1, 2, and 3.

Mass Balance

For each component of the chiller, the steady-state total mass balance equation can be expressed as:

$$\sum m_{in} = \sum m_{out}$$
 (1)

$$\sum m_{in} \cdot x_{in} = \sum m_{out} \cdot x_{out}$$
 (2)

Where the subscripts in and out mean the streams entering and leaving each of the components and x is a concentration of the water-LiBr solution.

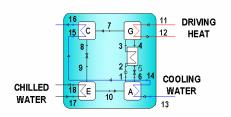


Figure 1. Schematic diagram of a SE absorption chiller

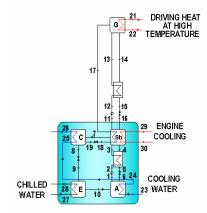


Figure 2. Schematic diagram of a DE absorption chiller

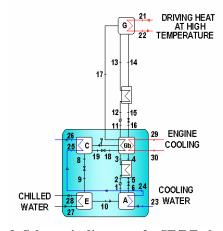


Figure 3. Schematic diagram of a SE/DE absorption chiller

Energy Balance

The steady state energy balance for each chiller component can be expressed as:

$$\dot{Q} + \sum m_i h_i = 0 \tag{3}$$

 $\overset{\cdot}{Q}$ is the heat transfer to or from the system, $\overset{\cdot}{m}$ is the mass flow of each stream and h is the enthalpy of each stream.

Heat transfer models

The UA-LMTD method is used to evaluate the heat transfer of the generator, condenser, evaporator and absorber with the externals flows of the chiller. The product of the overall heat transfer coefficient and the heat exchanger surface area (UA) is relatively constant throughout each heat exchanger at different charge level.

$$UA = \frac{Q}{\Delta T_{LMTD}} \tag{4}$$

The cycle solution heat exchanger is evaluated by the heat exchanger efficiency method (E). This efficiency heat exchanger is defined as the ratio of the actual heat transfer to the maximum possible heat transfer for the given inlet conditions:

$$E = \frac{Q_{act}}{Q_{max}} = \frac{T_{cold,out} - T_{cold,in}}{T_{hot,in} - T_{cold,in}}$$
(5)

Performance of the cycle

The performance of the each cycle is calculated as follows:

SE:
$$COP = \frac{Q_e}{Q_g}$$
 (6)

SE:
$$COP = \frac{Q_e}{Q_g}$$
 (6)
DE: $COP = \frac{Q_e}{Q_{ga}}$ (7)
DE/SE: $COP = \frac{Q_e}{Q_g + Q_{gb}}$ (8)

DE/SE:
$$COP = \frac{Q_e}{Q_g + Q_{gb}}$$
 (8)

DESCRIPTIONS OF THE TRIGENERATION CONFIGURATIONS

To characterise the different trigeneration configurations for buildings the main operating parameters are electricity production, efficiencies, temperatures and flow rates. The trigeneration configurations have been classified into basic and advanced configurations. The basic configurations are those in which chilled water is produced using waste heat at low temperature (around 90°C). The Advanced Configurations are those in which the chilled water is produced using directly the high temperature exhaust gases from a microturbine or a reciprocating engine.

Basic configurations

MGT+SE

This configuration shown in figure 4, is based on a micro gas turbine of 30 kW and an absorption chiller activated with hot water produced with the exhaust gas of the microturbine.

In this trigeneration system it is calculated the performance of the absorption chiller activated at diferent electrical loads of the microturbine (100, 75, 45 %). To tranfer the heat from the flue gas to the hot water it is used a gas/water heat exchanger. The heat exchanger duty available to drive the absorption chiller is 24, 18, 10.8 kW for each MGT load, respectively (Table 1).

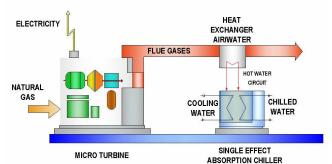


Figure 4. Schematic diagram of the MGT+SE trigeneration system

The operating conditions are showed in table 1. The performance and working parameters of the trigeneration system are listed in table 2.

	Gas/Hot water Heat exchanger					
	100 %	75 %	45%			
MGT exhaust gas temp (heat exchanger inlet) (°C)	276	253	231			
MGT exhaust gas temp (heat exchanger outlet) (°C)	205	190	132			
Flue gas flow rate (kg/s)	0.31	0.26	0.20			
Heat exchanger heat recovery (kW)	24	18	10.8			
Water temp in (°C)	90	88	87			
Water temp out (°C)	85	85	85			
Water flow rate (kg/s)	1.14	1.14	1.14			

Table 1. Operating conditions in the heat exchanger at different MGT loads

	Loading Rate of MGT						
	100 % 75 % 45 %						
Chw temp in/out (°C)	12/7	12/10	12/11				
Cw Temp in/out (°C)	28/33	28/30	28/29				
Hot water temp in/out (°C)	90/85	88/85	87/85				
Chiller capacity (kW)	19.4	14.8	8.6				
Cooling capacity (kW)	43.4	32.8	19.4				

Table 2. Performance of the absorption chiller at different MGT loads

ICE+SE

The SE absorption chiller is activated with the hot water of the engine cooling system (figure 5). The temperature at the hot water outlet of the engine is around 90 °C and 85 °C at the inlet. The flue gases at high temperatures could be used for other applications or to produce additional hot water at 90 °C. The main operating parameters of the system are shown in table 3.

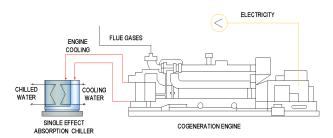


Figure 5. Schematic diagram of the ICE+SE trigeneration system

	ICE Load					
	100 %	75 %	45 %			
Chw temp in/out (°C)	12/7	12/7.9	12/8.8			
Cw temp in/out (°C)	28/44.7	28/41.1	28/38.1			
Hot water temp in/out (°C)	92/85	92/84	92/85			
Chiller capacity (kW)	74.1	57.8	44.3			
Cooling capacity (kW)	177.1	138.2	105.9			
ICE exhaust gas temp (Heat exchanger inlet) (°C)	719	660	587			
ICE exhaust gas temp (Heat exchanger oulet) (°C)	120	120	120			
Heat recovered (kW)	103	80.4	61.6			

Table 3. Performance of the ICE+SE configuration at ICE full and partial load

FC+SE

This trigeneration configuration consists of a fuel cell PEMFC and a single effect absorption chiller (figure 6). The PEMFC stack is designed to be operated with a diesel reformer still under development. This PEMFC has been tested in the INTA laboratories under different operating

conditions (temperature, pressure and voltages [8]. The results from these tests have been used to obtain the efficiency curves as function of fuel cell load. For 5 kWe of power capacity, the thermal efficiency of the FC is 0.37 [9]. The main characteristics of the configurations are shown in table 4.

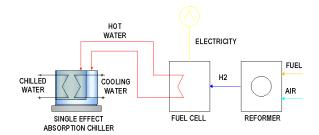


Figure 6. Schematic diagram of the FC+SE trigeneration system

FC+SE parameters	
Chw temperature in/out (°C)	13/10
Cw temperature in/out (°C)	25/32
Hot water temperature (°C)	70
Chiller capacity (kW)	5
Cooling capacity (kW)	12
Power capacity (kWe)	5
Heat recovered (kW)	7
Energy Hidrogen Consumption	18.91

Table 4. Performance of the FC + SE configuration

Advanced configurations

MTG+DE

The direct use of the exhaust gases from the MGT increases the performance of the absorption chiller since the higher activation temperature increases the overall performance of the system. The intermediate heat exchanger in this case is unnecessary, (figure 7). The exhaust gas passes directly through the generator of the double effect absorption chiller. The performance at different MGT loads is shown in table 5.

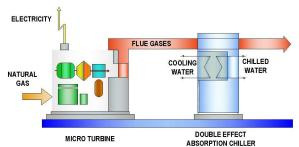


Figure 7. Schematic diagram of a MGT+DE trigeneration system

	MGT Load				
	100 %	75 %	45 %		
Chw temp in/out (°C)	12/7	12/8	12/9		
Cw temp in/out (°C)	28/36	28/34	28/31		
Chiller capacity (kW)	72	51.6	35.4		
Cooling capacity (kW)	132	94.6	64.9		
MGT exhaust gas temp (Generator inlet) (°C)	276	253	231.1		
MGT exhaust gas temp (Generator oulet) (°C)	130	131	134		
Heat recovered from exhaust gas (kW)	46	32	20.8		
Flow rate exhaust gas (kg/s)	0.31	0.26	0.20		
MGT fuel consumption (kW)	115.4	87	61.2		

Table 5. Performance of the MGT+DE trigeneration system at different MGT loads

ICE+SE/DE

In this configuration the absorption chiller is driven by heat recovered from the engine exhaust gas and from the water engine cooling system (Figure 8). The main performance parameters of this configuration are presented in table 6. The type of cogeneration engine considered in this configuration is based on a automotive derived internal combustion engine of 120 kW electrical and 195 kW thermal capacity.

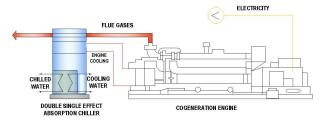


Figure 8. Schematic diagram of a ICE+SE/DE trigeneration system

	ICE Load				
	100 %	75 %	45 %		
Chw temp in/out (°C)	12/7	12/7	12/7		
Cw temp in/out (°C)	28/39	28/37	28/35		
Chiller capacity (kW)	177.5	126.2	100.9		
Cooling capacity (kW)	369.3	266	212		
ICE exhaust gas temp (°C)	719	660	587		
Flow rate exhaust gas (kg/s)	0.31	0.26	0.20		
Hot water temp in/out (°C)	92/85	92/84	92/85		
Recovered waste heat (ICE cooling) (kW)	103	80.4	61.6		

Table 6. Performance of the ICE+SE/DE trigeneration system at different ICE loads

ENERGY SAVING ANALYSIS

To evaluate the trigeneration configurations, a suitable indicator to assess the performance of a combined energy system should be used and compared with a "Conventional" system the one used here is the Trigeneration Primary Energy Saving (TPES) [10]:

$$TPES = \frac{F^{sp} - F_z}{F^{sp}} = 1 - \frac{F_z}{\frac{W_z}{\eta_e^{sp}} + \frac{Q_z}{\eta_e^{sp}} + \frac{R_z}{\eta_e^{sp} \cdot COP^{sp}}}$$

Where,

 F_z = Overall primary energy energy input.

 F^{sp} = Total fuel energy input required for the SP (Separate production) of the same energy vectors, W_z , Q_z , R_z produced in trigeneration configuration.

 W_z = The net trigenerated electricity output. –

 Q_z =The net useful trigenerated heat output.

 R_z = The net trigenerated cooling energy output.

To evaluate the impact of the selection of the numerical values for the *SP* three efficiency escenarios are defined (table 7).

	Efficiency	η_e^{sp}	$oldsymbol{\eta}_{\scriptscriptstyle t}^{\scriptscriptstyle sp}$	COP^{sp}
Α	Low efficiency	0.34	0.8	2.5
В	Intermediate	0.45	0.9	4
С	State of the art	0.55	0.98	6

Table 7 Efficiency Scenarios

For each configuration it was calculated the saving (TPES) with respect conventional system with separate production electricity, heat and cooling. This indicator and the CO₂ emmision savings have been calculated considering one hour of operation at each load level for the trigeneration system. The results are presented in tables 8 and 9. As a guide in this tables are guiven also estimates for the especific costs of each configuration. These have to be taken as tentative values because not all the components are fully commercialised. In all the cases, the energy saving are worst than the C scenario (state of the art of the conventional system). This is due to the high efficiency system considerate for the state of the art scenario (best technologies that can normally be encountered today). For the intermediate and low efficiency scenarios, some configurations have a higher energy saving than the reference scenario. The trigeneration configuration with the highest energy saving is ICE+(DE/SE and SE) in the A scenario (Low efficiency).

CONCLUSIONS

Basic and advanced trigeneration configurations have been simulated for one hour of operation to calculate an energy saving indicator with respect to the conventional case with separate production of electricity, heating and cooling. With the configuration ICE+DE/SE it is posible to obtain an energy saving up to 39 %, at 45% of the load in the low efficiency escenario, due to the variable operation of this engine and high efficiency at partial load, as mentioned previously. Engine characteristics relating to electrical and thermal efficiency are contants at different percentage of the engine load.

The relation of chiller capacity and the fuel comsuption in the ICE+SE/DE at 45 % of the load is more higher than of other engine load allow that the TPES value is increasing as the percentage of engine load decreases. The configuration with the highest CO₂ emissions savings assuming one hour of operation is the ICE+DE/SE with 39.7 kg of CO₂/hour. In the next phases of the project some of these configurations will be tested and the results compared with those of the present simulations.

ACKNOWLEDGMENTS

The authors would like to acknowledge the funding for this work provided by the Spanish Ministry of Education and Science (TRIGENED Project, ENE2006-15700-C02-01/CON). M.A. Marimón acknowledges for the scholarship, BES-2007-16086 of the Spanish Ministry of Education and Science.

REFERENCES

- [1] Bruno. J.C, Massagués. L.I and Coronas. A, Stand-alone and grid-connected performance analysis of a regenerative micro-gas turbine cogeneration plant, Inst Mech Eng, Part A: J Power Energ 218 (2004), pp. 15–22.
- [2] Bruno. J.C, Valero. A and Coronas. A. Performance analysis of combined microgas turbines and gas fired water/LiBr absorption

- chillers with post-combustion, Appl Therm Eng 25 (2005), pp. 87–99.
- [3] Badami. M, Casetti. A, Campanile. P, Anzioso. F. *Desing and performance of and innovative 120 kWe natural gas cogeneration system.* Energy 32 (2007) pp. 823-833.
- [4] Badami. M, Mura. M, Campanile. P, Anzioso. F. Desing and performance evaluation of an innovative small scale combined cycle cogeneration system. Energy 33 (2008) pp.1264-1276.
- [5] Bizarri. G, Morini. G.L. *Greenhouse gas reduction and primary energy saving via adoption of fuel cell Irbid plant in a hospital*. Applied Thermal Engineering, 24 (2004) pp 383-400.
- [6] Azmy A. M, Erlich. I. Intelligent operation managment of fuel cells and microturbines using genetic algorithms and neural networks. (2004) New and Renewable Energy Technologies for Sustainable Development (pp 53-66)
- [7] Engineering Equation Solver, (EES) F-Chart Software. www.fchart.com/ees/ees.shtml
- [8] Rosa. F, López. E, Briceño. Y, Sopeña. D, Navarro. R.M, Alvarez. M.C, Fierro. J.L.G. Bordons. C. *Desing of a diesel reformer coupled to a PEMFC*. Catalysis Today 116 (2006) pp.324-333.
- [9] Ortiga. J, Marimon. MA, Bruno. J.C, López. E, Coronas. A. *Integration of new small scale sorption chillers with a pem fuel cell of 5 kw*. HYCELTEC 2008. I Simposium Ibérico de Hidrógeno, Pilas de Combustible y Baterías Avanzadas. UPV Julio 2008 (Bilbao).
- [10] Chicco. G, Mancarella. P. Trigeneration primary energy saving evaluation for energy planning and policy development Energy Policy, 2007, vol. 35, issue 12, pp. 6132-6144.
- [11] WADE-World Alliance for Decentralized Energy. "Guide to descentralized energy technologies. www.localpower.org/
- [12] Absorsistem S.L., www.absorsistem.com.
- [15]Rotartica, www.rotartica.es.

CONFIGURATIONS		MGT+SE			ICE+SE		FC+SE	
Load Charge (%)	100	75	45	100	75	45	100	
Fuel Consumption (kW)	115.36	87.00	61.19	355.2	259.7	176.9	27.01	
Electricity (kWe)	28	21.75	13.95	117.21	88.29	58.37	5	
COP Absorption chiller	0.7	0.77	0.77	0.73	0.76	0.78	0.71	
Chiller Heat Input (kW)	23.94	18	10,8	103.7	80.4	61.6	7	
Chiller Capacity (kW)	18.35	13.86	8.34	75.4	61.8	48.6	5	
Unrecovered Waste Heat (kW)	35.8	25.74	8	92.3	60.8	35.8	0	
Scenario A - TPES Low (%)	22.41	22.63	-0.6	35.26	36.41	35.34	-31.19	
Scenario B - TPES Intermediate (%)	-2.82	-2.7	-37.4	12.25	12.88	9.97	-94.47	
Scenario C - TPES State of art (%)	-24.04	-24.26	-69.7	-7.61	-7.62	-12.39	-154.66	
Fuel Consumption (kWh) Trigeneration Configuration	115.36	87	61.1	355.5	259.7	176.9	27.01	
Fuel Consumption (kWh) Separate Production (Low)	148.69	112.45	60.84	549.12	408.40	273.62	20.58	
Kg CO ₂ /h Trigeneration Configuration	23.07	17.4	12.23	71.1	51.94	35.38	5.40	
Kg CO ₂ /h Separate Production (Low)	29.73	22.49	12.16	109.82	81.68	54.72	4.11	
Kg CO ₂ /h Saving (Low)	6.66	5.09	-0.07	38.72	29.74	19.34	-1.28	
Cogeneration Cost (€/kW)	generation Cost (€/kW) 1600 [11] 1000 [11]			3000 [11]				
Absorption Chiller Cost (€/kW)	1400 [12]		344 [12]			1800 [15]		
Total Investment Cost (€/kW)		3000			1344		4800	

Table 8 Energy saving at different load (%) and technology costs in the case of basic configurations

CONFIGURATIONS	1	MGT+DE			ICE+DE/SE		
Load Charge (%)	100	75	45	100	75	45	
Fuel Consumption (kW)	115.36	87.00	61.19	355,5	259,7	176,9	
Electricity (kWe)	28	21,75	13,95	117,3	88,2	58,3	
COP Absorption chiller	1.2	1.2	1.2	0.92	0.9	0.9	
Chiller Heat Input (kW)	46.41	32.46	20.81	191.2	139.7	111.1	
Chiller Capacity (kW)	58	32.5	20.8	177.5	126.2	100.9	
Unrecovered Waste Heat (kW)	10.23	8.86	7.85	0	0	0	
Scenario A - TPES Low (%)	29.3	23.1	18.7	35.81	36.37	39.08	
Scenario B - TPES Intermediate (%)	-9.00	-14.1	-19.3	1.06	2.48	4.78	
Scenario C – TPES State of art (%)	-46.1	-48.8	-54.2	-33.10	-30.6	-29.3	
Fuel Consumption (kWh) Trigeneration Configuration	0.11	0.087	0.06	0.35	0.25	0.17	
Fuel Consumption (kWh) Separate Production (Low)	0.16	0.11	0.075	0.55	0.40	0.29	
Kg CO ₂ /h Trigeneration Configuration	23.08	17.40	12.24	71.13	51.96	35.39	
Kg CO ₂ /h Separate Production (Low)	32.68	22.66	15.06	110	81.67	58.10	
Kg CO ₂ /h Saving (Low)	9.60	5.25	2.82	39.69	29.70	22.71	
Cogeneration Cost (€/kW)		1600			1000		
Absorption Chiller Cost (€/kW)	1600 160		1600				
Total Investment Cost (€)		3200			2600		

Table 9 Energy saving at different load (%) and technology costs in the case of advanced configurations

SPEEDING UP STARTUP OF A THERMAL POWERPLANT

Helge Didriksen* and Claus Perstrup **DONG Energy Denmark**

ABSTRACT

An installation of a new deNOx system at the thermal power plant "Studstrupværket" outside Århus, Denmark has resulted in new requirements for the startup of the plant. It is of greatest importance that the power plant, when taken out of operation, can be started up again faster than the contractual startup time of the plant, since the plant delivers district heating to the city of Århus.

This situation initiated an analysis/optimization of the startup problem. A key element in the work was development of a modular dynamic model of the optimization problem. The results of this work have been discussed with the operators at the power plant and have successfully contributed to a considerable reduction in the power plant startup time. Keywords: Dynamic simulation, thermal power plant, start up procedure, Matlab/Simulink

NOMENCLATURE

Nusselts number [-]

distance between heat

Nu

pitch

exchanger tubes [m]

Abbrevia	utions	Subscripts	
T	temperature [°C]	a	air
m	mass [kg]	m	metal
h	specific enthalpy [kJ/kg]	W	water (liquid)
	(used in energy balances)	S	steam (vapour)
W	mass flow [kg/s]	h	hot
Q	heat [kW]	c	cold
U	internal energy [kJ]	i	volume element number
V	volume [m ³]	tube	tube in heat exchanger
C_{p}	specific heat capacity [kJ/kg °C]	bank	bank of tubes, heat exchanger
h	heat transfer coefficient [kW/m ² °C]		
	(used in heat transfer)		
k	mass flow coefficient [kg/ m ³ s]	INTRODUCTION	
ρ	density [kg/m ³]		
ν	kinematic viscosity [m ² /s]	Thermal power plants are, from time to time, taken	
λ	thermal conductivity [kW/m°C]	out of operation from several possible reasons,	
V	air velocity [m/s]	planned audit, plant malfunction, the electricity	
d	heat exchanger tube diameter [m]	marked situation or local heat/electricity demand.	
Re	Reynolds number [-]	The power	r plant is normally not held warm in such
Pr	Prandtls number [-]		

^{*} Corresponding author: phone: +45 99 55 25 73

e-mail: heldi@dongenergy.dk

a situation and the whole plant is therefore cooled down. Getting the power plant back in production mode again requires a long startup procedure. The plant must be heated up again, some 2000 tons of steel for a medium size power plant. The plant must not be warmed up to quickly as the equipment, in that case, will be damaged. The boiler must even be heated up to a certain level before fuel can be added and ignited. This heating up can be time consuming, especially when only a small heat source is available.



Figure 1: "Studstrupværket" power plant

Recently, a new deNOx system was installed at DONG Energy's power plant "Studstrupværket" outside Århus, Denmark (figure 1). This resulted in a more complicated startup of the plant and the startup time became critical. This called for an optimization of the startup procedures involving process analysis, plant experiments and dynamic modeling and simulation.

Startup at "Studstrupværket"

In the early heat up procedure, which is in focus in this work, the boiler process is heated up by means of hot water from the feedwater tank. The feedwater tank represents a large reservoir of hot water. The water is pumped from the feedwater tank through the economizer and further through the evaporator tubes surrounding the lower part of the boiler room. Both the economizer and the evaporator are empty before the heating and the startup also includes a fill up of water in the boiler. The water flows from the evaporator through the separator vessel ("bottle"). From here, the water

can either be recirculated back to an inlet before the economizer or the water can be discharged into the cooling channel. Steam and cold water can (should) be added to the feedwater tank continuously to maintain a desired water level and temperature in the tank.

Before the new deNOx system was installed at the "Studstrupværket" plant, the early heating was a fairly easy task. The boiler was filled with hot water and the water was flowing through the evaporator tubes for some time. Preheated air was, at the same time, blown through the boiler room. One purpose here was to achieve a somewhat lukewarm boiler room to prevent the oil burners to extinguish shortly after ignition. Installation of the deNOx system has complicated the startup, however. It is absolutely necessary that the deNOx catalyst elements are heated up to a certain level before ignition of the burners. Otherwise condensation on the catalyst elements will occur and along with condensation fouling of the catalyst with dust and ashes. This will result in a degraded catalyst, and this is not an option.

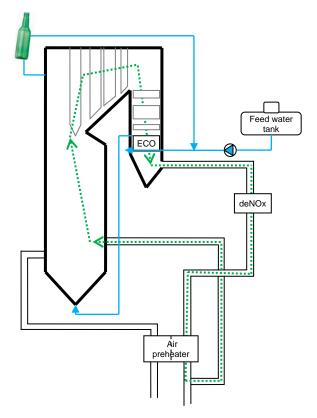


Figure 2: "Studstrupværket" boiler, schematic

Figure 2 shows the boiler process and the boiler elements being part of the early heating procedure. Air is flowing through the boiler system as indicated with the dashed line with arrows indicating the flow direction. Note that the air now is flowing recirculated in a "closed loop". Hot water is pumped from the feedwater tank through the economizer and evaporator and is possibly (partly) recirculated to an inlet before the economizer. Heat is transferred from the warm economizer to the deNOx system by the circulating airflow. Through the heated circulating air, heat is inevitably also transferred to the air/air preheater and the several superheaters in the boiler.

MODELING

In order to do some process analysis and optimization of the start-up procedure, a dynamic model of the relevant part of the boiler process was specifically developed, designed to simulation of this start up problem. The simulation/optimization problem is illustrated schematically in figure 3. Air is circulated in a closed loop and there is heat transfer between air and the different heat exchangers, shown as red arrows in the figure. The key temperature in the analysis is the air temperature after the deNOx equipment, indicated with a thermometer in the figure. This temperature should reach a value of 71 °C as quickly as possible.

The model must be able to simulate relevant temperatures at various positions in the process and at various conditions in the start-up sequence, variations initiated by different air flows and water flows and temperatures. The model is used to simulate slower changes in a sequence that has duration of 2-6 hours. Hence, the low frequency dynamic behavior is in focus. Making qualitative reasonable simulations with a reasonable accuracy is the scope and the use of a model that in some senses is a bit coarse, is justified.

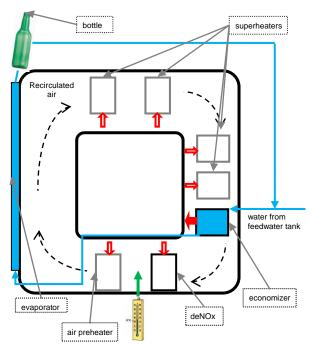


Figure 3: Elements of startup problem

The model is structurally designed by a number of model modules, each representing the different types of elements in the boiler process. The following modules are developed:

- economizer: mass and energy balances of water and metal (combined), heat transfer water/metal/air
- superheater/deNOx: energy balance of metal, heat transfer metal/air
- air/air preheater: energy balances of air cold and hot side, energy balance of metal, heat transfer air/metal/air
- boiler room: energy balances of air
- evaporator and pipe: mass and energy balances of water and metal (combined), heat transfer water/metal
- feedwater tank: mass and energy balance of water and metal

The model is based upon first principles, energy and mass balances of the water system, the air system and the many metal elements that are a part of the boiler process.

Model equations

The energy balances for water and metal are combined for the economizer, the pipe and the feedwater tank module. Hence the temperatures of metal and water are assumed to be identical for these modules.

The economizer and pipe modules are modeled as distributed parameter systems. This is done practically by representing these elements by 5 CSTR (Continuously Stirred Tank Reactors) in series, a common modeling procedure in such a case.

The boiler room is also made in this way and a number of volumes corresponding to the number of heat exchangers adjoining the boiler room. One boiler room volume exchanges heat with one heat exchanger.

Superheater and deNOx

$$Q_a = h_a (T_a - T_m) \tag{1}$$

$$\frac{dT_m}{dt} = Q_a / \left(m_m c_{p,m} \right) \tag{2}$$

Economizer

$$Q_a = h_a \left(T_a - T_m \right) \tag{3}$$

$$w_{w,i} = \left(m_{w,i}/\rho_w - V_i\right)k \tag{4}$$

$$\frac{dm_{w,i}}{dt} = w_{w,i-1} - w_{w,i} \tag{5}$$

$$\frac{dU_{w,i}}{dt} = w_{w,i-1}h_{w,i-1} - w_{w,i}h_{w,i}$$
 (6)

$$\begin{split} \frac{dT_{wm,i}}{dt} &= \left(\frac{dU_{w,i}}{dt} - \frac{dm_{w,i}}{dt}T_{wm,i}c_{p,w} - Q_a\right) / \\ \left(m_{w,i}c_{p,w} + m_{m,i}c_{p,m}\right) \end{split} \tag{7}$$

Air/air preheater

$$\frac{dT_{a,c}}{dt} = \left(w_a \left(h_{a,c,in} - h_{a,c} \right) + Q_{a,c} \right) / \left(m_{a,c} c_{p,a} \right)$$
 (8)

$$\frac{dT_{a,h}}{dt} = \left(w_a \left(h_{a,h,in} - h_{a,h} \right) - Q_{a,h} \right) / \left(m_{a,h} c_{p,a} \right) \quad (9)$$

$$\frac{dT_{met}}{dt} = \left(Q_{a,h} - Q_{a,c}\right) / \left(mc_{p,m}\right) \tag{10}$$

Boiler room

$$\frac{dT_{a,i}}{dt} = \left(w_a \left(h_{a,i-1} - h_{a,i} \right) - Q_{a,i} \right) / \left(m_a c_{p,a} \right)$$
 (11)

Feedwater tank

$$\frac{dm_{w}}{dt} = w_{w,in} - w_{w,out} + w_{s} \tag{12}$$

$$\frac{dU_{w}}{dt} = w_{w,in}h_{w,in} - w_{w,out}h_{w} + w_{s}h_{s}$$
 (13)

$$\frac{dT_{wm}}{dt} = \left(\frac{dU_{w}}{dt} - \frac{dm_{w}}{dt}T_{wm}c_{p,w}\right) / \left(m_{w}c_{p,w} + m_{m}c_{p,m}\right) \tag{14}$$

Evaporator and pipe

Same equations as economizer, but without Q_a and Q_w . The heat transfer from the evaporator to the circulating air is neglected.

The state variables in the model are temperatures of air, water and metal and masses of water.

Note that internal energies, U, are not state variables in the model, even though the equations (6) and (13) are expressed as differential equations. dU/dt are merely intermediate variables for the dT/dt expressions.

Energy balances for water and metal are combined for economizer, evaporator, pipe and feedwater tank (one joint temperature, T_{wm}).

Equation (4) expresses the mass flow from one CSTR-volume to the next. The mass flow exceeds zero only when the volume is totally filled with water. This ad hoc way of calculating the mass flow is done to simulate the filling of the pipes and economizer in a simple way.

The heat transfer coefficient for the heat transfer between metal and air is modeled in a rigorous way. This is done for several reasons. The air metal heat transfer is a very essential effect in the process taking place and in the heating of the deNOx material in particular. The model should be able to represent this effect with a reasonable accuracy. Furthermore, it is important that the model can capture the correlation between the boiler air flow and heat transfer. The air flow and air temperature is relatively low, compared to normal operation. However large variations in the airflow in percentage terms can occur, having a large effect on the heat transfer. The air/metal heat transfer is modeled according to the equations below [1].

$$Re = v_a d_{tube} / v_a (T_a)$$
 (15)

$$Nu_{tube} = 0.3 + \frac{0.62 \operatorname{Re}^{1/2} \operatorname{Pr}^{1/3}}{\left(1 + \left(0.4 \operatorname{Pr}\right)^{2/3}\right)^{1/4}}$$

$$Nu_{bank} = \left(1 + \frac{2}{3 + \operatorname{pitch}_{tubes}/d_{tube}}\right) Nu_{tube}$$
(15)

$$Nu_{bank} = \left(1 + \frac{2}{3 + pitch_{ubes}/d_{ube}}\right) Nu_{tube}$$
 (17)

$$h_a = \frac{Nu_{bank}\lambda_a(T_a)}{d_{ube}} \tag{18}$$

The final total dynamic model of the boiler startup process is accomplished rather easily by combining and connecting the different modules in such a way that the model represents the actual process and has the same structure as illustrated in figure 3.

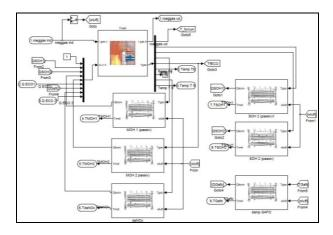


Figure 4: Boiler room, superheaters and deNOx modules connected.

modules implemented the are Matlab/Simulink modeling environment. Figure 4 shows a part of the model where superheater modules are connected with the boiler room module.

MODEL VERIFICATION

In connection with the analysis of the startup procedure, a startup test was performed at the "Studstrupværket" plant. The purpose of this test was to gain process knowledge in a more systematic way. The test was performed prior to the modeling work started and the test was not designed for model verification, specifically. The test was also made before the deNOx system elements were installed at the plant.

The start-up procedure used in the test was as follows (the short version):

- The boiler is filled with water from the feedwater tank and water is flowing through the boiler for approximately 30 minutes.
- A 50 minute "break" then follows (not planned) where there is no flow of water or air in the boiler.
- After this "break", water flows through the boiler again, this time with a high degree of recirculation of water from the separator vessel ("bottle").
- At the same time the temperature in the feedwater tank is raised slowly.
- Simultaneously, the circulation of air is started with 50 kg/s and then, 80 minutes later, raised to 80 kg/s.

The flow and temperature of the water entering the economizer is shown in figure 5 and figure 6.

The figures 7 and 8 compare the model simulation and the measured process data. Figure 7 shows the temperature in the boiler room before the superheaters and figure 8 shows the temperature of the water leaving the "bottle".

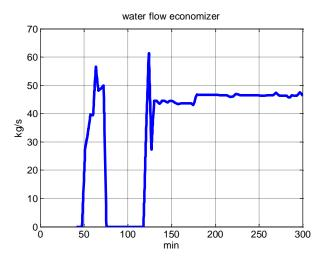


Figure 5: Water flow into economizer

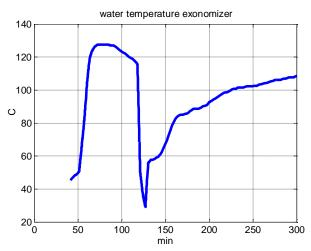


Figure 6: Temperature of water into economizer

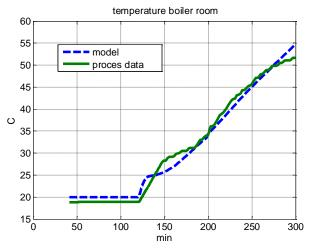


Figure 7: Temperature in boiler room

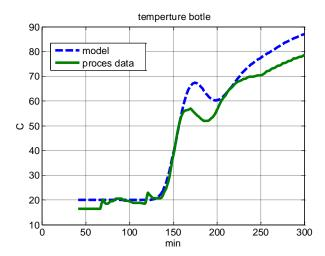


Figure 8: Temperature of water out of bottle

From the figures it is seen that there is not a perfect match between model results and the measured process values. Even though, the model is appraised to have "passed the test" and is trusted to be a valuable tool to evaluate the effects of changes in the start-up procedure.

It should also be mentioned here, that the model validation is sensitive to measurement errors/biases.

ANALYSIS AND OPTIMIZATION

The test procedure described above represented, at that time, an initial guess of a reasonable start-up procedure where much of the customary way of dealing with start up at the plant was maintained, (with an exception of the so called "break", which was unplanned). In the simulation exercise it is allowed, at no risk, to try out new solutions It may, of course, turn out that some of the suggested solutions based upon the simulation model turns out not to be feasible due to some practical reasons or restrictions. This will, if so, be exposed in a constructive dialogue with the operators at the plant.

There are a number of optimization handles in this optimization problem, a number of process variables that can be varied in time within some limits:

- The circulation air flow in the boiler
- The recirculated flow of water from the "bottle" into the economizer inlet
- The flow of water from the feedwater tank
- The setpoint to the temperature (actually pressure) of the feedwater tank (controlled by steam inlet flow)

A large number of simulations have been made. The many simulation results gave us an overview of the effects of making the different changes in the procedure. The simulations also made us confident that the altered procedures will not represent any risk for the boiler equipment.

It would not have been possible to carry out this investigation by making start up tests at the plant only.

The following recommendations were presented and discussed with the operators at "Studstrupværket":

- Minimize the recirculation of water from the "bottle" to the economizer inlet and preferably reduce the flow to zero.
- Start the circulation of air as early as possible, together with the filling of the boiler.
- Maximize the air flow circulation.
- Use a high water-flow from the feedwater tank (tank water level must be supervised).
- Raise the temperature in the feedwater tank.

Figure 9 shows the simulated air temperature after the deNOx system from three simulation cases.

The first case (solid line) is the "base case" which is more or less the same as the test case described in the model validation. The unplanned "break" is however left out and the process values are more ideal stair signals. The air temperature after the

deNOx system reaches 71 °C after approximately 300 minutes. An air temperature of 71 °C after deNOx is the "go signal" for ignition of the burners.

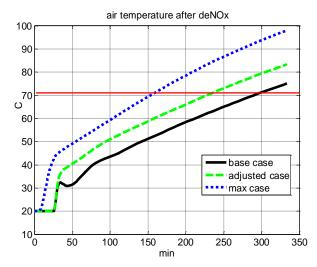


Figure 9: Air temperature after deNOx

In the next case (dashed line), "the adjusted case" one adjustment to the base case is made, only. The adjustment is that the flow of recirculated water flow from the bottle to the economizer inlet is omitted. This means that after the filling of the boiler is finished, the water flow through the boiler is reduced from 50 kg/s to 20 kg/s, and water comes directly from the feedwater tank only.

In the last case shown (dotted line), the max case, several other adjustments are made, in addition to the adjustment in "the adjustment case". The air flow is increased from 80 kg/s as in the previous cases, to 120 kg/s. Furthermore, the air circulation begins at the same time as the water starts flowing into the economizer. In the previous cases, the air circulation starts just after the boiler is filled with water. The temperature of the water in the feedwater tank is 140 °C from the very beginning while in the previous cases the temperature starts at 120 °C and increases towards 140 °C after the boiler is filled with water. Finally, the water flow from the feedwater tank is held at 30 kg/s after the boiler is filled with water (rather than 20 kg/s). The start-up time for this procedure is approximately 150 minutes, which is half of the time used in the base case.

CONCLUSION AND REMARKS

An analysis and optimization of the startup procedure at the "Studstrupværket" thermal power plant has been carried out successfully. A key element in this work has been development and use of a dynamic simulation model of the optimization problem. A valuable mapping of the effects of different changes in the startup procedure is achieved.

Based on the work described in this paper, the startup procedure at the power plant has been changed. It is estimated that a reduction in the startup time of 2 hours is achieved. This has contributed to the ability to keep the total startup time below the contractual startup time of the plant. On top of this, it is estimated that the reduced startup time has an economical profit of approximately 200.000 DKR per year.

The simulation tool is also being used to analyze and optimize the startup procedures for other thermal power plants in DONG Energy.

REFERENCES

[1] Mills A. F. Chapter 4 Convection fundamentals and correlations. In: Heat and mass transfer. Richard D. Irwin, INC, 1995.

Fuels 2



EXPERIMENTAL AND COMPUTATIONAL STUDY OF PARTICLE MINIMUM FLUIDIZATION VELOCITY AND BED EXPANSION IN A BUBBLING FLUIDIZED BED

Chameera K. Jayarathna¹, Britt M. Halvorsen^{1,2}

¹ Telemark University College, Porsgrunn, Norway ²Telemark Technological R&D Centre, Porsgrunn, Norway

chameera80@yahoo.com (Chameera Jayarathna)

ABSTRACT

The aim of this work is to study flow behavior in a fluidized bed with different mixtures of particles. The efficiency of fluidized bed reactors depends on bubble distribution, bubble size and bubble velocity within the reactor. The bubble behavior depends on the amount of excess air introduced to the reactor. Experiments are performed in a cylindrical bed with a uniform air distribution. Spherical glass particles with different mixtures of particles are used in the experiments. The minimum fluidization velocity and the bed expansion are observed for two different powders and mixtures of the powders. Corresponding simulations are performed by using the commercial CFD code Fluent 6.3. The computational results are compared to the experimental data and the discrepancies are discussed.

1 INTRODUCTION

Fluidized beds are widely used in industrial operations. Good mixing and large contact area between phases, enhances chemical reactions, heat transfer and mass transfer. Fluidized beds have the ability to operate smoothly because of a liquid like behavior of particles. In a well mixed bed, isothermal conditions are obtained and hence the operation can be controlled simply and consistently. Fluidized bed is used in chemical industry in two main types of reactions, in catalytic gas phase reactions where the particles influence on the reaction velocity without being consumed, and in gas-particle reactions. Pure silicon is needed in the production of solar cells and a gas-particle reaction in a fluidized bed can be used in one term of the purification process. The fluidized bed replaces the highly energy consuming process term that is commonly used today. The gas-particle reaction is a continuous process where the particles are fully consumed during the reaction and the particles in the reactor have large range of particle sizes. In a reactor like this, the temperature becomes very high, and it is extremely important to keep the particles fluidized and well mixed.

Fluidization and bubble formation depend very much on the particle characteristics. The behaviour of particles in fluidized beds depends on a combination of the particle size and density. Geldart fluidization diagram [1] is used to identify characteristics associated with fluidization of powders. Powders characterized within Group A are easily fluidized and give a high bed expansion before bubbles appear.

This type of powders has the most desirable properties for fluidization, and is mostly used as catalyst in fluidization system. For group B particles the bed expansion is low, and bubbles will appear as soon as the gas velocity reaches the minimum fluidization velocity [2]. Geldart diagram is based on mean particle diameters, but earlier studies have shown that powders with a range of particle sizes cannot be characterized from the mean diameter only [3, 4, 5, 6]. The fluidization properties are highly influenced of the bulk density, and the bulk density change with the particle distribution. The bubble behavior depends on the amount of excess air introduced to the reactor. The excess air is the actual superficial velocity minus the minimum fluidization velocity. The excess air is also defined as the air leaving the bed with the bubbles.

The amount of excess air should be sufficient to give a good mixing of the bed. In this work the minimum fluidization velocities for different mixtures of particles are studied.

2 COMPUTATIONAL MODEL

Two dimensional computational studies have been performed on the fluidized bed. The simulations are performed by using the commercial CFD code Fluent 6.3. The model is based on an Eulerian description of the gas and the particle phases. The combinations of models used in this work are presented in Table 1. Jayaratna et al. [7] did a computational studied of the influence of particle size distribution on flow behavior in fluidized beds, and by studying different combinations of models they concluded that this combination give the most realistic flow behavior.

Drag model	Syamlal&O'Brien
Granular viscosity	Syamlal&O'Brien
Granular bulk viscosity	Constant
Frictional viscosity	Schaeffer
Frictional pressure	Based-ktgf
Solid pressure	Ma-ahmadi
Radial distribution function	Ma-ahmadi

Table 1: Recommended combination of models [7]

The Syamlal &O'Brien drag model is used to express the solid-gas interaction. The Syamlal &O'Brien drag model is expressed in Eq (1) [8]:

$$\Phi_{sg} = C_D \frac{3\varepsilon_s \varepsilon_g \rho_g \left| \vec{U}_g - \vec{U}_s \right|}{4\nu_r^2 d_s}$$
 (1)

where ε_g and ε_s are the gas and solid fractions, ρ_g is the gas density, U_g and U_s are the gas and solid velocities and d_s is the particle diameter. The terminal velocity correlation for the solid phase, v_r , is a function of void fraction and Reynolds number [9]. In Eq. (2) the drag factor is expressed [10]:

$$C_D = \left(0.63 + \frac{4.8}{\sqrt{\text{Re}_s/\nu_r}}\right)^2 \tag{2}$$

The granular viscosity includes a collisional and a kinetic viscosity term. The collisional term is given in Eq (3):

$$\mu_{s,kin} = \frac{\varepsilon_s d_s \rho_s \sqrt{\Theta_s \pi}}{6(3e_{ss} - 1)} \left[1 + \frac{2}{5} (1 - e_{ss})(3e_{ss} - 1)\varepsilon_s g_{0,ss} \right]$$
(3)

and in Eq (4) the collisional term is presented:

$$\mu_{col} = \frac{4}{5} \varepsilon_s d_s \rho_s g_{0,ss} (1 + e_{ss}) \sqrt{\frac{\Theta_s}{\pi}}$$
(4)

where d_s e_s and Θ_s are the particle diameter, elasticity coefficient and the granular temperature of solid phase s respectively. The radial distribution function is presented by $g_{0,ss.}$. The radial distribution function included in the Syamlal-O'Brien-symmetric equation is expressed by Ma and Ahmadi [11].

The minimum fluidization velocity can be developed from the buoyant-equals-drag balance. The relation is expressed in Eq. (5)

$$(1 - \varepsilon_g)(\rho_s - \rho_g)g = \frac{\Phi_{sg}}{\varepsilon_g}(u_g - u_s)$$
 (5)

where the drag coefficient is developed by Syamlal&O'Brien. Eq (6) express the equation for minimum fluidization velocity [12]:

$$U_{mf} = \frac{\varepsilon_{mf}^{2} (1 - \varepsilon_{mf}) (\rho_{s} - \rho_{g}) g}{\Phi_{sg}}$$
(6)

Two particle phases are included in the simulations of mixtures. Syamlal-O'Briensymmetric, is used to express the particle-particle momentum exchange [13].

3 EXPERIMENTAL & COMPUTATIONAL SET-UP

Experiments and corresponding simulations are performed. The set-up is given in this chapter.

3.1 Experimental set up

A lab-scale fluidized bed with a uniform air distribution is constructed. The bed is cylindrical and is made of Lexan glass. The diameter and the height of the bed are 0.072 and 1.4 m respectively. The experimental rig is shown in Figure. 1. The gas flow rate is controlled by a pressure reduction valve, and measured by a digital flow meter. The pressure can be measured at eight positions in the bed.

Glass particles with two different mean particle sizes are used in this study. The particles have the size range $100{\sim}200~\mu m$ (small particles) and $400{\sim}600~\mu m$ (large particles).

The particle density is 2485 kg/m³. The bed and particle parameters are presented in Table. 2.

Experiments have been performed with 100% small particles, 100% large particles and mixtures of small particles with 20, 40, 50, 60 and 80% of large particles. The aim is to study how the different fractions of particle sizes influence on the minimum fluidization velocity and the bed expansion. Before the experiments with the mixtures started, the powders were well mixed and 2 liter of a compact mixture was weighted and filled into the bed. The void fractions at start and at minimum fluidization were calculated based on the weight and the volume.

Bed design			
Height		1.4 m	
Diameter		0.072 m	
Particles	(Spherical glass	s)	
Density		2485 kg/m^3	
Powder,	100~200 μm	400~600	Mixture
particle	(small)	μm	
range		(medium)	
Mean	154	488	
particle			
size			
(µm)			
% large			20, 40,
particles			50, 60,
			80

Table. 2: Experimental data

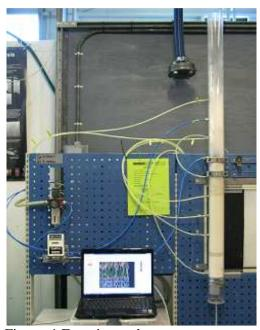


Figure. 1 Experimental set-up

3.2 Computational set-up

The simulations are performed with particles with diameters equal to the mean diameters of the glass powders used in the experiments. The simulations of the mixtures are performed with two particle phases. The data are given in Table. 3. Two particle sizes are used to simulate the mixtures of two powders with different mean particle size. The simulations are run with the same velocities and initial bed heights as in the experiments. Two-dimensional Cartesian coordinate system is used to describe the geometry. The dimensions of the computational bed are width 0.072 m and height 1.2 m. A grid resolution test is performed to find a suitable grid size. The grid is uniform and the size of a cell is 3x3 mm. The simulations have been run for 7 seconds. The simulations have been run with different gas flow rates, starting with low flow rates to determine the minimum fluidization velocities.

Simulation	% small	% large
no.	particles.	particles.
	Mean	Mean
	diameter 153	diameter 488
	μm	μm
1	100	0
2	80	20
3	60	40
4	50	50
5	40	60
6	20	80
7	0	100

Table. 3: Simulation martrix

4 RESULTS

This chapter presents the experimental bed expansion and the comparison of the experimental and computational minimum fluidization velocities.

4.1 Bed expansion

The bed expansion has been measured in the experimental rig for 100% small particles, 100% large particles and 5 different mixtures of small and large particles. The small particles have a mean diameter of 154 μ m, and according to Geldarts characterization diagram, the particles are characterized as Group B particles, but very close to Group A particles. Due to inter-particle forces, Group A particles expand significantly before bubbles appear.

Inter-particle forces are due to wetness, electrostatic charges and Van der Waals forces. For Group B particles the inter-particle forces are neglectible, and the bed expansion is at minimum fluidization velocity is rather low [2]. The small particles have a range of particle sizes from 100-200 μm .

The bed height as a function of fraction of large particles is shown in Figure. 2. The curves present the initial bed height and the bed height at minimum fluidization. Initially two liters of well mixed and maximum packed particles are filled into the experimental rig. This corresponds to a initial bed height of 491 mm as plotted with a dotted line. During the filling, the powder expanded, and the initial height of the bed therefore varies with the concentration of small and large particles. The initial bed height is 540 mm for 100% small particles and decreases to about 510 mm for mixtures with 40, 50 and 60% large particles, and increases to 548 mm for 100% large particles. The difference between maximum packed powder and bed height after filling are significant for all the mixtures, about 50, 20 and 60 mm for 100% small, 40-60% large and 100% large respectively. For the small particles this is due to the inter-particle forces as described above. The large particles are getting random packed during the filling, and the void fraction increases compared to maximum packing. In the mixtures, the properties of small and large particles influence on each other. The large particles settle and is randomly packed, and the small particles fill the spaces between the large particles.

The bed expansion for the small particles at minimum fluidization velocity is about 20 mm. About the same bed expansion is also observed for the mixtures with 20, 40, 50 and 60% large particles. This indicates that the fluidization properties in a fluidized bed reactor are significantly influenced of the smallest particles in the mixture. The bed expansion for 80 and 100% large particles is about 6 mm. This is a rather low bed expansion, which is typical for Group B particles.

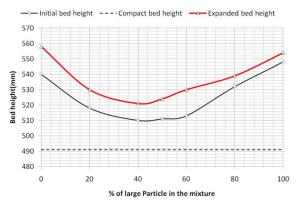


Figure. 2 Bed height as a function of particle mixtures.

4.2 Minimum fluidization velocity

Experiments are performed to study the minimum fluidization velocities for different mixtures of small and large particles. Corresponding studies have earlier performed with mixtures of 50% small and large particles which showed that the flow behavior is influenced of the smallest particles in the mixture [14]. The aim of this work is to study the flow behavior for the whole range of mixtures. The experiments are performed by starting with low velocities and increase the velocity until the minimum fluidization velocity is obtained and the powder starts to float. Corresponding simulations were performed, starting with the minimum fluidization velocities determined in the experiments. The comparison between the experimental and computational results is presented in Figure. 3.

The experimental minimum fluidization velocity is about 0.025 m/s for 100% small particles and 0.15 m/s for large particles. For the mixtures the minimum fluidization velocities increase from 0.027 to 0.039 m/s when the fraction of large particles is increased from 20 to 50%. The minimum fluidization velocities are 0.05 and 0.08m/s for the mixtures with 60 and 80% large particles. The minimum fluidization velocity is almost doubled when the fraction of large particles are increased from 80 to 100% large particles. This shows that the smallest particles in the mixture influence strongly on the fluidization behavior.

The results from the simulations show the same tendency as the experimental results. The minimum fluidization velocity for 100% small particles is 0.05 m/s.

When the fraction of large particles are changed from 0 to 40% no change in minimum fluidization velocity are observed. The minimum fluidization velocity increases slightly when the volume fraction of large particles is increased from 40 to 80%. The computational minimum fluidization velocities are 0.055, 0.06 and 0.075 for 50, 60 and 80% large particle mixtures respectively. The simulation with 100% large particles gives a minimum fluidization velocity of 0.255 m/s. This is more than three times the fluidization velocity observed for the mixture with 80% large particles.

The comparison between the experimental and computational results shows that the minimum fluidization velocities are strongly influenced of the smallest particles in the mixture. The computational minimum fluidization velocity is about double of the experimental fluidization velocity for small particles and mixtures with low concentrations of large particles. For the mixture with 50% large particles the deviation is smaller, and for the 60 and 80% mixtures the deviation between experimental and computational results are less than 10%. The difference between the experimental and computational minimum fluidization velocity is significant for the large particles.

The large deviation between the simulations and experiments for 100% small and 100% large particles can be explained by the difference in particle distribution. The small and the large particles used in the experiments are not mono sized particles but powders with a particle range of 100-200 µm and 400-600 µm respectively. This means that in the experiments many particle sizes are included, and this influence on the fluidization properties. In the simulations with 100% small and 100% large particles, the bed contains of mono sized particles, and this influence on the void fractions, packing of the bed and thereby on the fluidization properties. The minimum void fraction is significantly higher for mono sized particles than for a mixture of particle sizes. Higher void fraction in the bed requires a higher gas velocity to get the particles fluidized. To get a better agreement between simulations and experiments for the small and large particles, the simulations for these cases can be run with multiple particle phases to give a particle size distribution that corresponds to the experimental powder.

More than two particle phases can also be included in the simulations of the mixtures.

The deviation between the computational and experimental results may also partly be due to that the simulations are performed in a two dimensional system.

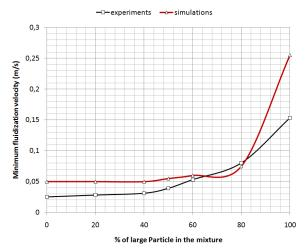


Figure. 3 Experimental and computational minimum fluidization

5 CONCLUSION

The efficiency of fluidized bed reactors depends on bubble distribution, bubble size and bubble velocity within the reactor. The bubble behavior depends on the amount of excess air introduced to the reactor. Excess air is the actual gas velocity minus the minimum fluidization velocity. The minimum fluidization velocities for different mixtures of particles are studied. A series of experiments are and simulations are performed. Experiments are performed in a cylindrical bed with a uniform air distribution. mixtures of spherical glass particles with mean diameter of 154 µm (small particles) and 488 µm (large particles) and mixtures of the small and the large particles are used in the experiments. Corresponding simulations are performed by using the commercial CFD code Fluent 6.3. In addition to the minimum fluidization velocity, the experimental bed expansion is measured. The bed expansion for small particles and mixtures including up to 60% of large particles is about 20 mm at minimum fluidization velocity. This indicates that the fluidization properties in a fluidized bed reactor are significantly influenced of the smallest particles in the mixture.

The bed expansion for 80 and 100% large particles is about 6 mm. This is a rather low bed expansion, which is typical for Group B particles. The comparison between the experimental and computational results shows that the minimum fluidization velocities are strongly influenced of the smallest particles in the mixture. The experimental and computational results show the same tendency, that the minimum fluidization velocities are low and about constant for mixtures of 0 to about 60% of large particles. The computational minimum fluidization velocity is about double of the experimental fluidization velocity for small particles and mixtures with low concentrations of large particles. Mixture with 50, 60 and 80% large particles give good agreement experimental between computational minimum fluidization velocities. The difference between the experimental and computational minimum fluidization velocity is significant for 100% large particles. The deviations are mainly due to the particle size range that is present in the experiments are not accounted for in the simulations of 100% small and 100% large particles. The deviations observed in the studies of the mixtures, may be reduced by using more than two particle phases to get a more representative particle size distribution.

REFERENCES

- [1] Geldart, D., Gas Fluidization Technology, John Wiley & Sons Ltd., 1986.
- [2] Kunii, D., Levenspiel, O., *Fluidization Engineering*, Second Edition, Butterworth-Heinemann, Newton, US, 1991.
- [3] Halvorsen, B.M., Lundberg J., Mathiesen, V. (2008), Computational study of fluidized bed, Conference on Heat Transfer, Fluid Mechanics and Thermodynamics, HEFAT 2008, June 30. –July 2., Pretoria, South Africa.
- [4] Ariyarathna, D.G.A.S.U, Wo, W.J., Halvorsen, B.M. (2008), Verifification of the importance of introducing particle size distributions to bubbling fluidized bed simulations, SIMS 2008, October 7th-8th, Oslo, Norway.

- [5] Wu, W.J., Ariyarathna, D. G. A. S. U., Halvorsen, B. M.(2008), Experimental study of effects of particle size distribution on bubble behaviour for validation of CFD modelling of bubbling fluidized bed, SIMS 2008, October 7th-8th, Oslo, Norway.
- [6] Jayarathna, S.A., Jayarathna, C.K., Wu, W.J., Halvorsen, B.M., (2008), Influence of particle size distributions on CFD simulations and experiments of bubbling fluidized beds. AIChE Annual Meeting 2008, November 16-21, Philadelphia, US.
- [7] Ariyarathna, D.G.A.S.U (2008).Recommendation of a Model for Simulating & Analysis of the Influence of Particle Size Distribution on the Simulations of Bubbling Fluidized Beds. In Thesis for the degree of MSc. Ing, pp. 22-46.
- [8] Syamlal, M., The Particle-Particle Drag Term in a Multiparticle Model of Fluidization., National Technical Information Service, Springfield, VA, 1987.
- [9] Garside, J. & Al Dibuouni, M.R., Velocity-Voidage Relationships for Fluidization and Sedimentation, I&EC Process Des. Dev., **16**, pp. 206-214, 1977
- [10] Dalla Valle, J.M., Micromeritics, Pitman, London, 1948.
- [11] Ma, D., Ahmadi, G., Thermodynamical Formulation for Dispersed Multi-phase Turbulent Flows, *Int. J. Multiphase Flow*, **16**, pp. 323-351, 1990.
- [12] Gidaspow, D., *Multiphase Flow and Fluidization*, Academic Press, Boston, 1994.
- [13] Syamlal, M., O'Brien, T.J., A Generalized Drag Correlation for Multiparticle Systems, Morgantown Energy Technology Center, 1987.
- [14] Halvorsen. B. M. (2005), An experimental and computational study of flow behaviour in bubbling fluidized beds.NTNU, 2005.

PREDICTING OPTIMAL TRIM CONFIGURATION OF MARINE VESSELS WITH RESPECT TO FUEL USAGE

Stefan Petursson,* Thomas Runarsson and Sven Sigurdsson
University of Iceland
Faculty of Industrial Engineering, Mechanical Engineering and Computer Science

Jon Agust Thorsteinsson, CEO, Marorka Ltd., Iceland

ABSTRACT

High fuel prices and environmental concerns are compelling shipping companies to consider how the fuel efficiency of vessels can be improved in order to reduce operating cost. Trim and displacement, i.e. the difference between the draught at the bow and at the stern, and the volume of sea displaced by the ship are controlled parameters worthy of attention with respect to fuel usage while the ship is cruising. Both can be controlled by arrangement of ballast. In this paper, black-box models are used to predict how the power consumption depends on the trim given various input parameters. The goal is to find the lowest power consumption with respect to the trim. The investigation is based on empirical data sampled at a passenger and freight vessel which has a cruising schedule in the North-Atlantic Ocean. The method presented here can likewise be applied to other types of vessels such as cruise liners, cargo ships and tank ships. The aim is to make such models part of an overall energy management system on board marine vessels.

Keywords: Black-Box Modelling, Energy Management, Functional Learning

NOMENCLATURE

C A penalty parameter in SVR

k Number of nearest points in kNN

p Pitch of the vessel

pp Pitch of the vessel's propeller

 P_E Vessel's effective power

 P_S Vessel's shaft power

S(p) A prediction score for pitch p

V Speed of the vessel in water

W A diagonal weight matrix

 \mathbf{x}_i A data point

 $\tilde{\mathbf{x}}(p)$ A generated data point for pitch p

γ A RBF kernel parameter in SVR

 ε An error margin parameter in SVR

 η An efficiency factor

INTRODUCTION

Many operational optimizations for marine vessels concentrate on minimizing the fuel consumption by optimizing the vessel speed or finding the optimal

*E-mail: stefan@marorka.com

route. Since the fuel cost is by far the largest portion of the operating cost of a vessel, fractional savings in fuel usage can result in considerable savings in operational costs. Furthermore, fuel savings have environmental benefits in the reduction of green-house gas emissions.

During a typical cruise the captain of the ship must meet a predefined schedule which limits the scope for speed optimizations. However, it has been shown that the power performance of vessels vary significantly with different trim configurations [1, 2, 3, 4]. Configuring the trim of a ship in harbour does not suffice due to the known *squat* effect [5]; the phenomenon of a vessel's increased immersion and trim when underway in water, as compared to calm water floating conditions. Often, the ship's trim configuration is such that it is not operated at the optimal efficiency level while the vessel is cruising. Thus, trimming the vessel correctly during a voyage could potentially save considerable amounts of money.

White-box models are based on physical laws and prior knowledge [6, 7, 8, 9, 10]. They describe how

the fuel is transformed into thrust through the propellers, in order to overcome the resistance to the motion so as to maintain a constant speed. They are quite effective but they lack the capacity to accurately include many aspects of the resistance such as the effects of waves [11], wind [12] and trim.

Alternatively, learning machines, also known as black-box models, such as support vector regression and k nearest neighbor, are on the other hand quite capable of including input parameters that are difficult or even impossible to include in a physical model, such as ocean waves and wind.

This paper examines the feasibility of utilizing such black-box models to predict the shaft power for different trim configurations. The objective is to create a simulation model to be used in a decision support system for potential fuel usage savings.

This paper starts by describing the data set, its characteristics and how it is preprocessed, followed by a short introduction to the black-box models. Results from an experimental study on the passenger and freight vessel Norröna are presented and the paper concludes with some remarks on the feasibility of this approach. A more detailed account is given in [13].

DATA SET

Norröna¹ is a ferry/cruiser with 4 main engines that have constant rotational velocity and two propellers to move the ship. Its length is approximately 160 m, the breadth is around 30 m and the mean draught is close to 6.5 m. Since the engines' revolutions are constant the speed of the vessel is controlled by changing the pitch of the propellers.

The output parameter of the models is the *shaft* power, P_S , that the propellers deliver to the water through the propulsion shaft. The shaft power can be measured directly (figure 1) and it is readily related to the fuel consumption via the specific fuel consumption of the engines. The fuel consumption itself is not suitable as an output parameter since the main engine is also used to run the electrical shaft generator.

The effective thrust delivered to the water, P_E , is related to P_S by a relation of the form

$$P_E = \eta(pp, V)P_S \tag{1}$$

where η denotes an efficiency factor dependent on the propeller pitch, pp, and the speed of the vessel, V, assuming constant rotational velocity of the shaft. P_E has, in turn, to balance the various resistance forces, $R_i(V)$, that may depend on V. Hence we have that

$$P_{S} = \frac{V \sum_{i} R_{i}(V)}{\eta(pp, V)} \tag{2}$$

It is this relationship that the black-box model has to reflect, where the focus is on how P_S varies with changes in *the trim*; defined as the difference between the draught of the hull at the bow and at the stern. The vessel's trim can be calculated directly from the pitch of the hull, cf. figure 2 (not to be confused with the propeller pitch), and since it is in fact the pitch that is measured (figure 1), reference will be made to the pitch rather than the trim in the remainder of this paper.

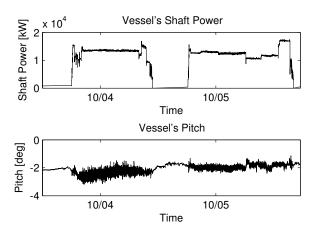


Figure 1: The shaft power consumption and pitch for two trips. These measurements are unfiltered.

However, since other resistance factors cannot be kept fixed, they also have to be included as input parameters. Apart from the shaft power and the pitch, numerous data series are sampled by the Maren² energy management system into a database at approximately 15 seconds interval. Only a handful of them are considered to be significant for the present study. The acquired data are measurements from various meters onboard the vessel; PLCs, systems using the NMEA and OPC protocols and, a SMC³ gyro motion sensor. It is assumed that all meters, excluding the gyroscope, are correctly set up and cali-

¹See http://www.smyril-line.com

 $^{^2}$ See http://www.marorka.com

³See http://www.shipmotion.se

brated and their accuracy will not be specifically questioned apart from noise. The data domain consists of 26 trips, each lasting approximately 20-22 hours, which were made in the fall of 2007, a total of approximately 90000 data points.

Input parameters of interest are now described briefly:

Log Speed The log speed is the speed of the vessel in the water.

Wind Speed and Direction The wind speed is the speed of the wind relative to the ship. The wind direction is the direction of the wind relative to the head of the ship.

Roll, Pitch and Wave The roll, pitch and heave of the ship are measured with a gyroscope which has the ability to measure the axial components along with the accelerometer component. As can be seen in figure 2 the roll is the measurement of the pitch along the Y-axis. The pitch refers to the pitch of the X-axis and the heave measures the acceleration of the ship up and down. From the heave measurements the estimate of the wave height is derived by calculating the highest absolute heave value between two consecutive zero crossings of the signal.

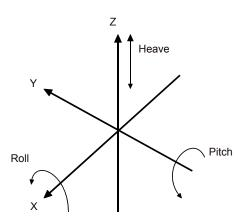


Figure 2: Roll, pitch and heave measured by the gyroscope.

Mean Draught The forward and aft measurements are the depth of the ship from the keel to the ocean surface - forward and aft respectively. Those measurements are not reliable under dynamic conditions since they are taken from sensors stationed forward and aft, which measure

the pressure on the hull. However, they are quite steady when the ship is in harbour and are thus utilized to correct the roll and the pitch. They are also used to estimate the *draught* of the ship, which gives some information on the ship's displacement.

Propeller Pitch The pitch of the two propeller blades relative to the shaft are used to control the vessel's speed, and change during voyage.

Thus the total of input parameters is 9.

Characteristics of the Data Set

In order to effectively apply a learning machine to the data it must be well formed and must therefore include synchronized measurements that correspond to reality as much as possible, while being devoid of corruption and outliers. In this study, this is not the case with the data series taken straight from the database. This section reviews those difficulties.

Data Sampling. The data series are *usually* sampled at 15 seconds interval into a database but they are neither necessarily logged at a uniform time interval nor simultaneously. These data series can, furthermore, be corrupt in the sense that they are either frozen, characterized by measurement values remaining the same although conditions alter, or the measurements are simply not arriving to the database system. Such defective data has to be detected and handled in a sensible way.

Noise and Outliers. Measurements made by the meters are often susceptible to noise, specifically in rough weather conditions as can be seen in figure 4. It is important to filter this noise as well as defective outliers.

Gyroscope Installation. The gyroscope was installed such that the head of the device was misaligned with the head of the ship. This resulted in a high correlation between the roll and the pitch measurements, which had to be remedied.

Data Range. The range of the data must be broad in order to successfully generate an adequate blackbox model that predicts the shaft power usage for various conditions. The difficulty with data sampled

under normal operational conditions is that the range of many of the parameter values can be quite narrow and may in turn limit the predictive accuracy of a regression model.

Furthermore, in this study, the focus is on how the shaft power changes with pitch while other input parameter values affecting the resistance remain fixed. Ideally, the data should be obtained from controlled experiments where the pitch is the only variable parameter. Clearly, this will not be the case when data is collected under operational conditions. Figure 3 illustrates this problem. The dots correspond to available data while the estimate is on data values along straight lines parallel to the pitch axis.

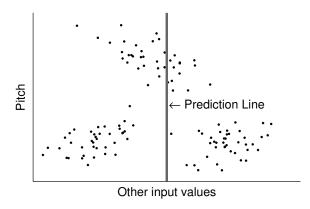


Figure 3: The distribution of the data is nonuniform making it difficult to predict how the shaft power changes with pitch, while other input values remain fixed.

DATA PREPROCESSING

To remedy the data complications some preprocessing must be performed on the data prior to application of black-box modelling.

Data Pruning

Some sections of the data must be removed manually, i.e. data series that are severely corrupted or are otherwise not desirable based on visual inspection. This applies, in particular, to series where data values seem to be frozen for too long.

Data Patching

Some series change slowly over time, where it is normal to have recurrent consecutive values. In cases where measurements have not arrived a linear interpolation is applied to "patch" the data series with data samples if the time gap is not too long. Gaps over 30 minutes are not patched as the condition of the ship might have changed too much for a simple linear interpolation correction.

Automatic Data Removal

Some data sections are not of interest in this problem and only introduce additional complexity if included. Data sections acquired while the ship is in harbour are removed since the most important component in terms of fuel savings is when the ship is sailing. Additionally, the data segments at the start and end of a journey, where the ship is accelerating, are removed since these are relatively short and thus do not play a significant role in the overall sailings.

Data Synchronization

After all unnecessary data sections have been removed the remaining data series are still not synchronized in time or of equal length.

All data series are broken down into data chunks corresponding to approximately one trip. The data series for a given trip are synchronized with each other by removing non-overlapping data sections.

Subsequently, the data points within each chunk are synchronized in time with the *shaft power* series by creating data points with linear interpolation and removing other points where applicable. This creates time series with nonuniform time intervals between data points.

Data Correction

The pitch and the roll measurements from the gyroscope are corrected so as to make them resemble the true pitch and roll measurements as much as possible and thus minimize the correlation between the roll and the pitch.

Filtering the Data

Noise and outliers are undesirable in data series when it comes to employing them as inputs and outputs in black-box modelling. The learning machine could simply learn the noise, since the root mean square (RMS) is used as the quality measure; rendering an unreliable model.

A filter based on local linear regression, which is resistant to outliers and can handle data points that are not uniformly sampled⁴, is applied to all data series. Figure 4 depicts how the noise is successfully removed and how the outlier is discarded without showing any sign of instability.

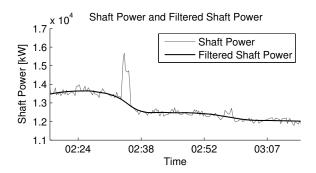


Figure 4: The shaft power series and a filtered shaft power series where the outlier has been discarded.

FUNCTIONAL LEARNING

This section briefly describes the two black-box models used in this study. Other black-box models were also tested; Classification And Regression Trees (CART), Bags of CART (bagging) and Artificial Neural Network (ANN) but they all gave similar or poorer results.

Support Vector Regression

Support Vector Regression (SVR) [14, 15, 16] is a learning machine that has yielded promising results in recent years. The attractiveness of SVRs stem from the process itself; first, the data is implicitly mapped, through the introduction of kernels of data point pairs, into a high dimensional feature space. In this space, a conventional linear regression can be applied to the mapped data, effectively handling noise and outliers implicitly. It is easy to find the linear function since the kernel ensures that the optimization problem will be convex. The corresponding function in the original data space will be nonlinear, but its shape will depend on the choice of kernels.

The kernel chosen for this study was the RBF kernel, which effectively measures the similarity between

data points \mathbf{x}_1 and \mathbf{x}_2 as $\exp\{-\gamma ||\mathbf{x}_1 - \mathbf{x}_2||^2\}$. Apart from the model parameter γ , two more parameters, C and ε , have to be specified, ε indicating an acceptable error margin, and C a penalty parameter on data points outside this error margin.

k Nearest Neighbor

The *k* Nearest Neighbor (*k*NN) regression [17, 18] consists of estimating the mean of the given output values at the *k* closest data points to a given point. The distance is a Euclidean distance metric where input parameter values are first normalized and subsequently given different weights to reduce the error and thus overcome the problem of the curse of dimensionality [17, 19].

The model-parameters are k, the number of neighborhood points, and the weights for the normalized coordinates of the Euclidean distance metric.

Data Entities

In order to generate a learning machine that performs well on unseen data it must be trained such that it will not overfit the training data. Since the data has to be filtered, care must be taken when splitting the data into training and test sets.

The data is split into approximately one hour chunks, each of which to be used as an entity. The entity is filtered as a whole and used either as training data or test data.

Entities are subsequently randomly selected into training and test data sets at ratio 80% vs. 20% respectively.

Implementation

Finding the model parameters is performed with a simple grid search on the parameters and a 5-fold cross validation [20] on the training data to choose the parameters that give the best fit.

EXPERIMENTAL STUDY

The black-box models are used to simulate the vessel for various external and operational conditions. They are, in particular, used to predict how the shaft power varies with different pitch configurations in an attempt to derive an optimal pitch configuration with respect to fuel usage.

⁴See rloess in Matlab

Results

The results from this study are twofold. First, the results of the overall quality of the model for shaft power prediction are displayed. Subsequently, the results on how the models perform in predicting the optimal pitch configuration are presented.

Predictive Results

Table 1 shows how the SVR model and the *k*NN model perform on unseen test data and how large their error RMS is compared to the RMS of the power shaft values.

Model	Error RMS	% of total RMS
ε-SVR	296	2.05
k-NN ($k = 20$)	290	2.01
Shaft Power	14442	

Table 1: RMS error results from black-box models.

Both models perform well indicating that they are viable as a model that can be used to predict how the shaft power usage varies with different configurations of the pitch. Figure 5 depicts the prediction result for the kNN model (the figure for the SVR model is quite similar). The black line is the pre-

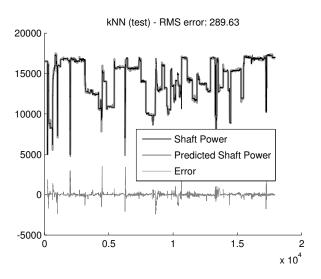


Figure 5: Shaft power prediction using the *k*NN model.

dicted shaft power, which essentially overlaps the original shaft power measurements, displayed as a thick grey line. The error is shown below.

It is of interest to note, that the introduction of weights for different normalized input parameter values reduces the RMS error over 20%, in the case of the kNN model. The propeller pitch parameters turn out to be assigned a dominant weight value, indicating that they are the most important input parameters in detecting optimal pitch values.

Optimal Pitch Configuration

Although the model thus predicts shaft power satisfactorily for unseen data of input parameters, it does not necessarily imply that it will accurately predict how shaft power varies with the pitch while keeping other input variables fixed. Figure 6 depicts how this prediction can be in certain situations.

The point X marked in the figure corresponds to a data point where all the input parameters, as well as the shaft power, are known. The vertical segment through the point shows the overall RMS error of 290. The curves then show how the predicted shaft power varies according to both models when all the input parameters except for the pitch are held constant at these values. The models are clearly not pre-

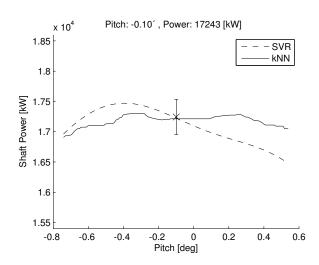


Figure 6: An example of a poor shaft power prediction for pitch values far from zero. The vertical segment through the known data point, marked with X, shows the RMS error of 290.

dicting correctly for pitch values far from zero. It suggests that the extreme pitch values, possibly beyond physical capacity, are the optimal ones. The problem stems from the external or operational conditions that the point presents. There are not enough

points in the data set that include similar conditions but with different pitch values. This causes the model to give predictive results induced from data points where the values of the remaining input variables differ significantly from the fixed ones. The data range is not broad enough to generate blackbox models that can predict the dependence of shaft power on pitch for these conditions.

By contrast, figure 7 illustrates where there is a general consensus between both models on a realistic location of the optimal pitch. This could be use-

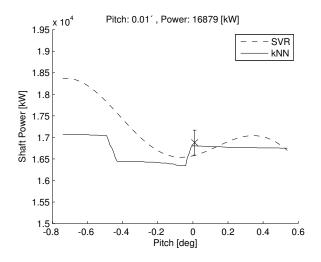


Figure 7: An example of both models agreeing on the optimal pitch location.

ful if the vessel happened to be incorrectly trimmed. It should further be noted that the output from the SVR-model is smoother than that of the *k*NN-model and seems to be more robust to changes in parameter values.

kNN Prediction Score

The variation of the prediction curves indicates a need of introducing some form of a prediction score, for a generated data point, reflecting the closeness of neighboring data points. It can be chosen such that values become 1 when the neighboring points coincide with the generated point. Equation 3 proposes a prediction score function of this kind, based on the kNN model, for a pitch value p:

$$S(p) = \frac{1}{k} \sum_{i=1}^{k} e^{-||\mathbf{W} \cdot (\mathbf{x}_i - \tilde{\mathbf{x}}(p))^{\mathrm{T}}||^2} \in]0, 1]$$
 (3)

The score is the average of the scaled weighted distance from a given point, $\tilde{\mathbf{x}}(p)$ with pitch p, to k

nearest points, \mathbf{x}_i , i=1,...,k. The weights in the diagonal matrix, \mathbf{W} , are the same as the ones used in the kNN model. The data points $\tilde{\mathbf{x}}(p)$ are generated input points where all the input parameters, excluding the pitch, are held constant.

Experiments indicate that a cut-off value as high as 0.99 may be needed to indicate reliable predictions but this remains to be investigated more fully.

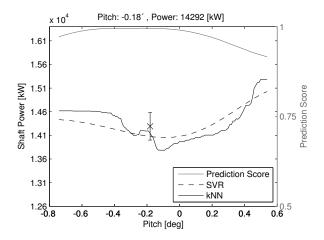


Figure 8: An example of how a prediction score can be displayed along with predicted values. The score indicates reliable predictions of values from -0.4 to -0.05.

Figure 8 illustrates this score function, displayed along with the model predictions. The score function suggests that the kNN model predicts adequately for pitch values from -0.4 to -0.05. If the vessel happened to be trimmed around -0.4 this figure would indicate that the ship should instead be trimmed around -0.1, in order to reduce the shaft power consumption by approximately 800 kW, which is outside the error margin of 300 kW. A power reduction of 500 kW for 20 hours (one trip) implies a 1.9 MT savings in fuel usage, given that the engines are running at $190 \ g/kWh$ in specific fuel consumption; a reduction of 3.4% or \$540 if the price for 1 MT is \$300⁵.

CONCLUSION

In this study, black-box models did not perform adequately in finding the optimal trim configuration in some cases. The main reason is the nature of the data set where the range of some of the parameters were

⁵See http://www.bunkerworld.com

too narrow to generate a complete model. Sampling more data to broaden the data set is not necessarily achievable since some of the parameters cannot be controlled due to external conditions.

Even though the models cannot predict fuel consumption accurately for all occasions there is evidence that it can aid the captain when the trim of the vessel is incorrectly configured. Specifically, if a prediction score would be used to indicate whether the estimate of the optimal trim configuration is reliable.

REFERENCES

- [1] Rocchi R. Delivered power trim and sinkage ship hull forms: an analysis of the effects of the trim variations on the power performance of a class of modern container ships Transactions on the Built Environment, Vol 5, WIT Press, 1994.
- [2] Journée JMJ. Review of the 1985 Full-Scale Calm Water Performance Tests Onboard m.v. Mighty Servant 3, report no. 1361, revision 07-11-2003, Ship Hydromechanics Laboratory, Delft University of Technology, August 2003.
- [3] Journée JMJ, Rijke RJ, Verleg GJH. *Marine Performance Surveillance with a Personal Computer*, report no. 753-P, Automation Days 87, Finish Society of Automatic Control, Helsinki, Finland, May 1987.
- [4] Comstock JP. *Principles of Naval Architecture*. Society of Naval Architects and Marine Engineers, New York, 1967.
- [5] Varyani KS. Squat effects on high speed craft in restricted waterways. Ocean Engineering 2006;33(3-4):365-381.
- [6] Holtrop J, Mennen GGJ. *An Approximate Power Prediction Method*. International Shipbuilding Progress 1982; 29(335):166-170.
- [7] Holtrop J. A Statistical Re-analysis of Resistance and Propulsion Data. International Shipbuilding Progress 1984;31(363):272-276.
- [8] Journée JMJ, Meijers JHC. Ship Routeing for Optimum Performance, report no. 529-P, Transactions IME, Conference on Operation of Ships in Rough Weather, February 1980.

- [9] Man and BW. *Basic principles of ship propulsion*. Technical report, 2005.
- [10] Thorsteinsson JA. Modelling of Fishing Vessel Operation for Energy System Optimisation. PhD thesis, Aalborg University, Aalborg, Denmark, 2004.
- [11] Steen S, Faltinsen OM. *Added Resistance of a Ship Moving in Small Sea States*. PRADS'98, The Hague, Netherlands, September 1998.
- [12] Isherwood RM. *Wind resistance of merchant ships*. Trans. of the Royal Institution of Naval Architects 1972;115:327-338.
- [13] Petursson S. Predicting Optimal Trim Configuration of Marine Vessels with respect to Fuel Usage. Master's thesis, University of Iceland, Reykjavik, Iceland, 2009.
- [14] Boser BE, Guyon I, Vapnik V. *A training algorithm for optimal margin classifiers*. In: COLT '92: Proceedings of the fifth annual workshop on Computational learning theory. Pittsburgh, Pennsylvania, United States. ACM, 1992. p. 144-152.
- [15] Christianini N, Shawe-Taylor J. An Introduction to Support Vector Machines and other kernel-based learning methods. Cambridge, UK, Cambridge University Press, 2000.
- [16] Smola AJ, Schölkopf B. *A tutorial on sup*port vector regression. Statistics and Computing 2008;14(3):199-222.
- [17] Duda R, Hart P, Stork D. *Pattern Classification, Second Edition*. USA, John Wiley & Sons, Inc., 2001.
- [18] Patrick EA, Fischer FP. *A generalized k-nearest neighbor rule*. Information and Control 1970;16(2):128-152.
- [19] Mitchell TM. *Machine Learning*. McGraw-Hill Higher Education, 1997.
- [20] Cover TM. Learning in pattern recognition. In: Satoshi Watanabe, editor, Methodologies of Pattern Recognition, Academic Press, New York, 1969. p. 111-132.

EVALUATING NEW AND EXISTING AUTOMATICALLY CONTROLLED DEEP WATER DRILLING CONCEPTS USING A HIGH-FIDELITY SIMULATION MODEL

Øyvind Breyholtz*, Gerhard Nygaard International Research Institute of Stavanger AS Department of Petroleum 5008 Bergen Norway

ABSTRACT

As more of the world's oil and gas reserves are located in deep waters, the petroleum industry demands new drilling concepts that make exploitation of these resources economically feasible. This paper will analyze drilling technologies developed to overcome the problems associated with deep water drilling. A low-order model of a deep water drilling system will be developed, and a Lyapounov stable observer will be presented. The use of model predictive control is proposed as a multivariable control framework to improve pressure control throughout the wellbore. Computer simulations show that the proposed controller structure efficiently coordinated the different manipulated inputs to control the pressure in the well.

Keywords: Automated drilling, Dual-Gradient drilling, Managed Pressure Drilling, Adaptive Observer, Model Predictive Control

NOMENCLATURE

ABP Annulus Backpressure
BHP Bottom Hole Pressure
CV Control Volume
DGD Dual Gradient Drilling
MPC Model Predictive Control
MPD Managed Pressure Drilling

INTRODUCTION

A large portion of the world's remaining offshore oil and gas reserves are located in deep water areas outside Brazil and in the Gulf of Mexico (GoM). Extraction of these reserves with conventional technology has turned out to be both technological and economical challenging.

The downhole pressure along the wellbore is critical for the success of a petroleum drilling process. The pressure in the wellbore, p_{well} , must be within the pressure range of the formation. The upper bound of the pressure range is the formation

fracturing pressure, p_{frac} , the lower bound is the formation collapse pressure, p_{coll} , or the reservoir pore pressure, p_{res} .

$$max(p_{coll}(t,x), p_{res}(t,x)) < p_{well}(t,x) < p_{frac}(t,x)$$

where x is the position along the open hole section and t is the time. When drilling, the formation will be exposed to the pressure in the wellbore. Since the density in the formation is usually higher than in the drilling fluid, the wellbore pressure will be closer to the fracturing pressure in the upper part of the open hole section, and closer to formation reservoir pressure in the lower part of the open hole section. Due to this, casings have to be set in order to protect the formation, and to allow drilling to continue. A casing is a steel pipe which are lowered into the open hole and permanently cemented in place. The purpose of the casing is to protect the formation, and enable the drilling to continue. A new casing has to be set when it is no longer possible to drill without exceeding the drilling window. One of the major challenges associated with deep water drilling is to obtain a

^{*}Corresponding author: Phone: +47 452 58 410 E-mail:Oyvind.Breyholtz@iris.no

favourable pressure profile in the well, resembling the natural hydrostatic pressure gradient of water and the pressure exerted by the rock formation. Drilling concepts resembling these two pressure gradients are often referred to as Dual-Gradient Drilling (DGD). As illustrated in Fig. 1 a single gradient mud column (conventional drilling) does not make a good fit of the pressure gradients of a deep water operation, and it becomes challenging for the drilling crew to maintain the pressure within the pressure window with conventional technology. Multiple casings have to be set in order to protect the formation when drilling towards the target depth. Setting a new casing is a time consuming procedure. Managing the pressure gradients in the well may be essential for the success of the operation. If a more favourable pressure profile in the well is achieved through DGD, longer sections can be drilled before a new casing has to be set. If the well can be completed with fewer casings than if conventional methods are used, it may decrease the number of days needed for the drilling operation and thereby the cost of the operation.

Drilling into mature and partly depleted zones may introduce increased complexity due to narrow pressure margins between the formation and pore pressure. Optimal co-ordination of the pump flows to suppress variations in the bottom hole pressure (BHP) may be difficult, and sometimes almost impossible to perform. Pressure surges in the BHP may be introduced by normal drilling operations, e.g. pipe connections and pipe movement. Introduction of automatic control may reduce these fluctuations and reduce the complexity of the operation for the drilling crew. In a recent paper from Breyholtz et al. (2009a) [2] a Model Predictive Control (MPC) scheme is suggested to include several manipulated inputs to efficiently co-ordinate the pressure in the well in a Managed Pressure Drilling (MPD) operation utilizing a topside choke, and in Breyholtz et al. (2009b) [3] an MPC scheme including pipe movement is presented.

This paper is divided into six main sections. In the following section the DGD operation is described in further detail, in section three the model, observer and the control theory are described. In section four, the simulations scenarios are presented, and in section five the simulation results are discussed. In the last section conclusions and suggestions for

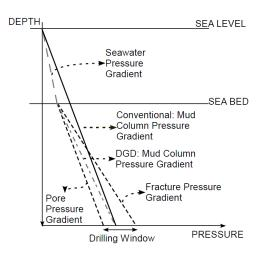


Figure 1: Hydrostatic pressure profile for dual gradient and conventional drilling

further work are given.

THE DUAL GRADIENT DRILLING CONCEPT

Dual gradient Drilling (DGD) is a relatively new drilling technology, which was introduced in the 90's to overcome the challenges associated with deep water operations. Common for these concepts is that they use a higher than normal mud density below the sea bed, and than actions are performed to reduce the efficient density in the riser section of the well, either by dilution or diversion. The different DGD technologies that have been introduced are the dilution-based concepts from Maurer Technology [5], which injects lightweight solid additives to reduce the density in the riser, and Louisiana State University [14], which has investigated how light-weight fluids can be injected into the riser to lower the efficient density. Divertion-based concepts have been proposed by Deep Vision [7], SubSea MudLift Drilling Joint Industry Project [22, 6], the Shell SubSea Pumping System [12, 11], the AGR's Riserless Mud Recovery concept [4, 9], and the Ocean Riser Systems' Low Return Riser System [8, 21]. Common for these concepts is that they have additional subsea extraction pumps which pump the mud through a separate mud return line to the surface.

A DGD drilling system consists of a rotating drill string which is placed into the well. The volume around the drill string is referred to as the annulus.

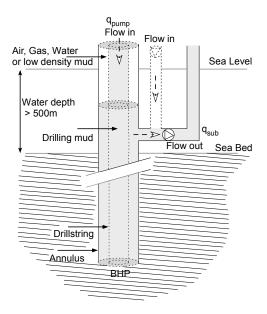


Figure 2: Dual-Gradient Drilling flow schematic

The main mud pump will pump drilling mud into the drill string. The mud circulates down into the drill string until it reaches the drill bit and enters the annulus section of the well. The mud will then circulate upwards between the walls of the well and the drill string, until it reaches the subsea arrangement at the seabed, where either (a) it is extracted through a separate mud return line and pumped back to the surface utilizing the subsea extraction mud pump or (b) gas, or light-weight solid additives are injected. At the surface cuttings from the drilling operation is removed, and the mud is reused. Two of the main objectives of the drilling mud is hole cleaning (removal of cuttings) and to maintain a certain pressure gradient along the open hole section of the well. An additional mud pump to re-inject mud directly into the riser at the seabed arrangement can also be present (illustrated in Fig 2).

APPLIED THEORY

This section is divided into three subsections. In the first subsection a low-order model of the drilling hydraulics is presented, the second subsection addresses an adaptive observer for the BHP, and at last the applied controller is discussed.

Model

In this section a low order hydraulic model of the drilling process will be developed and presented. Several low order models of the drilling process is developed in [13], [20] and [10]. These models are describing a drilling process known as Annulus Backpressure (ABP) which applies an additional topside pressure using a topside choke manifold. The ABP setup will not have the subsea arrangement described in this paper, and the riser will be filled to the surface with mud. The mud flow exiting the well at the surface can be restricted with the topside choke. The low order models developed for the ABP setup will form the basis for the model derived in this section. Especially for the drill string section of the well, the modelling will result in exactly the same low-order model for both systems.

The well will be modelled as three different control volumes interconnected by the flow and pressure dynamics. The first control volume (CV1) will be the drill string section of the well. The second control volume (CV2) is the annulus section of the well, stretching from the bottom of the well to the subsea arrangement at the riser base. The third and final control volume is the riser section of the well, stretching from the seabed arrangement to the surface (CV3). The modelling for CV1 and CV2 will be equal for all DGD systems.

Applying conservation of momentum theory for CV1 under the assumption of a turbulent flow regime yields

$$M_d \dot{q}_{pump} = p_p - p_{bit} - F_d |q_{pump}| q_{pump} + \rho_d g h_{TVD}$$
(1)

where q_{pump} is the flow rate from the main mud pump entering the drill string, p_p the main mud pump pressure, F_d the friction parameter in the drill string, ρ_d the density in the drill string, h_{TVD} the total vertical depth of the well, and p_{bit} the pressure at the bit. M_d is defined to be

$$M_d = \bar{\rho}_d \int_0^{lw} \frac{1}{A_d(x)} dx \tag{2}$$

where lw is the total length of the drill string. Conservation of mass in the drill string yields

$$\dot{p}_p = \frac{\beta_d}{V_d} \left(q_{pump} - q_{bit} \right) \tag{3}$$

where β_d is the compressibility factor in the drill string, and V_d the total volume in the drill string.

Applying conservation of momentum for CV2 yields

$$M_a \dot{q}_{bit} = p_{rb} - p_{bit} + F_a |q_{bit}| q_{bit} + \rho_a g [h_{TVD} - h_{rb}]$$
(4)

where q_{bit} is the flow rate through the bit, p_{rb} the pressure measurement at the riser base, F_a the friction parameter in the annulus, ρ_a the density in the annulus, h_{rb} the depth of the pressure measurement at the riser base. M_a is by definition

$$M_a = \bar{\rho}_a \int_{rb}^{lw} \frac{1}{A_a(x)} dx \tag{5}$$

The assumption that $\dot{q}_{pump} = \dot{q}_{bit}$ is made, and the expression for p_{bit} in equations 1 and 4 are set equal to obtain an expression for \dot{q}_{bit}

$$p_{rb} + \rho_{a}g(h_{TVD} - h_{rb}) + F_{a}|q_{bit}|q_{bit} + M_{a}\dot{q}_{bit}$$

= $p_{p} - F_{D}|q_{pump}|q_{pump} + \rho_{d}gh_{TVD} - M_{d}\dot{q}_{bit}$ (6)

Rearranging the equation to describe the flow dynamics through the bit yields

$$\dot{q}_{bit} = \frac{1}{M_d + M_a} (p_p - p_{rb} - F_d | q_{pump} | q_{pump} - F_a | q_{bit} | q_{bit} + g(\rho_d h_{TVD} - \rho_a [h_{TVD} - h_{rb}]))$$
(7)

For the final control volume, the riser section, the model for the systems will only consist of a hydrostatic pressure term. In this control volume the different DGD systems are described by different pressure and flow dynamics models. (Pressure and flow models for CV1 and CV2 can be used for all systems). To limit the scope of this paper, only two different diversion-based DGD concepts will be simulated in this section. The first concept (System 1) consists of a riser with a subsea extraction pump. In the riser the system will have a light-weight mud with density equal to sea water on top of the heavier mud. The second system (System 2) also consists of a riser with a subsea extraction pump. In addition this system will have a subsea injection pump. This concept will have a mud/air contact level in the riser somewhere below the sea surface.

$$q_{riser} = q_{bit} - q_{sub} + q_{inj} \tag{8}$$

where q_{sub} is the flow rate through the subsea extraction pump, and q_{inj} the optimal injection

pump. The dynamic of the mud height is

$$\dot{h}_{mud} = \frac{q_{riser}}{\pi (r_{ri}^2 - r_{do}^2)}$$
 (9)

where r_{ri} is the inner radius in the riser, and r_{do} is the outer drill string radius. To conclude the model of the pressure and flow dynamics the obtained expressions for the BHP is presented. The expression for the pressure at the riser base, p_{rb} , for system 1 yields

$$p_{rb} = p_0 + \bar{\rho}_r g h_{mud} \tag{10}$$

where p_0 is the atmospheric pressure, h_{mud} the mud height in the riser, and $\bar{\rho}_r$ the average density in the riser. For system 2 the expression for the pressure at the riser base yields

$$p_{rb} = p_0 + \bar{\rho}_r g h_{mud} + \rho_{sw} g (h_{rb} - h_{mud}) \qquad (11)$$

where ρ_{sw} is the density of sea water. Finally the pressure at the bottom of the well is presented

$$P_{bit} = p_{rb} + \rho_a g(h_{TVD} - h_{rb}) + F_a |q_{bit}| q_{bit} + M_a \dot{q}_{bit}$$

= $p_p - F_D |q_{pump}| q_{pump} + \rho_d g h_{TVD} - M_d \dot{q}_{bit}$ (12)

If the expression for \dot{q}_{bit} from Eq. (7) is inserted into the equation, the following expression for the BHP is obtained.

$$p_{bit} = \frac{1}{M_a + M_d} (M_a p_p + M_d p_{rb} + M_d F_a | q_{bit} | q_{bit} - M_a F_d | q_{pump} | q_{pump} + M_d \rho_a g [h_{tvd} - h_{rb}] + M_a g \rho_d h_{tvd})$$
(13)

Observer

During the drilling operation several measurements are available for the drilling crew, but unfortunately some of the key measurements, e.g. the BHP measurement, are not available at the frequency needed for control purposes. Normally this measurement is sent from the bottom hole assembly to the surface with a mud-pulse telemetry system. This system is inaccurate, and has a low bit rate. It is not unlikely that the BHP measurement will only be updated once every minute. It also needs a minimum flow to be able to transmit the measurement. Recently a major improvement in communication between the bottom hole assembly

and the surface has been achieved through telemetry drill pipe technology, where a wire from the bottom of the well to the surfaces increases the transmission rate to 1 Mbps [17]. This technology has recently been taken into use in offshore and onshore drilling operations. Even though telemetry pipe represents a huge improvement in quality and quantity of measurements almost all wells are drilled with conventional drill pipe, due to cost issues. However, as the technology matures and cost is reduced, the number of wells drilled with this technology is likely to increase. If such equipment is not available for the drilling crew, an observer for the BHP may be a helpful tool. In Stamnes et al. [24] an adaptive observer for a class of systems with parametric uncertainty in the unmeasured state dynamics are presented, and in [23] the latter theory is applied for a managed pressure drilling (MPD) system utilizing a topside choke. The MPD drilling system has similarities with the drilling system presented in this paper, and in this section it will be shown that the observer theory also can be applied to a DGD system. The observer will try to adapt to the friction in the annulus, and the parameter $\theta =$ F_a is introduced. The friction in the annulus is believed to be slowly changing variable ($\dot{\theta} \approx 0$) that will change accordingly to varying temperature, viscosity, roughness of walls, and flow regime. The first step in developing the observer is to introduce a change of coordinates.

$$\xi = q_{bit} + l_1 p_p \tag{14}$$

where l_1 is the feedback gain. The dynamics of ξ is

$$\dot{\xi} = \dot{q}_{bit} + l_1 \dot{p}_p \tag{15}$$

where \dot{q}_{bit} and \dot{p}_p can be found in Eq. (7) and (3). If these are inserted, the dynamics of ξ are found to be

$$\dot{\xi} = \frac{1}{M_d + M_a} (p_p - p_{rb} - F_d | q_{pump} | q_{pump} - \theta | q_{bit} | q_{bit} + g(\rho_d h_{TVD} - \rho_a [h_{TVD} - h_{rb}])) + l_1 \frac{\beta_d}{V_d} (q_{pump} - q_{bit}) \quad (16)$$

In the latter equation q_{bit} is unknown. An observer for q_{bit} is

$$\dot{\hat{\xi}} = \frac{1}{M_d + M_a} \left(p_p - p_{rb} - F_d | q_{pump} | q_{pump} - \hat{\theta} | \hat{q}_{bit} | \hat{q}_{bit} + g(\rho_d h_{TVD} - \rho_a [h_{TVD} - h_{rb}]) \right) + l_1 \frac{\beta_d}{V_J} \left(q_{pump} - \hat{q}_{bit} \right) \quad (17)$$

where \widehat{q}_{bit} can be estimated through

$$\widehat{q}_{bit} = \widehat{\xi} - l_1 p_p \tag{18}$$

The state estimation error is

$$\widetilde{\xi} = \xi - \widehat{\xi} = q_{bit} + l_1 p_p - \widehat{q}_{bit} - l_1 p_p$$

$$= q_{bit} - \widehat{q}_{bit} = \widetilde{q}_{bit} \quad (19)$$

where it can be seen that $\tilde{\xi} = \tilde{q}_{bit}$. The dynamic of the state estimation error is described through

$$\dot{\widetilde{\xi}} = \frac{1}{M_a + M_d} (\widehat{\theta} | \widehat{q}_{bit} | \widehat{q}_{bit} - \theta | q_{bit} | q_{bit})
+ l_1 \frac{\beta_d}{V_d} (\widehat{q}_{bit} - q_{bit})
= \frac{-1}{M_a + M_d} (\theta (|q_{bit}| q_{bit} - |\widehat{q}_{bit}| \widehat{q}_{bit}) + \widetilde{\theta} |\widehat{q}_{bit}| \widehat{q}_{bit})
- l_1 \frac{\beta_d}{V_d} \widetilde{q}_{bit} \quad (20)$$

Lyapunov Analysis

We will consider the following Lyapunov candidate function where the dynamics of $\tilde{\xi}$ are found in (20) and the dynamics of $\tilde{\theta}$ are still to be found.

$$U(\widetilde{\xi}, \widetilde{\theta}) = \frac{1}{2}\widetilde{\xi}^2 + \frac{1}{2\gamma}\widetilde{\theta}^2$$
 (21)

where $\gamma > 0$ is the adaption gain. The derivative of U and insertion of (20) gives

$$\dot{U}(\widetilde{\xi},\widetilde{\theta}) = \widetilde{\xi}\dot{\widetilde{\xi}} + \frac{1}{\gamma}\widetilde{\theta}\dot{\widetilde{\theta}}$$

$$= -l_1 \frac{\beta_d}{V_d} \widetilde{q}_{bit}^2 + \widetilde{q}_{bit} \frac{\theta}{M_a + M_d} (|q_{bit}| q_{bit} - |\widehat{q}_{bit}| \widehat{q}_{bit})$$

$$- \frac{\widetilde{\theta}}{M_a + M_d} |\widehat{q}_{bit}| \widehat{q}_{bit} \widetilde{q}_{bit} + \frac{1}{\gamma}\widetilde{\theta}\dot{\widetilde{\theta}} \quad (22)$$

From this expression it can be seen that by choosing

$$\dot{\widetilde{\theta}} = \frac{\gamma}{M_{-} + M_{A}} |\widehat{q}_{bit}| \widehat{q}_{bit} \widetilde{q}_{bit}$$
 (23)

 \dot{U} will become negative semi-definite since $\theta, M_a, M_d, \beta_d, V_d > 0$ and l_1 by choice is positive, and since $\widetilde{q}_{bit} \frac{\theta}{M_a + Md} (|q_{bit}|q_{bit} - |\widehat{q}_{bit}|\widehat{q}_{bit}) \geq 0$.

$$\dot{U} \le -\frac{\theta}{M_a + M_d} \tilde{q}_{bit}^2 - l_1 \frac{\beta_d}{V_d} \tilde{q}_{bit}^2$$
 (24)

From (20) and (23) it follows that $\tilde{q}_{bit} = \tilde{\theta} = 0$ is an equilibrium point for the system. If we follow the logic in [23] it can be concluded that

$$\lim_{t \to \infty} -\frac{\theta}{M_a + M_d} \widetilde{q}_{bit}^2 - l_1 \frac{\beta_d}{V_d} \widetilde{q}_{bit}^2 = 0 \qquad (25)$$

Adaption

Since \tilde{q}_{bit} is unknown in (20), the adaptive law can not be implemented as $\dot{\hat{\theta}} = -\dot{\tilde{\theta}}$. To overcome this problem a new function is defined

$$\sigma = \theta + \eta(\widehat{q}_{bit}) \tag{26}$$

where η is a function of known signals. The derivative of σ is found

$$\dot{\sigma} = \frac{\partial \eta}{\partial \widehat{q}_{bit}} \widehat{q}_{bit} \tag{27}$$

It has been assumed that θ is a slowly time-varying parameter ($\dot{\theta}=0$) and substitution of \hat{q}_{bit} yields

$$\dot{\sigma} = \frac{\partial \eta}{\partial \widehat{q}_{bit}} (\dot{\widehat{\xi}} - l_1 \dot{p}_p)
= -l_1 \frac{\partial \eta}{\partial \widehat{q}_{bit}} \frac{\beta_d}{V_d} (q_{pump} - q_{bit}) + \frac{\partial \eta}{\partial \widehat{q}_{bit}} \dot{\widehat{\xi}} \quad (28)$$

 q_{bit} is unknown, and thereby σ is also unknown. An estimate of σ can be found through

$$\dot{\hat{\sigma}} = -l_1 \frac{\partial \eta}{\partial \hat{q}_{bit}} \frac{\beta_d}{V_d} (q_{pump} - \hat{q}_{bit}) + \frac{\partial \eta}{\partial \hat{q}_{bit}} \dot{\hat{\xi}}$$
 (29)

And now final the expression for updating θ is found from Eq. 30

$$\widehat{\boldsymbol{\theta}} = \widehat{\boldsymbol{\sigma}} - \boldsymbol{\eta}(\widehat{q}_{bit}) \tag{30}$$

Noticing that $\widetilde{\theta} = \theta - \widehat{\theta} = \sigma - \widehat{\sigma} = \widetilde{\sigma}$, the error dynamics of the estimation is given by

$$\dot{\widetilde{\theta}} = \dot{\widehat{\sigma}} = l_1 \frac{\partial \eta}{\partial \widehat{q}_{bit}} \frac{\beta_d}{V_d} (q_{bit} - \widehat{q}_{bit})$$

$$= l_1 \frac{\partial \eta}{\partial \widehat{q}_{bit}} \frac{\beta_d}{V_d} \widetilde{q}_{bit} \quad (31)$$

This result is compared with (23)

$$l_1 \frac{\partial \eta}{\partial \widehat{q}_{bit}} \frac{\beta_d}{V_d} \widetilde{q}_{bit} = \frac{\gamma}{M_a + M_d} |\widehat{q}_{bit}| \widehat{q}_{bit} \widetilde{q}_{bit}$$
 (32)

and from the latter equation it can be concluded that $\eta(\widehat{q}_{bit})$ should be chosen such that

$$\frac{\partial \eta}{\partial \widehat{q}_{bit}} = \gamma \frac{V_d}{l_1(M_a + M_d)\beta_d} |\widehat{q}_{bit}| |\widehat{q}_{bit}$$
 (33)

Integrating with respect to \widehat{q}_{bit} gives the final expression for η

$$\eta(\widehat{q}_{bit}) = \gamma \frac{V_d}{3l_1(M_a + M_d)\beta_d} |\widehat{q}_{bit}|^3 \qquad (34)$$

Finally the estimate for the BHP is presented

$$\widehat{p}_{bit} = \frac{1}{M_a + M_d} (M_a p_p + M_d p_{rb} + M_d \widehat{\theta} | \widehat{q}_{bit} | \widehat{q}_{bit}$$

$$- M_a F_d | q_{pump} | q_{pump} + M_d \rho_a g [h_{tvd} - h_{rb}]$$

$$+ M_a g \rho_d h_{tvd}) \quad (35)$$

where the estimation error will be

$$\widetilde{p}_{bit} = \frac{1}{M_a + M_d} (\theta q_{bit} - \widehat{\theta} \widehat{q}_{bit})$$

$$= \frac{1}{M_a + M_d} (\theta \widetilde{q}_{bit} + \widetilde{\theta} \widehat{q}_{bit}) \quad (36)$$

Through the prior Lyapunov analysis it has been showned that $\widetilde{q}_{bit} \to 0$, and it because of the choice of θ it can be concluded that $\widetilde{\theta} \to 0$, and thereby $\widetilde{p}_{bit} \to 0$ for a nominal case. The adaptive observer which has been presented in this section uses the known pressure measurements from the main mud pump, and the riser base, together with the flow rate from the main mud pump and the parameters in Tab. 2 to estimate the flow through the bit, the bottom hole pressure and the friction parameter in the annulus section of the well.

CONTROLLER

MPC is a advanced control technique that has had a significant and widespread impact on industrial process control. The main reasons for its success are its ability to handle multivariable control problems naturally, take account of actuator limitations, and allow the process to operate closer to its constraints [15]. MPC is a form of control in which the 304

current control action is obtained by solving, at each sampling instant, a finite horizon open-loop optimal control problem, using the current state of the plant as the initial state. The optimization yields an optimal manipulated input sequence, of which only the first input value is applied to the plant [16]. In general, the model of the system to be controlled by MPC is described by difference equations

$$x_{k+1} = f(x_k, u_k) (37)$$

Constraints are usually of the form:

$$x_k \in X$$
 (38)

$$u_k \in U$$
 (39)

 $x_k \in \Re^n$ denotes the state vector of the system in deviation form at time k; $u_k \in \Re^m$ denotes the manipulated input vector in deviation form at time k; X is a convex, connected set (e.g. created by upper and lower-bound inequalities on states or inputs) that contains origin; and U is a convex, compact set, containing the origin [1]. The finite horizon MPC optimization problem is formulated as

$$\min_{\bar{u}_k} V(\bar{x}_k, \bar{u}_k) \tag{40}$$

subject to

$$\bar{x}_{k+1} = f(\bar{x}_k, \bar{u}_k) \tag{41}$$

$$\bar{x}_{k+j|k} \in X, \forall j = 1, ..., H_p$$
 (42)

$$\bar{u}_{k+i|k} \in U, \forall j = 0, ..., H_u - 1$$
 (43)

 \bar{u} denotes the input vector, and \bar{x} the system response to the input vector. The main objective of the system will be to maintain the desired BHP at its respective setpoint. The cost function $V(\bar{x}_k, \bar{u}_k)$ used for the system studied is

$$V(\bar{x}_{k}, \bar{u}_{k}) = \sum_{j=1}^{H_{p}} (\bar{x}_{k+j|k} - x_{k+j|k}^{set})^{T} Q(j) (\bar{x}_{k+j|k} - x_{k+j|k}^{set})$$

$$+ \sum_{j=0}^{H_{u}-1} \left[(\Delta \bar{u}_{k+j|k})^{T} R(j) (\Delta \bar{u}_{k+j|k}) + (\bar{u}_{k+j|k} - u_{k+j|k}^{set})^{T} S(j) (\bar{u}_{k+j|k} - u_{k+j|k}^{set}) \right]$$
(44)

where H_p is the prediction horizon, H_u the control input horizon, x^{set} the state setpoints, and u^{set} the ideal resting value of the input vector. The matrices Q(i) and S(i) are positive semi-definite $(Q(i), S(i) \ge 0)$, and R(i) is positive definite (R(i) > 0). The nonlinear solver used in the controller is a single shooting multi-step quasi-Newton method[18].

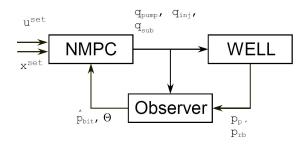


Figure 3: Float diagram

CASE DESCRIPTION

The two systems will be tested with three different control setups. Control setup A: In this case it will be assumed that a telemetry pipe is used, feeding down hole information by-wire to the surface. In this control setup the MPC application will try to control all mud pumps, and totally remove the direct control of the inputs from the driller. The driller will be able to give setpoints to both down hole pressures and inputs (pumps).

Control setup B: Again the presence of a telemetry pipe is assumed. In this setup the driller will have direct control of the main mud pump, and the control application will try to control the BHP by setting the subsea extraction volume flow.

Control setup C: In this setup a conventional drill string will be used. The down hole measurements are sent to the surface with an inadequate bit rate for control purposes. The adaptive observer presented in section is implemented, and the MPC application controls directly on the estimated pressure.

Both systems with the three different controller setups will be tested on a tracking case. The reference for the BHP will be changed with ± 5 bars in each step. The different test cases are briefly described in Tab. 1.

All simulations are performed with a high-fidelity model as process. This model has been proven through several onshore and offshore tests [19]. The test case used in this paper is based on a close to vertical well in the Gulf of Mexico which is 9590 m deep. The different parameters listed in Tab. 2 has been used for the low-order model for prediction purposes and in the observer. These parameters have been adjusted to fit the high-fidelity model.

Case	Description		
1-A	System 1: Telemetry pipe. Inputs are		
	main mud pump and subsea extraction		
	pump		
1-B	System 1: Telemetry pipe. Input is		
	subsea extraction pumpp		
1-C	System 1: Observer based control.		
	Input is subsea extraction pump		
2-A	System 2: Telemetry pipe. Inputs are		
	main mud pump, subsea extraction and		
	insertion pumps		
2-B	System 2: Telemetry pipe. Inputs are		
	subsea extraction and insertion pumps		
2-C	System 2: Observer based control.		
	Inputs are subsea extraction and		
	insertion pumps		

Table 1: Case description

Parameter	Value	Unit	Description
M_a	2052.3	$[10^{-8} \frac{kg}{m^4}]$	Eq. (5)
M_d	17976	$[10^{-8} \frac{kg}{m^4}]$ $[10^6 \frac{s^2 bar}{m^6}]$	Eq. (2)
F_d	297340	$[10^6 \frac{s^2 bar}{m^6}]$	Drill string
			friction factor
$F_a(0)$	58000	$[10^6 \frac{s^2 bar}{m^6}]$	Annulus
		m .	friction factor
$ ho_a$	0.01757	$[10^{-5} \frac{kg}{m^3}]$	Density in
			annulus
$ ho_d$	0.01757	$[10^{-5} \frac{kg}{m^3}]$	Density in
			drill string
h_{tvd}	9587	[<i>m</i>]	Total vertical
_			depth
h_{rb}	2150	[<i>m</i>]	Depth of riser
0			base
$oldsymbol{eta}_d$	14000	[bar]	Bulk modulus
* 7	00.0054	F 33	drill string
V_d	88.9954	$[m^3]$	Volume in
			drill string

Table 2: Parameters in low-order model

RESULTS AND DISCUSSIONS

The results for system 1 with all three controller setups are presented in Fig. 4-11, and the results for system 2 are presented in Fig. 12-20. Even though a telemetry pipe is used for cases A and B, the observer will still be implemented and used for calculations of the friction parameter in the annulus, which will be used for predictions in the MPC application. In general, the observer converges to a reasonable value for the BHP during steady-state conditions in the well. However, the observer has problems estimating the correct BHP when the volume flow from the main mud is changed. The estimate of q_{bit} does not converge to the correct value, and during transients inverse responses occur before it settles at a new value. The problems related to estimation of the flow rate through the bit also affects the estimate of θ . Since this value is directly used in the MPC application, the performance of the controller will be affected if the observer estimates an incorrect flow and friction. The estimates of \hat{p}_{bit} , \widehat{q}_{bit} , and $\widehat{\theta}$, and the problems associated with these estimates can be found illustrated in Fig. 8, 9, and 10 for system 1 and in Fig. 16, 17, and 18 for system

If system 1 and 2 are compared, it is clear that system 2 is more efficient when changing the reference for the BHP. Since this system does not have a lightweight fluid on top of the heavier mud, an increase of the mud level in the riser will more efficiently contribute to an increased BHP. For system 1 the difference of the density of the heavy mud and the lightweight fluid affects how fast the BHP can be increased by increasing the heavy mud level in the riser. To illustrate the difference between the two concepts, some simple calculations will be performed. If the BHP is to be increased by 5 Bars and a 1.75 SG mud is used for system 2, the mud column has to be increased by 28.6 meters. If the same calculation is performed for system 1, the mud column has to be increased by 66.7 meters.

From the industry's point of view, the BHP in a DGD system is to be controlled by changing the height of the mud column. Increasing the BHP is a time consuming process, since normally large risers has to be used in deep water operation to handle the enormous pressures that the riser might be exposed to. The difference between the inner diameter of the riser and the outer volume of the drill string

will directly affect how fast the system can change the BHP if only the extraction and insertion pumps are used for controlling the pressure, which is the accepted control solution in the industry today. Such a design will only be able to adapt to slowly varying conditions in the well. Fast pressure disturbances in the well, which can be induced by pipe movement, can not be handled by such a design. Since the extraction pumps, and the optional injection pump, only can suppress slowly varying disturbances the main mud pump is the only available option when it comes to suppression of fast changing variations in the BHP. For a DGD concept the main mud pump is the fastest, the most efficient, and thereby the most important control input. If this pump flow is part of the control algorithm other mud objectives as hole cleaning must be taken into consideration, e.g. in form of a minimum accepted flow rate. For case 1-A and 2-A, the main mud pump is included as an input in the controller. The results are illustrated in Fig. 7, and the flow rate in Fig. 5 for system 1, and in Fig. 15 and the flow rate in Fig. 13 for system 2. The results shows that the main mud rapidly affects the BHP, unfortunately the prediction in the controller is affected by the adaption in the observer, which does not converge to the correct value. From the plots it can be seen that the controller changes the flow rate from the main mud pump to control the BHP, but since the prediction misses due to the friction parameter, the controller has depend on integral action to bring the value to the reference. The co-ordinated control shows promising results by the fast initial response, but the settling time is in this case not faster than if only the extraction pump is used to control the BHP.

CONCLUSIONS AND FUTURE WORKS

In this paper a hydraulic model of DGD, an observer which estimates the BHP and the friction in the annulus, and MPC control scheme has been presented.

This paper is the first paper which addresses co-ordinated control for DGD. It can be concluded from this paper that more work is needed both on the controller, and for the observer of the BHP. The observer must be modified to be reliable in all possible scenarios. A controller for this drilling system has to be tested on various scenarios, both for modelled dynamics and un-modelled dynamics.

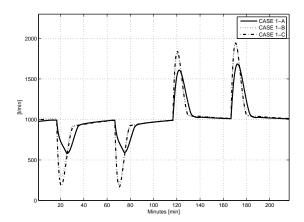


Figure 4: Extraction pump flow

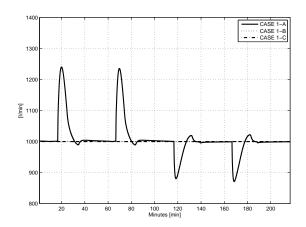


Figure 5: Main pump flow

Normal drilling operations that the controller should be tested on, is pipe connections, tripping in and out of the hole, and well control incidents (influx from the reservoir).

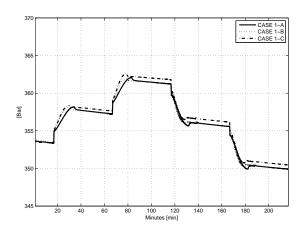


Figure 6: Riser base pressure

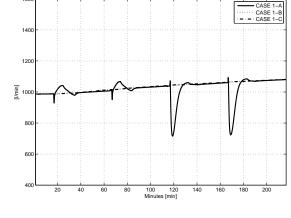


Figure 9: Estimated flow through bit

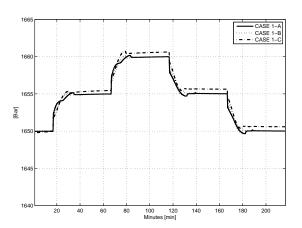


Figure 7: Bottom hole pressure

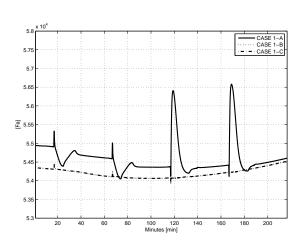


Figure 10: Estimated friction parameter in annulus

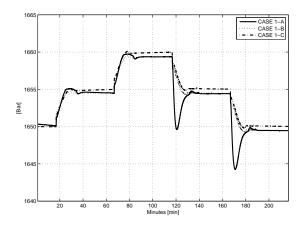


Figure 8: Estimated bottom hole pressure

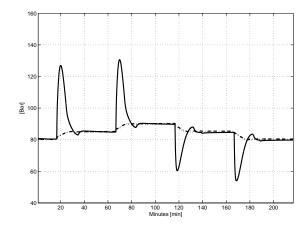


Figure 11: Main mud pump pressure

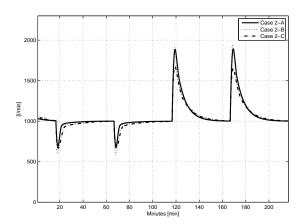


Figure 12: Extraction pump flow

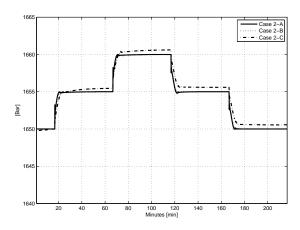


Figure 15: Bottom hole pressure

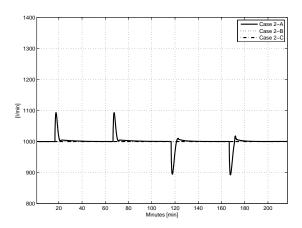


Figure 13: Main pump flow

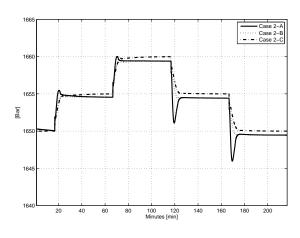


Figure 16: Estimated bottom hole pressure

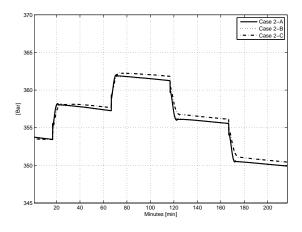


Figure 14: Riser base pressure

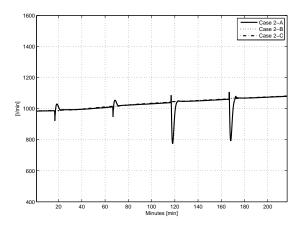


Figure 17: Estimated flow through bit

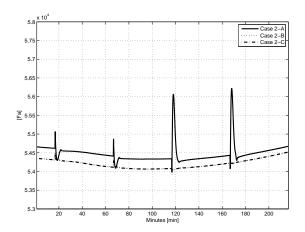


Figure 18: Estimated friction parameter in annulus

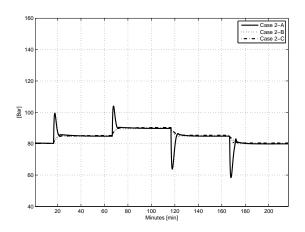


Figure 19: Main mud pump pressure

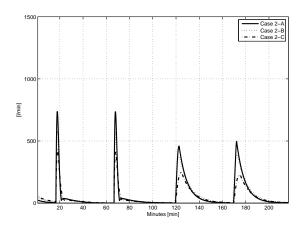


Figure 20: Injection pump flow rate

REFERENCES

- [1] F. Allgöwer, F. Findeisen, and Z. K. Nagy. Nonlinear model predictive control: From theory to application. *J. Chin. Inst. Chem. Engrs.*, 35(3):299–315, 2004.
- [2] Ø. Breyholtz, G. Nygaard, J.-M. Godhavn, and E. H. Vefring. Evaluating control designs for co-ordinating pump rates and choke valve during managed pressure drilling operations. In ACCEPTED 18th IEEE international Conference on Control Applications, St. Petersburg, Russia, 2009.
- [3] Ø. Breyholtz, G. Nygaard, and M. Nikolaou. Advanced automatic control for dual-gradient drilling. In SPE 124631- Presented at the 2009 SPE Annual Technical Conference and Exhibiton, New Orleands, Louisiana, USA, 4-7 October, 2009.
- [4] J. D. Brown, V. V. Urvant, J. L. Thorogood, and N. L. Rolland. Deployment of a riserless mud-recovery system offshore sakhalin island. In SPE/IADC Drilling Conference, Amsterdam, The Netherlands, 2007.
- [5] J.H. Cohen and G. Deskins. Use of lightweight solid additives to reduce the weight of drilling fluid in the riser. In *IADC/SPE Drilling Conference, Miami, Fl, U.S.A.*, 2006.
- [6] J. C. Eggemeyer, M. E. Akins, R. R. Brainard, R. A. Judge, C. P. Peterman, L. J. Scavone, and K. S. Thehti. Subsea mudlift drilling: Design and implementation of a dual gradient drilling system. In SPE Annual technical Conference and Exhibition, New Orleans, LA, U.S.A., 2001.
- [7] N. Forrest and T. Bailey. Subsea equipment for deep water drilling using dual gradient mud system. In SPE/IADC Drilling Conference, 2001.
- [8] B. Fossli and S. Sangesland. Controlled mud-cap drilling for subsea applications: Well-control challenges in deep waters. SPE Drilling & Completion, 21:133–140, 2006.
- [9] J. Frøyen, R. Rommetveit, H. Jaising, and N. L. Stave, R. Rolland. Riserless mud

- recovery (rmr) system evaluation for top hole drilling with shallow gas. In *SPE Russian Oil* and Gas Technical Conference and Exhibition, Moscow, Russia, 2006.
- [10] J.-M. Godhavn. Control requirements for high-end automatic MPD operations. In SPE/IADC Drilling Conference and Exhibition, Amsterdam, The Netherlands, 2009.
- [11] R. Gonzalez. Deepwater drill string shut-off valve system and method for controlling mud circulation. In *US. patent* 6,263,981, 1998.
- [12] R. Gonzalez. Shell drilling system. In DOE/MMS Deepwater Dual-Density Drilling Workshop, 2000.
- [13] G.-O. Kaasa. A simple dynamic model of drilling for control. Technical report, StatoilHydro, Researc Centre Porsgrunn, 2007.
- [14] C. A. Lopes and A. T. Bourgoyne. The dual density riser solution. In *SPE/IADC Drilling Conference*, 1997.
- [15] J. M. Maciejowski. *Predictive Control with Constraints*. PrenticeHall, Harlow, England, 2002.
- [16] D. Mayne, J. B. Rawlings, C. V. Rao, and P. O. M. Scokaert. Constrained model predictive control: Stability and optimality. *Automatica*, 36:789–814, 2000.
- [17] D. McNeill, M. Reeves, M. Hernandez, B. Lawrence, L. Redmond, and R. Russel. 'intelligent' wired drill-pipe system allows operators to take full advantage of latest downhole sensor developments. In *International Petroleum Technology Conference*, 2008.
- [18] P. Meum, P. Tøndel, J.-M. Godhavn, and O. M. Aamo. Optimization of smart well production through nonlinear model predictive control. In 2008 SPE Intelligent Energy Conference and Exhibition, Amsterdam, The Netherlands, 2008.

- [19] G. Nygaard and J.E. Gravdal. Wemod for matlab user's guide. Technical report, International Research Institue of Stavanger AS (IRIS), Bergen, Norway, nr 2007/234, 2007.
- [20] G. Nygaard and G.-O. Kaasa. Control algorithms applied to managed pressure drilling operations in depleted reservoirs. Science and Technology in Gas Industry. (In Russian, Nauka i Technologya v gazovoi promushlennosti), 2(34):88–98, 2008.
- [21] S. Sangesland and B. Fossli. Low riser return and mud-lift system. In *the XIV Deep offshore Tech. Conf. New Orleans, U.S.A.*, 2002.
- [22] K. L. Smith, A. D. Gault, D. E. Witt, and C. E. Weddle. Subsea mudlift drilling joint industry project: Delivering dual gradient drilling technology to industry. In *SPE Annual Technical Conference and Exhibition*, 2001.
- [23] Ø. N. Stamnes, J. Zhou, O. M. Aamo, and G.-O. Kaasa. Adaptive observer design for the bottomhole pressure of a managed pressure drilling system. In 47th IEEE Conference on Decision and Control, Dec 9.-11, Cancun, Mexico, 2008.
- [24] Ø. N. Stamnes, J. Zhou, O. M. Aamo, and G.-O. Kaasa. Adaptive observer design for nonlinear systems with parametric uncertainties in unmeasured state dynamics. In *Proceedings of the 48th IEEE Conference on Decision and Control*, 2009.

Refrigeration 2



EFFECT OF REFRIGERANT MAL-DISTRIBUTION IN FIN-AND-TUBE **EVAPORATORS ON SYSTEM PERFORMANCE**

Martin Rvhl Kærn* and Lars Finn Sloth Larsen Danfoss A/S **Refrigeration and Air-Conditioning DK-6430 Nordborg** Denmark

Brian Elmegaard Technical University of Denmark Department of Mechanical Engineering DK-2800 Lyngby Denmark

ABSTRACT

Refrigerant mal-distribution in fin-and-tube evaporators for residential air-conditioning (RAC) is investigated numerically in this paper. A model of the system is developed in the object-oriented modeling language Modelica. The models of the compressor and expansion valve are static, whereas the condenser is a dynamic moving boundary model. The evaporator model is a dynamic distributed one-dimensional homogeneous equilibrium model, in order to capture the distribution phenomena. Fin-and-tube heat exchangers usually have a complex circuitry, however the evaporator will be simplified to be two straight tubes. The refrigerant mal-distribution is then induced to the evaporator by varying the vapor quality at the inlet to each feeder tube, the pressure drop through each feeder tube and the air-flow across each tube. Finally it is shown that air-flow mal-distribution can be compensated by an intelligent distributor, that ensures equal superheat in both tubes. The refrigerant

Keywords: Mal-distribution, air-conditioning, evaporator, modeling, Modelica.

Overall heat transfer coefficient [W/m²K] **NOMENCLATURE** VVelocity [m/s] AArea [m²] V Volumetric flow rate [m³/s] Outer tube diameter [m] DVapor quality [-] х d Inner tube diameter [m] Pressure drop [Pa] Δp Distribution factor [-] Efficiency [-] GMass flux [kg/m²s] Specific enthalpy [J/kg] h **Subscripts** Tube length [m] L air Air Mass [kg] MCondenser cond Mass flow rate [kg/s] Correlation corr Number of control volumes [-] Evaporator evap Pressure [Pa] Friction Heat flow rate [J/s] Frontal frTTemperature [°C] Feeder tube ft Time [s] inInlet Internal energy [J] Isentropic is *Corresponding author: Phone: +45 7488 2572 Fax: +45 Mean m 7488 5635 E-mail: martin@danfoss.com Outlet

out

sh Superheat

tot Total

- 1 Tube 1
- 2 Tube 2

INTRODUCTION

Energy consumption and refrigerant charge in refrigeration systems are becoming increasingly important for environmental, legislative and economic reasons. Hence compact dry-expansion multichannel heat exchangers are of interest for future refrigeration technology. The use of more channels in evaporators gives rise to mal-distribution phenomena, which have shown to reduce evaporator capacity and thus system energy efficiency. Refrigerant mal-distribution can be caused by different reasons, such as air-flow mal-distribution, non-uniform air-temperature, fouling, improper heat-exchanger or distributor design and installation, or interactions of these.

Several studies on mal-distribution in evaporators and its impact on cooling capacity and coefficient of performance (COP) have been made. Payne and Domanski [1], Lee et al. [2] and Kim et al. [3] studied air-flow mal-distribution, and Nakayama et al. [4] and Li et al. [5] studied refrigerant flow distribution in distributors. Particularly Payne and Domanski [1] and Kim et al. [3] demonstrated that individual superheat control of each circuit could recover most of the cooling capacity and COP.

Typically A-coils are employed in RAC systems as the indoor coil, i.e. as the evaporator. The coil forms an A-shape in order to minimize the size of the airduct. A drawback is that the air-flow becomes nonperpendicular to the face coil, resulting in air-flow mal-distribution. Steady state models capable of handling user-defined air-flow mal-distribution exist in the literature such as Domanski [6], and Jiang et al. [7]. Recently Domanski and Yashar [8] used computational fluid dynamics (CFD) and particle image velocimetry (PIV) to obtain the air-velocity profile through an A-coil. Likewise AbdelAziz et al. [9] applied CFD to analyze the air-flow in an A-coil. Both showed that air-flow mal-distribution occur.

Domanski and Yashar [8] applies a novel optimization system called ISHED (intelligent system for heat exchanger design) to optimize refrigerant circuitry (tube connections) in order to compensate airflow mal-distribution. They show that cooling capa-

city is increased by 4.2% compared to an interlaced type of circuitry.

This study focuses on understanding the effect of refrigerant mal-distribution in the evaporator and methods of compensation. The objective is to quantify the influence of the distributor and the air-flow on refrigerant mal-distribution, UA-value and COP. A system model is made capable of simulating refrigerant mal-distribution in the evaporator. The evaporator model is ideal, i.e. two straight tubes, in order to perform simple and basic investigation of refrigerant mal-distribution in the evaporator and its effect on system performance. The refrigerant maldistribution is then induced to the model by varying the vapor quality distribution in the distributor, the bending of the distributor feeder tubes and the airflow distribution across the tubes. Finally the hypotheses implied by Payne and Domanski [1] and Kim et al. [3] as mentioned above is investigated, that is "controlling individual superheats results in recovered cooling capacity and COP at air-flow maldistribution".

MODEL DESCRIPTION

The main interest in this study is the refrigerant maldistribution and its effect on system performance. Thus the model of the compressor and the expansion valve are static and not particularly detailed, i.e the volumetric flow rate and the isentropic efficiency are constant. The model of the condenser is a bit more detailed and relies on the requirement to model refrigerant mass distribution between the condenser and evaporator in this project. The moving boundary model formulation as proposed by Zhang and Zhang [10] was chosen for this.

The evaporator model needs to capture the mass flow distribution through the tubes, thus pressure drop needs to be modeled. The simplest form of the distributed models is chosen for this, i.e. the homogeneous equilibrium model. In the following the evaporator model is explained in more detail. Information about the moving boundary model used as condenser is available in Zhang and Zhang [10], where the homogeneous void fraction is employed together with similar heat transfer correlations, to be comparable to the evaporator model (see Table 1).

The evaporator model

The main assumptions of the distributed evaporator model is:

- The refrigerant flow is one-dimensional.
- The refrigerant vapor and liquid are in thermodynamic equilibrium.
- The refrigerant flow is homogeneous.
- The refrigerant kinetic and potential energies are negligible.
- The heat transfer coefficient on the air-side is uniform on each segment.
- The air is dry, incompressible and does not accumulate mass or energy.
- The axial heat conduction of the wall is negligible.

Further assumptions with regards to the two-phase flow formulation are explained in the following. The inertia term in the momentum equation (the derivative term w.r.t. time) is important for modeling propagation of pressure fluctuations and other effects of very small time scales (see Richter [11]), which is not important in the current study and will be neglected. Also accelerational pressure drop is typically small compared to frictional pressure drop and will also be neglected (see Jiang [12]). The one-dimensional homogeneous two-phase flow formulation for horizontal tubes is then

$$\frac{dM}{dt} = \dot{m}_{in} - \dot{m}_{out} \tag{1}$$

$$\frac{dU}{dt} = (\dot{m}h)_{in} - (\dot{m}h)_{out} + \dot{Q}$$
 (2)

$$(p_{in} - p_{out}) = \Delta p_f \tag{3}$$

where equation 1, 2 and 3 are the mass conservation, energy conservation and momentum equation, respectively. The model has been implemented as described by Jensen [13] and has been verified in steady state by Coil-Designer (Jiang et al. [7]). Additional information needs to be given such as heat transfer coefficient and friction coefficient. The model also includes the thermal mass of the tube wall and employs the effectiveness-NTU relations for each segment similarly to Jiang [12] for cross-flow heat exchangers. Table 1 gives an overview of the correlations used.

The evaporator also consists of a distributor and a manifold, that serve to split and join the refrigerant flow, respectively. The pressure drop across the

Table 1: Overview of correlations

Air-side	
Heat transfer coefficient	Wang et al. [14]
Fin efficiency	Schmidt [15]
-	(Schmidt approximation)
Two-phase	
Heat transfer coefficient	Shah [16]
Friction coefficient	Müller-Steinhagen and
	Heck [17]
Single phase	
Heat transfer coefficient	Gnielinski [18]
Friction coefficient	Blasius [19]

distributor feeder tubes is modeled by the Müller-Steinhagen and Heck [17] correlation, where the inner diameter of the feeder tube is 3 mm and the length is 250 mm. Other pressure drops from a sudden enlargement or a tee branch etc. are not considered. Both energy and mass conservation is applied to the distributor and the manifold.

IMPLEMENTATION

The models are implemented in Dymola 7.1 [20]. Dymola solvers are able to integrate large-scale differential and algebraic equations (DAEs) efficiently. Dymola is based on the Modelica language and supports object-oriented programming, that is important for model reuse and extension. Equations can be written in a casual manner and supports event driven procedures. Dymola has been well tested within the field of air-conditioning and refrigeration (Eborn et al. [21], Richter [11]). Thermophysical properties are provided by the RefEqn package (Skovrup [22]). A given heat exchanger geometry within the applicable range of the correlations is chosen for both evaporator and condenser, where the considered fin type is louvered. The only difference is that the total length of the condenser is twice as long as the total length of the evaporator. Typically the geometric difference is around one and a half, however the air velocity is higher for the condenser, thus a geometric difference of two is reasonable when the air velocity is set equal. The main input parameters to the models are depicted in Table 2.

In the following three important parameters will be introduced to analyze the mal-distribution in the evaporator. These will be referred to as the distribution parameters. The first and the second are distribution parameters used for the distributor. The first is used

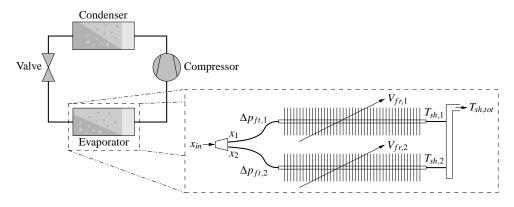


Figure 1: Sketch of model setup

Table 2: Main input parameters

Tuble 2. Main input p	arameters
Compressor	
Volumetric flow rate, \dot{V}	$3.25 \text{ m}^3/\text{h}$
Isentropic efficiency, η_{is}	0.8
Condenser	
Inlet air temperature, $T_{air,cond}$	310 K (36.85 °C)
Total tube length, L_{cond}	28 m
Evaporator	
Inlet air temperature, $T_{air,evap}$	300 K (26.85 °C)
Tube length, L_{evap}	7 m (per tube)
Number of control volumes, <i>n</i>	30 (per tube)
Evaporator and condenser	
Mean air frontal velocity, V_m	1.5 m/s
Tube inner diameter, d	7.6 mm
Tube outer diameter, D	9.6 mm

for distribution of liquid and vapor phases and is defined as $F_x = x_2/x_{in}$. Figure 1 shows a sketch of the model setup including these symbols. When F_x is equal to one, the vapor quality into the feeder tubes is equal, when F_x is equal to zero, only liquid comes into feeder tube 2.

The second parameter is used to induce different pressure drops in the feeder tubes, that could be caused by different bending. This distribution factor is defined, so that $\Delta p_{ft,1} = F_{ft} \Delta p_{ft,1,corr}$ and $\Delta p_{ft,2} = \Delta p_{ft,2,corr}$, which means that the factor is multiplied to the pressure drop correlation for tube 1 only. When F_{ft} is equal to one, the pressure drop across the feeder tubes are equal. When F_{ft} is above 1, the pressure drop becomes higher across feeder tube 1.

The third distribution parameter is a similar parameter used for the air-flow distribution and is defined as $F_{air} = V_{fr,1}/V_m$. When F_{air} is equal to one, the air-flow is distributed equally across the 2 tubes, when

 F_{air} is equal to zero, air only travels across tube 2. This leads to 3 cases that are simulated in this study, where each distribution parameter is varied individually. F_x and F_{air} are varied from 1 to 0.1 and F_{ft} is varied from 1 to 5.5. The total superheat $T_{sh,tot}$ is controlled to 5 K throughout the simulations by the mass flow rate through the expansion device. A fourth case is also investigated, that is, control of individual superheats to 5 K by controlling individual mass flow rates at air-flow mal-distribution. This requires that the pressure drop across each tube is no longer the same, in order to control individual mass flow rate. This is so to say done by an intelligent distributor.

For initialization a linear enthalpy and a linear pressure drop along the tubes are used for the evaporator. These correspond to an inlet quality of 0.2 into the distributor, a pressure of 10 bar into the distributor and individual tube superheats of 5 K, i.e. no maldistribution. The initial condenser pressure was set to 25 bar, together with a superheated length of 15%, two-phase length of 75% and a subcooled length of 10%. Fast transients happen at the beginning of each simulation, however at no mal-distribution (i.e. $F_x =$ $F_{ft} = F_{air} = 1$), from which the simulations starts, the steady state becomes the same for all cases, and is thus comparable. After initialization the steady state at no mal-distribution gives a pressure in the distributor at 10.95 bar (10.4 °C), inlet quality at 0.26, manifold pressure at 10.43 bar (8.8 °C), condenser pressure at 29.08 bar (48.2 °C) and a subcooling at 5.7 K. It is important to note that this steady state is determined by the initialization, which again determines the mass of refrigerant in the system. Another initialization would give another steady state and hence mass of refrigerant.

RESULTS Mal-distribution from the distributor

In this section the results of the aforementioned case 1 and 2 will be presented, i.e. mal-distribution of liquid and vapor phases in the distributor (F_x , case 1) and mal-distribution caused by different feeder tube bending (F_{ft} , case 2). Figure 2 depicts the mass flux distribution through each tube as F_x goes to zero (case 1) and F_{ft} goes to six (case 2).

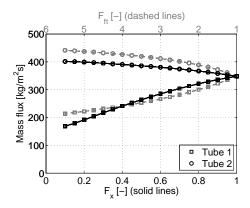


Figure 2: Mass fluxes vs. F_x and F_{ft} (case 1-2)

It shows that mass flux distribution is dependent on the quality factor F_x , so that more mass comes through the tube with lower inlet quality (tube 2) and less mass comes through the tube with higher inlet quality (tube 1). When F_{ft} goes to six a similar mass distribution trend is seen. This is determined by the pressure drop across the tubes. If the inlet vapor quality becomes lower the pressure drop will become lower, because of the difference in liquid and vapor pressure drop, which is higher for the vapor phase. In order to ensure equal pressure drop through the tubes, the mass flux becomes higher for the tube with lower inlet vapor quality. Similarly when F_{ft} goes to six the pressure drop across tube 1 becomes higher, and more refrigerant will travel through tube 2 to maintain equal pressure drop.

The consequence of different mass flux distribution is seen on figure 3, which shows the individual and total superheats. At $F_x = 0.8$ liquid is coming out of tube 1 (case 1) and at $F_{ft} = 2.75$ liquid is coming out of tube 1 (case 2). These points are important because the two-phase zone decreases, when full evaporation is not reached. A higher superheated zone in tube 1 is required in order to evaporate this surplus liquid, thus the UA-value is decreased. The UA-value also decreases when the total mass flux

decreases. The total mass flux decreases in both cases in order to maintain the total superheat of 5 K. The UA-value degradation is showed on figure 4, together with the COP of the system. It shows that mal-distribution of inlet vapor quality is more significant than different feeder tube pressure drop. Note that a compact fin-and-tube heat-exchanger usually consists of more passes and thus U-bends. This would reduce the influence of the distributor pressure drop even more compared to the inlet vapor quality.

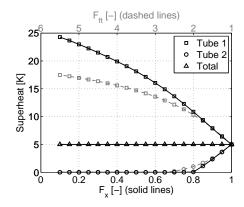


Figure 3: Superheats vs. F_x and F_{ft} (case 1-2)

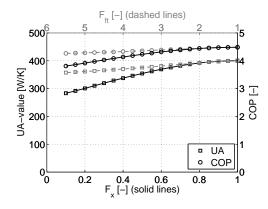


Figure 4: Evaporator UA-value and COP vs. F_x and F_{ft} (case 1-2)

The UA-value decreases 29% and 11% as F_x goes to 0.1 and F_{ft} goes to 6, where the COP decreases 15% and 5% as F_x goes to 0.1 and F_{ft} goes to 6. Because the UA-value decreases, the evaporating temperature decreases. This is seen on figure 5 and 6. The results show that the different feeder tube bending has a minor impact on UA-value and COP, whereas the distribution of liquid and vapor phases has a higher impact. The two are not considered by

the authors to interact significantly, i.e. the distribution of liquid and vapor phases is a separation phenomena in the distributor, and thus not affected by different feeder tube pressure drop.

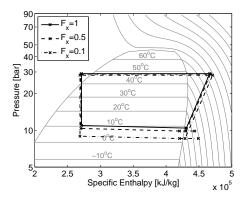


Figure 5: $\log p$ -h diagram at different F_x (case 1)

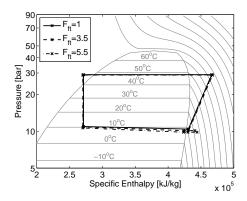


Figure 6: $\log p$ -h diagram at different F_{ft} (case 2)

Mal-distribution from the air-flow and compensation

In this section the results of the aforementioned case 3 and 4 will be presented, i.e. air-flow mal-distribution (F_{air} , case 3) and compensation of air-flow mal-distribution by controlling individual superheats (F_{air} , case 4). Figure 7 shows the mass flux distribution.

Interestingly the mass fluxes are almost equal for case 3 with no individual control of the superheat, however reduced significantly. The reduction of mass flux together with different superheated zones have a degrading effect on the UA-value, as depicted on figure 8, however it can be compensated considerably if individual superheats are controlled as in

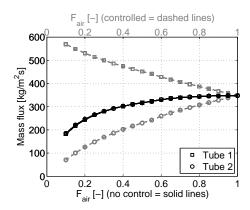


Figure 7: Mass fluxes vs. F_{air} (case 3 and 4)

case 4. For this case the refrigerant mass flux distribution is optimized to compensate the air-flow maldistribution.

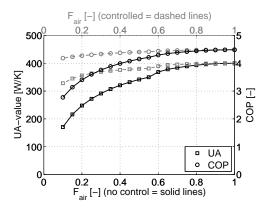


Figure 8: Evaporator UA-value and COP vs. F_{air} (case 3 and 4)

The UA-value and the COP decrease 57% and 38% as F_{air} goes to 0.1 for case 3, where the UA-value and the COP decrease 18% and 7% as F_{air} goes to 0.1 for case 4. Again the UA-value reduction decreases the evaporating temperature. This reduction causes a degradation of the COP. The $\log p$ -h diagrams of case 3 and 4 are depicted on figure 9 and 10.

DISCUSSION

The results of this paper should be used as guidelines to what occurs in evaporators, where maldistribution is present, whenever it comes from the distributor or the air-flow. It is difficult to extend the results of this work to a given type of evaporator or system, in order to estimate the degradation of the UA-value and COP. The problem is that it is dif-

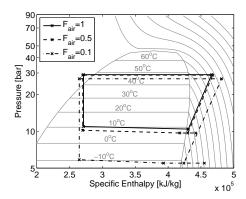


Figure 9: $\log p$ -h diagram at different F_{air} (case 3)

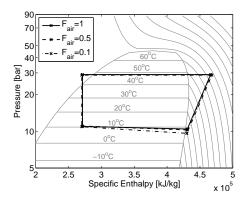


Figure 10: $\log p$ -h diagram at different F_{air} (case 4)

ficult to quantify and distinguish between the maldistribution of the different sources, i.e. vapor quality distribution, feeder tube pressure drop difference (in bends) or air-flow mal-distribution. These can be different for different types of heat exchangers.

The trends of the results in this paper are similar to studies of Brix [23] and Kærn and Elmegaard [24], where the former showed these trends on a microchannel evaporator. However the inlet pressure was fixed for these analysis, which only focused on the evaporator as a separate component. Thus the system level influence was not addressed. The latter did not take into account the feeder tube pressure drop in fin-and-tube evaporators, hence addressed in the present study. The feeder tube pressure drop was in the present study about half of the total pressure drop through the evaporator. Thus the inclusion of the feeder tube pressure drop has significant effect when it comes to mal-distribution from the distributor. Because the mass flux is distributed evenly at mal-distribution from the air-flow, the feeder tube pressure drop has no particular effect here.

Kim et al. [3] also performed system level analysis of mal-distribution in evaporators, and showed that the cooling capacity and COP could be recovered to 99.9% at $F_{air} = 0.75$, by controlling individual superheat. The result of this study shows a UA-value recovery of 99.2% and a COP recovery of 99.6% at $F_{air} = 0.75$. The trends are also similar, thus the model appears verified with earlier work.

CONCLUSION

It can be concluded that mal-distribution in fin-and-tube evaporators reduces the UA-value and COP, whenever it comes from a mal-functioning distributor or a non-uniform air-flow. It turns out that the non-uniform air-flow significantly reduces the UA-value and COP, whereas the mal-functioning distributor has a smaller impact.

Four cases were studied, i.e case 1 at mal-distribution of liquid and vapor phases, case 2 at mal-distribution by different feeder tube bending, case 3 at air-flow mal-distribution and case 4 at air-flow mal-distribution with compensation by individual superheat control. Case 1, 2 and 3 showed a degradation of up to 15%, 5% and 38% in COP, respectively, as F_x went to 0.1, F_{ft} went to 6 and F_{air} went to 0.1. Case 4 showed that the degradation of up to 38% could be compensated to only 7% as F_{air} went to 0.1.

With regards to the distributor, it is important to secure a good distribution of liquid and vapor phases, whereas the different feeder tube bending were found to have minor degradation effect.

The overall picture shows that the UA-value and COP reduction becomes significant when full evaporation is not reached in one of the tubes. Also airflow mal-distribution can be compensated by controlling individual superheats.

This investigation gave rise to another important issue, that is, what is the benefits of optimizing refrigerant circuitry, if refrigerant distribution is controllable and how could the two interact?

REFERENCES

[1] W. V. Payne, P. A. Domanski, Potential benefits of smart refrigerant distributors, Final report No. ARTI-21CR/610-20050-01, Air-Conditioning and Refrigeration Technology Institute, Arlington, VA, USA (2003).

- [2] J. Lee, Y.-C. Kwon, M. H. Kim, An improved method for analyzing a fin and tube evaporator containing a zeotropic mixture refrigerant with air maldistribution, International Journal of Refrigeration 26 (2003) 707–720.
- [3] J.-H. Kim, J. E. Braun, E. A. Groll, Analysis of refrigerant flow distribution in evaporators, in: 12th International Refrigeration and Air Conditioning Conference at Purdue, no. 2353, West Lafayette, IN, USA, 2008.
- [4] M. Nakayama, Y. Sumida, S. Hirakuni, A. Mochizuki, Development of a refrigerant two-phase flow distributor for a room air conditioner, in: 8th International Refrigeration Conference at Purdue, West Lafayette, IN, USA, 2000, pp. 313–319.
- [5] G. Li, S. Frankel, J. E. Braun, E. A. Groll, Application of cfd models to two-phase flow in refrigeration distributors, HVAC&R Research 11 (1) (2005) 45–62.
- [6] P. A. Domanski, Finned-tube evaporator model with a visual interface, in: 20th International Congress of Refrigeration, Sydney, Australia, 1999.
- [7] H. Jiang, V. Aute, R. Radermacher, Coildesigner: A general-purpose simulation and design tool for air to refrigerant heat exchangers, International Journal of Refrigeration 29 (2006) 601–610.
- [8] P. A. Domanski, D. Yashar, Application of an evolution program for refrigerant circuitry optimization, in: ACRECONF "Challenges To Sustainability", New Delhi, India, 2007.
- [9] O. AbdelAziz, V. Singh, V. Aute, R. Radermacher, A-type heat exchanger simulation using 2-d cfd for airside heat transfer and pressure drop, in: 12th International Refrigeration and Air Conditioning Conference at Purdue, no. 2200, West Lafayette, IN, USA, 2008.
- [10] W.-J. Zhang, C.-L. Zhang, A generalized movingbounary model for transient simulation of dryexpansion evaporators under larger disturbances, International Journal of Refrigeration 29 (2006) 1119–1127.
- [11] C. C. Richter, Proposal of new object-oriented equation-based model libraries for thermodynamic systems, Ph.D. thesis, Technische Universität Carolo-Wilhelmina zu Braunschweig, Fakultät für Maschinenbau (2008).

- [12] H. Jiang, Development of a simulation and optimization tool for heat-exchanger design, Ph.D. thesis, University of Maryland at College Park, Department of Mechanical Engineering (2003).
- [13] J. M. Jensen, Dynamic modelling of thermo-fluid systems with focus on evaporators for refrigeration, Ph.D. thesis, Technical University of Denmark, Department of Mechanical Engineering (2003).
- [14] C.-C. Wang, C.-J. Lee, C.-T. Chang, S.-P. Lin, Heat transfer and friction correlation for compact louvered fin-and-tube heat exchangers, International Journal of Heat and Mass Transfer 42 (1999) 1945–1956.
- [15] T. E. Schmidt, Heat transfer calculations for extended surfaces, Refrigerating Engineering (1949) 351–357.
- [16] M. M. Shah, Chart correlation for saturated boiling heat transfer: Equations and further study, ASHRAE Transactions 88 (1982) 185–196.
- [17] H. Müller-Steinhagen, K. Heck, A simple friction pressure drop correlation for two-phase flow in pipes, Chemical engineering and processing 20 (1986) 297–308.
- [18] V. Gnielinski, New equation for heat and mass transfer in turbulent pipe and channel flow, International Chemical Engineering 16 (1976) 359–368.
- [19] P. R. H. Blasius, VDI Wärmeatlas, 9th Edition, Springer-Verlag, Ch. Lab., 2002.
- [20] Dynasim AB, Research Park Ideon SE-223 70, Lund, Sweden, Dynamic Modeling Laboratory, Dymola User's Manual, version 7.1 (2008).
- [21] J. Eborn, H. Tummescheit, K. Prölß, Airconditioning a modelica library for dynamic simulation of ac systems, in: 4th International Modelica Conference, Hamburg, Germany, 2005, pp. 185–192.
- [22] M. J. Skovrup, Thermodynamic and thermophysical properties of refrigerants, Department of Energy Engineering, Technical University of Denmark, Nils Koppels Allé, Building 402, DK-2800 Lyngby, Denmark.
- [23] W. Brix, Modelling of refrigerant distribution in microchannel evaporators, in: Danske Køledage 2008, 2008, pp. 71–79.
- [24] M. R. Kærn, B. Elmegaard, Analysis of refrigerant mal-distribution in fin-and-tube evaporators, in: Danske Køledage 2009, 2009, pp. 25–35.

NUMERICAL MODELING IN MAGNETIC REFRIGERATION

R. Bjørk*, C. R. H. Bahl, A. Smith and N. Pryds,
Technical University of Denmark
Fuel Cells and Solid State Chemistry Division
Risø National Laboratory for Sustainable Energy
DK-4000 Roskilde
Denmark

K. K. Nielsen and J. Hattel Technical University of Denmark Department of Mechanical Engineering DK-2800 Lyngby Denmark

ABSTRACT

A magnetic refrigeration device built at Risø DTU is presented. For this device there are two important physical systems whose design must be carefully considered. The first is the permanent magnet assembly where the optimal economic values for the magnet design are found based on numerical simulations. A physical magnet was constructed and measurements of the flux density are compared with simulation, showing a good agreement. The second is the design of the so-called Active Magnetic Regenerator (AMR) which is the active core of the refrigeration system. A transient heat transfer 2.5-dimensional numerical model to model AMR is presented. The model is shown to reproduce experimental data from the Risø DTU magnetic refrigeration device.

Keywords: Magnetic refrigeration, Magnetic field, Heat transfer, Finite element, Finite difference

INTRODUCTION

Magnetic refrigeration is an evolving technology that has the potential of high energy efficiency and the usage of environmentally friendly refrigerants [1]. Magnetic refrigeration is based on the magnetocaloric effect (MCE). The MCE is observed in magnetic materials when subjected to a change in magnetic field. Under adiabatic conditions, most materials exhibit an increase in temperature when the field change is positive and a decrease when the change is negative. An increase in magnetic field tends to order the magnetic moments and thus lowers the magnetic entropy. Since the total entropy is constant under adiabatic conditions the lattice and electron entropies must increase and thus the temperature of the material rises. If the MCE of the material is reversible, the temperature will decrease when the field is removed since the direction of the magnetic moments will be randomized when no external field is present. This increase/decrease in temperature is called the adiabatic temperature change, $\Delta T_{\rm ad}$. Magnetocaloric materials exhibit a maximum in the MCE at the transition temperature between a ferromagnetic and a paramagnetic phase, known as the Curie temperature, $T_{\rm c}$. Different magnetocaloric materials have different values of $T_{\rm c}[2]$.

One of the keystones of using magnetocaloric materials (MCMs) as refrigerants is their inherent reversibility (for materials of interest), which allows for an efficient refrigeration process. However, the MCE in the best materials currently available show a temperature change of no more than around 4 K in an magnetic field of around 1 T. Thus a simple reverse thermodynamic cycle will not be able to produce significant refrigeration at reachable magnetic

 $^{^*}$ Corresponding author: E-mail:rabj@risoe.dtu.dk

fields from permanent magnets. Therefore the active magnetic regeneration (AMR) cycle is applied. This process combines the MCE of the MCM as work input with the MCM, i.e. the refrigerant, at the same time working as a regenerator. A heat transfer fluid is used to exchange heat between the solid and heat exchangers at the hot and cold ends respectively. Four steps are normally used to characterize the AMR process. These are

- 1. Adiabatic magnetization, which increases the temperature of the refrigerant.
- 2. The hot blow period, where the heat transfer fluid is blown from the cold to the hot end, allowing heat from the solid to be rejected at the hot end.
- 3. Adiabatic demagnetization, which lowers the temperature of the refrigerant.
- 4. The cold blow where the heat transfer fluid is blown from the hot end to the cold end and thus absorbs a cooling load in the cold end.

The regenerator is a porous structure made of the MCM, with the heat transfer fluid filling the void space. The AMR system cannot be described by a conventional refrigeration cycle since each differential element of the regenerator undergoes its own specific thermodynamic cycle. The scientific problem of magnetic refrigeration consists of a combination of regenerator-effectiveness, the non-linear MCE and an application of an external magnetic field.

In this paper the focus is on the numerical modeling of a magnetic refrigeration test machine constructed at Risø DTU [3, 4]. The test machine is a reciprocating device using parallel plates of magnetocaloric material and using a cylindrical permanent magnet assembly to create the magnetic field.

THE RISØ DTU MAGNETIC REFRIGERATION DEVICE

The test machine, which is pictured in Fig. 1, consists of a regenerator core in the middle of a plastic tube with an outer diameter of 40 mm and an inner diameter of 34 mm. The regenerator core contains 13 precision machined grooves to hold plates of magnetocaloric material with dimensions 40 mm along the flow direction, 0.9 mm thick and 25 mm

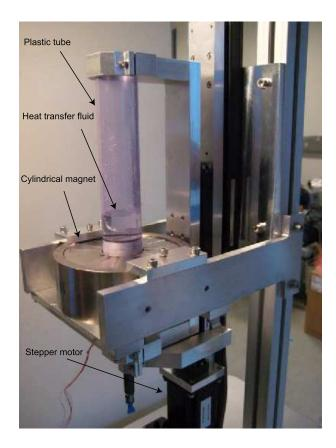


Figure 1: The test machine in its operational environment. The cylindrical permanent magnet assembly can be seen in the center of the picture. Also the plastic tube, filled with water, holding the regenerator core (not visible) can be seen. The regenerator core is inside the magnet. The motor for moving the regenerator core is visible at the bottom of the photo.

wide. The plates are separated by a 0.8 mm spacing which is then the thickness of the fluid channel. A close up photo of the regenerator can be seen in Fig. 2

The heat transfer fluid is moved using a piston. Five type E thermocouples are placed in the center flow channel of the regenerator so the temperature profile in the AMR can be recorded during an experiment. The permanent magnet assembly that provides the magnetic field can be seen in Fig. 1. This has the shape of a cylinder. The assembly provides a maximum magnetic field of 1.1 T. The regenerator is moved in and out of the magnetic field by a stepper motor

The total system is compact and is generally easy to handle. The setup allows for easy change of the plates of MCM as well as the heat transfer fluid. Dif-

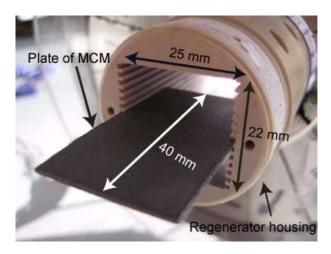


Figure 2: A close-up of the experimental AMR regenerator bed with a plate of MCM material sticking out of the regenerator. The regenerator bed can contain 13 parallel plates.

ferent AMR parameters such as piston stroke length and cycle time are easily adjustable using a custom LabView computer controlled interface.

THE PERMANENT MAGNET ASSEMBLY

In general a magnetic field can be produced by an electromagnet or by a permanent magnet assembly. For the test machine the permanent magnet assembly was chosen as it requires no external power source to produce a magnetic field. The design requirement for the permanent magnet assembly is that it produces a homogenous high flux density magnetic field in a confined region of space and a very weak field elsewhere. The Halbach cylinder design [5, 6] was chosen, because it fulfills the requirements, is compact and relatively simple to assemble.

A Halbach cylinder consists of a permanent magnetic material with a bore along the cylinder symmetry axis in which the magnetic field is concentrated. The magnet is magnetized such that the direction of magnetization varies continuously as, in polar coordinates,

$$B_{\text{rem},r} = B_{\text{rem}} \cos(\phi)$$

 $B_{\text{rem},\phi} = B_{\text{rem}} \sin(\phi)$, (1)

where B_{rem} is the magnitude of the remanent flux density. An illustration of the Halbach cylinder can be seen in Fig. 3. The Halbach cylinder can be char-

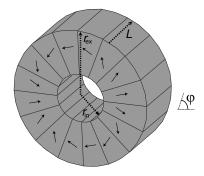


Figure 3: A illustration of a 16 segmented Halbach magnet. Shown as arrows is the direction of magnetization. The internal and external radii, r_{in} and r_{ex} , respectively, and the length, L are also shown.

acterized by three parameters: the internal and external radii, $r_{\rm in}$ and $r_{\rm ex}$, respectively, and the length, L. For practical applications the Halbach cylinder is built up from segments each with their own direction of magnetization. The Halbach cylinder used for the test machine consists of 16 blocks of permanent magnets. This configuration yields 95% of the flux density of an unsegmented continuous Halbach cylinder [7].

Dimensioning the magnet

As the magnet is the single most expensive part of a magnetic refrigeration device the magnet must be dimensioned such that it uses the minimum amount of magnetic material while at the same time producing a homogenous high flux density over as large a volume as possible. Based on these requirements a magnet assembly can be characterized by three parameters. The first is the volume in which the magnetic field is created, in this case the volume of the cylinder bore. The second is the volume of magnet used to create the magnetic field, in this case the volume of the Halbach cylinder. The third is the flux density of the created magnetic field.

To find the optimal dimensions of the Halbach cylinder for the test machine we have conducted a series of parameter variation simulations using the commercially available finite element multiphysics program, *Comsol Multiphysics*[8]. The Comsol Multiphysics code has previously been validated through a number of NAFEMS (National Agency for Finite Element Methods and Standards) benchmark studies [9].

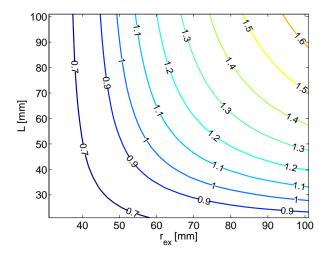


Figure 4: Contours of the mean flux density as a function of external radius and length. Each contour is labeled by its mean flux density. The maximum flux density is obtained by maximizing both $r_{\rm ex}$ and L.

The equation solved in the simulations is the magnetic vector potential equation,

$$\nabla \times (\boldsymbol{\mu}_0^{-1} \boldsymbol{\mu}_r^{-1} (\nabla \times \mathbf{A} - \mathbf{B}_{\text{rem}})) = 0, \tag{2}$$

where $\bf A$ is the magnetic vector potential, $\bf B_{rem}$ is the remanent flux density, μ_0 is the permeability of free space and μ_r is the relative permeability assumed to be isotropic. A finite element mesh is used as this provides high resolution near geometric connections, e.g. corners. The solver used to solve Eq. 2 on the simulation mesh is *Pardiso* which is a parallel sparse direct linear solver [10, 11]. Boundary conditions are chosen such that the boundaries of the computational volume, which is many times larger than the Halbach cylinder, are magnetically insulating, while all other (internal) boundaries are continuous.

The parameters that were varied were the external radius and the length of the Halbach cylinder. The internal radius of the Halbach cylinder was fixed at $r_{\rm in}=21$ mm to fit the regenerator bed. The external radius was varied in the range $r_{\rm ex}=31-101$ mm in steps of 1 mm while the length was varied in the range L=21-101 mm in steps of 1 mm. All in all 5751 simulations were performed. For all simulations a remanent magnetization of the individual magnet of 1.4 T was used.

Shown in Fig. 4 are contours of equal mean flux density in the cylinder bore as a function of external

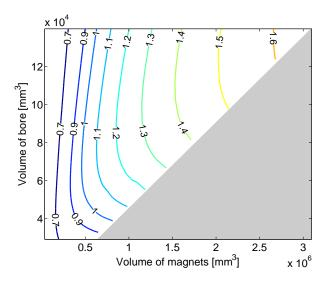


Figure 5: Contours of the mean flux density as a function of the volume of magnets used and the volume of the cylinder bore. It is seen that there is a minimum amount of magnet for each mean flux density contour. Also the volume of the bore can be significantly increased by slightly increasing the volume of the magnets.

radius and length. From this figure it can be seen that increasing the external radius or the length will increase the mean flux density in the cylinder bore. However it cannot be seen which parameters produce the largest flux density over the biggest volume with the minimum amount of magnetic material.

In Fig. 5 contours of equal mean flux density are plotted as a function of the volume of the magnet and the volume of the bore. Using these variables it can be seen that for each flux density there is a minimum value of the volume of the magnet. This is the most economic design as it uses the minimum amount of magnetic material to produce a given mean flux density. However it can also be seen that by increasing the amount of magnetic material slightly the volume of the bore can be significantly increased.

The data points in Fig. 5 (not shown) can be mapped to a specific value of the external radius and length. By finding the minimum value of the volume of the magnet for a range of mean flux densities and recording the external radius and length for this configuration the optimal economic values for $r_{\rm ex}$ and L are found. These are shown in Fig. 6.

From this figure one can get the external radius and length of the Halbach cylinder with the minimum volume of the magnet that produces a given mean

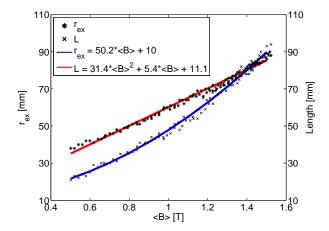


Figure 6: The optimal $r_{\rm ex}$ and L as functions of the mean flux density. Polynomia have been fitted to the data to ease interpolation. Building a Halbach cylinder with an internal radius of 21 mm with dimensions different from the dimensions given here means that more magnetic material is used than need be, if one does not care about the volume of the bore.

flux density. A first order polynomial has been fitted to the external radius data points while a second order polynomial has been fitted to the length data points.

Based on Fig. 6 and a design requirement that the magnet for the test machine should provide a mean flux density of around 1 T, an external radius of the Halbach cylinder of 60 mm and a length of 50 mm was chosen.

The physical magnet

Having found the dimensions of the ideal Halbach cylinder for the test machine a magnet was constructed. The actual Halbach cylinder, part of which can be seen on Fig. 1, has an inner radius of 21 mm, an outer radius of 60 mm and a length of 50 mm. The volume of the magnet is 0.50 L and the volume of the cylinder bore is 0.07 L. We have measured the flux density along the central axis of the Halbach cylinder using a Hall probe and the result is shown in Figure 7. Also shown is the flux density obtained from simulation. As can be seen from the figure the numerical simulation and the experimental measurements agree, and show that a high flux density is produced in the center of the cylinder bore. The small difference between simulation and measurement can be due to uncertainty in the

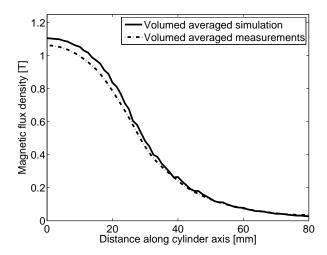


Figure 7: The measured and simulated flux density for the Halbach cylinder for the test machine.

magnet specifications and manufacturing processes as well as measuring uncertainty.

THE AMR MODEL

As the coupling between magnetic field, MCE, fluidsolid heat transfer and the thermal properties of the MCM is highly non-linear, numerical modeling is needed to understand the physics and response of the AMR system to changes in geometry, operating parameters and material composition. Such a model has developed at Risø DTU [12, 14]. The model is 2-dimensional, resolving the flow-direction (parallel to the MCM plates) and the direction perpendicular to the flow and the plane of the plates. Thus the internal gradients are resolved, while the plates are assumed wide enough that boundary effects are negligible. However, the model features an option to model the ambient temperature in the not-resolved dimension through a simple thermal resistive formulation. The governing equations are for the fluid

$$\rho_{\rm f} c_{\rm p,f} \left(\frac{\partial T_{\rm f}}{\partial t} + (\mathbf{u} \cdot \nabla) T_{\rm f} \right) = k_{\rm f} \nabla^2 T_{\rm f}, \tag{3}$$

and solid

$$\rho_{\rm s}c_{\rm p,s}\frac{\partial T_{\rm s}}{\partial t} = k_{\rm s}\nabla^2 T_{\rm s},\tag{4}$$

respectively. Subscripts f and s stand for fluid and solid respectively. The thermal properties are mass density, ρ , and thermal conductivity k, both assumed constant, and specific heat capacity, c_p , which is a

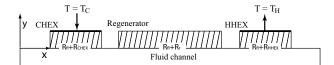


Figure 8: The 2-dimensional geometry of the AMR model. The model exploits symmetry and thus only half a fluid channel and half the solid domains are modeled. All thermal boundary conditions are isolating except those otherwise indicated.

function of temperature and magnetic field. Temperature is denoted T and time is t. Finally, the velocity of the fluid is denoted \mathbf{u} . The solid and fluid domains are coupled via inner boundaries. These slide to simulate the fluid movement and the resulting velocity profile is

$$u(y) = \tilde{u}\left(\frac{6y^2}{H_{\rm f}^2} - 1/2\right). \tag{5}$$

Here the y-direction is perpendicular to the flow and the plane of the MCM-plates. The velocity profile only has a component in the x-direction (parallel to the flow) since it is assumed to be fully developed, laminar and incompressible. The mean fluid velocity is denoted \tilde{u} and the thickness of the fluid channel is H_f .

The geometry of the model is displayed in Fig. 8. The model exploits symmetry and thus only half a fluid channel and half a solid domain are modeled. The model is solved using a spatial discretization based on finite differences of 2nd order and the alternate direction implicit (ADI) method for the temporal integration. The code is written by the authors and maintained at Risø DTU and available in generic Fortran. A detailed description of the model is available in [12].

The magnetocaloric effect (MCE) can be modeled either using the mean field theory (MFT) [13] or using experimental data when available).

Thermal parasitic losses

The model is able to include thermal parasitic losses to the ambient in the *z*-direction, i.e. the dimension not resolved spatially. This formulation is straightforwardly written in terms of thermal resistances

$$Q_{\rm loss} = \frac{T_{\infty} - T}{\sum_{i} R_{i}}.$$
 (6)

The ambient temperature is denoted T_{∞} and the thermal resistances are denoted R_i . This expression is applied for each grid cell, which individually has the temperature T. The thermal resistance sum has three main contributors namely the resistance in the domain under consideration (MCM or fluid), the plastic housing and finally natural convection between the housing and the ambient. Thus, the sum becomes

$$\sum R_i = \frac{1/2\Delta z_f}{k_f \Delta x \Delta y} + \frac{\Delta z_{\text{pl}}}{k_{\text{pl}} \Delta x \Delta y} + \frac{1}{h_{\text{conv}} \Delta x \Delta y}, \quad (7)$$

in the case of the fluid (the subscript is simply substituted for the appropriate domain). In this expression the thickness of the domain, $\Delta z_{\rm f}$, has been introduced as well as the area of the individual grid cell perpendicular to the *z*-direction, $\Delta x \Delta y$. The subscript pl stands for plastic. Finally, the natural convection parameter is denoted $h_{\rm conv}$.

The purpose of including the parasitic losses to the ambient is to model in detail the exterior circumstances to a specific AMR experiment. For ideal modeling, i.e. where the optimal performance is sought for the theoretical AMR device, such losses are without meaning. However, when modeling experimental results they can be of great significance. The expression in Eq. 6 is added as a source term in Eqs. 3 and 4.

Results from the AMR modeling

A wide range of results exist from the current AMR model. These range from theoretical AMR modeling, which aims at understanding the basic principles of active magnetic regeneration both in terms of regenerator efficiency and material composition [15], to modeling of the actual test machine located at Risø DTU [16]. In the latter case e.g. the thermal parasitic losses are taken into account. This way of modeling the AMR problem from different perspectives provides a basis for understanding how to obtain the optimal performance as well as understanding the short-commings of the experiment (e.g. significance of thermal losses, demagnetization effects [17] etc).

Results from a fluid-displacement variation experiment using gadolinium as MCM and water as heat transfer fluid are showed in Fig. 9. The figure shows a clear dependency of the zero heat-load temperature span as function of fluid displacement. Furthermore,

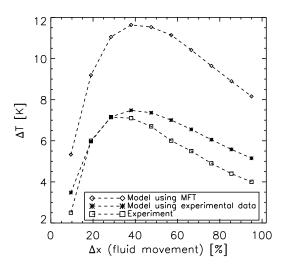


Figure 9: An example of a result from the numerical AMR model compared to the experimental device. The ambient temperature was set to 298 K and gadolinium was used as the MCM and water as the heat transfer fluid. In this figure the no heat-load temperature span is plotted as function of fluid displacement during the AMR process. The two different modeling situations are different in the sense that one uses the mean field theory (MFT) to calculate the MCE and the other uses experimental data from [17]. Reproduced from [12].

it is evident from the figure that the input MCE should be carefully used. The clearly overestimating model-curve is from a modeling series where the mean field theory (MFT) was used to calculated the MCE (see [18] for details on the MFT). The model-curve that is almost overlying with the experimental values uses experimentally obtained data. This shows that the model is quite sensitive to the input MCE, which is important since magnetocaloric data in general are not abundant for most MCMs and thus an effort towards characterizing MCMs in detail is needed.

Figure 10 shows the significance of including the thermal parasitic losses. The experiment was run using gadolinium as MCM and water as heat transfer fluid at a total cycle timing of about 9 seconds, and thus the parasitic losses have plenty of time to destroy the regeneration.

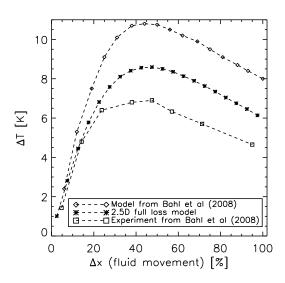


Figure 10: An example of the impact of including the thermal parasitic losses (denoted 2.5D full loss model). The losses are seen to have a significant impact on the experimental results. Reproduced from [12].

CONCLUSION

A magnetic refrigeration test device made at Risø DTU was presented. The Halbach cylinder magnet design for the device was discussed and optimal economic dimensions for the magnet were found. The magnet was constructed and the flux density was measured and compared with simulation and a good agreement was found. Also a numerical AMR model was presented and some results discussed. The modeling shows that the magnetocaloric effect should be carefully implemented, i.e. when modeling experiments real experimental MCE data should be applied when available. Furthermore, it was shown that including the thermal parasitic losses to the ambient greatly improves the resembles of the model and the experiment. Thus, an important point when designing an AMR experiment is to minimize the impact of parasitic losses. This can be done be e.g. increasing the operating frequency.

ACKNOWLEDGEMENTS

We thank Mr. Jørgen Geyti for his technical help. The authors further acknowledge the support of the Programme Commission on Energy and Environment (EnMi) (Contract No. 2104-06-0032), which is part of the Danish Council for Strategic Research.

REFERENCES

- [1] Gschneidner Jr K A and Pecharsky V. *Thirty* years of near room temperature magnetic cooling: Where we are today and future prospects. Int. J. Refrig., 2008;31(6):945.
- [2] Pecharsky V K and Gschneidner K A Jr. *Advanced magnetocaloric materials: What does the future hold?* Int. J. Refrig. 2006;29:1239-1249.
- [3] Bahl C R H, Petersen T F, Pryds N and Smith, A. A versatile magnetic refrigeration test device Rev. Sci. Inst. 2008;79(9):093906
- [4] Engelbrecht K, Jensen J B, Bahl C R H and Pryds N. 2009. *Experiments on a modular magnetic refrigeration device* Proc. 3rd Int. Conf. on Magn. Refrig. at Room Temp. 2009;IIF/IIR.
- [5] Mallinson J C. One-sided Fluxes A Magnetic Curiosity? IEEE Trans. Magn. 1973;9(4):678.
- [6] Halbach K. Design of permanent multipole magnets with oriented rare earth cobalt material Nucl. Instrum. Methods 1980;169.
- [7] Bjørk R, Bahl C R H, Smith A and Pryds N. *Optimization and improvement of Halbach cylinder design* J. Appl. Phys. 2008;104:13910.
- [8] COMSOL AB, Tegnrgatan 23, SE-111 40 Stockholm, Sweden.
- [9] Comsol, Comsol Multiphysics Model Library, third ed. COMSOL AB, Chalmers Teknikpark 412 88 G (2005).
- [10] Schenk O, Gärtner K, Fichtner W and Stricker A., *PARDISO: A High-Performance Serial and Parallel Sparse Linear Solver in Semiconductor Device Simulation* J. of Future Gener. Comput. Syst. 2001;18:69.
- [11] Schenk O and G\u00e4rtner K. Two-Level Scheduling in PARDISO: Improved Scalability on Shared Memory Multiprocessing Systems Parallel Comput. 2002;28

- [12] Nielsen K K, Bahl C R H, Smith A, Pryds N, Bjørk R and Hattel J. *Detailed numerical modeling of a linear parallel-plate active magnetic regenerator* Int. J. Refrig. 2009, doi:10.1016/j.ijrefrig.2009.03.003
- [13] Morrish *The physical principles of magnetism*. New York: John Wiley and Sons Inc., 1965.
- [14] Nielsen K K, Pryds N, Smith A, Bahl C R H and Hattel J. 2-dimensional numerical modeling of active magnetic regeneration Proc. 3rd Int. Conf. on Magn. Refrig. at Room Temp. 2009;IIF/IIR.
- [15] Nielsen K K, Bahl C R H, Smith A., Pryds N. and Hattel J. *On the ideal cooling capacity of gadolinium in active magnetic regenerative refrigeration* 2009;In prep.
- [16] Nielsen K K, Engelbrecht K, Bahl C R H, Smith A, Pryds N and Hattel J. *Numerical modeling of multi-material active magnetic regeneration* Proc. 7th World Conf. on Exp. Heat Transf., Fluid Mech. and Thermodyn. 2009.
- [17] Bahl, C R H and Nielsen, K K. The effect of demagnetization on the magnetocaloric properties of gadolinium. J. Appl. Phys. 2009;105:013916.
- [18] Petersen T F, Pryds N, Smith A, Hattel J, Schmidt H and Knudsen H. *Two-dimensional mathematical model of a reciprocating room-temperature active magnetic regenerator.* Int. J. Refrig. 2008;31:432.
- [19] Rowe A & Barclay J. Ideal magnetocaloric effect for active magnetic regenerators J. Appl. Phys. 2003;93:1672

Simulation Tools 2



SOLUTION TO AN IMPLEMENTATION ISSUE FOR A TWO-STEP ARX ALGORITHM, WITH APPLICATION TO THE CZOCHRALSKI **CRYSTALLIZATION PROCESS**

Magnus Komperød Østfold University College **Faculty of Engineering** 1757 Halden Norway

John Atle Bones **SINTEF Materials and Chemistry Department of Metallurgy** 7465 Trondheim **Norway**

Bernt Lie * **Telemark University College Faculty of Technology** 3901 Porsgrunn Norway

ABSTRACT

DSR E is a system identification algorithm for identification of linear time-invariant systems. DARX is a two-step ARX algorithm which approximates DSR E. The second step of DARX slightly differs from the standard ARX form. Apparently this prevents standard ARX software from being used, requiring a tailor-made implementation of ARX. This paper presents a rewriting of the second step of DARX. Applying this rewriting standard ARX software can be used also for the second step of DARX, simplifying the overall implementation of DARX. The rewriting is validated using timeseries logged at a real-life Czochralski crystallization process.

Keywords: Applied linear algebra, ARX, Czochralski crystallization process, DSR E, System identification.

NOMENCLATURE

- Polynomial in z^{-1} , $A(z) = 1 + \sum_{i=1}^{n_A} a_i z^{-i}$. Polynomial in z^{-1} , $B(z) = \sum_{i=1}^{n_B} b_i z^{-i}$. Polynomial in z^{-1} , $C(z) = 1 + \sum_{i=1}^{n_C} c_i z^{-i}$.
- B(z)
- C(z)
- eActual ("true") innovation process.
- Identified innovation process.
- kTimestep index.
- P Control signal for heating power [%].
- TRaw signal from temperature sensor [V].
- Deterministic system input.
- *Corresponding author: Phone: +47 35 57 51 69 Fax: +47 35 57 52 50 E-mail: bernt.lie@hit.no

- Value of *x* at timestep *k*, for $x \in \{e, f, u, y\}$.
- Measured system output.
- The timeshift operator of the Z-transform, $z^{-1} x_k \stackrel{\text{def}}{=} x_{k-1}.$

Text written in teletype font refers to MAT-LAB commands, for example arx.

INTRODUCTION

Modeling of dynamic systems is a most important part of today's science and engineering. Empirical modeling is a commonly used modeling approach which is based on observations of the systems to be modeled. Empirical modeling used for developing *dynamic* models is referred to as system identification. System identification is commonly used for developing models for model-based control, predictors, and state estimators.

ARX is an algorithm for system identification of linear, time-invariant (LTI) systems. ARX is a simple, commonly used algorithm, which is based on the ordinary least squares method (OLS). Although ARX identifies good models for many systems, it has significant disadvantages compared to other, more advanced methods. DSR E is a more advanced algorithm for system identification of LTI systems. The DSR E algorithm is a two-step algorithm [1, 4].

Reference [2] shows that the DSR E algorithm can be approximated by a two-step ARX algorithm. This approximation of the DSR E algorithm is referred to as the DARX algorithm. Unfortunately, the second ARX step of DARX is slightly different than the standard ARX form. This apparently requires an implementation of a tailor-made ARX algorithm, instead of using standard ARX software, such as the MATLAB command arx. Implementing a tailor-made ARX algorithm will increase the complexity of the otherwise simple implementation of DARX.

The main contribution of this paper is to present a rewriting of the second step of DARX. This rewriting allows standard ARX software to be used for both steps of DARX. Hence the implementation of DARX is significantly simplified. Only strictly proper, single input, single output (SISO) systems will be considered in this paper. Although not tested, it is believed that the results presented in this paper can be applied directly to biproper systems and multiple input systems as well. With respect to multiple output systems, the general challenges caused by a complex internal structure and a large number of parameters must be handled. Multiple output systems have not been considered by the authors.

The Czochralski (CZ) crystallization process is used to grow monocrystals (single crystals). Among the most important applications of the CZ process is production of monocrystalline silicon. Monocrystalline silicon is used for production of solar cells and in computers and electronics.

The rewriting of the second step of DARX is validated using timeseries logged at a real-life CZ process.

INNOVATION PROCESS

The actual ("true") innovation process, e_k , is the part of the measured system output, y_k , that can *not* be explained from previous system inputs, $u_{-\infty}, \dots, u_{k-1}$, and previous system outputs, $y_{-\infty}, \dots, y_{k-1}$, under the assumption of no model errors. For biproper systems, the current input, u_k , is also included in the explanation of y_k . The actual innovation process is typically caused by non-measured process disturbances and measurement noise.

The identified innovation process, f_k , is an estimate of the actual innovation process, e_k . The differences between the actual innovation process and the identified innovation process are typically caused by imperfect models and limited number of previous inputs and previous outputs being available.

A known input which has no measurement error is referred to as a deterministic input. A system having only deterministic inputs is referred to as a deterministic system. A system having both deterministic inputs and nonzero innovation process is referred to as a deterministic / stochastic system.

ARX AND ARMAX

The term ARX refers to a dynamic model on the form of Eq. 1.

$$A(z) y_k = B(z) u_k + f_k \tag{1}$$

The term ARX also refers to a system identification algorithm that identifies models on the form of Eq. 1. This algorithm is derived as follows: Using the definitions of A(z), B(z), and z from the nomenclature, Eq. 1 can be written as Eq. 2.

$$y_k = -a_1 y_{k-1} - \dots - a_{n_A} y_{k-n_A}$$

$$+b_1 u_{k-1} + \dots + b_{n_B} u_{k-n_B} + f_k$$
(2)

Define the column vector \mathbf{u}_k as in Eq. 3.

$$\mathbf{u}_{k} \stackrel{\text{def}}{=} \begin{bmatrix} u_{k} & u_{k+1} & \dots \end{bmatrix}^{T} \tag{3}$$

Here k is the timestep index of the first element in the vector. The number of elements in the vector will be discussed shortly. The column vectors \mathbf{f}_k and \mathbf{y}_k are defined similarly for f and y, respectively. Define the regression matrix \mathbf{R}_k and the parameter vector \mathbf{p} as in Eq. 4 and Eq. 5.

$$\mathbf{R}_{k} \stackrel{\text{def}}{=} \begin{bmatrix} -\mathbf{y}_{k-1} & \dots & -\mathbf{y}_{k-n_{A}} & \mathbf{u}_{k-1} & \dots & \mathbf{u}_{k-n_{B}} \end{bmatrix}$$
(4)

$$\mathbf{p} \stackrel{\text{def}}{=} \left[a_1 \dots a_{n_A} b_1 \dots b_{n_B} \right]^T$$
 (5)

Multiple instances of Eq. 2, for increasing values of k, can be stacked in a column vector and then written in the form of Eq. 6.

$$\mathbf{y}_k = \mathbf{R}_k \, \mathbf{p} + \mathbf{f}_k \tag{6}$$

The *i*th row of Eq. 6 is equivalent to Eq. 2 for k := k + i - 1. Assuming that the first timestep in a timeseries has index 1, the lowest value for k is $k = \max(n_A, n_B) + 1$. The number of rows in Eq. 6 is limited by the number of samples in the timeseries. The ARX algorithm is to solve Eq. 6 with respect to **p** using the ordinary least squares (OLS) method, where \mathbf{f}_k is considered the residual. Hence the model identified by the ARX algorithm is given by Eq. 1 or, equivalently, by Eq. 2, where the model parameters are given by the parameter vector **p** computed from Eq. 7.

$$\mathbf{p} = (\mathbf{R}_k^T \, \mathbf{R}_k)^{-1} \, \mathbf{R}_k^T \, \mathbf{y}_k \tag{7}$$

The term ARMAX refers to a dynamic model on the form of Eq. 8. The DARX algorithm uses the ARX algorithm twice to identify a model on the ARMAX form.

$$A(z) y_k = B(z) u_k + C(z) f_k$$
 (8)

DSR E AND DARX

DSR E is a system identification algorithm for identification of deterministic / stochastic linear time-invariant (LTI) systems. Two somewhat different versions of DSR E are derived in references [1] and [4], respectively.

The DSR E algorithm consists of two steps. Step 1: The identification problem is reduced from a deterministic / stochastic problem to a deterministic problem. The purpose of this reduction is that identification of a deterministic system is a much simpler problem. The stochastic part of the problem is eliminated by identifying the innovation process, f, and then consider the identified innovation process

as a deterministic input. Step 2: Identify the deterministic system having u and f as deterministic inputs, and y as output. For a detailed explanation of DSR E, please refer to references [1, 4].

Reference [2] shows that the first step of DSR E is mathematically identical to the ARX algorithm: The identified innovation process, f, is mathematically identical to the one-step-ahead prediction error as the identified ARX model is simulated on its own training dataset. After this first step, the problem is reduced to a deterministic identification problem. This deterministic problem can be solved using ARX. Hence each of the two steps of DSR E can be replaced by or approximated by the ARX algorithm. The total DSR E algorithm can then be approximated by a two-step ARX algorithm. This approximation is referred to as the DARX algorithm [2].

It should be emphasized that DARX is *not* a new system identification algorithm. It is an approximation of DSR E that may be easier to understand and easier to implement in a computer program. DARX is also interesting because it shows the close relationship between ARX and DSR E, even though their derivations may seem quite different.

The DARX algorithm is derived as follows: Define matrix S_k as in Eq. 9.

$$\mathbf{S}_{k} \stackrel{\text{def}}{=} \begin{bmatrix} -\mathbf{y}_{k-1} & \dots & -\mathbf{y}_{k-J} & \mathbf{u}_{k-1} & \dots & \mathbf{u}_{k-J} \end{bmatrix}$$
(9)

Matrix S_k is to be used during the first step of the DARX algorithm. It is identical to \mathbf{R}_k of Eq. 4, with n_A and n_B set to J. Define matrix \mathbf{M}_k as in Eq. 10.

$$\mathbf{M}_k = \mathbf{S}_k \left(\mathbf{S}_k^T \mathbf{S}_k \right)^{-1} \mathbf{S}_k^T \tag{10}$$

Matrix \mathbf{M}_k is a projection matrix projecting onto the column space of \mathbf{S}_k . Putting Eq. 7 into Eq. 6, replacing \mathbf{R}_k by \mathbf{S}_k , and using Eq. 10 gives Eq. 11.

$$\mathbf{y}_k = \mathbf{M}_k \, \mathbf{y}_k + \mathbf{f}_k \tag{11}$$

The term $\mathbf{M}_k \mathbf{y}_k$ is the projection of \mathbf{y}_k onto the column space of \mathbf{S}_k . Equivalently: $\mathbf{M}_k \mathbf{y}_k$ is the part of \mathbf{y}_k that can be explained from the inputs, u, and outputs, y, as organized in the matrix \mathbf{S}_k . The part of \mathbf{y}_k that can *not* be explained from \mathbf{S}_k is the residual \mathbf{f}_k . DARX uses \mathbf{f}_k , as solved from Eq. 11, as an estimate of the innovation process, i.e. the *identified* innovation process. In other words: The first step of DARX

is to compute \mathbf{f}_k by solving Eq. 11 with respect to \mathbf{f}_k . The choice of J in Eq. 9 is most important. This is discussed in reference [2].

The second step of DARX is to develop an ARMAX model, i.e. a model on the form of Eq. 8. This model is the final model identified by DARX. Under the assumptions that the system to be identified is a perfect LTI system, and that the innovation process is perfectly identified, i.e. $f_k = e_k \forall k$, the second step of DARX is a deterministic identification problem. Even though these assumptions are not perfectly met for most real-life systems, the second step of DARX is still considered as a deterministic identification problem. During the second step of DARX, both u and f are considered deterministic inputs. The output is y.

The ARMAX model of Eq. 8 can be written as Eq. 12.

$$y_{k} = -a_{1} y_{k-1} - \dots - a_{n_{A}} y_{k-n_{A}}$$

$$+b_{1} u_{k-1} + \dots + b_{n_{B}} u_{k-n_{B}}$$

$$+f_{k} + c_{1} f_{k-1} + \dots + c_{n_{C}} f_{k-n_{C}}$$

$$(12)$$

Please notice that no coefficient is associated with f_k in Eq. 12. Moving f_k to the left side gives Eq. 13.

$$y_{k} - f_{k} = -a_{1} y_{k-1} - \dots - a_{n_{A}} y_{k-n_{A}}$$

$$+b_{1} u_{k-1} + \dots + b_{n_{B}} u_{k-n_{B}}$$

$$+c_{1} f_{k-1} + \dots + c_{n_{C}} f_{k-n_{C}}$$

$$(13)$$

In Eq. 13 all y, u, and f on the right side are associated with coefficients. Multiple instances of Eq. 13, for increasing values of k, can be stacked in a column vector and then written in the form of Eq. 14.

$$\mathbf{y}_k - \mathbf{f}_k = \mathbf{T}_k \, \mathbf{q} \tag{14}$$

The regression matrix \mathbf{T}_k contains, from left to right, the column vectors $-\mathbf{y}_{k-1}$, ..., $-\mathbf{y}_{k-n_A}$, \mathbf{u}_{k-1} , ..., \mathbf{u}_{k-n_B} , \mathbf{f}_{k-1} , ..., \mathbf{f}_{k-n_C} . The parameter vector \mathbf{q} is a column vector containing the elements a_1 , ..., a_{n_A} , b_1 , ..., b_{n_B} , c_1 , ..., c_{n_C} . Using OLS the parameter vector \mathbf{q} is given by Eq. 15.

$$\mathbf{q} = (\mathbf{T}_k^T \mathbf{T}_k)^{-1} \mathbf{T}_k^T (\mathbf{y}_k - \mathbf{f}_k)$$
 (15)

Hence the final model identified by the DARX algorithm is an ARMAX model, where the parameters of the polynomials A(z), B(z), and C(z) are the

elements of the parameter vector \mathbf{q} . It is most important to understand that the definition of the innovation process requires the constant term of C(z) to be 1, i.e. no coefficient can be associated with f_k in Eq. 12. How to select n_A , n_B , and n_C is a most important issue. However, this issue is beyond the scope of this paper.

IMPLEMENTATION OF DARX

When implementing DARX in a computer program, the implementation can be simplified using standard ARX software, such as the MATLAB command arx, instead of implementing the ARX algorithm from scratch. Using MATLAB, the first step of DARX is straight forward: An ARX model is identified using arx, then the innovation process, f, is identified using pe (prediction error).

Unfortunately, it is *not* straight forward to use arx to implement the second step of DARX. The main contribution of this paper is to explain the reason for this issue, and to provide a rewriting such that arx can be used for the second step of DARX after all. To simplify the discussion, the values $n_A = 1$, $n_B = 1$, and $n_C = 1$ will be used, unless otherwise is specified. However, the result to be presented is valid for any values of n_A , n_B , and n_C .

During the second step of DARX, u and f are considered deterministic inputs. The output is y. Using arx straight forward, a model will be identified by solving the linear regression problem of Eq. 16.

$$\mathbf{y}_{k} = \begin{bmatrix} -\mathbf{y}_{k-1} & \mathbf{u}_{k-1} & \mathbf{f}_{k} & \mathbf{f}_{k-1} \\ \times \begin{bmatrix} a_{1} & b_{1} & c_{0} & c_{1} \end{bmatrix}^{T} \end{bmatrix}$$
(16)

The problem to be handled is the parameter c_0 . This parameter should *not* be subject to identification, because its value must be 1 according to the definition of innovation process. The solution is to remove c_0 from the parameter vector and move the column vector \mathbf{f}_k to the left side. Define $\mathbf{\bar{y}}_k \stackrel{\text{def}}{=} \mathbf{y}_k - \mathbf{f}_k \ \forall \ k$. The regression problem is then on the form of Eq. 17.

$$\bar{\mathbf{y}}_{k} = \begin{bmatrix} -\mathbf{y}_{k-1} & \mathbf{u}_{k-1} & \mathbf{f}_{k-1} \\ \times \begin{bmatrix} a_{1} & b_{1} & c_{1} \end{bmatrix}^{T} \end{bmatrix}$$
(17)

Eq. 17 violates the standard ARX form of Eq. 16, because Eq. 17 has $\bar{\mathbf{y}}_k$ on the left side, but the column in the regression matrix associated with a_1 is $-\mathbf{y}_{k-1}$.

The standard ARX form requires either \mathbf{y}_k on the left side and $-\mathbf{y}_{k-1}$ associated with a_1 , or $\bar{\mathbf{y}}_k$ on the left side and $-\bar{\mathbf{y}}_{k-1}$ associated with a_1 . As the standard ARX form is violated, arx can not be used directly to identify the parameter vector of Eq. 17.

A solution to this problem is to implement from scratch a tailor-made, non-standard ARX algorithm that assumes the form of Eq. 17. However, this will complicate the implementation of DARX. The simpler solution is to rewrite Eq. 17 to the standard ARX form. This rewriting is split into two cases: Case 1 is to be applied when $n_A \leq n_C$. Case 2 is to be applied when $n_A \geq n_C$. When $n_A = n_C$, either of the cases can be applied.

Case 1: $n_A \leq n_C$

This derivation is valid for any values of n_A , n_B , and n_C which obey the constraint $n_A \le n_C$. The values $n_A = 1$, $n_B = 1$, and $n_C = 2$ will be used to simplify the discussion. Eq. 18 is identical to Eq. 17, except that n_C is increased from 1 to 2.

$$\bar{\mathbf{y}}_{k} = \begin{bmatrix} -\mathbf{y}_{k-1} & \mathbf{u}_{k-1} & \mathbf{f}_{k-1} & \mathbf{f}_{k-2} \\ \times \begin{bmatrix} a_{1} & b_{1} & c_{1} & c_{2} \end{bmatrix}^{T} \end{bmatrix} (18)$$

The issue is how to rewrite Eq. 18 to the standard ARX form, so that arx can be used to identify the parameter vector. The column of the regression matrix associated with the parameter a_1 must be $-\bar{\mathbf{y}}_{k-1}$, not $-\mathbf{y}_{k-1}$, because the left side is $\bar{\mathbf{y}}_k$, not \mathbf{y}_k . It must be required that the rewriting does not change the column space of the regression matrix, otherwise the parameter vector will be identified erroneously. Adding a column of a matrix to another column of the same matrix does not change the column space of the matrix. This is a basic result of linear algebra. The desired rewriting is achieved by adding the column \mathbf{f}_{k-1} to the column $-\mathbf{y}_{k-1}$. This column summation changes Eq. 18 into the form of Eq. 19.

$$\bar{\mathbf{y}}_{k} = \begin{bmatrix}
-\bar{\mathbf{y}}_{k-1} & \mathbf{u}_{k-1} & \mathbf{f}_{k-1} & \mathbf{f}_{k-2} \\
\times \begin{bmatrix} \bar{a}_{1} & \bar{b}_{1} & \bar{c}_{1} & \bar{c}_{2} \end{bmatrix}^{T}
\end{cases} (19)$$

Eq. 19 is on the standard ARX form. Hence the parameter vector of Eq. 19 can be identified using arx. Three important comments regarding this derivation: (i) The output specified to arx should be $\bar{y} = y - f$, not y. The deterministic inputs are

u and f. (ii) The columns \mathbf{u}_k and \mathbf{f}_k are not in the regression matrix of Eq. 19. This is equivalent to the transfer functions from u to \bar{y} , and from f to \bar{y} , having a time delay of one sample. This should be specified to arx by setting the time delay parameter nk to 1 for both inputs. (iii) The parameter vectors of Eq. 18 and Eq. 19 differ (the elements in the parameter vector of Eq. 19 have bars). The desired parameter vector of Eq. 18 is related to the identified parameter vector of Eq. 19 by $a_1 = \bar{a}_1$, $b_1 = \bar{b}_1$, $c_1 = \bar{a}_1 + \bar{c}_1$, and $c_2 = \bar{c}_2$.

This derivation can easily be generalized to any values of n_A , n_B , and n_C that obey the constraint $n_A \le n_C$. The desired parameter vector of Eq. 18 is related to the identified parameter vector of Eq. 19 by $a_i = \bar{a}_i \, \forall \, i, \, b_i = \bar{b}_i \, \forall \, i, \, c_i = \bar{a}_i + \bar{c}_i \, \forall \, i \in \{1, \dots, n_A\},$ and $c_i = \bar{c}_i \, \forall \, i > n_A$.

Case 2: $n_A > n_C$

The case $n_A \ge n_C$ is somewhat more complex. The derivation to be presented is valid for any n_A , n_B , and n_C which obey the constraint $n_A \ge n_C$. The values $n_A = 2$, $n_B = 1$, and $n_C = 1$ will be used to simplify the discussion. Eq. 20 is identical to Eq. 17, except that n_A is increased from 1 to 2.

$$\bar{\mathbf{y}}_{k} = \begin{bmatrix} -\mathbf{y}_{k-1} & -\mathbf{y}_{k-2} & \mathbf{u}_{k-1} & \mathbf{f}_{k-1} \\ \times \begin{bmatrix} a_{1} & a_{2} & b_{1} & c_{1} \end{bmatrix}^{T} \end{bmatrix} (20)$$

For $n_A > n_C$ the rewriting presented for $n_A \le n_C$ can not be applied. In Eq. 20 the column $-\mathbf{y}_{k-1}$ can be changed to $-\bar{\mathbf{y}}_{k-1}$ by adding the column \mathbf{f}_{k-1} . However, the column $-\mathbf{y}_{k-2}$ can *not* be changed to $-\bar{\mathbf{y}}_{k-2}$, because \mathbf{f}_{k-2} is not in the column space of the regression matrix. In other words: Adding \mathbf{f}_{k-2} would change the column space of the regression matrix. This would cause the DARX implementation to identify erroneous models.

Rewriting the $n_A \ge n_C$ case includes rearranging the columns of the regression matrix. The columns $-\mathbf{y}_{k-1}$ and $-\mathbf{y}_{k-2}$ are moved to the right, and the column \mathbf{f}_{k-1} is moved to the left as shown in Eq. 21.

$$\bar{\mathbf{y}}_{k} = \begin{bmatrix} \mathbf{f}_{k-1} & \mathbf{u}_{k-1} & -\mathbf{y}_{k-1} & -\mathbf{y}_{k-2} \\ \times \begin{bmatrix} \bar{a}_{1} & \bar{b}_{1} & \bar{c}_{1} & \bar{c}_{2} \end{bmatrix}^{T} \end{bmatrix} (21)$$

Please note the change of the parameter vector from Eq. 20 to Eq. 21. The column \mathbf{f}_{k-1} can be changed

to the desired form, $-\bar{\mathbf{y}}_{k-1}$, by adding the column $-\mathbf{y}_{k-1}$. This column summation does not change the column space of the regression matrix. The regression problem is now on the form of Eq. 22.

$$\bar{\mathbf{y}}_{k} = \begin{bmatrix}
-\bar{\mathbf{y}}_{k-1} & \mathbf{u}_{k-1} & -\mathbf{y}_{k-1} & -\mathbf{y}_{k-2} \\
\times \begin{bmatrix} \tilde{a}_{1} & \tilde{b}_{1} & \tilde{c}_{1} & \tilde{c}_{2} \end{bmatrix}^{T}
\end{bmatrix} (22)$$

Please note the change of the parameter vector from Eq. 21 to Eq. 22. Eq. 22 is on the standard ARX form. Hence its parameter vector can be identified using arx. There are three important comments also for this derivation: (i) The inputs specified to arx are u and -y, and the output is $\bar{y} = y - f$. (ii) The time delay parameter nk of arx should be set to 1 for both inputs. (iii) The desired parameter vector of Eq. 20 is related to the identified parameter vector of Eq. 22 by $a_1 = \tilde{a}_1 + \tilde{c}_1$, $a_2 = \tilde{c}_2$, $b_1 = \tilde{b}_1$, and $c_1 = \tilde{a}_1$.

This derivation can easily be generalized to any values of n_A , n_B , and n_C which obey the constraint $n_A \ge n_C$. The desired parameter vector of Eq. 20 is related to the identified parameter vector of Eq. 22 by $a_i = \tilde{a}_i + \tilde{c}_i \, \forall \, i \in \{1, \dots, n_C\}, \, a_i = \tilde{c}_i \, \forall \, i > n_C, \, b_i = \tilde{b}_i \, \forall \, i$, and $c_i = \tilde{a}_i \, \forall \, i$.

THE CZOCHRALSKI PROCESS

The Czochralski (CZ) crystallization process is named after its inventor, the Polish scientist Jan Czochralski. The CZ process is used to grow monocrystals (single crystals). Production of monocrystalline silicon is among the most important applications of the CZ process. Monocrystalline silicon is used in solar cells as well as computers and electronics.

The CZ process is a batch process. Initially multicrystalline silicon is melted in a crucible. Dopant materials, such as boron or phosphorus, may be added to the crucible. When the silicon is all molten, a seed crystal of monocrystalline silicon is dipped into the melt. As the seed crystal is slowly elevated, the molten silicon solidifies on the seed crystal. The seed crystal then grows radially and axially, while preserving its crystal structure. The produced rod of monocrystalline silicon is referred to as the ingot. The CZ process is performed in an inert atmosphere, such as an argon atmosphere. Figure 1 illustrates the principle of operation of the CZ process for production of monocrystalline silicon.

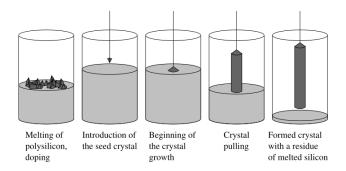


Figure 1: The Czochralski process, principle of operation. Illustration from Wikipedia.

With respect to control of the CZ process, a tight control of the ingot diameter is most important in order to minimize cutting waste. There are also several quality parameters that should be met, such as dislocation level, impurity content, and dopant distribution. Unfortunately, these quality parameters can not be measured online and can therefore not be used as control objectives for control strategies [3].

A control strategy for the CZ process is presented in reference [3]. This control strategy is based on single loop control, cascade control, and feedforward trajectories. The control strategy is thoroughly explained in reference [3] and will not be repeated here.

VALIDATION OF THE DARX REWRITING

This paper presents a rewriting of the second step of the DARX algorithm. This rewriting allows arx to be used also for the second step of DARX, canceling the need for implementing a tailor-made ARX algorithm. Hence the rewriting simplifies the overall implementation of DARX.

In this section the DARX rewriting is validated using timeseries logged at a real-life CZ process owned and operated by SINTEF Materials and Chemistry in Trondheim, Norway. At this CZ process the temperature of the crucible is controlled by adjusting the electric power to a heating element using TRIACs. The temperature is measured using a pyrometer. The DARX rewriting is validated by identifying the transfer function from the control signal of the TRIACs, P, to the voltage output signal from the pyrometer, T. The timeseries used for identification are shown in Figure 2. These timeseries were logged during heating of the crucible before the actual crystal pulling started, because it then could be

done larger excitations in *P* than during the crystal pulling.

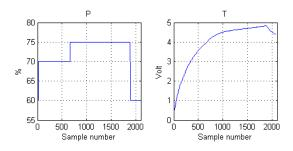


Figure 2: Timeseries *P* and *T* used for identification of the transfer function from *P* to *T*.

In this validation four implementations of DARX, referred to as A, B, C, and D, will be compared. Implementation A uses a tailor-made, non-standard ARX algorithm to handle the second step of DARX. In other words: Implementation A handles the form of Eq. 17 directly. The main disadvantage of this approach is that implementing the tailor-made ARX algorithm significantly complicates the implementation of DARX. Implementations B, C, and D use the rewriting presented in this paper and arx to handle the second step of DARX. Implementation B implements only case 1, i.e. $n_A \leq n_C$. Implementation C implements only case 2, i.e. $n_A \ge n_C$. Implementation D calls implementation B as a sub-routine if $n_A \leq n_C$, otherwise implementation D calls implementation C. Implementations A, B, C, and D all use arx for the first step of DARX.

The validation of the DARX rewriting consists of three tests. In each test the transfer function from the control signal P to the measurement signal T is identified based on the timeseries shown in Figure 2. The same timeseries are used in all three tests. In each test four models are identified, one for each of the implementations A to D. Implementation A is known to work correctly and is used as a reference for validating the other implementations.

In test #1 the values $n_A = 1$, $n_B = 1$, and $n_C = 2$ are used. Hence the parameters a_1 , b_1 , c_1 , and c_2 are to be identified. The identified parameters are shown in Figure 3. Implementations A, B, and D identify the parameters identically. Hence B and D identify the parameters correctly as A is known to be correct. This was expected, because B is implemented to handle the constraint $n_A \le n_C$, which is obeyed, and D calls B as a sub-routine when this constraint

is obeyed. Implementation C identifies the parameters erroneously. This is because C assumes the constraint $n_A \ge n_C$, which is violated.

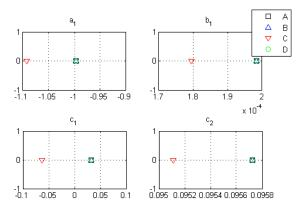


Figure 3: Parameters a_1 , b_1 , c_1 , and c_2 as identified in test #1.

Test #2 uses the values $n_A = 2$, $n_B = 1$, and $n_C = 1$. The parameters a_1 , a_2 , b_1 , and c_1 are then to be identified. The identified parameters are shown in Figure 4. In this test C and D identify the parameters correctly, while B does not. This is because B assumes the constraint $n_A \le n_C$, which is violated in this test.

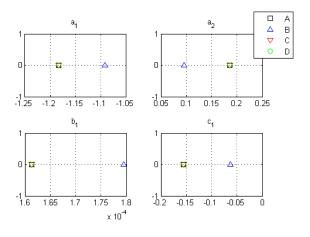


Figure 4: Parameters a_1 , a_2 , b_1 , and c_1 as identified in test #2.

In test #3, the values $n_A = 2$, $n_B = 1$, and $n_C = 2$ are used. Hence the parameters a_1 , a_2 , b_1 , c_1 , and c_2 are to be identified. In this test, all implementations identify the parameters correctly, because the constraints $n_A \le n_C$ and $n_A \ge n_C$ both are obeyed. This result is *not* illustrated graphically.

In all three tests the parameter J, which was intro-

duced in Eq. 9, was set to J = 10. This parameter does not influence the validation result because it is only used during step 1 of DARX, while the rewriting only considers step 2.

Summing up the tests shows that implementation B, which is based on case 1, identifies the parameters correctly if and only if the constraint $n_A \le n_C$ is obeyed. Implementation C, which is based on case 2, identifies the parameters correctly if and only if the constraint $n_A \ge n_C$ is obeyed. Hence the results of the validation back up the mathematical derivation of the rewriting. It is then concluded that the rewriting works correctly.

CONCLUSION

DARX is a two-step ARX algorithm which approximates the DSR E system identification algorithm. The first step of DARX is on the standard ARX form, allowing standard ARX software, such as the MATLAB command arx, to be used directly. The second step of DARX slightly differs from the standard ARX form. This issue can be handled by implementing from scratch a tailor-made, non-standard ARX algorithm. However, this approach significantly complicates the otherwise simple implementation of DARX.

The main contribution of this paper is to present a rewriting of the second step of DARX. Using this rewriting standard ARX software can be used also for the second step of DARX. Hence the need for a tailor-made ARX algorithm is canceled.

The Czochralski (CZ) crystallization process is used to grow monocrystals (single crystals). Production of monocrystalline silicon is among the most important applications of the CZ process. Monocrystalline silicon is used in solar cells, computers, and electronics.

The rewriting of the second step of DARX has been validated by comparing four implementations of DARX. These implementations were tested by identifying a transfer function in the CZ process based on timeseries logged at a real-life CZ process. One implementation uses a tailor-made, non-standard ARX algorithm to handle the second step of DARX. The other three implementations use the rewriting presented in this paper. As the results of this validation back up the mathematical derivation, it is concluded that the rewriting is correct.

ACKNOWLEDGMENTS

The authors are most grateful to SINTEF Materials and Chemistry in Trondheim, Norway, for allowing timeseries logged at a CZ process owned and operated by the organization to be used in this paper. The authors are also very grateful to Eivind Johannes Øvrelid at SINTEF Materials and Chemistry for sharing his knowledge and experience of the CZ process. Beathe Furenes at Prediktor AS is acknowledged for her participation and contribution to the CZ batch of which the timeseries used in this paper were logged.

The main author is most grateful for the financial support of his PhD study from NorSun AS, Østfold Energi AS, and the Norwegian Research Council. The cooperation with NorSun AS, Prediktor AS, and SINTEF Materials and Chemistry is also very much appreciated.

REFERENCES

- [1] D. Di Ruscio. Subspace system identification of the Kalman filter: Open and closed loop systems. In *The 6th international conference on Computing, Communication and Control Technologies (CCCT 2008)*, Orlando, Florida, June 29th July 2nd 2008.
- [2] M. Komperød, TA. Hauge, D. Di Ruscio, and B. Lie. Empirical modeling: Approximating the DSR E sub-space system identification algorithm by a two-step ARX algorithm. In *The* 49th Scandinavian Conference on Simulation and Modeling (SIMS 2008), October 7th 8th 2008.
- [3] K. Lee, D. Lee, J. Park, and M. Lee. MPC based feedforward trajectory for pulling speed tracking control in the commercial Czochralski crystallization process. *International Journal of Control, Automation, and Systems*, 3:252–257, 2005.
- [4] GW. Nilsen. Topics in Open and Closed Loop Subspace System Identification: Finite Data-Based Methods. PhD thesis, Norwegian University of Science and Technology / Telemark University College, Trondheim / Porsgrunn, Norway, 2006.

DYNAMIC SIMULATION OF SOLAR COLLECTOR FIELDS IN CHANGING OPERATING CONDITIONS

Esko K. Juuso*
Control Engineering Laboratory
Department of Process and Environmental Engineering,
P.O. Box 4300, FI-90014 University of Oulu, Finland

ABSTRACT

Solar power plants should be designed to collect all the available thermal energy in a usable form within a desired temperature range. In cloudy conditions, the collector field is maintained in a standby mode ready for full-scale operation when the intensity of the sunlight rises again. Control is achieved by means of varying the flow of oil pumped through the pipes during the plant operation. Dynamic linguistic equation (LE) models provide a smooth and accurate overall behaviour, which can be further extended by specialized fuzzy models, distributed parameter models, and uncertainty processing with fuzzy interval analysis. The multilevel LE controller with predefined adaptation models, smart features and a cascade controller results a smooth operation. The whole LE system, which is efficiently parameterised, can be tuned with genetic algorithms without using penalty functions.

Keywords: Solar energy, intelligent control, nonlinear systems, adaptation, efficiency, linguistic equations, modelling, simulation

NOMENCLATURE		e(t)	noise
A	cross section of the pipe line $[m^2]$	$e_j(k)$	error
A_{eff}	effective collector area $[m^2]$	f_j, f_{out}	scaling functions
A_{ij}, B_i, A_{iout}	parameters of LE models	h	heat transfer coefficient $[Wm^{-2}K^{-1}]$
D	pipe diameter $[m]$	n_k	delay number
F	flow rate of the oil $[m^3s^{-1}]$	t	time [s]
$ ilde{F}$	scaled flow rate of the oil	wp	working point
I_{eff}	effective irradiation $[Wm^{-2}]$	X	length coordinate [m]
$egin{aligned} I_{eff} \ \widetilde{I}_{eff} \ T \end{aligned}$	scaled effective irradiation	x_j, u	input variable
T	oil temperature $[{}^{o}C]$	x_{out}, y	output variable
T_{amb}	ambient temperature $[{}^{o}C]$	y_0	initial condition
$ ilde{T}_{amb}$	scaled ambient temperature	$lpha_i^-, lpha_i^+$	support coefficients
T_{diff}	temperature difference $[{}^{o}C]$	$\Delta c_i^-, \Delta c_i^+$	core around the working point
$ ilde{T}_{diff}$	scaled temperature difference	$\Delta e_{i}^{j}(k)$	derivative of the error
T_I	time period of integration	Δt	time step $[s]$
T_{in}	inlet temperature $[{}^{o}C]$	$\Delta u_i(k)$	change of control
T_{out}	outlet temperature $[{}^{o}C]$	η_0	optical efficiency
W	width of the mirror $[m]$	η_p	a general loss factor
a_i, b_1	constant coefficients	ρ	oil density kgm^{-3}
c	specific heat of oil $[Jkg^{-1}K^{-1}]$	•	• 0
c_j	working point		

^{*}Corresponding author: Phone: +358 8 5532463 Fax +358 8 5532304 E-mail:esko.juuso@oulu.fi

INTRODUCTION

Solar power plants should collect any available thermal energy is in a usable form at the desired temperature range, which improves the overall system efficiency and reduces the demands placed on auxiliary equipments. In cloudy conditions, the collector field is maintained in a state of readiness for the resumption of full-scale operation when the intensity of the sunlight rises once again.

Solar collector field is good test platform for various control methodologies [1, 2]. An overview of possible control strategies presented in [1] include basic feedforward and PID schemes, adaptive control, model-based predictive control, frequency domain and robust optimal control and fuzzy logic control. A comparison of several intelligent controllers was presented in [2].

Models have been integrated to various control schemes. Feedforward approaches based directly on the steady state energy balance relationships can use measurements of solar radiation and inlet temperature [3]. Lumped parameter models taking into account the sun position, the field geometry, the mirror reflectivity, the solar radiation and the inlet oil temperature have been developed for a solar collector field [1]. A feedforward controller has been combined with different feedback controllers, even PID controllers operate for this purpose [4]. The classical internal model control (IMC) can operate efficiently in varying time delay conditions [5].

An object oriented dynamic model, which is based in the thermohydraulic modelling framework ThermoFluid, within the Modelica modelling language, has been presented in [6].

Linguistic equations have been used in various industrial applications [2, 7]. Modelling and control activities with the LE methodology started by the first LE controllers implemented in 1996 [8] and the first dynamic LE models developed in 1999 [9]. The robust dynamic simulator based on linguistic equations is an essential tool in fine—tuning of these controllers [10]. This data-driven dynamic LE modelling approach has been combined with a dynamic energy balance and extended to developing distributed parameter models [11]. The operating area of LE controllers has been extended by using model-based adaptation and feedforward features, which are aimed for preventing overheating. The present controller takes also care of the actual

set points of the temperature [12]. The overall system is used in control design [13].

Genetic algorithms with binary coding combined with simulation and model-based predictive control have further reduced temperature differences between collector loops [14]. An advanced tuning approach has been introduced in [15].

All the experiments have been carried out in the *Acurex Solar Collectors Field of the Plataforma Solar de Almeria* in Spain. An extensive number of daily data sets are available as the process needs to be controlled all the operating time. Test campaigns include step changes and load disturbances but they cannot be planned in detail because of changing weather conditions, e.g. irradiation disturbances.

This paper presents a multilevel, parameterised LE simulation system used in control design of a solar collector field.

SOLAR COLLECTOR FIELD

The aim of solar thermal power plants is to provide thermal energy for use in an industrial process such as seawater desalination or electricity generation. In addition to seasonal and daily cyclic variations, the intensity depends also on atmospheric conditions such as cloud cover, humidity, and air transparency. Unnecessary shutdowns and start-ups of the collector field are both wasteful and time consuming. Finally if the control is fast and well damped, the plant can be operated close to the design limits thereby improving the productivity of the plant [16].

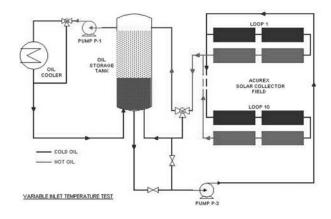


Figure 1: Layout of the Acurex solar collector field.

The Acurex solar collector field supplies thermal energy $(1 MW_t)$ in form of hot oil: the consists

of parabolic–trough collectors (Figure 1): 480 distributed solar collectors modules are arranged in 10 parallel rows. Each row contains 4 groups with 12 modules each group, i.e. 48 modules, see [6, 8]. Control is achieved by means of varying the flow pumped through the pipes during the plant operation. The oil is stored in a thermal storage tank of $140 \, m^3$ capacity: the oil properties permit stratified energy storage according to its density, allowing the use of only one tank for both cold and hot oil, the hottest oil being situated at the top of the tank. The stored energy is then transformed via a conversion system that can either be a steam turbine for generating electricity, or a desalination plant [6].

The collector field status must be monitored to prevent potentially hazards situations, e.g. oil temperatures greater than $300\,^{o}C$. The oil flow rate is limited between 2 and $10\,l/s$. In beginning of the daily operation, high flow rates should not be used. The temperature increase in the field may rise up to $110\,$ degrees, preferably it should be less than $80\,^{o}C$. In the beginning of the daily operation, the oil is circulated in the field, and the valve to storage system (Figure 1) is open when an appropriate outlet temperature is achieved.

The maximum of the outlet temperatures of the loops The collector loops do not operate identically: the difference between loops increases when the flow of oil is changed rapidly [11]. Therefore, the maximum loop temperatures as well as the maximum temperature differences over the loops are important in keeping the field in good condition.

Energy balance

The *energy balance* of the collector field can be represented by expression [4]

$$I_{eff}A_{eff} = (1 - \eta_p)F\rho cT_{diff} \tag{1}$$

where I_{eff} is effective irradiation (Wm^{-2}) , A_{eff} effective collector area (m^2) , η_p a general loss factor, F flow rate of the oil (m^3s^{-1}) , ρ oil density kgm^{-3} , c specific heat of oil $(Jkg^{-1}K^{-1})$ and T_{diff} temperature difference between the inlet and the outlet $({}^oC)$. The effective irradiation is the direct irradiation modified by taking into account the solar time, declination and azimuth.

A simple feedforward controller

$$F = \alpha \frac{I_{eff}}{T_{out} - T_{in}} \tag{2}$$

can be obtained by combining the oil characteristics and geometrical parameters into a term

$$\alpha = \frac{A_{eff}}{(1 - \eta_p)\rho c}.$$
 (3)

Moving averages or medians are needed to achieve smooth changes for the outlet temperature, T_{out} , in changing operating conditions: clouds are seen in I_{eff} and load disturbances in inlet temperature T_{in} . For example, small clouds do not have effect on the overall energy collection although they may cause drastic fluctuations in the irradiation measurement.

Distributed parameter system

Differences between collector loops are handled with distributed parameter models based on the energy balance: energy stored = Irradiation - Energy transferred - Heat loss. For a unit volume this can be represented by

$$\rho cA \frac{\partial T}{\partial t} = I_{eff} W \eta_0 - \rho cF \frac{\partial T}{\partial x} - hD(T - T_{amb})$$
 (4)

where A is cross section of the pipe line (m^2) , c specific heat of oil $(Jkg^{-1}K^{-1})$, D pipe diameter (m), I_{eff} irradiation (Wm^{-2}) , h heat transfer coefficient $(Wm^{-2}K^{-1})$, T oil temperature (^{o}C) , T_{amb} ambient temperature (^{o}C) , x length coordinate (m), F flow rate (m^3s^{-1}) , W width of the mirror (m), η_0 optical efficiency, ρ oil density kgm^{-3} , t time (s).

Oil properties depend drastically on temperature, and therefore operating conditions change considerably during the working day, e.g. during the start-up stage, the oil flow is limited by the high viscosity. Large temperature differences between loops are detected when the operating conditions change drastically, i.e. start-up, strongly variating cloudiness and load disturbances. Since the irradiation is not known in different parts of the collector field, the local energy balance (4) can be used only for sensitivity analysis.

LINGUISTIC EQUATION MODELLING

Linguistic equation (LE) models consist of two parts: *interactions* are handled with linear equations, and nonlinearities are taken into account by *membership definitions* [2]. In the LE models, the nonlinear scaling is performed twice: first scaling from real values to the interval [-2, 2] before applying

linguistic equations, and then scaling from the interval [-2, 2] to real values after applying linguistic equations (Fig. 2(a)). The linguistic level of the input variable x_j is calculated the inverse functions of the polynomials [7].

Steady state LE models

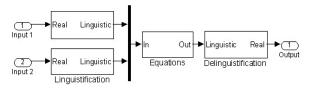
Steady state LE models are represented by

$$x_{out} = f_{out} \left(-\frac{\sum_{j=1, j \neq out}^{m} A_{ij} f_j^{-1}(x_j) + B_i}{A_{iout}} \right)$$
 (5)

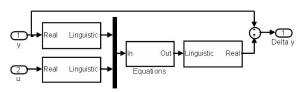
where the functions f_j and f_{out} are membership definitions of input variables x_j and output x_{out} , respectively. The variable specific functions are defined by a set

$$\{c_j, \Delta c_j^-, \Delta c_j^+, \alpha_j^-, \alpha_j^+\}$$
 (6)

where c_j is the working point, increments Δc_j^- and Δc_j^+ define the core around the working point, i.e. [-1, 1]. The coefficients α_j^- and α_j^+ , which expand the definitions to the support [-2, 2], are restricted to the range $\frac{1}{3}$...3 to get monotonously increasing scaling functions [15].



(a) A steady state LE model for two inputs and one output.



(b) Dynamic LE model of Δy .

Figure 2: LE models.

Dynamic LE models

Dynamic LE models are rather simple input-output models, where the old value of the simulated variable and the current value of the control variable as inputs and the new value of the simulated variable as an output, can be used since nonlinearities are taken into account by membership definitions (Fig. 2(b)).

For the default LE model, all the degrees of the polynomials in parametric models become very low, i.e. all the parametric models become the same

$$y(t) + a_1 y(t-1) = b_1 u(t - n_k) + e(t).$$
 (7)

This model is a special case with three variables, y(t), y(t-1) and $u(t-n_k)$, and a zero bias.

The output, the derivative of the variable *y*, is integrated with numerical integration methods:

$$y = \int_0^{T_I} F(t, y, u) dt + y_0,$$
 (8)

where T_I is the time period for integration, and y_0 the initial condition. Usually, several values from the integration step or the previous steps are used in evaluating the new value. Step size control adapts the simulation to changing operating conditions.

Effective time delays depend on the working conditions (process case), e.g. the delays are closely related to the production rate in many industrial processes. In the block shown in Figure 3, the delay of the variable *Var1* depends on the variable *Var2*: the linguistic level of the variable *Var2* is multiplied by 1 or -1 to get the linguistic level of the delay for the variable *Var1*, coefficient 1 means that the delay increases when the variable *Var2* increases. The real value of the delay is obtained by the delinguistification block.

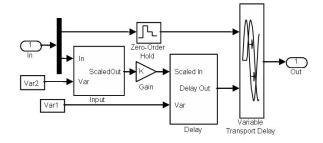


Figure 3: Variable delay.

Uncertainty

Universal approximators for fuzzy functions can be constructed as extension principle extensions of continuous real-valued functions which continuously map fuzzy numbers into fuzzy numbers [17, 18]. The dynamic LE models with fuzzy inputs were introduced in forecasting of batch cooking in a pulp

mill [19], and later adapted to dynamic modelling of a fluidised bed granulator used in production of pharmaceuticals [20], and dynamic simulation of a fed-batch enzyme fermentation process [21].

In this approach, LE models are extended to fuzzy inputs with this approach if the membership definitions, i.e. functions f_j and the corresponding inverse functions, are replaced by corresponding extension principle extensions of these functions. The argument of the function f_{out} in (5) is obtained by fuzzy arithmetic. Only addition and subtraction are needed if the interaction coefficients are crisp. Fuzzy LE models with fuzzy inputs can be constructed by using multiplication and division as well. Fuzzy extension of the classical interval analysis [22] suits very well to these calculations. Finally, the delinguistication block uses also second order polynomials defined.

GENETIC TUNING

Structural restrictions of the LE models are beneficial for tuning and adaptation. Manual tuning consists two independent parts: scaling and interactions. Both can be defined manually but the constraints must be taken into account when defining the scaling functions. Neural tuning reduces the error between the model and the training data [2]: membership definitions are tuned for one variable of the equation at a time with a linear neural network. For matrix equations, only one variable from each equation can be selected for tuning. Recursive implementations of the regression or the linear network make on-line adaptation possible.

Genetic algorithms can handle the whole system simultaneously by comparing the effects of the parameters defined by the scaling functions, interactions, time delays, and the weights of the models [15]. Scaling functions of the variables and time delays are tuned with the parameter sets (6). This coding is essential for handling hybrid models. All alternative parameter sets result acceptable models if the coefficients α_j^- and α_j^+ are restricted to the range $\frac{1}{3}\dots 3$. Penalty terms can be used for reducing model complexity.

The fitness values of the models are obtained through simulation, and the new approach reduces the simulation runs considerably. Genetic tuning is controlled by population size, number of bits, and probabilities of crossover and mutation.

SOLAR PLANT MODELS

The LE approach has been applied in modelling of the solar collector field shown in Figure 1.

Working point model

The volumetric heat capacity increases very fast in the start-up stage but later remains almost constant because the normal operating temperature range is fairly narrow. This nonlinear effect is handled with the working point LE model

$$wp = a_1 \tilde{I}_{eff} + a_2 \tilde{T}_{diff} + a_3 \tilde{T}_{amb} + a_4, \qquad (9)$$

where \tilde{I}_{eff} , \tilde{T}_{diff} and \tilde{T}_{amb} , which are obtained by nonlinear scaling of variables I_{eff} , $T_{diff} = T_{out} - T_{in}$, and T_{amb} , correspondingly. Interactions are defined by constant coefficients a_1 , a_2 , a_3 and a_4 . Working point, wp, represents a fluctuation from the normal operation.

The working point variables already define the overall normal behaviour of the solar collector field, e.g. oscillatory behaviour is a problem when the temperature difference is higher than the normal. This type of model can be used for feedforward control but the chosen control strategy will effect to the coefficients.

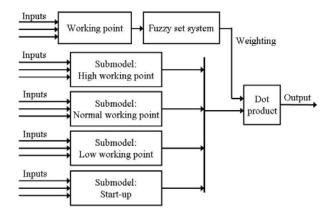


Figure 4: Dynamic LE multimodel.

Weighting of the submodels are defined by the working point model (Figure 4): the input variables are the effective solar irradiation, I_{eff} , the temperature difference between inlet and outlet temperatures, T_{diff} , and the ambient temperature T_{amb} . In the normal working point (wp = 0), the irradiation \tilde{I}_{eff} and the temperature difference, \tilde{T}_{diff} , are on the same level. High working point (wp > 0) means low \tilde{T}_{diff}

compared to the irradiation level \tilde{I}_{eff} . Correspondingly, low working point (wp < 0) means high \tilde{T}_{diff} compared to the irradiation level \tilde{I}_{eff} . The ambient temperature has a minor effect. The fuzzy set system in Figure 4 fuzzifies the wp value into four labels: start-up, low, normal and high.

Each fully nonlinear membership definition requires three parameters more than is needed for normalisation, and each equation is defined by as many parameters as there are variables [15]. As the working point does not need scaling, the number of parameters is 18.

Dynamic LE model

Conventional mechanistic models do not work: there are problems with oscillations and irradiation disturbances. In dynamic LE models, the new temperature difference $\tilde{T}_{diff}(t + \Delta t)$ between the inlet and outlet depends on the irradiation, oil flow and previous temperature difference:

$$\tilde{T}_{diff}(t + \Delta t) = a_1 \tilde{T}_{diff}(t) + a_2 \tilde{I}_{eff}(t) + a_3 \tilde{F}(t) + a_4,$$
(10)

where coefficients a_1 , a_2 , a_3 and a_4 depend on operating conditions, i.e. each submodel in Figure 4 has different coefficients. According to the tests, the fuzzy LE system with four operating areas is clearly the best overall model [10]: the simulator moves smoothly from start-up mode via low mode to normal mode and later visits shortly in high mode and low mode before returning to low mode in the afternoon. Even oscillatory conditions are handled correctly.

The dynamic LE simulator predicts well the average behaviour but requires improvements for predicting the maximum temperature since the process changes considerably during the first hour. For radiation disturbances, the LE simulator operates quite well: the temperature is on an appropriate range all the time and the timing of the changes is very good. For handling special situations, additional fuzzy models have been developed on the basis of the Fuzzy–ROSA method. For the period after radiation disturbances, the combined model improves the result considerably. [9].

The membership definition of the outlet temperature does not depend on time; the bias term $a_4 = 0$. Model coefficients and the scaling functions for T_{diff} , I_{eff} and F are all model specific. The total

number of parameters is 60 for variables, 12 model coefficients, and 12 for time delays.

Distributed parameter models

In distributed parameter models, the collector field is divided into modules, where the dynamic LE models are applied in a distributed way [11]. Element locations are defined by the flow rate. In cloudy conditions, the heating effect can be strongly uneven. These effects are simulated by introducing irradiation disturbances. Uneven distributions of the oil flow are important if the oil flow changes are rapid since some loops may be unable to follow.

The distributed parameter model is aimed for control design. It extends the operability of the simulator to evaluating the controller performance for drastic changes, e.g. start-up and large load disturbances, and local disturbances and malfunctioning. This extension is important for controlling the maximum temperature of the collector field as the previous models were capable only for the simulation of the average temperature.

LE MODELS IN CONTROL DESIGN

Trial and error type controller tuning does not work since the operating conditions cannot be reproduced or planned in detail because of changing weather conditions. As the process must be controlled all the time, modelling is based on process data from controlled process.

The solar collector field i controlled by varying the flow of oil pumped through the pipes during the plant operation. Feedback linguistic equation (LE) controllers use error $e_i(k)$ and derivative of the error $\Delta e_i(k)$ to obtain the change of control $\Delta u_i(k)$. The nonlinear scaling described above is used for these variables as well. Oscillations are considerably reduced by modifying the operation of the controller by adaptive scaling of the manipulating variable. The adaptive part contains additional braking and asymmetrical actions. The predefined adaption is not enough in fast changes of operating conditions. Too high temperatures are avoided by additional smart actions. Cascade control is used in the start-up to facilitate fast temperature increase without oscillatory behaviour. Similar reduction of the set point is activated for load disturbances. In cloudy conditions the cascade control reduces considerably the overshoot after clouds. [13, 23]

The simulation system consisting of the working point model and the dynamic models has been tuned by using data from several test campaigns. This model has then used for tuning the LE control system in different operating conditions. The distributed parameter models and the fuzzy models have been used for testing the controller. The fuzzy LE model is aimed for supporting decisions on proper working point.

Harmful operating conditions are avoided. Fast start-up and efficient energy collection in variable operating condition extend considerably the operating time of the collector field.

According to the test results the solar collector field operates well also in less favourable conditions if the multilevel LE controller is used. Start-up is very fast in good weather conditions, and the increase of irradiation is utilised efficiently. Short irradiation disturbances do not have any effect on the outlet temperature. Fast start-up and recovery from the load disturbances are clear benefits resulting from the predefined adaptation and the cascade control. In good weather conditions, the thermal power around $1 MW_t$, and the efficiency is around 0.5 for most of the time. The start-up period has lower efficiencies, and higher efficiencies are achieved when the field is in the high operation limit.

On a cloudy day, the operation time is shorter, but quite high temperatures are achieved. Start-up is very fast and fairly good operating conditions can be kept for whole day in spite of drastic changes in irradiation. The multilevel LE controller is necessary in these cases: all the special features described above are used. In cloudy conditions, irradiation is fluctuating and there are periods of very low irradiation. Naturally, the efficiency decreases, but even short sunny spells are utilised quite well. The thermal power almost reaches 1 MW_t , and the efficiency is almost 0.5 for long periods, even for low irradiation. The temperature difference is usually kept rather low for safety reasons. Although the efficiencies are almost on the same level as in good weather conditions, the total collected thermal energy reduces, since there is less solar energy available. In many cases, this energy can be collected only with the aid of the advanced LE controller tuned with the full multilevel LE simulator.

CONCLUSION

Dynamic linguistic equation models, which provide a smooth and accurate overall behaviour, has been successfully used in control design. The system can be further extended by specialized fuzzy models, distributed parameter models, and uncertainty processing with fuzzy interval analysis. The whole LE system, which is efficiently parameterised, can be tuned with genetic algorithms without using penalty functions.

REFERENCES

- [1] E. Camacho, M. Berenguel, and F. R. Rubio. *Adaptive Control of Solar Plants*. Springer, London, 1997.
- [2] E. K. Juuso. Fuzzy control in process industry: The linguistic equation approach. In H. B. Verbruggen, H.-J. Zimmermann, and R. Babuska, editors, *Fuzzy Algorithms for Control, International Series in Intelligent Technologies*, pages 243–300. Kluwer, Boston, 1999.
- [3] E.F Camacho, F.R. Rubio, and F.M. Hughes. Self-tuning control of a solar power plant with a distributed collector field. *IEEE System Control Magazine*, (April):72–78, 1992.
- [4] L. Valenzuela and P. Balsa. Series and parallel feedforward control schemes to regulate the operation of a solar collector field. In *Proceedings of the 2nd User Workshop Training and Mobility of Researchers Programme at Plataforma Solar de Almeria*, pages 19–24. Ciemat, 1998.
- [5] I. Farkas and I. Vajk. Internal modelbased controller for a solar plant. In CD-ROM Preprints of the 15th Triennial World Congress, 6 pp. IFAC, 2002.
- [6] L. J. Yebra, M. Berenguel, J. Bonilla, L. Roca, S. Dormido, and E. Zarza. Object oriented modelling and simulation of Acurex solar thermal power plant. In 6th Vienna Conference on Mathematical Modelling - MATHMOD 2009, Argesim Report no. 35, pages 2025–2033. Argesim, 2009.
- [7] E. K. Juuso. Integration of intelligent systems in development of smart adaptive systems. *In*-

- ternational Journal of Approximate Reasoning, 35:307–337, 2004.
- [8] E. K. Juuso, P. Balsa, and K. Leiviskä. Linguistic Equation Controller Applied to a Solar Collectors Field. In *Proceedings of the European Control Conference -ECC'97*, *Brussels*, volume Volume 5, TH-E I4, paper 267 (CD-ROM), 6 pp. 1997.
- [9] E. K. Juuso, D. Schauten, T. Slawinski, and H. Kiendl. Combination of linguistic equations and the fuzzy-rosa method in dynamic simulation of a solar collector field. In *Proceedings of TOOLMET 2000 Symposium Tool Environments and Development Methods for Intelligent Systems*, pages 63–77, Oulu, 2000. Oulun yliopistopaino.
- [10] E. K. Juuso. Intelligent dynamic simulation of a solar collector field. In *Simulation in Industry, 15th European Simulation Symposium ESS* 2003, pages 443–449. SCS, Gruner Druck, Erlangen, Germany, 2003.
- [11] E. K. Juuso. Dynamic simulation of a solar collector field with intelligent distributed parameter models. In *Proceedings of SIMS 2004 the 45th Scandinavian Conference on Simulation and Modelling*, pages 141–153. DTU, Lungby, Denmark, 2004.
- [12] E. K. Juuso and L. Valenzuela. Adaptive intelligent control of a solar collector field. In *Proceedings of Eunite 2003 European Symposium on Intelligent Technologies, Hybrid Systems and their implementation on Smart Adaptive Systems*, pages 26–35. Wissenschaftsverlag Mainz, Aachen, 2003.
- [13] E. K. Juuso. Modelling and control of a solar thermal power plant. In *Preprints of 16th IFAC World Congress*. IFAC, 2005. Th-A16-TO/5, 6 pp.
- [14] E. K. Juuso. Modelling and simulation in development and tuning of intelligent controllers. In *Proceedings of 5th Vienna Symposium on Mathematical Modelling, Argesim Report 30*, pages 6–1 10. Argesin Verlag, Vienna, 2006.
- [15] E. K. Juuso. Tuning of large-scale linguistic equation (le) models with genetic algorithms.

- In Proceedings of the International Conference on Adaptive and Natural Computing Algorithms ICANNGA 2009, Lecture Notes in Computer Science, volume LNCS 5495, pages 161–170. Springer-Verlag, Heidelberg, 2009.
- [16] E. K. Juuso, P. Balsa, and L. Valenzuela. Multilevel linguistic equation controller applied to a 1 mw solar power plant. In *Proceedings of the ACC* '98, volume 6, pages 3891–3895. ACC, 1998.
- [17] J. J. Buckley and T. Feuring. Universal approximators for fuzzy functions. *Fuzzy Sets and Systems*, 113:411–415, 2000.
- [18] J. J. Buckley and Y. Hayashi. Can neural nets be universal approximators for fuzzy functions? *Fuzzy Sets and Systems*, 101:323–330, 1999.
- [19] E. K. Juuso. Forecasting batch cooking results with intelligent dynamic simulation. In *Proceedings of the 6th EUROSIM Congress on Modelling and Simulation*, volume 2, 8 pp. University of Ljubljana, Ljubljana, Slovenia, 2007.
- [20] E. K. Juuso. Intelligent modelling of a fluidised bed granulator used in production of pharmaceuticals. In Conference Proceedings of SIMS 2007 The 48th Scandinavian Conference on Simulation and Modeling, Göteborg (Särö), pages 101–108. Linköping University Electronic Press, Linköping, Sweden, 2007.
- [21] E. K. Juuso. Intelligent dynamic simulation of a fed-batch enzyme fermentation process. In Tenth International Conference on Computer Modelling and Simulation, EUROSIM/UKSim, pages 301–306. The Institute of Electrical and Electronics Engineers IEEE, 2008.
- [22] R. E. Moore. Interval Analysis. Prentice Hall, Englewood Cliffs, NJ, 1966.
- [23] E. K. Juuso. Intelligent control of solar collector fields in changing operating conditions. In Preprints of the IFAC Symposium on PP & PS Power Plants and Power System Control, 6 pp. IFAC, 2009.

ENHANCED INTEGRITY AND PRODUCTION OF THE KOC PIPELINE NETWORK OPERATION THROUGH DYNAMIC SIMULATION

Tiina M. Komulainen¹ (Ph.D., Senior process engineer) Kongsberg Oil&Gas Technologies

> Farrukh Waheed (Process Specialist) Kuwait Oil Company

Ray J. Davies (Head of Section) and Tony D. Alfano (M.Sc., Project Engineer) Asset Risk Management, Det Norske Veritas

ABSTRACT

Over the next few years production through the Kuwait Oil Company (KOC) pipeline network will be increased significantly. This means that the capacity and the integrity of the pipeline network have to be ensured. In order to do this, dynamic simulation models were built and case studies of various transient and maximum production cases were conducted.

The model scope included a vast underground network of pipelines, transporting five different hydrocarbon fluids, with a total length exceeding 3200 km. The models were implemented using a D-SPICE simulation environment. Physical pipeline data was used to parameterize the models and operational data was used to run the models to steady state. Relevant simulation scenarios, including transients, such as pump trips, shutdowns, valve closures and leakages and maximum production cases, were defined.

Based on the results from simulation case runs, the pipelines with integrity issues and pipeline network bottlenecks were identified. Actions to ensure that all the pipelines remain under maximum pressure and erosion velocity limits as well as actions solving the pipeline network bottlenecks were tested. Benefits of the simulation are illustrated with case examples of both integrity and operational issues.

It is shown that dynamic simulation is a powerful tool for planning of production changes. Through dynamic simulations, the actions required to meet the planned production targets, without sacrificing pipeline network integrity, can easily be tested and evaluated. The dynamic simulation models provide a further basis for enhancement of the pipeline integrity using a leak detection system.

Keywords: Dynamic simulation, pipeline integrity, oil and gas pipeline network, debottlenecking, industrial application

NOMENCLATURE & ABBREVIATIONS		IONS	BS	Booster Station	
				CMM	Central Mixing Manifold
0	ampirical cons	tont []he	$\frac{1}{2} / ft \cdot s^2$	DNV	Det Norske Veritas
	c empirical constant $[\sqrt{lbs/ft \cdot s^2}]$		$f f i \cdot s$	D-SPICE	Kongsberg's simulation software
Pm	•	[lbs/ft ³]		GC	Gathering Center
MAOP		allowed	operating	HP	High Pressure
		[psig]		KOC	Kuwait Oil Company
MAEV		allowed	erosional	LP	Low Pressure
	velocity	[ft/s]		NTF	North Tank Farm

Corresponding author: Phone: +47 6780 4805, Fax: +47 6780 4830 E-mail: tiina.komulainen@kongsberg.com.

349

INTRODUCTION

Kuwait oil company (KOC) owns and operates a vast network of hydrocarbon pipelines in the State of Kuwait. The network consists of underground pipelines with varying sizes, from 3-inch to 52inch diameter, and the total length exceeds 3200 km. These pipelines, transferring crude oil, condensate, water, high pressure rich gas, low pressure rich gas and fuel gas, connect different Gathering Centers (GCs) and Booster Stations (BSs) through distribution manifolds to tank farms, refineries, consumers and export facilities. Due to the increasing global oil production demand, KOC is heavily expanding production. This means that ensuring sufficient transfer capacity, safety and integrity of the pipeline networks is of crucial importance. Monitoring of the fluid conditions in the pipelines is a challenge due to the limited number of measurements in the installed systems.

In continuation of KOC's advanced efforts in the area of risk management, KOC intended to conduct an integrated risk assessment and simulation studies of their entire pipeline network. Det Norske Veritas (DNV) was awarded the contract and completed the risk assessment part of the project that consisted of data gathering, hazard identification, quantitative risk assessment and cost benefit analysis [1]. Kongsberg Oil and Gas Technologies completed the simulation study part of the project. This consisted of data gathering, dynamic modelling and simulation studies of the KOC pipeline network, and holding a simulator training course for the KOC personnel.

The overall objective of the simulation part of the project was to define the sensitivity of the KOC pipeline networks to sudden transients, such as pump trips, shutdowns, valve closures and leakages in the KOC pipeline networks. A further objective of this study was to identify areas of KOC's pipeline networks that need debottlenecking and to determine if future production demands can be met.

METHODS

Applied methodology

The following approach was used to enhance the operation of KOC pipeline networks by simulation, as presented in Figure 1. The modelling and simulation studies were conducted using Kongsberg's proprietary dynamic simulation software D-SPICE.

The current and design operational conditions of the pipeline networks were used for the model implementation. A total of 44 simulation cases, including realistic worst case dynamic transients (such as pump trips, manifold closures and leaks) and maximum production / bottleneck steady state scenarios, were defined in co-operation with KOC and DNV. The consequences of the simulation events were studied and capacity and integrity issues were identified. The capacity issues included identification of the bottlenecks and calculation of the maximum throughputs of the pipeline networks. Pipeline integrity was analyzed by considering the maximum allowed erosion velocity and maximum allowed operating pressure limits. For each capacity and integrity issue remedies that did not sacrifice production goals were to be found through simulation. Based on these recommendations, safe production through KOC pipelines was ensured.

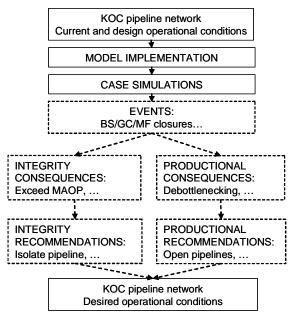


Figure 1: Illustration of the applied methodology.

Description of relevant D-SPICE modules

The dynamic simulation models were implemented with D-SPICE using standard D-SPICE modules [2].

The pipeline module DPipe solves fundamental equations for mass, momentum and energy transfer along the pipeline axis. It is thus a one dimensional model. The construction and layout of the pipeline (i.e. varying diameter, thickness, elevation) is accounted for in the flow calculation as well as the fluid composition in the thermodynamic calculations. DPipe calculates single phase fluid flow (liquid or gas), and thus any multiphase flow through pipe is calculated based on average properties. Local physical properties are calculated from pressure and temperature for each time step. The governing equations are solved by means of a finite difference technique using SIMPLE algorithm by Patankar and Spalding.

The *Valve module* uses standard Masoneilan flow correlations with due regard taken for flowing medium conditions (gas, liquid, two-phase). Parameters such as design C_v, valve characteristic, opening/closing time are included.

The *pressure node module* represents the volume of a manifold and calculates component and energy balances (gas, liquid, two-phase).

All the necessary modules are implemented and combined into a *pressure-flow network*, where each module calculates either flow or pressure. Mathematically this network consists of nonlinear algebraic equations of flow pressure relations and mainly linear differential mass balance equations of node pressures. These equations are solved simultaneously using a multidimensional Newton-Raphson method that is based on the mass balance for each node.

Pipeline integrity criteria

The maximum allowed operating pressure (MAOP) was given for each pipeline in the pipeline specification. Maximum allowed operational pressure is determined based on the pipeline material, thickness and current condition. Exceeding MAOP might cause severe damage to the pipeline, thereby creating a safety hazard.

The maximum allowed erosional velocity (MAEV) in feet/second was calculated as follows:

$$MAEV = \frac{c}{\sqrt{pm}} \tag{1}$$

Where pm in [lbs/ft³] is the fluid density at flowing pressure and temperature, and c is an empirical constant with a value less than 100 for continuous service of fluids with solid particles, as described in [3]. Exceeding the maximum allowed erosional velocity will increase the corrosion of the pipeline, and thus in time might cause leaks and other safety hazards.

KOC PIPELINE NETWORK MODELS

Scope of the models

The simulation model scope included eight separate pipeline networks: Crude oil South-East (SEK), Crude oil West (WK), Crude oil North (NK), Crude oil Export, HP rich gas, LP rich gas, HP fuel gas and Condensate. The pipeline network topology included simplified inlets to the pipeline network (sending station), the pipeline network with pipelines, valves and manifolds, and simplified outlets from the pipeline network (receiving stations). Pressures, flow rates and velocities in the pipelines and manifolds were the main monitored variables.

Data

Physical pipeline data was collected from KOC's advanced Total Pipeline Integrity Management System (TPIMS), which included various physical properties of each pipeline. The essential data for the simulation models consisted of lengths, thicknesses, diameters and elevation profiles.

A heat and material balance table was constructed from fluid and operational data provided by KOC. The operational data included the current flow rates, pressures and temperatures for the inlet streams to the pipeline network (sending stations) and the backpressure at the outlet streams of the pipeline network (receiving stations). The fluid composition and other properties for each inlet stream were based on laboratory analyses.

Model implementation

The pipeline network models were implemented in the D-SPICE simulation environment by connecting D-SPICE process modules (pipelines, nodes, valves) according to the pipeline network layout plans and by configuring the parameters of each module according to the KOC data, see subnetworks in Appendix A and B.

An inlet was configured as a mass flow source with specific temperature, pressure and composition combined with a flow rate controller. The flow rate and fluid properties were set according to the heat and material balance table. In the liquid networks, parts of the inlet process equipment, such as a pump, were included in order to make the case simulations more realistic. An outlet was configured as a valve with constant backpressure, as defined by the heat and material balance table.

A pipeline was configured by applying the pipeline physical data. The following assumptions were made for all the pipelines: ambient temperature is assumed to be constant 35°C, Young's Modulus 2.03 GPa, total heat transfer coefficient 10 W/m² K, roughness 0.046 mm, and the Colebrook friction calculation method was used.

The nodes representing manifolds were parameterized by setting volumes and elevations. The valves were parameterized assuming the pipeline size with standard ball valve/ control valve parameters.

Table 1: Number of the main model components in each pipeline network model.

Pipeline	Inlets	Outlets	Pipe	Mani
			lines	folds
Crude oil	14	12	50	17
SEK				
Crude oil	6	4	12	3
WK				
Crude oil	3	3	13	4
NK				
Crude oil	16	18	60+	17
Export				
HP rich gas	21	7	68	21
LP rich gas	20	5	39	14
HP fuel gas	2	41	70	37
Condensate	19	5	60	25

A total of eight different pipeline network models were implemented. The descriptions of the implemented models are given here as the number of inlets, outlets, pipelines/ sub-pipelines, and manifolds, listed in Table 1. The models were run to a steady state that reflected the normal operating conditions of the pipeline networks.

RESULTS AND DISCUSSION

Enhance integrity

The maximum pressure and velocity in each pipeline was evaluated in each study case. Correcting actions to ensure integrity of the pipeline, such as isolation of a pipeline, a flow rate limitation, change of pipeline configuration in manifolds or addition of a parallel pipeline, were tested with the simulator, and recommendations were given.

In dynamic transient situations with current production targets, MAEV limits were not exceeded, but other integrity issues such as overpressurization of pipelines, liquid hammer and vacuum occurred.

Liquid hammer was obtained during fast valve closures. The recommended action was to increase the valve closure time and possibly open other pipelines, as presented in Example 2.

Typically a vacuum situation occurred when a pump tripped at the inlet of a liquid pipeline with decreasing elevation profile. The remedy for this is to increase pressure at the pipeline outlet or to close the pipeline outlet before stopping the pump. In the dynamic leak study cases the effects of leaks in liquid and gas pipeline networks were evaluated. The leaks were detected as sudden pressure drops in the nearby manifolds, see Example 1. Thus, the simulation models would provide a basis for a leak detection system if additional measurements were installed.

The design production cases led to exceeding the integrity limits in pipelines with low MAOP limits or pipelines with small diameter and high flow rate. Remedies to avoid excessive pressures are isolation of a pipeline with low MAOP limit, opening of other pipelines or building parallel pipelines, and decreasing of pump discharge pressure. In order to avoid overpressurizing pipelines with low MAOP limits, the pressure

alarm High-High limit should be set lower at the upstream gathering center. In all solutions, the effect of the remedies on the production rates at each gathering center was studied to avoid a loss of production. Refer to Example 3.

Exceeding MAEV limit can be avoided by opening parallel pipelines or decreasing flow rate from pipeline inlet (Gathering center), see Example 4.

Example 1: Leak detection in gas pipeline network

The possibilitites of detecting a 25% gas leak on a LP rich gas pipeline were studied. The LP rich gas pipeline consists of 14 inlets (GC) two main outlets (BS) and 32 pipelines. The pipeline studied is located between two main manifolds, close to the two receiving stations and a residential area.

The initial conditions were as per current operating conditions. The leak was simulated by opening a valve representing a 4 inch hole in a 36 inch LP rich gas pipeline. Pressure trends along the pipeline are shown in Figure 2. Pressure in the nearby manifolds decreases by around 0.3 psig, and total LP gas flow rate to the receiving stations decreases by 0.38 MSm³/d. Leak volume after one hour was 15384 Sm³.

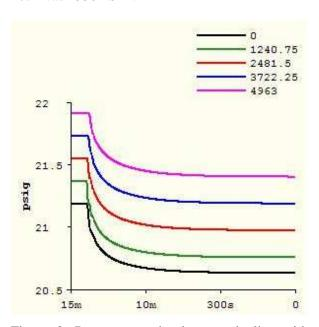


Figure 2: Pressure trends along a pipeline with 25% leak, pipeline in LP rich gas network.

Example2: Avoid overpressurization and liquid hammer

The possibility to avoid liquid hammer on closure of a main crude oil pipeline was studied.

North Kuwait Crude oil pipeline network includes three inlets (GC), and four main transit pipelines (CRN111, CRN112, CRN121, CRN122) to the four outlets at CMM, NTF and PS1. The pipeline network is shown in Figure 3. The initial conditions were as per current operating conditions with isolated pipelines CRN111 and CRN112.

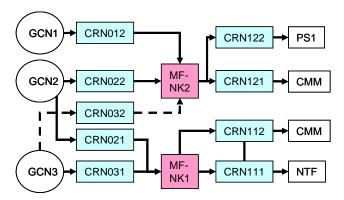


Figure 3: Simplified presentation of crude oil North Kuwait pipeline network.

Remedies for avoiding liquid hammer with valve closure at the outlet of pipeline CRN121 were studied. The initial valve closing time was 54 This caused liquid hammer and overpressurization of the pipeline, due to higher PAHH limits at GCs than the MAOP limits at the pipelines. The MAOP limit was exceeded in CRN121 (850 psig) and in CRN122 (530 psig). The flow rate and pressure trends for pipeline CRN121 are presented in Figure 4 and Figure 5. Increasing the valve opening time from 54 seconds to 10 minutes did not remove the liquid hammer and overpressurization, but opening of the two other pipelines was necessary. Also the closure time had to be increased to 30 minutes. The flow rate and pressure trends for pipeline CRN121 are presented in Figure 6 and Figure 7. It was recommended to revise pump PAHH limits in gathering centers GC_N1, GC_N2 and GC_N3.

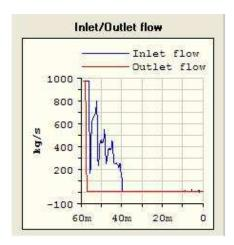


Figure 4: Flow rate at the inlet and outlet of pipeline CRN121.

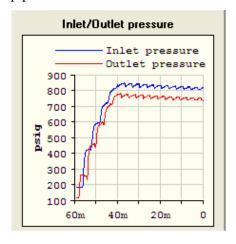


Figure 5: Pressure at the inlet and outlet of pipeline CRN121.

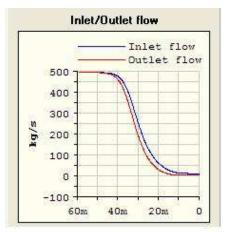


Figure 6: Flow rate at the inlet and outlet of pipeline CRN121 after implemented remedies.

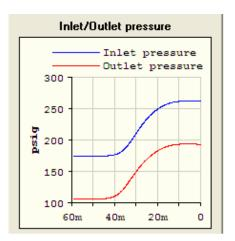


Figure 7: Pressure at the inlet and outlet of pipeline CRN121 after implemented remedies.

Example 3: Avoid exceeding MAOP limit

The aim of this sub-study was to find remedies to avoid exceeding MAOP limit while increasing flow rates from nominal to design.

The analyzed sub-part of South East Kuwait crude oil pipeline network is illustrated in Figure 8. This sub-network consists of inlets GC_S1 and GC_S2, five pipelines, and four manifolds. In addition, crude oil from GC_S2 can be routed through pipeline CR02A to MF-T22. There are no check valves, other gathering centers and manifolds are connected to the system through manifolds MF-T11 and MF-T22.

The initial condition is as per the design flow rate, where the outlets of CR0TT to MF-T11 and MF-T02 are closed and only the outlet to MF-T01 is open.

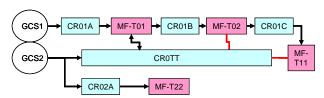


Figure 8: Subpart of South East Kuwait crude oil pipeline network.

For the design flow rate case, the MAOP limit of 230 psig was exceeded in pipeline CR0TT, as shown in Figure 9.

The mitigating measure was to change the manifold configuration at some of the manifolds, while ensuring design production from the other gathering centers in the area. The successful remedy was to open the valve only to MF-T11. When this was done, the nearby GCs continued delivering design flow rates and the maximum pressure of pipeline CR0TT remained under MAOP limit.

If changing of the manifold configuration is not possible, it is recommended that the pipeline is isolated. In this case, this option is feasible: crude oil can be transferred through pipeline CR02A without violating the design flow rate targets at other parts of the crude oil South East Kuwait network.

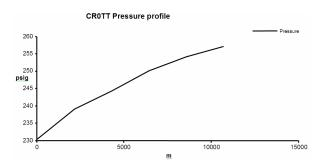


Figure 9: Pressure profile of pipeline CR0TT with design flow rates.

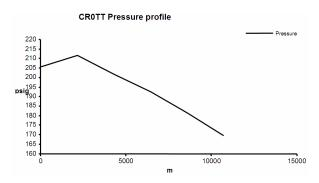


Figure 10: Pressure profile of pipeline CR0TT with design flow rates, open outlet to MF-T11.

Example 4: Avoid exceeding MAEV limit

The aim of this sub-study was to find ways to avoid exceeding MAEV limit while increasing flow rates from nominal to design.

A sub-part of South East Kuwait crude oil pipeline network is shown in Figure 11. This sub-network consists of the inlets GCS2 and GCS3, pipelines CR003A, CR0AA, CR0BB and CR02A, and the manifolds MF-1 and MF-T22.

The maximum allowed velocity limit (4.02 m/s) is exceeded in pipeline CR015 (4.73 m/s) when production from GCS3 is increased to the design production target 160 000 BPD.

If only one pipeline from the gathering center to manifold MF-1 is available, the production target has to be decreased under 141000 BPD in order to remain below the MAEV limit. Decreasing flow rate in GCS3 does not affect design flow rates in other parts of the system.

In order to reach the production target in GCS3 without violating pipeline integrity, it is recommended to add parallel pipelines, CR0AA and CR0BB, which route flow from GCS3 through MF-T22 to MF-1.

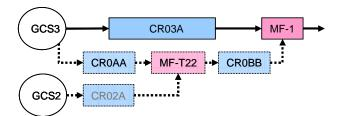


Figure 11: Subpart of South East Kuwait crude oil pipeline network.

Enhance production

Achievement of production targets were verified in each study case. Pipelines and manifolds that limit transmission at the required production rates were identified. Mitigating measures that increase flow rate through these bottlenecks were designed and tested with the simulator. Recommendations on opening pipelines or addition of parallel pipelines, changes in the manifold configuration and possibly changes in the sending/receiving stations, were given. Examples of debottlenecking are presented for gas pipeline networks in Example 5 and for liquid pipeline networks in Example 6.

Example 5: De-bottlenecking in gas pipeline networks

The aim of this sub-study was to find out how to meet all design flow rate targets in the fuel gas network without addition of pipelines.

The main fuel gas pipeline network consists of one inlet (LPG), over 60 pipelines, around 40 manifolds and over 40 receiving stations like

power stations and gathering centers. A simplified illustration of the power station (PS) connections to the fuel gas pipeline network is given in Figure 12. The aim was to find if the design flow rates could be delivered to the power stations with a backpressure of 304 psig. It was found that back pressure in the vicinity of power station PS2 should be decreased to 250 psig, whereas the power stations that are further away (PS1, PS4, PS5) require backpressures as low as 175 psig to receive the design flow rates.

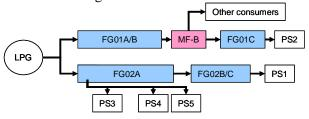


Figure 12: Simplification of fuel gas pipeline network.

Example 6: Debottlenecking of liquid pipeline networks

The aim of this sub-study was to debottleneck crude oil transit through manifold MF-2 at design flow rates.

The sub-network of South East Kuwait crude oil pipeline network is illustrated in Figure 13. This sub-network includes the gathering centers GCE1, GCE2 and GCE3. These produce exclusively to the main manifold MF-2. The only open transit pipeline from the manifold is CRT04. In the current manifold configuration, transit pipelines CRT01, CRT02 and CRT03 bypass manifold MF-2 and the transit pipeline CRT05 is isolated.

The initial requirement is a design flow rate of 1.6 MBPD, which at the current manifold configuration cannot be met in GCE01 (0.8 MBPD) and GCE3 (1.2 MBPD).

A feasible solution to achieve the production targets is to open at least one of the transit pipelines from MF-2 together with transit pipeline CRT05 from MF-1. This transit pipeline will transfer part of the crude oil production from the three gathering centers feeding to MF-1.

CONCLUSIONS

To meet increasing oil and gas production demands, transfer capacity and integrity of the KOC pipeline network have to be ensured. Up-todate dynamic simulation models of the KOC networks, implemented using pipeline simulation D-SPICE environment. provide reliable methods to plan the production changes and to test effects of planned shutdowns. Ways to avoid possible integrity issues and production losses can be evaluated quickly and easily through simulation. The dynamic simulation models provide a further basis for the future enhancement of the pipeline integrity using a leak detection system.

ACKNOWLEDGEMENTS

The authors would like to thank the Management of Kuwait Oil Company for permission to publish this paper and acknowledge the support of the "Subject Matter Experts" who contributed to the success of the project.

REFERENCES

- [1] Davies, R.J., Alfano, T.D., Waheed, F., Komulainen, T.M., A root cause analysis approach to risk assessment of a pipeline network for Kuwait Oil Company, In: Proceedings of Rio Pipeline 2009 Conference & Exposition, Rio De Janeiro, 2009.
- [2] Information about Kongsberg and D-SPICE http://www.km.kongsberg.com/processsimulation [3] API RP 14E: Recommended Practice for Design and Installation of Offshore Production Platform Piping Systems, American Petroleum Institute, 1991, p. 23.

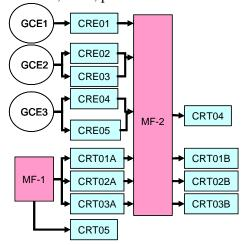


Figure 13: A subnetwork of South East Kuwait Crude oil pipeline network.

Author Index

Abboudi, Said, 87	Farrokh, Mohammad, 173
Agap, Adelina, 115	Fayad, Sahar, 87
Alfano, Tony, 349	Feddersen, Henrik, 151
Alic, Mirnes, 157	Finn Sloth Larsen, Lars, 315
Alne, Sveinung, 3	Fritzson, Peter, 21
Andersen, Peter B., 107	, ,
Avelin, Anders, 125	Glende, Erik, 3
, , , , , , , , , , , , , , , , , , , ,	Green, Torben, 71
Bahl, Christian, 323	Gudmundsson, Oddgeir, 165
Bakke, Rune, 221	_
Bang-Møller, Christian, 189	Halvorsen, Britt M., 285
Barahona, Braulio, 97, 107	Hansen Sass, Bent, 151
Bjørk, Rasmus, 323	Hansen, Anca D., 97, 107
Bleaja, Gheorghe, 211	Hattel, Jesper, 323
Bones, John Atle, 333	Hauge, Tor Anders, 157
Botheju, Deshai, 221	Heikkinen, Mikko, 237
Braun, Robert, 229	Hiltunen, Teri, 237
Breyholtz, Øyvind, 299	Hiltunen, Yrjö, 237
Brix, Wiebke, 79	Houbak, Niels, 229
Bruno, Joan Carles, 259, 267	Hälikkä, Eero, 237
Cameron, David, 3	Iov, Florin, 115
Cameron, David, 3 Chassin, David, 131	Iov, Florin, 115 Izadi-Zamanabadi, Roozbeh, 71
Chassin, David, 131	Iov, Florin, 115 Izadi-Zamanabadi, Roozbeh, 71
Chassin, David, 131 Chen, Liang, 71	
Chassin, David, 131 Chen, Liang, 71 Chen, Min, 247	Izadi-Zamanabadi, Roozbeh, 71
Chassin, David, 131 Chen, Liang, 71 Chen, Min, 247 Chiriac, Radu, 211	Izadi-Zamanabadi, Roozbeh, 71 Jayarathna, Chameera K., 285 Jayarathna, Sanoja A., 13
Chassin, David, 131 Chen, Liang, 71 Chen, Min, 247 Chiriac, Radu, 211 Christensen, Torkild, 143	Izadi-Zamanabadi, Roozbeh, 71 Jayarathna, Chameera K., 285
Chassin, David, 131 Chen, Liang, 71 Chen, Min, 247 Chiriac, Radu, 211 Christensen, Torkild, 143 Ciobanu, Cristina, 211	Izadi-Zamanabadi, Roozbeh, 71 Jayarathna, Chameera K., 285 Jayarathna, Sanoja A., 13
Chassin, David, 131 Chen, Liang, 71 Chen, Min, 247 Chiriac, Radu, 211 Christensen, Torkild, 143 Ciobanu, Cristina, 211 Clausen, Lasse, 229	Izadi-Zamanabadi, Roozbeh, 71 Jayarathna, Chameera K., 285 Jayarathna, Sanoja A., 13 Juuso, Esko, 341
Chassin, David, 131 Chen, Liang, 71 Chen, Min, 247 Chiriac, Radu, 211 Christensen, Torkild, 143 Ciobanu, Cristina, 211 Clausen, Lasse, 229 Constantin, Adrian, 115	Izadi-Zamanabadi, Roozbeh, 71 Jayarathna, Chameera K., 285 Jayarathna, Sanoja A., 13 Juuso, Esko, 341 Komperød, Magnus, 333
Chassin, David, 131 Chen, Liang, 71 Chen, Min, 247 Chiriac, Radu, 211 Christensen, Torkild, 143 Ciobanu, Cristina, 211 Clausen, Lasse, 229 Constantin, Adrian, 115 Coronas, Alberto, 259, 267	Izadi-Zamanabadi, Roozbeh, 71 Jayarathna, Chameera K., 285 Jayarathna, Sanoja A., 13 Juuso, Esko, 341 Komperød, Magnus, 333 Komulainen, Tiina, 349
Chassin, David, 131 Chen, Liang, 71 Chen, Min, 247 Chiriac, Radu, 211 Christensen, Torkild, 143 Ciobanu, Cristina, 211 Clausen, Lasse, 229 Constantin, Adrian, 115	Izadi-Zamanabadi, Roozbeh, 71 Jayarathna, Chameera K., 285 Jayarathna, Sanoja A., 13 Juuso, Esko, 341 Komperød, Magnus, 333 Komulainen, Tiina, 349
Chassin, David, 131 Chen, Liang, 71 Chen, Min, 247 Chiriac, Radu, 211 Christensen, Torkild, 143 Ciobanu, Cristina, 211 Clausen, Lasse, 229 Constantin, Adrian, 115 Coronas, Alberto, 259, 267	Izadi-Zamanabadi, Roozbeh, 71 Jayarathna, Chameera K., 285 Jayarathna, Sanoja A., 13 Juuso, Esko, 341 Komperød, Magnus, 333 Komulainen, Tiina, 349 Kær, Søren Knudsen, 197
Chassin, David, 131 Chen, Liang, 71 Chen, Min, 247 Chiriac, Radu, 211 Christensen, Torkild, 143 Ciobanu, Cristina, 211 Clausen, Lasse, 229 Constantin, Adrian, 115 Coronas, Alberto, 259, 267 Cutululis, Nicolaos A., 97, 107	Izadi-Zamanabadi, Roozbeh, 71 Jayarathna, Chameera K., 285 Jayarathna, Sanoja A., 13 Juuso, Esko, 341 Komperød, Magnus, 333 Komulainen, Tiina, 349 Kær, Søren Knudsen, 197 Larsen, Lars F. S., 71
Chassin, David, 131 Chen, Liang, 71 Chen, Min, 247 Chiriac, Radu, 211 Christensen, Torkild, 143 Ciobanu, Cristina, 211 Clausen, Lasse, 229 Constantin, Adrian, 115 Coronas, Alberto, 259, 267 Cutululis, Nicolaos A., 97, 107 Dahlquist, Erik, 53, 125	Izadi-Zamanabadi, Roozbeh, 71 Jayarathna, Chameera K., 285 Jayarathna, Sanoja A., 13 Juuso, Esko, 341 Komperød, Magnus, 333 Komulainen, Tiina, 349 Kær, Søren Knudsen, 197 Larsen, Lars F. S., 71 Lie, Bernt, 13, 157, 221, 333
Chassin, David, 131 Chen, Liang, 71 Chen, Min, 247 Chiriac, Radu, 211 Christensen, Torkild, 143 Ciobanu, Cristina, 211 Clausen, Lasse, 229 Constantin, Adrian, 115 Coronas, Alberto, 259, 267 Cutululis, Nicolaos A., 97, 107 Dahlquist, Erik, 53, 125 Darde, Victor, 29	Izadi-Zamanabadi, Roozbeh, 71 Jayarathna, Chameera K., 285 Jayarathna, Sanoja A., 13 Juuso, Esko, 341 Komperød, Magnus, 333 Komulainen, Tiina, 349 Kær, Søren Knudsen, 197 Larsen, Lars F. S., 71 Lie, Bernt, 13, 157, 221, 333 Liso, Vincenzo, 197
Chassin, David, 131 Chen, Liang, 71 Chen, Min, 247 Chiriac, Radu, 211 Christensen, Torkild, 143 Ciobanu, Cristina, 211 Clausen, Lasse, 229 Constantin, Adrian, 115 Coronas, Alberto, 259, 267 Cutululis, Nicolaos A., 97, 107 Dahlquist, Erik, 53, 125 Darde, Victor, 29 Davies, Ray, 349	Izadi-Zamanabadi, Roozbeh, 71 Jayarathna, Chameera K., 285 Jayarathna, Sanoja A., 13 Juuso, Esko, 341 Komperød, Magnus, 333 Komulainen, Tiina, 349 Kær, Søren Knudsen, 197 Larsen, Lars F. S., 71 Lie, Bernt, 13, 157, 221, 333 Liso, Vincenzo, 197 Liukkonen, Mika, 237 Lohne, Hans Petter, 37
Chassin, David, 131 Chen, Liang, 71 Chen, Min, 247 Chiriac, Radu, 211 Christensen, Torkild, 143 Ciobanu, Cristina, 211 Clausen, Lasse, 229 Constantin, Adrian, 115 Coronas, Alberto, 259, 267 Cutululis, Nicolaos A., 97, 107 Dahlquist, Erik, 53, 125 Darde, Victor, 29 Davies, Ray, 349 Didriksen, Helge, 143, 275 Dragan, Cristina, 115	Izadi-Zamanabadi, Roozbeh, 71 Jayarathna, Chameera K., 285 Jayarathna, Sanoja A., 13 Juuso, Esko, 341 Komperød, Magnus, 333 Komulainen, Tiina, 349 Kær, Søren Knudsen, 197 Larsen, Lars F. S., 71 Lie, Bernt, 13, 157, 221, 333 Liso, Vincenzo, 197 Liukkonen, Mika, 237 Lohne, Hans Petter, 37 Madsen, Søren, 63
Chassin, David, 131 Chen, Liang, 71 Chen, Min, 247 Chiriac, Radu, 211 Christensen, Torkild, 143 Ciobanu, Cristina, 211 Clausen, Lasse, 229 Constantin, Adrian, 115 Coronas, Alberto, 259, 267 Cutululis, Nicolaos A., 97, 107 Dahlquist, Erik, 53, 125 Darde, Victor, 29 Davies, Ray, 349 Didriksen, Helge, 143, 275 Dragan, Cristina, 115 Eguía, Pablo, 259	Izadi-Zamanabadi, Roozbeh, 71 Jayarathna, Chameera K., 285 Jayarathna, Sanoja A., 13 Juuso, Esko, 341 Komperød, Magnus, 333 Komulainen, Tiina, 349 Kær, Søren Knudsen, 197 Larsen, Lars F. S., 71 Lie, Bernt, 13, 157, 221, 333 Liso, Vincenzo, 197 Liukkonen, Mika, 237 Lohne, Hans Petter, 37 Madsen, Søren, 63 Mahmoudi, Jafar, 45, 173
Chassin, David, 131 Chen, Liang, 71 Chen, Min, 247 Chiriac, Radu, 211 Christensen, Torkild, 143 Ciobanu, Cristina, 211 Clausen, Lasse, 229 Constantin, Adrian, 115 Coronas, Alberto, 259, 267 Cutululis, Nicolaos A., 97, 107 Dahlquist, Erik, 53, 125 Darde, Victor, 29 Davies, Ray, 349 Didriksen, Helge, 143, 275 Dragan, Cristina, 115	Izadi-Zamanabadi, Roozbeh, 71 Jayarathna, Chameera K., 285 Jayarathna, Sanoja A., 13 Juuso, Esko, 341 Komperød, Magnus, 333 Komulainen, Tiina, 349 Kær, Søren Knudsen, 197 Larsen, Lars F. S., 71 Lie, Bernt, 13, 157, 221, 333 Liso, Vincenzo, 197 Liukkonen, Mika, 237 Lohne, Hans Petter, 37 Madsen, Søren, 63

Martínez, David, 259 Melaaen, Morten C., 13 Moya, Marta, 259 Nabati, Hamid, 45 Nielsen, Kaspar, 323 Nielsen, Mads Pagh, 197 Nygaard, Gerhard, 37, 299	Waheed, Farrukh, 349 Weberg, Trond, 3 Widarsson, Björn, 125 Willatzen, Morten, 63 Woetman Nielsen, Niels, 151 Xu, Jianhua, 131
Ortiga, Jordi, 267	Younes, Rafic, 87 Zamora, Inmaculada, 259
Pagh Nielsen, Kristian, 151 Palsson, Halldor, 165 Palsson, Olafur Petur, 165 Pedersen, Claus, 151 Perstrup, Claus, 275 Petcu, Cristian, 211 Petursson, Stefan, 291 Pop, Adrian, 21 Popa, Elena, 211 Poulsen, Kristian, 143 Pourian, Bijan, 53 Prisecaru, Malina, 211 Prisecaru, Tudor, 211 Pryds, Nini, 323	
Rokni, Masoud, 181, 189 Rosendahl, Lasse, 247 Runarsson, Thomas, 291 Ryhl Kærn, Martin, 315	
Sattler, Kai, 151 Scappin, Fabio, 181 Sigurdsson, Sven, 291 Sjölund, Martin, 21 Smith, Anders, 323 Stenby, Erling H., 29 Sørensen, Poul, 97, 107	
Teodorescu, Mihai, 211 Thomsen, Kaj, 29 Thorsteinsson, Jon Agust, 291 Time, Rune, 37 Time, Rune Wiggo, 45 Torabzadeh-Tari, Mohsen, 21 Torres, Esther, 259	
van Well, Willy J.M, 29 Vedel, Henrik, 151 Veje, Christian T., 63	